PHYSICAL CHEMISTRY AND CHEMICAL PHYSICS EDITOR'S PICK 2021

EDITED BY: Malgorzata Biczysko

PUBLISHED IN: Frontiers in Chemistry and Frontiers in Physics

frontiers Research Topics

ISSN 1664-8714
ISBN 978-2-88971-110-9
DOI 10.3389/978-2-88971-110-9

About Frontiers

Frontiers is more than just an open-access publisher of scholarly articles: it is a pioneering approach to the world of academia, radically improving the way scholarly research is managed. The grand vision of Frontiers is a world where all people have an equal opportunity to seek, share and generate knowledge. Frontiers provides immediate and permanent online open access to all its publications, but this alone is not enough to realize our grand goals.

Frontiers Journal Series

The Frontiers Journal Series is a multi-tier and interdisciplinary set of open-access, online journals, promising a paradigm shift from the current review, selection and dissemination processes in academic publishing. All Frontiers journals are driven by researchers for researchers; therefore, they constitute a service to the scholarly community. At the same time, the Frontiers Journal Series operates on a revolutionary invention, the tiered publishing system, initially addressing specific communities of scholars, and gradually climbing up to broader public understanding, thus serving the interests of the lay society, too.

Dedication to Quality

Each Frontiers article is a landmark of the highest quality, thanks to genuinely collaborative interactions between authors and review editors, who include some of the world's best academicians. Research must be certified by peers before entering a stream of knowledge that may eventually reach the public - and shape society; therefore, Frontiers only applies the most rigorous and unbiased reviews.
Frontiers revolutionizes research publishing by freely delivering the most outstanding research, evaluated with no bias from both the academic and social point of view. By applying the most advanced information technologies, Frontiers is catapulting scholarly publishing into a new generation.

What are Frontiers Research Topics?

Frontiers Research Topics are very popular trademarks of the Frontiers Journals Series: they are collections of at least ten articles, all centered on a particular subject. With their unique mix of varied contributions from Original Research to Review Articles, Frontiers Research Topics unify the most influential researchers, the latest key findings and historical advances in a hot research area! Find out more on how to host your own Frontiers Research Topic or contribute to one as an author by contacting the Frontiers Editorial Office: frontiersin.org/about/contact

PHYSICAL CHEMISTRY AND CHEMICAL PHYSICS EDITOR'S PICK 2021

Topic Editor:
Malgorzata Biczysko, Shanghai University, China

Citation: Biczysko, M., ed. (2021). Physical Chemistry and Chemical Physics Editor's Pick 2021. Lausanne: Frontiers Media SA. doi: 10.3389/978-2-88971-110-9

Table of Contents

frontiers in Chemistry

ORIGINAL RESEARCH
published: 19 March 2019
doi: 10.3389/fchem.2019.00122

Rational Design of Low-Band Gap Star-Shaped Molecules With 2,4,6-Triphenyl-1,3,5-triazine as Core and Diketopyrrolopyrrole Derivatives as Arms for Organic Solar Cells Applications

Xinhao Zhang [1,2] *and Ruifa Jin* [1,2]*

[1] *Inner Mongolia Key Laboratory of Photoelectric Functional Materials, Chifeng University, Chifeng, China,* [2] *College of Chemistry and Chemical Engineering, Chifeng University, Chifeng, China*

OPEN ACCESS

Edited by:
Doo Soo Chung,
Seoul National University, South Korea

Reviewed by:
Sungu Hwang,
Pusan National University, South Korea
Ahmad Irfan,
King Khalid University, Saudi Arabia

***Correspondence:**
Ruifa Jin
ruifajin@163.com

Specialty section:
This article was submitted to Physical Chemistry and Chemical Physics, a section of the journal Frontiers in Chemistry

Received: *04 December 2018*
Accepted: *15 February 2019*
Published: *19 March 2019*

Citation:
Zhang X and Jin R (2019) Rational Design of Low-Band Gap Star-Shaped Molecules With 2,4,6-Triphenyl-1,3,5-triazine as Core and Diketopyrrolopyrrole Derivatives as Arms for Organic Solar Cells Applications. Front. Chem. 7:122. doi: 10.3389/fchem.2019.00122

A series of D–A novel star-shaped molecules with 2,4,6-triphenyl-1,3,5-triazine (TPTA) as core, diketopyrrolo[3,4-c]pyrrole (DPP) derivatives as arms, and triphenylamine (TPA) derivatives as end groups have been systematically investigated for organic solar cells (OSCs) applications. The electronic, optical, and charge transport properties were studied using density functional theory (DFT) and time-dependent DFT (TD-DFT) approaches. The parameters such as energetic driving force ΔE_{L-L}, adiabatic ionization potential *AIP*, and adiabatic electron affinity *AEA* were also calculated at the same level. The calculated results show that the introduction of different groups to the side of DPP backbones in the star-shaped molecules can tune the frontier molecular orbitals (FMOs) energy of the designed molecules. The designed molecules can provide match well with those of typical acceptors PCBM ([6,6]-phenyl-C61-butyric acid methyl ester) and PC71BM ([6,6]-phenyl-C71-butyric acid methyl ester). Additionally, the absorption wavelengths of the designed molecules show bathochromic shifts compared with that of the original molecule, respectively. The introduction of different groups can extend the absorption spectrum toward longer wavelengths, which is beneficial to harvest more sunlight. The calculated reorganization energies suggest that the designed molecules are expected to be the promising candidates for ambipolar charge transport materials except molecule with benzo[c]isothiazole group can be used as hole and electron transport material. Moreover, the different substituent groups do not significantly affect the stability of the designed molecules.

Keywords: star-shaped molecules, diketopyrrolopyrrole derivatives, optical and electronic properties, frontier molecular orbitals (FMOs), organic solar cells (OSCs)

INTRODUCTION

Nowadays, organic π-conjugated small molecules (SMs) used as the donors in organic solar cells (OSCs) have drawn intense attention because of their outstanding advantages, such as excellent reproducibility, easy purification, well-defined chemical and optoelectronic properties (Coughlin et al., 2014; Yao et al., 2016; Bin et al., 2017). Owing to the tremendous efforts on improving the performance of OSCs based on SMs, their power conversion efficiency (PCE) has surpassed over 10% recently (Zhou et al., 2012; Kan et al., 2015). However, it is worth noting that their overall performance still falls behind that of their polymer counterparts (Ni et al., 2013; Lin and Zhan, 2016). Accordingly, to address this issue, it is a big challenge to design and synthesize high-performance and desirable donor novel SMs (Chaudhry et al., 2018; Irfan et al., 2018; Wazzan et al., 2018). In general, the high-efficiency SMs donor materials should possess suitable frontier molecular orbital (FMOs) (including the highest occupied molecular orbital, HOMO, and lowest unoccupied molecular orbital, LUMO) energy levels, high charge carrier mobility, broad absorption region, and miscibility with fullerene derivatives. In this regard, the HOMO level of the designed donor materials should been reduced to increase the open circuit voltage (V_{oc}), because the HOMO of donor and the LUMO of acceptor are closely relate to the V_{oc}. With the aim to harvest more sunlight, the energy gaps of the designed donor materials should been decreased, which results in an increase in the short circuit current density (J_{sc}) (Loser et al., 2017; Maglione et al., 2017; Zhang et al., 2017). Moreover, a key factor that impact on the efficient exciton splitting and charge dissociation is the downhill energetic driving force (ΔE_{L-L}), which is the energy differences between the LUMOs of the donor and acceptor. The ΔE_{L-L} value should be about 0.3 eV to ensure efficient charge transfer, exciton splitting, and charge dissociation (Scharber et al., 2006). Therefore, an ideal donor material should have narrowing the HOMO-LUMO gap (E_g) and suitable FMOs energy levels with PCBM ([6,6]-phenyl-C61-butyric acid methyl ester) and PC71BM ([6,6]-phenyl-C71 butyric acid methyl ester), which are widely employed as acceptors in OSCs (He et al., 2007; Lenes et al., 2008). Among the various approaches to design organic π-conjugated SMs materials with the long range absorption, one of the successful approaches is to incorporate the electron-donating (D) and electron-accepting (A) moieties in π-conjugated SMs (Qu and Tian, 2012; Guo et al., 2017; Wang et al., 2017). The FMOs energy levels, absorption and emission properties as well as intermolecular charge transfer of these materials can be tuned effectively by altering the chemistries of the donor and acceptor units. At the same time, adjusting the donor and acceptor units can also affect their self-assembly in the solid state. Among the various D–A type SMs donors for OSCs, diketopyrrolo[3,4-c]pyrrole (DPP)-based molecules are promising building blocks owing to their excellent coplanarity, broader absorption region, and thermal stability (Chen et al., 2013; Lin et al., 2013; Zhang et al., 2014). Furthermore, the introduction of the planar heteroarenes into the strong electron-withdrawing DPP-based molecules backbones can lead to lower the band gap because of increasing effective conjugation length (Dutta et al., 2012; Patra et al., 2013). In addition, star-shaped SMs materials with π-conjugated arms can harvest sunlight effectively because of their extended dimensionality. Meanwhile, their steric hindrances can prevent the formation of an ordered, long-range, and coplanar π-π stacking, which are beneficial for their charge transport property (Irfan et al., 2017). Therefore, the star-shaped D–A type DPP-based molecules may possess narrower band gap, broader absorption region, strong light absorption, and high charge carrier mobility (Sharma et al., 2014; Shiau et al., 2015).

Considering these merits and characteristics mentioned above, in this contribution, we report the design of a series of novel star-shaped DPP-based molecules with electron-accepting 2,4,6-triphenyl-1,3,5-triazine (TPTA) as core, electron accepting DPP derivatives as arms, and electron-donating triphenylamine derivatives (TPA) as end groups for OSCs applications (as shown in **Scheme 1**). With the aim to investigate the relationships between structure and properties of the designed molecules, the different planar heteroarenes have been introduced into the side of DPP molecules backbones in the star-shaped molecules. The HOMO energy (E_{HOMO}), LUMO energy (E_{LUMO}), HOMO–LUMO gap (E_g), energetic driving force ΔE_{L-L}, and absorption spectra of the designed molecules were systematically investigated by applying density functional theory (DFT) and time-dependent DFT (TD-DFT) methodology. The charge transfer properties (reorganization energy, λ) were also simulated.

COMPUTATIONAL DETAILS

Using the Gaussian 09 W software package (Frisch et al., 2009), all the geometry optimizations and frequency for the designed molecules in the gas phase were performed with the DFT method. No imaginary frequency was used to ensure the nature of the stationary point for the optimized molecules. On the basis of the optimized structures, the absorption spectra of the designed molecules were predicted using the TD-DFT method. The 6-31G (d,p) basis set was employed for all calculations in this work. For the FMOs energy levels of the designed molecules, because it is difficult to describe the virtual orbitals theoretically (Wu et al., 2013). The LUMO energy levels can be calculated with the equation, $E_{LUMO} = E_{HOMO} + E^{ex}$, where E^{ex} represents the first vertical excited energy (Zhang and Musgrave, 2007; Ku et al., 2011; Zhang et al., 2012). A crucial step in the theoretical investigations is to select an appropriate exchange correlation functional. With the aim to select an appropriate approach, we chose various functionals such as B3LYP (Lee et al., 1988), PBE0 (Adamo and Barone, 1999), LC-wPBE (Tawada et al., 2004), M062X (Zhao and Truhlar, 2008), and CAM-B3LYP (Yanai et al., 2004) to optimize the geometries of the parent molecule **1**. Based on the optimized geometries, the absorptions were predicted using the TD-DFT method. The longest wavelengths of absorption (λ_{abs}) as well as the experimental data are shown in **Figure 1**. As showing **Figure 1**, the calculated λ_{abs} value obtained at PBE0 (543 nm) level provided better agreement with the experimental value (523 nm) (Shiau et al., 2015) than those obtained with other levels of theory, with the deviation being 20 nm. Although B3LYP appeared adapted to 1,3,5-triazine and

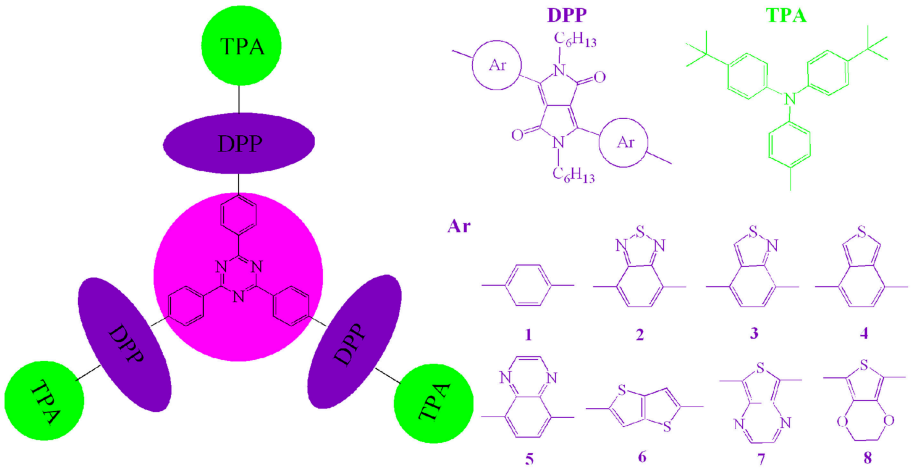

SCHEME 1 | Molecule models of **1**–**8** investigated in this work.

DPP derivatives in literature (Feng et al., 2014; Vala et al., 2014; Jin, 2015; Jin and Irfan, 2015; Jin and Xiao, 2015; Fujii et al., 2016), the λ_{abs} value obtained at the B3LYP/6-31G (d,p) level is worsen accordance with the experimental data (the deviation is 48 nm) than that for at the PBE0/6-31G (d,p) level (the deviation is 20 nm). Additionally, we also calculated the FMOs energy levels of molecule **1** using both at PBE0 and B3LYP methods. The calculated E_{HOMO} and E_{LUMO} values (−5.04 and −2.76 eV) at the PBE0/6-31G (d,p) level are more close to the electrochemical measurements data (−5.47 and −3.41 eV) (Shiau et al., 2015) than those obtained at the B3LYP/6-31G (d,p) level (−4.82 and −2.67 eV), respectively. Furthermore, in order to make further investigation of the validity of the selected approach, both PBE0 and B3LYP methods were also employed to optimize the structure of PCBM and PC71BM. The calculated E_{HOMO} and E_{LUMO} of PCBM and PC71BM along with available experimental data are listed in **Table S1**. Inspection of **Table S1** reveals clearly that the E_{HOMO} and E_{LUMO} at the PBE0/6-31G (d,p) level of PCBM are −5.98 and −3.99 eV, and the corresponding values of PC71BM are −5.92 and −3.82 eV, respectively. These are well reproduce the experimental values of PCBM (−6.00 and −3.80 eV) (Jeon et al., 2016) and PC71BM (−6.00 and −3.95 eV) (Chandrasekharam et al., 2014), respectively. However, at B3LYP/6-31G (d,p) level, the calculated E_{HOMO} and E_{LUMO} of PCBM are −5.67 and −3.75 eV, while the corresponding values of PC71BM are −5.61 and −3.60 eV, respectively. It was noticed that B3LYP overestimate the E_{HOMO} and E_{LUMO} of PCBM and PC71BM. The B3LYP overestimate the E_{HOMO} and E_{LUMO} compared with experimental value, as reported in the literature (Blouin et al., 2008; Xiao et al., 2010; Abbotto et al., 2012). Therefore, PBE0 functional is reasonable to investigate the current system. In order to obtain insight into the method to describe and the influence of functionals on the optical properties, the absorption spectrum of the designed molecules were also simulated at B3LYP/6-31G (d,p) levels.

It is well-known that the reorganization energy (λ) play the dominant role in the effective charge transfer according

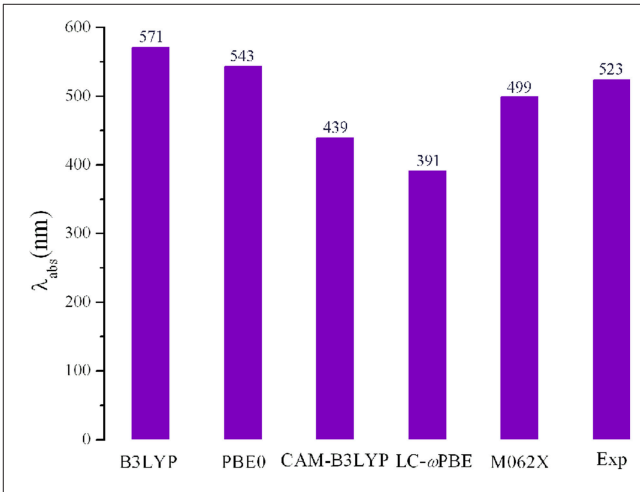

FIGURE 1 | Calculated absorption wavelengths (λ_{abs}) of **1** using various functionals, together with the experimental result.

to the Marcus theory (Marcus, 1964, 1993). A good charge transfer materials should possess lower λ values, which led to higher charge transfer rate. We only pay attention to the internal reorganization energy in this work owing to the low dielectric constant of medium in OSCs materials (Marcus, 1964). The electron (λ_e) and hole (λ_h) reorganization energy can be expressed as follows (Köse et al., 2007; Sancho-García, 2007):

$$\lambda e = \left(E_0^- - E_-^-\right) + \left(E_-^0 - E_0^0\right) \quad (1)$$

$$\lambda h = \left(E_0^+ - E_+^+\right) + \left(E_+^0 - E_0^0\right) \quad (2)$$

Here, $E_0^{\pm}$ and $E_{\pm}^{\pm}$ are the energies of the cationic (anionic) states with the optimized neutral and cationic (anionic) geometry, respectively. $E_{\pm}^0$ and E_0^0 represent the energy of the neutral states with the optimized geometry of the cationic (anionic) and neutral structures, respectively. The λ_e and λ_h of the designed molecules were predicted at the PBE0/6-31G(d,p) level.

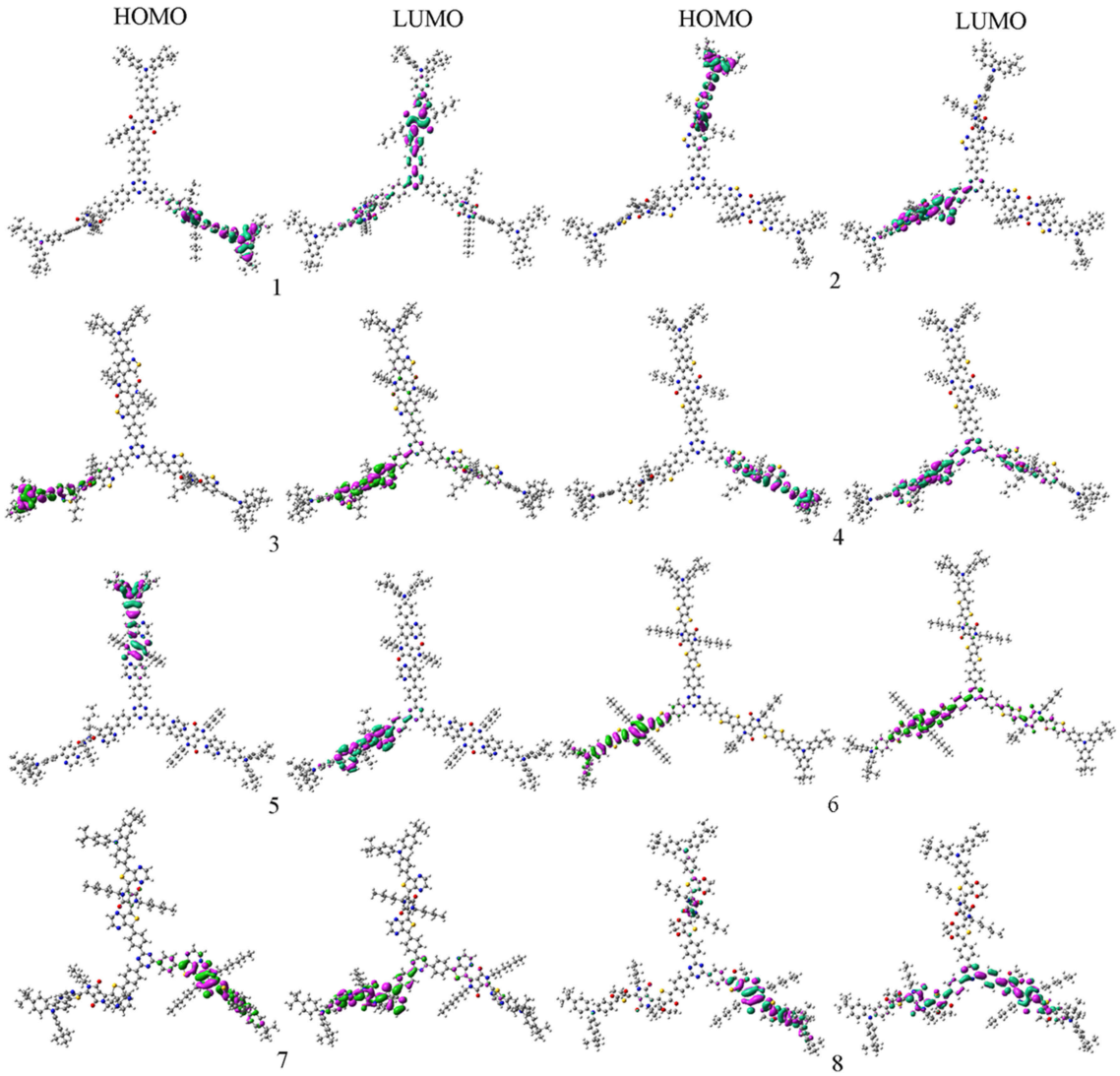

FIGURE 2 | The FMOs of the designed molecules at the PBE0/6-31G(d,p) level.

It is noteworthy that the stability is the most important criteria to evaluate the nature of devices for OSCs. Generally, the absolute hardness (η) was applied to explore the stability of the materials. From a viewpoint of conceptual density functional theory, the η values of the designed molecules were calculated with the following equation (Cheung and Troisi, 2010):

$$\eta = \frac{1}{2}\left(\frac{\partial \mu}{\partial N}\right) = \frac{1}{2}\left(\frac{\partial^2 E}{\partial N^2}\right) = \frac{AIP - AEA}{2} \quad (3)$$

Here, μ and N correspond to the chemical potential and total electron number, respectively. The adiabatic ionization potential (AIP) is the energy difference between the cation radical specie and its neutral specie, while the adiabatic electron affinity (AEA) represents the energy difference between the neutral molecule and its anion radical molecule.

RESULTS AND DISCUSSION

Frontier Molecular Orbitals and Band Gaps

In order to characterize the optical and electronic properties, we investigated the distributions of the FMOs for the designed molecules. The distribution of HOMOs and LUMOs are plotted in **Figure 2**. Based on Mulliken population analysis, molecular orbital contribution (%) from core TPTA, arms DPP, and end groups TPA to the FMOs of **1**–**8** are given in **Table 1**. The corresponding contributions (%) from TPTA, DPP, and TPA groups to the HOMOs-1 and LUMOs+1 of **1**–**8** are given in **Table S2**. As visualized in **Figure 2**, the distribution of HOMOs and LUMOs are spread over the conjugated backbone and show π orbital features. The HOMOs are mainly localized on the arm groups DPP and end groups TPA with only minor contributions from the core fragments TPTA. The sum contributions of DPP and TPA fragments are larger than 96.1%, while the

TABLE 1 | Molecular orbital contribution (%) from core TPTA, arms DPP, and end groups TPA to the FMOs of **1**–**8** at the PBE0/6-31G(d,p).

Species	HOMO			LUMO		
	TPTA	DPP	TPA	TPTA	DPP	TPA
1	0.7	32.5	66.4	17.8	79.4	2.8
2	0.6	34.5	64.9	8.3	88.4	3.3
3	0.3	18.3	81.4	8.4	88.5	3.1
4	0.8	53.7	45.5	17.2	80.9	2.0
5	0.3	29.8	69.9	8.4	89.	2.5
6	2.4	76.5	21.1	16.9	79.9	3.2
7	3.9	71.1	25.0	11.6	82.7	5.6
8	3.1	69.6	27.3	25.8	69.9	4.3

TPTA, 2,4,6-triphenyl-1,3,5-triazine moieties; DPP, diketopyrrolopyrrole moieties; TPA, triphenylamine moieties.

TABLE 2 | Calculated E_{HOMO}, E_{LUMO}, E_g, and ΔE_{L-L} (all in eV) for investigated molecules at the PBE0/6-31G(d,p).

Species	E_{HOMO}	E_{LUMO}	E_g	$\Delta E_{L\text{-}L}$[a]	$\Delta E_{L\text{-}L}$[b]
1	−5.04	−2.76	2.28	1.23	1.06
2	−5.07	−3.26	1.81	0.73	0.56
3	−5.03	−3.05	1.98	0.94	0.77
4	−5.02	−2.84	2.18	1.15	0.98
5	−5.02	−2.94	2.08	1.05	0.88
6	−4.86	−2.95	1.91	1.04	0.87
7	−4.80	−3.25	1.55	0.74	0.57
8	−4.69	−2.63	2.06	1.36	1.19

[a]*Energetic driving force for PCBM as donor.*
[b]*Energetic driving force for PC71BM as donor.*

corresponding values of TPTA fragments are within 3.9% for HOMOs. On the contrary, the LUMOs are mainly distributed on the DPP and TPTA moieties with minor contributions from TPA fragments. The sum contributions of DPP and TPTA fragments for LUMOs are larger than 94.4%, while the corresponding values of TPA fragments are within 5.6%. Obviously, the contributions of both DPP and TPTA fragments for LUMOs are larger than those of for HOMOs, respectively. The contributions of TPA fragments to LUMOs are decreased compared with those of to HOMOs, respectively. Similar phenomena are found for the HOMOs-1 and LUMOs+1 of **1**–**8**. The changes in contributions suggest that the electronic density flow from the end groups TPA to the arms groups DPP and cores groups TPTA for HOMOs → LUMOs excitations. This indicates that the end groups TPA serve as donors, whereas, the arm groups DPP and core groups TPTA serve as acceptors, respectively.

It is worth noting that the E_{HOMO}, E_{LUMO}, E_g, and ΔE_{L-L} are strongly related to the optical and electronic properties. The calculated values of E_{HOMO}, E_{LUMO}, E_g, and ΔE_{L-L} of the designed molecules are given in **Table 2** and depicted in **Figure 3**. As shown in **Figure 3**, it is clear that the E_{HOMO} values of **3**–**8** increase, while the corresponding value of **2** decreases compared with that of **1**. The E_{HOMO} values is in the order

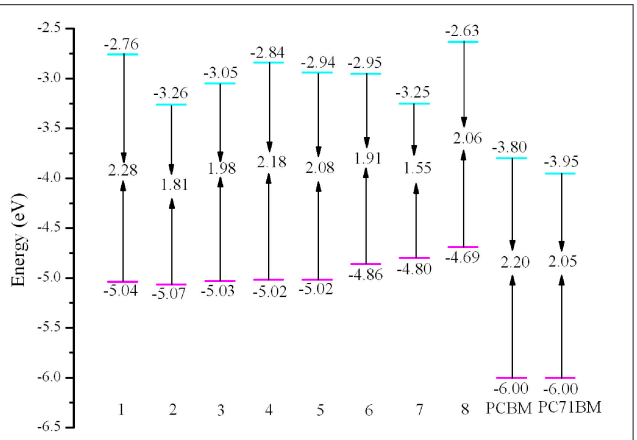

FIGURE 3 | Evaluation of calculated FMO energies for the designed molecules as well as FMO energies for PCBM and PC70BM at the PBE0/6-31G(d,p) level.

of **8** > **7** > **6** > **4** ≈ **5** > **3** > **1** > **2**. On the other hand, the E_{LUMO} values of **2**–**7** decrease, while the corresponding value of **8** increases compared with that of **1**. The sequence of E_{LUMO} values is **8** > **1** > **4** > **5** > **6** > **3** > **2** > **7**. Therefore, the E_g values of **2**–**8** decrease compared with that of **1**. The E_g values are in the order of **1** < **4** < **5** < **8** < **3** < **6** < **2** < **7**. The analysis indicates that the decrease of E_g is mainly attributable to the increased E_{HOMO} and declined E_{LUMO}. The reducing the E_g of the designed molecules should leads to bathochromic shifts of the maximum absorption compared with that of **1**. Consequently, the introduction of different groups to the side of DPP molecules backbones in the star-shaped molecules can tune the FMOs energy and E_g values of the original molecule. It provides a powerful strategy for design high-performance and desirable donor novel SMs. Furthermore, in order to ensure efficient charge transfer, the ΔE_{L-L} values must exceed the binding energy (0.2 ∼ 1.0 eV) (Hill et al., 2000; Knupfer, 2003). From **Table 2**, it is noteworthy that the ΔE_{L-L} values of the designed molecules are all beyond the binding energy with regard to PCBM and PC71BM as acceptors. It is clear that the sequence of the values of ΔE_{L-L} with regard to PCBM and PC71BM are all **8** > **1** > **4** > **5** > **6** > **3** > **7** > **2**. In addition, the differences between the E_{HOMO} of **1**–**8** and the E_{LUMO} of PCBM and PC71BM are larger than 0.73 and 0.56 eV, respectively. Thus, it is quite clear that the designed molecules can provide match well with PCBM and PC71BM as acceptors.

Absorption Spectra

The absorption wavelengths λ_{abs} (in nm), the oscillator strength *f*, and main assignments (coefficient), and the absorption region *R* of **1**–**8** at the PBE0/6-31G(d,p) level are listed in **Table 3**. *R* denotes for the difference of the longest and shortest wavelength values with oscillator strength larger than 0.01 considering the first 15 excited states (see **Table S3**). The simulated absorption spectra of **1**–**8** are shown in **Figure 4**, which were plotted by

TABLE 3 | The electronic transition, absorption wavelengths λ_{abs} (in nm), the oscillator strength *f*, main assignments (coefficient), and the absorption region *R* of **1**–**8** at the TD-PBE0/6-31G(d,p)//PBE0/6-31G(d,p) level, along with available experimental data.

Species	λ_{abs}	*f*	Assignment	*R*
1	543.4	1.79	H → L (0.12) H-2 → L (0.50) H-1 → L (0.20)	72.2
2	686.4	1.30	H-2 → L (0.66) H-5 → L (−0.17)	142.2
3	626.4	1.37	H → L (0.59) H → L+2 (0.21) H-2 → L+1 (0.21)	155.3
4	569.5	1.79	H → L (0.30) H-1 → L (0.43) H-1 → L+2 (−0.22)	82.3
5	597.2	1.01	H-2 → L (0.64) H-5 → L (0.23)	106.1
6	648.0	3.13	H → L (0.60) H → L+2 (0.21) H-2 → L+1 (−0.19)	139.1
7	799.6	2.19	H → L (0.24) H-2 → L (0.45) H → L+1 (−0.41)	225.7
8	602.4	2.83	H → L (0.51) H-2 → L (0.20), H-2 → L+1 (0.30)	152.7
Exp	523			

*Exp, Experimental results of **1** in thin film were taken from Sharma et al. (2014), Shiau et al. (2015).*

using the GaussSum 1.0 program (O'Boyle and Vos, 2003). As expected, the results displayed in **Table 3** reveals that the λ_{abs} of **2**–**8** exhibit bathochromic shifts compared with that of **1**. The bathochromic shifts values of **2**–**8** are 143, 83, 26.1, 53.8, 104.6, 256.2, and 59.0 nm (3834, 2439, 844, 1658, 2971, 5897, and 1803 cm^{-1}), respectively. Moreover, the λ_{abs} values are in the order of **7** > **2** > **6** > **3** > **8** > **5** > **4** > **1**, which is in excellent agreement with the corresponding reverse sequence of their E_g values. It reveals that the introduction of different groups to the side of DPP molecules backbones leads to bathochromic shifts of the maximum absorption for the original molecule. The order of the bathochromic shifts values compared with that of **1** is thieno[3,4-b]pyrazine (**7**) > benzo[c][1,2,5]thiadiazole (**2**) > thieno[3,2-b]thiophene (**6**) > benzo[c]isothiazole (**3**) > 2,3-dihydrothieno[3,4-b][1,4]dioxine (**8**) > quinoxaline (**5**) > benzo[c]thiophene (**4**). Additionally, one can find that **6**–**8** have larger oscillator strengths, while the corresponding values of **2**, **3**, and **5** possess slightly < that of **1**. The oscillator strength value of **4** is almost equal to that of **1**, indicating that the designed molecules shown large absorption intensity. At the same time, the designed molecules have large absorption region *R* (82.3–225.7 nm). The *R* values of 2–8 are larger than that of parent compound 1. It suggests that the introduction of different groups to the side of DPP molecules backbones lead to the increase of R values compared with parent molecule 1. The order of *R* values compared with that of **1** is thieno[3,4-b]pyrazine (**7**) > benzo[c]isothiazole (**3**) > 2,3-dihydrothieno[3,4-b][1,4]dioxine (**8**) > benzo[c][1,2,5]thiadiazole (**2**) > thieno[3,2-b]thiophene (**6**) > quinoxaline (**5**) > benzo[c]thiophene (**4**). It is noticeable that a good overlap between the absorption spectrum of the designed molecules and the solar emission spectrum, which can improve the light-absorption efficiency. It clearly shows that the introduction of different groups can extend the absorption spectrum toward longer wavelengths, which is beneficial to harvest more sunlight. These results imply that the designed compounds have strong absorption and are expected to be the promising candidates for donor materials in OSCs applications.

The calculated λ_{abs}, *f*, and main assignments (coefficient) of **1**–**8** at the B3LYP/6-31G(d,p) level are listed in **Table S4**. Comparing the results shown in **Table 3** with **Table S4**, one can find that the calculated λ_{abs} values of **1**–**8** at the B3LYP/6-31G(d,p) are larger than those obtained at the PBE0/6-31G(d,p), respectively. The differences between λ_{abs} at the B3LYP/6-31G(d,p) and PBE0/6-31G(d,p) levels are about 30 ∼ 50 nm. It should be mentioned that although the E_{HOMO} and E_{LUMO} are overestimated with both the PBE0 and B3LYP functionals, the predicted λ_{abs} values using PBE0 are found to be closer to the experimental findings. The trend for λ_{abs} at B3LYP/6-31G(d,p) is similar to using PBE0/6-31G(d,p) method. Obviously, B3LYP functional underestimate the E_g value, resulting in the large λ_{abs} compared with experimental value. Considering the FMOs energy levels and the predicted absorption spectra mentioned above, the PBE0/6-31G(d,p) approach is the best choice to well reproduce the experimental results. Therefore, the λ, η, *AIP*, and *AEA* of the designed molecules were computed at PBE0/6-31G(d,p).

Adiabatic Ionization Potential and Electron Affinity

It is well known that *AIP* and *AEA* are two major parameters that determine the charge transfer behavior for materials. The carrier polarity of materials can be adjusted by the *AIP* and *AEA* values (Chen and Chao, 2005; Liu et al., 2010). The lower *AIP* and higher *AEA* revealed that material would be better hole and electron transporter, respectively (Li et al., 2012). The calculated *AIP* and *AEA* of **1**–**8** are collected in **Table 4**. Obviously, the results displayed in **Table 4** show that the increasing sequence of *AIP* values is **8** < **7** < **6** < **4** < **5** < **1** < **3** < **2**. On the other hand, the decreasing order of *AEA* values is **7** > **2** > **3** > **6** > **5** > **4** > **1** > **8**. It indicates that the introduction of benzo[c]thiophene (**4**), quinoxaline (**5**), thieno[3,2-b]thiophene (**6**), and thieno[3,4-b]pyrazine (**7**) groups can decrease/increase *AIP*/*AEA* values compared with that of **1**. However, the benzo[c][1,2,5]thiadiazole (**2**) and benzo[c]isothiazole (**3**) groups can increase both *AIP* and *AEA* values, whereas 2,3-dihydrothieno[3,4-b][1,4]dioxine (**8**) group can decrease both *AIP* and *AEA* values compared with that of **1**. It is noticeable that the introduction of different aromatic heterocyclic group to the side of DPP molecules backbones can affect the *AIP* and *AEA* of the designed molecules.

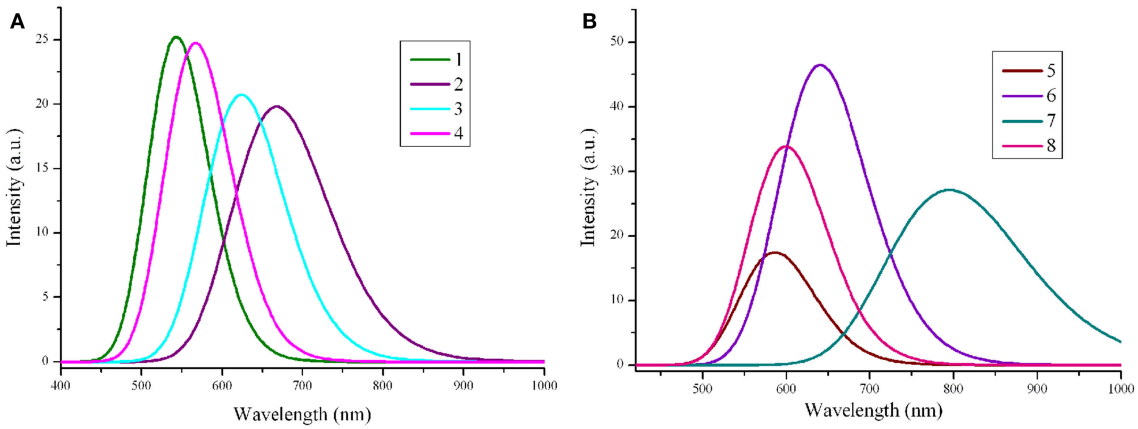

FIGURE 4 | The calculated absorption spectra of the investigated molecules (value of full width at half maximum is 3,000 cm^{-1}). **(A)** Molecules **1**–**4**; **(B)** Molecules **5**–**8**.

TABLE 4 | Calculated molecular *AIP* and *AEA* (both in eV) of **1**–**8** at the PBE0/6-31G(d,p) level.

Species	*AIP*	*AEA*
1	5.404	1.953
2	5.435	2.372
3	5.406	2.272
4	5.362	1.979
5	5.378	2.068
6	5.209	2.196
7	5.163	2.449
8	5.048	1.781

TABLE 5 | Calculated molecular λ_e, λ_h, and η (all in eV) of **1**–**8** at the PBE0/6-31G(d,p) level.

Species	λ_h	λ_e	η
1	0.054	0.134	1.725
2	0.058	0.112	1.532
3	0.046	0.209	1.567
4	0.090	0.135	1.692
5	0.051	0.138	1.655
6	0.107	0.091	1.506
7	0.129	0.122	1.357
8	0.128	0.128	1.633

Reorganization Energies and Stability Properties

The calculated λ_e, λ_h, and η of **1**–**8** are listed in **Table 5**. It is worth noting that the lower the reorganization energy values can be beneficial to the higher charge transfer rate (Marcus, 1964, 1993). Usually, tris(8-hydroxyquinolinato)aluminum(III) (Alq3, λ_e = 0.276 eV) and N,N′-diphenyl-N,N′-bis(3- methlphenyl)-(1,1′-biphenyl)-4,4′-diamine (TPD, λ_h = 0.290 eV) are taken as typical electron and hole transport materials, respectively (Gruhn et al., 2002; Lin et al., 2005). It is clear from **Table 5** that the λ_h values of **1**–**8** (0.046–0.129 eV) are smaller than that of TPD. It indicates that the hole transfer rates of **1**–**8** are higher than that of TPD. On the other hand, the λ_e values of **1**–**8** (0.091–0.209 eV) are smaller than that of Alq3. It implies that the electron transfer rates of **1**–**8** might be higher than that of Alq3. The λ_h values of **1**–**5** are slightly smaller than those of **6**–**8**, suggesting that the hole transfer rates of **1**–**5** should be higher than those of **6**–**8**, respectively. It indicates that the introduction of benzene (**1**), benzo[c][1,2,5]thiadiazole (**2**), benzo[c]isothiazole (**3**), benzo[c]thiophene (**4**), and quinoxaline (**5**) groups may lead to higher charge transfer rates than that of thieno[3,2-b]thiophene (**6**), thieno[3,4-b]pyrazine (**7**), and 2,3-dihydrothieno[3,4-b][1,4]dioxine (**8**) groups, respectively. The λ_e values is in the order of **3** > **5** > **4** > **1** > **8** > **7** > **2** > **6**. It suggests that molecules with benzo[c][1,2,5]thiadiazole (**2**), thieno[3,2-b]thiophene (**6**), thieno[3,4-b]pyrazine (**7**), and 2,3-dihydrothieno[3,4-b][1,4]dioxine (**8**) possess higher electron transfer rates, while molecules with benzo[c]isothiazole (**3**), benzo[c]thiophene (**4**), and quinoxaline (**5**) groups have lower electron transfer rates compared with that of **1**, respectively. Additionally, the λ_h values of **1**–**5** are smaller than those of their λ_e values, suggesting that the carrier mobility of the hole is larger than that of the electron. However, the λ_e values of **6** and **7** are smaller than those of their λ_h values, implying that the carrier mobility of the electron is larger than that of the hole. Moreover, the differences between λ_e and λ_h values of the designed molecules are in the region of 0.00 ∼ 0.087 eV except the corresponding value of **3** is 0.163 eV, respectively. It indicates that they exhibit better equilibrium feature for hole and electron transport. Therefore, **1**, **2**, and **4**–**8** are expected to be the promising candidates for ambipolar charge transports materials, whereas **3** can be used as hole and electron transport material.

The absolute hardness η of **1**–**8** were calculated and shown in **Table 5**. The η values is in the order of **1** > **4** > **5** > **8** > **3** > **2** > **6** > **7**. Inspection of **Table 5** reveals clearly that the η values of

2–**8** are smaller slightly than the value of **1**, which may be owing to the steric hindrances of the heterocyclic groups introduced to the side of DPP backbones in star-shaped DPP-based molecules. It implies that the introduction of different heterocyclic groups do not significantly affect the stability of the designed molecules.

CONCLUSION

In this contribution, a series of novel star-shaped molecules have been systematically investigated. Their electronic, optical, and charge transport properties studied using DFT and TD-DFT approaches. The calculated results show that the introduction of different groups to the side of DPP backbones in the star-shaped molecules can tune the FMOs energy and E_g values of the original molecule. The designed molecules can provide match well with PCBM and PC71BM as acceptors. Additionally, the λ_{abs} of **2**–**8** show bathochromic shifts compared with that of the original molecule **1**, respectively. The introduction of different groups can extend the absorption spectrum toward longer wavelengths, which is beneficial to harvest more sunlight. Our results suggest that the designed molecules are expected to be the promising candidates for ambipolar charge transport materials except molecule with benzo[c]isothiazole group (**3**) can be used as hole and electron transport material. Moreover, the different substituent groups do not significantly affect the stability of the designed molecules.

AUTHOR CONTRIBUTIONS

RJ conceived and designed the research and headed, wrote, and revised the manuscript. XZ contributed to the performance and analysis of the frontier molecular orbitals, absorption spectra the reorganization energies. Both authors contributed to manuscript revision, read, and approved the submitted version.

ACKNOWLEDGMENTS

This work was supported by NSFC (No. 21563002) and the Research Program of Sciences at Universities of Inner Mongolia Autonomous Region (No. NJZY19223).

SUPPLEMENTARY MATERIAL

The Supplementary Material for this article can be found online at: https://www.frontiersin.org/articles/10.3389/fchem.2019.00122/full#supplementary-material

REFERENCES

Abbotto, A., Seri, M., Dangate, M. S., De Angelis, F., Manfredi, N., Mosconi, E., et al. (2012). A vinylene-linked benzo[1,2-b:4,5-b′]dithiophene-2,1,3-benzothiadiazole low-bandgap polymer. *J. Polym. Sci. Pol. Chem.* 50, 2829–2840. doi: 10.1002/pola.26046

Adamo, C., and Barone, V. (1999). Toward reliable density functional methods without adjustable parameters: the PBE0 model. *HJ. Chem. Phys.* 110, 6158–6170. doi: 10.1063/1.478522

Bin, H., Yang, Y., Zhang, Z. G., Ye, L., Ghasemi, M., Chen, S., et al. (2017). 9.73% efficiency nonfullerene all organic small molecule solar cells with absorption-complementary donor and acceptor. *J. Am. Chem. Soc.* 139, 5085–5094. doi: 10.1021/jacs.6b12826

Blouin, N., Michaud, A., Gendron, D., Wakim, S., Blair, E., Neagu-Plesu, R., et al. (2008). Toward a rational design of poly(2,7-carbazole) derivatives for solar cells. *J. Am. Chem. Soc.* 130, 732–742. doi: 10.1021/ja0771989

Chandrasekharam, M., Anil Reddy, M., Ganesh, K., Sharma, G. D., Singh, S. P. J., and Rao, L. (2014). Synthesis and photovoltaic properties of D-A-D type small molecules containing diketopyrrolopyrrole (DPP) acceptor central unit with different donor terminal units. *Org. Electron.* 15, 2116–2125. doi: 10.1016/j.orgel.2014.05.033

Chaudhry, A. R., Muhammad, S., Irfan, A., Al-Sehemi, A. G., Haq, B. U., and Hussain, S. (2018). Structural, electronic, and nonlinear optical properties of novel derivatives of 9,12-diiodo-1,2-dicarba-closo-dodecaborane: density functional theory approach. *Z. Naturforsch. A* 73, 1037–1045. doi: 10.1515/zna-2018-0123

Chen, H. Y., and Chao, I. (2005). Effect of perfluorination on the charge-transport properties of organic semiconductors: density functional theory study of perfluorinated pentacene and sexithiophene. *Chem. Phys. Lett.* 401, 539–545. doi: 10.1016/j.cplett.2004.11.125

Chen, Y., Wan, X., and Long, G. (2013). High performance photovoltaic applications using solution-processed small molecules. *Acc. Chem. Res.* 46, 2645–2655. doi: 10.1021/ar400088c

Cheung, D. L., and Troisi, A. (2010). Theoretical study of the organic photovoltaic electron acceptor PCBM: morphology, electronic structure, and charge localization. *J. Phys. Chem. C* 114, 20479–20488. doi: 10.1021/jp1049167

Coughlin, J. E., Henson, Z. B., Welch, G. C., and Bazan, G. C. (2014). Design and synthesis of molecular donors for solution-processed high-efficiency organic solar cells. *Acc. Chem. Res.* 47, 257–270. doi: 10.1021/ar400136b

Dutta, P., Yang, W., Eom, S. H., Lee, W. H., Kang, I. N., and Lee, S. H. (2012). Development of naphtho[1,2-b:5,6-b′]dithiophene based novel small molecules for efficient bulk-heterojunction organic solar cells. *Chem. Commun.* 48 573–575. doi: 10.1039/C1CC15465F

Feng, H. F., Fu, W. F., Li, L., Yu, Q. C., Lu, H., Wan, J. H., et al. (2014). Triphenylamine modified bis-diketopyrrolopyrrole molecular donor materials with extended conjugation for bulk heterojunction solar cells. *Org. Electron.* 15, 2575–2586. doi: 10.1016/j.orgel.2014.07.020

Frisch, M. J., Trucks, G. W., Schlegel, H. B., Scuseria, G. E., Robb, M. A., Cheeseman, J. R., et al. (2009). *Gaussian 09*. Wallingford, CT: Gaussian, Inc.

Fujii, M., Shin,W., Yasuda, T., and Yamashita, K. (2016). Photon-absorbing charge-bridging states in organic bulk heterojunctions consisting of diketopyrrolopyrrole derivatives and PCBM. *Phys. Chem. Chem. Phys.* 18, 9514–9523. doi: 10.1039/C5CP06183K

Gruhn, N. E., da Silva Filho, D. A., Bill, T. G., Malagoli, M., Coropceanu, V., Kahn, A., et al. (2002). The vibrational reorganization energy in pentacene: molecular influences on charge transport. *J. Am. Chem. Soc.* 124, 7918–7919. doi: 10.1021/ja0175892

Guo, Y. Q., Wang, Y., Song, L. C., Liu, F., Wan, X., Zhang, H., et al. (2017). Small molecules with asymmetric 4-alkyl-8-alkoxybenzo[1,2-*b*:4,5-*b*′]dithiophene as the central unit for high-performance solar cells with high fill factors. *Chem. Mater.* 29, 3694–3703. doi: 10.1021/acs.chemmater.7b00642

He, C., He, Q. G., Yang, X. D., Wu, G. L., Yang, C. H., Bai, F. L., et al. (2007). Synthesis and photovoltaic properties of a solution-processable organic molecule containing triphenylamine and DCM moieties. *J. Phys. Chem. C* 111, 8661–8666. doi: 10.1021/jp070714x

Hill, I. G., Kahn, A., Soos, Z. G., and Pascal, R. A Jr. (2000). Charge-separation energy in films of π-conjugated organic molecules. *Chem. Phys. Lett.* 327, 181–188. doi: 10.1016/S0009-2614(00)00882-4

Irfan, A., Assiri, M., and Al-Sehemi, A. G. (2018). Exploring the optoelectronic and charge transfer performance of diaza[5]helicenes at molecular and bulk level. *Org. Electron.* 57, 211–220. doi: 10.1016/j.orgel.2018.03.022

Irfan, A., Muhammad, S., Chaudhry, A. R., Al-Sehemi, A. G., and Jin, R. (2017). Tuning of optoelectronic and charge transport properties in star shaped anthracenothiophene-pyrimidine derivatives as multifunctional materials. *Optik* 149, 321–331. doi: 10.1016/j.ijleo.2017.09.065

Jeon, I., Delacou, C., Nakagawa, T., and Yutaka Matsuo, Y. (2016). Enhancement of open-circuit voltage by using the 58-p silylmethyl fullerenes in small-molecule organic solar cells. *Chem. Asian J.* 11, 1268–272. doi: 10.1002/asia.201501400

Jin, R. (2015). Theoretical study of the optical and charge transport properties of star-shaped molecules with 1,3,5-triazine-core derivatives as organic light-emitting and organic solar cells materials. *C. R. Chimie.* 18, 954–959. doi: 10.1016/j.crci.2015.05.021

Jin, R., and Irfan, A. (2015). Theoretical study on photophysical properties of multifunctional star-shaped molecules with 1,8-naphthalimide core for organic light-emitting diode and organic solar cell application. *Theor. Chem. Acc.* 134:89. doi: 10.1007/s00214-015-1693-8

Jin, R., and Xiao, W. (2015). Rational design of organoboron heteroarene derivatives as luminescent and charge transport materials for organic light-emitting diodes. *New J. Chem.* 39, 8188–8194. doi: 10.1039/C5NJ01499A

Kan, B., Li, M., Zhang, Q., Liu, F., Wan, X., Wang, Y., et al. (2015). A series of simple oligomer-like small molecules based on oligothiophenes for solution-processed solar cells with high efficiency. *J. Am. Chem. Soc.* 137, 3886–3893. doi: 10.1021/jacs.5b00305

Knupfer, M. (2003). Exciton binding energies in organic semiconductors. *Appl. Phys. A* 77, 623–626. doi: 10.1007/s00339-003-2182-9

Köse, M. E., Mitchell, W. J., Kopidakis, N., Chang, C. H., Shaheen, S. E., Kim, K., et al. (2007). Theoretical studies on conjugated phenyl-cored thiophene dendrimers for photovoltaic applications. *J. Am. Chem. Soc.* 129, 14257–14270. doi: 10.1021/ja073455y

Ku, J., Lansac, Y., and Jang, Y. H. (2011). Time-dependent density functional theory study on benzothiadiazole-based low-band-gap fused-ring copolymers for organic solar cell applications, *J. Phys. Chem. C* 115, 21508–21516. doi: 10.1021/jp2062207

Lee, C., Yang, W., and Parr, R. G. (1988). Development of the colle–salvetti correlation-energy formula into a functional of the electron density. *Phys. Rev. B* 37, 785–789. doi: 10.1103/PhysRevB.37.785

Lenes, M., Wetzelaer, G. -J. A. H., Kooistra, F. B., Veenstra, S. C., Hummelen, J. C., and Blom, P. W. M. (2008). Fullerene bisadducts for enhanced open-circuit voltages and efficiencies in polymer solar cells. *Adv. Mater.* 20, 2116–2119. doi: 10.1002/adma.200702438

Li, G., Zhu, R., and Yang, Y. (2012). Polymer solar cells. *Nat. Photonics.* 6, 153–161. doi: 10.1038/nphoton.2012.11

Lin, B. C., Cheng, C. P., You, Z. Q., and Hsu, C. P. (2005). Charge transport properties of tris(8-hydroxyquinolinato)aluminum(III): why it is an electron transporter. *J. Am. Chem. Soc.* 127, 66–67. doi: 10.1021/ja045087t

Lin, Y., and Zhan, X. (2016). Oligomer molecules for efficient organic photovoltaics. *Acc. Chem. Res.* 49, 175–183. doi: 10.1021/acs.accounts.5b00363

Lin, Y. Z., Ma, L. C., Li, Y. F., Liu, Y. Q., Zhu, D. B., and Zhan, X. W. (2013). A solution-processable small molecule based on benzodithiophene and diketopyrrolopyrrole for high-performance organic solar cells. *Adv. Energy. Mater.* 3, 1166–1170. doi: 10.1002/aenm.201300181

Liu, C. C., Mao, S. W., and Kuo, M. Y. (2010). Cyanated pentaceno[2,3-*c*]chalcogenophenes for potential application in air-stable ambipolar organic thin-film transistors. *J. Phys. Chem. C* 114, 22316–22321. doi: 10.1021/jp1099464

Loser, S., Lou, S. J., Savoie, B. M., Bruns, C. J., Timalsina, A., Leonardi, M. J., et al. (2017). Systematic evaluation of structure–property relationships in heteroacene–diketopyrrolopyrrole molecular donors for organic solar cell. *J. Mater. Chem. A* 5, 9217–9232. doi: 10.1039/C7TA02037F

Maglione, C., Carella, A., Centore, R., Chávez, P., Lévêque, P., Fall, S., et al. (2017). Novel low bandgap phenothiazine functionalized DPP derivatives prepared by direct heteroarylation: application in bulk heterojunction organic solar cells. *Dyes. Pigments.* 141, 169–178. doi: 10.1016/j.dyepig.2017.02.012

Marcus, R. A. (1964). Chemical and electrochemical electron-transfer theory. *Annu. Rev. Phys. Chem.* 15, 155–196.

Marcus, R. A. (1993). Electron transfer reactions in chemistry. theory and experiment. *Rev. Mod. Phys.* 65, 599–610.

Ni, D., Zhao, B., Shi, T., Ma, S., Tu, G., and Wu, H. (2013). Monodisperse low-bandgap macromolecule-based 5,5′-bibenzo[c][1,2,5]thiadiazole swivel cruciform for organic solar cells. *ACS. Macro. Lett.* 2, 621–624. doi: 10.1021/mz4002436

O'Boyle, N. M., and Vos, J. G. (2003). *GaussSum 1.0*. Dublin: Dublin City University.

Patra, D., Huang, T. Y., Chiang, C. C., Maturana, R. O., Pao, C. W., Ho, K. C., et al. (2013). 2-Alkyl-5-thienyl-substituted benzo[1,2-b:4,5-b]dithiophene-based donor molecules for solution-processed organic solar cells. *ACS Appl. Mater. Interfaces* 5, 9494–9500. doi: 10.1021/am4021928

Qu, S., and Tian, H. (2012). Diketopyrrolopyrrole (dpp)-based materials for organic photovoltaics. *Chem. Commun.* 48, 3039–3051. doi: 10.1039/c2cc17886a

Sancho-García, J. C. (2007). Assessment of density-functional models for organic molecular semiconductors: the role of Hartree–Fock exchange in charge-transfer processes. *Chem. Phys.* 331, 321–331. doi: 10.1016/j.chemphys.2006.11.002

Scharber, M. C., Wuhlbacher, D., Koppe, M., Denk, P., Waldauf, C., Heeger, A. J., et al. (2006). Design rules for donors in bulk-heterojunction solar cells-towards 10 % energy-conversion efficiency. *Adv. Mater.* 18, 789–794. doi: 10.1002/adma.200501717

Sharma, G. D., Zervaki, G. E., Angaridis, P. A., Kitsopoulos, T. N., and Coutsolelos, A. G. (2014). Triazine-bridged porphyrin triad as electron donor for solution-processed bulk hetero-junction organic solar cells. *J. Phys. Chem. C* 118, 5968–5977. doi: 10.1021/jp500090h

Shiau, S. Y., Chang, C. H., Chen, W. J., Wang, H. J., Jeng, R. J., and Lee, R. H. (2015). Star-shaped organic semiconductors with planar triazine core and diketopyrrolopyrrole branches for solution-processed small-molecule organic solar cells. *Dyes. Pigments* 115, 35–49. doi: 10.1016/j.dyepig.2014.12.007

Tawada, Y., Tsuneda, T., Yanagisawa, S., Yanai, T., and Hirao, K. (2004). A long-range-corrected time-dependent density functional theory. *J. Chem. Phys.* 120, 8425–8433. doi: 10.1063/1.1688752

Vala, M., Krajčovič, J., Luňák, Jr., S., Ouzzane, I., Bouillon, J. P., and Weiter, M. (2014). HOMO and LUMO energy levels of N,N′-dinitrophenyl-substituted polar diketopyrrolopyrroles (DPPs). *Dyes Pigments* 106, 136–142. doi: 10.1016/j.dyepig.2014.03.005

Wang, J. L., Liu, K. K., Liu, S., Xiao, F., Chang, Z. F., Zheng, Y. Q., et al. (2017). Donor end-capped hexafluorinated oligomers for organic solar cells with 9.3% efficiency by engineering the position of π-bridge and sequence of two-step annealing. *Chem. Mater.* 29, 1036–1046. doi: 10.1021/acs.chemmater.6b03796

Wazzan, N., El-Shishtawy, R. M., and Irfan, A. (2018). DFT and TD–DFT calculations of the electronic structures and photophysical properties of newly designed pyrene-core arylamine derivatives as hole-transporting materials for perovskite solar cells. *Theor. Chem. Acc.* 137:9. doi: 10.1007/s00214-017-2183-y

Wu, J., Kan, Y. -H., Wu, Y., and Su, Z. -M. (2013). Computational design of host materials suitable for green-(deep) blue phosphors through effectively tuning the triplet energy while maintaining the ambipolar property. *J. Phys. Chem. C* 117, 8420–8428. doi: 10.1021/jp4008174

Xiao, S., Stuart, A. C., Liu, S., Zhou, H., and You, W. (2010). Conjugated polymer based on polycyclic aromatics for bulk heterojunction organic solar cells: a case study of quadrathienonaphthalene polymers with 2% efficiency. *Adv. Funct. Mater.* 20, 635–643. doi: 10.1002/adfm.200901407

Yanai, T., Tew, D. P., and Handy, N. C. (2004). A new hybrid exchange–correlation functional using the coulomb-attenuating method (CAM-B3LYP). *Chem. Phys. Lett.* 393, 51–57. doi: 10.1016/j.cplett.2004.06.011

Yao, H., Ye, L., Zhang, H., Li, S., Zhang, S., and Hou, J. (2016). Molecular design of benzodithiophene-based organic photovoltaic materials. *Chem. Rev.* 116, 7397–7457. doi: 10.1021/acs.chemrev.6b00176

Zhang, G., and Musgrave, C. B. (2007). Comparison of DFT methods for molecular orbital eigenvalue calculations. *J. Phys. Chem. A* 111, 1554–1561. doi: 10.1021/jp061633o

Zhang, L., Pei, K., Yu, M., Huang, Y., Zhao, H., Zeng, M., et al. (2012). Theoretical investigations on donor-acceptor conjugated copolymers based on naphtha [1, 2-c: 5, 6-c] bis [1, 2, 5] thiadiazole for organic solar

cell applications. *J. Phys. Chem. C* 116, 26154–26161. doi: 10.1021/jp306656c

Zhang, Y. M., Tan, H., Xiao, M. J., Bao, X. C., Tao, Q., and Wang, Y. F. (2014). D–A–Ar-type small molecules with enlarged π-system of phenanthrene at terminal for high-performance solution processed organic solar cells. *Org. Electron.* 15, 1173–1183. doi: 10.1016/j.orgel.2014.03.011

Zhang, Z., Zhou, Z., Hu, Q., Liu, F., Russell, T. P., and Zhu, X. (2017). 1, 3-bis (thieno [3, 4-b] thiophen-6-yl)-4 H-thieno [3, 4-c] pyrrole-4, 6 (5 H)-dione-Based small-molecule donor for efficient solution-processed solar cells. *ACS Appl. Mater. Interfaces* 9, 6213–6219. doi: 10.1021/acsami.6b14572

Zhao, Y., and Truhlar, D. G. (2008). The M06 suite of density functionals for main group thermochemistry, thermochemical kinetics, noncovalent interactions, excited states, and transition elements: two new functionals and systematic testing of four M06-class functionals and 12 other functionals. *Theor. Chem. Acc.* 120, 215–241.

Zhou, H., Yang, L., and You, W. (2012). Rational design of high performance conjugated polymers for organic solar cells. *Macromolecules* 45, 607–632. doi: 10.1021/ma201648t

Conflict of Interest Statement: The authors declare that the research was conducted in the absence of any commercial or financial relationships that could be construed as a potential conflict of interest.

frontiers in Chemistry

ORIGINAL RESEARCH
published: 04 October 2019
doi: 10.3389/fchem.2019.00642

Surface Study of Fe_3O_4 Nanoparticles Functionalized With Biocompatible Adsorbed Molecules

Beata Lesiak[1], N. Rangam[1]*, P. Jiricek[2], I. Gordeev[2], J. Tóth[3], L. Kövér[3], M. Mohai[4] and P. Borowicz[1]*

[1] Institute of Physical Chemistry, Polish Academy of Sciences, Warsaw, Poland, [2] Institute of Physics, Academy of Sciences of the Czech Republic, Prague, Czechia, [3] Institute for Nuclear Research, Hungarian Academy of Sciences, Debrecen, Hungary, [4] Research Centre for Natural Sciences, Institute of Materials and Environmental Chemistry, Hungarian Academy of Sciences, Budapest, Hungary

OPEN ACCESS

Edited by:
Ralph Ernstorfer,
Fritz-Haber-Institut, Germany

Reviewed by:
Enio Lima,
Bariloche Atomic Centre (CNEA), Argentina
Rodica Turcu,
National Institute for Research and Development of Isotopic and Molecular Technologies, Romania

***Correspondence:**
Beata Lesiak
blesiak-orlowska@ichf.edu.pl
N. Rangam
nrangam@ichf.edu.pl

Specialty section:
This article was submitted to Physical Chemistry and Chemical Physics, a section of the journal Frontiers in Chemistry

Received: 28 May 2019
Accepted: 09 September 2019
Published: 04 October 2019

Citation:
Lesiak B, Rangam N, Jiricek P, Gordeev I, Tóth J, Kövér L, Mohai M and Borowicz P (2019) Surface Study of Fe_3O_4 Nanoparticles Functionalized With Biocompatible Adsorbed Molecules. Front. Chem. 7:642. doi: 10.3389/fchem.2019.00642

Surfaces of iron oxide of ferrimagnetic magnetite (Fe_3O_4) nanoparticles (MNPs) prepared by Massart's method and their functionalized form (f-MNPs) with succinic acid, L-arginine, oxalic acid, citric acid, and glutamic acid were studied by dynamic light scattering (DLS), Fourier transform infrared spectroscopy (FTIR-S), UV-vis, thermogravimetric analysis (TGA)/differential scanning calorimetry (DSC), X-ray photoelectron spectroscopy (XPS), and reflection electron energy loss spectroscopy (REELS). The XPS analysis of elements and their chemical states at the surface of MNPs and f-MNPs revealed differences in chemical bonding of atoms, content of carbon–oxygen groups, iron oxide forms, iron oxide magnetic properties, adsorbed molecules, surface coverage, and overlayer thickness, whereas the Auger parameters (derived from XPS and Auger spectra) and elastic and inelastic scattering probabilities of electrons on atoms and valence band electrons (derived from REELS spectra) indicated modification of surface charge redistribution, electronic, and optical properties. These modified properties of f-MNPs influenced their biological properties. The surfaces biocompatible for L929 cells showed various cytotoxicity for HeLa cells (10.8–5.3% of cell death), the highest for MNPs functionalized with oxalic acid. The samples exhibiting the largest efficiency possessed smaller surface coverage and thickness of adsorbed molecules layers, the highest content of oxygen and carbon–oxygen functionalizing groups, the highest ratio of lattice O^{2-} and OH^- to C sp^2 hybridizations on MNP surface, the highest ratio of adsorbed O^- and OH^- to C sp^2 hybridizations on adsorbed molecule layers, the closest electronic and optical properties to Fe_3O_4, and the lowest degree of admolecule polymerization. This high cytotoxicity was attributed to interaction of cells with a surface, where increased content of oxygen groups, adsorbed O^-, and OH^- may play the role of additional adsorption and catalytic sites and a large content of adsorbed molecule layers of carboxylic groups facilitating Fenton reaction kinetics leading to cell damage.

Keywords: ferrimagnetic magnetite (Fe_3O_4) magnetic nanoparticles, biocompatible acid functionalization, DLS, FTIR-S, TGA/DSC, XPS, REELS, HeLa cells

INTRODUCTION

The iron oxide nanoparticles, i.e., ferrimagnetic maghemite (γ-Fe_2O_3) with Fe^{3+} vacancies and ferrimagnetic magnetite ($Fe_3O_4 \equiv FeO{\bullet}Fe_2O_3$) with Fe^{2+} and Fe^{3+} vacancies, have already been applied in the field of medicine due to their biocompatibility, biodegradability, and possibility to tailor magnetic behavior (Sangaiya and Jayaprakash, 2018), where the change of nanoparticle size, morphology, agglomeration, magnetic, and electronic properties influences the biological effect (Liu et al., 2016). Although magnetic targeting iron nanoparticles serve as platforms for attaching drugs like, e.g., doxorubicin (DOX), they were also applied in a tumor therapy, which resulted in a hyperthermia and oxidative stress leading to tumor cell damage (Rangam et al., 2017; Petran et al., 2018; Sangaiya and Jayaprakash, 2018). Enhancement of antitumor effect was obtained by functionalization of nanoparticles by a conventional DOX drug (Liu et al., 2016; Rangam et al., 2017) and/or doping with rare metals (Petran et al., 2018). Additional functionalization of iron nanoparticles may lead to enhancement of their biocompatibility, colloidal stability, and enlargement of number of groups, through which the required antitumor effect can be obtained.

The cytotoxicity of Fe_3O_4 MNPs coated with a wide variety of biocompatible admolecules has been recently extensively studied (Gupta and Gupta, 2005; Kim et al., 2009, 2010; Tomitaka et al., 2012; Mahdavi et al., 2013; Sahu et al., 2015; Taghavi et al., 2016; Hu et al., 2017; Linh et al., 2018). These several studies showed that cytotoxicity depends on the type of the investigated cells, type of biocompatible adlayer on MNPs, MNP size, concentration of MNPs, pH of solution, and time of incubation. The functionalization of MNPs with biocompatible molecules like polyethylene glycol, pluronic acid, and others providing a better biocompatibility may also affect the cytotoxicity due to modification of physical and chemical properties of the material, its interaction with biological cells, and ability of forming reactive oxygen species (ROS). The coating of Fe_3O_4 MNPs may provide a positive charge, which facilitates interaction of a specimen with negatively charged cell membrane (Taghavi et al., 2016). For the concentration range of 0.012–0.1 mg mL^{-1}, the generation of ROS by Fe_3O_4 nanoparticles was found to be smaller in comparison to Pt and PEGylated mesoporous iron–platinum–iron(II, III) (FePt-Fe_3O_4) nanoparticles (Sahu et al., 2015). Recently, it has been reported that Fe_3O_4 MNPs exhibited no cytotoxicity for HeLa cells during incubation time from 24 to 72 h, whereas coated MNPs showed the cytotoxicity after 72 h (Linh et al., 2018). No effect of Fe_3O_4 MNPs on cytotoxicity for HeLa cells was observed for incubation time of 24 h elsewhere (Gupta and Gupta, 2005; Kim et al., 2009, 2010; Tomitaka et al., 2012).

Functionalized nanoparticles of Fe_3O_4 iron oxide prepared by Massart's method (Massart, 1981; Runowski and Lis, 2016) (f-MNPs) using functionalization with succinic acid [$(CH_2)_2(CO_2H)_2$], L-arginine ($C_6H_{14}N_4$), oxalic acid ($C_2H_2O_4$), citric acid ($C_6H_8O_7$), and glutamic acid ($C_5H_9O_4N$) showed similar biocompatibility on fibroblasts (Rangam et al., 2017). Their average efficiency on HeLa cell treatment (% of HeLa cell deaths) in an f-MNP concentration range of 3.125–100 μg mL^{-1} and incubation time of 24 h decreased in the following order: 10.8% (oxalic acid), 10.7% (succinic acid), 9.2% (glutamic acid), 7.5% (citric acid) and 5.3% (L-arginine) (Rangam et al., 2017). The respective f-MNPs loaded with DOX showed about six times higher efficiency on HeLa cell therapy decreasing in different order, i.e., 64.2% (oxalic acid), 55.2% (L-arginine), 42.8% (glutamic acid), 42.2% (succinic acid), and 32.7% (citric acid), which is attributed to DOX adsorption and modified surface properties (Rangam et al., 2017).

The reason for the different cytotoxicity of Fe_3O_4 MNPs functionalized with oxalic, succinic, glutamic acids, and L-arginine for HeLa cells was investigated by X-ray photoelectron spectroscopy (XPS), X-ray excited Auger electron spectroscopy (XAES), and reflected electron loss spectroscopy (REELS) revealing the chemical groups at the surface and modification of surface electronic properties. These studies were supported by dynamic light scattering (DLS), Fourier transform infrared spectroscopy (FTIR-S), UV-vis, thermogravimetric analysis (TGA), and differential scanning calorimetry (DSC).

EXPERIMENTAL

Samples

Details on synthesis of nanoparticles of iron oxide (Fe_3O_4) by Massart's method (MNPs) (Massart, 1981; Runowski and Lis, 2016) and their functionalization at a temperature of 70°C–80°C at pH ca. 6–7 for 30 min with succinic acid [$(CH_2)_2(CO_2H)_2$], L-arginine ($C_6H_{14}N_4$), oxalic acid ($C_2H_2O_4$), citric acid ($C_6H_8O_7$), and glutamic acid ($C_5H_9O_4N$) (samples denoted as I, II, III, IV, and V, respectively) were described elsewhere (Rangam et al., 2017). The structural formulae of functionalizing adsorbed molecules are shown in **Supplementary Figure S1**. The prepared samples' (Fe_3O_4 MNPs and Fe_3O_4 f-MNPs I–V) chemical, structural, and magnetic properties were characterized previously by energy dispersive X-ray spectroscopy (EDX), scanning electron microscopy (SEM), transmission electron microscopy (TEM), X-ray diffraction (XRD), and vibrating sample magnetometer (Rangam et al., 2017).

DLS, FTIR-S, UV-vis, and TGA/DSC Apparatuses

The DLS measurements were carried out using Brookhaven Instruments Particle Size Analyzer 90+ to determine nanoparticles' hydrodynamic diameter (D_H), polydispersity index (PDI), and zeta potential. The measurements were performed in a water suspension of concentration of 0.01 mg mL^{-1} at pH ca. 6.

The FTIR spectra were recorded in Fourier spectrophotometer Vertex 80 V (Bruker Inc., USA) in a configuration of attenuated total reflectance (ATR) at a pressure below 5 hPa, which reduces negative factors like carbon dioxide and water. In order to obtain a high spectral resolution and signal-to-noise ratio, the following apparatus conditions were applied during the measurement: spectral resolution of 2 cm^{-1} and number of scans of 1,024.

The UV-vis spectra were recorded in deionized water solution by a Shimazu UV-2401 spectrophotometer.

The TGS/DSC data were recorded using Mettler Toledo TGA/DSC 3+ apparatus in nitrogen flow in a temperature range from room temperature (RT) to 800°C at a heating rate of 10°C min^{-1}.

XPS Spectrometer

The XPS spectra of Fe_3O_4 MNPs and Fe_3O_4 f-MNPs I–V were measured in an ultra-high vacuum (UHV) AXIS Supra photoelectron spectrometer (Kratos Analytical, UK). The incidence angle of the monochrome Al K_α radiation (1 mm^2 irradiation area, 300 × 700 μm analyzed area) was set to 54.4° and the photoelectron emission angle was $\alpha_{out} = 0°$, with respect to the surface normal. The hemispherical electron energy analyzer operated in the constant analyzer energy (CAE) mode at an analyzer pass energy of $E_p = 80$ eV (survey spectra) and $E_p = 10$ eV (high-resolution detailed spectra). The data acquisition was performed using ESCApe Kratos software. The samples were investigated without any UHV pretreatment. The binding energies (BE) of all the spectra were referenced to BE of 284.4 eV of C 1s line.

The REELS measurements proceeded in an ultra-high-vacuum (UHV) chamber using the ESA-31 electron spectrometer (home-made) (Kövér et al., 1992). The spectrometer is equipped with a hemispherical electron energy analyzer of high energy resolution, an electron gun (LEG62-VG Microtech), a home-made X-ray excitation source (Al Kα X-rays $h\nu = 1486.67$ eV), and an Ar^+ ion source of AG21 (VG Scientific). The REELS spectra were measured at fixed retardation ratio (FRR) mode using the retardation ratio of $k = 41$. The electron beam parameters were as follows: a primary electron energy of 4 keV, a beam current of about 11.5 nA measured with a Faraday cup, and electron incidence and emission angles of 50° and 0° with respect to the surface normal of the specimen, respectively.

RESULTS AND DISCUSSION

DLS, FTIR-S, UV-vis, and TGA/DSC

The investigated Fe_3O_4 MNPs and Fe_3O_4 f-MNPs I–V exhibit various values of D_H, PDI, and zeta potential. The values of D_H vary in a range of 217.9–871.2 nm (III < V < I < Fe_3O_4 < IV < II). Larger values of D_H in comparison to SEM values (Rangam et al., 2017) would suggest polymeric coating formed from adsorbed molecules on Fe_3O_4 MNPs. The values of polydispersity are in a range of 0.039–0.853 (IV < I < Fe_3O_4 < II < V < III) indicating different agglomeration/aggregation of nanoparticles in a solution. The value of zeta potential at pH ca. 6 is at a range of −0.53 to 0.83 mV (I < II < IV < V < Fe_3O_4 < III).

The ATR-FTIR spectra of Fe_3O_4 MNPs and f-MNPs I–V are shown in **Figure 1A**. All spectra show the characteristic peak of iron oxides, i.e., Fe-O at 548 cm^{-1}. The literature reports this peak at 580 cm^{-1} (Wei et al., 2012; Asgari et al., 2014; Bordbar et al., 2014). However, these reported data result from measurements in a polar environment of KBr pellet, which may shift the peak position. The spectrum of Fe_3O_4 MNPs exhibits modes typical for organic groups in regions of 760–1800 cm^{-1}, about 2,000 cm^{-1}, and 2,500–3,600 cm^{-1}. The spectra of Fe_3O_4 MNPs I–V samples confirm the presence of adsorbed molecule layers. All the spectra were normalized to the intensity of the Fe–O peak at 548 cm^{-1} in order to compare the intensity of peaks at different spectra regions for various adsorbed molecules. The FTIR spectra can be divided into the following regions: 760–1,180 cm^{-1}, 1,180–1,480 cm^{-1}, 1,480–1,800 cm^{-1}, region about 2,000 cm^{-1}, and 2,500–3,600 cm^{-1}. In the region of 760–1,180 cm^{-1}, C–C stretching (strong) and C–N stretching (medium) exist (Infrared Spectroscopy-MSU Chemistry, 2013). This region encloses the complex skeleton modes involving few vibration local modes due to modification of length of the bonds and angles between the bonds. Such vibration modes have been previously observed for L-arginine (Kumar and Rai, 2010) and glutamic acid (Sengupta and Krimm, 1985). For Fe_3O_4 f-MNPs II and V, dominating signal should result from C–C stretching. In the region of 1,180–1,480 cm^{-1}, the functionalized MNP modes characteristic for COOH group exist, i.e., stretching C–O mode (medium strong) (Silverstein et al., 1981; Infrared Spectroscopy-MSU Chemistry, 2013), bending C–O–H mode (medium), and bending C–H mode (Silverstein et al., 1981). For the investigated admolecules, the literature reports symmetric stretching $COOH^-$ mode for succinic acid (Krishnan et al., 2007); CH_3 symmetric bending mode for L-arginine (Kumar and Rai, 2010); stretching C–O mode for oxalic acid (Muthuselvi et al., 2016); scissoring C–O–H, CH_2, CH_3 modes, wagging CH_2, and CH_3 modes for citric acid (Bichara et al., 2011); and different types of bending C–H and stretching C–O modes for glutamic acid (Sengupta and Krimm, 1985). In the region of 1,480–1,800 cm^{-1}, C=O stretching mode (strong) is dominating (Silverstein et al., 1981; Infrared Spectroscopy-MSU Chemistry, 2013). For sample MNPs III, this mode is shifted to higher frequencies, and among all the samples, this mode resembles the structure of the COOH group in oxalic acid. For sample MNPs I and IV, this mode is shifted to lower frequencies, i.e., to 1,550 cm^{-1}. The structure of sample MNPs III is more rigid than the structure of sample MNPs I and MNPs IV. The interaction of COOH groups in f-MNPs III with Fe_3O_4 is weak. This is shown in bending of a mode at about 1,705 cm^{-1} typical for the COOH group interacting weakly with Fe_3O_4 MNPs. The main mode maximum at about 1,645 cm^{-1} is attributed to the C=O mode of stronger interaction with MNPs. For sample MNPs I and IV, their less rigid structure allows for attraction of all COOH groups to Fe_3O_4, which results in a larger frequency shift of C=O mode to lower values. For sample MNPs II and V, the mode in a range of 1,490–1,705 cm^{-1}, there is an overlap of stretching C=O mode (strong) (Silverstein et al., 1981; Infrared Spectroscopy-MSU Chemistry, 2013) and bending N–H mode (medium/medium-strong) typical for amine and amide (Silverstein et al., 1981; Infrared Spectroscopy-MSU Chemistry, 2013). Contribution of bending N–H mode and interaction of COOH with Fe_3O_4 result in a mode position and shape, where, for smaller frequencies, the slope responsible for bending N–H mode is smaller than that for stretching C=O mode. The region at about 2,000 cm^{-1} consists of weak modes responsible for combination and overtones of basic modes. The region of 2,500–3,600 cm^{-1} encloses stretching O–H modes (strong and

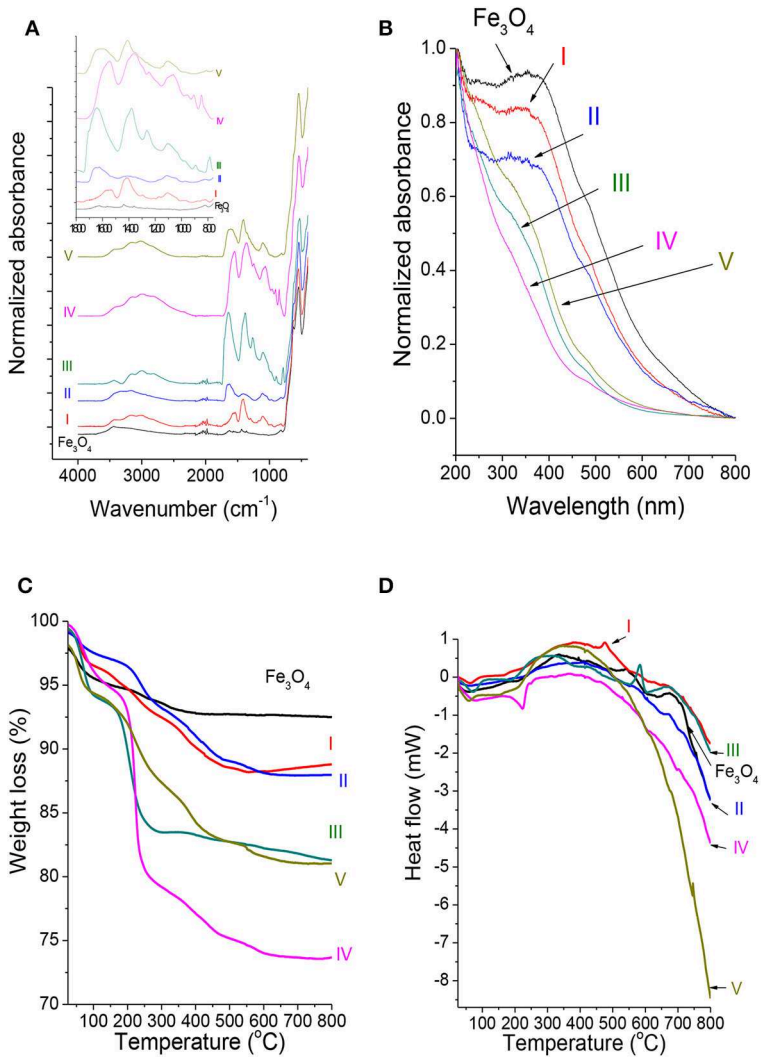

FIGURE 1 | (A) The ATR-FTIR, **(B)** UV-vis spectra, and **(C)** TGA and **(D)** DSC curves of the investigated Fe_3O_4 MNPs and Fe_3O_4 f-MNPs I–V.

wide depending on the environment), stretching C–H modes (generally strong), and stretching N–H mode typical for amine groups (sample MNPs II and V) (Silverstein et al., 1981; Infrared Spectroscopy-MSU Chemistry, 2013). Since the intensity of N–H stretching mode in this region is weak, the main components are stretching O–H and C–H modes with contributions depending on the sample.

The UV-vis spectra of Fe_3O_4 MNPs (**Figure 1B**) indicate the absorption band between 400 and 420 nm characteristic for Fe_3O_4 nanoparticles as reported elsewhere (Bahadur et al., 2017) and at about 300 nm reported previously for Fe_2O_3 (Bian et al., 2017). Less intense absorption bands with intensity decreasing in the order of I > II > III ≈ V > IV and shifted to smaller wavelengths exhibit Fe_3O_4 f-MNPs I–V samples due to adsorbed molecules. The shift may be attributed to adsorbed molecules, where L-arginine absorption band at 226–278 nm has been reported (Kumar and Rai, 2010).

The TGA curves (**Figure 1C**, **Supplementary Figure S2**) indicate various weight loss for every investigated sample in different temperature regions. The temperature range of 30–150°C is characteristic for a loss of residual water and other contaminations, as well as for physically adsorbed molecules. In the temperature range of 150–600°C, carboxyl, hydroxyl, carbonyl, and nitrogen groups of chemically adsorbed molecules undergo decomposition (Lesiak et al., 2009; Stobinski et al., 2010, 2012; Linh et al., 2018), contributing to this weight loss, whereas higher temperatures are more characteristic for phase transformations. The weight loss for all the investigated samples in the first range varies from 2.3 to 5.4% and is larger for oxalic (5.4%) and citric (4.6%) acids indicating either higher surface hydrophilicity and/or physical adsorption. The weight loss in the second region is 2.8% for Fe_3O_4 MNPs, 8 and 8.5% for L-arginine and succinic acid, 10.5 and 10.9% for oxalic and glutamic acid, and 21.4% for citric acid. This weight loss

between 10.5 and 21.4% indicates citric, oxalic, and glutamic acid dissolution in Fe_3O_4, where dissolution in oxalic acid was reported elsewhere (Panias et al., 1996). Thermal stability decreases in the following order: Fe_3O_4 MNPs > II (f-L-arginine) > I (f-succininc acid) > III (f-oxalic acid) > V (f-glutamic acid) > IV (f-citric acid).

The DSC curves (**Figure 1D**, **Supplementary Figure S2**) show endothermic and exothermic peaks indicating, respectively, heat absorption and release. The endothermic peaks are attributed to phase transitions, reduction, and most decomposition reactions, whereas exothermic peaks are related with oxidation, decomposition reactions, and crystallization. The first endothermic peaks visible for all the samples at 50.5–71.3°C can be attributed to desorption and/or evaporation of water and is related with the weight loss from 1.9% for Fe_3O_4 MNPs to 5.4% for f-MNPs I–V. The endothermic peaks in a range of 190–224°C can be attributed to desorption and/or decomposition of carboxylic groups and are related with the weight loss of 1.7–15.7%. This peak maximum temperature shift, i.e., Fe_3O_4 MNPs < I ≈ III < IV ≈ V < II, indicates increasing binding energy between MNPs and carboxylic groups from functionalizing molecules. The other broad exothermic peaks in a range of 320–420°C (Fe_3O_4 MNPs < I < V < II < IV) with a weight loss of 1.1–5.7% (Fe_3O_4 MNPs < I < V < II < IV) may be attributed to hydroxyl, carbonyl, and nitrogen group decomposition (Lesiak et al., 2009; Stobinski et al., 2010, 2012; Linh et al., 2018). The narrow exothermic peak at 475°C for sample I (f-succininc acid) with a weight loss of 1.3% and at 583°C for sample III (f-oxalic acid) with a weight loss of 2.2% may be related to decomposition of carbonyl groups forming a stronger bond with MNPs (Lesiak et al., 2009; Stobinski et al., 2010, 2012). The above results indicate different thermal decomposition, confirming the results by FTIR-S indicating various adsorption behaviors of molecules via MNP surface interaction.

Quantitative Surface Analysis

The survey XPS spectra (**Figure 2**) showed Fe, C, O, and N and contaminations of S and Cl at the surface. The quantitative surface analysis was performed using the peak areas (Fe 2p, C 1s, O 1s, N 1s, S 2p, and Cl 2p) after Tougaard background subtraction (Tougaard, 1999–2001) using the XPS MultiQuant software (Mohai, 1999-2001, 2004) considering a homogeneous surface distribution of elements, Scofield subshell photoionization cross sections (Scofield, 1976), and correction for analyzer transmission function and electron elastic scattering. The atomic composition of samples Fe_3O_4 and I–V is listed in **Supplementary Table S1**. The Fe_3O_4 MNPs show contamination of only Cl. The N from functionalizing adsorbed molecules was present in samples II and V, whereas samples III and IV indicated contamination of N. Otherwise, all f-MNPs show contamination of Cl and sample IV contamination of S. Contaminations of Cl and S result from precursors used in the Massart's synthesis of Fe_3O_4 MNPs, whereas contamination of N from ammonia and N gas flow conditions applied in the above mentioned synthesis.

Comparison of elemental ratios at the surface resulting from XPS to those in the bulk resulting from EDX, published elsewhere (Rangam et al., 2017), is shown in **Figure 3**. The ratios of C/Fe and O/Fe atomic contents at the surface (XPS) are larger than the respective ratios in the bulk (EDX), indicating remarkably larger carbon and oxygen content after functionalization, which result from the formation of a carbon–oxygen layer at the surface of Fe_3O_4 f-MNPs. The ratio of O/C atomic content being smaller at the surface than in the bulk indicates oxygen deficiency of functionalizing surface layers in comparison to the bulk Fe_3O_4 MNPs. Differences in these ratio values for MNPs and f-MNPs denoted as I–V confirm various adsorbed molecules layer of different surface coverages.

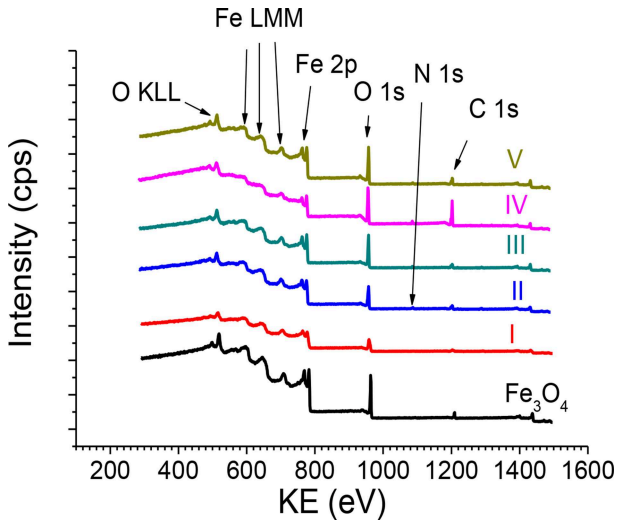

FIGURE 2 | The survey XPS spectra recorded from Fe_3O_4 MNPs and Fe_3O_4 f-MNPs I–V.

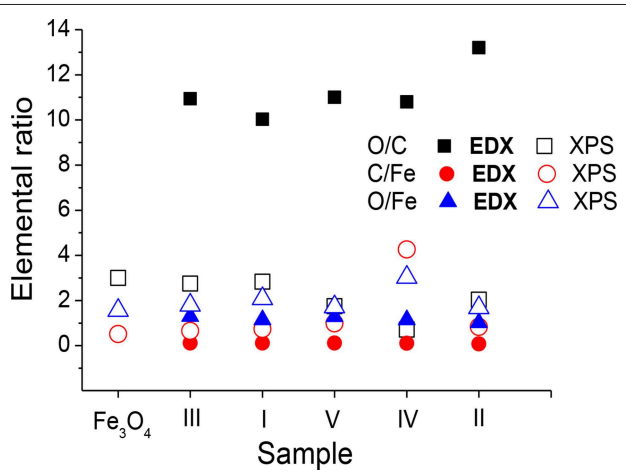

FIGURE 3 | Comparison of ratios of elemental contents at the surface (XPS) and in the bulk (EDX) (Rangam et al., 2017) of Fe_3O_4 and Fe_3O_4 f-MNPs I–V. Sample f-MNPs I–V are listed in the order of decreasing cytotoxicity.

Chemical State of Carbon, Oxygen, and Nitrogen

Fitting of C 1s, O 1s, and N 1s spectra was performed after Tougaard background subtraction using the XPSPeakfit41 software (Kwok, 2000). The fitting of C 1s, O 1s, and N 1s

spectra was focused on determination of the chemical forms of functionalizing overlayers and the Fe_3O_4 MNP substrate. The expected C chemical forms at the surface of Fe_3O_4 MNPs are carbon atoms forming sp^2 and/or sp^3 hybridizations and sp^2 and/or sp^3 carbon bonded to oxygen groups like carbonyl (C=O), hydroxyl (C–OH), and carboxyl (C–OOH) resulting from oxygen adsorption, whereas functionalization of the Fe_3O_4 MNP substrate is expected to provide increased number of carbon forms resulting from the chemical treatment with biocompatible molecules I–V, which consist mainly of C sp^2/sp^3 and carboxylic bonds (**Supplementary Figure S1**). These carbon oxygen bonds resulting from oxidation of carbon layer on Fe_3O_4 MNPs and the MNP additional functionalization, i.e., C=O, C–OH, and C–OOH, are expected to be present in the O 1s spectrum. However, the O 1s spectrum should also provide information on oxidized forms of Fe. Previously reported experimental and theoretical results (Butenko et al., 2005; Shim et al., 2012; Wagner et al., 2012; Fujimoto et al., 2016; Lesiak et al., 2018) provided and compiled the values of binding energy (BE) for C 1s and O 1s spectra typical for these carbon–oxygen groups for different carbon nanomaterials. Similarly, different oxidized forms of Fe due to iron treatment with oxygen and water were reported previously including the respective BE values (Grosvenor et al., 2004a,b), as well as carbon–nitrogen chemical forms (Wagner et al., 2012).

The resulting C 1s, O 1s, and N 1s spectra for sample III are shown in **Figure 4**, whereas the spectra recorded and fitted for all the samples are presented in **Supplementary Figures S3A–C**. The atomic contents of carbon, oxygen, and nitrogen chemical states resulting from C 1s, O 1s, and N 1s

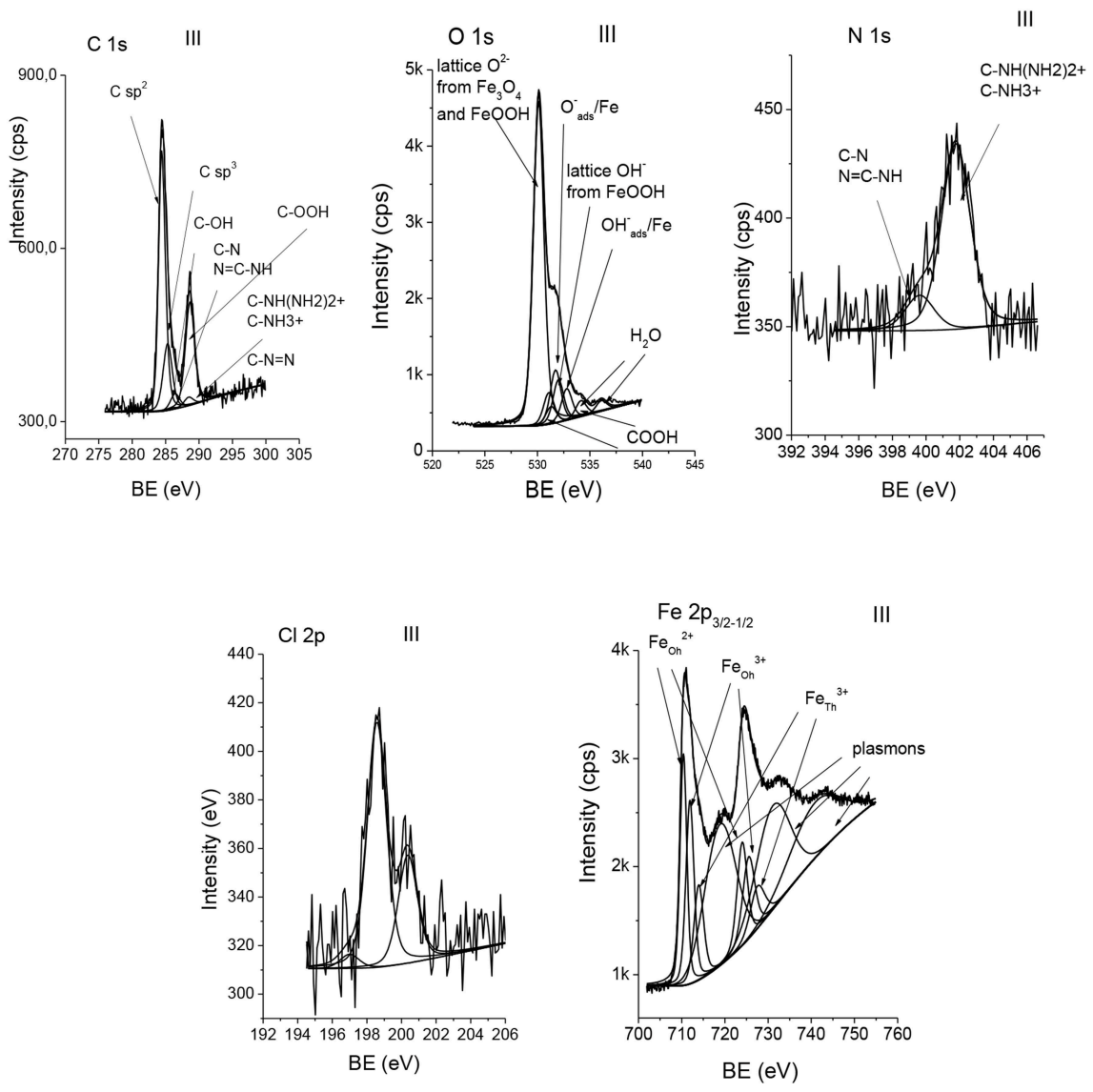

FIGURE 4 | The XPS C 1s, O 1s, N 1s, Cl 2p, and Fe 2p spectra fitted to different chemical forms for exemplary Fe_3O_4 f-MNPs III.

spectra fitting are listed in **Supplementary Tables S2A–C**. **Supplementary Tables S2A–C** also contains the respective BE values for C 1s, O 1s, and N 1s electrons characterizing the chemical states of the components of the adsorbed molecule layers and the Fe_3O_4 substrate. At the surface of Fe_3O_4 MNPs, the C–OH and C–OOH bonds are present, whereas f-MNPs I–V surfaces exhibit a large amount of C–OOH bonds (**Supplementary Table S2A**) due to functionalizing adsorbed molecules consisting profoundly of carboxylic bonds (**Supplementary Figure S1**). A small amount of C–OH bonds at the surface of sample III results probably from decomposition of carboxylic groups due to X-ray damage. The O 1s spectrum (**Supplementary Table S2B**) indicates the same amount of C–OOH groups resulting from adsorbed molecules and iron oxide forms interpreted as the lattice O^{2-} and adsorbed O^- from Fe_3O_4 and/or FeOOH and lattice OH^- and adsorbed OH^- from FeOOH, where adsorbed forms refer to those confirmed by the angular resolved measurement forms at the outer surface (Grosvenor et al., 2004a,b) and finally water adsorbed at the surface. Although, O^- and OH^- species would adsorb as atomic or molecular form, they receive the negative charge from tunneling electrons from the metal to the surface, as it has been suggested to occur during oxidation of Fe. Therefore, the notation of adsorbed O^- and OH^- includes a partial negative charge, which allows their BE values to be close to BEs for the lattice O^{2-} and OH^-. At the surface of Fe_3O_4 MNPs and their I–V functionalized MNPs, the largest amount of lattice O^{2-} is observed, then lattice OH^-, and then adsorbed OH^- and O^- forms and water. The comparison of the atomic contents of carbon and oxygen chemical states (**Supplementary Tables S2A,B**) for Fe_3O_4 MNPs and f-MNPs I–V in the order of decreasing cytotoxicity on HeLa cells is shown in **Figures 5A,B**, respectively.

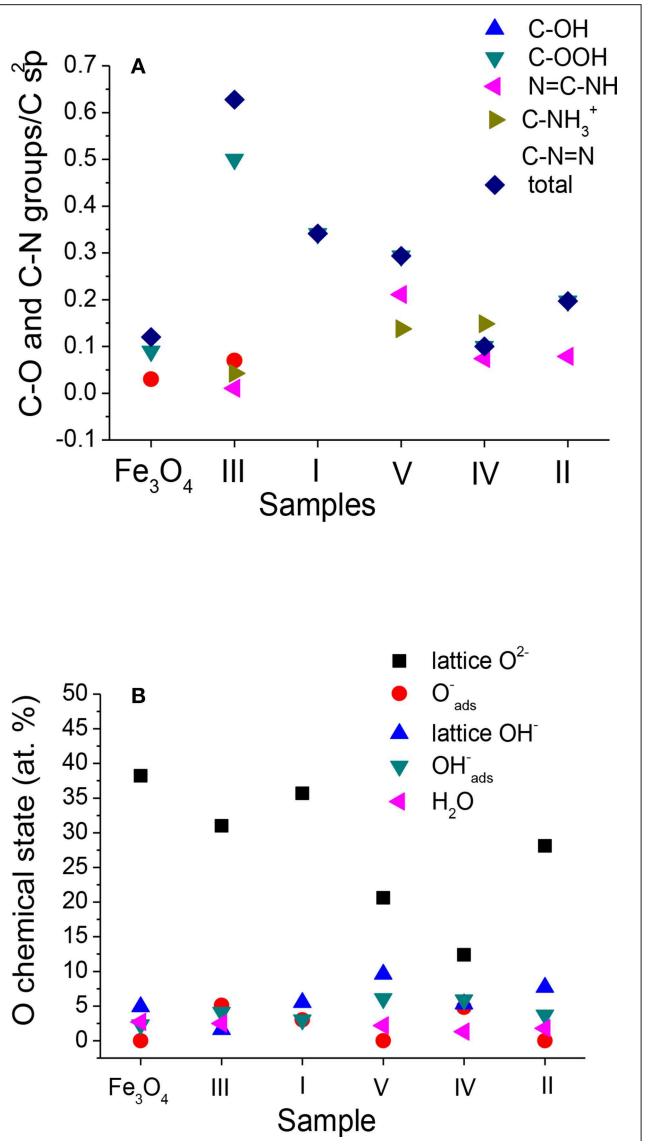

FIGURE 5 | Contents of **(A)** carbon–oxygen and carbon–nitrogen groups resulting from fitting of C 1s spectra normalized to C sp^2 and **(B)** oxygen chemical states resulting from fitting of O 1s spectra in Fe_3O_4 MNPs and Fe_3O_4 f-MNPs I–V. Sample f-MNPs I–V are listed in the order of decreasing cytotoxicity.

Chemical State of Fe

The stoichiometric magnetite Fe_3O_4 of cubic close packed oxygen sublattice can be alternatively expressed as $FeO{\bullet}Fe_2O_3$. Therefore, it consists of iron ions Fe^{2+} and Fe^{3+} occupying the tetrahedral (denoted as Th) and octahedral (denoted as Oh) interstices of cubic spinel type structure. The ideal Fe_3O_4 atomic ratio of Fe^{2+}:Fe^{3+} is 1:2, and precisely the ratio of $Fe_{Oh}{}^{2+}$:$Fe_{Oh}{}^{3+}$:$Fe_{Th}{}^{3+}$ is 1:1:1. The fitting of Fe 2p spectra accounted for Fe^{2+} and Fe^{3+} octahedral and Fe^{3+} tetrahedral spectra component parameters like Fe $2p_{3/2}$ BE and FWHM values reported in the literature (Yamashita and Hayes, 2008; Poulin et al., 2010; Eltouny and Ariya, 2014; Herng et al., 2015; Liu et al., 2016; Li et al., 2018; Petran et al., 2018). Exemplary Fe 2p spectra fitting results are shown in **Figure 4**, whereas all the fitted spectra are shown in **Supplementary Figure S4**. **Table 1** provides the parameters of the fitted Fe $2p_{3/2}$ spectra recorded for Fe_3O_4 MNPs and f-MNPs I–V. For Fe_3O_4 MNPs, the obtained values of BE for Fe^{2+} octahedral and Fe^{3+} tetrahedral and octahedral components, as well as intensity ratios of Fe^{3+} and Fe^{2+} tetrahedral and octahedral components equal to 1:1:1, are in agreement with those reported previously (Poulin et al., 2010), confirming Fe_3O_4 MNPs (**Table 1**). The temperature functionalization of Fe_3O_4 surface by biocompatible admolecules (samples I–V) at 70–80°C modifies the stoichiometry of Fe_3O_4, i.e., $FeO{\bullet}Fe_2O_3$, leading to changes of ratio of Fe^{2+} octahedral and Fe^{3+} tetrahedral and octahedral components, their BE values, and separation between the octahedral Fe^{2+} component and plasmon loss of the octahedral Fe^{2+} component ($\Delta Fe_{Oh}{}^{2+}$) of the Fe 2 $p_{3/2}$ spectra, which are also reflected in magnetic properties. Consistently increasing values of BE due to functionalization, values of ratio of Fe^{2+} and Fe^{3+} components, and values of separation between Fe $2p_{3/2}$ octahedral 2+ component and values of separation between plasmon loss of Fe $2p_{3/2}$ octahedral 2+ component ($\Delta Fe_{Oh}{}^{2+}$) ranging from 8.11 to 8.77 eV (**Table 1**) indicate surface oxidation. Such separation

TABLE 1 | The percentage of Fe^{2+}/ Fe^{3+} octahedral (Oh) and Fe^{3+} tetrahedral (Th) chemical states including BE values of Fe $2p_{3/2}$ components; ratio of separation between Fe $2p_{3/2}$ octahedral 2+ component and plasmon loss; ratios of Fe_{Oh}^{2+}, Fe_{Oh}^{3+}, and Fe_{Th}^{3+} components; ratio of plasmon loss to the total area and separation of Fe_{Oh}^{2+} components from plasmon loss in Fe $2p_{3/2}$ spectra recorded from Fe_3O_4 and Fe_3O_4 f-MNPs I–V.

Sample	Fe chemical state						Fe_{Oh}^{2+}/ Fe_{Oh}^{3+} + Fe_{Th}^{3+}	Fe_{Oh}^{2+}:Fe_{Oh}^{3+}:Fe_{Th}^{3+}	A_{Plas}/ A_{Total}	ΔFe_{Oh}^{2+} -plasmon
	Fe_{Oh}^{2+}		Fe_{Oh}^{3+}		Fe_{Th}^{3+}					
	(%)	BE (eV)	(%)	BE (eV)	(%)	BE (eV)				
Fe_3O_4	33	710.0	33	711.4	34	713.3	0.49	1:1:1	0.5844	8.77
III	39	710.4	38	711.9	23	713.9	0.64	1:0.97:0.59	0.5857	8.52
I	30	710.8	35	712.2	35	714.0	0.43	0.86:1:1	0.5007	8.90
V	34.5	710.5	34.5	711.9	31.0	713.8	0.53	1:1:0.90	0.5855	8.32
IV	40	710.0	34	711.4	26	713.3	0.67	1:0.85:0.65	0.5986	8.11
II	37.0	710.5	39.0	712.0	24.0	714.1	0.59	0.95:1:0.62	0.5815	8.49

Sample f-MNPs I–V are listed in the order of decreasing cytotoxicity.

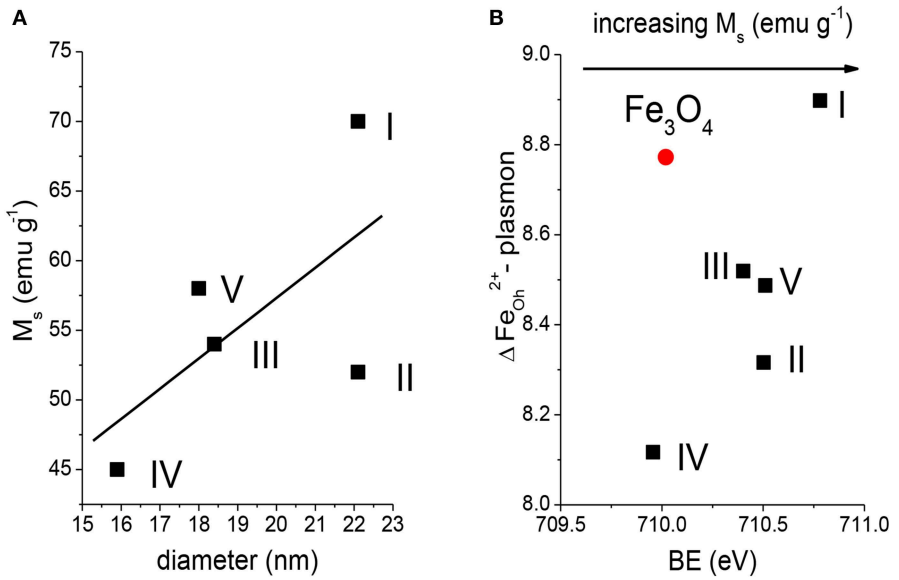

FIGURE 6 | Dependence of **(A)** Fe_3O_4 f-MNPs I–V diameters determined from XRD (Rangam et al., 2017) as a function of saturation magnetization. **(B)** BE of Fe 2p 2+ octahedral component on separation between Fe $2p_{3/2}$ 2+ octahedral component and plasmon loss in Fe $2p_{3/2}$ spectra recorded from Fe_3O_4 MNPs and Fe_3O_4 f-MNPs I–V.

values (ΔFe_{Oh}^{2+}), i.e., from 8.0 to 8.5 eV, were observed for α- and γ-FeOOH and Fe_2O_3 (Grosvenor et al., 2004c).

As reported previously (Rangam et al., 2017), the value of saturation magnetization, M_s, for Fe_3O_4 f-MNPs I–V, determined as a maximum magnetization characterized by parallel orientations of magnetic moments, varies from 45 to 70 emu g^{-1}, as a result of nanoparticle size and surface oxidation (**Figures 6A,B**). These values are smaller than the respective value for a bulk Fe_3O_4, i.e., 89–92 emu g^{-1}, and within agreement with various size Fe_3O_4 nanoparticles modified by different organic material. Generally, the value of M_s increases with increasing nanoparticle size (Herng et al., 2015). This remains in agreement with the results obtained by Rangam et al. (2017), where increasing M_s values are observed with increasing diameters obtained from XRD (**Figure 6A**). However, diamagnetic coating of nanoparticles causes decrease of M_s due to introducing surface spin disorder. Previously reported results provided evidences on modification of magnetic properties of Fe_3O_4 due to adsorption (Li et al., 2018), grain size (Liu et al., 2016), and functionalization (Soares et al., 2015). The oxidation of the surface interface of Fe_3O_4 MNPs I–V is reflected in increasing Fe $2p_{3/2}$ BE values and separation between Fe $2p_{3/2}$ octahedral 2+ component and plasmon loss of Fe $2p_{3/2}$ octahedral 2+ component (ΔFe_{Oh}^{2+}) (**Figure 6B**), justifying modification of magnetic properties resulting from slight modification of Fe_3O_4 stoichiometry and spin flipping at

the interface of MNPs and functionalizing adsorbed molecules. The saturation magnetization increases in the following order: sample IV < sample II < sample III < sample V < sample I.

Chemical State of Chlorine and Sulfur Contaminations

Chlorine was observed in Fe_3O_4 and samples I–V (0.1–1.9 at. %), and sulfur (1.1 at. %) was observed in sample IV (**Supplementary Table S1**). The chemical states of chlorine and sulfur contaminations were analyzed by fitting of Cl 2p (**Figure 4**, **Supplementary Figure S5A**, **Supplementary Table S3**) and S 2s (**Supplementary Figure S5B**) spectra. Chlorine chemical states are interpreted as follows: (i) $[(CH_3)_4N]Cl$ and/or $[N(C_2H_5)_4]Cl$ (BE = 196.6 ± 0.3 eV), (ii) $C(NH_2)_3Cl$ (BE = 198.2 ± 0.3 eV), and (iii) Met-Cl and/or $(-CH_2CHO(Cl)-)_n$ (BE = 199.9 ± 0.3 eV) (Wagner et al., 2012). Sulfur chemical state was interpreted as $-SO_4$ (BE = 168.6 eV) (Wagner et al., 2012). The resulting BE values providing information on the chemical states of Cl and S indicate that ionic Cl and S are bonded to Fe_3O_4 MNPs and adsorbed functionalizing molecules, which may result from segregation due to applied temperature conditions (70°C–80°C) during functionalization of MNPs.

Auger Parameters

The Auger parameters are not sensitive to uniform charging of non-conductive specimens. Combining information resulting from photoelectron peak positions and peak positions of the Auger transitions (**Figure 7**), providing the Auger parameters, is a powerful tool for exploring the electronic structure of surfaces and interfaces in XPS-XAES studies.

The local electronic changes in charge redistribution and transfer at the atomic level can be investigated, analyzing the final state Auger parameter (Equation 1a) and the initial state Auger parameter (Equation 1b) defined as (Wagner, 1972; Gaarenstroom and Winograd, 1977):

$$\alpha = E_A + E_B \quad (1a)$$

$$\beta = E_A + 3E_B, \quad (1b)$$

where E_A is the kinetic energy (KE) of the Auger electron and E_B is the binding energy (BE) of the photoelectron. Changes in the Auger parameter between two environments due to the atomic potentials in the core of the atom and the core hole screening efficiency (extra-atomic relaxation), ΔR (Equation 2a), as well as between atomic potentials in the core of the atom at the atomic site, ΔV (Equation 2b) are defined as (Cole and Weightman, 1994; Cole et al., 1995):

$$\Delta\alpha = \alpha_{Fe3O4} - \alpha_{env} = 2\Delta R \quad (2a)$$

$$\Delta\beta = \beta_{Fe3O4} - \beta_{env} = 2\Delta V, \quad (2b)$$

where α_{env} and β_{env} refer to functionalized Fe_3O_4 MNP surface. The final state effects (ΔR) refer to a shift in polarization energy at the core-ionized atom. This shift considers the charge transfer in a local valence band orbital of the core ionized atom and the contribution to the electronic relaxation energy of all the other atoms in the system. The initial state effects (ΔV) represent a chemical shift as a result of a ground state electronic structure and depend on bonding to neighboring atomic valence states. This shift is related to electronic states like, e.g., band structures, bond directionality, and structural parameters like atomic positions and Madelung constants of the bonded atom.

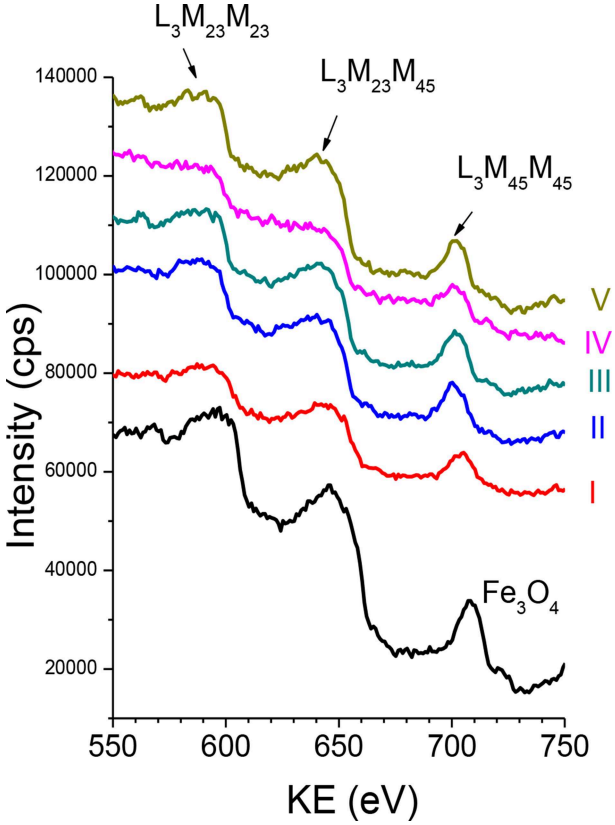

FIGURE 7 | The Fe L_3VV Auger spectra recorded from Fe_3O_4 MNPs and Fe_3O_4 f-MNPs I–V.

The Wagner plot for a given element and/or compound, known also as chemical state plot or chemical state diagram, displays in a compact form the values of photoelectron BE, Auger electron KE, and Auger parameters. Positions of compounds on this plot indicate relaxation shifts of various species and initial and final state effect contributions of various species. Therefore, Wagner plot information is related to the concept of ionicity, electronegativity, and polarizability. The Wagner plots for Auger Fe $L_3M_{45}M_{45}$ electrons–Fe $2p_{3/2}$ photoelectron spectra and Auger O KLL electrons–O 1s photoelectron spectra representing the investigated Fe_3O_4 and Fe_3O_4 MNPs I–V samples are shown in **Figure 8**, whereas values of Auger spectra KE, BE of photoelectron spectra, and Auger parameters resulting from Equations 1a—2b are provided in **Supplementary Tables S4A,B**. It should be noted that Equations 2a and 2b are a good approximation in the case of core–core–core Auger transitions.

The spectral shape of Auger transition (**Figure 7**) is influenced by the valence band density of states and also by changes in the local density of states resulting from the screening of

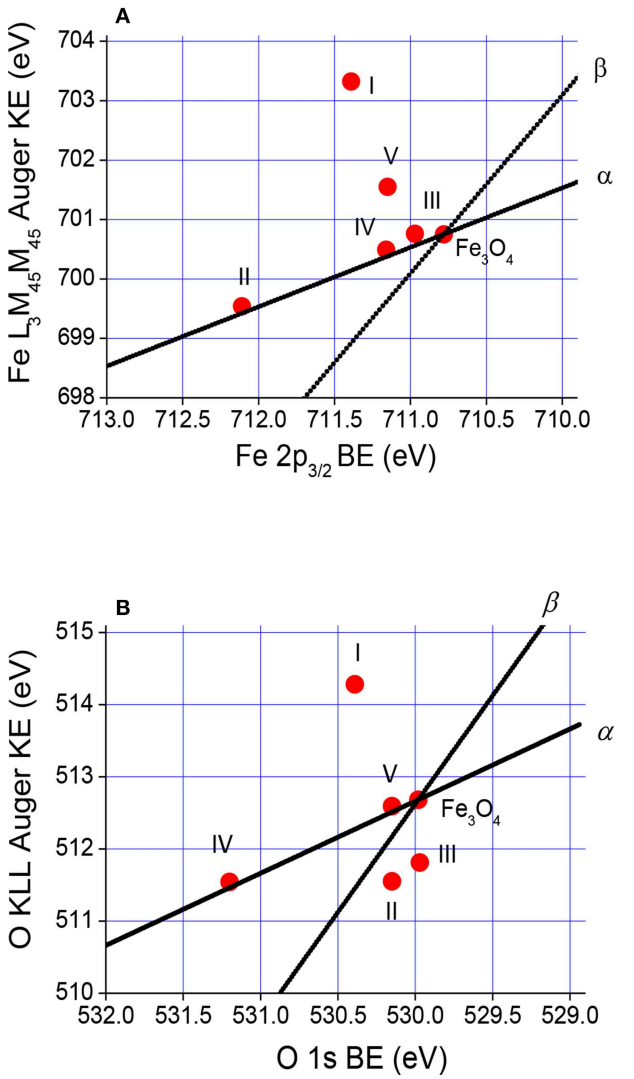

FIGURE 8 | Wagner plots for **(A)** Fe $L_3M_{45}M_{45}$ and Fe $2p_{3/2}$ spectra and **(B)** O KLL and O 1s spectra representing the investigated Fe_3O_4 MNPs and Fe_3O_4 f-MNPs I–V.

the initial core-hole. Therefore, any change of Auger spectral profile indicates modification of the local density of states. The core–core–core Auger electrons ($L_3M_{23}M_{2,3}$) are not involved into bonding in contrast to core–core–valence Auger electrons ($L_3M_{23}M_{45}$). The number of electrons from the Fe atom in the d states of the valence band, n^d, evaluated from the ratio of core–core–valence to core–core–core Auger intensities (Allen et al., 1977) decreases in the following order: 0.92 (sample I), 0.89 (Fe_3O_4 MNPs), 0.86 (sample III), 0.85 (samples II and IV), and 0.83 (sample V), and exhibits no direct relation with cytotoxicity.

Overlayer Thickness

The thickness of adsorbed molecule overlayers was evaluated using the following methods:

1. QUASES-Analyze (Tougaard, 1994–2002),
2. XPS MultiQuant (Mohai, 1999-2001, 2004), and
3. attenuation equation (Jablonski and Zemek, 2009)

and applying the inelastic mean free path (IMFP) values of photoelectrons from the G1 equation of Gries (1996).

QUASES-Analyze (Tougaard, 1994–2002) evaluates the surface morphology, i.e., type of depth profile, percent coverage and layer thickness from XPS spectra, and an inelastic background in the vicinity of the photoelectron peak. Exemplary results of QUASES-Analyze evaluations using the Buried Layer (BL) model without a standard and models of BL and Active Substrate (AS) with a Fe_3O_4 standard are shown in **Supplementary Figures S6A–C**, respectively. The values of surface coverage, adsorbed molecule overlayer thickness resulting from QUASES-Analyze BL and AS models without and with Fe_3O_4 standard, and averaged overlayer thickness are listed in **Table 2**.

The thickness resulting from XPS MultiQuant (Mohai, 1999-2001, 2004) was evaluated using the Layers-on-Sphere model. Although the particles are small, the large difference between the IMFP of the overlayer and a core allows using it (particle radius set to 10 nm). The composition, molecular weight, and IMFP values from G1 equation (Gries, 1996) for each adsorbed molecules are listed in **Table 3**. Other parameters applied are as follows: Al K_α excitation, Scofield cross section, and Reilman angular corrections for an analyzer input angle of 54.4°. The surface of Fe_3O_4 nanoparticles is oxygen deficient in comparison to functionalized nanoparticles I–V (**Figure 3**). After functionalization, the calculated thickness of contamination assuming CH_x hydrocarbon and possible other oxidized states (**Table 1**) is almost the same but the quantity of the missing oxygen is different. Due to the oxygen deficiency of the nanoparticles and their original carbonaceous contamination, the calculated layer thickness must be considered critically; presumably, the values calculated without oxygen are closer to reality. In the case of nitrogen-containing molecules, the nitrogen deficiency suggests that beside the adsorbed molecules, carbonaceous contamination is also present. It may be true for the other molecules as well. The values of overlayer thickness evaluated from XPS MultiQuant are listed in **Table 3**.

The following attenuation equation was applied (Jablonski and Zemek, 2009):

$$t = \lambda \cos\alpha \ln(R + 1) \tag{3}$$

Where λ is the IMFP from Gries G1 equation (Gries, 1996) and R is given by Equation 4:

$$R = \left(\frac{I_i^l}{I_j^s}\right)\left(\frac{I_j^o}{I_i^\infty}\right) \tag{4}$$

Where I_i^∞ is the intensity of the photoelectron signal from an infinitely thick layer, I_j^o is the signal intensity from the uncovered substrate, I_i^l is the intensity of the photoelectron signal from a layer of a thickness t, and I_j^s is the intensity of photoelectron signal from a substrate covered by a layer of thickness t.

TABLE 2 | Coverage and overlayer thickness resulting from QUASES-Analyze Buried Layer (BL) model without a standard, and BL and Active Substrate (AS) models with a Fe_3O_4 standard.

Sample	Analyze BL No standard thickness (nm)	Analyze BL Cov. (%)	Analyze BL Thickness (nm)	Analyze AS Thickness (nm)	Av. Thickness (nm)
III	1.34	50.6	1.19	1.2	1.24 ± 0.08
I	1.5	42.2	1.6	1.58	1.56 ± 0.05
V	1.51	70.5	1.58	1.59	1.56 ± 0.04
IV	2.38	61.0	2.26	2.27	2.30 ± 0.07
II	1.38	58.9	1.5	1.5	1.46 ± 0.07

Evaluation is performed from Fe $2p_{3/2}$ spectra recorded from Fe_3O_4 and Fe_3O_4 f-MNPs I–V. Sample f-MNPs I–V are listed in the order of decreasing cytotoxicity.

TABLE 3 | Parameters for determining overlayer thickness from XPS MultiQuant (Mohai, 1999-2001, 2004), attenuation equation (Equation 3) (Jablonski and Zemek, 2009), IMFP values for various overlayers from Gries G1 equation (Gries, 1996), and comparison of overlayer thickness values resulting from XPS MultiQuant, attenuation equation and effective thickness from QUASES-Analyze for Fe_3O_4 MNPs and Fe_3O_4 f-MNPs I–V.

Sample	Density (g cm^{-3})	Atomic weight (g mol^{-1})	N_v	Overlayers $IMFP_{Gries}$ (nm)	*t* (nm) Equation (3) ($IMFP_{Gries}$)	*t* (nm) XPS MultiQuant ($IMFP_{Gries}$)	Effective Av. thickness QUASES-analyze (nm) ($IMFP_{Gries}$)
Fe_3O_4	5.18	231.533	–	1.55	–	–	–
III	1.90	90.03 (anhydrous)	34	2.20	1.0	1.11	0.63
I	1.56	118.09	46	2.06	0.74	0.68	0.66
V	1.4601	147.13	58	2.11	1.42	1.04	1.10
IV	1.665	192.12 (anhydrous)	74	2.16	1.22	–	1.40
II	1.43	174.20	70	2.00	1.37	0.66	0.86

Sample f-MNPs I–V are listed in the order of decreasing cytotoxicity. The IMFP values were calculated for Fe $2p_{3/2}$ photoelectron kinetic energy.

The $\frac{I_i^\infty}{I_j^o}$ can be measured in a separate experiment and/or calculated from Equation 5:

$$\frac{I_i^\infty}{I_j^o} = \frac{S(E_i)\, M^l \lambda_i^l \left(d\sigma_x/d\Omega\right)_i}{S\left(E_j\right) M^s \lambda_j^s \left(d\sigma_x/d\Omega\right)_i} \tag{5}$$

where S is the spectrometer function, $d\sigma_x/d\Omega$ is a differential photoelectric cross section, M is atomic density of a given element (number of atoms in unit volume), $M = \frac{No\rho}{A}$, N_o is Avogadro number, λ_i^l is the IMFP for photoelectrons emitted in a layer l and moving in a layer l, λ_j^s is the IMFP for photoelectrons emitted in a substrate s and moving in a layer l, ρ is a density, A is atomic mass, and α is a detection angle with respect to the surface normal. The values of parameters for determining the layer thickness from Equation 3, IMFPs from Gries G1 equation (Gries, 1996), and the layer thickness resulting from Equation 3 are provided in **Table 3**. Comparison of adsorbed molecule layer thicknesses obtained from QUASES-Analyze (so-called effective layer thickness, i.e., layer thickness multiplied by a coverage), XPS MultiQuant, and attenuation equation (Equation 3), respectively, is provided in **Table 3** and **Figure 9**.

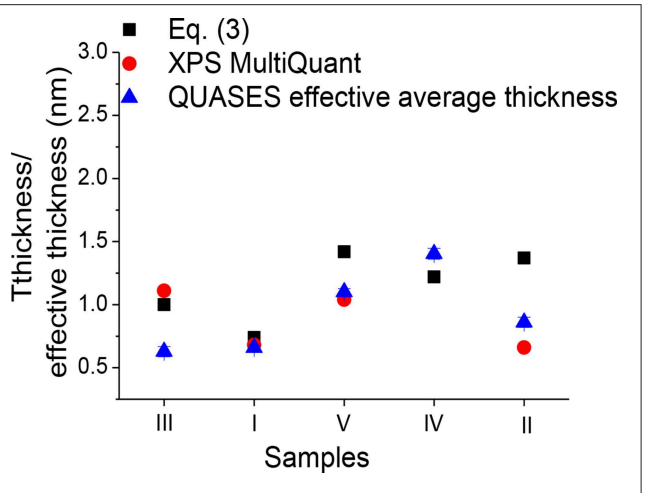

FIGURE 9 | Comparison of overlayer thickness resulting from attenuation equation (Equation 3) (solid square), XPS MultiQuant (solid circle), and effective average thickness resulting from QUASES-Analyze (solid triangle) for Fe_3O_4 f-MNPs I–V. Sample f-MNPs I–V are shown in the order of decreasing cytotoxicity.

REELS Spectra

Comparison of REELS spectra recorded from Fe_3O_4 MNPs and f-MNPs I–V and parameters derived from these spectra are shown in **Figure 10**. The electron scattering probabilities (elastic peak intensities) at 0 eV and inelastic scattering probabilities on valence band electrons in the region of about 80 eV above the

elastic peak (electron inelastic losses) show variations due to functionalization (**Figures 10A,B**) with no remarkable changes in elastic peak full width at half maximum (FWHM) of 0.83 ± 0.02 eV. The presented changes (**Figures 10A,B**) reflect modification of surface electronic and optical properties. The quantitative analysis of REELS spectra combined with Tougaard QUEELS algorithm (Tougaard and Yubero, 2008) may provide detailed information on parameters of surface electronic and optical properties (Tougaard and Yubero, 2008; Tahir et al., 2018). The band gap energy (E_g) value can be evaluated from REELS spectra since the plasmon loss peak exhibiting broad peaks with the energy in the vicinity of the elastic peak at 0 eV appears below the electron-hole interband transition. The onset of the loss spectrum is due to electron-hole excitation. The band gap energy was estimated from a linear fit line along the maximum negative slope at a point near the onset of the loss signal spectrum to the background level. The crossing of the linear fit line and the background level provides the band gap value (**Figure 10C**). The band gap energy values for Fe_3O_4 MNPs is 2.45 eV similarly as reported previously, i.e., 2.5 eV (Tahir et al., 2018). These values for Fe_3O_4 f-MNPs increase from 2.45 to 2.7 eV and exhibit decreasing dependence of band gap energy with decreasing carbon content and increasing nanoparticle size (**Figure 10D**). Similarly, increasing band gap energy values, i.e., from 2.4 to 2.9 eV, with increasing carbon content in Fe_3O_4 (Tahir et al., 2018) and decreasing Fe_3O_4 nanoparticle size (Kouotou et al., 2018) were reported previously. The inelastic scattering probability values showing changes due to functionalization (**Figures 10A–D**) provide evidences on modified optical and dielectric properties of the investigated surface (Tahir et al., 2018). No direct dependence of band gap energy of f-Fe_3O_4 MNPs on cytotoxicity tested for HeLa was observed, although this cytotoxicity was the highest for sample III of an intermediate nanoparticle size, the lowest carbon content, and the band gap energy value closest to that for Fe_3O_4.

Dependence of Cytotoxicity Tested for HeLa Cells on Surface Properties of Functionalized Fe_3O_4 Nanoparticles

Compilation of features indicating the differences in structural and chemical properties in the investigated surfaces Fe_3O_4 f-MNPs I–V in the order of decreasing cytotoxicity is compiled in **Table 4**. The highest cytotoxicity is observed for Fe_3O_4 f-MNPs with (i) the smaller surface coverage and thickness of biocompatible adsorbed molecules layers, (ii) the highest content of oxygen and carbon–oxygen functionalizing groups, (iii) the highest ratio of lattice O^{2-} and OH^- to C sp^2 hybridizations on MNP surface, (iv) the highest ratio of adsorbed O^- and OH^- to C sp^2 hybridizations due to adsorbed molecule layers, and (v) the closest electronic and optical properties to Fe_3O_4 shown in Auger parameters of XPS and Auger lines from Fe (**Figure 8A**) and REELS spectra (**Figures 10A–D**). No dependence of Cl and S contaminations and band gap energy was observed. No dependence of cytotoxicity on PDI and zeta potential values in the recorded range was shown. This would indicate that for the applied conditions of concentration, temperature, and pH, the sample homogeneity and ability for attachment to a negatively charged cell membrane are less important than the content of adsorbed molecule oxygen groups, which are responsible for generating ROS. Higher cytotoxicity is observed for MNPs of smaller hydrodynamic diameters (217.9–527.9 nm), indicating that adlayers of smaller polymerization degree will favor ROS generation.

Although different iron oxides and also Fe_3O_4 have been previously applied for diagnosis and in tumor therapy (Sangaiya and Jayaprakash, 2018), the biocompatibility of functionalized Fe_3O_4 MNPs is competitive to Fe_3O_4 nanoparticles. The enhanced cytotoxicity for HeLa cells has been previously reported for L-cysteine-conjugated ruthenium oxy-hydroxide ($RuO_x(OH)_y$) in comparison to $RuO_x(OH)_y$ (Ganguly et al., 2018). This cytotoxicity of L-cysteine-conjugated $RuO_x(OH)_y$ increasing with the concentration of this agent was attributed to the selective ability of HeLa cells to create bonding with this surface. According to the above, the cytotoxicity of f-MNPs seems to be related to interaction of cells with the applied agent surface, where both oxygen groups, Fe_3O_4 lattice O^{2-} and OH^-, and adsorbed O^- and OH^- play a role of adsorption and catalytic sites leading to the cytotoxicity of HeLa cells. Cytotoxicity was found to be higher for systems with a larger amount of double-carboxylic groups, which could enhance kinetics of Fenton reaction.

CONCLUSIONS

Functionalization of Fe_3O_4 MNPs with different adsorbed molecules (samples I–V) to increase biocompatibility of Fe_3O_4 MNPs provides no modification in biocompatibility on L929 cells. However, it leads to variation in cytotoxicity on HeLa cells decreasing in the order III ≈ I > V > IV > II due to chemical and morphology modification of Fe_3O_4 MNPs.

The adsorbed layers provide f-MNPs of various physicochemical properties since adsorption of amino acids leads to modification of their surface and interface, providing nanoparticles of different hydrodynamic diameters, polydispersities, and zeta potentials. Functionalization provides adsorbed layers on Fe_3O_4 MNPs of various thicknesses and partial dissolution of oxalic, glutamic, and citric acids in nanoparticles. The presence of Fe_3O_4 MNPs and adsorbed layer of different thicknesses is confirmed by FTIR-S and UV-vis absorption spectra. The adlayer thickness values resulting from UV-vis and QUASES are in a reasonable agreement. The adsorbed layers have different degrees of polymerization confirmed by hydrodynamic diameter value. The adsorption behavior of amino acids on MNPs confirmed by FTIR-S results in weaker (oxalic acid) and/or stronger (succinic, L-arginine, citric, glutamic acids) interactions between adlayers and MNPs and different zeta potential values of nanoparticles. The C/O atomic content ratio is larger at the surface than in the bulk, indicating formation of functionalizing carbon–oxygen layers with oxygen deficiency in comparison to Fe_3O_4 MNPs. These carbon–oxygen layers show C sp^2, C sp^3, and carboxyl (C–OOH) groups and also C–N, C–NH_3^+, C–NO_2, and C–NO_3 from adsorbed molecule

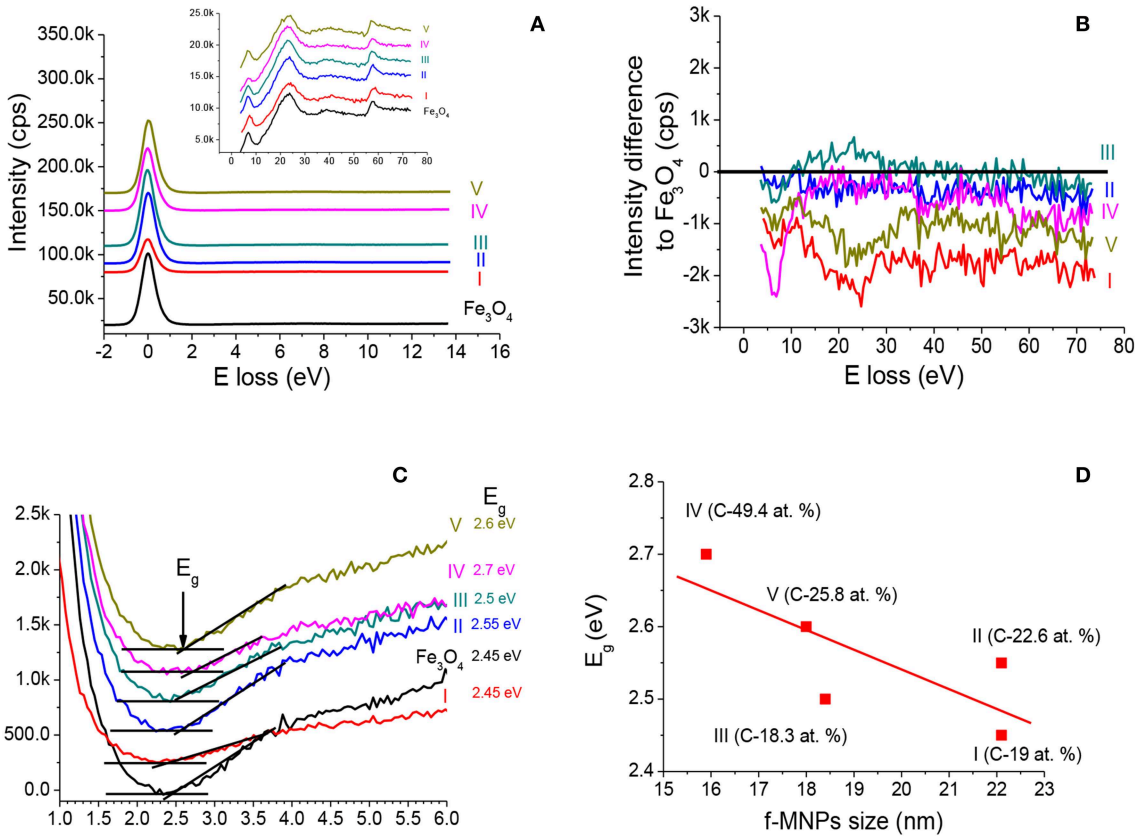

FIGURE 10 | (A) Comparison of elastic peak and spectrum of inelastic losses of electrons on valence band electrons recorded from Fe_3O_4 MNPs and f-MNPs. **(B)** Differences between the spectrum of inelastic losses of electrons on valence band electrons recorded from Fe_3O_4 f-MNPs and the respective spectrum recorded from Fe_3O_4 MNPs. **(C)** Evaluation of band gap energy values from REELS spectra recorded from Fe_3O_4 MNPs and f-MNPs. **(D)** Dependence of band gap energy values on Fe_3O_4 f-MNPs nanoparticle size (Rangam et al., 2017) and surface carbon content (**Supplementary Table S1**).

TABLE 4 | Dependence of cytotoxicity tested for HeLa cells on surface properties of Fe_3O_4 f-MNPs I–V.

Sample	Av.% cell death	Cov. (%)	Av. *t* (nm)	C–OOH +C–OH C 1s (at. %)	Total O/C sp^2 C 1s	Lattice O^{2-}+OH^-/C sp^2	Ads $(O^-+OH^-)_{ads}$ /C sp^2	D_H (nm)	PDI	Zeta potential (mV)	Overlayer interaction with MNPs
Fe_3O_4	–	–	–	1.7	0.12	3.01	0.16	601.3	0.171	0.56	–
III	10.8	50.6	0.91	5.4	0.57	3.47	0.98	217.9	0.853	0.83	Weaker
I	10.7	42.2	0.69	4.3	0.34	3.27	0.48	527.9	0.101	−0.53	Stronger
V	9.2	70.5	1.19	3.2	0.29	2.77	0.56	256.7	0.246	0.28	Stronger
IV	7.5	61.0	1.31	3.1	0.10	0.57	0.35	717.7	0.039	0.19	Stronger
II	5.3	58.9	0.96	2.5	0.20	0.36	0.29	871.2	0.237	−0.23	Stronger

Sample f-MNPs I–V are listed in the order of decreasing cytotoxicity. D_H, hydrodynamic diameter; PDI, polydispersity.

layers present at the surface, whereas Fe_3O_4 MNPs and f-MNPs show the presence of lattice O^{2-} and OH^- and adsorbed O^- and OH^-. The coverage of functionalizing adsorbed layers is 40–50% (oxalic and succinic acids) and 60–70% (L-arginine and citric and glutamic acid) and overlayer effective thickness is 0.69–1.31 nm. Such functionalization influences the magnetic, electronic, and optical properties of Fe_3O_4 MNPs. The modification of magnetic properties is manifested in changes of ratio of Fe $2p_{3/2}$ 2+ and 3+ tetrahedral and octahedral components and separation of Fe $2p_{3/2}$ photoelectron transition from inelastic plasmon. Modification of surface electronic charge redistribution and electronic and optical properties of f-MNPs is shown in the Auger parameters (derived from XPS and Auger spectra) and elastic/inelastic scattering probabilities of

electrons on atoms and valence band electrons (derived from REELS spectra).

No dependence of cytotoxicity on polydispersity and zeta potential of Fe_3O_4 f-MNPs is observed, whereas the highest cytotoxicity is observed for f-MNPs with (i) a lower degree of polymerization, (ii) the smaller surface coverage and thickness of biocompatible adsorbed molecules layers, (iii) the highest content of oxygen and carbon–oxygen functionalizing groups, (iv) the highest ratio of lattice O^{2-} and OH^- to C sp^2 hybridizations on MNP surface, (v) the highest ratio of adsorbed O^- and OH^- to C sp^2 hybridizations on adsorbed molecule layers, and (vi) the closest electronic and optical properties to Fe_3O_4 shown in Auger parameters of XPS and Auger lines from Fe and REELS spectra. No dependence of Cl and S contaminations, band gap energy, and number of electrons from the Fe atom in the d states of the valence band was observed.

The enhancement of cytotoxicity of f-MNPs is related to interaction of cells with these surfaces, where both oxygen groups and increasing content of lattice O^{2-} and OH^-, as well as adsorbed O^- and OH^- from biocompatible layers play a role of adsorption and catalytic sites and a large amount of double-carboxylic groups enhancing kinetics of Fenton reaction leading to cell damage. Since the cell viability and the type and mechanism of cell death are a more complex process, the results of the present work provide an indicative comparison of toxicity of the nanoparticles observed for HeLa cells focusing on nanoparticle surface properties and possible HeLa adsorption behavior.

DATA AVAILABILITY STATEMENT

All datasets generated for this study are included in the manuscript/**Supplementary Files**.

AUTHOR CONTRIBUTIONS

BL: XPS and REELS data evaluation, preparation of the manuscript. NR: XPS data evaluation, participating in preparation of the manuscript. PJ and IG: XPS data measurement, participating in preparation of the manuscript. JT: REELS data measurement, participating in preparation of the manuscript. LK: participating in preparation of the manuscript. MM: MultiQuant data evaluation, participating in preparation of the manuscript. PB: FTIR-S measurements and interpretation, participating in preparation of the manuscript.

FUNDING

Polish Academy of Sciences—supporting exchange visits, no funds for open access fees. Hungarian Academy of Sciences—supporting exchange visits, no funds for open access fees. Academy of Sciences and Academy of Sciences of the Czech Republic—supporting exchange visits, no funds for open access fees. European Regional Development Fund and Hungary in the frame of the project GINOP-2.2.1-15-2016-00012—funds for Hungarian laboratory, no funds for open access fees. Horizon 2020 MSCA-COFUND agreement No. 711859—Ph.D. scholarship funds, limited funds for open access fees. Financial resources for science in the years 2017-2021 for an international co-financed project (3549/H2020/COFUND/2016/2)—limited funds for open access fees. Ministry of Education, Youth and Sports of the Czech Republic, grant number LM2015088, no funds for open access fees.

ACKNOWLEDGMENTS

BL, LK, JT, and MM acknowledge the support of a bilateral project between the Polish Academy of Sciences and the Hungarian Academy of Sciences. BL and PJ acknowledge the support of a bilateral project between the Polish Academy of Sciences and the Academy of Sciences of the Czech Republic. JT acknowledges the support by the European Regional Development Fund and Hungary in the frame of the project GINOP-2.2.1-15-2016-00012. BL, NR, and LK acknowledge the support of Horizon 2020 MSCA-COFUND agreement No. 711859 and the financial resources for science in the years 2017–2021 for an international co-financed project (3549/H2020/COFUND/2016/2). IG and PJ acknowledge support via the grant LM2015088 of the Ministry of Education, Youth and Sports of the Czech Republic. The authors would like to thank Prof. N. K. Sahu (Center for Nanotechnology and Research, VIT University Vellore, India) for helpful discussion and comments. The authors would like to thank Dr. A. Wiśniewska (Institute of Physical Chemistry, Polish Academy of Sciences) for TGA/DSC measurements.

SUPPLEMENTARY MATERIAL

The Supplementary Material for this article can be found online at: https://www.frontiersin.org/articles/10.3389/fchem.2019.00642/full#supplementary-material

REFERENCES

Allen, G. C., Tucker, P. M., and Wild, R. K. (1977). High resolution LMM Auger electron spectra of some first row transition elements. *Surf. Sci.* 68, 469–469. doi: 10.1016/0039-6028(77)90240-0

Asgari, S., Fakhari, Z., and Berijani, S. (2014). Synthesis and characterization of Fe_3O_4 magnetic nanoparticles coated with carboxymethyl chitosan grafted sodium methacrylate. *Nanostructures* 4, 55–63. doi: 10.7508/JNS.2014.01.007

Bahadur, A., Saeed, A., Shoaib, M., Iqbal, S., Bashir, M. I., Waqas, M., et al. (2017). Eco-friendly synthesis of magnetite (Fe_3O_4) nanoparticles with tunable size: dielectric, magnetic, thermal and optical studies. *Mater. Chem. Phys.* 198, 229–235. doi: 10.1016/j.matchemphys.2017.05.061

Bian, J., Wang, Y., Zhang, Q., Fang, X., Feng, J., and Li, C. (2017). Fatty acid decarboxylation reaction kinetics and pathway of co-conversion with amino acids on supported iron oxide catalysts. *RSC Adv.* 7, 47279–47287. doi: 10.1039/C7RA08507A

Bichara, L. C., Lanús, H. E., Ferrer, E. G., Gramajo, M. B., and Brandán, S. A. (2011). Vibrational study and force field pf the citric acid dimer based on the SQM methodology. *Adv. Phys. Chem.* 2011:347072. doi: 10.1155/2011/347072

Bordbar, A. K., Rastegari, A. A., Amiri, R., Ranjbakhsh, E., Abbasi, M., and Khosropour, A. R. (2014). Characterization of modified magnetite nanoparticles for albumin immobilization. *Biotechnol. Res. Int.* 2014:705068. doi: 10.1155/2014/705068

Butenko, Y. V., Krishnamurthy, S., Chakraborty, A. K., Kuznetsov, V. L., Dhanak, V. R., Hunt, M. C., et al. (2005). Photoemission study of onion like carbons produced by annealing nanodiamonds. *Phys. Rev. B* 71, 75420–75410. doi: 10.1103/PhysRevB.71.075420

Cole, R. J., Brooks, N. J., Weightman, P., and Matthew, J. A. D. (1995). Onset of d screening in alkali and alkaline earths. *Phys. Rev. B* 52, 2976–2982. doi: 10.1103/PhysRevB.52.2976

Cole, R. J., and Weightman, P. (1994). Separating ground state and screening contributions to chemical shifts. *J. Phys. Condens. Matter* 6, 5783–5790. doi: 10.1088/0953-8984/6/29/020

Eltouny, N., and Ariya, P. A. (2014). Competing reactions of selected atmospheric gases on Fe_3O_4 nanoparticles surfaces. *Phys. Chem. Chem. Phys.* 6, 23056–23066. doi: 10.1039/C4CP02379J

Fujimoto, A., Yamada, Y., Koinuma, M., and Sata, S. (2016). Origins of sp^3C peaks in C_{1s} X-ray photoelectron spectra of carbon materials. *Anal. Chem.* 88, 6110–6114. doi: 10.1021/acs.analchem.6b01327

Gaarenstroom, D. W., and Winograd, N. (1977). Initial and final state effects in the ESCA spectra of cadmium and silver oxides. *J. Chem. Phys.* 67, 3500–3506. doi: 10.1063/1.435347

Ganguly, B. N., Maity, B., Maity, T. K., Manna, J., Roy, M., Mukherjee, M., et al. (2018). L-cysteine-conjugated ruthenium hydrous oxide nanomaterials with anticancer active application. *Langmuir* 34, 1447–1456. doi: 10.1021/acs.langmuir.7b01408

Gries, W. H. (1996). An universal predictive formula for the inelastic mean free pathlengths of x-ray photoelectrons and Auger electrons. *Surf. Interface Anal.* 24, 38–50.

Grosvenor, A. P., Cobe, B. A., and McIntyre, N. S. (2004a). Examination of the oxidation of iron by oxygen using X-ray photoelectron spectroscopy and QUASES. *Surf. Sci.* 565, 151–162. doi: 10.1016/j.susc.2004.06.210

Grosvenor, A. P., Cobe, B. A., and McIntyre, N. S. (2004b). Studies of the oxidation of iron by water vapour using X-ray photoelectron spectroscopy and QUASES. *Surf. Sci.* 572, 217–227. doi: 10.1016/j.susc.2004.08.035

Grosvenor, A. P., Kobe, B. A., Biesinger, M. C., and Mcintyre, N. S. (2004c). Investigation od multiplet splitting of Fe 2p XPS spectra and bonding in iron compounds. *Surf. Interface Anal.* 36, 1564–1574. doi: 10.1002/sia.1984

Gupta, A. K., and Gupta, M. (2005). Cytotoxicity suppression and cellular uptake enhancement of surface modified magnetic nanoparticles. *Biomaterials* 26, 1565–1573. doi: 10.1016/j.biomaterials.2004.05.022

Herng, T. S., Xiao, W., Poh, S. M., He, F., Sutarto, R., Zhu, X., et al. (2015). Achieving a high magnetization in sub-nanostructured magnetite films by spin-flipping of tetrahedral Fe^{3+} cations. *Nano Res.* 8, 2935–2945. doi: 10.1007/s12274-015-0798-7

Hu, Y., Liu, W., and Wu, F. (2017). Novel multi-responsive polymer magnetic microgels with folate or methyltetrahydrofolate. *RSC Adv.* 7, 10333–10344. doi: 10.1039/C6RA27114F

Infrared Spectroscopy-MSU Chemistry (2013). Available online at: http://www2.chemistry.msu.edu/faculty/reusch/virttxtjml/Spectrpy/InfraRed/infrared.htm (accessed July 31, 2019).

Jablonski, A., and Zemek, J. (2009). Overlayer thickness determination by XPS using the multiline approach. *Surf. Interface Anal.* 41, 193–204. doi: 10.1002/sia.3005

Kim, D.-H., Kim, K.-N., Kim, K.-M., and Lee, Y.-K. (2009). Targeting to carcinoma cells with chitosan- and starch-coated magnetic nanoparticles for magnetic hyperthermia. *J. Biomater. Res. A* 88, 1–11. doi: 10.1002/jbm.a.31775

Kim, J., Jung, J., Lee, J., Na, K., Park, S., and Hyun, J. (2010). Amphiphilic comblike polymers enhance the colloidal stability of Fe_3O_4 nanoparticles. *Colloids Surf. B Biointerfaces* 76, 236–240. doi: 10.1016/j.colsurfb.2009.10.042

Kouotou, P. M., El-Kasmi, A., Wu, L. N., Wagas, M., and Tian, Z. Y. (2018). Particle size-band gap energy–catalytic properties relationship of PSE-CVD-derived Fe_3O_4 thin films. *J. Taiwan Inst. Chem. Engineers* 93, 427–435. doi: 10.1016/j.jtice.2018.08.014

Kövér, L., Varga, D., Cserny, I., Tóth, J., and Tokési, J. (1992). Some applications of high-energy, high-resolution Auger-electron spectroscopy using Bremsstrahlung radiation. *Surf. Interface Anal.* 19, 9–15. doi: 10.1002/sia.740190106

Krishnan, S., Raj, J. C., Robert, R., Ramanand, A., and Das, J. S. (2007). Growth and characterization of succinic acid single crystals. *Cryst. Res. Technol.* 42, 1087–1090. doi: 10.1002/crat.200710981

Kumar, S., and Rai, S. B. (2010). Spectroscopic studies of L-arginine molecule. *Indian J. Pure Appl.* Physics 48, 251–255. Available online at: http://nopr.niscair.res.in/handle/123456789/7643

Kwok, R. W. M. (2000). *XPS Peak Fitting Program for WIN95/98 XPSPEAK, ver. 4.1*. Shatin: Department of Chemistry, The Chinese University of Hong Kong.

Lesiak, B., Kövér, L., Tóth, J., Zemek, L., Jiricek, P., Kromka, A., et al. (2018). C sp^2/sp^3 hybridisations in carbon nanomaterials—XPS and (X)AES study. *Appl. Surf. Sci.* 452, 223–231. doi: 10.1016/j.apsusc.2018.04.269

Lesiak, B., Zemek, J., Jiricek, P., and Stobinski, L. (2009). Temperature modification of oxidized multiwall carbon nanotubes studied by electron spectroscopy methods. *Phys. Status Solidi B* 246, 2645–2649. doi: 10.1002/pssb.200982268

Li, Z. Y., Jibran, M., Sun, X., Pratt, A., Wang, B., Yamauchi, Y., et al. (2018). Enhancement of the spin polarization of an Fe_3O_4(100) surface by nitric oxide adsorption. *Phys. Chem. Chem. Phys.* 20, 15871–15875. doi: 10.1039/C8CP02361A

Linh, P. H., Chien, N. V., Dung, D. D., Nam, P. H., Hoa, D. T., Anh, N. T. N., et al. (2018). Biocompatible nanoclusters of O-carboxymethyl chitosan-coated Fe_3O_4 nanoparticles: synthesis, characterization and magnetic heating efficiency. *J. Mater. Sci.* 53, 8887–8900. doi: 10.1007/s10853-018-2180-0

Liu, Y., Cui, T., Li, Y., Zhao, Y., Ye, Y., Wu, W., et al. (2016). Effects of crystal size and sphere diameter on static magnetic and electromagnetic properties of monodisperse Fe_3O_4 microspheres. *Mater. Chem. Phys.* 173, 152–160. doi: 10.1016/j.matchemphys.2016.01.053

Mahdavi, M., Namvar, F., Ahmad, M. B., and Mahamad, R. (2013). Green biosynthesis and characterization of magnetic iron oxide (Fe_3O_4) nanoparticles using seaweed (*Sargassum muticum*). *Molecules* 18, 5954–5964. doi: 10.3390/molecules18055954

Massart, R. (1981). Preparation of aqueous magnetic liquids in alkaline and acidic media. *IEEE Trans. Magn.* 17, 1247–1248. doi: 10.1109/TMAG.1981.1061188

Mohai, M. (1999-2001). Multimodel of X-ray photoelectron spectroscopy quantification program for 32-bit Windows, XPS MultiQuant, ver. 7.

Mohai, M. (2004). XPS MultiQuant: multimodel XPS quantification software. *Surf. Interface Anal.* 36, 828–832. doi: 10.1002/sia.1775

Muthuselvi, C., Arunkumar, A., and Rajaperumal,. G. (2016). Growth and characterization of oxalic acid doped with tryptophan crystal for antimicrobial activity. *Der Chimica Sinica* 7, 55–62. Available online at: https://www.researchgate.net/publication/319327894

Panias, D., Taxiarchou, M., Paspaliaris, I., and Kontopoulos, A. (1996). Mechanisms of dissolution of iron oxides in aqueous oxalic acid solutions. *Hydrometallurgy* 42, 257–265. doi: 10.1016/0304-386X(95)00104-O

Petran, A., Radu, T., Borodi, G., Nan, A., Suciu, M., and Turcu, R. (2018). Effects of rare earth doping on multi-core iron oxide nanoparticles properties. *Appl. Surf. Sci.* 428, 492–499. doi: 10.1016/j.apsusc.2017.09.160

Poulin, S., França, R., Moreau-Bélanger, L., and Sacher, E. (2010). Confirmation of X-ray photoelectron spectroscopy peak attributions of nanoparticulate iron oxides, using symmetric peak component line shapes. *J. Phys. Chem. C* 114, 10711–10718. doi: 10.1021/jp100964x

Rangam, N., Sahu, N. K., Jaiswal, A., and Jayesh, B. (2017). Synthesis of surface grafted mesoporous magnetic nanoparticles for cancer therapy. *J. Nanosci. Nanotech.* 17, 5181–5188. doi: 10.1166/jnn.2017.13853

Runowski, M., and Lis, S. (2016). Synthesis, surface modification/decoration of luminescent-magnetic core/shell nanomaterials, based on the lanthanide doped fluorides ($Fe_3O_4/SiO_2/NH_2/PAA/LnF_3$). *J. Luminescence* 170, 484–490. doi: 10.1016/j.jlumin.2015.05.037

Sahu, N. K., Gupta, J., and Bahadur, D. (2015). PEGylated FePt-Fe_3O_4 composite nanoassemblies (CNAs): *in vitro* hyperthermia, drug delivery and generation of reactive oxygen species (ROS). *Dalton Trans.* 44, 9103–9113. doi: 10.1039/C4DT03470H

Sangaiya, P., and Jayaprakash, R. (2018). A review on iron oxide nanoparticles and their biomedical applications. *J. Supercond. Novel Magn.* 31, 3397–3413. doi: 10.1007/s10948-018-4841-2

Scofield, H. (1976). Hartree-Slater Subshell Photoionization Cross-sections at 1254 and 1487 eV. *J. Electron Spectrosc. Relat. Phenom.* 8, 129–137. doi: 10.1016/0368-2048(76)80015-1

Sengupta, P. K., and Krimm, S. (1985). Vibrational analysis of peptides, polypeptides, and proteins. *Biopolymers* 24, 1479–1491. doi: 10.1002/bip.360240805

Shim, S. H., Kim, K. T., Lee, Y. U., and Jo, W. H. (2012). Facile method to functionalize graphene oxide and its application to poly(ethylene terephthalate)/graphene composite. *ACS Appl. Mater. Interfaces* 4, 4184–4191. doi: 10.1021/am300906z

Silverstein, R. M., Bassler, G. C., and Morrill, T. C. (1981). *Spectrometric Identification of Organic Compounds*. 4th ed. New York, NY: John Wiley and Sons. Available online at: http://www2.ups.edu/faculty/hanson/Spectroscopy/IR/IRfrequencies.html

Soares, P. I. P., Lochte, F., Echeverria, C., Pereira, L. C. J., Coutinho, J. T., Ferreira, I. M. M., et al. (2015). Thermal and magnetic properties of iron oxide colloids: Influence of surfactants. *Nanotechnology* 26:425704. doi: 10.1088/0957-4484/26/42/425704

Stobinski, L., Lesiak, B., Zemek, J., and Jiricek, P. (2012). Time dependent thermal treatment of oxidized MWCNTs studied by the electron and mass spectroscopy methods. *Appl. Surf. Sci.* 258, 7912–7917. doi: 10.1016/j.apsusc.2012.04.127

Stobinski, L., Lesiak, B., Zemek, J., Jiricek, P., Biniak, S., and Trykowski, G. (2010). Studies of oxidized multiwall carbon nanotubes in the temperature range from RT to 630 °C by the infrared and electron spectroscopy methods. *J. Alloys Comp.* 505, 379–384. doi: 10.1016/j.jallcom.2010.05.185

Taghavi, F., Saljooghi, A. S., Gholizadeh, M., and Ramezani, M. (2016). Deferasirox-coated iron oxide nanoparticles as a potential cytotoxic agent. *Med. Chem. Commun.* 7, 2290–2298. doi: 10.1039/C6MD00293E

Tahir, D., Ilvas, S., Abdullah, B., Armynah, B., and Kang, H. J. (2018). Electronic properties of composite iron (II, III) oxide Fe_3O_4 carbonaceous absorber materials by electron spectroscopy. *J. Electron Spectrosc. Rel. Phenom.* 229, 47–51. doi: 10.1016/j.elspec.2018.09.008

Tomitaka, A., Yamaga, T., and Takemura, Y. (2012). Magnetic nanoparticle hyperthermia using pluronic-coated Fe_3O_4 nanoparticles: an *in vitro* study. *J. Nanomater.* 2012:480626. doi: 10.1155/2012/480626

Tougaard, S. (1994–2002). *Software for Quantitative XPS/AES of Surface Nano-Structures by Analysis of the Peak Shape and Background, ver. 5.0*. Odense: QUASES-Tougaard Inc.

Tougaard, S. (1999–2001). *Background Analysis of XPS/AES-QUASES Simple Backgrounds, ver. 2.2*. Odense: QUASES-Tougaard Inc. Available online at: http://www.quases.com

Tougaard, S., and Yubero, F. (2008). *QUEELS-ε(k,ω)-REELS: Quantitative Analysis of Electron Energy Loss Spectra: Dielectric Function Determined by Reflection Electron Energy Loss Spectroscopy, ver. 3.0*. Odense: QUASES-Tougaard Inc.

Wagner, C. D. (1972). Auger lines in x-ray photoelectron spectrometry. *Anal. Chem.* 44, 967–973. doi: 10.1021/ac60314a015

Wagner, C. D., Naumkin, A. V., Kraut-Vass, A., Allison, J. W., Powell, C. J., and Rumble, J. R. Jr. (2012). *NIST X-Ray Photoelectron Database, NIST SRD 20, ver. 4.1., online, PC*. Gaithersburg: NIST, U.S. Department of Commerce.

Wei, Y., Han, B., Hu, X., Lin, Y., Wang, X., and Deng, X. (2012). Synthesis of Fe_3O_4 nanoparticles and their magnetic properties. *Proc. Engineering* 27, 632–637. doi: 10.1016/j.proeng.2011.12.498

Yamashita, T., and Hayes, P. (2008). Analysis of XPS spectra of Fe^{2+} and Fe^{3+} ions in oxide materials. *Appl. Surf. Sci.* 254, 492–499. doi: 10.1016/j.apsusc.2007.09.063

Conflict of Interest: The authors declare that the research was conducted in the absence of any commercial or financial relationships that could be construed as a potential conflict of interest.

frontiers in Chemistry

ORIGINAL RESEARCH
published: 01 November 2019
doi: 10.3389/fchem.2019.00722

Synthesis of Graphene Oxide Interspersed in Hexagonal WO_3 Nanorods for High-Efficiency Visible-Light Driven Photocatalysis and NH_3 Gas Sensing

*Tarek M. Salama[1], Mohamed Morsy[2], Rabab M. Abou Shahba[3], Shimaa H. Mohamed[3] and Mohamed Mokhtar Mohamed[4]**

[1] Department of Chemistry, Faculty of Science, Al-Azhar University, Cairo, Egypt, [2] Building Physics and Environment Institute, Housing and Building National Research Center (HBRC), Giza, Egypt, [3] Department of Chemistry, Faculty of Science (Girls Branch), Al-Azhar University, Cairo, Egypt, [4] Chemistry Department, Faculty of Science, Benha University, Benha, Egypt

OPEN ACCESS

Edited by:
Min-Cherl Jung,
Nara Institute of Science and Technology (NAIST), Japan

Reviewed by:
Jianhui Sun,
Henan Normal University, China
Jung Ho Yun,
University of Queensland, Australia

***Correspondence:**
Mohamed Mokhtar Mohamed
mohmok2000@yahoo.com

Specialty section:
This article was submitted to Physical Chemistry and Chemical Physics, a section of the journal Frontiers in Chemistry

Received: 20 April 2019
Accepted: 10 October 2019
Published: 01 November 2019

Citation:
Salama TM, Morsy M, Abou Shahba RM, Mohamed SH and Mohamed MM (2019) Synthesis of Graphene Oxide Interspersed in Hexagonal WO_3 Nanorods for High-Efficiency Visible-Light Driven Photocatalysis and NH_3 Gas Sensing. Front. Chem. 7:722. doi: 10.3389/fchem.2019.00722

WO_3 nanorods and GO (at 1 wt% loading) doped WO_3 were synthesized using a template free deposition-hydrothermal route and thoroughly characterized by various techniques including XRD, FTIR, Raman, TEM-SAED, PL, UV-Vis, XPS, and N_2 adsorption. The nano-materials performance was investigated toward photocatalytic degradation of methylene blue dye (20 ppm) under visible light illumination (160 W, $\lambda > 420$) and gas sensing ability for ammonia gas (10–100 ppm) at 200°C. HRTEM investigation of the 1%GO.WO_3 composite revealed WO_3 nanorods of a major *d*-spacing value of 0.16 nm indexed to the crystal plane (221). That relevant plane was absent in pure WO_3 establishing the intercalation with GO. The MB degradation activity was considerably enhanced over the 1%GO.WO_3 catalyst with a rate constant of 0.0154 min^{-1} exceeding that of WO_3 by 15 times. The reaction mechanism was justified dependent on electrons, holes and •OH reactive species as determined via scavenger examination tests and characterization techniques. The drop in both band gap (2.49 eV) and PL intensity was the main reason responsible for enhancing the photo-degradation activity of the 1%GO.WO_3 catalyst. The later catalyst initiated the two electron O_2 reduction forming H_2O_2, that contributed in the photoactivity improvement via forming •OH moieties. The hexagonal structure of 1%GO.WO_3 showed a better gas sensing performance for ammonia gas at 100 ppm (R_a-R_g/R_g = 17.6) exceeding that of pure WO_3 nanorods (1.27). The superiority of the gas-sensing property of the 1%GO.WO_3 catalyst was mainly ascribed to the high dispersity of GO onto WO_3 surfaces by which different carbon species served as mediators to hinder the recombination rate of photo-generated electron-hole pairs and therefore facilitated the electron transition. The dominancy of the lattice plane (221) in 1%GO.WO_3 formed between GO and WO_3 improved the electron transport in the gas-sensing process.

Keywords: hexagonal WO_3, graphene oxide, hydrothermal method, gas sensing, MB photocatalysis, visible light irradiation

INTRODUCTION

The nanoscience and nanotechnology have allowed the development of nanosized materials of unique electronic and optical properties quite different from those of their bulk states (Pang et al., 2010). Metal nanoparticles were recognized to reveal sum of unique optical and electronic properties, which result largely from surface plasmon resonance phenomenon. However, the high cost and low stability following annealing usually limits their applications. Nevertheless, composite materials including metal oxide nanoparticles have drawn great attention due to their unique chemical and physical properties, which make them applicable for use in photocatalysis and gas sensing (Bittencourt et al., 2006; Guo et al., 2012; Chen et al., 2013). Among the existing metal oxides, tungsten oxide (WO_3) as an n-type semiconductor of a band gap of 2.5–2.8 eV owns important applications in numerous fields (Zeng et al., 2012; Gui et al., 2015; Behera and Chandra, 2018). WO_3-based nanomaterials with various morphologies have been widely investigated for chemical gas sensors (Chu et al., 2017; Kaur et al., 2018; Gao et al., 2019) such as for detecting NH_3, H_2, and ethanol (Tsai et al., 2017; Chen et al., 2018; Morsy et al., 2018, 2019). Besides, it has attracted a lot of interest in photocatalysis theme because of its strong adsorption, manipulated energy band gap and visible light absorption (Zhang et al., 2017). However, the application of WO_3 as gas sensors is reduced by the bad selectivity, long response time, low sensitivity and high resistivity (Urasinska-Wojcik et al., 2016). Generally, nanocrystalline semiconductors have poor charge mobility and thus produce very limited photocurrent. This regards as one of the biggest obstacle that hinder the usage of WO_3 as practical photocatalysts. Thus, many attempts have been made to improve the behavior of WO_3 such as morphology control, surface hybridization and forming hybrid composites (Li et al., 2015; Galstyan et al., 2016; Shendage et al., 2017). Improved photocatalytic activities and gas sensing performances have been demonstrated for WO_3-graphene composite. Recently, graphene-based composites have received considerable attention due to their potential applications in many useful fields including photocatalysis (Zhang et al., 2015; Luna et al., 2018) and gas sensors (Behera and Chandra, 2018). The enhanced performance was based on the composite high conductivity, large surface area and the P-type conductivity created due to adsorbed oxygen molecules localized on graphene structure. With attaching an n-type semiconductor, it might be feasible to boost the reaction activity based on the facile charge transfer via the p-n junction interface. Expectedly, graphene not only can facilitate the nucleation and growth of the nanocrystals but also help achieving its stability and size beside it can orientate the oxide crystal growth (Zhang et al., 2015; Quan et al., 2017).

For the purpose of optimizing WO_3 nanoparticles for improving ammonia gas sensing and MB photocatalytic degradation, the surface hybridization of WO_3 with a small loading of GO was carried out. Thus, GO at 1 wt% loading was successfully dispersed in the matrix of WO_3 hexagonal structure as synthesized by the *in-situ* deposition hydrothermal technique. The 1%GO.WO_3 and WO_3 free GO catalysts were well-characterized using various techniques including XRD, TEM-SAED, UV-Vis, PL, FTIR, Raman, XPS, and N_2 sorptiometry. The catalysts were then tested as visible light photocatalysts toward methylene blue (MB) degradation and as gas sensors for NH_3 gas.

EXPERIMENTAL

Materials and Methods

Sodium tungstate dihydrate (Nice Chemicals, India), hydrochloric acid (Fisher Scientific, UK), oxalic acid (Adwic, Egypt), potassium permanganate, and sulfuric acid (Sigma-Aldrich, Germany), sodium nitrite (BDH Prolabo chemicals, USA), graphite (Merck, Germany), hydrogen peroxide (GFS Chemicals, USA), and methylene blue dye (S.D. Fine-Chem Limited, India) were used as obtained.

Synthesis of WO_3 Nanorods

Sodium tungstate (6.6 g, 0.2 mol) was dissolved in 100 ml distilled water and then acidified with HCl till pH 1, to form an immediate white precipitate. This precipitate was dissolved in 30 ml distilled water containing 0.4 g oxalic acid to obtain clear and transparent solution. The final solution was transferred to 40 ml Teflon stainless steel autoclave and maintained at 180°C for 26 h. After reaction, the product was washed several times with distilled water and ethanol to remove any unreacted residuals and finally dried at 100°C for 1 h.

Synthesis of Graphene Oxide-Loaded Tungsten Oxide Nanorods

A typical synthesis procedure of GO loaded onto WO_3 nanorods with a GO loading of 1% by weight was as follows. A definite amount of GO was dissolved in 50 ml distilled water to form a pasty brownish color solution. To this solution, a proper sodium tungstate (6.6 g, 0.2 mol) solution was slowly added and the pH of the mixture was adjusted to 1 by addition of aqueous HCl. Then, 0.4 g of oxalic acid dissolved in 30 ml water was added and stirred continuously at room temperature for 3 h. The latter mixture was transferred into a 250 ml Teflon stainless steel autoclave and maintained at 180°C for 26 h to get the final product. This catalyst is denoted as 1%GO.WO_3.

Physical Methods and Analysis

The powder X-ray diffraction (XRD) patterns were recorded, on Ni-filtered copper radiation (λ =1.5404 Å) at 45 kV and 40 mA with a scanning speed of $2\theta = 2.5°$/min, on a Bruker diffractometer, type D8 ADVANCE (Germany). The TEM micrographs were measured with a FEI Tecnai G20 Super-Twin microscope (USA), at an accelerating voltage of 200 kV. The powder samples were put on carbon foils with a microgrid and the TEM images were measured with minimum electron irradiation to prevent the samples damage, together with the selected area electron diffraction patterns. Fourier transform infrared (FT-IR) spectra were recorded via a single beam Perkin-Elmer Spectrometer (RXI, USA) with a resolution of 2 cm^{-1} in the region 4,000–400 cm^{-1}. Raman spectra were obtained with a Bruker Senterra Raman spectrometer (Germany), using the 532 nm line as the excitation beam. The incident laser power

and resolution were 5 mW and 2 cm^{-1}, respectively. The surface properties namely BET surface area, total pore volume (V_p) and mean pore radius (r^-) were determined from the nitrogen adsorption isotherms measured at −196°C using a Nova 3200 porosimeter, USA. The solid samples were out-gassed at 473 K for 2 h under a reduced pressure of 10^{-4} Torr before starting the measurements. Diffuse Reflectance UV–Vis spectra (UV–Vis DRS) were recorded using a UV–Vis JASCO spectrophotometer (V-570, Japan) in the range of 200–1,000 nm. The edge energy (E_g) was determined by finding the intercept of the straight line in the low-energy rise of the plot of $[F(R_\infty)h\nu]^2$, for the direct allowed transition vs. hν, where hν is the incident photon energy. The photoluminescence (PL) excitation and emission spectra were measured on a FL/FS 900 time resolved fluorescence spectrometer. The measurements were conducted at room temperature using a He-Cd laser (310 nm), as an excitation source. X-ray photoelectron spectroscopy (XPS) equipped with an Al-Kα x-ray source at energy of 1486.6 eV was utilized to distinguish the surface chemical composition of the catalysts. Electrochemical measurements were determined using Digi-Ivy 2116 B, USA, in 6.0 M KOH aqueous solution for determining either N_D or N_A concentration using the Mott-schottky plot. More details information about the measurement conditions can be found elsewhere (Mohamed et al., 2017).

Photocatalytic Degradation Experiments

The photocatalyst (100 mg) was suspended in 100 mL aqueous solution containing 20 mg L^{-1} methylene blue (MB). For each experiment, the suspension was stirred in dark for 60 min to establish the adsorption–desorption equilibrium between the MB and the catalyst, followed by irradiation with a high-pressure Philips lamp of 160 W with an average light intensity of 60 $mWcm^{-2}$, emitting only visible light (400–700 nm) via using a cut-off filter. Three ml aliquot containing dye and catalyst powder was taken out followed by centrifuging at 3,000 rpm for 5 min. After the catalyst separation, the change in MB concentration was determined through the absorbance variation at the wavelength of 664 nm. The absorption spectra of the aqueous solution of the MB after adsorption and degradation were measured using a Shimadzu UV-2350 spectrophotometer, Japan. The reactive species were also determined to stand on the degradation mechanism via employing various scavengers.

Sensor Fabrication and Evaluation

Fluorinated tin oxide (FTO) glass substrate has been used for sensors fabrication. In a typical procedure, 1 mm gap was created on the conductive FTO substrate using an electric arc followed by washing/cleaning processes via soaking in a soap solution for 10 min, flowed by distilled water and acetone. Finally, the FTO substrate was dried under N_2 flux. The electrical contacts were established via attaching two copper foils with conductive adhesive onto the FTO substrate. A proper amount of the GO.WO_3 composite was mixed with deionized water in a mortar forming a paste. The paste was then applied onto the FTO substrate and annealed at 80°C for 4 h. The sensor was aged at 5 V for 36 h to enhance its stability. Following stabilization of the sensor resistance, a known concentration of ammonia gas was generated by injection into a fixed volume chamber supplied with heater. The ammonia gas concentration in ppm was calculated using the following equation: $\boldsymbol{Vi = C.V.MW/22.45\ D}$, Where MW is the molecular weight of ammonia, D is the density of ammonia, V is the chamber volume, C is the concentration of ammonia in ppm, and Vi is the injected volume of ammonia. The real time resistance variation was recorded every 3 s by a digital precision pico-ammeter type keithley-6487 interfaced to a computer. The response of the sensor (R_a- R_g/R_g) ∗ 100 was defined as the ratio of the resistances of the sensor in air (R_a) to that in ammonia (R_g). The response time was defined as the time taken by the sensor to achieve 90% of the total resistance changes.

RESULTS AND DISCUSSION

X-Ray Diffractometry (XRD)

Figure 1 illustrates the XRD patterns of the WO_3 nanorods, graphene oxide (GO) and WO_3 nanorods doped with 1% GO. As for GO, an intense reflection related to GO appears at $2\theta = 10.64°$ diffracted from the (002) plane. By applying Bragg's law, the calculated interlayer spacing of GO is 0.83 nm, providing an expansion than graphite analog depicted at 0.34 nm. This is interpreted in terms of elongation of the c-axis during graphite oxidation to GO via creation of oxygen-containing functional groups. The pure WO_3 sample is well-crystallized in a single phase with exposing diffraction peaks at 2θ equal 24.68°, 28.17°, 36.52°, 49.85°, and 55.43°, indexed to hexagonal WO_3 (JCPDS 85-2459). The average crystallite size of WO_3 determined via Scherer's equation is 20 nm. All reflections due to the 1%GO.WO_3 pattern are associated with a single phase hexagonal WO_3. This sample exhibits more intense reflections when compared with the GO free WO_3 sample, endorsing an average crystallite size of 25 nm. Besides, the peak of GO disappears in the 1%GO.WO_3 pattern, which is likely due to the thimbleful of GO in

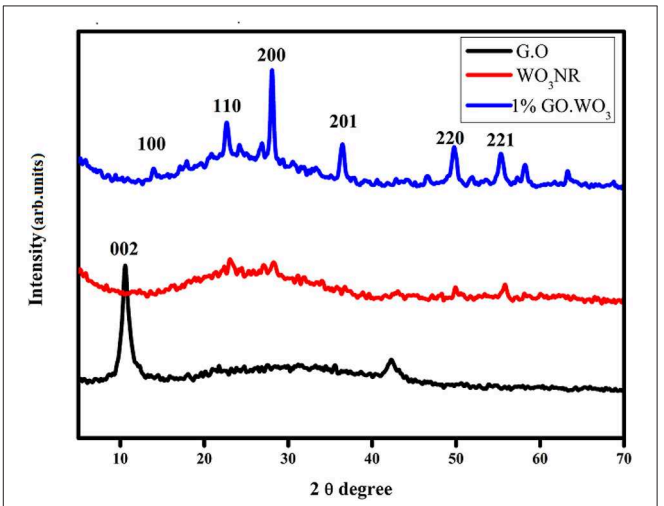

FIGURE 1 | XRD patterns of GO, WO_3, 1%GO.WO_3 catalysts.

the composite. However, the revealed broadness in the latter pattern for the peak at 24.68°, along with the expansion in d values is indicative of the dispersion of GO into the WO_3 hexagonal structure.

High-Resolution Transmission Electron Microscopy (HRTEM)

Particle morphology, crystallinity and selected area electron diffraction (SAED) analyses of the synthesized samples are studied by means of HRTEM (**Figure 2**). The HRTEM image of WO_3 shows that it owns nanorods shape with an average diameter of 4.11 nm. The magnified HRTEM image in the inset of the WO_3 Figure shows good crystallinity and spacing's of well-resolved lattice fringes at ∼0.35 nm, coincidently matching the (110) diffraction plane of WO_3 (JCPDS 85-2459). On the other hand, the SAED pattern of this sample shows a distorted hexagon with d = 0.24 nm corresponding to the (201) plane of WO_3 nanorods. The HRTEM image of the 1%GO.WO_3 composite shows clear nanorods with an average diameter of 17.6 nm and lattice spacing's equal 0.16 nm due to the (221) plane. This plane is not apparent in pure WO_3 nanorods. The SAED pattern in the inset of the latter Figure shows six-fold symmetry diffraction bright spots appears as well-defined diffraction hexagonal form, unlike that of pure WO_3 nanorods, emphasizing the interaction of GO with WO_3.

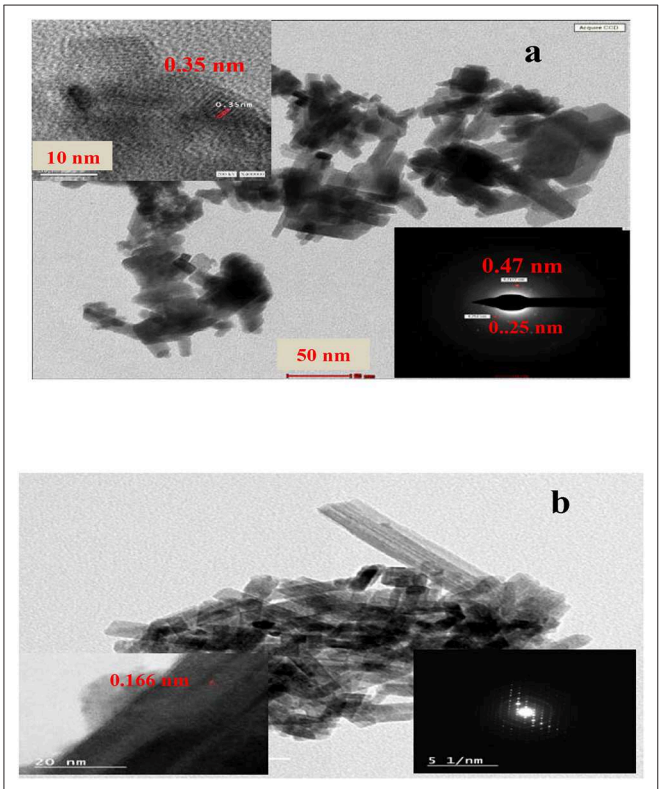

FIGURE 2 | TEM, HREM, and SAED (inset) images of GO inset in **(a)** WO3 **(a)** 1%GO.WO3 **(b)** catalysts.

FTIR Spectra

The interaction between WO_3 and GO is confirmed by the FTIR spectroscopy as exemplified in **Figure 3A**. The FTIR spectrum of GO exhibits a broad band with a maximum at 3,424 cm^{-1} corresponding to the OH stretching vibration (ν_{OH}). The substantial OH band broadening is a result of the strong hydrogen bonding interaction of hydroxyl containing groups, while the small band at 1,719 cm^{-1} is due to the C=O stretching vibration from the residual COOH groups on the GO surfaces. The sp^2 carbon network revealed from the band at 1,623 cm^{-1} is assigned to the C=C skeletal asymmetric vibration of unoxidized graphitic domains (Poongodi et al., 2017). The bands at 1,423 and 1,054 cm^{-1} correspond to the stretching vibrations of the C-OH and C-O groups, respectively (Shendage et al., 2017). For WO_3 nanorods, the small broad band observed at 3,417 cm^{-1} corresponds to the OH stretching, and the strong bands at 808 and 639 cm^{-1} to the stretching vibration of O-W_b-O and O-W_c-O links in the WO_3 structure, respectively (Han et al., 2018). The peak related to the W=O stretching vibration, proposed for dangling oxygen bonds, is obscured by the strong absorption of the former peak. The 1%GO.WO_3 composite shows a band at 3,436 cm^{-1} ascribed to the OH stretching vibration. By comparing with that of GO, this band becomes stronger, narrower and shifts to a higher frequency in the spectrum of 1%GO.WO_3 composite, i.e., from 3,424 to 3,436 cm^{-1}. This reflects the interspersion of GO matrix within the WO_3 structure (Zhang et al., 2010). In addition, the carbonyl C=O band at 1,719 cm^{-1} is disappeared in the spectrum of 1%GO.WO_3. This result implies that the carboxylic functional groups of GO are involved in the GO.WO_3 interactions (Saidi et al., 2018). The peaks due to O–W–O stretching vibrations are decreased in intensity and red shifted to 707 and 611 cm^{-1}, inferring the GO dispersion into the WO_3 hexagonal structure (Saidi et al., 2018). A small band at 877 cm^{-1} characteristics of

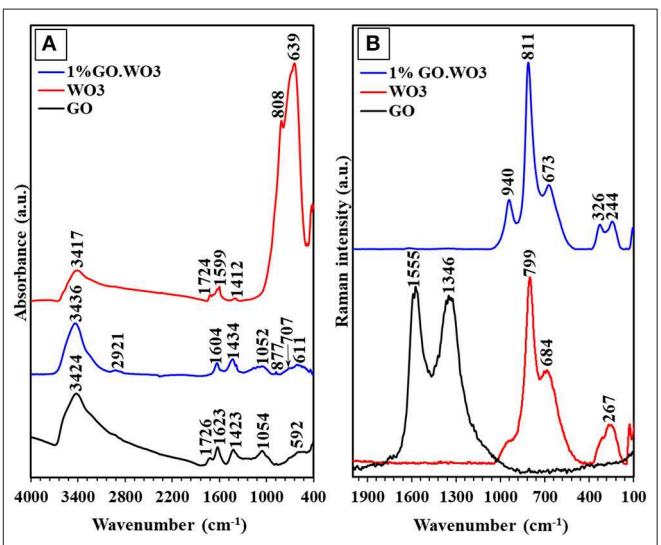

FIGURE 3 | FTIR spectra **(A)** and Raman spectra **(B)** of GO, WO_3, 1%GO.WO_3 catalysts.

the stretching W=O vibration is noticed, which never seen in the GO free WO_3 (Saidi et al., 2018). This indeed confirms the strong interaction between the two-component forming composite in which GO contributes in the formation of W=O bonds. The GO doping is rather confirmed from the presence of peaks assignable to C=C and C-OH stretching vibrations at 1,604 and 1,434 cm^{-1}, respectively. In this case, it is observed that the shift of bands at 1,604 and 1,434 cm^{-1} in 1%GO.WO_3 toward higher and lower values when compared with those for individual GO (1,623 and 1,423 cm^{-1}), respectively, reflects the strong interaction between the components forming the composite. In addition, there is almost no change in the peak at 1,052 cm^{-1} both in GO and 1%GO.WO_3 confirming that C-O groups did not take part in the reaction between GO and WO_3, unlike COOH and C-OH functional groups.

Raman Spectra

Figure 3B shows the Raman spectra of GO, WO_3 nanorods and 1%GO.WO_3. The GO spectrum exhibits two intense bands at 1,346 and 1,559 cm^{-1}; the former D-band represents the disordering sp^2-hybridized C atoms of GO, while the latter G-band corresponds to the structural integrity of the sp^2-hybridized C atoms of GO (Zeng et al., 2012). The Raman spectrum of pure WO_3 nanorods is characterized by two bands at 799 and 684 cm^{-1} assigned to the W-O-W stretching vibrations, which according to previous reports signified to the distances of the W-O bonds in pure WO_3 (Gao et al., 2019). The shoulder near 920 cm^{-1} is assigned to the stretching frequency of the terminal W=O on the nanostructural boundaries of WO_3 (Kaur et al., 2018), whereas Raman frequencies at 326 and 267 cm^{-1} are most likely due to the O-W-O deformation modes. The Raman spectrum of 1%GO.WO_3 is only dominated by the W-O-W stretching modes at 799 and 684 cm^{-1} (**Figure 3B**), and their relevant deformation ones occurred at 326 and 244 cm^{-1}. It is observed that the molecular structure of GO (D- and G-bands) is vanished after inclusion of GO onto the WO_3 nanorods. This agrees with the low content of GO (1 %) in the sample. The Raman peaks of 1%GO.WO_3 at 940 and 811 cm^{-1} are weakened and rather shifted to higher frequencies as compared to 920 and 799 cm^{-1} for WO_3, advocating strong interaction between WO_3 and GO matrix. Similarly, developing of two peaks at 244 and 326 cm^{-1} in 1%GO.WO_3 contrary to only one peak at 267 cm^{-1} in WO_3, features a distortion in the nanostructured WO_3 (shortening O-W-O bonds) revealing its strong bonding with GO, as typically confirmed from the XRD analysis of 1%GO.WO_3.

N_2 Sorptiometry

Figure 4 shows the adsorption-desorption isotherms and pore size distribution curves (inset) of all the samples. The WO_3 nanorods isotherm fits type IV of mesoporous materials, in agreement with the IUPAC assembling. The adsorption-desorption coincides at P/P_o of 0.5, revealing the existence of wide pores with H4 type. Where in 1%GO.WO_3 the adsorption-desorption isotherm coincides at P/P_o of 0.46 indicating narrowing of the pores as a result of GO incorporation within the WO_3 pores. In concordance, the pore radius of WO_3 nanorods indicates a value of 6.5 nm where it becomes narrower for 1%GO.WO_3 at 3.9 nm. The pore size distribution (PSD) of WO_3 nanorods in the inset of **Figure 4** manifests a monomodal type of pore maximized at 7.5 Å that extends to 20 Å. Contrarily, the 1%GO.WO_3 indicates PSD at 4.0 Å, proposing the evolution of more narrow pores, to comprehend the role of GO in narrowing the pore mouth of the WO_3 hexagonal array. The surface area of WO_3 nanorods (54.3 m^2/g) exceeds that of the 1%GO.WO_3 composite (14.2 m^2/g); a concurrent trend involving a lager pore volume for the former (0.084 cm^3/g) than for the latter (0.024 cm^3/g). This result emphasizes the inclusion of GO precursor into the WO_3 nanorods.

Optical Characteristics

Figures 5A,B present the PL emission spectra of WO_3 NRs and 1%GO.WO_3 excited at 320 nm at different wavelengths margin. A clear main broad emission peak at 447 nm is observed in the PL spectra of both samples. Based on previous investigations in literature (Jung et al., 2010; Chu et al., 2017), this peak may originate from the presence of oxygen vacancies or defects in WO_3 NRs. The decrease in PL emission intensity at 447 nm for 1%GO.WO_3 compared to that for WO_3 NPs (**Figure 5B**) is likely a consequence of an electron transfer from the WO_3 conduction band to GO networks. Such quenching of PL emission of 1%GO.WO_3 discloses that GO could acts as an electron transfer channel in the GO-encompassed semiconductor materials, as indicated in previous studies (Min et al., 2012; Dong et al., 2014). GO can thus virtually lower the rate of the electron-hole recombination, leading to maximizing charge separations and conserving more reactive species for high photocatalytic activity. Another emission peak at 560 nm is seen in **Figure 5B** for both samples however, the peak of 1%GO.WO_3 was of lower intensity reflecting the decrease in the electron-hole recombination.

Figure 5C shows the UV–Vis absorption spectra of WO_3 NRs and 1%GO.WO_3 (inset) in comparison with GO spectrum. The latter spectrum indicates bands at 250, 280 and 320 nm comprehending the presence of π-π^* and n-π^*(C=O), respectively. This indeed indicates the presence of both graphene and graphene oxide structures. The WO_3 NRs, and 1%GO.WO_3 samples exhibit wide absorption bands at 304 and 330 nm, respectively. Meanwhile, the latter reveals an absorption edge at 430 nm, which is lower in energy than the relevant of 1%GO.WO_3 at 480 nm. This could give an indication of decreasing the oxygen deficiencies on WO_3 NRs as consequence of GO incorporation. Besides, the 1%GO.WO_3 catalyst displays absorption in the visible region from 400 to 700 nm stronger than that of free WO_3, signifying the presence of W-O-C linkages in the composite. This manifests the expected photocatalytic capability of 1%GO.WO_3 under visible light irradiation. The band gaps of the catalysts calculated from the absorption spectra using the Tauc draw (**Figure 5D**) are 2.49, 2.8, and 0.55 eV for 1%GO.WO_3, WO_3 NRs, and GO, respectively. Indeed, the incorporation of GO might led to the decrease in the bond length of W=O and/or O-W-O, possibly due to the strong interaction between WO_3 and GO and via elaborating bonds such as C-O-W and C-W.

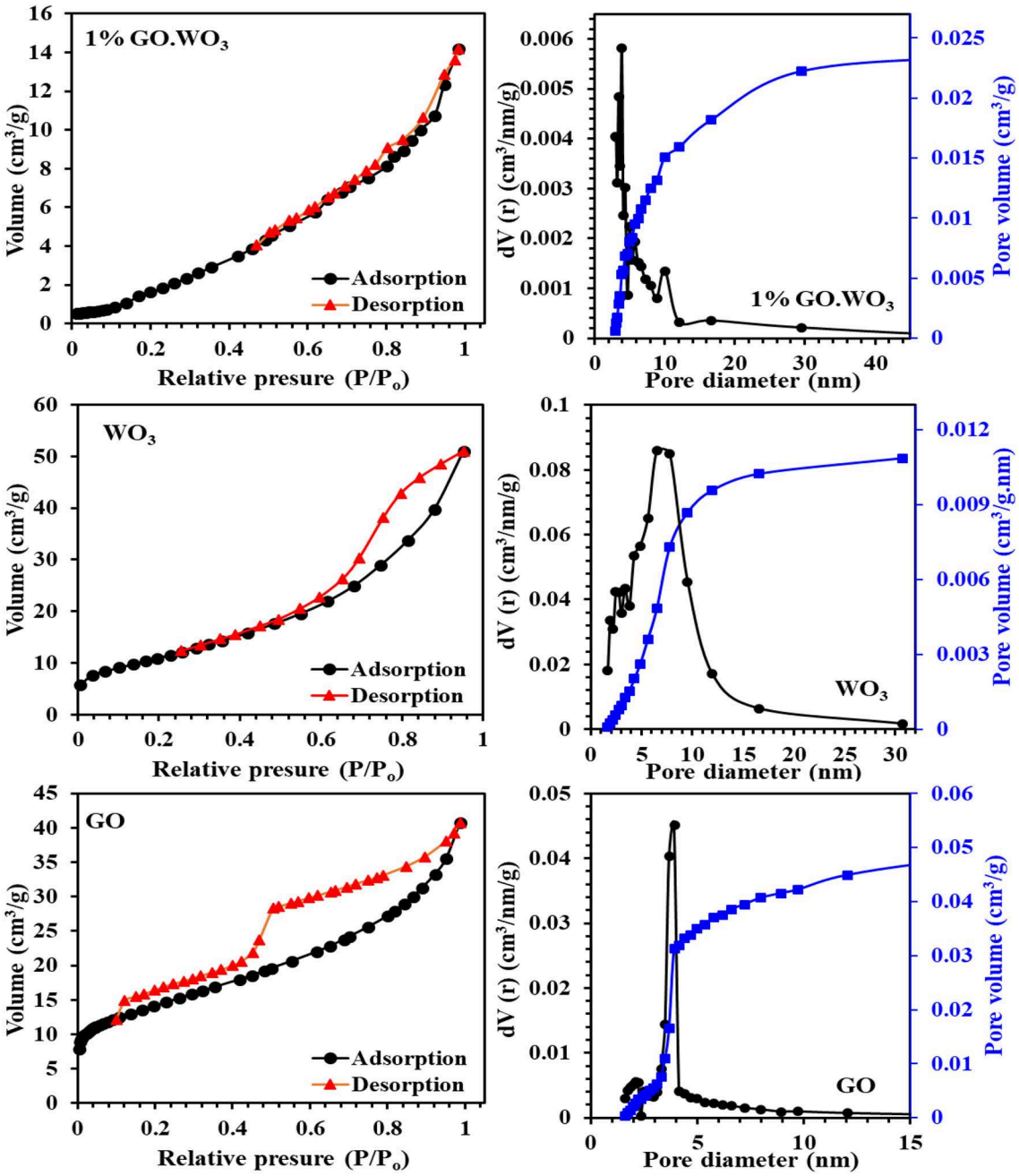

FIGURE 4 | Adsorption-desorption isotherms and pore size distribution curves (in-set) of GO, WO_3, 1%GO.WO_3 catalysts.

XPS Study

XPS, illustrated in **Figure 6**, is used to have an idea about WO_3 chemical composition as well as tracing the changes in WO_3 chemical states following GO incorporation. XPS survey scan (not shown) verifies the presence of W, C and O elements in both pure WO_3 nanorods and 1%GO.WO_3 samples. The core-level W4f XPS of WO_3 nanorods (**Figure 6A**) shows the presence of strong two peaks at 35.92 and 38.09 eV together with their satellite band at 41.88 eV due to the spin-orbit split levels of W(4f7/2) and W(4f5/2), respectively. The spectral deconvolution indicates two subpeaks at 35.4 and 37.3 eV due to W^{5+} state. The high-resolution W4f spectrum of 1%GO.WO_3 (**Figure 6B**) shows two well-defined feature peaks located at 36.6 and 38.8 eV to fit W4f7/2 and W4f5/2, consistent with W^{6+} state in the form of WO_3 together with a loss feature at 42.6 eV of W(4f3/2) (Naseri et al., 2011). The latter confirms the successful incorporation of GO into WO_3 structure, manifested by the exhibited shift of all W4f peaks into higher binding

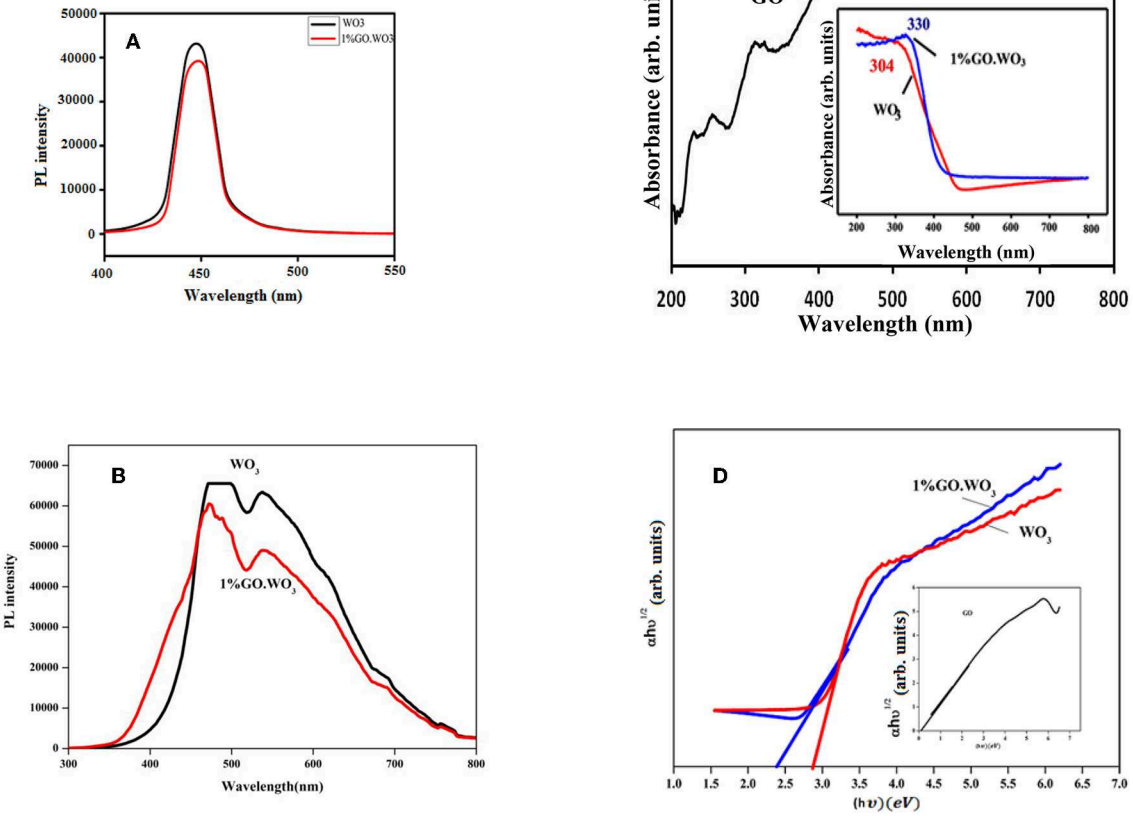

FIGURE 5 | Photoluminescence (PL) emission spectra of WO_3 and 1%GO.WO_3 in the margin of 400–550 nm **(A)**, WO_3 and 1%GO.WO_3 in the margin of 300–800 nm all excited at 320 nm **(B)**, beside UV-visible spectra **(C)**, and gap energy plots **(D)** of the GO (inset), WO_3, 1%GO.WO_3 catalysts.

energies. Also, this shift indicates that the low valence W^{5+} state seen in WO_3 nanorods is no longer detectable in 1%GO.WO_3 featuring the absence of substoichiometric WO_{3-x} following the GO incorporation.

The high-resolution C 1 s spectrum (**Figure 6C**) of 1%GO.WO_3 owns a strong peak of C=C species positioned at 285.2 eV. This spectrum is also divided into three bands at 285.84, 286.45, and 287.69 eV attributed to C-C, C-O, and C=O groups, respectively. The surface atomic percentages show that C=C represents the highest ratio (62.2%) reflecting a reduction in the oxygen content of GO in 1%GO.WO_3. The latter deduction is justified by ratios of C=O (29.46%), C-C (3.93%) and C-O (4.39%). This result verifies the successful formation of a hybridized structure of GO.WO_3.

The normalized XPS O 1 s spectrum shown in **Figure 6D** of WO_3 NRs shows one peak at BE of 530.73 eV, assigned to the O_2^- 1s ion (lattice oxygen). The XPS spectrum of the O 1 s of 1%GO.WO_3 (**Figure 6E**) is splitted into two component peaks localized at 531.51 and 531. 15 eV ascribed, respectively, to O1s O-C and O_2^- states, which represent a total surface oxygen moiety of 53.89 vs. 100% at the surfaces of WO_3 NRs. This indeed advocates the GO involvement in the WO_3 structure. Conclusively, the majority of GO is reduced to graphene (62.2%) with exposing residual oxides correlated to C=O (29.46%) and C-O (4.39%) moieties on GO amounted to the promotion of P-type conducting nature. This is capable of forming conducting transition when amalgamated with WO_3 (n-type) to boost the charge transfer via the p-n junction interface and thus the reaction activity.

Photocatalytic Degradation of MB

The photocatalytic activities of WO_3 NRs and 1%GO.WO_3 toward the degradation of methylene blue dye (MB; 20 ppm) under visible light illumination are shown in **Figure 7A**. Prior irradiation, the suspension formed between the catalyst and the dye is stirred in dark for 1 h to ensure diffusion from the bulk of dye to the interfacial zone and to accomplish adsorption-desorption equilibrium between them. The MB adsorption ability of 1%GO.WO_3 increases over 17% above WO_3 NRs, elaborating that GO-doping of WO_3 with small amount as 1% does not effectively improve the electrostatic attraction between MB and the catalyst. The result in **Figure 7A** shows

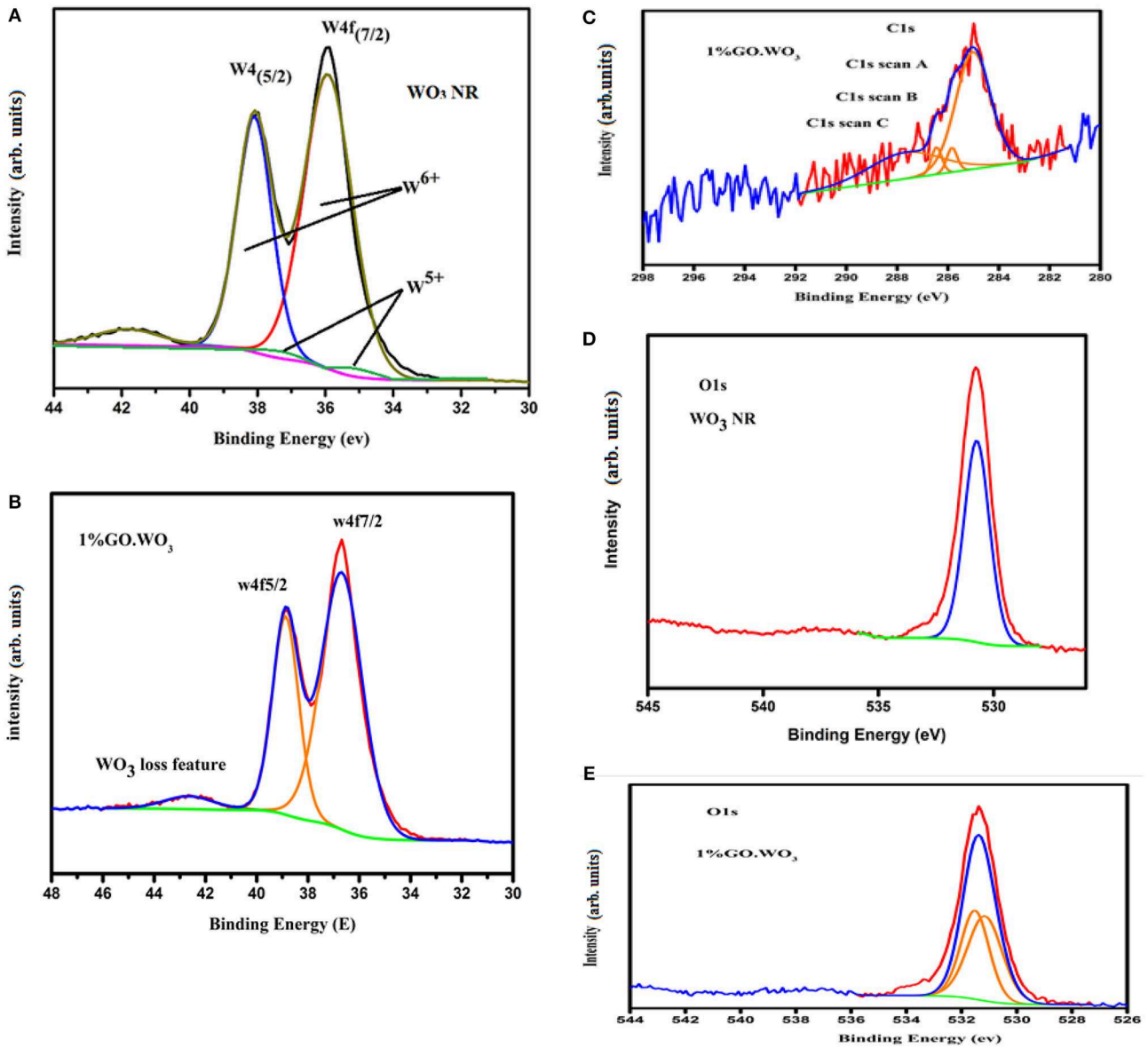

FIGURE 6 | W 4f XPS spectra of WO_3 **(A)** and 1%GO.WO_3 **(B)**, beside the C1S of 1%GO.WO_3 **(C)**, and O1S of WO_3 **(D)** and 1% GO.WO_3 **(E)** catalysts.

an enhanced degradation of the MB dye over 1%WO_3.GO under visible light irradiation through a complete degradation (100%) in 180 min at a rate constant of 0.0154 min^{-1}; as shown in **Figure 7B**, in front of 34% degradation with a rate of 0.001 min^{-1} for WO_3 NRs. **Figure 7C** shows the UV-vis spectra of the MB photodegradation over 1%GO.WO_3 as a function of elapsed time elucidating the consequences of the MB degradation. These results indicate that the marked increase in activity of the 1%GO.WO_3 catalyst is explained by the slight increase in the visible light absorption beside lowering both the band gap and the PL intensity; reflecting the slow recombination between electrons and holes. Also, the high dispersity of GO in WO_3 NRs; as emphasized by the FTIR, Raman and XPS data, evokes the involvement of carbons via hindering the recombination rate of photo-generated electron-hole pairs within the WO_3 hexagonal structure, facilitating the electron transition. Performing the MB degradation over WO_3 incorporated higher GO weight percentages (such as 5 and 10%) indicates adsorption behavior rather than photocatalysis trend (not shown). That is why we were only restricted to the 1%GO ratio. Executing the MB degradation (20 ppm) over 1%GO.WO_3 in presence of various scavengers under visible light illumination (**Figure 7D**) results in a significant decrease in the rate constant, compared to 0.0124 min^{-1}; evaluated in the absence of any scavenger. From **Figure 7D**, the maximum decease in the rate constant

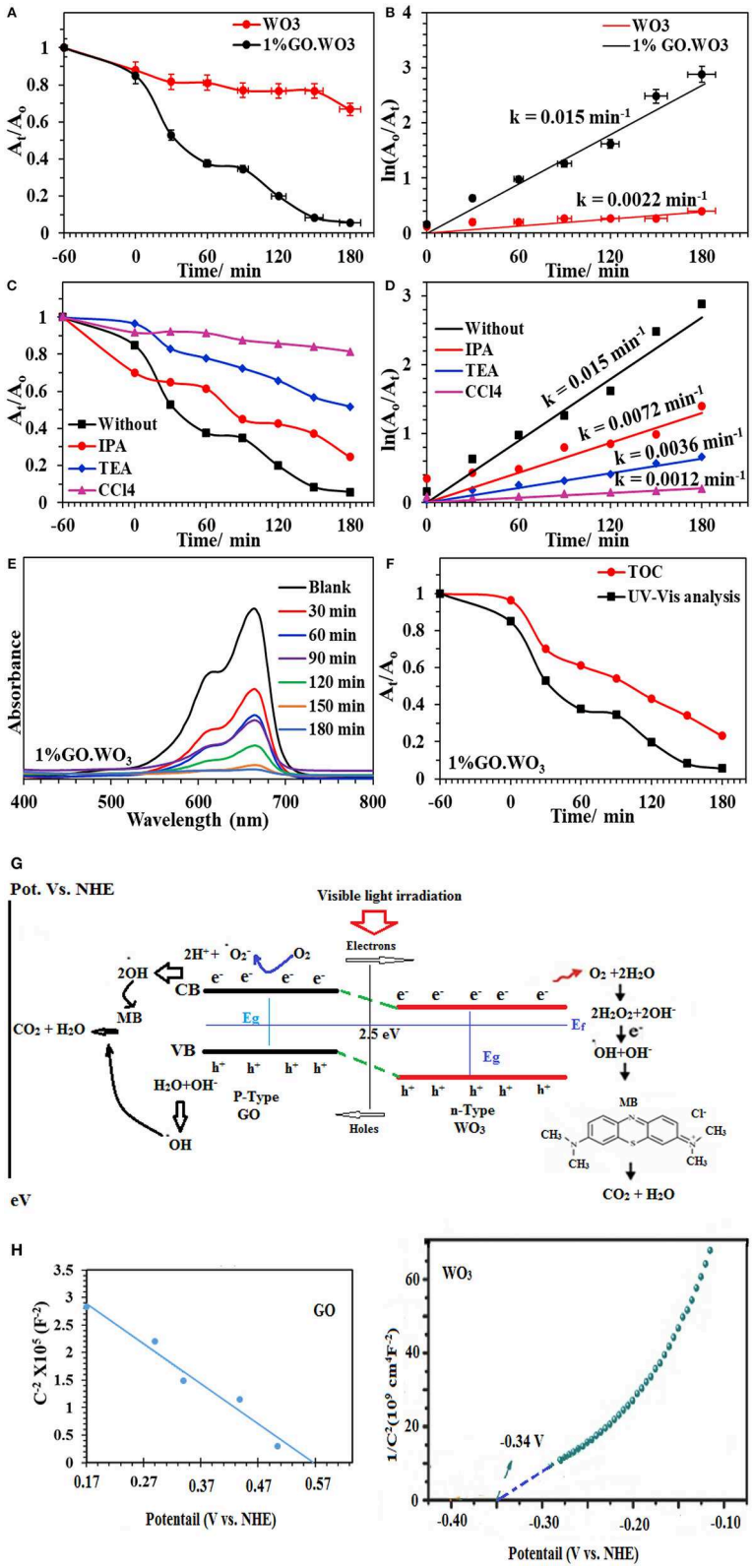

FIGURE 7 | A_t/A_o plot of the MB (20 ppm) degradation over WO_3 and 1%GO.WO_3 catalysts at the dose of 1.0 g/l under visible light illumination (160 W, $\lambda > 420$) **(A)** and their kinetic curves of ln A_o/A_t vs. time **(B)** Effect of scavengers on the catalytic degradation of MB over 1%GO.WO_3 with time **(C)** and their kinetic curves with time **(D)** beside UV-Vis. absorbance spectra of the MB over 1wt% GO.WO_3 with time **(E)**, Decrease in TOC and change in absorbance as function of irradiation time for the MB dye **(F)**, the expected reaction mechanism of the MB degradation over 1%GO.WO_3 **(G)** and Mott–Schottky plots of WO_3 and GO **(H)**.

is for that depicted for the CCl_4 scavenger (0.0008 min^{-1}), implying that electrons are the most reactive species affecting the MB degradation, followed by triethanolamine (0.0029 min^{-1}) and isopropanol (0.0053 min^{-1}), configuring in sequence the importance of holes and •OH after electrons. **Figure 7E** depicts the UV-Vis spectra of the MB dye as a function of time in the presence of the 1%GO.WO_3 photocatalyst. A magnificent decrease after 180 min is well-illustrated. Interestingly, the enhanced photocatalytic activity for photodegradation of MB is acquired over WO_3 modified low conc. of GO (1%) of eco-friendly synthesis conditions. To identify the extent of MB mineralization, **Figure 7F** shows the reduction in TOC in comparison to the dye degradation curve. Apparently, the TOC curve decreases significantly to 77% in 180 min confirming the presence of none degradable products and rather affirming the high mineralization capability of the catalyst.

The above mentioned results suggest that electrons, holes and •OH are the main reactive species in the process of MB photodegradation over the 1%GO.WO_3 catalyst. This is not mean the insignificant effect of holes but it works as an indirect way as elaborated in the mechanism to deliver •OH. Based on the above outcomes, a suggested mechanism for the photocatalytic reaction is depicted as in the scheme shown in **Figure 7G**. Under visible light irradiation, the valence band (VB) electrons are excited to the conduction band (CB) of the WO_3 semiconductor, creating holes (h^+) in the VB. The conduction band (CB) edge and valence band (VB) edge can be calculated by the following equations (Sadakane et al., 2010):

$$EVB = X - E^e + 1/2\ Eg \quad (1)$$

$$ECB = EVB - Eg \quad (2)$$

Where EVB and ECB are the valence band and conduction band edge potentials respectively where χ is the geometric mean of electronegativity of the constituent atoms semiconductor. The values of χ for GO.WO_3 and WO_3 are calculated as 6.39 eV and 6.59 eV according to the literature (Pearson, 1988). E^e is the energy of free electrons vs. hydrogen (4.5 eV) scale and Eg is the band gap energy of the semiconductor. A Mott-Schottky analysis is constructed to examine the carrier density and flat band potential for both WO_3 and GO. The E_{fb} is estimated by extrapolating each Mott–Schottky plot to the x-axis to obtain the intercept value and the N_d is estimated by the slope following Equations 3 and 4 (Mohamed et al., 2018a,b);

$$1/C^2 = [2/(e\varepsilon\varepsilon_0 N_d)](E - E_{fb} - \kappa T/e) \quad (3)$$

$$N_d = 2/(e\varepsilon\varepsilon_0)[d(1/C^2)/d(E)]^{-1} \quad (4)$$

Where C is the capacitance of the space charge layer, N_d is the number of donors, e (1.602×10^{-19} C) is the electron charge, ε (20 for WO_3) is the dielectric constant, and ε_0 (8.85×10^{-14} F cm^{-1}) is the vacuum permittivity, and κ (1.38×10^{-23} J K^{-1}) is the Boltzmann constant. First, the positive slopes indicate the n-type nature of the WO_3 samples (**Figure 7H**). Moreover, the calculated N_d is 1.30×10^{20} cm^{-3}, thus enormously promoting the charge transport efficiency. In the meantime, the flat band potential equal −0.34 V. The flat band potential of GO is measured at 0.57 V. Assuming that majority of the depletion width is located in GO film, the depletion width in the 1%GO.WO_3 interface is estimated according to following equation:

$$V_{bi}(p) = qN_A x_p^2/2\varepsilon GO \quad (5)$$

Where N_A, ε and εGO are acceptor concentration and absolute permittivities of WO_3 and GO respectively. Of particular interest, GO shows a negative slope corresponding to p-type conductivity manifesting the presence of high oxygen vacant defects with carrier concentration (N_A-holes) of 1.6×10^{18} cm^{-3}. Apparently, GO shows a positive shift of the flat-band potential as compared to the WO_3 electrode and rather indicates a lower concentration as compared to the N donor.

The band potential alignment of the as prepared GO.WO_3 vs. NHE shown in **Figure 7G** illustrates higher activity since its CB edge potential is more active than that of WO_3 indicating that photogenerated electrons from GO.WO_3 are easily transferrable than that of WO_3 via the former formed interface. Alike, the VB edge potential of GO.WO_3 is less positive than WO_3, specifying that the lower potential of the former facilitates its holes energetics. Accordingly, sticking a large number of electrons in the conduction band of GO.WO_3 as well as holes in its valence band increases the life time of e^--h^+ and slow down their recombination to markedly enhance the photocatalytic performance of GO.WO_3. The electrons may transport into the carbons of GO rather than recombined with the holes in the prevented band. The rest of the electrons on the WO_3 nanorods surface can react to form reactive oxygen moieties ($\cdot O_2^-$); of reduced lifetime, which react accordingly with $2H^+$ to form •OH. The latter reactive species can also be formed from the reaction of holes with the OH^-/H_2O species, to degrade the MB dye more efficiently (Zhang and Yi-Jun, 2016). The two-electron reduction of O_2 to form H_2O_2; as a common role of RGO-constructed composite photocatalysts (Weng et al., 2014), is augmented on the 1%GO.WO_3 surface. Here, the presence of H_2O_2 is determined via using the Ghormley triiodide method (Björkbacka et al., 2015), by which an electron acceptor is donated to form ·OH species. Based on the difference in work function of the GO in favors of that of WO_3 an electron transfer into the latter from the former is expected, and thus increases the electron density. Rendering the n-type conductivity to WO_3 surface in front of the p-type of the residual oxygen in GO facilitates the n–p semiconducting boundary interface that causes an enhanced photocatalysis. Accordingly, the electron transfer is found to be efficient in 1%GO.WO_3 rather than in GO free WO_3 catalyst. The latter showed high recombination rates of charge carriers of revealed insignificant lifetime, leading to a lower photocatalytic performance. Apparently, our catalyst shows higher photocatalytic efficiency compared with some WO_3-based graphene composites toward the degradation of the MB dye (Fan et al., 2012; Azimirad and Safa, 2015; Sun et al., 2015; Dinari et al., 2016; Liu et al., 2017). As revealed, their photocatalytic efficiencies are found to be in the range 65–95% within 56–180 min as well as with lower rates than ours.

Gas Sensing Behavior

The I-V characteristic curves of bare WO_3 NRs and 1%GO.WO_3 catalysts shown in **Figure 8A** indicate an Ohmic contact to ensure the sensing performance of the composite itself and not due to the contact between the composite and the electrode (Morsy et al., 2018). It is obvious that the electrical conductivity of the 1%GO.WO_3 catalyst is much higher than that of bare WO_3 NRs. Generally, metal oxides exhibit very poor electrical conductivity, and many strategies are devoted to overcome such poor conductivity. In order to investigate the gas-sensing effect of WO_3 NRs, and 1%GO.WO_3, these materials are subjected to different ammonia concentrations (10-100 ppm) at 200°C and the relationship between the sensor's response/recovery and ammonia gas is summarized in **Figures 8B,C**. The WO_3 NRs sensor shows no response at room temperature, while 1%GO.WO_3 shows a moderate sensitivity at room temperature (not shown). For comparison, the response/recovery of WO_3 NRs and 1%GO.WO_3 sensors toward ammonia gas evaluated at 200°C is performed as similarly depicted in some literatures (Bittencourt et al., 2006; Guo et al., 2012; Zeng et al., 2012; Chen et al., 2013; Gui et al., 2015; Zhang et al., 2017). The sensitivity of 1%GO.WO_3 to ammonia gas is estimated to be 2, 2.6, 5.1, 7.9, and 17.6 at 10, 20, 50, 70, and 100 ppm, respectively. For GO free WO_3, the sensitivity was 0.2, 0.4, 0.89, 1.02, and 1.27 at 10, 20, 50, 70, and 100 ppm, respectively. Therefore, the sensitivity to ammonia processed preferentially on 1%GO.WO_3 is ∼14 times higher than that on WO_3 NRs sensor. This could be due to the conductivity enhancement as a result of the strong interaction exhibited between partially reduced GO and WO_3 NRs, which is in accordant with the analysis data of TEM, XPS and Raman. It is also observed that the response increase with increasing ammonia concentration. The sensors response curves show that the resistance of sensors recovers its initial value after ammonia gas interruption, indicating a good reversibility. As a general trend for both sensors, the sensors interact directly with ammonia gas, which may lead to the reduction in the electrical resistivity. Rendering the n–p conductivity enhances the sensing response. Apparently, the numbers of oxygen vacancies formed on the WO_3 surfaces provide many active sites for the gas sensing reactions. In addition, the formed heterojunction is effectively accelerated the electron transfer and helps reducing the activation energy and enthalpy of the adsorbed gas molecules and thus enhances the sensing response; as shown in **Figure 8D**. The formed hetero-junction also accelerates the sensing response with the target gas that passes through the interface leading to electronic sensitization via modulation of depletion layers at the heterojunction area.

The principal of semiconductor metal oxide gas sensors depends on the material change in electrical resistance due to the interaction between the target gas and the material. When the sensor subjected to air, the oxygen molecules adsorbed on the conduction band of WO_3 get ionized to oxygen ions such as O_2^-, O^-, and O^{2-} through capturing free electrons from the surface of the WO_3 and result in an electron depletion layer at the WO_3 surface.

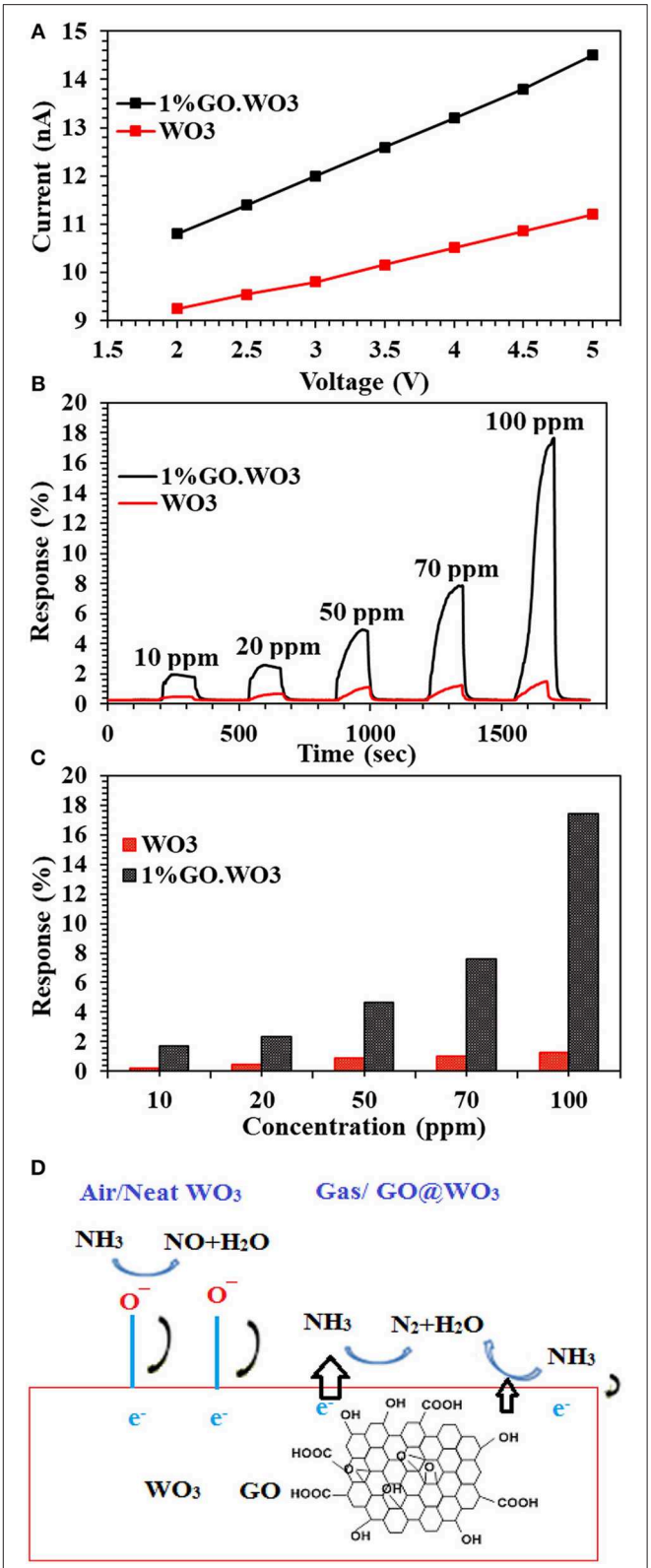

FIGURE 8 | I-V characteristic curves of WO_3 and 1%GO.WO_3 catalysts **(A)**, and their response transient to different ammonia concentration (10–100 ppm) at 200°C **(B)** response Vs. NH_3 concentration for WO_3 and 1 % GO.WO_3 **(C)** beside the mechanism of NH_3 gas sensing on the 1%GO.WO_3 catalyst **(D)**.

TABLE 1 | Comparison of ammonia gas sensing on some WO_3 based catalysts.

Catalyst name	Analyte gas	Temperature(°C)	Conc. ppm	Response sensitivity	Response/recovery time(s)	References
WO_3 nanorod	NH_3	225	10	16	145/155 s	Prabhu et al., 2018
SnO_2-WO_3 nanofilm	NH_3	300	50–1,000	1.9–20.3	12/58 s	Behera and Chandra, 2018
WO_3 nanwire	NH_3	200, 250, 300	100–1,500	2.39–9.67	16, 7, 15/16, 8, 13 s	Toan et al., 2017
Hemispherical WO_3/G	NH_3	R. T.	100	10	–	Hieu et al., 2011
WO_3 nanofiber	NH_3	350	50–500	low	20 s	Gui et al., 2015
1%GO.WO_3 nanorods	NH_3	200	10–100	17.6	10–15 s	This work

The chemical reaction can be composed as follows;

$$O_{2(ads)} + e^- \Rightarrow O_2^- \quad (6)$$

$$O_{2(ads)} + 2e^- \Rightarrow O^- \quad (7)$$

$$O_{2(ads)} + 4e^- \Rightarrow O^{2-} \quad (8)$$

These forms of the absorbed oxygen species are function in the operating temperature. The first form, as evidenced by XPS and represents major species, (O_2^-, Equation 1) onsets at room temperature and rests at ∼100°C. The second form (O^-, Equation 2) is acquired in the temperature range of 100–225°C. The third form of adsorbed oxygen species (O^{2-}, Equation 3) is excited between 225 and 400°C (Chen et al., 2018). This may explain why the optimum working condition for WO_3 is approximately around 200°C. During ammonia (reducing gas) exposure, the pre-adsorbed oxygen ions release electrons to the WO_3 surface, causing a decrease in the depletion layer, thereby decreases the electrical resistance (Urasinska-Wojcik et al., 2016).

$$2NH_3 + 3O^-(ads) \rightarrow N_2 + 3H_2O + 3e^- \quad (9)$$

When 1%GO.WO_3 sensor is exposed to NH_3 atmosphere, the electron transfer occurs through the formed 1%GO.WO_3 interface (**Figure 8D**), whereby both of which can provide effective adsorption sites. Rendering the n-type conductivity to WO_3 surface in front of the p-type of the residual oxygen in GO facilitates the n-p sensing for enhancing the response. GO acts as a catalytic promoter favoring surface reactions between ammonia gas and the adsorbed oxygen species on the sensor surface. Our results exhibited higher response toward ammonia gas sensing (see **Table 1**) in a relatively shorter time when compared with some various structural WO_3 catalysts, GO.WO_3 composites and when WO_3 forms heterojunction with other oxides (Wang et al., 2006; Hieu et al., 2011, 2012; Toan et al., 2017; Behera and Chandra, 2018; Prabhu et al., 2018).

CONCLUSION

The highly dispersed 1% GO in WO_3 hexagonal array heterojunction is successfully synthesized using a template free deposition-hydrothermal route for photocatalytic remediation of the MB (20 ppm) dye and for NH_3 gas sensing (10–100 ppm). The characterization results conducted using various physicochemical techniques show that the high dispersity of GO onto WO_3 nanorods surface causes an increase in the observed visible light absorptivity for the 1%GO.WO_3 composite and consequently decreases both energy band gap and PL intensity. The latter two factors are chiefly responsible for enhancing the MB degradation under visible illumination (in 180 min; 0.0154 min^{-1}) via freeing electrons of expanded lifetime, as well as played a role in promotion and enhancing the ammonia gas sensing sensitivity to 17.6%.

DATA AVAILABILITY STATEMENT

The raw data supporting the conclusions of this manuscript will be made available by the authors, without undue reservation, to any qualified researcher.

AUTHOR CONTRIBUTIONS

All authors listed have made a substantial, direct and intellectual contribution to the work, and approved it for publication.

REFERENCES

Azimirad, R., and Safa, S. (2015). Preparation of three dimensional graphene foam WO_3 nanocomposite with enhanced visible light photocatalytic activity. *Mater. Chem. Phys.* 162, 686–691. doi: 10.1016/j.matchemphys.2015.06.043

Behera, B., and Chandra, S. (2018). Synthesis of WO_3 nanorods by thermal oxidation technique for NO_2 gas sensing application. *Mater. Sci. Semi. Process.* 86, 79–84. doi: 10.1016/j.mssp.2018.06.022

Bittencourt, C., Felten, A., Espinosa, E. H., Ioneescu, R., Liobetr, E., Pireaux, J. J, et al. (2006). WO_3 films modified with functionalized multi-wall carbon nanotubes: morphological, compositional and gas response studies. *Sens. Actuators B Chem.* 115, 33–41. doi: 10.1016/j.snb.2005.07.067

Björkbacka, A., Yang, M., Gasparrini, C., Leygraf, C., and Jonsson, M. (2015). Kinetics and mechanisms of reactions between H_2O_2 and copper and copper oxides. *Dalton Trans.* 44, 16045–11651. doi: 10.1039/C5DT02024G

Chen, D., Yin, L., Ge, L., Fan, B., Zhang, R., Sun, J., et al. (2013). Low temperature and highly selective NO-Sensing performance of WO_3 nanoplates decorated with silver nanoparticles. *Sens. Actuator. B Chem.* 185, 445–455. doi: 10.1016/j.snb.2013.05.006

Chen, L., Huang, L., Lin, Y., Sai, L., hong, Q., Wang, C., et al. (2018). Chemical Fully gravure-printed WO_3/Pt-decorated rGO nanosheets composite

film for detection of acetone. *Sens. Actuators B. Chem*. 255, 1482–1490. doi: 10.1016/j.snb.2017.08.158

Chu, J., Lu, D., Wang, X., Wang, X., and Xiong, S. (2017). WO_3 nanoflower coated with graphene nanosheet: synergetic energy storage composite electrode for supercapacitor application. *J. Alloys. Compd*. 702, 568–572. doi: 10.1016/j.jallcom.2017.01.226

Dinari, M., Momeni, M. M., and Ahangarpour, M. (2016). Efficient degradation of methylene blue dye over tungsten trioxide/multi-walled carbon nanotube system as a novel photocatalyst. *Appl. Phys. A* 2122, 876–882. doi: 10.1007/s00339-016-0403-2

Dong, S., Cui, Y., Wang, Y., Li, Y., Hu, L., Sun, J., et al. (2014). Designing three-dimensional acicular sheaf shaped $BiVO_4$/reduced graphene oxide composites for efficient sunlight-driven photocatalytic degradation of dye wastewater. *Chem. Eng. J*. 249, 102–110. doi: 10.1016/j.cej.2014.03.071

Fan, H., Zhao, X., Yang, J., Shan, X., Yang, L., Zhang, Y., et al. (2012). ZnO-graphene composite for photocatalytic degradation of methylene blue dye. *Catal. Commun*. 29, 29–34. doi: 10.1016/j.catcom.2012.09.013

Galstyan, V., Comini, E., Kholmanov, I., Faglia, G., and Sberveglieri, G. (2016). Reduced graphene oxide/ZnO nanocomposite for application in chemical gas sensors. *RSC Adv*. 6, 34225–34232. doi: 10.1039/C6RA01913G

Gao, H., Yu, Q., Chen, K., Sun, P., Liu, F., Yan, X., et al. (2019). Ultrasensitive gas sensor based on hollow tungsten trioxide-nickel oxide (WO_3-NiO) nanoflowers for fast and selective xylene detection. *J. Colloid Interf. Sci*. 535, 458–468. doi: 10.1016/j.jcis.2018.10.010

Gui, Y., Zhao, J., Wang, W., Tian, J., and Zhao, M. (2015). Synthesis of hemispherical WO_3/graphene nanocomposite by a microwave-assisted hydrothermal method and the gas-sensing properties to trimethylamine. *Mater. Lett*. 155, 4–7. doi: 10.1016/j.matlet.2015.04.100

Guo, J. J., Li, Y., Zhu, S., Chen, Z., Liu, Q., Zhang, D., et al. (2012). Synthesis of WO_3 Graphene composite for enhanced photocatalytic Oxygen evolution from water. *RSC Adv*. 2, 1356–1363. doi: 10.1039/C1RA00621E

Han, L., Chen, J., Zhang, Y., Liu, Y., Zhang, L., and Cao, S. (2018). Facile synthesis of hierarchical carpet-like WO_3 Micro flowers for high NO_2 gas sensing performance. *Mater. Lett*. 210, 8–11. doi: 10.1016/j.matlet.2017.08.065

Hieu, N. V., Hoang, V., Day, N. V., and Hoa N. D. (2012). A morphological control of tungsten oxide nanowires by thermal evaporation method for sub-ppm NO_2 gas sensor application. *Sens. Actuators B Chem.* 171-172, 760–768. doi: 10.1016/j.snb.2012.05.069

Hieu, N. V., Quang, V. V., Hoa, N. D., and Kim, D. (2011). Preparing large-scale WO_3 nanowire-like structure for high sensitivity NH_3 gas sensor through a simple route. *Curr. Appl. Phys*. 11, 657–661. doi: 10.1016/j.cap.2010.11.002

Jung, J. H., Cheon, D. S., Liu, F., Lee, K. B., and Seo, T. S. (2010). A graphene oxide based immuno-biosensor for pathogen detection. *Angew. Chem. Int. Ed. Engl.* 49, 5708–5711. doi: 10.1002/anie.201001428

Kaur, J., Anand, K., Kaur, A., and Singh, R. C. (2018). Sensitive and selective acetone sensor based on Gd doped WO_3/reduced graphene oxide nanocomposite. *Sens. Actuators B Chem*. 258, 1022–1035. doi: 10.1016/j.snb.2017.11.159

Li, X., Wang, J., Xie, D., Xu, J., Dai, R., Xiang, L., et al. (2015). Reduced graphene oxide/hierarchical flower-like zinc oxide hybrid films for room temperature formaldehyde detection. *Sens. Actuators B Chem*. 221, 1290–1298. doi: 10.1016/j.snb.2015.07.102

Liu, X., Jin, A., Jia, Y., Xia, T., Deng, C., Zhu, M., et al. (2017). Synergy of adsorption and visible-light photocatalytic degradation of methylene blue by a bifunctional Z-scheme heterojunction of WO_3/g-C_3N_4. *Appl. Surface Sci*. 405 359–371. doi: 10.1016/j.apsusc.2017.02.025

Luna, T., Chongfei, Y., Yinlan, Z., Hui, C., Siyu, Y., Jingyu, S., et al. (2018). Fabrication of WO_3 nanorods on reduced graphene oxide sheets with augmented visible light photocatalytic activity for efficient mineralization of dye. *J. Alloys Comp*. 769, 83–91. doi: 10.1016/j.jallcom.2018.07.176

Min, Y.-L., Zhang, K., Chen, Y.-C., and Zhang, Y.-G. (2012). Enhanced photocatalytic performance of Bi_2WO_6 by graphene supporter as charge transfer channel. *Sep. Purif. Technol*. 86, 98–105. doi: 10.1016/j.seppur.2011.10.025

Mohamed, M. M., Khairy, M., and Eid, S. (2017). Surfactant-assited formation of silver titanates as active catalysts for methanol electro-oxidation. *Appl. Catal. A* 547, 205–213. doi: 10.1016/j.apcata.2017.08.031

Mohamed, M. M., Khairy, M., and Eid, S. (2018b). Polyethylene glycol assisted one-pot hydrothermal synthesis of $NiWO_4$/WO_3 heterojunction for direct Methanol fuel cells. *Electrochim. Acta*. 263, 286–298. doi: 10.1016/j.electacta.2018.01.063

Mohamed, M. M., Khairy, M., and Ibrahem, A. (2018a). Dispersed Ag_2O/Ag on CNT-graphene composite: an implication for magnificent photoreduction and energy storage applications. *Front. Chem*. 6:250. doi: 10.3389/fchem.2018.00250

Morsy, M., Yahia, I. S., and Zahran, H. Y. (2018). Low cost alcoholic breath sensor based on SnO_2 modified with CNTs. *J. Korean Phys. Soc*. 73, 1437–1443. doi: 10.3938/jkps.73.1437

Morsy, M., Yahia, I. S., Zahran, H. Y., and Ibrahim, M. (2019). Hydrothermal synthesis of CNTs/Co_3O_4@rGO mesoporous nanocomposite for enhanced VOCs. *J. Inorg Organomet. Polym*. 29, 416–422. doi: 10.1007/s10904-018-1011-8

Naseri, N., Yousefzadeh, S., Daryaei, E., and Moshfegh, A. Z. (2011). Photoresponse and H_2 production of topographically controlled PEG assisted Sol-gel WO_3 nanocrystalline thin films. *Int. J. Hydrogen Energy*. 36, 13461–13472. doi: 10.1016/j.ijhydene.2011.07.129

Pang, Y., Chen, Q., Shen, X., Tang, L., and Qian, H. (2010). Size-Controlled Ag nanoparticle modified WO_3 composite films for adjustment of electrochromic properties. *Thin Solid Films*. 518, 1920–1924. doi: 10.1016/j.tsf.2009.07.138

Pearson, R. G. (1988). Absolute electronegativity and hardness: application to inorganic chemistry. *Inorg. Chem*. 27, 734–740. doi: 10.1021/ic00277a030

Poongodi, S., Kumar, P. S., Mangalaraj, D., Ponpandian, N., Meena, P., Masuda, Y., et al. (2017). Electrodeposition of WO_3 nanostructured thinfilms for electrochromic and H_2S gas sensor applications. *J. Alloys. Compd*. 719, 71–81. doi: 10.1016/j.jallcom.2017.05.122

Prabhu, S., Manikumar, S., Cindrella, L., and Kwon, O. J. (2018). Charge transfer and intrinsic electronic properties of rGO-WO_3 nanostructures for efficient photoelectrochemical and photocatalytic applications. *Mater. Sci. Semicond. Process*. 74, 136–146. doi: 10.1016/j.mssp.2017.10.041

Quan, Q., Xin, L., Zhang, N., and Yi-Jun, X. (2017). Graphene and its derivatives as versatile templates for materials synthesis and functional applications, *Nanoscale* 9, 2398–2416. doi: 10.1039/C6NR09439B

Sadakane, M., Sasaki, K., Kunioku, H., Ohtani, B., Abe, R., and Ueda, W. (2010). Preparation of 3-D ordered macroporous tungsten oxides and nano-crystalline particulate tungsten oxides using a colloidal crystal template method, and their structural characterization and application as photocatalysts under visible light irradiation. *J. Mater. Chem*. 20, 1811–1818. doi: 10.1039/b922416e

Saidi, T., Palmowski, D., Kiewlicz, S. B., Welearegay, T. G., El Bari, N., Ionescu, R., et al. (2018). Exhaled breath gas sensing using pristine and functionalized WO_3 nanowire sensors enhanced by UV-light irradiation. *Sens. Actuators B Chem*. 273 1719–1729. doi: 10.1016/j.snb.2018.07.098

Shendage, S. S., Patil, V. L., Vanalakar, S. A., Patil, S. P., and Harale, N. S. (2017). Sensitive and selective NO_2 gas sensor based on WO_3 nanoplates. *Sens. Actuators B Chem*. 240, 426–433. doi: 10.1016/j.snb.2016.08.177

Sun, M., Li, W., Sun, S., He, J., Zhang, Q., and Shi, Y. (2015). One-step in situ synthesis of graphene-TiO_2 nanorod hybrid composites with enhanced photocatalytic activity. *Mater. Res. Bull*. 61, 280–286. doi: 10.1016/j.materresbull.2014.10.040

Toan, N. V., Hung, C. M., Duy, N. V., Hoa, N. D., Le, D. T. T., and Hieu, N. V. (2017). Bilayer SnO_2-WO_3 nanofilms for enhanced NH_3 gas sensing performance. *Mater. Sci. Eng. B* 224, 163–170. doi: 10.1016/j.mseb.2017.08.004

Tsai, M., Lu, C., and Su, P. (2017). One-pot synthesis of AuNPs/RGO/WO_3 nanocomposite for simultaneously sensing hydroquinone and catechol. *Mater. Chem. Phys*. 215, 293–298. doi: 10.1016/j.matchemphys.2018.05.058

Urasinska-Wojcik, B., Vincent, T. A., Chowdhury, M. F., and Gardner, J. W. (2016). Ultrasensitive WO_3 as sensors for NO_2 detection in air and low oxygen environment. *Sens. Actuators. B Chem*. 239, 1051–1059. doi: 10.1016/j.snb.2016.08.080

Wang, G., Ji, Y., Huang, X., Yang, X., Gouma, P. I., and Dudley, M. (2006). Fabrication and characterization of polycrystalline WO_3 nanofibers and their application for ammonia sensing. *J. Phys. Chem. B* 110, 23777–23782. doi: 10.1021/jp0635819

Weng, B., Wu, J., Zhang, N., and Xu, Y.-J. (2014). Observing the role of graphene in boosting the two-electron reduction of oxygen in graphene–WO_3 nanorod photocatalysts. *Langmuir* 30, 5574–5584. doi: 10.1021/la4048566

Zeng, J., Hu, M., Wang, W., Chen, H., and Qin, Y. (2012). NO_2-sensing properties of porous WO_3 gas sensor based on anodized sputtered tungsten thin film. *Sens. Actuators B Chem.* 161, 447–452. doi: 10.1016/j.snb.2011.10.059

Zhang, D., Sun, Y., Jiang, C., and Zhang, Y. (2017). Room temperature hydrogen gas sensor based on palladium decorated tin oxide/molybdenum disulfide ternary hybrid via hydrothermal route. *Sen. Actuators. B Chem.* 242, 15–24. doi: 10.1016/j.snb.2016.11.005

Zhang, N., Min-Quan, Y., Siqi, L., Yugang, S., and Yi-Jun, X. (2015). Waltzing with the versatile platform of graphene to synthesize composite photocatalysts. *Chem. Rev.* 115, 10307–10377. doi: 10.1021/acs.chemrev.5b00267

Zhang, N., and Yi-Jun, X. (2016). The endeavour to advance graphene–semiconductor composite-based photocatalysis. *Cryst. Eng. Comm.* 18, 24–37. doi: 10.1039/C5CE01712B

Zhang, W., He, W., and Jing, X. (2010). Preparation of a stable graphene dispersion with high concentration by ultrasound. *Phys. Chem. B* 114, 10368–10373. doi: 10.1021/jp1037443

Conflict of Interest: The authors declare that the research was conducted in the absence of any commercial or financial relationships that could be construed as a potential conflict of interest.

frontiers in Chemistry

ORIGINAL RESEARCH
published: 23 January 2020
doi: 10.3389/fchem.2019.00890

Vapor–Liquid Equilibrium Study of LiBr + H_2O and LiBr + $CaCl_2$ + H_2O Systems

*Huinan Wang, Hongfei Chen, Wanhao Chen, Haoran Sun and Xianzhen Xu**

Laboratory of Fiber Materials and Modern Textile, Shandong Sino-Japanese Center for Collaborative Research of Carbon Nanomaterials, Collaborative Innovation Center for Marine Biomass Fiber Materials and Textiles, College of Chemistry and Chemical Engineering, Qingdao University, Qingdao, China

Vapor–liquid equilibrium (VLE) data and modeling for LiBr + H_2O and LiBr + $CaCl_2$ + H_2O are reported in this paper. This work focuses on the experimental determination of the boiling point of LiBr + H_2O and LiBr + $CaCl_2$ + H_2O solutions with vapor pressures between 6 and 101.3 kPa and the total molality of salt ranging from 0 to 21.05 mol•kg^{-1}. The procedures were carried out in a computer-controlled glass apparatus. The relationship between the boiling point and saturated vapor pressure is obtained, and Xu's model is used to correlate and predict the VLE. By correlation of the data (literature and experimental) for LiBr + H_2O and LiBr + $CaCl_2$ + H_2O, the parameters are obtained. We compared the results with the ElecNRTL model and Pitzer model. The parameters for the LiBr + H_2O, $CaCl_2$ + H_2O, and LiBr + $CaCl_2$ + H_2O systems can be successfully used to calculate and predict the VLE data.

Keywords: electrolyte solution, vapor–liquid equilibrium (VLE), measurement, modeling, thermodynamics

OPEN ACCESS

Edited by:
Ramesh L. Gardas, Indian Institute of Technology Madras, India

Reviewed by:
Jun Gao, Shandong University of Science and Technology, China
Andres Mejia, University of Concepcion, Chile

****Correspondence:***
Xianzhen Xu
xuxianzhen@qdu.edu.cn

Specialty section:
This article was submitted to Physical Chemistry and Chemical Physics, a section of the journal Frontiers in Chemistry

Received: *30 October 2019*
Accepted: *10 December 2019*
Published: *23 January 2020*

Citation:
Wang H, Chen H, Chen W, Sun H and Xu X (2020) Vapor–Liquid Equilibrium Study of LiBr + H_2O and LiBr + $CaCl_2$ + H_2O Systems. Front. Chem. 7:890. doi: 10.3389/fchem.2019.00890

INTRODUCTION

The vapor–liquid equilibrium (VLE) of electrolyte solutions is widely used in industries, natural processes, chemistry, and chemical engineering. LiCl, LiBr, and $CaCl_2$ aqueous solutions have extensive applications in the field of refrigeration, cooling, and heat transforming systems based on absorption cycles (Lan et al., 2017; Li et al., 2017). Simultaneously, the thermodynamic properties of the solutions play a key role in the absorption cycles.

Due to the strong demand for absorption and separation process design, an increasing number of researchers have studied the VLE of electrolyte systems. Massive quantities of phase equilibrium data have been reported in recent years. Some solubility isotherms of the LiCl + $CaCl_2$ + H_2O system have been measured (Filippov and Mikhelson, 1977; Zeng et al., 2008), and VLE data of LiCl + H_2O, $CaCl_2$ + H_2O, and LiCl + $CaCl_2$ + H_2O systems have been obtained (Xu et al., 2014, 2019a). Lan et al. (2017) and N'Tsoukpoe et al. (2013) experimentally determined the saturated vapor pressure of LiBr aqueous solution with mass fractions ranging from 43.14 to 65.26 wt.% at high temperature. Chua et al. (2000) presented a thermodynamically consistent set of specific enthalpy, entropy, and heat capacity fields for a LiBr + H_2O solution. However, the phase equilibrium data of the systems containing LiBr with a wide range of pressures and temperatures are still rare.

The experimental data and thermodynamic models are equally important (Xu et al., 2019b). Significant improvements have been made in calculating thermodynamic properties using theoretical models; most models are based on the Wilson model (Wilson, 1964), NRTL model (Renon and Prausnitz, 1968), and UNIQUAC model (Abrams and Prausnitz, 1975). For electrolyte solutions, the Pitzer model (Pitzer, 1973), ElecNRTL model (Chen et al., 1982; Chen and Evans, 1986), Lu–Maurer model (Lu and Maurer, 1993; Lu et al., 1996), extended

UNIQUAC model (Thomsen et al., 1998), and Xu model (Xu et al., 2016, 2019c) have been widely utilized. The thermodynamic properties of the binary systems ($CaCl_2 + H_2O$ and $LiCl + H_2O$) were simulated by the Pitzer–Simonson–Clegg (PSC) model in Li's work (Li et al., 2015, 2016). Patek and Klomfar (2006) developed an effective formulation of the thermodynamic properties of $LiBr–H_2O$ solutions from 273 to 500 K. Despite the aforementioned research works, thermodynamic property calculations for some electrolyte systems still face great challenges, and more accurate models over a wide range of pressures, temperatures, and concentrations are needed.

Due to the lack of VLE data for systems containing LiBr at a wide range of pressures and temperatures, in this work, VLE data of $LiBr + H_2O$ and $LiBr + CaCl_2 + H_2O$ systems are experimentally measured at concentrations ranging from 0 to 21.05 mol•kg^{-1} and pressures ranging from 6 to 101.3 kPa. In addition, the obtained data are used to parameterize Xu's model (Xu et al., 2016). We expand the scope of the model, such as concentration, pressure, and temperature. Correlation and prediction of the VLE of $LiBr + H_2O$ and $LiBr + CaCl_2 + H_2O$ were successfully developed.

EXPERIMENTAL SECTION

Materials

Anhydrous LiBr (purity ≥ 99.5%) and anhydrous $CaCl_2$ (purity ≥ 99.99%) were purchased from Adamas-Beta. Distilled water (18.2 Ω cm) was used for the preparation of solutions.

Apparatus and Procedures

A dual circulation glass ebulliometer (40 ml) was used in the VLE measurements, as shown in **Figure 1**. The main experimental instruments are listed in **Table 1**, including a vacuum pump in the ebulliometer, a pressure controller, a heating mantle, and a temperature controller.

The reliability of the experiment has been verified in the literature (Xu et al., 2014, 2019a) (i.e., $CaCl_2 + H_2O$ and $NaCl + KCl + H_2O$), as shown in **Figure 2**. The experimental data for the $LiBr + H_2O$ and $LiBr + CaCl_2 + H_2O$ systems at different molalities are listed in **Tables 2–6**. Each VLE experimental data in this work are averages taken after three experiments. For the systems containing LiBr, the solubility of the salt is relatively high, with a value of 21.05 mol•kg^{-1} at 298.15 K. The absorption

TABLE 1 | The main experimental instruments.

Instrument	Model	Manufacturer	Uncertainty
Dual circulation glass ebulliometer	40 cm^3	Tianjin Wuqing Beiyang Chemical Factory	
Pressure controller	Ruska Series 7000 controller	Ruska Instrument Corp., Houston, USA	±0.01 kPa
Temperature controller	Model SRS13A	SHIMADEN, Japan	±0.05 K
Electronic balances	SECURA225D-1CEU balances	Sartorius Lab Instruments GmbH & Co. KG 37070 Gorttingen, Germany	±0.0001 g

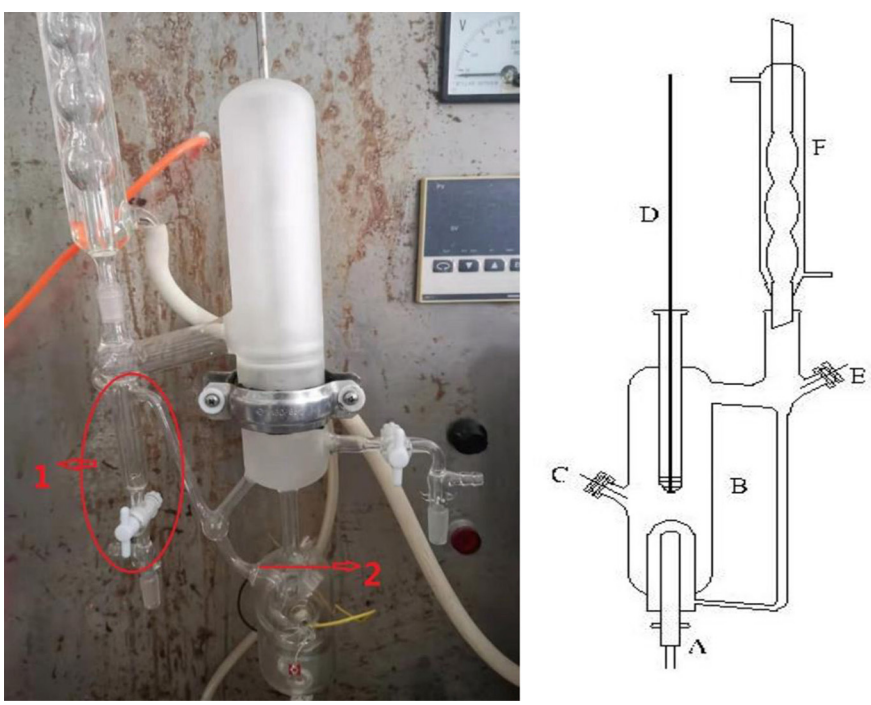

FIGURE 1 | A dual circulation glass ebulliometer.

is relatively strong at higher salt concentrations. The pressure (6–101.3 kPa) is an important factor for the design of absorption and separation processes.

The experimental procedures are as follows: (1) During the experiments, the sample was placed into the glass ebulliometer. When we were ready to add the sample into the ebulliometer, we filled the sample solution in the part marked 1 in **Figure 1**. Because of the problem of water condensation, if the part was not filled with the sample solution, the experimental results would have a large error. The sample should be added to the height of mark 2 shown in **Figure 1**. (2) The ebulliometer was heated by the heating mantle and was controlled by the voltage controller. (3) The operation pressure was controlled by the vacuum pump, the pressure sensor, and the control valve. (4) After the sample was added, we turned on the heater and controlled the heating voltage. Then, we stably controlled the pressure in the ebulliometer through the pressure controller. (5) The vapor H_2O was condensed in a spherical condenser (length 40 cm) and then returned to the mixing chamber for recirculation. The time was 0.5–1 h in the first equilibrium, and the following equilibrium time was 10–20 min. The judging standard of the VLE is an important factor. The condensate reflux of the ebulliometer was controlled at two to three drops per second and was stably refluxed for ∼15 min to establish an equilibrium state. (6) After the VLE was reached, we recorded the temperature and pressure.

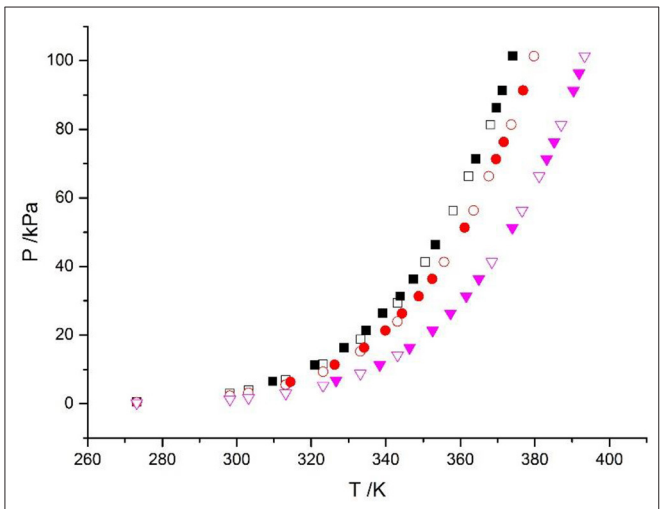

FIGURE 2 | Vapor-liquid equilibrium in the $CaCl_2 + H_2O$ system. Empty symbols (□, $m = 1$ mol/kg; ○, $m = 3$ mol/kg; ▽, $m = 6$ mol/kg): literature data (Xu et al., 2014, 2016; Lan et al., 2017); full symbols (■, $m = 1$ mol/kg; ●, $m = 3$ mol/kg; ▼, $m = 6$ mol/kg): experimental data (Xu et al., 2014).

MODEL DESCRIPTION

Xu Model

In the Xu model (Xu et al., 2016) for mixed electrolyte solution systems, the equation was based on the NRTL model:

$$\frac{n_t G^e_{NRTL}}{RT} = m_x m_w \left(\frac{\tau_{w,x} G_{w,x}}{m_x + m_w G_{w,x}} + \frac{\tau_{x,w} G_{x,w}}{m_w + m_x G_{x,w}} \right) \quad (1)$$

TABLE 2 | Experimental VLE data for temperature T, pressure P, and molality m—LiBr for the LiBr + H_2O system.

m = 21.05 mol•kg^{-1}		m = 16.5 mol•kg^{-1}		m = 11 mol•kg^{-1}		m = 9.01 mol•kg^{-1}	
T (K)	P (kPa)	T (K)	P (kPa)	T (K)	P (kPa)	T (K)	P (kPa)
319.65	6.29	318.35	6.405	333.15	6.3	324.75	5.94
332.25	11.875	329.45	11.33	345.05	10.955	338.35	11.085
340.85	16.38	337.35	16.265	354.55	16.61	347.95	16.405
347.15	21.3	343.35	21.365	360.95	21.185	354.25	21.495
352.05	26.205	347.95	26.21	366.35	26.225	359.45	26.05
356.45	31.075	352.35	31.295	371.25	31.235	363.85	30.94
360.45	36.075	356.05	36.2	375.35	36.23	368.25	36.08
363.85	41.23	359.45	41.34	378.95	41.27	371.95	41.07
366.85	45.98	362.25	46.14	382.05	46.38	375.05	46.155
369.55	50.96	364.85	51.26	384.95	51.445	378.05	51.24
372.25	56.165	367.55	56.34	387.65	56.3	380.85	56.25
374.55	60.865	369.95	61.305	390.05	61.51	383.45	61.33
376.75	66.715	371.95	66.18	392.45	66.575	385.55	66.22
378.85	70.91	374.05	70.78	394.65	71.02	387.55	71.035
380.85	76.2	376.15	75.75	396.55	75.885	389.75	76.63
382.65	80.975	377.85	81.11	398.05	81.205	391.45	81.26
384.45	86.145	379.85	86.355	399.95	86.255	393.25	86.31
386.05	91.315	381.45	91.26	401.95	91.27	395.15	91.29
387.65	96.12	383.05	96.165	403.25	96.265	396.75	96.26
389.15	101.255	384.45	101.235	404.55	101.245	398.25	101.245

Standard uncertainties u are u(P) = 0.1 kPa, u(T) = 0.05 K, u(m) = 0.0001 g, respectively.

TABLE 3 | Experimental VLE data for temperature *T*, pressure *P*, and molality *m*—LiBr for the LiBr + H_2O system.

$m = 7$ mol•kg^{-1}		$m = 4.8$ mol•kg^{-1}		$m = 4$ mol•kg^{-1}		$m = 1.5$ mol•kg^{-1}	
***T* (K)**	***P* (kPa)**	***T* (K)**	***P* (kPa)**	***T* (K)**	***P* (kPa)**	***T* (K)**	***P* (kPa)**
319.65	6.29	318.35	6.405	316.95	6.51	311.65	6.59
332.25	11.875	329.45	11.33	326.95	11.29	322.45	11.59
340.85	16.38	337.35	16.265	334.35	16.105	329.35	16.245
347.15	21.3	343.35	21.365	340.35	21.29	335.25	21.24
352.05	26.205	347.95	26.21	344.85	26.4	339.85	26.31
356.45	31.075	352.35	31.295	348.95	31.685	343.75	31.175
360.45	36.075	356.05	36.2	352.65	36.345	347.45	36.31
363.85	41.23	359.45	41.34	355.55	41.405	350.95	41.495
366.85	45.98	362.25	46.14	358.45	46.485	353.45	46.22
369.55	50.96	364.85	51.26	361.15	50.965	356.05	51.24
372.25	56.165	367.55	56.34	363.55	56.36	358.45	56.425
374.55	60.865	369.95	61.305	365.85	61.45	360.65	61.25
376.75	66.715	371.95	66.18	368.15	66.235	362.75	66.155
378.85	70.91	374.05	70.78	370.35	71.355	364.65	71.31
380.85	76.2	376.15	75.75	372.15	76.435	366.45	76.295
382.65	80.975	377.85	81.11	373.95	81.22	368.35	81.345
384.45	86.145	379.85	86.355	375.65	86.105	370.05	86.325
386.05	91.315	381.45	91.26	377.65	91.5	371.65	91.185
387.65	96.12	383.05	96.165	378.55	96.155	373.25	96.375
389.15	101.255	384.45	101.235	380.25	101.235	374.65	101.325

Standard uncertainties u are u(P) = 0.1 kPa, u(T) = 0.05 K, u(m) = 0.0001 g, respectively.

TABLE 4 | Experimental VLE data for temperature *T*, pressure *P*, and molality *m* (*ma*—LiBr, *mb*—$CaCl_2$) for the LiBr + $CaCl_2$ + H_2O system.

$ma = 21.05$ mol•kg^{-1} $mb = 0$ mol•kg^{-1}		$ma = 1.5$ mol•kg^{-1} $mb = 8.5$ mol•kg^{-1}		$ma = 3.08$ mol•kg^{-1} $mb = 8.1$ mol•kg^{-1}		$ma = 4.12$ mol•kg^{-1} $mb = 7.1$ mol•kg^{-1}	
***T* (K)**	***P* (kPa)**	***T* (K)**	***P* (kPa)**	***T* (K)**	***P* (kPa)**	***T* (K)**	***P* (kPa)**
362.25	6.425	337.55	6.395	338.65	6.475	337.95	5.98
375.95	11.295	349.65	11.165	351.35	11.445	352.25	11.425
384.95	16.17	357.95	16.18	359.95	16.27	360.95	16.415
391.95	21.31	364.15	21.305	366.35	20.955	366.75	21.08
398.15	26.78	368.85	26.14	371.55	26.195	371.95	26.465
401.95	31.48	373.25	31.28	376.35	31.315	376.35	31.47
404.95	35.5	376.45	36.145	380.05	36.31	380.45	36.315
408.45	40.55	379.75	41.1	382.25	41.22	383.55	40.975
410.65	45	382.35	46.32	384.45	46.345	386.65	46.43
413.35	51.055	384.55	51.22	386.95	51.235	389.25	51.26
416.35	56.455	386.85	56.385	389.55	56.155	392.05	55.95
418.65	60.87	389.45	61.25	391.95	61.27	394.15	61.16
420.55	66.18	392.35	66.84	394.35	66.245	396.25	65.83
422.45	70.975	394.15	71.165	395.55	71.865	398.85	71.2
424.15	76.595	395.75	76.385	397.35	75.785	401.25	76.33
425.35	81.26	397.75	81.47	398.45	81.33	402.75	81.125
426.45	86.265	399.25	86.19	399.25	86.355	404.35	86.33
427.65	91.445	400.85	91.265	400.25	91.31	405.65	91.33
428.75	96.74	401.85	96.27	402.35	96.32	407.25	96.34
429.65	101.225	403.45	101.235	402.75	101.205	408.35	101.215

Standard uncertainties u are u(P) = 0.1 kPa, u(T) = 0.05 K, u(m) = 0.0001 g, respectively.

TABLE 5 | Experimental VLE data for temperature *T*, pressure *P*, and molality *m* (*ma*—LiBr, *mb*—$CaCl_2$) for the LiBr + $CaCl_2$ + H_2O system.

***ma* = 5.5 mol•kg^{-1} *mb* = 6.1 mol•kg^{-1}**		***ma* = 7.1 mol•kg^{-1} *mb* = 4.7 mol•kg^{-1}**		***ma* = 8.95 mol•kg^{-1} *mb* = 4.08 mol•kg^{-1}**		***ma* = 11 mol•kg^{-1} *mb* = 3.3 mol•kg^{-1}**	
***T* (K)**	***P* (kPa)**	***T* (K)**	***P* (kPa)**	***T* (K)**	***P* (kPa)**	***T* (K)**	***P* (kPa)**
338.35	6.33	336.85	6.05	342.45	6.2	342.65	6.145
349.85	10.935	351.95	11.47	355.85	11.095	357.45	11.29
359.25	16.14	360.15	16.145	365.25	16.465	366.25	16.17
366.05	21.285	368.85	21.365	372.05	21.31	373.05	21.385
371.85	26.21	373.65	25.91	377.45	26.205	379.25	26.18
376.25	31.47	378.95	31.255	382.05	30.935	384.25	31.135
380.05	36.41	382.85	35.87	386.05	36.12	388.05	38.31
383.45	41.37	386.95	41.225	389.95	41.255	391.65	40.875
386.45	46.425	390.35	46.09	392.55	46.245	395.15	46.28
388.95	51.01	393.25	51.085	395.35	50.98	398.05	51.445
391.85	56.31	395.85	56.265	398.15	56.05	400.75	56.175
394.65	62.045	398.65	61.32	400.55	61.39	403.45	61.26
396.35	66.41	401.05	65.955	402.75	66.225	405.25	65.89
398.15	71.4	402.55	71.155	405.15	71.005	407.15	71.31
399.75	76.48	404.75	76.185	407.15	76.435	408.95	74.16
400.95	81.27	406.85	81.28	408.45	81.255	410.75	81.31
402.65	86.205	408.35	86.185	409.95	86.395	412.95	86.175
403.95	91.285	410.15	91.385	411.45	91.36	415.05	91.265
404.55	96.29	411.45	96.34	412.85	96.35	416.45	96.405
405.65	101.315	412.75	101.185	415.65	101.205	416.85	101.215

Standard uncertainties u are u(P) = 0.1 kPa, u(T) = 0.05 K, u(m) = 0.0001 g, respectively.

$$G_{w,x} = \exp(-\alpha\tau_{w,x}) \quad (2)$$

$$G_{x,w} = \exp(-\alpha\tau_{x,w}) \quad (3)$$

$$m_w = \frac{1000}{Ms} - \sum_{i=1}^{n}(h_i m_i) \quad (4)$$

$$\tau_{w,x} = \sum_{i=1}^{n}(\tau_{w,i}m_i)/\sum_{i=1}^{n}(m_i) \quad (5)$$

$$\tau_{x,w} = \sum_{i=1}^{n}(\tau_{i,w}m_i)/\sum_{i=1}^{n}(m_i) \quad (6)$$

$$\tau_{w,i} = \tau_{w,i}^{(0)} + \tau_{w,i}^{(1)}/T \quad (7)$$

$$\tau_{i,w} = \tau_{i,w}^{(0)} + \tau_{i,w}^{(1)}/T \quad (8)$$

The final equation can be written as:

$$\ln a_w = \left(\frac{\sum_{i=1}^{n}(\tau_{w,i}m_i)G_{w,x}}{\sum_{i=1}^{n}(m_i) + m_w G_{w,x}} + \frac{\sum_{i=1}^{n}(\tau_{i,w}m_i)G_{x,w}}{m_w + \sum_{i=1}^{n}(m_i)G_{x,w}}\right) + m_w\left(\frac{-\sum_{i=1}^{n}(\tau_{w,i}m_i)G_{w,x}^2}{\left(\sum_{i=1}^{n}(m_i) + m_w G_{w,x}\right)^2} - \frac{\sum_{i=1}^{n}(\tau_{i,w}m_i)\,G_{x,w}}{\left(m_w + \sum_{i=1}^{n}(m_i)G_{x,w}\right)^2}\right) + \ln\left(\frac{1000/Ms}{1000/Ms + \sum_{i=1}^{n}(m_i)}\right) \quad (9)$$

In this model, Equation (9) is the final objective function. Five parameters (h, $\tau_{w,i}^{(0)}$, $\tau_{w,i}^{(1)}$, $\tau_{i,w}^{(0)}$, and $\tau_{i,w}^{(1)}$) need to be calculated in the equation. Experimental data (**Tables 2–6**) and the data in the literature (Xu et al., 2014, 2016) were used for correlation. $\tau_{w,i}$ and $\tau_{i,w}$ are related to the temperature, and the temperature range is between 298.15 and 440.15 K.

The physical meaning of parameters (n, m_x, m_i, m_w, h_i, n_t, Ms, $\tau_{w,x}$, $\tau_{x,w}$, $\tau_{w,i}$, and $\tau_{i,w}$) in this model is shown in the NOMENCLATURE. In this model, the reference state of activity coefficients is $\gamma_i \to 1$ as $x_i(=n_i/n_t) \to 1$. Five parameters (h, $\tau_{w,i}^{(0)}$, $\tau_{w,i}^{(1)}$, $\tau_{i,w}^{(0)}$, and $\tau_{i,w}^{(1)}$) were fitted to the VLE data for the LiBr + $CaCl_2$ + H_2O system in the final equations. The 1stOpt 7.0 (7D-Soft High Technology Inc.) optimization software was chosen as the main tool for simulation calculations.

RESULTS AND DISCUSSION

In this work, the VLE data of the LiBr + H_2O and LiBr + $CaCl_2$ + H_2O systems were experimentally measured at concentrations ranging from 0 to 21.05 mol•kg^{-1} and pressures ranging from 6 to 101.3 kPa; the data are listed in **Tables 2–6**. Analysis and summary of the experimental data are shown in **Figures 3**, **4**.

TABLE 6 | Experimental VLE data for temperature *T*, pressure *P*, and molality *m* (*ma*—LiBr, *mb*—$CaCl_2$) for the LiBr + $CaCl_2$ + H_2O system.

***ma* = 16.6 mol•kg^{-1} *mb* = 1.5 mol•kg^{-1}**		***ma* = 0 mol•kg^{-1} *mb* = 8.91 mol•kg^{-1}**	
***T* (K)**	***P* (kPa)**	***T* (K)**	***P* (kPa)**
350.85	6.35	336.55	6.395
366.45	11.51	348.55	11.375
377.15	17.65	356.85	16.2
381.15	19.75	363.35	21.405
385.45	23.835	368.25	26.235
390.75	28.625	372.25	31.565
394.85	33.67	376.15	36.325
400.15	38.815	379.65	41.295
403.55	44.15	382.85	46.26
406.85	48.96	385.45	51.2
409.55	54.155	387.75	56.31
412.05	58.805	390.75	61.41
413.95	63.71	392.95	66.27
415.85	68.79	394.85	71.475
417.95	74.95	396.85	76.49
419.55	80.885	398.45	81.21
421.05	86.415	400.25	86.175
422.15	90.845	401.75	91.085
423.65	96.35	403.15	96.275
425	101.225	404.45	101.245

Standard uncertainties u are u(P) = 0.1 kPa, u(T) = 0.05 K, u(m) = 0.0001 g, respectively.

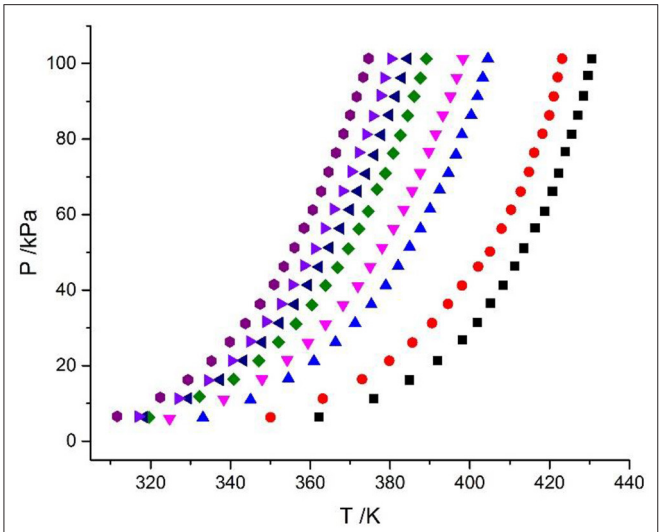

FIGURE 3 | Vapor–liquid equilibrium in the LiBr + H_2O system. Full symbols (■, *m* = 21.05 mol/kg; ⬢, *m* = 16.5 mol/kg; ▲, *m* = 11 mol/kg; ▼, *m* = 9 mol/kg; ◆, *m* = 7 mol/kg; ◀, *m* = 5.5 mol/kg; ▶, *m* = 4 mol/kg; ⬢, *m* = 3 mol/kg): experimental data.

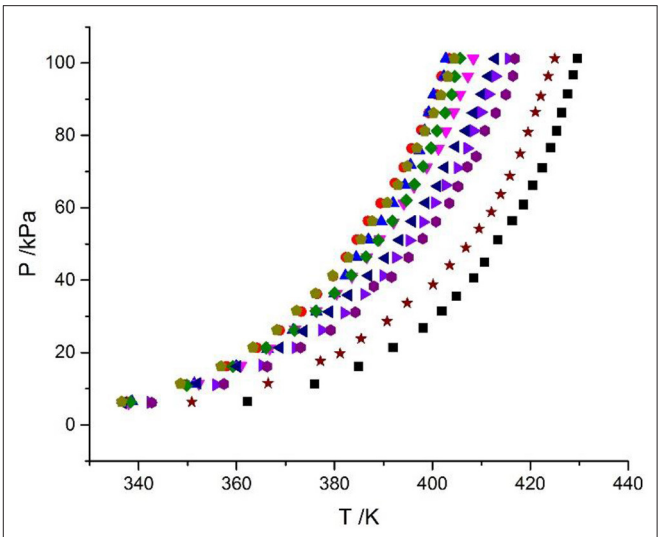

FIGURE 4 | Experimental VLE data for the LiBr + $CaCl_2$ + H_2O system. Symbols (■, ma = 21.05 mol/kg, mb = 0 mol/kg; ⬢, ma = 1.5 mol/kg, mb = 8.5 mol/kg; ▲, ma = 3.08 mol/kg, mb = 8.1 mol/kg; ▼, ma = 4.12 mol/kg, mb = 7.1 mol/kg; ◆, ma = 5.5 mol/kg, mb = 6.1 mol/kg; ◀, ma = 7.1 mol/kg, mb = 4.7 mol/kg; ▶, ma = 8.95 mol/kg, mb = 4.08 mol/kg; ⬢, ma = 11 mol/kg, mb = 3.3 mol/kg; ★, ma = 16.5 mol/kg, mb = 1.5 mol/kg; ⬟, ma = 0 mol/kg, mb = 8.91 mol/kg): experimental data (this work).

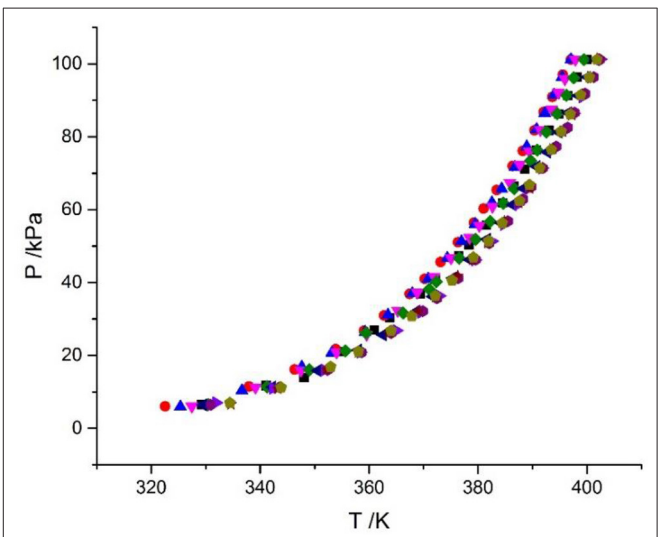

FIGURE 5 | VLE data for the LiCl + $CaCl_2$ + H_2O system (Xu et al., 2019a). Symbols (■, ma = 20.08 mol/kg, mb = 0 mol/kg; ⬢, ma = 15.63 mol/kg, mb = 1.3 mol/kg; ▲, ma = 10.4 mol/kg, mb = 3.14 mol/kg; ▼, ma = 8.83 mol/kg, mb = 4.07 mol/kg; ◆, ma = 7.46 mol/kg, mb = 4.68 mol/kg; ◀, ma = 5.41 mol/kg, mb = 5.95 mol/kg; ▶, ma = 3.73 mol/kg, mb = 6.73 mol/kg; ⬢, ma = 2.43 mol/kg, mb = 7.08 mol/kg; ★, ma = 1.66 mol/kg, mb = 7.14 mol/kg; ⬟, ma = 0 mol/kg, mb = 7.72 mol/kg).

For the study of the activity coefficient model for electrolyte solutions, we usually choose the activity coefficient of the molality concentration standard. Thus, we only need to study the activity data of water in the electrolyte solutions (Chen et al., 1982; Chen and Evans, 1986; Xu et al., 2014). The Xu model was used to correlate and predict the VLE for the LiBr + H_2O and LiBr + $CaCl_2$ + H_2O systems. The applicable system of the model was extended in this work. The correlation and prediction results were used to compare the Pitzer model (Pitzer, 1973), ElecNRTL model (Chen et al., 1982; Chen and Evans, 1986), and Xu model,

and the VLE behavior of the LiBr + $CaCl_2$ + H_2O system was investigated.

Discussion of Experimental Results

The LiBr + H_2O and LiBr + $CaCl_2$ + H_2O systems were chosen to study the VLE, as shown in **Tables 2–6** and **Figures 3**, **4**. The tables and figures show that the VLE of LiBr + H_2O and LiBr + $CaCl_2$ + H_2O are similar. It is well-known that as the salt concentration increases in the LiBr + H_2O and LiBr + $CaCl_2$ + H_2O systems, the vapor pressure of water decreases. From **Tables 2–6** and **Figures 3**, **4**, we can see that the vapor pressure at m_{LiBr} = 21.05 mol•kg^{-1} and m_{CaCl2} = 0 mol•kg^{-1} in the LiBr + $CaCl_2$ + H_2O system is lowest, and the activity at the corresponding temperature is lowest.

The VLE of the $CaCl_2$ + H_2O, LiBr + H_2O, LiBr + $CaCl_2$ + H_2O, and LiCl + $CaCl_2$ + H_2O systems are shown in **Figures 4**, **5**. From the figures, it can be known that the LiBr + H_2O curve at saturated solubility (m = 21.05 mol•kg^{-1}) and normal temperature is lower than that of $CaCl_2$ + H_2O, LiBr + $CaCl_2$ + H_2O, and LiCl + $CaCl_2$ + H_2O. The LiBr + $CaCl_2$ + H_2O curve at the same concentration and temperature is lower than that of LiCl + $CaCl_2$ + H_2O. Therefore, the hygroscopicity of some systems containing LiBr is also relatively high, and the hygroscopicity of the LiBr + H_2O system at saturated solubility (m = 21.05 mol•kg^{-1}) is the highest.

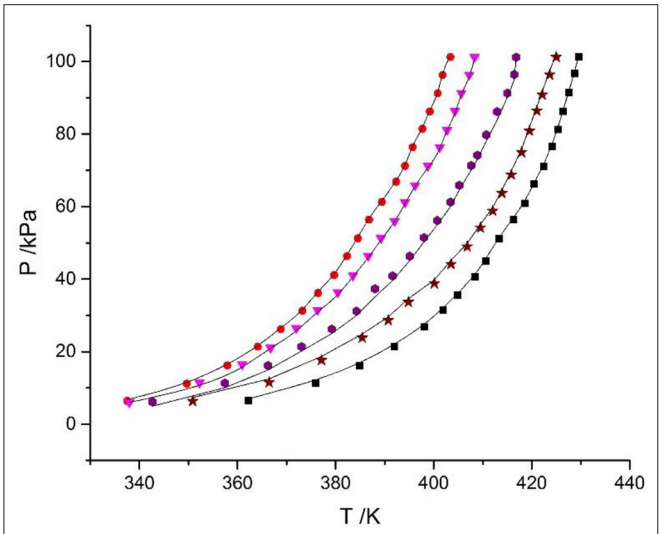

FIGURE 6 | Correlation of experimental VLE data for the LiBr + $CaCl_2$ + H_2O system. Symbols (■, ma = 21.05 mol/kg, mb = 0 mol/kg; ●, ma = 1.5 mol/kg, mb = 8.5 mol/kg; ▼, ma = 4.12 mol/kg, mb = 7.1 mol/kg; ⬢, ma = 11 mol/kg, mb = 3.3 mol/kg; ★, ma = 16.5 mol/kg, mb = 1.5 mol/kg): experimental data (this work); lines: correlation of the model.

Results of the Modeling

Correlation of the VLE

Equation (9) was used to correlate VLE data for the LiBr + H_2O and LiBr + $CaCl_2$ + H_2O systems. The results of the correlation for the LiBr + $CaCl_2$ + H_2O system are shown in **Figure 6**. The deviation between the literature and the calculated values for the LiBr + H_2O, $CaCl_2$ + H_2O, and LiBr + $CaCl_2$ + H_2O systems are listed in **Table 8**. Parameters, $\tau^0_{1,2}$, $\tau^0_{2,1}$, $\tau^0_{1,3}$, $\tau^0_{3,1}$, $\tau^0_{2,3}$, $\tau^0_{3,2}$, $\tau^1_{1,2}$, $\tau^1_{2,1}$, $\tau^1_{1,3}$, $\tau^1_{3,1}$, $\tau^1_{2,3}$, $\tau^1_{3,2}$, h_1, and $h_2$were obtained from the correlation of the experimental and literature data, as listed in **Table 7**. For LiBr + $CaCl_2$ + H_2O, it can be seen from **Table 8** that dY = 0.31 kPa and dP = 2.55%. dY and dP were calculated via the

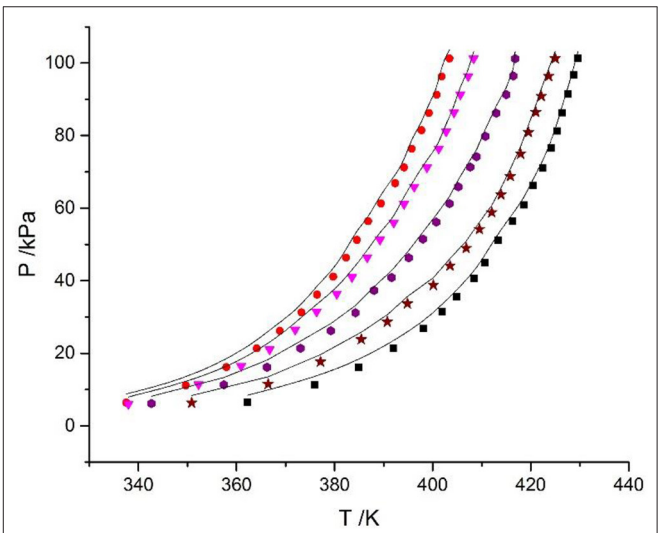

FIGURE 7 | Prediction of experimental VLE data for the LiBr + $CaCl_2$ + H_2O system. Symbols (■, ma = 21.05 mol/kg, mb = 0 mol/kg; ●, ma = 1.5 mol/kg, mb = 8.5 mol/kg; ▼, ma = 4.12 mol/kg, mb = 7.1 mol/kg; ⬢, ma = 11 mol/kg, mb = 3.3 mol/kg; ★, ma = 16.5 mol/kg, mb = 1.5 mol/kg): experimental data (this work); lines: prediction of the model.

TABLE 8 | Correlation results of VLE data.

System	p (kPa)	Data points	This work		Data source
			dY (kPa)[a]	dP (%)[b]	
$CaCl_2$-H_2O	5–101.3	322	0.081	1.82	4, 15
LiBr-H_2O	5–101.3	180	0.191	2.15	Experiment
LiBr-$CaCl_2$-H_2O	5–101.3	200	0.31	2.55	Experiment

[a] $dY = (1/N)\sum|P_{exp} - P_{cal}|$, where N is the number of data points.
[b] $dP = (1/N)\sum|P_{exp} - P_{cal}|/P_{exp} \times 100\%$, where N is the number of data points.

TABLE 7 | Model parameters for the $CaCl_2$-H_2O, LiBr-H_2O, and LiBr-$CaCl_2$-H_2O systems.

System			a	h	$\tau^{(0)}_{i,w}$	$\tau^{(0)}_{w,i}$	$\tau^{(1)}_{i,w}$	$\tau^{(1)}_{w,i}$
$CaCl_2$-H_2O	$CaCl_2$	Reference 4	0.3	1.1	781.44	−3771.77	−98.47	−6010.44
LiBr-H_2O	LiBr	Correlated in this work	0.3	0.8	−5.47	56.87	510.23	−23,153.41
LiBr-$CaCl_2$-H_2O	LiBr	Correlated in this work	0.3	−25.82	−5.14	−5129.97	−1949.2	2,149,363.27
	$CaCl_2$			−66.64	−8.4	4740.2	−1046.8	−1,973,929.6

TABLE 9 | Comparison of models for the electrolyte solutions.

System	*p* (kPa)	Data points	Chen-NRTL		Pitzer		This work (correlation using the Xu model)		This work (prediction using the Xu model)		Data source
			dY (kPa)[a]	*dP* (%)[b]	*dY* (kPa)[a]	*dP* (%)[b]	*dY* (kPa)[a]	*dP* (%)[b]	*dY* (kPa)[a]	*dP* (%)[b]	
LiBr-$CaCl_2$-H_2O	5–101.3	200	4.1	8.96	2.75	4.51	0.31	2.55	3.1	5.96	Experiment

[a] $dY = (1/N)\sum|P_{exp} - P_{cal}|$, where N is the number of data points.
[b] $dP = (1/N)\sum|P_{exp} - P_{cal}|/P_{exp} \times 100\%$, where N is the number of data points.

following equations:

$$dY = (1/N)\sum\left|P_{\text{exp}} - P_{\text{cal}}\right| \quad (10)$$

$$dP = (1/N)\sum\left|P_{\text{exp}} - P_{\text{cal}}\right|/P_{\text{exp}} \times 100 \quad (11)$$

where N denotes the number of data points, and P_{exp} and P_{cal} denote experimental vapor pressure and calculated vapor pressure, respectively.

Prediction of the VLE

The Xu model was chosen to correlate and predict the VLE. In previous work, the model was also successfully applied to predict the VLE data in mixed electrolyte solution systems with binary parameters (Xu et al., 2016). However, the parameters of LiBr are lacking. The prediction parameters of $CaCl_2$ were obtained from the literature (Xu et al., 2019a), the parameters of LiBr were calculated using LiBr + H_2O experimental data in this work, as listed in **Table 7**. The prediction result is shown in **Figure 7**, where $dY = 3.1$ kPa and $dP = 5.96\%$, which are worse than the correlation results.

Comparison With Other Methods

For the LiBr + $CaCl_2$ + H_2O system calculation, we choose the ElecNRTL model and Pitzer model for comparison with this work. The Pitzer equation for the thermodynamic properties of electrolytes is developed on the basis of theoretical insights from improved analysis of the Debye-Huckel model. The system of equations developed in the first paper of this series is successfully applied to the available free energy data at room temperature for 227 pure aqueous electrolytes in which one or both ions are univalent. The ElecNRTL model proposed by Chen et al. (1982) is generalized to represent the excess Gibbs energy of aqueous multicomponent electrolyte systems. Using only binary parameters, the model correlates and predicts the deviation from ideality of aqueous multicomponent electrolyte systems over the entire range of temperatures and concentrations. The comparison results are shown in **Table 9**. Note that the results from both the ElecNRTL and Pitzer models were calculated by the software Aspen Plus 8.1 (Xu et al., 2019a).

For the LiBr + $CaCl_2$ + H_2O system, the dY value (0.31 kPa) of this work (correlation) using the Xu model is smaller than that of the ElecNRTL model ($dY = 4.1$ kPa) and Pitzer model ($dY = 2.75$ kPa). Likewise, the dP value (2.55%) of this work (correlation) is smaller than that of the ElecNRTL model ($dP =$ 8.96%) and Pitzer model ($dP = 4.51\%$).

In this work, we expand the scope of the model based on previous work (Xu et al., 2014, 2019a). The parameters of the LiBr + H_2O system were obtained in this paper. Then, the binary parameters of LiBr + H_2O and $CaCl_2$ + H_2O were used to predict the VLE for the LiBr + $CaCl_2$ + H_2O system. However, the results are not satisfactory. Therefore, we recommend using the correlated parameters of LiBr + $CaCl_2$ + H_2O in **Table 8** to calculate the VLE.

CONCLUSIONS

In this paper, VLE data for LiBr + H_2O and LiBr + $CaCl_2$ + H_2O systems were measured and reported. By the analysis, it is shown that the type and concentration of salt are important factors affecting the VLE. The VLE curve of the LiBr + H_2O system at saturated solubility ($m = 21.05$ mol•kg^{-1}) and 25°C is lower than that of $CaCl_2$ + H_2O, LiBr + $CaCl_2$ + H_2O, and LiCl + $CaCl_2$ + H_2O. The hygroscopicity of some systems containing LiBr is also relatively high, and the hygroscopicity of the LiBr + H_2O system at saturated solubility ($m = 21.05$ mol•kg^{-1}) is the highest.

By correlation of the experimental data, the parameters of the LiBr + H_2O and LiBr + $CaCl_2$ + H_2O systems were obtained in this paper. The correlation results and prediction results were compared to those of the ElecNRTL and Pitzer model. By comparison, the correlation results of the LiBr + $CaCl_2$ + H_2O system in this work are better than those of the ElecNRTL and Pitzer models. The model can be used to successfully calculate VLE data for LiBr + H_2O and LiBr + $CaCl_2$ + H_2O systems.

DATA AVAILABILITY STATEMENT

All datasets generated for this study are included in the article/supplementary material.

AUTHOR CONTRIBUTIONS

HW: experimental design and data processing. HC: experimental design and experimental equipment assembly. WC: experimental operation and data processing. HS: data processing and modeling. XX: overall planning of the article and modeling.

FUNDING

This work was supported by the National Natural Science Foundation of China (no. 21703115).

REFERENCES

Abrams, D. S., and Prausnitz, J. M. (1975). Statistical thermodynamics of liquid mixtures: a new expression for the excess Gibbs energy of partly or completely miscible systems. *AIChE J.* 21, 116–128. doi: 10.1002/aic.690210115

Chen, C. C., Britt, H. I., Boston, J., and Evans, L. (1982). Local composition model for excess Gibbs energy of electrolyte systems. Part I: Single solvent, single completely dissociated electrolyte systems. *AIChE J.* 28, 588–596. doi: 10.1002/aic.690280410

Chen, C. C., and Evans, L. B. (1986). A local composition model for the excess Gibbs energy of aqueous electrolyte systems. *AIChE J.* 32, 444–454. doi: 10.1002/aic.690320311

Chua, H., Toh, H., Malek, A., Ng, K., and Srinivasan, K. (2000). Improved thermodynamic property fields of LiBr–H_2O solution. *Int. J. Refrig.* 23, 412–429. doi: 10.1016/S0140-7007(99)00076-6

Filippov, V., and Mikhelson, K. (1977). A thermodynamic study of the system LiCl-$CaCl_2$-H_2O at 25 and 35 C. *Zh. Neorg. Khim.* 22, 1689–1694.

Lan, Z., Ma, X., Hao, Z., and Jiang, R. (2017). Experiments on saturated vapor pressure of aqueous lithium bromide solution at high temperatures. *Int. J. Refrig.* 76, 73–83. doi: 10.1016/j.ijrefrig.2016.11.025

Li, D., Li, S., Meng, L., Deng, T., and Guo, Y. (2017). Solid–liquid phase equilibria of ternary systems LiCl–LiBr–H_2O and $CaCl_2$-$CaBr_2$-H_2O at 288.15 K. *J. Chem. Eng. Data* 62, 833–838. doi: 10.1021/acs.jced.6b00855

Li, D., Zeng, D., Han, H., Guo, L., Yin, X., and Yao, Y. (2015). Phase diagrams and thermochemical modeling of salt lake brine systems. I. LiCl + H_2O system. *Calphad* 51, 1–12. doi: 10.1016/j.calphad.2015.05.001

Li, D., Zeng, D., Yin, X., Han, H., Guo, L., and Yao, Y. (2016). Phase diagrams and thermochemical modeling of salt lake brine systems. II. NaCl + H_2O, KCl + H_2O, $MgCl_2$ + H_2O and $CaCl_2$ + H_2O systems. *Calphad* 53, 78–89. doi: 10.1016/j.calphad.2016.03.007

Lu, X., Zhang, L., Wang, Y., Shi, J., and Maurer, G. (1996). Prediction of activity coefficients of electrolytes in aqueous solutions at high temperatures. *Ind. Eng. Chem. Res.* 35, 1777–1784. doi: 10.1021/ie950474k

Lu, X. H., and Maurer, G. (1993). Model for describing activity coefficients in mixed electrolyte aqueous solutions. *AIChE J.* 39, 1527–1538. doi: 10.1002/aic.690390912

N'Tsoukpoe, K., Le Pierrès, N., and Luo, L. (2013). Experimentation of a LiBr–H_2O absorption process for long-term solar thermal storage: prototype design and first results. *Energy* 53, 179–198. doi: 10.1016/j.energy.2013.02.023

Patek, J., and Klomfar, J. (2006). A computationally effective formulation of the thermodynamic properties of LiBr–H_2O solutions from 273 to 500 K over full composition range. *Int. J. Refrig.* 29, 566–578. doi: 10.1016/j.ijrefrig.2005.10.007

Pitzer, K. S. (1973). Thermodynamics of electrolytes. I. Theoretical basis and general equations. *J. Phys. Chem.* 77, 268–277. doi: 10.1021/j100621a026

Renon, H., and Prausnitz, J. M. (1968). Local compositions in thermodynamic excess functions for liquid mixtures. *AIChE J.* 14, 135–144. doi: 10.1002/aic.690140124

Thomsen, K., Rasmussen, P., and Gani, R. (1998). Simulation and optimization of fractional crystallization processes. *Chem. Eng. Sci.* 53, 1551–1564. doi: 10.1016/S0009-2509(97)00447-8

Wilson, G. M. (1964). Vapor-liquid equilibrium. XI. A new expression for the excess free energy of mixing. *J. Am. Chem. Soc.* 86, 127–130. doi: 10.1021/ja01056a002

Xu, X., Cao, D., Liu, J., Gao, J., and Wang, X. (2019c). Research on ultrasound-assisted demulsification/dehydration for crude oil. *Ultrason. Sonochem.* 57, 185–192. doi: 10.1016/j.ultsonch.2019.05.024

Xu, X., Gu, X., Wang, Z., Shatner, W., and Wang, Z. (2019b). Progress, challenges and solutions of research on photosynthetic carbon sequestration efficiency of microalgae. *Renew. Sustain. Energy Rev.* 110, 65–82. doi: 10.1016/j.rser.2019.04.050

Xu, X., Hu, Y., Wang, X., and Wu, L. (2016). Experimental and modeling of vapor–liquid equilibria for mixed electrolyte solution systems. *J. Chem. Eng. Data* 61, 2311–2320. doi: 10.1021/acs.jced.5b01028

Xu, X., Hu, Y., Wu, L., and Zhang, S. (2014). Experimental and modeling of vapor–liquid equilibria for electrolyte solution systems. *J. Chem. Eng. Data* 59, 3741–3748. doi: 10.1021/je500623w

Xu, X., Wang, Y., Sun, X., and Zhou, Y. (2019a). Vapor–liquid equilibria study of the LiCl + $CaCl_2$ + H_2O System. *ACS Omega* 4, 4390–4396. doi: 10.1021/acsomega.8b03570

Zeng, D., Xu, W., Voigt, W., and Xia, Y. (2008). Thermodynamic study of the system (LiCl + CaCl + HO). *J. Chem. Thermodynamics* 40, 1157–1165. doi: 10.1016/j.jct.2008.02.010

Conflict of Interest: The authors declare that the research was conducted in the absence of any commercial or financial relationships that could be construed as a potential conflict of interest.

NOMENCLATURE

a	activity
G^e	excess Gibbs energy, J•mol^{-1}
R	gas constant, J•mol^{-1}•kg^{-1}
m	molality, mol•kg^{-1}
n	mole, mol
m_x	total molality of solute, mol•kg^{-1}
m_w	molar of free water, mol•kg^{-1}
h	hydration numbers of the solute
Z	solvation parameters
T	temperature, K
Ms	molecular weight of water
γ	activity coefficients
n_t	integral molar quantity, mol
τ	parameter
i	component i
j	component j
dY	mean absolute error, mol•kg^{-1}
dP	mean relative error, %

frontiers in Chemistry

ORIGINAL RESEARCH
published: 28 January 2020
doi: 10.3389/fchem.2020.00020

A Theoretical Study on Laser Cooling Feasibility of Group IVA Hydrides XH (X = Si, Ge, Sn, and Pb): The Role of Electronic State Crossing

Donghui Li[1,2], *Mingkai Fu*[3], *Haitao Ma*[1]*, *Wensheng Bian*[1,2]*, *Zheng Du*[4] and *Congmei Chen*[4]

[1] Beijing National Laboratory for Molecular Sciences, Institute of Chemistry, Chinese Academy of Sciences, Beijing, China, [2] School of Chemical Sciences, University of Chinese Academy of Sciences, Beijing, China, [3] Institute of Electrical Engineering, Chinese Academy of Sciences, Beijing, China, [4] National Supercomputing Center in Shenzhen, Shenzhen University Town, Shenzhen, China

The feasibility of direct laser cooling of SiH, GeH, SnH, and PbH is investigated and assessed based upon first principles. The internally contracted multi-reference configuration interaction method with the Davidson correction is applied. Very good agreement is obtained between our computed spectroscopic constants and the available experimental data. We find that the locations of crossing point between the $B^2\Sigma^-$ and $A^2\Delta$ states have the tendency of moving downwards from CH to SnH relative to the bottom of the corresponding $A^2\Delta$ potential, which precludes the laser cooling of GeH, SnH, and PbH. By including the spin-orbit coupling effects and on the basis of the $A^2\Delta_{5/2} \rightarrow X^2\Pi_{3/2}$ transition, we propose a feasible laser cooling scheme for SiH using three lasers with wavelengths varying from 400 to 500 nm, which features a very large vibrational branching ratio (0.9954) and a very short radiative lifetime (575 ns). Moreover, similar studies are extended to carbon monosulfide (CS) with a feasible laser cooling scheme proposed. The importance of electronic state crossing in molecular laser cooling is underscored, and our work suggests useful caveats to the choice of promising candidates for producing ultracold molecules.

Keywords: laser cooling, *ab initio*, spin-orbit coupling, electronic state crossing, group IVA hydrides

OPEN ACCESS

Edited by:
Zhuhua Zhang,
Nanjing University of Aeronautics and Astronautics, China

Reviewed by:
Jiangtan Yuan,
Northwestern University, United States
Sunny Gupta,
Rice University, United States

***Correspondence:**
Haitao Ma
mht@iccas.ac.cn
Wensheng Bian
bian@iccas.ac.cn

Specialty section:
This article was submitted to Physical Chemistry and Chemical Physics, a section of the journal Frontiers in Chemistry

Received: *10 October 2019*
Accepted: *08 January 2020*
Published: *28 January 2020*

Citation:
Li D, Fu M, Ma H, Bian W, Du Z and Chen C (2020) A Theoretical Study on Laser Cooling Feasibility of Group IVA Hydrides XH (X = Si, Ge, Sn, and Pb): The Role of Electronic State Crossing. Front. Chem. 8:20. doi: 10.3389/fchem.2020.00020

1. INTRODUCTION

Laser cooling of diatomic molecule is an issue of great interest owing to their promising applications in many fields such as quantum computing and precision measurement (Carr et al., 2009; Hudson et al., 2011; Yan et al., 2013; Baron et al., 2014). Direct laser cooling of SrF molecules to μK level was firstly achieved with only three laser beams (Shuman et al., 2010). In addition, transverse and longitudinal laser cooling experiment was applied to YO (Hummon et al., 2013) and CaF (Zhelyazkova et al., 2014), respectively. So far only a few molecules including SrF, CaF, and YO have been cooled to the ultracold temperature experimentally, and there is an urgent need to search for more suitable molecular candidates for laser cooling. Recently, a number of theoretical efforts have been made in searching for promising molecular laser cooling candidates (Wells and Lane, 2011a; Fu et al., 2016a; Cao et al., 2019; González-Sánchez et al., 2019; Xu et al., 2019). It is generally accepted (Di Rosa, 2004; Fu et al., 2016b) that, a suitable laser-cooling candidate must meet the

following three criteria: highly diagonal Franck-Condon factors (FCFs), a short lifetime, and no intermediate electronic-state interference. Here we reveal that the crossing between two electronic states may damage the cooling scheme, and may be regarded as the fourth criterion that should be checked beforehand in choosing laser-cooling candidates. We will demonstrate this point by investigating the laser cooling of group IVA hydrides.

There have been a lot of studies on SiH and GeH (Kleman and Werhagen, 1953a; Ram et al., 1998), while SnH and PbH have not been sufficiently studied (Alekseyev et al., 1996; Zhao et al., 2017). SiH radical has been attracting great interest over many years, since it plays a significant role in many industrial processes such as plasma vapor deposition (Ram et al., 1998). In 1930, the emission spectrum of SiH was observed using an arc source, and a strong transition near 410 nm was assigned to as the $A^2\Delta \rightarrow X^2\Pi$ transition (Jackson, 1930). In 1969, the lifetime of the $A^2\Delta$ state was measured as 700±100 ns with phase-shift technique (Smith, 1969). Later, the high-resolution spectrograms of 325 nm bands for SiH were measured with rotational analysis (Bollmark et al., 1971). In 1979, the accurate spectroscopic parameters and molecular constants of SiH were summarized and reported in the literature (Huber and Herzberg, 1979). In 1980, the emission spectroscopy of SiH in a silane glow-discharge was measured with a moderate spectrometer (Perrin and Delafosse, 1980). In 1989, the spectrum of SiH radical was observed over the laser wavelength between 426 and 430 nm by resonance-enhanced multiphoton ionization spectroscopy, and new state was tentatively assigned as $^2\Pi$ state with further computer simulation (Johnson and Hudgens, 1989). Parallel to extensive studies on SiH, the spectra of GeH are well-studied in experiment, especially for the low-lying electronic states. In 1953, the spectra of $A^4\Sigma^- \rightarrow X^2\Pi$ and $A^2\Delta \rightarrow X^2\Pi$ band for GeH were first observed (Kleman and Werhagen, 1953a,b). Subsequently, the spectroscopic constants of the $A^2\Delta$ state of GeH were deduced with rotational analysis (Klynning and Lindgren, 1966). In 1989, the radiative lifetime of the $A^2\Delta$ state of GeH was measured as 93±10 ns with laser-induced fluorescence technique (Bauer et al., 1989). In 1938, the emission spectrum of PbH was firstly detected using arc-excitation in hydrogen atmosphere (Watson, 1938). In 2008, the near-infrared emission spectra of $X^2\Pi_{3/2} \rightarrow {}^2\Pi_{1/2}$ transitions of PbH were observed using high-resolution Fourier-transform spectrometry (Setzer et al., 2008).

Theoretically, in 1967 the first *ab initio* calculations on the SiH radical were performed with the Hartree-Fock method (Cade and Huo, 1967), in which the potential energy curve (PEC) of the ground-state was obtained. In 1983, the PECs of SiH were evaluated with the multi-reference double-excitation configuration interaction calculations (Lewerenz et al., 1983). In recent years, there are many calculations about spectroscopic constants of SiH (Ram et al., 1998; Kalemos et al., 2002; Shi et al., 2008, 2013; Zhang et al., 2018). In 2013, the PECs of eleven Ω states generated from seven Λ-S states of SiH radical were calculated by the internally contracted multi-reference configuration interaction method with the Davidson correction (icMRCI+Q) (Shi et al., 2013). In 2001, the $X^2\Pi$ and $a^4\Sigma^-$ states of GeH were investigated with the MRCI approach and the spectroscopic parameters for the two states were reported (Bruna and Grein, 2001). In 2015, the lifetimes of $A^2\Delta$ and $a^4\Sigma^-$ states of GeH were obtained (Li et al., 2015). Some *ab initio* calculations on SnH and PbH were also reported (Alekseyev et al., 1996; Zhao et al., 2017).

The $A^2\Delta \rightarrow X^2\Pi$ transition of CH was pointed out to be dominated by diagonal bands, making it a potential cooling candidate (Wells and Lane, 2011b). SiH is considered to be suitable for laser cooling by Zhang et al. (2018), although they ignored the SOC effects in their laser cooling schemes. In addition, they did not consider the effect of electronic state crossing. According to previous investigations (Fu et al., 2017; Xia et al., 2017), the SOC effects are important for laser cooling molecules and will be taken into account in this work. There have not been theoretical studies reported on laser cooling of GeH, SnH, and PbH. In this work, by means of highly accurate *ab initio* and dynamical calculations, we investigate the laser cooling of group IVA hydrides and the importance of electronic state crossing in molecular laser cooling is underscored. Additionally, based on the fourth criterion mentioned above, laser cooling of CS is investigated.

The paper is organized as follows. The theoretical methods and computational details are briefly described in section 2. The results and discussion are shown in section 3. The conclusions are given in section 4.

2. METHODS AND COMPUTATIONAL DETAILS

In this paper, all the *ab initio* calculations of SiH, GeH, SnH, and PbH are performed using the MOLPRO 2012.1 program package (Werner et al., 2012). For each Λ-S state, the energies are computed using the complete active space self-consistent field (CASSCF) (Werner and Knowles, 1985) approach followed by the icMRCI+Q (Langhoff and Davidson, 1974). The lowest electronic configuration of Si is (core)$3s^2 3p^2$ corresponding to the atomic states ^3P and ^1D. In combination with the 1 s function of a H atom, the lowest electronic configuration of SiH in $X^2\Pi$ is invariably (core)$4\sigma^2 5\sigma^2 6\sigma^0 2\pi^1$ and the next is (core)$4\sigma^2 5\sigma^1 6\sigma^0 2\pi^2$ leading to the multiplets $^4\Sigma^-$, $^2\Delta$, $^2\Sigma^-$, and $^2\Sigma^+$, which could be considered as involving a $p\sigma \rightarrow p\pi$ transition within the Si atom. In asymptote region, the 5σ molecular orbital origins from the 1s on hydrogen, while the 6σ and 2π correspond to the $3p$ on silicon.

The choice of active space is very important in the CASSCF and MRCI+Q calculations (Liu et al., 2009; Yu and Bian, 2011, 2012). The active space of SiH used here consists of ten orbitals corresponding to Si 2p3s3p4p$_\pi$ and H 1s, and is referred to as (11e, 10o), which is carefully chosen to include proper orbitals, and large enough for the present calculations. Our test calculations indicate that the full valence space is inadequate, and thus additional five orbitals are added into the active space. The inner shell orbitals are included to account for the core-valence correlation effects and the outer virtual orbitals are added to give a better description on the dissociation behavior and Rydberg character, especially for excited electronic states (Shen

et al., 2017). In fact, a completely satisfactory set could neither be found by increasing the active orbital space nor by including more states (Simah et al., 1999). The best compromise we could achieve is to distribute the eleven electrons in 10 active orbitals. As for the basis set, we use the aug-cc-pV5Z basis sets for Si and H atom. In the SOC calculations, the SO eigenstates are obtained by diagonalizing $\hat{H}^{el} + \hat{H}^{SO}$ in the basis of eigenfunctions of $\hat{H}^{el}$. In addition, the $\hat{H}^{el}$ and $\hat{H}^{SO}$ are obtained from the icMRCI+Q calculations and icMRCI+Q waves functions, respectively. The active space for GeH in the present work is (9e, 9o), which consists of the Ge $3d_\pi 4s4p5p_\pi$ and H 1s orbitals. The accuracy and computational performance are compromised, thus the active space of GeH includes the $3d_\pi$ orbitals, valence orbitals and $5p_\pi$ orbitals. The aug-cc-pV5Z-DK basis sets are used for GeH. Here, the active space for SnH consists of the Sn 4d5s5p and H 1s orbitals and is referred as (15e, 10o). The aug-cc-pVQZ basis sets are used for H and aug-cc-pwCVQZ-PP with ECP28MDF effective core potentials for Sn. Similarly, the active space for PbH is (15e, 10o), which consists of the Pb 5d6s6p and H 1s orbitals. We use the aug-cc-pVQZ basis sets for H and aug-cc-pwCVQZ-PP with ECP60MDF for Pb. In addition, the active space used for the study of CS is (10e, 8o) corresponding to the C 2s2p and S 3s3p, and we use the aug-cc-pV5Z basis sets for both C and S atoms.

The Einstein spontaneous emission coefficient $A_{v'v}$ is calculated by the following expression (Herzberg, 1950),

$$A_{v'v} = \frac{16\pi^3}{3\epsilon_0 \hbar} \frac{S(J', J)}{2J' + 1} \nu^3 |\Psi_{v',J'}|M(r)|\Psi_{v,J}|^2 \quad (1)$$

where $A_{v'v}$ is in units of s^{-1}, ε_0 is the vacuum permittivity in units of F· cm^{-1}, $M(r)$ is the transition dipole function in Debye unit, ν is emission frequency in units of cm^{-1}, $\Psi_{v',J'}$ and $\Psi_{v,J}$ are normalized radial wave functions, $\hbar$ is the Planck constant and $S(J', J)$ is the Hönl-London rotational intensity factor. The radiative lifetime for a given vibrational level v' can be obtained by the following equation,

$$\tau_{v'v} = 1/\sum_{v} A_{v'v} \quad (2)$$

The spectroscopic parameters of group IVA hydrides, including the equilibrium bond length (R_e), the harmonic vibrational constant (ω_e), the rotational constant (B_e), and adiabatic relative electronic energy referred to the ground state (T_e) are obtained using the Le Royv's LEVEL program (Le Roy, 2007).

3. RESULTS AND DISCUSSION

3.1. PECs of the Λ-S States and Spectroscopic Constants

For the group IVA hydrides, the main configuration of the ground state ($X^2\Pi$) is (core)$4\sigma^2 5\sigma^2 6\sigma^0 2\pi^1$. The second lowest state here is the $A^2\Delta$, whose main configuration is (core)$4\sigma^2 5\sigma^1 6\sigma^0 2\pi^2$. The PECs of SiH, GeH, SnH, and PbH computed using the icMRCI+Q method are shown in **Figures 1**–**4**, respectively. The weights of ionic configuration

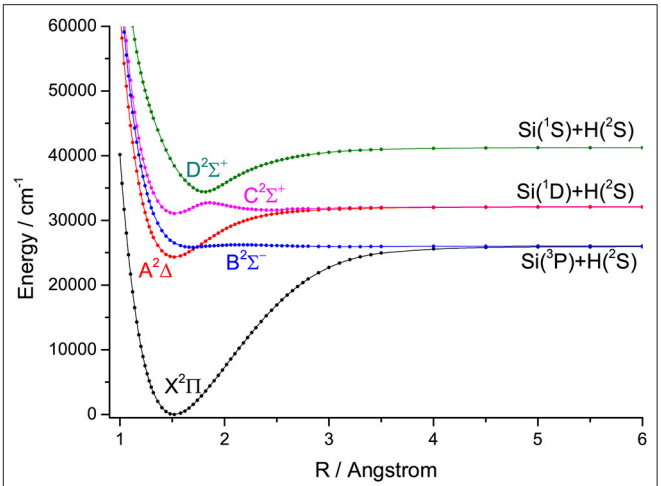

FIGURE 1 | Potential energy curves of SiH for the five Λ-S states at the icMRCI+Q level.

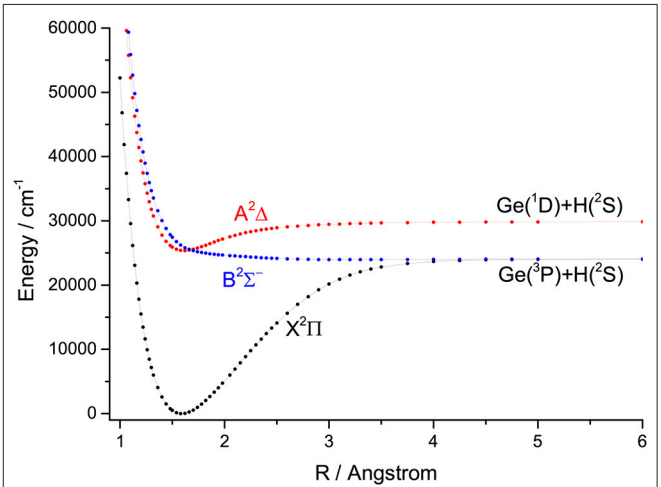

FIGURE 2 | Potential energy curves of GeH for the three Λ-S states at the icMRCI+Q level.

in the $X^2\Pi$ and $A^2\Delta$ states decrease gradually with increasing internuclear distances. As seen in **Figure 1**, the five states of SiH correlate to the three dissociation limits. The $X^2\Pi$ and $A^2\Delta$ states are the two energetically lowest lying electronic state and correlate to the neutral atomic Si(^{3}P)+H(^{2}S) limit and Si(^{1}D)+H(^{2}S) limit, respectively. From **Figures 2**–**4**, we can see that the $X^2\Pi$ and $A^2\Delta$ states of GeH, SnH, and PbH correlate to the neutral atomic Ge/Sn/Pb(^{3}P)+H(^{2}S) limit and Ge/Sn/Pb(^{1}D)+H(^{2}S) limit, respectively. The PEC of the $B^2\Sigma^-$ crosses with that of $A^2\Delta$ will be discussed in details in section 3.2. The PECs of the $B^2\Sigma^-$ and $X^2\Pi$ correlate to the same neutral atomic Si(^{3}P)+H(^{2}S) limit.

Since the spectroscopic constants of the $X^2\Pi$ and $A^2\Delta$ states have been measured in experiment for SiH, GeH, SnH, and PbH, comparing with experimental data could provide an indicator of the reliability of our calculations. We present our calculated

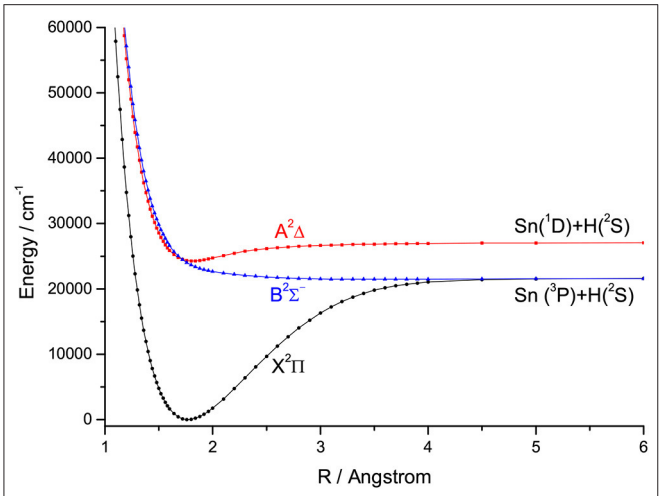

FIGURE 3 | Potential energy curves of SnH for the three Λ-S states at the icMRCI+Q level.

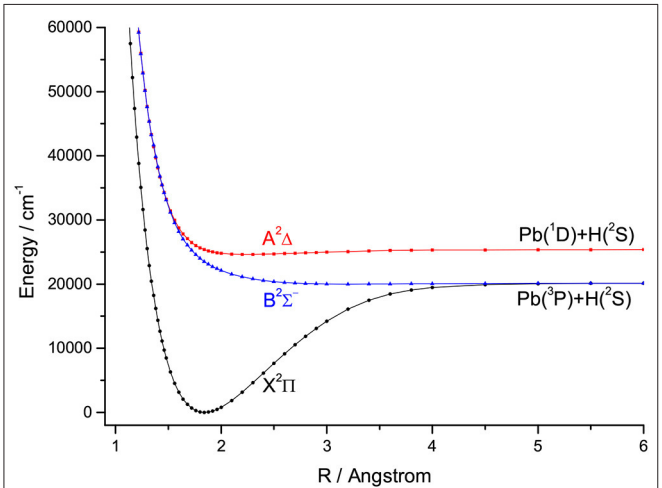

FIGURE 4 | Potential energy curves of PbH for the three Λ-S states at the icMRCI+Q level.

spectroscopic constants of SiH, GeH, and SnH in **Tables 1**, **2** and **Table S1**, together with previous theoretical and experimental values for comparison. The calculated R_e and ω_e of the $X^2\Pi$ of SiH are 1.5200 Å and 2047.71 cm^{-1}, respectively, which are in good agreement with the corresponding experiment data (1.5201 Å and 2041.80 cm^{-1}) (Huber and Herzberg, 1979). The contributions from non-valence orbitals to correlation energy are relatively small for the ground state, however, they become very important for the excited states and lead to noticeable differences. In particular, the experimental T_e is 24300.4 cm^{-1} (Huber and Herzberg, 1979) and our calculated one with a better active space is 24299.20 cm^{-1}, whereas that obtained by Zhang et al. (2018) is 25080.92 cm^{-1}, which deviates from experimental value by about 780 cm^{-1}. When additional virtual orbitals are taken into account by Kalemos et al. (2002), the deviation is

TABLE 1 | Spectroscopic constants of the $A^2\Delta$ and $X^2\Pi$ states for SiH.

State	Method	T_e (cm^{-1})	R_e (Å)	ω_e (cm^{-1})	v^a	T_v (cm^{-1})	B_e (cm^{-1})	μ_e (Debye)
$X^2\Pi$	This work		1.5200	2047.71	0	1018.07	7.5083	0.1451
					1	2996.15		
					2	4904.97		
	Expt.[b]		1.5201	2041.80			7.4996	
	Expt.[c]		1.5197	2042.52			7.5039	
	Calc.[d]		1.5223	2043.15				
	Calc.[e]		1.5223	2046.91			7.4779	
	Calc.[f]		1.5154	2043.47			7.7258	
$A^2\Delta$	This work	24299.20	1.5238	1859.72	0	25277.40	7.5164	0.134
					1	26988.69		
					2	28485.89		
	Expt.[b]	24300.4	1.5234	1858.90			7.4664	
	Expt.[g]	24255.51	1.5198				7.5027	
	Calc.[h]	24923.56	1.546	1797			7.253	0.118
	Calc.[d]	24129.60	1.5240	1853.15				
	Calc.[f]	24323.28	1.5148	1857.63			7.5021	

[a] *The vibrational levels are represented by v.*
[b] *Huber and Herzberg (1979).*
[c] *Betrencourt et al. (1986).*
[d] *Kalemos et al. (2002).*
[e] *Shi et al. (2008).*
[f] *Shi et al. (2013).*
[g] *Ram et al. (1998).*
[h] *Lewerenz et al. (1983).*

reduced to around 200 cm^{-1}. The spectroscopic constants of GeH obtained from the active space (9e, 9o) are shown in **Table 2**. The calculated R_e and ω_e of the $X^2\Pi$ of GeH are 1.5885 Å and 1902.32 cm^{-1}, respectively, which are in very good agreement with the corresponding experiment data (1.5872 Å and 1900.38 cm^{-1}) (Towle and Brown, 1993). The $A^2\Delta$ state of GeH, the experimental T_e is 25454 cm^{-1} (Huber and Herzberg, 1979), whereas our calculated T_e is 25386.63 cm^{-1}, which is much improvement compared with previous computational value 25774 cm^{-1} (Li et al., 2015).

The permanent dipole moments (PDMs) and absolute values transition dipole moments (TDMs) for the $A^2\Delta \rightarrow X^2\Pi$ transition of SiH at the icMRCI+Q level are represented in **Figure 5**. The TDMs for the $A^2\Delta \rightarrow X^2\Pi$ transition of SiH are 0.6231 D at R_e and decrease with the increasing bond length. The calculated TDMs for the $A^2\Delta \rightarrow X^2\Pi$ transition of GeH are given in **Figure S1**. The Einstein A coefficients and vibrational branching ratio of the $A^2\Delta \rightarrow X^2\Pi$ transition of GeH are listed in **Table S2**. The calculated radiative lifetime for the $A^2\Delta(v' = 0)$ state of SiH is 613 ns, which is in very good agreement with the experimental value (534 ± 23 ns) (Bauer et al., 1984). The FCFs $f_{v'v}$ of the $A^2\Delta \rightarrow X^2\Pi$ transition for GeH are calculated and plotted in **Figure S2**. In this work, the f_{00} (0.995) of SiH is in excellent agreement with the value (0.994) derived from experiment (Smith and Liszt, 1971). The computational value of f_{00} for GeH (0.940) is in very good agreement with the experimental value 0.928 (Erman et al., 1983).

TABLE 2 | Spectroscopic constants of the $A^2\Delta$ and $X^2\Pi$ states for GeH.

State	Method	T_e (cm^{-1})	R_e (Å)	ω_e (cm^{-1})	v^a	T_v (cm^{-1})	B_e (cm^{-1})	μ_e (Debye)
$X^2\Pi$	This work		1.5885	1902.32	0	943.46	6.7107	0.1076
					1	2777.80		
					2	4546.19		
	Expt.[b]		1.5872	1900.38			6.73	
	Expt.[c]		1.5880	1833.77			6.7259	
	Calc.[d]							0.097
	Calc.[e]		1.5823	1914.93			6.7688	
$A^2\Delta$	This work	25386.63	1.6100	1308.62	0	26159.92	6.5408	0.257
					1	27380.21		
					2	28307.39		
	Expt.[c]	25454	1.611	1185.15			6.535	
	Calc.[d]	26663	1.66	1302				
	Calc.[e]	25774	1.617	1306.36			6.5343	0.356

[a] *The vibrational levels are represented by v.*
[b] *Towle and Brown (1993).*
[c] *Huber and Herzberg (1979).*
[d] *Chapman et al. (1988).*
[e] *Li et al. (2015).*

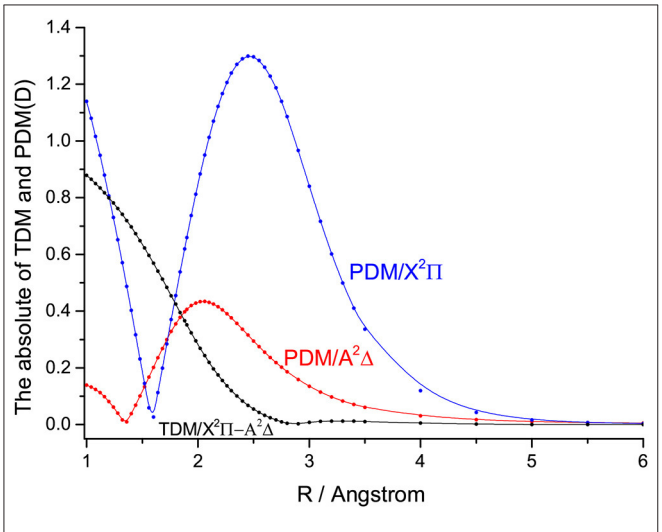

FIGURE 5 | The permanent dipole moments (PDMs) and transition dipole moments (TDMs) for the $X^2\Pi$ and $A^2\Delta$ states of SiH at the icMRCI+Q level.

3.2. The Comparison of the Feasibility of Laser Cooling for Group IVA Hydrides

There are some similar properties of group IVA hydrides. The inner closed-shell orbitals are occupied with 2, 10, 28, 46, and 78 electrons for CH, SiH, GeH, SnH, and PbH, respectively. The equilibrium bond length R_e increases regularly from CH to PbH, while the harmonic constant ω_e decreases in the order of CH>SiH>GeH>SnH>PbH (Huber and Herzberg, 1979; Alekseyev et al., 1996; Zhao et al., 2017). The comparison of the feasibility of laser cooling for group IVA hydrides is summarized here. An amplified view of crossing regions of PECs for SiH, GeH, SnH, and PbH is shown in **Figure 6**, we see that the dissociation energies of the $A^2\Delta$ states of SiH, GeH, SnH, and PbH are 7735.89, 4465.21, 2849.26, and 798.36 cm^{-1}, respectively. This trend is consistent when the second-row CH is included and the corresponding dissociation energy is 16641.68 cm^{-1} (Wells and Lane, 2011b). The depths of the $A^2\Delta$ state decrease from CH to PbH, and it supports only one vibrational level for PbH. In equilibrium region, two electrons anti-parallelly are distributed on one ($np_x^{\uparrow\downarrow}/np_y^{\uparrow\downarrow}$) and two ($np_x^{\uparrow}np_y^{\downarrow}$) sp^3 hybridized orbitals for the $B^2\Sigma^-$ and $A^2\Delta$ states, respectively. The hybridized orbital effect vanishes as the internuclear distance increases to the asymptotic region. Where, $np_x^{\uparrow\downarrow}/np_y^{\uparrow\downarrow}$ goes to X(^{3}P) and $np_x^{\uparrow}np_y^{\downarrow}$ goes to X(^{1}D). Therefore, there is a crossing point between the $B^2\Sigma^-$ and $A^2\Delta$ states of group IVA hydrides. The electronic state crossing between the $B^2\Sigma^-$ and $A^2\Delta$ states can lead to nonradiative transition (Wu et al., 2019), and may cause predissociation. This kind of electronic state crossing in a diatomic molecule will become potential energy surface intersections in the polyatomic cases involving multiple electronic states (Liu et al., 2003; Zhao et al., 2006). We find that the locations of crossing point between the $B^2\Sigma^-$ and $A^2\Delta$ states have the tendency of moving downwards from CH to SnH relative to the bottom of the corresponding $A^2\Delta$ state potential. The locations of crossing point between the $B^2\Sigma^-$ and $A^2\Delta$ states of GeH and SnH are 591 and 255 cm^{-1} lower than the corresponding vibrational level $v' = 0$ in the $A^2\Delta$, while that of third-row SiH is 670 cm^{-1} higher than the vibrational level $v' = 0$ in the $A^2\Delta$. This trend is consistent when the second-row CH is included since the corresponding crossing point is 3,000 cm^{-1} higher (Wells and Lane, 2011b).

The location of crossing point between the $B^2\Sigma^-$ and $A^2\Delta$ states of SiH is higher than the vibrational level $v' = 0$ in the $A^2\Delta$, indicating that laser cooling of SiH in the $A^2\Delta \rightarrow X^2\Pi$ transition may not be affected by electronic state crossing. However, our results imply that the crossing between the $B^2\Sigma^-$ and $A^2\Delta$ states of GeH will lead to predissociation of all vibrational levels of the $A^2\Delta$ state, which is backed up by experiments of Erman et al. (1983) using high frequency deflection technique. They reported that, 80–90% of the GeH molecules excited to the $A^2\Delta$ state decay via predissociation to their ground state atomic constituents, and fewer than 20% of the molecules follow the regular decay route to the ground state. Furthermore, the $A^2\Delta$ states of SnH and PbH have a similar problem to that of GeH, although there has been no relevant experimental measurements reported. It is clear that GeH and SnH can not be used for laser cooling due to the electronic state crossing. In addition, the small Franck-Condon factor f_{00} (0.08) of PbH also suggests that it is not suitable for laser cooling.

It seems that both CH and SiH are very good laser cooling candidates, and we make a comparison in the following. The f_{00} of SiH (0.995) is close to that of CH (0.9957) (Wells and Lane, 2011b). The radiative lifetimes of the $A^2\Delta$ state of SiH and CH are 575 and 536 ns (Wells and Lane, 2011b), respectively. The $T_{Doppler}$ and T_{recoil} of SiH (6.65 and 3.89 μK) are also similar to that of CH (7.13 and 7.91 μK) (Wells and Lane, 2011b). The

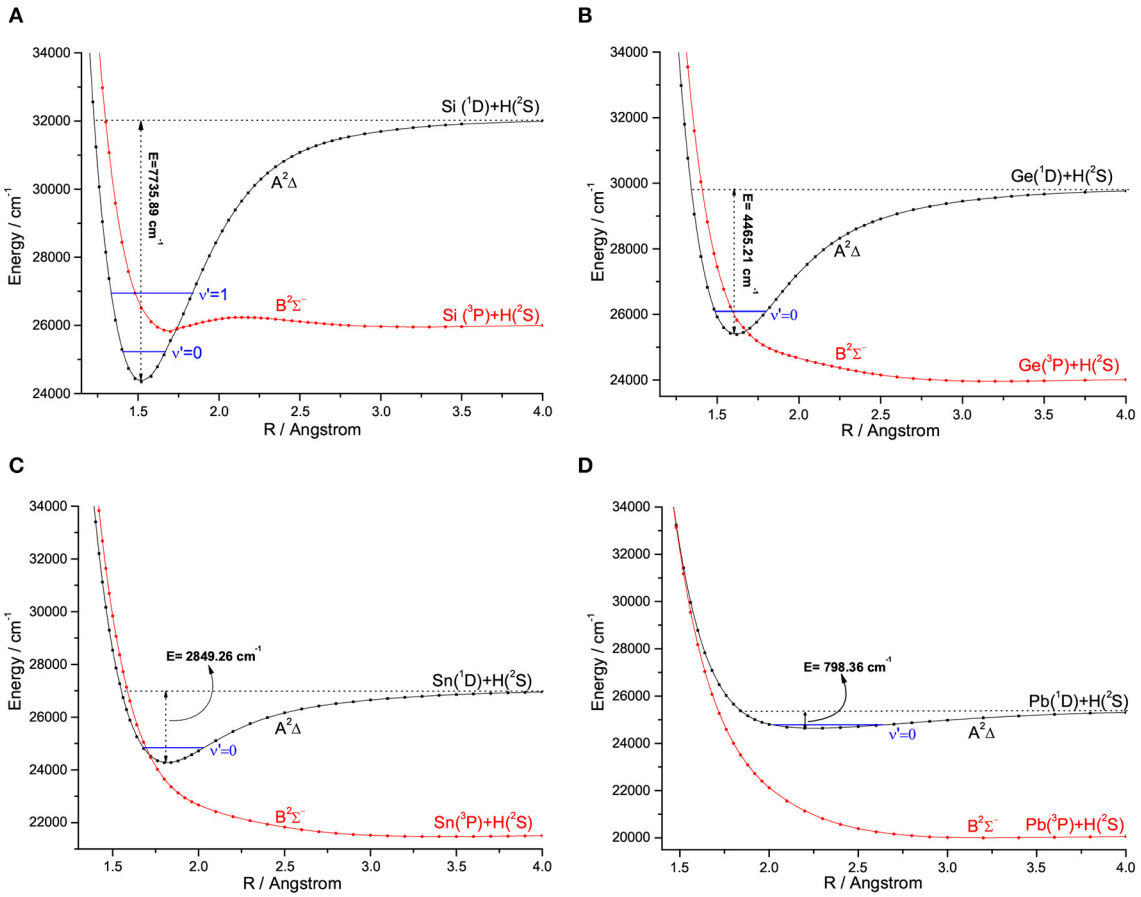

FIGURE 6 | An amplified view of crossing regions of potential energy curves for SiH **(A)**, GeH **(B)**, SnH **(C)**, and PbH **(D)**.

calculated pump and repump wavelengths for SiH and CH are all in the visible region. The electronic state crossing between the $B^2\Sigma^-$ and $A^2\Delta$ states of CH is higher than that of SiH, with both crossing points located above the corresponding vibrational $v' = 0$ levels in the $A^2\Delta$ state. Generally speaking, a larger atomic mass difference for the diatomic candidate is desirable by experimentalists, and in this respect, SiH is better than CH. Furthermore, we will propose a scheme using two spin-orbit states for SiH in the next section, which is more feasible than the one using two Λ-S states for CH. The $A^2\Delta \rightarrow X^2\Pi$ transition of CH was used to establish a laser cooling scheme, and the SOC effects were not included (Wells and Lane, 2011a). With the inclusion of the SOC effects into the icMRCI wave functions in our calculations, accurate Ω states are determined. The calculated spectroscopic constants of SiH are in very good accordance with experimental measurements. The prospect for the production of ultracold SiH molecules by means of direct laser cooling method is discussed below.

3.3. Laser Cooling Scheme for SiH

When the SOC effects are taken into account, seven Ω states, involving four states with $\Omega = 1/2$, two states with $\Omega = 3/2$ and one state with $\Omega = 5/2$, are generated from the five Λ-S states of SiH. The PECs of the Ω states are depicted in **Figure 7**. The SOC splitting of the $X^2\Pi$ and $A^2\Delta$ states of SiH is shown in **Table 3**. As seen, the energy separation of the $X^2\Pi_{1/2}$ and $X^2\Pi_{3/2}$ is 140.18 cm^{-1} in this work, which is in excellent agreement with the experimental value (142.83 cm^{-1}) (Huber and Herzberg, 1979). For the $A^2\Delta_{3/2}$ and $A^2\Delta_{5/2}$ states, the energy separation is 3.01 cm^{-1}.

We find that, the $A^2\Delta_{5/2} \rightarrow X^2\Pi_{3/2}$ transition is suitable for laser cooling in three possible transitions, $A^2\Delta_{3/2} \rightarrow X^2\Pi_{1/2}$, $A^2\Delta_{3/2} \rightarrow X^2\Pi_{3/2}$, and $A^2\Delta_{5/2} \rightarrow X^2\Pi_{3/2}$. In the $A^2\Delta_{5/2} \rightarrow X^2\Pi_{3/2}$ transition, SiH molecules will jump from the $X^2\Pi_{3/2}(v = 0)$ to the $A^2\Delta_{5/2}(v' = 0)$, then the $A^2\Delta_{5/2}(v' = 0)$ state will decay to the $X^2\Pi_{3/2}$ rather than $X^2\Pi_{1/2}$ according to the selection rules. The $A^2\Delta_{5/2} \rightarrow X^2\Pi_{3/2}$ transition can ensure a closed-loop cooling cycle, while the other two transitions can not. The three-laser cooling scheme proposed in the following using the $A^2\Delta_{5/2} \rightarrow X^2\Pi_{3/2}$ transition is more feasible than the one proposed by Zhang et al. (2018) without including the SOC effects. More importantly, they did not consider the effect of electronic state crossing, and proposed a laser cooling cycle for SiH involving the $v' = 1$ vibrational level of the $A^2\Delta$ state, which would predissociation before the radiative transition and can not be used to establish laser cooling cycles.

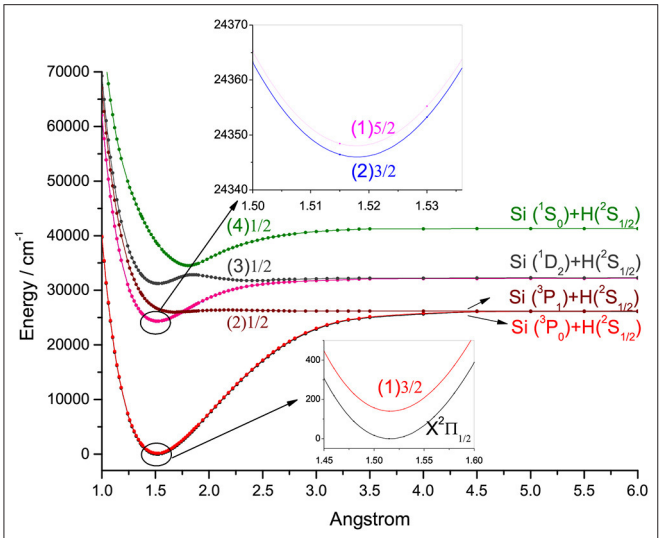

FIGURE 7 | Potential energy curves of SiH for the seven Ω states at the icMRCI+Q level.

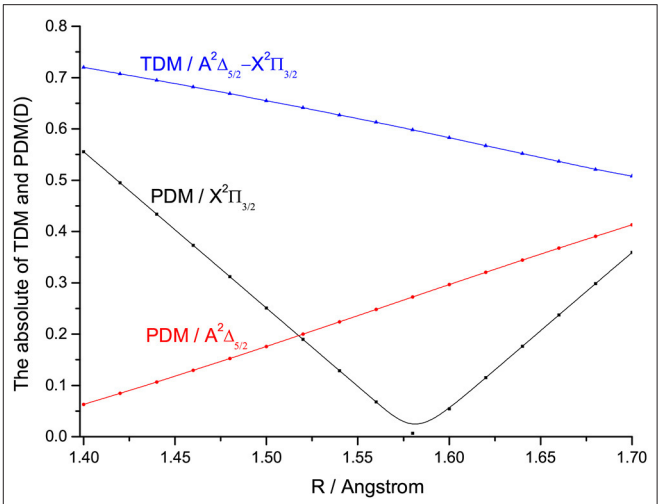

FIGURE 8 | The permanent dipole moments (PDMs) and transition dipole moments (TDMs) for the $X^2\Pi_{3/2}$ and $A^2\Delta_{5/2}$ states of SiH at the icMRCI+Q level.

TABLE 3 | The spin-orbit coupling (SOC) splitting for SiH.

State	Method	SOC splitting(cm^{-1})
X1/2, (1)3/2	This work	140.18
	Expt.[a]	142.83
	Calc.[b]	141.12
	Calc.[c]	118.5
	Calc.[d]	141.0343
(2)3/2, (1)5/2	This work	3.01
	Expt.[a]	3.58
	Calc.[b]	5.19
	Calc.[c]	0.1
	Calc.[d]	2.7135

[a]*Huber and Herzberg (1979).*
[b]*Shi et al. (2013).*
[c]*Li et al. (2008).*
[d]*Zhang et al. (2018).*

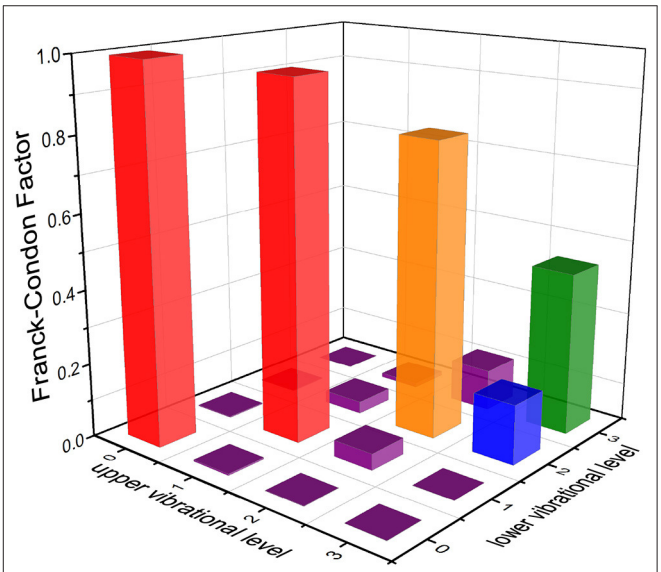

FIGURE 9 | Franck-Condon factors of the $A^2\Delta_{5/2}(v'\leq3)\rightarrow X^2\Pi_{3/2}(v\leq3)$ transition for SiH, calculated at the icMRCI+Q level.

The TDMs of SiH for the $A^2\Delta_{5/2}\rightarrow X^2\Pi_{3/2}$ transition at the icMRCI+Q level are represented in **Figure 8**. The TDMs of SiH is 0.6157 D at R_e. The FCFs values of the $A^2\Delta_{5/2}\rightarrow X^2\Pi_{3/2}$ transition for SiH are computed and shown in **Figure 9**. As seen, the $\Delta v = 0$ transitions are significantly larger than those for the off-diagonal terms. The present value of f_{00} (0.9949) is so large that the spontaneous decays to $v = 1,2$ vibrational levels in the $X^2\Pi_{3/2}$ are significantly restrained. Additionally, the relative strengths of the photon loss pathways are more directly related to the vibrational branching ratios than the FCFs in the laser cooling cycle (Lane, 2015). Furthermore, we calculate the Einstein A coefficients $A_{v'v}$ and vibrational branching ratios $R_{v'v}$ of the $A^2\Delta_{5/2}\rightarrow X^2\Pi_{3/2}$ transition for SiH. The $A_{v'v}$ and $R_{v'v}$ of the $A^2\Delta_{5/2}\rightarrow X^2\Pi_{3/2}$ transition are listed in **Table 4**. As seen in **Table 4**, a very large A_{00} (1.73×10^6 s^{-1}) and very low scattering probabilities into off-diagonal bands ($R_{01} = 3.61 \times 10^{-3}$, $R_{02} = 9.83 \times 10^{-4}$, $R_{03} = 9.20 \times 10^{-8}$) of SiH contribute to a desirable condition for rapid and efficient laser cooling. It should be noted that R_{00} (0.9954) is slightly larger than f_{00} (0.9949), indicating that the probability of spontaneous decay to the $X^2\Pi_{3/2}(v = 0)$ increases when the variations in transition wavelength are taken into account.

The vibrational branching ratios $R_{v'v}$ is determined by the following expression:

$$R_{v'v} = A_{v'v} / \sum_{v} A_{v'v} \quad (3)$$

TABLE 4 | Calculated Einstein A coefficients $A_{\nu'\nu}$ and vibrational branching ratio $R_{\nu'\nu}$ of the $A^2\Delta_{5/2}$ (ν') $\rightarrow X^2\Pi_{3/2}(\nu)$ transition for SiH.

	$\nu' = 0$		$\nu' = 1$		$\nu' = 2$		$\nu' = 3$	
	$A_{\nu'\nu}$	$R_{\nu'\nu}$	$A_{\nu'\nu}$	$R_{\nu'\nu}$	$A_{\nu'\nu}$	$R_{\nu'\nu}$	$A_{\nu'\nu}$	$R_{\nu'\nu}$
$\nu = 0$	1.73×10^6	0.9954	5.83×10^4	4.13×10^{-3}	3.50	2.83×10^{-6}	5.49×10^2	5.61×10^{-4}
$\nu = 1$	6.28×10^3	3.61×10^{-3}	1.40×10^6	0.9954	2.06×10^5	0.166	8.76×10^3	8.95×10^{-3}
$\nu = 2$	1.71×10^3	9.83×10^{-4}	3.55×10^2	2.52×10^{-5}	1.00×10^6	0.807	3.99×10^5	0.41
$\nu = 3$	0.16	9.20×10^{-8}	6.43×10^3	4.56×10^{-4}	1.59×10^4	1.28×10^{-2}	4.83×10^5	0.49

Moreover, the Doppler temperature ($T_{Doppler}$) is the achievable minimum temperature of translational cooling with the Doppler method, it is obtained by the following expression:

$$T_{Doppler} = h/(4k_B\pi\tau), \tag{4}$$

where k_B and h are Boltzmann′s constant and Planck′s constant, respectively (You et al., 2016). The radiative lifetime (τ) for the $A^2\Delta_{5/2}(\nu' = 0)$ of SiH is 575 ns and $T_{Doppler}$ is 6.65 μK. Additionally, the recoil temperature (T_{recoil}) is calculated by the following expression:

$$T_{recoil} = h^2/(mk_B\lambda^2), \tag{5}$$

and the obtained T_{recoil} for the $A^2\Delta_{5/2}(\nu' = 0) \rightarrow X^2\Pi_{3/2}(\nu = 0)$ transition of SiH is 3.89 μK.

The proposed scheme to facilitate the laser cooling of SiH is shown in **Figure 10**. The large R_{00} (0.9954) of SiH indicates that the $A^2\Delta_{5/2}(\nu' = 0) \rightarrow X^2\Pi_{3/2}(\nu = 0)$ transition has the largest probabilities. A desirable laser cooling cycle needs to solve the vibrational branching loss. Therefore, the off-diagonal vibrational branching ratios $R_{\nu'\nu}$ of SiH are calculated, and the probabilities of decay from the $A^2\Delta_{5/2}(\nu' = 0)$ to the $X^2\Pi_{3/2}(\nu = 1, 2)$ are firstly obtained ($R_{01} = 3.61\times10^{-3}$ and $R_{02} = 9.83\times10^{-4}$). Besides, the probabilities of the unwanted decay channels are also computed by using $R_{03^+} + R_{02}\times R_{13^+}$. The negligible value of 1.0×10^{-5} means that the present scheme will allow for at least 1.0×10^5 photon absorption/emission cycles, which are sufficient enough to decelerate SiH in a cryogenic beam, in principle (Shuman et al., 2010). The laser cooling scheme takes the transition $A^2\Delta_{5/2}(\nu' = 0) \leftarrow X^2\Pi_{3/2}(\nu = 0)$ as the main pump, $A^2\Delta_{5/2}(\nu' = 0) \leftarrow X^2\Pi_{3/2}(\nu = 1)$ and $A^2\Delta_{5/2}(\nu' = 0) \leftarrow X^2\Pi_{3/2}(\nu = 2)$ as the first and second vibrational repump, respectively. Accurate T_e is crucial for estimating the pump and repump wavelengths in laser cooling cycles, and our calculated T_e values, which are very close to experimental ones, give confidence in the subsequent study on laser cooling, especially, for SiH. The calculated value of wavelength λ_{01} should be larger than λ_{00}, however, the wavelengths λ_{01} obtained by Zhang et al. (2018), is 376.88 nm, which is smaller than that of their main pump. In our laser-driven cycling, the calculated pump and repump wavelengths of λ_{00}, λ_{01}, and λ_{02} are 412.6, 449.7, and 491.8 nm, respectively. The required wavelengths are all in the range of 400–500 nm and can be produced with the frequency doubled semiconductor laser, which has been used for the laser cooling experiment of the strontium atom (Wang et al., 2009). The SiH molecules will stay in the laser cooling cycle until the decay to $\nu \geq 3$ ($X^2\Pi_{3/2}$).

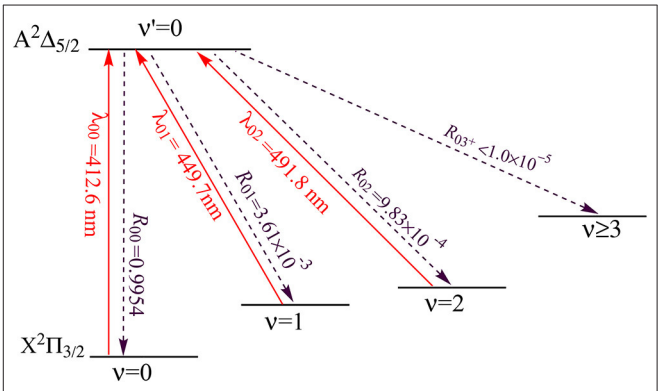

FIGURE 10 | Proposed three-laser cooling scheme for SiH using the $A^2\Delta_{5/2} \rightarrow X^2\Pi_{3/2}$ transitions. Solid arrows indicate laser-driven transitions at certain wavelengths $\lambda_{\nu'\nu}$. Dashed arrows indicate spontaneous decays from the $A^2\Delta_{5/2}(\nu' = 0)$ state with the calculated $R_{\nu'\nu}$.

3.4. Laser Cooling Scheme for CS

We further find that CS is a promising candidate based on the criteria mentioned above. The PECs of CS, obtained at the icMRCI+Q level, is shown in **Figure 11**. Our calculated R_e and ω_e of the $X^1\Sigma^+$ of CS are 1.5380 Å and 1288.63 cm^{-1}, respectively, which are in very good accordance with the corresponding experimental values (1.5349 Å and 1285.1 cm^{-1}) (Huber and Herzberg, 1979). As for the $A^2\Delta$ state of CS, our calculated T_e 39175.96 cm^{-1} is in agreement with the experimental value 38,904 cm^{-1} (Huber and Herzberg, 1979). The calculated vibrational branching ratio R_{00} is 0.885, which is highly diagonal.

As shown in **Figure 11**, the PEC of $A^1\Pi$ crosses with those of two other electronic states, however, from an amplified view of the crossing regions we see that, the two crossing points are higher than the $\nu' = 0$ vibrational level of the $A^1\Pi$ state. So this kind of crossing would not affect laser cooling cycles using the $A^1\Pi(\nu' = 0) \rightarrow X^1\Sigma^+(\nu<3)$ transition. A suitable laser cooling scheme using the $A^1\Pi \rightarrow X^1\Sigma^+$ transition of CS is proposed and

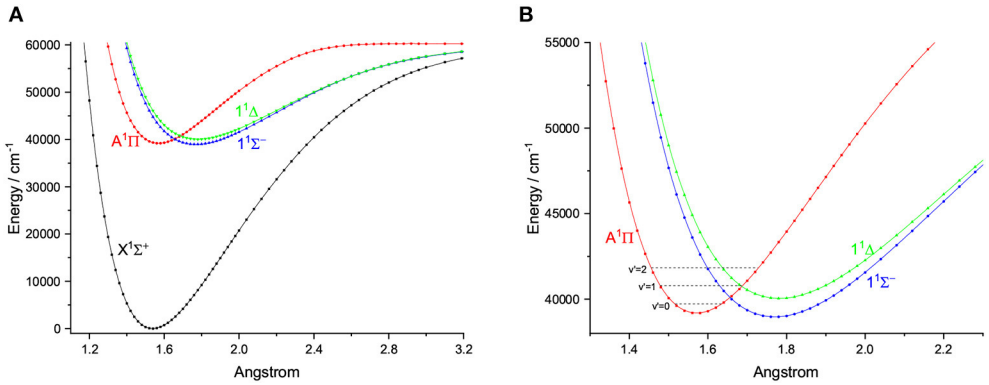

FIGURE 11 | Potential energy curves of CS for the four Λ-S states at the icMRCI+Q level **(A)** and an amplified view of crossing regions of potential energy curves **(B)**.

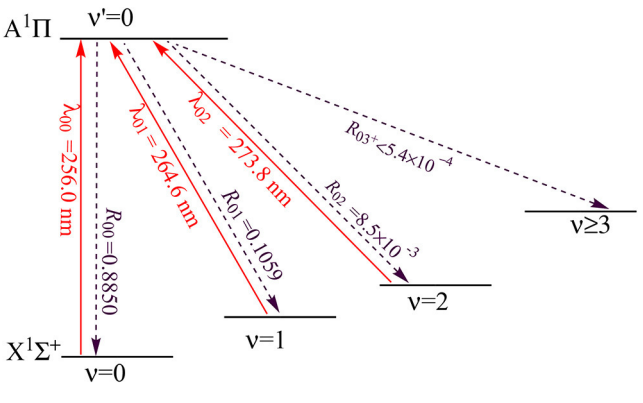

FIGURE 12 | Proposed three-laser cooling scheme for CS using the $A^1\Pi \rightarrow X^1\Sigma^+$ transitions. Solid arrows indicate laser-driven transitions at certain wavelengths $\lambda_{v'v}$. Dashed arrows indicate spontaneous decays from the $A^1\Pi(v' = 0)$ state with the calculated $R_{v'v}$.

shown in **Figure 12**. The scheme takes the transition $A^1\Pi(v' = 0) \rightarrow X^1\Sigma^+(v = 0)$ as the main pump, $A^1\Pi(v' = 0) \rightarrow X^1\Sigma^+(v = 1)$ and $A^1\Pi(v' = 0) \rightarrow X^1\Sigma^+(v = 2)$ as the first and second vibrational repump, respectively. The radiative lifetime of the $A^1\Pi$ state is 70 ns, whereas the $T_{Doppler}$ and T_{recoil} of the $A^1\Pi \rightarrow X^1\Sigma^+$ transition are 54.61 and 6.64 μK, respectively. The large R_{00}, short radiative lifetime and ultracold temperatures suggest CS as a promising candidate for rapid and efficient laser cooling.

4. CONCLUSIONS

The fourth criterion for molecular laser cooling is proposed in this work, that is, there is no electronic-state crossing, or the crossing point is high enough in energy. Its importance is demonstrated by investigating the laser cooling feasibility of group IVA hydrides and carbon monosulfide.

Ab initio and dynamical calculations are performed, and the calculated spectroscopic constants are in very good agreement with the available experimental data. We find that the locations of crossing point between the $B^2\Sigma^-$ and $A^2\Delta$ states have the tendency of moving downwards from CH to SnH relative to the bottom of the corresponding $A^2\Delta$ potential, and this would lead to failure of cooling GeH and SnH. The potential wells of the $A^2\Delta$ state of group IVA hydrides become shallower and shallower from CH to PbH, with the Franck-Condon factor decreasing, which results in a very small Franck-Condon factor for PbH. It is clear that PbH is not a suitable candidate for laser cooling either. We further propose a practical and efficient laser-cooling scheme for SiH using the $A^2\Delta_{5/2} \rightarrow X^2\Pi_{3/2}$ transition. The calculated excitation energy is 24299.20 cm^{-1}, which is in perfect agreement with the experimental data (24300.4 cm^{-1}). This allows us accurately estimate the pump and repump wavelengths in laser cooling cycles, which is shown to vary from 400 to 500 nm and are easily accessible in experiment. The Doppler temperature and recoil temperature of SiH for the $A^2\Delta_{5/2} \rightarrow X^2\Pi_{3/2}$ transition are 6.65 and 3.89 μK, respectively. The computed radiative lifetime is 575 ns, and the vibrational branching ratio is highly diagonally distributed with the R_{00} being 0.9954. Furthermore, we performed additional calculations, and find that, the carbon monosulfide (CS) is a promising candidate which meets the four criteria, and we further propose a suitable laser cooling scheme. We hope that this work will be helpful in searching for promising candidates for producing ultracold molecules.

DATA AVAILABILITY STATEMENT

All datasets generated for this study are available within the article and from the corresponding author on request.

AUTHOR CONTRIBUTIONS

DL carried out the MRCI calculations. DL, MF, HM, and WB analyzed the data and interpreted the results. ZD and CC provided computing assistance. DL, HM, and WB developed

the theoretical scheme and wrote the paper. WB supervised the research and proposed the fourth criterion for molecular laser cooling.

FUNDING

This work was supported by the National Natural Science Foundation of China (Nos. 21773251, 21973098), the Beijing National Laboratory for Molecular Sciences and Chinese Academy of Sciences.

SUPPLEMENTARY MATERIAL

The Supplementary Material for this article can be found online at: https://www.frontiersin.org/articles/10.3389/fchem.2020.00020/full#supplementary-material

REFERENCES

Alekseyev, A. B., Liebermann, H. P., Buenker, R. J., and Hirsch, G. (1996). Ab initio study of the low-lying states of SnH. *Mol. Phys.* 88, 591–603. doi: 10.1080/00268979609482439

Baron, J., Campbell, W. C., Demille, D., Doyle, J. M., Gabrielse, G., Gurevich, Y. V., et al. (2014). Order of magnitude smaller limit on the electric dipole moment of the electron. *Science* 343, 269–272. doi: 10.1126/science.1248213

Bauer, W., Becker, K. H., Düren, R., Hubrich, C., and Meuser, R. (1984). Radiative lifetime measurements of SiH ($A^2\Delta$) by laser-induced fluorescence. *Chem. Phys. Lett.* 108, 560–561. doi: 10.1016/0009-2614(84)85054-X

Bauer, W., Engelhardt, B., Wiesen, P., and Becker, K. H. (1989). Lifetime measurements of GeH and CH in the $A^2\Delta$, $v' = 0$ state by laser induced fluorescence. *Chem. Phys. Lett.* 158, 321–324. doi: 10.1016/0009-2614(89)87344-0

Betrencourt, M., Boudjaadar, D., Chollet, P., Guelachvili, G., and Morillon-Chapey, M. (1986). Infrared emission spectrum of the radical ^{28}SiH: observation and analysis of the rovibrational bands 1−0, 2−1, and 3−2 in the $X^2\Pi$ ground state. *J. Chem. Phys.* 84, 4121–4126. doi: 10.1063/1.450081

Bollmark, P., Klynning, L., and Pages, P. (1971). Rotational analysis of the 3250 Å bands of SiH and SiD. *Phys. Scripta* 185, 219–222. doi: 10.1088/0031-8949/3/5/004

Bruna, P. J., and Grein, F. (2001). Ab initio study of the $X^3\Sigma^-$, $a^1\Delta$, $b^1\Sigma^+$ states of GeH^-, and electron affinity of GeH. *J. Mol. Spectrosc.* 599, 261–269. doi: 10.1016/S0022-2860(01)00829-8

Cade, P. E., and Huo, W. M. (1967). Electronic structure of diatomic molecules. VI.A. Hartree-Fock wavefunctions and energy quantities for the ground states of the second-row hydrides, AH. *J. Chem. Phys.* 47, 614–648. doi: 10.1063/1.1711938

Cao, J., Li, F., Xia, W., and Bian, W. (2019). van der Waals interactions in bimolecular reactions. *Chinese J. Chem. Phys.* 32, 157–166. doi: 10.1063/1674-0068/cjcp1901007

Carr, L., Demille, D., Krems, R., and Ye, J. (2009). Cold and ultracold molecules: science, technology and applications. *New J. Phys.* 11:055049. doi: 10.1088/1367-2630/11/5/055049

Chapman, D. A., Li, J., Balasubramanian, K., and Lin, S. H. (1988). Theoretical study of electric dipole and transition moments of GeH, SnH and PbH. *J. Chem. Phys.* 88, 3826–3833. doi: 10.1063/1.453883

Di Rosa, M. D. (2004). Laser-cooling molecules: concept, candidates, and supporting hyperfine-resolved measurements of rotational lines in the A-X(0,0) band of CaH. *Eur. Phys. J. D* 31, 395–402. doi: 10.1140/epjd/e2004-00167-2

Erman, P., Gustafsson, O., and Larsson, M. (1983). New predissociations in GeH affecting all the $A^2\Delta$ state levels. *Phys. Scripta* 27, 256–260. doi: 10.1088/0031-8949/27/4/006

Fu, M., Cao, J., Ma, H., and Bian, W. (2016a). Laser cooling of copper monofluoride: a theoretical study including spin-orbit coupling. *RSC Adv.* 6, 100568–100576. doi: 10.1039/C6RA07835D

Fu, M., Ma, H., Cao, J., and Bian, W. (2016b). Extensive theoretical study on electronically excited states of calcium monochloride: molecular laser cooling and production of ultracold chlorine atoms. *J. Chem. Phys.* 144:184302. doi: 10.1063/1.4948631

Fu, M., Ma, H., Cao, J., and Bian, W. (2017). Laser cooling of CaBr molecules and production of ultracold Br atoms: a theoretical study including spin-orbit coupling. *J. Chem. Phys.* 146:134309. doi: 10.1063/1.4979566

González-Sánchez, L., Gómez-Carrasco, S., Santadaría, A., Wester, R., and Gianturco, F. (2019). Collisional quantum dynamics for MgH^- ($^1\Sigma^+$) with He as a buffer gas: ionic state-changing reactions in cold traps. *Front. Chem.* 7:64. doi: 10.3389/fchem.2019.00064

Herzberg, G. (1950). *Spectra of Diatomic Molecules, Vol. 235*. New York, NY: Van Nostrand Reinhold.

Huber, K. P., and Herzberg, G. (1979). *Molecular Spectra and Molecular Structure IV: Constants of Diatomic Molecules*. New York, NY: Van Nostrand Reinhold.

Hudson, J. J., Kara, D. M., Smallman, I. J., Sauer, B. E., Tarbutt, M. R., and Hinds, E. A. (2011). Improved measurement of the shape of the electron. *Nature* 473, 493–496. doi: 10.1038/nature10104

Hummon, M. T., Yeo, M., Stuhl, B. K., Collopy, A. L., Xia, Y., and Ye, J. (2013). 2D Magneto-optical trapping of diatomic molecules. *Phys. Rev. Lett.* 110:143001. doi: 10.1103/PhysRevLett.110.143001

Jackson, C. V. (1930). The spectrum of silicon hydride. *Proc. R. Soc. Lond. Ser. A* 126, 373–405. doi: 10.1098/rspa.1930.0015

Johnson, R. D. III, and Hudgens, J. W. (1989). New electronic state of silylidyne and silylidyned radicals observed by resonance-enhance multiphoton ionization spectroscopy. *J. Phys. Chem.* 93, 6268–6270. doi: 10.1021/j100354a003

Kalemos, A., Mavridis, A., and Metropoulos, A. (2002). An accurate description of the ground and excited states of SiH. *J. Chem. Phys.* 116, 6529–6540. doi: 10.1063/1.1461817

Kleman, B., and Werhagen, E. (1953a). $A^2\Delta \rightarrow X^2\Pi$ system in germanium hydride (GeH). *Arkiv Fysik* 6:359.

Kleman, B., and Werhagen, E. (1953b). $A^4\Sigma^- \rightarrow X^2\Pi$ system in germanium hydride (GeH). *Arkiv Fysik* 6:399.

Klynning, L., and Lindgren, B. (1966). Rotational analysis of the $^2\Delta \rightarrow {}^2\Pi$ band system of germanium hydride and of deuteride germanium. *Arkiv Fysik* 32:575.

Lane, I. C. (2015). Production of ultracold hydrogen and deuterium production via Doppler-cooled Feshbach molecules. *Phys. Rev. A* 92:022511. doi: 10.1103/PhysRevA.92.022511

Langhoff, S. R., and Davidson, E. R. (1974). Configuration interaction calculations on the nitrogen molecule. *Int. J. Quant. Chem.* 8, 61–72. doi: 10.1002/qua.560080106

Le Roy, R. J. (2007). *LEVEL 8.0: A Computer Program for Solving the Radial Schrödinger Equation for Bound and Quasibound Levels, Chemical Physics Research Report CPRR-663*. University of Waterloo. Available online at: http://leroy.uwaterloo.ca

Lewerenz, M., Bruna, P. J., Peyerimhoff, S. D., and Buenker, R. J. (1983). *Ab initio* MRD-CI study of the electronic spectrum of SiH. *Mol. Phys.* 49, 1–24. doi: 10.1080/00268978300101001

Li, G., Gao, T., and Zhang, Y. (2008). The splitting of low-lying or low excited states for hydride molecules (cations) of the third period under spin-orbit coupling. *Chinese Phys. B* 17, 2040–2047. doi: 10.1088/1674-1056/17/6/018

Li, R., Zhai, Z., Zhang, X., Jin, M., Xu, H., and Yan, B. (2015). All-electron spin-orbit configuration interaction study on the valence and low-lying Rydberg electronic states of GeH. *J. Quant. Spectrosc. Radiat. Transf.* 157, 42–53. doi: 10.1016/j.jqsrt.2015.02.009

Liu, C., Zhang, D., and Bian, W. (2003). Theoretical investigation of the reaction of Co^+ with OCS. *J. Phys. Chem. A* 107, 8618–8622. doi: 10.1021/jp034693s

Liu, K., Yu, L., and Bian, W. (2009). Extensive theoretical study on various low-lying electronic states of silicon monochloride cation including spin-orbit coupling. *J. Phys. Chem. A* 113:1678. doi: 10.1021/jp809618y

Perrin, J., and Delafosse, E. (1980). Emission spectroscopy of SiH in a silane glow-discharge. *J. Phys. D Appl. Phys.* 13:759. doi: 10.1088/0022-3727/13/5/009

Ram, R. S., Engleman, R., and Bernath, P. F. (1998). Fourier transform emission spectroscopy of the $A^2\Delta \rightarrow X^2\Pi$ transition of SiH and SiD. *J. Mol. Spectrosc.* 190, 341–352. doi: 10.1006/jmsp.1998.7582

Setzer, K. D., Borkowska-Burnecka, J., Zyrnicki, W., and Fink, E. H. (2008). High-resolution fourier-transform study of the $X_2{}^2\Pi_{3/2} \rightarrow X_1{}^2\Pi_{1/2}$ fine structure transitions of PbH and PbD. *J. Mol. Spectrosc.* 252, 176–184. doi: 10.1016/j.jms.2008.08.003

Shen, Z., Ma, H., Zhang, C., Fu, M., Wu, Y., Bian, W., et al. (2017). Dynamical importance of van der Waals saddle and excited potential surface in $C(^1D)+D_2$ complex-forming reaction. *Nat. Commun.* 8:14094. doi: 10.1038/ncomms14094

Shi, D., Li, P., Zhu, Z., and Sun, J. (2013). Spin-orbit coupling splitting in the $X^2\Pi$, $A^2\Delta$, $B^2\Sigma^-$, $C^2\Sigma^+$, $D^2\Sigma^+$, $F^2\Pi$ and $a^4\Sigma^-$ Λ-S states of SiH radical. *Spectrochim. Acta Part A* 115, 259–268. doi: 10.1016/j.saa.2013.06.038

Shi, D., Zhang, J., Sun, J., Zhu, Z., Yu, B., and Liu, Y. (2008). Investigations on spectroscopic properties of SiH ($X^2\Pi$) radical using coupled-cluster theory in combination with the correlation-consistent quintuple basis set. *J. Mol. Struct. Theochem* 851, 30–34. doi: 10.1016/j.theochem.2007.10.033

Shuman, E. S., Barry, J. F., and Demille, D. (2010). Laser cooling of a diatomic molecule. *Nature* 467, 820–823. doi: 10.1038/nature09443

Simah, D., Hartke, B., and Werner, H. J. (1999). Photodissociation dynamics of H_2S on new coupled ab initio potential energy surfaces. *J. Chem. Phys.* 111, 4523–4534. doi: 10.1063/1.479214

Smith, W. H. (1969). Lifetimes and total transition probabilities for NH, SiH, and SiD. *J. Chem. Phys.* 51, 520–524. doi: 10.1063/1.1672027

Smith, W. H., and Liszt, H. S. (1971). Franck-Condon factors and absolute oscillator strengths for NH, SiH, S_2 and SO. *J. Quant. Spectrosc. Radiat. Transf.* 11, 45–54. doi: 10.1016/0022-4073(71)90160-9

Towle, J. P., and Brown, J. M. (1993). The infrared spectrum of the GeH radical. *Mol. Phys.* 79, 249–261. doi: 10.1080/00268979300100211

Wang, S., Wang, Q., Lin, Y., Wang, M., Lin, B., Zang, E., et al. (2009). Cooling and trapping ^{88}Sr atoms with 461 nm laser. *Chinese Phys. Lett.* 26:093202. doi: 10.1088/0256-307X/26/9/093202

Watson, W. W. (1938). The spectrum of lead hydride. *Phys. Rev.* 54, 639–642. doi: 10.1103/PhysRev.53.639

Wells, N., and Lane, I. C. (2011a). Electronic states and spin-forbidden cooling transitions of AlH and AlF. *Phys. Chem. Chem. Phys.* 13, 19018–19025. doi: 10.1039/c1cp21313j

Wells, N., and Lane, I. C. (2011b). Prospects for ultracold carbon via charge exchange reactions and laser cooled carbides. *Phys. Chem. Chem. Phys.* 13, 19036–19051. doi: 10.1039/c1cp21304k

Werner, H.-J., and Knowles, P. J. (1985). A second order multiconfiguration SCF procedure with optimum convergence. *J. Chem. Phys.* 82, 5053–5063. doi: 10.1063/1.448627

Werner, H.-J., Knowles, P. J., Lindh, R., Manby, F. R., Schütz, M., Celani, P., et al. (2012). *Molpro, Version 2012.1, A Package of* Ab Initio *Programs*. Available online at: http://www.molpro.net

Wu, Y., Cao, J., Ma, H., Zhang, C., Bian, W., Nunez-Reyes, D., et al. (2019). Conical intersection–regulated intermediates in bimolecular reactions: insights from $C(^1D)$ + HD dynamics. *Sci. Adv.* 5:eaaw0446. doi: 10.1126/sciadv.aaw0446

Xia, W., Fu, M., Ma, H., and Bian, W. (2017). A theoretical study on laser cooling of silicon monofluoride. *Chem. Phys.* 485–486, 29–34. doi: 10.1016/j.chemphys.2017.01.007

Xu, S., Xia, M., Yin, Y., Gu, R., Xia, Y., and Yin, J. (2019). Determination of the normal $A^2\Pi$ state in MgF with application to direct laser cooling of molecules. *J. Chem. Phys.* 150:084302. doi: 10.1063/1.5083898

Yan, B., Moses, S. A., Gadway, B., Covey, J. P., Hazzard, K. R. A., Rey, A. M., et al. (2013). Observation of dipolar spin-exchange interactions with lattice-confined polar molecules. *Nature* 501, 521–525. doi: 10.1038/nature12483

You, Y., Yang, C. L., Zhang, Q. Q., Wang, M. S., Ma, X. G., and Liu, W. W. (2016). *Ab initio* studies on the spin-forbidden cooling transitions of the LiRb molecule. *Phys. Chem. Chem. Phys.* 18:19838. doi: 10.1039/C6CP01618A

Yu, L., and Bian, W. (2011). Extensive theoretical study on electronically excited states and predissociation mechanisms of sulfur monoxide including spin-orbit coupling. *J. Comput. Chem.* 32, 1577–1588. doi: 10.1002/jcc.21737

Yu, L., and Bian, W. (2012). Electronically excited-state properties and predissociation mechanisms of phosphorus monofluoride: a theoretical study including spin-orbit coupling. *J. Chem. Phys.* 137:014313. doi: 10.1063/1.4731635

Zhang, Y., Dou, G., Qi, J., and Cui, J. (2018). *Ab inito* study on the electronic structure and laser cooling of SiH. *Comput. Theor. Chem.* 1134, 8–14. doi: 10.1016/j.comptc.2018.04.014

Zhao, H., Bian, W., and Liu, K. (2006). A theoretical study of the reaction of $O(^3P)$ with isobutene. *J. Phys. Chem. A* 110, 7858–7866. doi: 10.1021/jp060583k

Zhao, S., Li, R., Zhang, H., and Li, H. (2017). MRCI+Q calculations on spectroscopic properties of excited states of PbH including spin-orbit coupling. *Chem. Phys. Lett.* 671, 92–99. doi: 10.1016/j.cplett.2017.01.016

Zhelyazkova, V., Cournol, A., Wall, T. E., Matsushima, A., Hudson, J. J., Hinds, E. A., et al. (2014). Laser cooling and slowing of CaF molecules. *Phys. Rev. A* 89, 12707–12715. doi: 10.1103/PhysRevA.89.053416

Conflict of Interest: The authors declare that the research was conducted in the absence of any commercial or financial relationships that could be construed as a potential conflict of interest.

frontiers in Physics

ORIGINAL RESEARCH
published: 30 January 2020
doi: 10.3389/fphy.2020.00005

A Circuit Topology Approach to Categorizing Changes in Biomolecular Structure

Otto Schullian[1†], *Jaie Woodard*[2†], *Arash Tirandaz*[3,4†] *and Alireza Mashaghi*[4*]

[1] *Max Planck Institute of Colloids and Interfaces, Department Theory and Biosystems, Potsdam, Germany,* [2] *Chemistry and Chemical Biology, Harvard University, Cambridge, MA, United States,* [3] *School of Biological Sciences, Institute for Research in Fundamental Sciences (IPM), Tehran, Iran,* [4] *Faculty of Mathematics and Natural Sciences, Leiden Academic Centre for Drug Research, Leiden University, Leiden, Netherlands*

The biological world is composed of folded linear molecules of bewildering topological complexity and diversity. The topology of folded biomolecules such as proteins and ribonucleic acids is often subject to change during biological processes. Despite intense research, we lack a solid mathematical framework that summarizes these operations in a principled manner. Circuit topology, which formalizes the arrangements of intramolecular contacts, serves as a general mathematical framework to analyze the topological characteristics of folded linear molecules. In this work, we translate familiar molecular operations in biology, such as duplication, permutation, and elimination of contacts, into the language of circuit topology. We show that for such operations there are corresponding matrix representations as well as basic rules that serve as a foundation for understanding these operations within the context of a coherent algebraic framework. We present several biological examples and provide a simple computational framework for creating and analyzing the circuit diagrams of proteins and nucleic acids. We expect our study and future developments in this direction to facilitate a deeper understanding of natural molecular processes and to provide guidance to engineers for generating complex polymeric materials.

Keywords: topology, matrix representation, protein folding, protein engineering, permutation, duplication, elimination

OPEN ACCESS

Edited by:
Sabre Kais,
Purdue University, United States

Reviewed by:
Kelin Xia,
Nanyang Technological University, Singapore
Ross Douglas Hoehn,
Qatar Environment and Energy Research Institute, Qatar

***Correspondence:**
Alireza Mashaghi
a.mashaghi.tabari@lacdr.leidenuniv.nl

[†]*These authors have contributed equally to this work*

Specialty section:
This article was submitted to Physical Chemistry and Chemical Physics, a section of the journal Frontiers in Physics

Received: *02 April 2019*
Accepted: *06 January 2020*
Published: *30 January 2020*

Citation:
Schullian O, Woodard J, Tirandaz A and Mashaghi A (2020) A Circuit Topology Approach to Categorizing Changes in Biomolecular Structure. Front. Phys. 8:5. doi: 10.3389/fphy.2020.00005

1. INTRODUCTION

Topology is a mathematical concept that refers to specific properties of objects that remain invariant under continuous operations like stretching, bending, or shrinking [1]. Objects that transform to each other by such continuous deformations fall into the same topological class. For instance, circles and triangles are topologically alike since they can interconvert by bending or stretching. There is a close relationship between the functional and physical properties of molecular structures and their topological features [2, 3]. Moreover, topology provides elementary rules that help us to engineer molecules in a desired way and to synthesize new structures [4–6]. Emergent properties may be seen in such synthetic molecules that have no counterpart in the biochemical world [7, 8].

In chemistry there are general frameworks, such as group theory, that aid in investigating the topological and geometrical properties of molecules. In biology, however, we lack similar

frameworks. The diversity and complexity of biological molecules make it difficult to reduce the structural and functional properties of molecules to simple rules of symmetry. Consequently, creating a topological language for biochemistry and biochemical engineering is an interesting scientific challenge. Such a framework would be a powerful tool for unifying the diversity of molecules within a coherent closed theory. Many applications can be envisioned, as the relation between topology and biomolecular function or dysfunction has been addressed frequently in health and disease [9, 10]. Topological approaches have already been implemented in powerful machine learning algorithms to correctly predict protein-ligand binding affinities, mutation induced globular protein folding free energy changes, and mutation induced membrane protein folding free energy changes [11, 12].

Biological circuit topology is a mathematical approach that describes the relationships between intramolecular contacts within a folded molecule [13–20]. In this framework, pairwise relations between contacts can be defined using the logic rules of set theory [13, 14]. Irrespective of the kind of molecule or its complexity, two contacts may have one of a few general symmetry relations with one another. For binary contacts, they might be in parallel, in series, or in cross arrangement, or in corresponding concerted arrangements if two contacts share a site. **Figure 1** demonstrates these arrangements and the associated matrices showing connectivity of sites. Completeness of these relations can be proved [13], and they can be considered as necessary and sufficient to describe the topology of folded molecules (formed by di- or multivalent contacts). Circuit topology forms a set of rules that can be used to find unknown topological relations between contacts from known relations. In this approach, topology is represented in matrix forms, and equivalent topologies are inferred from identical matrix representations. Biological circuit topology makes it possible to determine the topology of a more complex molecule resulting from the combination of simpler molecules. The folding rates and number of unfolding paths of a macromolecule can be estimated using circuit topology rules [14].

The circuit topology of biomolecules is subject to changes during folding/unfolding and biochemical reactions as well as during evolution. Here we ask how the topology changes upon basic molecular operations such as permutation of contacts, duplication, or elimination. We develop a simple algebraic formalism to describe the effect of these operations. Briefly, each topological state can be described by a connectivity matrix, and topological changes can be described as transformations of the matrix, for which linear algebra already provides all the necessary tools. We show that the outcome of operations on molecules with complex topologies can be readily predicted from this approach. Our results are relevant to understanding the evolution and structural similarities of proteins and other biological molecules, and they may help provide a guideline to molecular engineers interested in engineering folded molecules, active materials, and smart structures.

2. CIRCUIT TOPOLOGY AND MOLECULAR OPERATIONS

We will introduce here a new way of describing both the topological state of a folded linear polymer and molecular operations on the structure. Both the topological state and changes to this state are represented using permutation matrices (representations of S_n) and are connected with the well known tools of matrix multiplication.

2.1. Circuit Topology

In the following, we redefine basic concepts of circuit topology to allow for the ability to use simple algebraic operations, rather than relying on combinatorical algorithms. In this generalized approach, we show that any structure of a linear molecule can be uniquely represented by a permutation matrix $\mathcal{S}$ and a vector d, called the **connectivity matrix** and **backbone**, respectively.

A mathematic permutation is an exchange of elements. The abstract map is often denoted with a greek letter (we will often use π) and maps an integer onto another integer $\pi(i) = j$. If and only if a permutation exchanges only two elements it is called a transposition. The abstract permutation can be represented by a permutation matrix. A permutation matrix exchanges elements of a vector according to the permutation. It has only entries of 1 and 0, and the sum of each row and the sum of each column is 1. In the case of circuit topology not any permutation matrix can be used. First of all, $\mathcal{S}$ must be symmetric, i.e., it consists only of commutating transpositions. The matrix

$$\mathcal{S} = \begin{pmatrix} 0 & 1 & 0 \\ 1 & 0 & 0 \\ 0 & 0 & 1 \end{pmatrix} \tag{1}$$

for example, exchanges element 1 with 2 and leaves the element 3 unchanged [it is often represented as (12) (3) or (12)]. In biological circuit topology this represents a connection between the element 1 and 2 of the backbone d.

The backbone d is a vector that holds the information of the underlying molecular structure. It may consist of the indices of all the aminoacids in a protein or nucleotides in a DNA sequence, or it can be the length of the string/chain up to a particular point d_i. d need not be complete (i.e., it need not contain the whole array of indices), for example $d = (2, 5, 20, 21)$ is a valid backbone vector. In addition the values need not be unique. This means e.g., $d = (1, 2, 2, 3)$ is also acceptable and in some cases even required. If the elements of d are distances, then d_i can be any real number, e.g., $d = (1.23, 1.938, 5.392)$. If an element is not exchanged by the connectivity matrix (for example the element 3 in Equation 1) then it can safely be eliminated from the representation without changing the state of the molecule:

$$\mathcal{S} = \begin{pmatrix} 0 & 1 \\ 1 & 0 \end{pmatrix} \tag{2}$$

When changing the pair $(\mathcal{S}, d)$ in this way, the molecule itself is not changed, but the representation is minimalized. A more detailed discussion on transformations can be found in the next section.

$$\text{P:}\quad \begin{pmatrix} 0 & 0 & 0 & 1 \\ 0 & 0 & 1 & 0 \\ 0 & 1 & 0 & 0 \\ 1 & 0 & 0 & 0 \end{pmatrix} \quad d = \begin{pmatrix} 1 \\ 2 \\ 3 \\ 4 \end{pmatrix}$$

$$\text{S:}\quad \begin{pmatrix} 0 & 1 & 0 & 0 \\ 1 & 0 & 0 & 0 \\ 0 & 0 & 0 & 1 \\ 0 & 0 & 1 & 0 \end{pmatrix} \quad d = \begin{pmatrix} 1 \\ 2 \\ 3 \\ 4 \end{pmatrix}$$

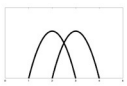

$$\text{X:}\quad \begin{pmatrix} 0 & 0 & 1 & 0 \\ 0 & 0 & 0 & 1 \\ 1 & 0 & 0 & 0 \\ 0 & 1 & 0 & 0 \end{pmatrix} \quad d = \begin{pmatrix} 1 \\ 2 \\ 3 \\ 4 \end{pmatrix}$$

$$\text{CS:}\quad \begin{pmatrix} 0 & 1 & 0 & 0 \\ 1 & 0 & 0 & 0 \\ 0 & 0 & 0 & 1 \\ 0 & 0 & 1 & 0 \end{pmatrix} \quad d = \begin{pmatrix} 1 \\ 2 \\ 2 \\ 3 \end{pmatrix}$$

$$\text{CP:}\quad \begin{pmatrix} 0 & 0 & 1 & 0 \\ 0 & 0 & 0 & 1 \\ 1 & 0 & 0 & 0 \\ 0 & 1 & 0 & 0 \end{pmatrix} \quad d = \begin{pmatrix} 1 \\ 1 \\ 2 \\ 3 \end{pmatrix}$$

FIGURE 1 | The five types of circuit topology relations representes as a connectivity matrix $\mathcal{S}$ and the corresponding graph.

The pair $(\mathcal{S}, d)$ defines a state of a linear molecule (e.g., protein, DNA), where d defines the bonding sites and $\mathcal{S}$ the connectivity of these bonding sites. **Figure 1** shows a two-bond system with all possible relations. The possible relations are series (S), cross (X), and parallel (P). Two special connectivity relations (concerted parallel and concerted series) are discussed below. Note that only P is non-reflexive and has an inverse relation P^{-1}, for more detailed information see Mashaghi et al. [13].

For most of the connectivity relations the connectivity map $\mathcal{S}$ is identical to the contact map, however two special connectivity relations lead to different matrices: concerted parallel (CP) and concerted series (CS). For a contact with residue 1 and 2 and contact 2 with 3 (CS) the contact map is given by

$$\mathcal{S} = \begin{pmatrix} 0 & 1 & 0 \\ 1 & 0 & 1 \\ 0 & 1 & 0 \end{pmatrix} \tag{3}$$

This is however not a permutation matrix and therefore forbidden as a connectivity matrix. In order to represent this system in the circuit topology framework d must contain the contact site 2 twice, one of which being in contact with 1 and the other with 3. One might think of it as fictionally separating the site 2 into two separate and distinct sites, 2 and 2', forming the connection and then bringing them together by $2 = 2'$. The correct connectivity matrix and backbone for CS are therefore

$$\mathcal{S} = \begin{pmatrix} 0 & 1 & 0 & 0 \\ 1 & 0 & 0 & 0 \\ 0 & 0 & 0 & 1 \\ 0 & 0 & 1 & 0 \end{pmatrix} \qquad d = \begin{pmatrix} 1 \\ 2 \\ 2 \\ 3 \end{pmatrix}. \tag{4}$$

Figure 1 also shows the correct representation for *CP*.

The demand for uniqueness requires additional restrictions on d and $\mathcal{S}$. If d only contains each value once, then ordering is sufficient for uniqueness; however if this is not the case, then several equivalent arrangements of d will lead to different $\mathcal{S}$ (for example, swapping index 2 with 3 in Equation 4). We define the ordered state therefore as follows: for all i and j with $i < j$ we have $d_i \leq d_j$ and if $d_i = d_j$ then it follows that $\pi(i) < \pi(j)$, where π is the permutation that is represented by $\mathcal{S}$. For example,

$$\mathcal{S} = \begin{pmatrix} 0 & 0 & 1 & 0 \\ 0 & 0 & 0 & 1 \\ 1 & 0 & 0 & 0 \\ 0 & 1 & 0 & 0 \end{pmatrix} \qquad d = \begin{pmatrix} 1 \\ 2 \\ 2 \\ 3 \end{pmatrix} \tag{5}$$

is the same state as in Equation (4), however for $d_2 = d_3$ but $4 = \pi(2) \not< \pi(3) = 1$, therefore the only correct representation is in Equation (4).

In addition we also impose the rule that there can not be contact between identical sites and that any bond can occur at most once. This means that a contact like

$$\mathcal{S} = \begin{pmatrix} 0 & 1 \\ 1 & 0 \end{pmatrix} \qquad d = \begin{pmatrix} 1 \\ 1 \end{pmatrix}, \tag{6}$$

is never allowed. With these restriction (d is ordered, $\mathcal{S}$ is ordered for $d_i = d_j$ and no contacts between equal sites) $\mathcal{S}$ is said to be reduced. This gives uniqueness and the ordering is consistent with previously defined orders [20]. For the complete proof see **Supplementary Information**.

Finally, we introduce the relations matrix [13]. The relations matrix is a $n \times n$-matrix that contains the relation between bonds, where n is the number of contacts. The relations are the known $X, P, P^{-1}, S \ldots$. This representation is mostly for the purpose of display, because it is smaller than $\mathcal{S}$ and the relation between bonds can immediately be read out.

Finally we will propose a simple way of comparing different states:

- identical: $d = d'$ and $\mathcal{S} = \mathcal{S}'$
- partially equivalent: $\mathcal{S} = \mathcal{S}'$ and both d and d' are ordered in a similar way, where $\mathcal{S}$ and d exclude any elements without connections.
- non-equivalent: otherwise.

The description of the topological state of a protein using the pair $(\mathcal{S}, d)$ provides a powerful tool to perform transformations using algebraic operations which are well-known and readily available. The various types of transformations are discussed in the next section.

2.2. Molecular Operations

2.2.1. General

A molecular operation is any map such that $\mathcal{T}:(\mathcal{S},d)\mapsto(\mathcal{S}',d')$. We can loosely classify these operations as rearrangements or as operations where the topological state of the molecule is changed (molecular operation), or as a combination of both types. Clearly, we are interested in the molecular operations where both the pre-image and the image are ordered and reduced. The restriction is necessary because it will conveniently directly lead to a unique map that describes the change explicitly [without any additional combinatorial (re)arrangements]. We first describe three types of transformations, that give the transformations a clear interpretation.

The first set of transformations are type-0 transformations. Type-0 deformation do not change the topological state of the molecule, and form a group that consist of reordering, extending and reducing of d.

The first subgroup consists of the ordering transformations. If d is not ordered, then one can order it using a permutation matrix O, which swaps the corresponding elements in d. This must lead to a change in $\mathcal{S}$ for the system to remain unchanged. The change is described by $\mathcal{S}'=O\mathcal{S}O^{-1}$. In summary, the pair $(\mathcal{S},d)$ and $(\mathcal{S}',d')=(O\mathcal{S}O^{-1},Od)$ describe the same state, but are different representations. Visually it can be thought as relabeling the residues in a protein, without changing the sequence or the connectivity.

For example, we consider the state where residue 1 with 2, as well as residue 3 and 4 share a connection. The system is described by the following $\mathcal{S}$ and d

$$\mathcal{S}=\begin{pmatrix}0&0&1&0\\0&0&0&1\\1&0&0&0\\0&1&0&0\end{pmatrix}\qquad d=\begin{pmatrix}1\\3\\2\\4\end{pmatrix}. \tag{7}$$

d is however not ordered, which might lead to confusion, as S could be mistaken for a X state. Redordering demand that the element d_2 and d_3 are exchanged. The corresponding permutation matrix O is given by

$$O=\begin{pmatrix}1&0&0&0\\0&0&1&0\\0&1&0&0\\0&0&0&1\end{pmatrix} \tag{8}$$

and we can calculate the transformed d' and $\mathcal{S}'$

$$d'=O\begin{pmatrix}1\\3\\2\\4\end{pmatrix}=\begin{pmatrix}1\\2\\3\\4\end{pmatrix}, \tag{9}$$

$$\mathcal{S}'=\begin{pmatrix}1&0&0&0\\0&0&1&0\\0&1&0&0\\0&0&0&1\end{pmatrix}\begin{pmatrix}0&0&1&0\\0&0&0&1\\1&0&0&0\\0&1&0&0\end{pmatrix}\begin{pmatrix}1&0&0&0\\0&0&1&0\\0&1&0&0\\0&0&0&1\end{pmatrix}^{-1} \tag{10}$$

$$=\begin{pmatrix}1&0&0&0\\0&0&1&0\\0&1&0&0\\0&0&0&1\end{pmatrix}\begin{pmatrix}0&1&0&0\\0&0&0&1\\1&0&0&0\\0&0&1&0\end{pmatrix} \tag{11}$$

$$=\begin{pmatrix}0&1&0&0\\1&0&0&0\\0&0&0&1\\0&0&1&0\end{pmatrix} \tag{12}$$

The pair $(\mathcal{S}',d')$ clearly describe the same state, however the fact that d is ordered, makes it easier to interpret and prevents reading errors. This is especially of importance when transformations of other types (see below) produce an unordered d that might be not noticed.

The other group of transformations of type-0 increase or decrease the length of d but do not change the topological state of molecule. The reduction, for example, can be used to eliminate unbound contact sites, to give a smaller $\mathcal{S}$ still containing all the necessary information. The extension does the opposite. It may, for instance, add another entry in d so that additional bonds can be formed, or it may reintroduce whole blocks of the protein which were disregarded because they might not have been of importance. An example for a type-0 transformation is given by

$$\mathcal{S}=\begin{pmatrix}0&1&0\\1&0&0\\0&0&1\end{pmatrix}\mapsto\ \mathcal{S}'=\begin{pmatrix}0&1\\1&0\end{pmatrix}. \tag{13}$$

The molecular operations that literally change the molecule can be separated into (i) transformations that change the contacts (Type I), and (ii) transformations that change the backbone (Type II).

1. Type-I transformations lead to a change of the contacts. This means that either new contacts are formed (creation), existing contacts are broken (annihilation), or both. Both operations are performed with the same operator, which is a permutation matrix which transposes the elements that are affected. The operator matrix is multiplied to the $\mathcal{S}$ matrix, but one must be careful to perform the annihilation(s) first. In some cases the final state is unordered and must be reordered again. Reordering is a type-0 transformation and requires $(\mathcal{S}',d')=(O\mathcal{S}O^{-1},Od)$. For the simple case of $\mathcal{S}=(23)$ where the bond (23) is broken and a bond (12) is created we use

$$\begin{aligned}\mathcal{S}'&=T^{(12)}T^{(23)}\mathcal{S}\\&=\begin{pmatrix}0&1&0\\1&0&0\\0&0&1\end{pmatrix}\begin{pmatrix}1&0&0\\0&0&1\\0&1&0\end{pmatrix}\begin{pmatrix}1&0&0\\0&0&1\\0&1&0\end{pmatrix}\\&=\begin{pmatrix}0&1&0\\1&0&0\\0&0&1\end{pmatrix}\end{aligned} \tag{14}$$

If, on the other hand, the initial and final states are known the total transformation matrix can directly be calculated with $T=\mathcal{S}'\mathcal{S}^{-1}=\mathcal{S}'\mathcal{S}$. This also gives the shortest path from $\mathcal{S}$ to $\mathcal{S}'$ because any transposition is its own inverse. For

example, the transformation $(12)(34)(56) \mapsto (12)(36)$ will give $T = (12)(36) \cdot (12)(34)(56) = (12)(12)(34)(56)(36) = (12)(12)(36)(34)(56) = (36)(34)(56)$. This shows that at the most three operations need to be performed. (The same result would be obtained using matrices).

As mentioned already, if the resulting state is unordered, it must be reordered again. Otherwise operations might arise that do not actually change the system. This is only the case if d contains a value multiple times. For example, consider $d = (1, 2, 2)$ and $\mathcal{S} = (12)$. Annihilation of (12) and creation of (13) would give $\mathcal{S}' = (13)$. This is not ordered however because for $i = 2 < 3 = j$ will give $d_2 = 2 = d_3$ but $\pi(2) = 2 > \pi(3) = 1$ which is contrary to the assumption of $(\mathcal{S}, d)$ being ordered. Reordering will give $\mathcal{S}'' = O\mathcal{S}'O^{-1} = (23)(13)(23) = (12) = \mathcal{S}$, so the same as the initial state. The transformation described is therefore actually only the unity map.

2. Type-II transformations: these types of transformation literally change the backbone of the molecule. The map acts therefore mostly on d which afterwards must be ordered again. For simple categories as below, simple transformations are readily available but in theory almost any map on d is possible. For example when a part is cut out reattached then: $d = (1, 2, 3, 4) \mapsto d = (1, 2, 4, 3)$. This d however has to be reordered with $O = (34)$ and in turn $\mathcal{S}' = OSO^{-1}$ also changes.

The biological difference of type-I and type-II is clear, however from a mathematical perspective they may be equivalent. As long as the same resulting state appears the map is mathematically identical and interchangeable. If a type-I and a type-II transformation are equivalent, and one might be much more complex to perform, it can easily be reproduced with the other transformation. This is comparable to coordinate transformation: one can either rotate a point in space with respect to a fixed coordinate system or rotate the coordinates and leave the point fixed. Both transformations yield the same result but the mathematical procedure is different. The same can be said about type-I and type-II transformations.

In the following, we redefine the most important molecular operations using the logic of circuit topology. Specifically, we treat circular and standard permutation, inversion, duplication, and elimination. These operations are of much relevance to biomolecular evolution, conformational dynamics and folding, and structural comparison. We discuss these operations in detail in the context of biological circuit topology, and we demonstrate specific applications to the analysis of protein and RNA structure. In the **Supplementary Information**, we present the complete mathematical framework, citing specific examples in the main text.

2.2.2. Permutation

Permutation changes contacts through restructuring or reordering, resulting in a new structure with different connectivity. Mathematically it can either be a type-I or type-II molecular operation, it is however simpler to treat this transformation as a type-II molecular operation. This does not necessarily imply that biologically it is a type-II transformation, it is just simpler to calculate it as such. That such changes have relevance to biomolecules is well-established, and algorithmic approaches have even been proposed for the detection of permutation [21–23]. Here, we focus on two types of permutation, namely standard permutation and circular permutation.

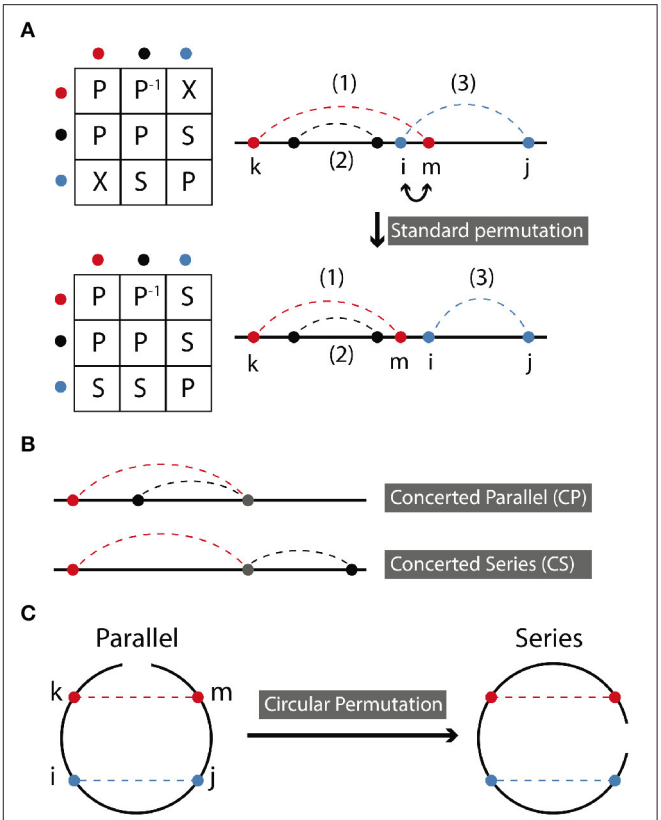

FIGURE 2 | (A) Standard permutation takes place when two nearest neighbor sites are exchanged. $aP^{-1}b$, where a and b are abstract notations for bond a and bond b means that b is in parallel with a. Here, colors red, black, and blue, each stand for a specific bond. Relationships between bonds are represented by a letter, as described in the text. **(B)** Concerted parallel (CP) and concerted series (CS) are depicted. **(C)** Circular permutation occurs by rotating the endpoint of the molecule. It can transform a series relation to parallel and vice versa depending on the position of the ending point.

2.2.2.1. Standard permutation

In standard permutation, two sites are swapped (replaced with each other), while preserving other aspects of connectivity. **Figure 2A** demonstrates a standard permutation in which sites i and m are swapped, thereby transforming a cross relation into a series relation. Following the specific example shown in **Figure 2A**, permutation takes place between the middle sites of (1) and (3) which are in cross arrangement. The resulting symmetry of the two contacts in the new molecule will be series. The symmetry relations of contact (2) and other contacts remain unchanged, i.e., in parallel with (1) and in series with (2) as before.

The matrix formalism for standard permutation is described in the previous section. In the case of the example discussed above, the original arrangement of contacts is given by the connectivity matrix (which in this instance is identical to the contact map).

$$\mathcal{S} = \begin{pmatrix} 0&0&0&0&1&0 \\ 0&0&1&0&0&0 \\ 0&1&0&0&0&0 \\ 0&0&0&0&0&1 \\ 1&0&0&0&0&0 \\ 0&0&0&1&0&0 \end{pmatrix} \tag{15}$$

For instance, the first site is bonded to the fifth, and so there is a 1 at column 5 of the first row, and so on. There are three contacts, each containing unique sites, so the size of the contact matrix is 6 $\times$ 6, and the matrix is of course symmetric (if 2 contacts 3, then 3 will contact 2). By definition, no site is in contact with itself. The permutation matrix for exchange of sites 4 and 5 is given by

$$O = \begin{pmatrix} 1&0&0&0&0&0 \\ 0&1&0&0&0&0 \\ 0&0&1&0&0&0 \\ 0&0&0&0&1&0 \\ 0&0&0&1&0&0 \\ 0&0&0&0&0&1 \end{pmatrix} \tag{16}$$

Then we have $\mathcal{S}' = OSO^{-1}$ which is equal to

$$\mathcal{S}' = \begin{pmatrix} 0&0&0&1&0&0 \\ 0&0&1&0&0&0 \\ 0&1&0&0&0&0 \\ 1&0&0&0&0&0 \\ 0&0&0&0&0&1 \\ 0&0&0&0&1&0 \end{pmatrix} \tag{17}$$

Table 1 summarizes all possible results of standard permutation for a system containing two contacts. For instance, a cross, series, or parallel relation can be converted into any other of the three relations by application of the appropriate transformation. In the context of biological molecules, two contacts may share a contact site, resulting in concerted parallel (CP) or concerted series (CS) relations, as shown in **Figure 2B**. The effect of standard permutation on these relations is summarized in **Table 2**, where each "site" represent, for instance, a secondary structural element or nucleotide. For two contacts, there are four sites: two adjacent inner sites and two outer sites; sites may either be neighboring or non-neighboring.

Inversion can be understood in terms of standard permutation operations and is discussed in the **Supplementary Information**.

We further illustrate the concept of standard permutation using an example from protein structure. For details of the computational approach for diagram generation (see **Figure S2**). In this and other examples, we assume some familiarity with biomolecular structure; for readers less familiar with this field, excellent introductions can be found in references [24, 25].

The simple circuit diagram of an eight-stranded beta barrel protein is shown in **Figure 3A** (color added to help visualize the effect of permutation), with the protein structure shown in **Figure 3C**. Each strand is connected to the next strand in the sequence, and the last strand is connected to the first. Note that here we depict reduced diagrams, with each beta strand corresponding to a node of the diagram. A standard permutation of sites 4 and 8 of the beta barrel diagram yields the greek key barrel (**Figure 3B**, protein structure shown in **Figure 3D**). Permutation clearly changes the contact map (**Figures 3E,F**) and also affects the map of relations (**Figures 3G,H**), increasing the number of parallel and cross relations relative to series. Our framework thus illustrates detailed properties of a structural relation between two well-known protein folds.

TABLE 1 | Result of standard permutation between each pair of sites within two contacts.

Init.	Middle	Outer	Mid., term. N.	Mid., term. N.N.
P	P	P	X	S
X	S	S	P	X
S	X	X	S	P

Contacts begin in parallel (P), cross (X), or series (S) relation. Shown are the initial symmetry and result of permutation between middle sites, outer sites, middle and terminal neighboring sites, and middle and terminal non-neighboring sites.

TABLE 2 | Result of standard permutation, starting from concerted parallel (CP) or concerted series (CS) relations.

Init. symmetry	Mid., shared	Mid., unshared	Term.
CP	CS	CP	CP
CS	N/A	CP	CS

The shared terminal site refers to the site common to the two contacts in concerted parallel relation.

2.2.2.2. Circular permutation

In circular permutation, the two ends of the molecule are joined, and a single cut is made elsewhere in the molecule, resulting in a topology with identical contacts, but, in general, different relations between them. For a molecule with two contacts, this can be pictured easily as shown in **Figure 2C**. Hence, circular permutation can transform a parallel relation to a series relation and vice versa depending on the position of the ending point of circulation. The resulting symmetry ultimately depends on the location of this ending point with respect to the positions of the contact sites. Topology can be determined according to the following rules, using the points-on-a-line visualization of **Figures 1**, **2A,B**. If the two contacts are initially in series, then placing the new endpoint within the interval of either contact leads to parallel symmetry; otherwise series symmetry is preserved. If the two contacts are in parallel, then placing the endpoint within the interval of one contact but not the other leads to series symmetry; otherwise parallel symmetry results. CP and CS relations can be treated as parallel and series above. If the two contacts are in cross relation, any circular permutation will result in cross relation.

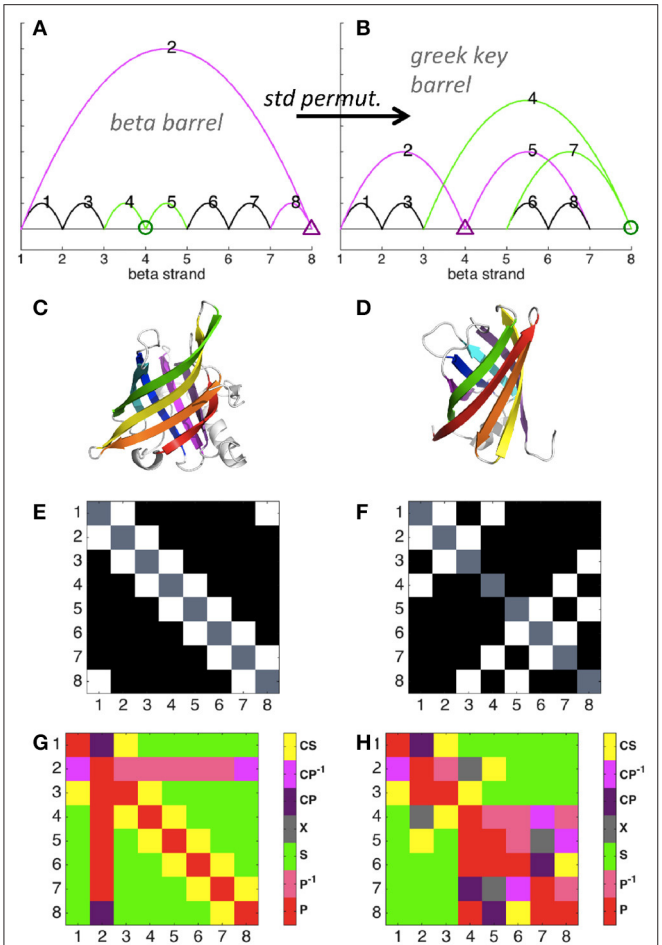

FIGURE 3 | Circuit diagram examples. Diagrams were calculated with distance cutoff 3.5 Angstroms and number cutoff 6 (see explanation in **Figure S2**). Maps were reduced such that each contacting site represents a node (1, 2, 3, 4, *etc*.) and non-bonded sites were excluded. **(A)** Beta barrel (pdb ID 1rbp) diagram. Sites and contacts involved in (4, 8) standard permutation are shown in green and magenta. **(B)** Greek key beta barrel (4cv7) diagram. **(C)** Beta barrel structure. **(D)** Greek key barrel structure. **(E)** Contact map of the beta barrel structure. Axes denote beta strand number, with contacts shown in white. **(F)** Contact map of the greek key barrel structure. **(G)** Relations between contacts of the beta barrel, numbered as shown in **(A)**. **(H)** Relations between contacts of the greek key barrel, numbered as shown in **(B)**.

The example in **Figure 2C** contains just four contact sites. The original matrix, depicting two contacts in parallel is

$$\mathcal{S} = \begin{pmatrix} 0 & 0 & 0 & 1 \\ 0 & 0 & 1 & 0 \\ 0 & 1 & 0 & 0 \\ 1 & 0 & 0 & 0 \end{pmatrix} \tag{18}$$

and the permutation matrix for a single clockwise rotation of the endpoint is

$$O = \begin{pmatrix} 0 & 0 & 0 & 1 \\ 1 & 0 & 0 & 0 \\ 0 & 1 & 0 & 0 \\ 0 & 0 & 1 & 0 \end{pmatrix} \tag{19}$$

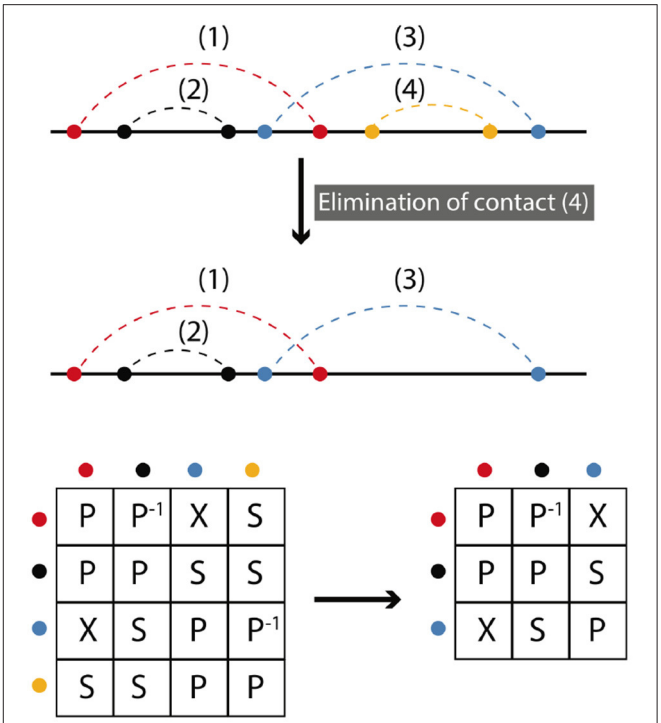

FIGURE 4 | Elimination corresponds to the deletion of contacts. In the simplest case only one contact is removed. The resulting matrix form is obtained by omitting the row and column of the eliminated contact. A matrix formalism for the elimination processes can be found in the **Supplementary Information**.

Then $\mathcal{S}' = OSO^{-1}$ is

$$\mathcal{S}' = \begin{pmatrix} 0 & 1 & 0 & 0 \\ 1 & 0 & 0 & 0 \\ 0 & 0 & 0 & 1 \\ 0 & 0 & 1 & 0 \end{pmatrix} \tag{20}$$

Standard and circular permutation are relevant to protein evolution [26, 27], as discussed in **Figure S3** and the corresponding discussion.

2.2.3. Elimination

Elimination is the deletion of a contact or set of contacts. Elimination does not change the symmetry relations between remaining contacts. **Figure 4** shows a simple example, where we begin with four contacts and contact (4) is eliminated. Matrix representations before and after elimination are depicted. To find the final representation after elimination we omit the row and the column that (4) belongs to. The matrix framework for elimination can be found in the **Supplementary Information**.

We illustrate elimination in **Figure 5**, showing that elimination of four contacts within the eight-stranded beta barrel topology leads to the fundamental topology of tRNA. **Figures 5A,B** show that the basic tRNA topology (apparent from visual inspection of hydrogen bonding patterns) can be deduced by starting from the beta barrel topology and introducing four

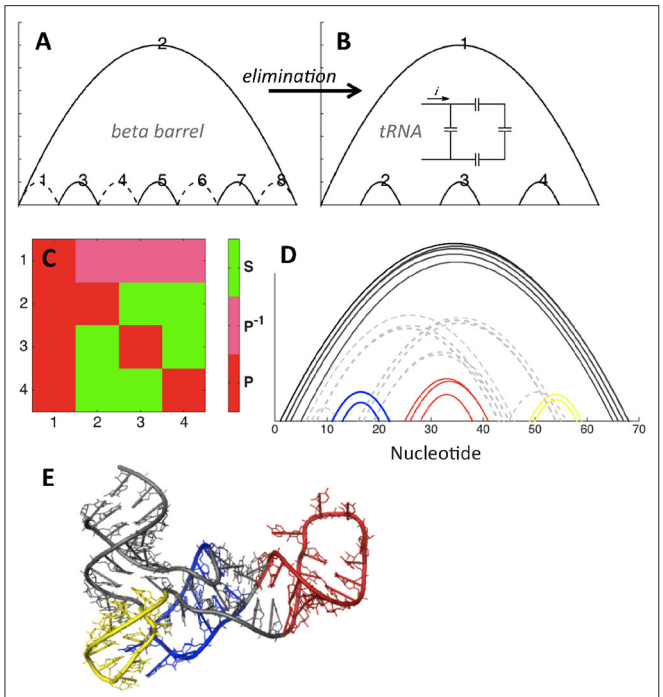

FIGURE 5 | tRNA topology (PDB ID 4kr2). **(A,B)** Elimination of contacts within the beta barrel motif **(A)** leads to the tRNA motif **(B)**. Topologically equivalent capacitor schematic shown in the inset. **(C)** Relations matrix for **(B)**. **(D)** Contacts between ribonucleotides of tRNA, PDB ID 4kr2. Cutoffs: 3.5, 6. Color and dashes added for emphasis. **(E)** tRNA structure, colored as shown in **(D)**.

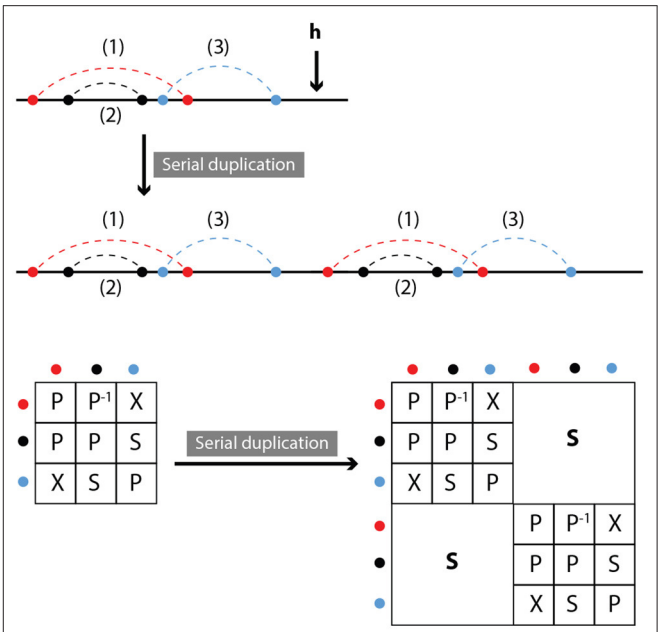

FIGURE 6 | Serial duplication: Part of a molecule is duplicated and inserted outside the original, at position *h*. Symmetry relations between duplicated and original contacts are series.

eliminations, shown as dotted lines in **Figure 5A**. This structure contains no concerted relations, and in fact it is possible to draw a simple analogy to electronic circuits, with the topologically equivalent capacitor schematic depicted in the inset of **Figure 5B**. **Figure 5C** confirms that contacts 2, 3, and 4 are in parallel with contact 1, while contacts 2, 3, and 4 are in series with each other (each contact is in parallel with itself by definition). Our heavy-atom contact analysis procedure (**Figure 5D**) demonstrates that the diagram in **Figure 5B** is indeed the basic topology of the example tRNA structure.

2.2.4. Addition

Addition, the reverse of elimination, can be accomplished by either adding one or more contacts between (potential) contact sites, as occurs in protein folding, or by insertion: the splicing of a new molecule (backbone and contacts) into the backbone of an existing one. In the case of insertion, relations within each molecule are unchanged. Relations between the new molecule and the one into which it is spliced will be either in series or in parallel, depending on the location of insertion.

2.2.5. Duplication

We define duplication as the attachment of a copy of the original molecule in series with the molecule itself. Clearly, relations between the contacts within the original molecule or its copy do not change, while all contacts between the original and copied molecule are in series (see **Figure 6**). In other words,

$$\mathcal{S}' = \mathcal{S} \oplus \mathcal{S} = \left(\begin{array}{c|c} \mathcal{S} & 0 \\ \hline 0 & \mathcal{S} \end{array}\right) \tag{21}$$

In biological polymers, the two linked molecules may be connected by a "linker" region, and new contacts between the two molecules, or between either molecule and the linker, may form. Consider the Greek key barrel diagram, shown again in the inset of **Figure 7C**, and perform the two eliminations indicated in magenta. The result is the beta/gamma crystallin diagram, present in the protein Nitrollin (**Figure 7C**, picture in **Figure 7A**). Duplication (plus elimination and addition of a contact) leads to the beta-B1 crystallin diagram shown in **Figure 7D** (picture in **Figure 7B**). In fact, evolutionarily, the beta/gamma crystallins emerged from an ancestral single-domain protein [28].

2.2.6. Additional Discussion

Domain swapping is a protein-protein interaction that involves exchange of contacts between proteins, such that contacts disrupted in the original protein chain are reformed with the corresponding portion of the other protein. A simpler representation is to consider each swapped segment as a node, in which case the standard permutation of the second and fourth nodes of two contacts in series leads to two contacts in parallel (**Figures 7E,F**). Consider such a simplistic representation of beta/gamma crystallin, where each domain consists of two contacting subdomains. Imagine a domain swap between N-terminal domains, a standard permutation between nodes 2 and 6 (**Figures 7E,F**). Say the molecules are connected in a single molecule pulling experiment, and the C-terminal domain is

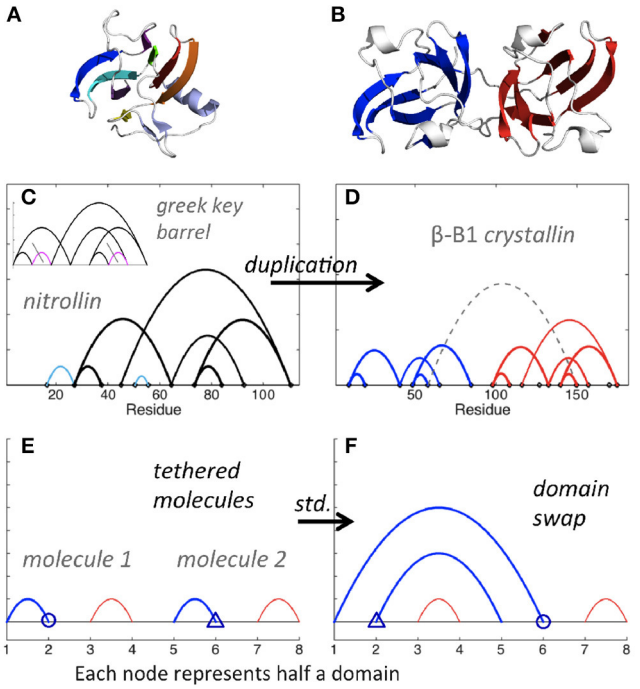

FIGURE 7 | Crystallin and nitrollin diagrams. **(A)** Nitrollin. **(B)** Beta-B1 crystallin. **(C)** Circuit diagram for Nitrollin (3ent), calculated with cutoffs: 3.6, 5. Inset: Greek key barrel with eliminations leading to the nitrollin diagram shown in magenta with gray slashes. **(D)** Beta-B1 crystallin (1oki), with cutoffs 3.6, 5, and bridge beta sites included. **(E)** Simplified representation of a crystallin molecule. Here std stands for standard permutation. **(F)** Simplified representation of hypothesized intramolecular domain swap. Color added for emphasis in all diagrams.

less mechanically resilient. Then, upon application of a force pulling at the two ends, we would expect unfolding of the second C-terminal domain first, followed by the swapped N-terminal domains, sequentially, followed by the first C-terminal domain. This is exactly the model proposed by Garcia-Manyes et al. in a recent publication [29], based on single molecule force spectroscopy experiments. Biological circuit topology provides a simple illustration of this prediction, also illustrating how our framework may be applied to provide insights relevant to the interpretation of experiment.

It is apparent from **Figure 6A** that, starting from the crystallin motif, loss of just a single contact can lead to a topologically isolated N-terminal hairpin, i.e., a single contact between beta strands, not bound to the rest of the protein. In fact, detachment of the N-terminal hairpin of gamma-D crystallin is an early event in Monte Carlo unfolding simulations of this protein [30]. Analysis of biological circuit topology may help to identify possible unfolding mechanisms [14] and structural weaknesses that can lead to unfolding and aggregation in biological proteins. The high content of parallel and cross relations in the crystallin motif may be a reason for its high stability in many proteins.

In summary, we believe that our method represents a useful and intuitive approach to circuit diagram generation, providing insights into key properties of biomolecular structures and the relations between them. We plan to extend and improve our approach to allow for more automated bioinformatic analyses. While we apply our approach to biological structures in the Protein Data Bank, we note that it could also be used in conjunction with Molecular dynamics and analysis tools to study dynamic transitions in biomolecules, including transient structure in intrinsically disordered proteins.

The complete code and documentation is available online.

3. CONCLUSION

In this article, we developed a framework that can be used to describe, compare, and predict the topological properties of a molecule that is subject to specific molecular operations. More specifically, we considered several generic operations, namely permutation, duplication, inversion, addition/insertion, and elimination. We used examples from structural biology to demonstrate how relationships between molecules can be understood in terms of the biological circuit topology framework, and we introduced a simple toolset for drawing, analyzing, and manipulating circuit diagrams of proteins. Altogether, we present a mathematical approach to the analysis of protein and nucleic acid structure and structural changes that may also be applied to other linear polymers. We expect the formalism extended here and future developments to be relevant to the process of engineering and manipulating molecules according to symmetry rules between their constituents, and we believe our methods and insights could help foster interdisciplinary collaboration and learning in mathematics, chemistry, biology, and related disciplines.

DATA AVAILABILITY STATEMENT

All datasets generated for this study are included in the article/**Supplementary Material**.

AUTHOR CONTRIBUTIONS

AM conceived, designed, and supervised the research. OS and AT conducted the theoretical analysis. JW conducted the biomolecular modeling part and wrote the script. OS, AT, JW, and AM discussed the results and the interpretations. All authors contributed to writing of the manuscript and approved the final version.

ACKNOWLEDGMENTS

OS thanks V. Satarifard for introducing him into the subject and H. Antila, M. Miettinen, and A. Valleriani for their helpful discussions.

SUPPLEMENTARY MATERIAL

The Supplementary Material for this article can be found online at: https://www.frontiersin.org/articles/10.3389/fphy.2020.00005/full#supplementary-material

REFERENCES

1. Mizuguchi K, Go N. Seeking significance in three-dimensional protein structure comparisons. *Curr Opin Struct Biol.* (1995) **5**:377–82. doi: 10.1016/0959-440x(95)80100-6
2. Brown ID. Topology and chemistry. *Struct Chem.* (2002) **13**:339–55. doi: 10.1023/A:1015872125545
3. Flapan E. *When Topology Meets Chemistry: A Topological Look at Molecular Chirality*. Cambridge, UK: Cambridge University Press (2000).
4. Ayme JF, Beves JE, Leigh DA, McBurney RT, Rissanen K, Schultz D. A synthetic molecular pentafoil knot. *Nat Chem*. (2011) **11**:15–20. doi: 10.1038/nchem.1193
5. Blankenship JW, Dawson PE. Threading a peptide through a peptide: protein loops, rotaxanes, and knots. *Protein Sci*. (2007) **16**:1249–56. doi: 10.1110/ps.062673207
6. Coskun A, Banaszak M, Astumian RD, Stoddart JF, Grzybowski BA. Great expectations: can artificial molecular machines deliver on their promise? *Chem Soc Rev*. (2012) **41**:19–30. doi: 10.1039/C1CS15262A
7. Kamien RD. Topology from the bottom up. *Science.* (2003) **299**:1671–3. doi: 10.1126/science.1082510
8. Siegel JS. Chemical topology and interlocking molecules. *Science.* (2004) **304**:1256–8. doi: 10.1126/science.1099216
9. Bailor MH, Sun X, Al-Hashimi HM. Topology links RNA secondary structure with global conformation, dynamics, and adaptation. *Science*. (2010) **327**:202–6. doi: 10.1126/science.1181085
10. Cavalli G, Misteli T. Functional implications of genome topology. *Nat Struct Mol Biol.* (2013) **20**:290–9. doi: 10.1038/nsmb.2474
11. Cang Z, Wei GW. TopologyNet: topology based deep convolutional and multi-task neural networks for biomolecular property predictions. *PLoS Comput Biol*. (2017) **13**:e1005690. doi: 10.1371/journal.pcbi.1005690
12. Cang Z, Mu L, Wei GW. Representability of algebraic topology for biomolecules in machine learning based scoring and virtual screening. *PLoS Comput Biol*. (2017) **14**:e1005929. doi: 10.1371/journal.pcbi.1005929
13. Mashaghi A, van Wijk RJ, Tans SJ. Circuit topology of proteins and nucleic acids. *Structure.* (2014) **22**:1227–37. doi: 10.1016/j.str.2014.06.015
14. Mugler A, Tans SJ, Mashaghi A. Circuit topology of self-interacting chains: implications for folding and unfolding dynamics. *Phys Chem Chem Phys.* (2014) **16**:22537–44. doi: 10.1039/C4CP03402C
15. Verovšek SK, Mashaghi A. Extended topological persistence and contact arrangements in folded linear molecules. *Front Appl Math Stat*. (2016) **2**:6. doi: 10.3389/fams.2016.00006
16. Nikoofard N, Mashaghi A. Topology sorting and characterization of folded polymers using nano-pores. *Nanoscale.* (2016) **8**:4643–9. doi: 10.1039/C5NR08828C
17. Heidari M, Satarifard V, Tans SJ, Ejtehadi MR, Mashaghi S, Mashaghi A. Topology of internally constrained polymer chains. *Phys Chem Chem Phys.* (2017) **19**:18389–93. doi: 10.1039/C7CP02145C
18. Satarifard V, Heidari M, Mashaghi S, Tans SJ, Ejtehadi MR, Mashaghi A. Topology of polymer chains under nanoscale confinement. *Nanoscale.* (2017) **9**:12170–7. doi: 10.1039/C7NR04220E
19. Mashaghi A, Ramezanpour A. Circuit topology of linear polymers: a statistical mechanical treatment. *RSC Adv*. (2015) **5**:51682–9. doi: 10.1039/C5RA08106H
20. Mashaghi A, Ramezanpour A. Distance measures and evolution of polymer chains in their topological space. *Soft Matter*. (2015) **11**:6576–85. doi: 10.1039/C5SM01482D
21. Bachar O, Fischer D, Nussinov R, Wolfson H. A computer vision based technique for 3-D sequence-independent structural comparison of proteins. *Protein Eng Design Select*. (1993) **6**:279–87. doi: 10.1093/protein/6.3.279
22. Prlić A, Bourne PE, Bliven SE. Detection of circular permutations within protein structures using CE-CP. *Bioinformatics.* (2014) **31**:1316–8. doi: 10.1093/bioinformatics/btu823
23. Wang L, Wu LY, Wang Y, Zhang XS, Chen L. SANA: an algorithm for sequential and non-sequential protein structure alignment. *Amino Acids.* (2010) **39**:417–25. doi: 10.1007/s00726-009-0457-y
24. Branden C, Tooze J. *Introduction to Protein Structure.* 2nd Edn. New York, NY: Garland Science (1999).
25. Hubbard TJ, Murzin AG, Brenner SE, Chothia C. SCOP: a structural classification of proteins database. *Nucleic Acids Res.* (1997) **25**:236–9.
26. Grishin NV. Fold change in evolution of protein structures. *J Struct Biol.* (2001) **134**:167–85. doi: 10.1006/jsbi.2001.4335
27. Bliven S, Prlić A. Circular permutation in proteins. *PLoS Comput Biol*. (2012) **8**:e1002445. doi: 10.1371/journal.pcbi.1002445
28. Kappé G, Purkiss AG, van Genesen ST, Slingsby C, Lubsen NH. Explosive expansion of betagamma-crystallin genes in the ancestral vertebrate. *J Mol Evol*. (2010) **71**:219–30. doi: 10.1007/s00239-010-9379-2
29. Garcia-Manyes S, Giganti D, Badilla CL, Lezamiz A, Perales-Calvo J, Beedle AEM, et al. Single-molecule force spectroscopy predicts a misfolded, domain-swapped conformation in human YD-crystallin protein. *J Biol Chem*. (2016) **291**:4226–35. doi: 10.1074/jbc.M115.673871
30. Serebryany E, Woodard JC, Adkar BV, Shabab M, King JA, Shakhnovich EI. An internal disulfide locks a misfolded aggregation-prone intermediate in cataract-linked mutants of human YD-crystallin. *J Biol Chem*. (2016) **291**:19172–83. doi: 10.1074/jbc.M116.735977

Conflict of Interest: The authors declare that the research was conducted in the absence of any commercial or financial relationships that could be construed as a potential conflict of interest.

frontiers in Chemistry

ORIGINAL RESEARCH
published: 24 March 2020
doi: 10.3389/fchem.2020.00208

Design and Characterization of Naphthalene Ionic Liquids

Verónica Fernández-Stefanuto[1], *Alba Somoza*[2], *Raquel Corchero*[2], *Emilia Tojo*[1] *and Ana Soto*[2]*

[1] Department of Organic Chemistry, Faculty of Chemistry, Universidade de Vigo, Vigo, Spain, [2] Department of Chemical Engineering, Cretus Institute, Universidade de Santiago de Compostela, Santiago de Compostela, Spain

Surfactants have a great number of applications. Among these chemicals, petroleum sulfonates have been widely used due to their effectiveness in reducing interfacial tension. This is the case of sodium octylnaphthalene sulfonate which is a solid with a very low solubility in water. To overcome these drawbacks, this work aimed to synthesize new surface active ionic liquids based on a naphthalene sulfonate anion and traditional cations of these salts (imidazolium, pyrrolidinium, and pyridinium). The new chemicals showed high thermal stability, ionic liquid nature, and a stronger surfactant character than the original naphthalene. Moreover, they were found to be water soluble which greatly facilitates their application in the form of aqueous formulations. 1-Hexyl-3-methylimidazolium 4-(*n*-octyl)naphthalene-1-sulfonate showed the best capacity to reduce water-air and water-oil interfacial tension.

Keywords: synthesis, characterization, surfactant, ionic liquid, enhanced oil recovery

OPEN ACCESS

Edited by:
Ramesh L. Gardas, Indian Institute of Technology Madras, India

Reviewed by:
Johan Jacquemin, Université de Tours, France
Dilip H. Dagade, Shivaji University, India

***Correspondence:**
Ana Soto
ana.soto@usc.es

Specialty section:
This article was submitted to Physical Chemistry and Chemical Physics, a section of the journal Frontiers in Chemistry

Received: *16 December 2019*
Accepted: *05 March 2020*
Published: *24 March 2020*

Citation:
Fernández-Stefanuto V, Somoza A, Corchero R, Tojo E and Soto A (2020) Design and Characterization of Naphthalene Ionic Liquids. Front. Chem. 8:208. doi: 10.3389/fchem.2020.00208

INTRODUCTION

Surfactants are extensively used not only in the chemical industry but also in daily life. Applications include: detergents, emulsifiers, de-emulsifiers, dispersants, lubricant additives, wetting agents, corrosion inhibitors, foaming agents, enhancing additives in oil recovery, phase transfer or drug delivery agents, chemical reaction media (e.g., for micellar catalysis), etc. Most applications of surface active agents derive from two fundamental properties in aqueous solution: adsorption at the interface and aggregation. Adsorption at the air/water interface allows reduction of the surface tension and modification of wetting and foam-forming properties of the surfactant-containing water. Adsorption at the oil/water interface is the first step in emulsification, while at the interface of water with suspended solids, it affects flocculation and coagulation. The aggregation of surfactants is the basis of applications involving the formation of micelles, microemulsions, and liquid crystals. Thus, the study of the behavior of these chemicals in water is the first step in their application.

Among the surfactants, petroleum sulfonates have been widely used because they are effective at attaining low interfacial tension, relatively inexpensive and chemically stable. Petroleum sulfonates are produced when an intermediate-molecular-weight refinery stream is sulfonated, and synthetic sulfonates are the result of sulfonating a relatively pure organic compound (Green and Willhite, 1998). The first synthetic surfactants based on fossil raw materials were the alkylnaphthalenesulfonates. They are used in many applications as detailed below. They offer acid, base and thermal stability. They have excellent wetting and dispersing properties, and also can be designed to have different foaming tendencies. Abdel-Raouf et al. (2011) synthesized several alkylnaphthalene and alkylphenanthrene sulfonates by means of a Wurtz–Fittig reaction. Aggregation properties were studied in water and the detergency power of the prepared surfactants shown. These kinds of surfactants are also used as lubricant additives because they

impart thermal and thermo-oxidative stability. The electron-rich naphthalene ring has the ability to absorb energy, resonate, and then disperse that energy (Hunter, 2017). Finally, perhaps one of the most promising applications for these compounds is Enhanced Oil Recovery (EOR). Their ability to reduce water/oil interfacial tension make them desired components in surfactant or microemulsion formulations designed to liberate oil trapped in the pores of rocks.

Gong et al. (2005) synthesized sodium and sodium methyl naphthalene sulfonates by naphthalene sulfonation with chlorosulfonic acid in carbon tetrachloride at low temperature, followed by neutralization with NaOH solution. The interfacial tension (IFT) between these surfactants and Liaohe or Shengli crude oil was measured. It was found that the rigid aromatic ring could play the role of a hydrophobic group and that the effect of the alkyl group was not very significant. The surfactants proved effective in lowering the IFT. However, formulations with NaCl, alkali, and other surfactants were required to obtain ultra-low interfacial tension ($\sim 10^{-3}$ mN/m). Wurtz–Fittig and sulfonation reactions were also used by Tan et al. (2004a) to synthesize sodium alkylnaphthalene sulfonates with longer alkyl chains (C_6, C_8, C_{10}). Comparing the aggregation capacity of different sulfonate surfactants, they found that critical micelle concentration decreases according to *n*-alkyl > *n*-alkylbenzene > *n*-alkylnaphthalene. Moreover, in the case of the latter, the higher the alkyl chain length, the lower the critical micelle concentration (cmc) of these surfactants in water. Similar conclusions were obtained by these authors (Tan et al., 2004b) using fluorescence techniques instead of surface tension measurements to characterize the micellization and microenvironmental properties of these surfactants. Optimal formulations for EOR containing sodium alkylnaphtalene sulfonates were defined by Chu et al. (2004). Ultra-low interfacial tensions were achieved in surfactant/alkali/acidic oil systems. The synergism between the sulfonates and surface-active components in crude oil was controlled by sulfonate and alkali concentration, alkaline type and ionic strength. The alkylation of β-methylnaphthalene with a series of different chain lengths of *n*-bromoalkanes led to the synthesis of alkyl (C_6-C_{14}) methylnaphthalene sulfonate surfactants. All of the synthesized surfactants except for hexyl methylnaphthalene sulfonate were able to reduce the interfacial tension between Shengli oil and water to ultra-low values in the absence of alkali (Zhao et al., 2006, 2007).

The design of new sulfonate surfactants based on the naphthalene ring was accomplished by Berger and Lee (2002). They carried out the simultaneous sulfonation and alkylation of aromatic compounds using olefin sulfonic acids. Alkylnaphthalene sulfonic acids were obtained, among other surfactants, but in this case the sulfonic group was attached to the end of the alkyl chain instead of the aromatic ring as usual. The authors propose these new compounds not only for use in EOR but also as dispersants and emulsifiers for cleaners, detergents, agriculture, oilfield drilling muds, cement, metal treating, etc.

One of the most highlighted properties of ionic liquids (ILs) is their tunability. By selecting the ions, the alkyl chains, functional groups, etc. a great number of chemical designs which improve the characteristics or the applicability of these chemicals are possible (Pirkwieser et al., 2018; Lethesh et al., 2019). With this idea in mind, and due to the interest in alkylnaphtalene sulfonate surfactants, the aim of this work is the design of new kinds of surfactants containing this anion and typical IL cations (imidazolium, pyrrolidinium and pyridinium). An imidazolium ring was considered as the archetypal cation of ILs, and pyrrolidinium and pyridinium as more biodegradable alternatives. An alkyl chain length able to produce ILs with high solubility in water and low cmc was selected. The objectives include reducing the melting point of these traditional surfactants, and analyzing the aggregation capacity of the resultant chemicals.

MATERIALS AND METHODS

Reagents used in the metathesis reactions were prepared as reported in literature: N-methylpyrrolidinium dihydrogen phosphate [C_1Pyr][H_2PO_4] (Pal and Saini, 2019), 1-hexyl-3-methylimidazolium chloride [C_1C_6Im]Cl (Min et al., 2006), 1-ethylpyridinium bromide [C_2Py]Br (Potangale et al., 2017), and 1-butylpyridinium chloride [C_4Py]Cl (Potangale et al., 2017). These starting materials were purified as indicated in **Supplementary Material**. That is: Na[ONS] (2) was recrystallized from an ethanol/water mixture (50:50, vol/vol), [C_1C_6Im]Cl, [C_2Py]Br, and [C_4Py]Cl were washed with AcOEt to remove possible unreacted starting reagents and dried under reduced pressure, while [C_1Pyr][H_2PO_4] was just heated under reduced pressure to remove volatile starting materials. From the NMR spectra and MS data a purity ≥99%wt was estimated for all of them. Tetrahydrofuran was distilled from sodium/benzophenone prior to use. All other materials were reagent grade purchased from commercial suppliers: Acros Organics (*n*-octylmagnesium bromide 2M solution in diethyl ether, zinc chloride > 97%wt, 1-bromonaphtalene 96%wt, chlorosulfonic acid 97%wt) and Sigma Aldrich (Ni(dppp)Cl_2 ≤100%wt), and employed without further purification.

The chemicals used in the dynamic interfacial tension measurements were: *n*-octane purchased from Sigma-Aldrich with a purity >99%wt, and crude oil kindly supplied by Repsol (A Coruña, Spain). Main properties of the oil are shown in **Table 1**.

The glass material employed in the synthetic reactions was dried in an oven at 333 K for 24 h before use. The evolution of the reactions was monitored by thin layer chromatography (t.l.c.) employing silica-gel sheets (Merck, TLC Silica gel 60 F254). Spectroscopic data were provided by the Center of Scientific-Technological Support to Research (CACTI) of the University of

TABLE 1 | Crude oil properties (provided by supplier).

Density at 288.15 K (kg/m^3)	811.1
Reid vapor pressure (kPa)	44.9
Viscosity at 293.15 K (cSt)	4.861
Carbon residue (%wt)	1.2522
Asphaltenes (%wt)	0.4624

Vigo. ^{1}H and ^{13}C NMR spectra were recorded on a BRUKER ARX 4CO spectrometer at 400.1621 (^{1}H) and 100.6314 (^{13}C) MHz, respectively. $CDCl_3$ (ACROS Organics, 99.6+ atom % D) and D_2O (ACROS Organics, 99.8+ atom % D) were employed as deuterated solvents. Chemical shifts are quoted in parts per million (ppm) relative to the signals corresponding to the residual non-deuterated solvents ($CDCl_3$: $\delta H = 7.26$ ppm, $\delta C = 77.16$ ppm). Coupling constants are given in hertz (Hz). Low and high resolution ESI mass spectra were recorded on a BRUKER FTMS APEXIII spectrometer, while ICP-MS analyses were carried out on an X Series ICP-MS (Thermo Elemental) equipment. All solutions for ICP-MS analyses were prepared using ultra-high purity Milli-Q water.

Karl-Fischer titration was used to measure water content of the original surfactant and synthesized ILs. In the case of the solid materials, they were solubilized in 2-propanol and their water content corrected according to the water content of the solvent.

Thermogravimetric analysis (TGA) and differential scanning calorimetry (DSC) were used to characterize the synthesized ILs. Thermal decomposition of the samples was analyzed in a TA Instruments Q500 thermogravimetric analyzer with a weight precision of ±0.01%. This apparatus was weight-calibrated with weights of certified mass, and temperature-calibrated with nickel of high purity (99.9945%wt) by means of the determination of its Curie temperature. An open platinum pan loaded with ∼12 mg of sample was used in each case. A simple heating ramp of 10 $K{\cdot}min^{-1}$ from room temperature to 900 K was applied, using nitrogen gas (Praxair, 99.999%) as both balance purge gas (40 $mL{\cdot}min^{-1}$) and sample purge gas (60 $mL{\cdot}min^{-1}$). In addition, since it is well-known that isothermal experiments give safer values of temperature operation for ILs, isothermal studies were also carried out at different temperatures. All the experiments were performed at least twice to ensure repeatability.

DSC runs were carried out in a TA Instruments Q2000 differential scanning calorimeter, equipped with an RCS 90 refrigerated cooling system. The apparatus was calibrated with high purity indium (99.99%wt) by means of the determination of its onset melting temperature. Approximately 12 mg of each sample were placed in a 40 μL aluminum pan, sealed hermetically with a lid of the same material and loaded into the measuring chamber with an autosampler. An identical empty pan with its corresponding lid was used as reference. Nitrogen gas (Praxair, 99.999%wt), at a flowrate of 50 $mL{\cdot}min^{-1}$, was used as sample purge gas. The thermal program consisted of a cooling ramp and then a heating ramp from 190 K to a temperature below the decomposition at a rate of 5 $K{\cdot}min^{-1}$. The procedure was repeated, with intercalated 10-min isotherms at both ends of the temperature range, and when the curves were coincident (usually in the second and third cycle) results were analyzed. A second study was carried out at 3 $K{\cdot}min^{-1}$ in order to confirm results obtained at the highest rate.

Surface tensions of the synthesized ILs in aqueous solutions were measured using the Wilhelmy plate method in a Krüss K11 tensiometer in order to determine the cmc. An external thermostat (Selecta Frigiterm 6000382) maintained the temperature at 298.15 K. Dynamic interfacial tensions between the surfactant IL solutions and octane or crude oil were measured using a Krüss SITE 100 spinning drop tensiometer. Temperature was controlled circulating oil from a thermostatic bath Julabo model EH-5. The capillary was filled with the heavy phase (aqueous solution) and a drop of the light phase (oil) was injected. Rotating velocities between 3000 and 7000 rpm were applied. The interfacial tension was calculated according to the following equation:

$$\gamma = \frac{\Delta\rho\omega^2 D^3}{32} \quad (1)$$

where ω is the angular velocity, D is the diameter of the oil drop and $\Delta\rho$ the density difference between the aqueous phase and the oil. All the experiments were performed at least twice to ensure repeatability.

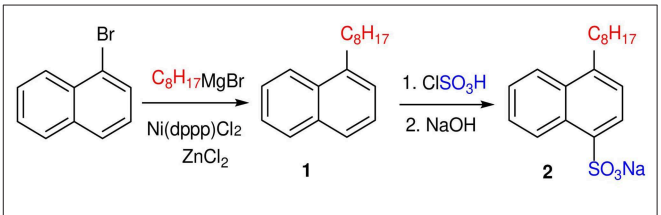

SCHEME 1 | Synthetic procedure applied to obtain sodium 4-octylnaphthalene-1-sulfonate (2).

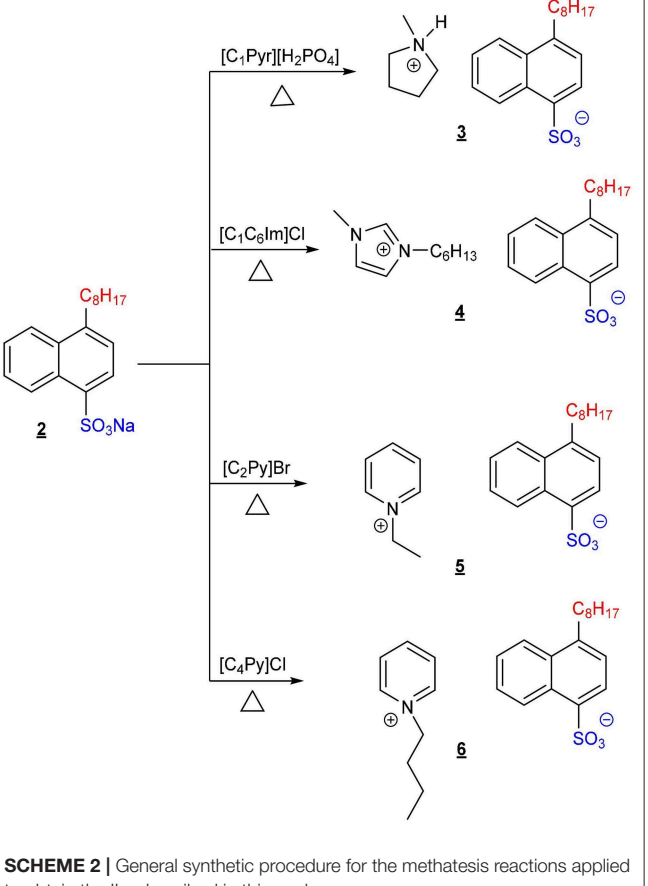

SCHEME 2 | General synthetic procedure for the methatesis reactions applied to obtain the ILs described in this work.

RESULTS AND DISCUSSION

Synthesis

The ILs described in this work were obtained by applying a synthetic procedure of three steps (**Schemes 1**, **2**). The first one involved the alkylation of 1-bromonaphthalene in the presence of Ni(dppp)Cl_2 and $ZnCl_2$ to obtain 1-*n*-octylnaphthalene (1) with high yield (Palmaerts et al., 2009; Nietfeld et al., 2011). The later sulfonation of 1-*n*-octylnaphthalene (1) by treatment with chlorosulfonic acid and neutralization with NaOH gave sodium 4-(*n*-octyl)naphthalene-1-sulfonate Na[ONS] (2) with a high yield as the only product after recrystallization (Tan et al., 2004a). Finally, the exchange of Na^+ for the desired cations was carried out by the corresponding metathesis reactions of sulfonate 2 with the ILs N-methylpyrrolidinium dihydrogen phosphate [C_1Pyr][H_2PO_4], 1-hexyl-3-methylimidazolium

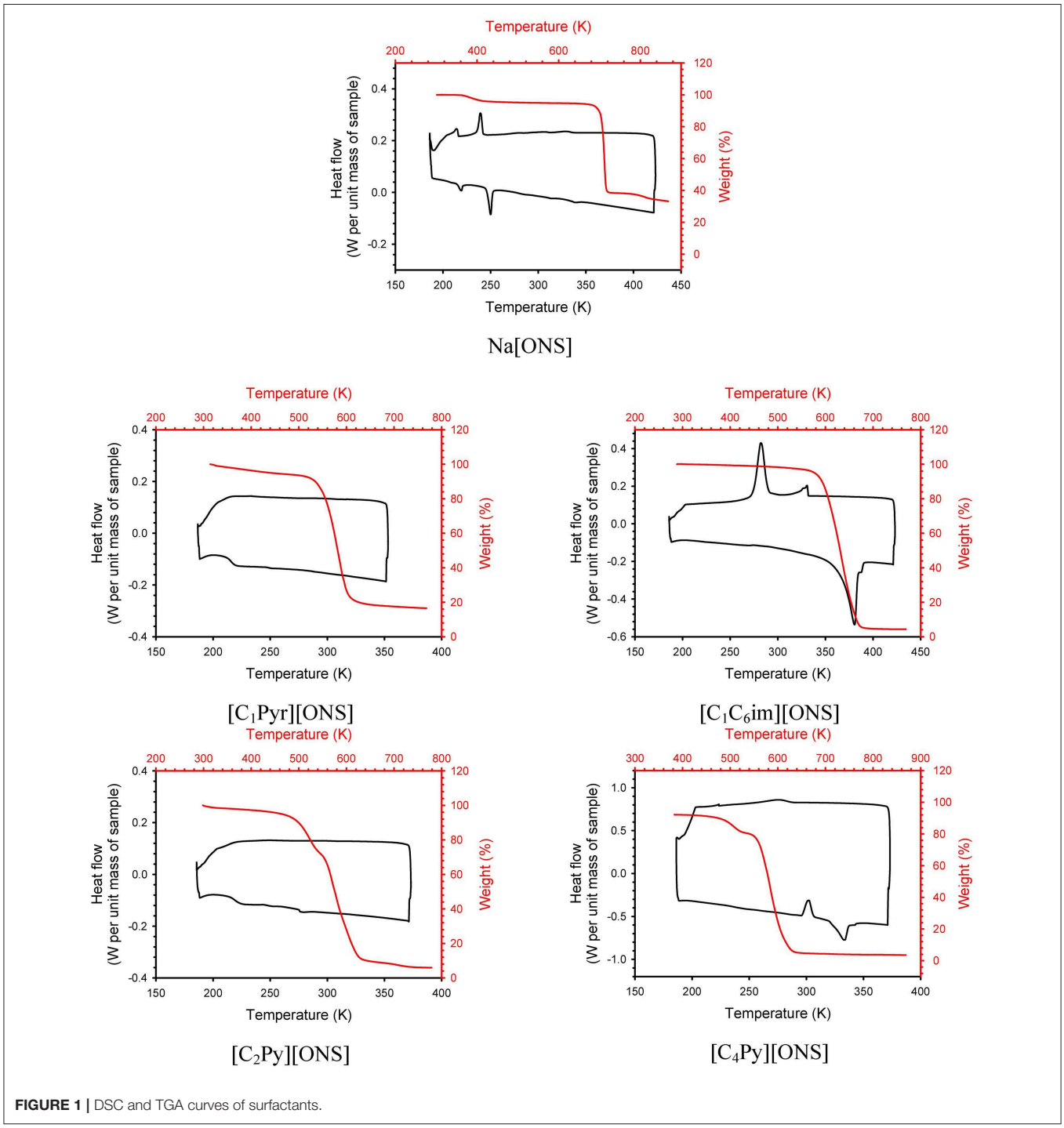

FIGURE 1 | DSC and TGA curves of surfactants.

TABLE 2 | Thermal characterization of surfactants at 0.1 MPa.

Surfactant	T_c(K)	T_{cc}(K)	$T_{ss-Cool}$(K)	T_g(K)	$T_{ss-Heat}$(K)	T_m(K)	$T_{d,5\%onset}$ (K)
Na[ONS]			215/236		215/246		686
[C_1Pyr][ONS]				216			522
[C_1C_6Im][ONS]	289/332					367	571
[C_2Py][ONS]				219			473
[C_4Py][ONS]		296				323	488

Standard uncertainties: u(P) = 5 kPa, u(T) = 1 K.

TABLE 3 | cmc and surface tension of surfactants in aqueous solutions at 298.15 K and 0.1 MPa.

Surfactant	*cmc* (mmol/kg)	γ_{cmc} (mN/m)
Na[ONS]	3.86	41.0
[C_1Pyr][ONS]	0.78	37.4
[C_1C_6Im][ONS]	0.39	29.7
[C_2Py][ONS]	1.17	36.9
[C_4Py][ONS]	0.74	36.8

Standard uncertainties: u(P) = 5 kPa, u(T) = 0.05 K, u(cmc) = 0.01, u(γ) = 0.3 mN/m.

chloride [C_1C_6Im]Cl, 1-ethylpyridinium bromide [C_2Py]Br, and 1-butylpyridinium chloride [C_4Py]Cl.

The resulting reaction products of the metathesis reactions were dissolved in CH_2Cl_2 to precipitate the formed inorganic salt (NaH_2PO_4, NaCl or NaBr), which was filtered off. The filtrate was then concentrated and dried under high vacuum (2×10^{-1} Pa) to obtain alkylnaphthalene-ILs: N-methylpirrolidinium 4-(*n*-octyl)naphthalene-1-sulfonate [C_1Pyr][ONS] (3), 1-hexyl-3-methylimidazolium 4-(*n*-octyl)naphthalene-1-sulfonate [C_1C_6Im][ONS] (4), 1-ethylpyridinium 4-(*n*-octyl)naphthalene-1-sulfonate [C_2Py][ONS] (5) and 1-butylpyridinium 4-(*n*-octyl)naphthalene-1-sulfonate [C_4Py][ONS] (6). The ^{1}H and ^{13}C NMR spectra of the synthesized ILs, as well as their HR-MS data, confirmed their structure and showed the absence of unreacted starting materials. The base peak observed in the HR-MS spectra corresponded to $[A_2B]^+$ ion associations (A = cation mass, B = anion mass), frequently observed in ILs MS spectra. In addition, the ICP-MS analyses allowed quantifying the concentration of the inorganic ions that could remain after the metathesis reactions. It was found to be lower than 0.17%wt in all cases (see **Supplementary Material**). From the NMR spectra and MS data, a purity ≥99%wt is estimated for all the ILs synthesized in this study. Water content of ILs is also presented in **Supplementary Material**.

All of the synthesized ILs were found to be water soluble.

Thermal Characterization

The thermal stability of the original surfactant (sodium 4-(n-octyl)naphthalene-1-sulfonate) and the four synthesized surfactant ILs was investigated via TGA experiments. TGA curves can be seen in **Figure 1**. **Table 2** shows the 5% onset decomposition temperature ($T_{d,5\%onset}$), a more conservative value than the usual $T_{d,onset}$ in order to define a safe temperature of operation with these ILs. As could be expected, the incorporation of a large and asymmetrical organic cation leads to a decrease of the thermal stability. Isothermal scans at temperatures lower than calculated $T_{d,5\%onset}$ are presented in **Supplementary Material**. The influence of the cation on the thermal stability is confirmed, with a decrease of the stability according to: Na > [C_1C_6Im] > [C_1Pyr] > [C_4Py] > [C_2Py]. However, at least 100 K below $T_{d,5\%onset}$ are required in order to have insignificant loss weigh when surfactants are maintained at high temperature for a long period of time.

Thermal events for the ILs were investigated via DSC experiments and results at a working rate of 5 K/min are shown in **Table 2** (**Figure 1** shows the third cycle). Temperatures were calculated as the extrapolated onset-temperature. This temperature is the intersection point of the extrapolated baseline and the inflectional tangent at the beginning of the peak. The baseline and the inflectional tangent are determined from the temperature-dependent heat flow signal. In contrast to peak-temperature, the onset-temperature is less dependent on heating rate and sample mass. In the case of the Na[ONS] surfactant, two endothermic peaks were found in the heating ramp and two exothermic peaks in the cooling ramp, at 215/236 and 215/246 K, respectively. No other peaks were found heating up to the decomposition temperature of this chemical. In order to confirm that these thermal events correspond to solid-solid transitions, a sample was heated in an oven up to 473 K and no melting was observed. [C_1Pyr][ONS] has a glass transition temperature at 216 K. It is a viscous liquid at room temperature. [C_1C_6Im][ONS] shows melting at 367 K and crystallization at 332K. Another small exothermic peak appears in the cooling ramp at 289 K. This suggests a polymorphic-like behavior that leads to the formation of crystals with different structures (Calvar et al., 2013; Villanueva et al., 2015). In the case of the surfactants with a pyridinium cation, their thermograms are quite different despite the similarity of their structures. Only a glass transition temperature (219 K) was detected in the case of [C_2Py][ONS], however it has a solid appearance at room temperature. In the case of [C_4Py][ONS] a different profile was observed. A cold crystallization peak appears at 296 K and a melting point at 323 K. In order to check the nature of the peaks obtained, DSC runs were also carried out at a rate of 3 K/min (**Supplementary Material** shows all the cycles at this rate). All the thermal events presented in **Table 2** are confirmed (kinetic events appearing at higher temperatures). Only in the case of [C_1C_6Im][ONS] a new cold crystallization was observed. This is not unusual. The ILs possess great crystallization and glass-forming ability (Lobo Ferreira et al., 2019) strongly dependent on their water content and operation conditions.

Aggregation in Water

The critical micelle concentration (cmc) of the original surfactant and the synthesized ILs was measured in aqueous solution at 298.15 K using surface tension measurements. Results can be seen in **Table 3**. In the case of the surfactant Na[ONS], this parameter was previously published. Tan et al. (2004a,b) obtained at 303.15 K a cmc value of 2.36 mmol/L with a surface tension at

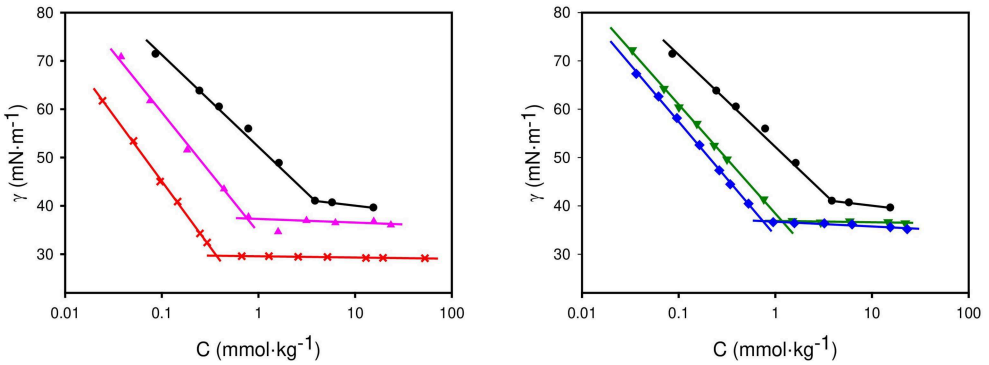

FIGURE 2 | Surface tension of aqueous solutions of surfactants at 298.15 K. • Na [ONS] , ▲ [C_1Pyr] [ONS] , × [C_1C_6Im] [ONS] , ▼ [C_2Py] [ONS] , ♦ [C_4Py] [ONS].

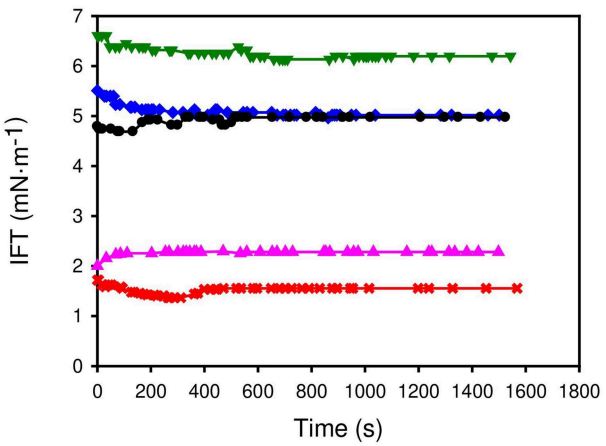

FIGURE 3 | Dynamic interfacial tension between aqueous solutions of the surfactants (concentration is twice the cmc) and *n*-octane. • Na [ONS] , ▲ [C_1Pyr] [ONS] , × [C_1C_6Im] [ONS] , ▼ [C_2Py] [ONS] , ♦ [C_4Py] [ONS].

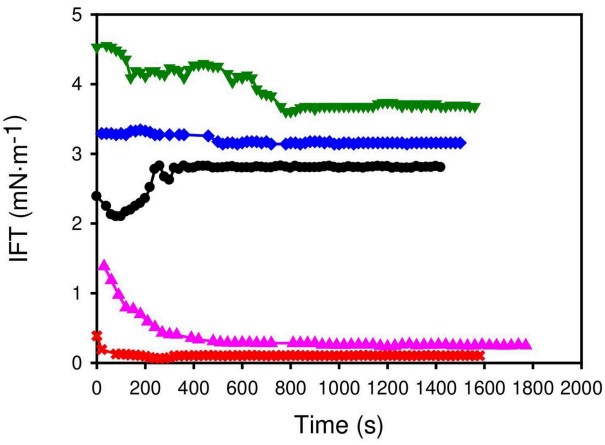

FIGURE 4 | Dynamic interfacial tension between aqueous solutions of the surfactants (concentration is twice the cmc) and crude oil. • Na [ONS] , ▲ [C_1Pyr] [ONS] , × [C_1C_6Im] [ONS] , ▼ [C_2Py] [ONS] , ♦ [C_4Py] [ONS].

this concentration (γ_{cmc}= 39.3 mN/m) while Abdel-Raouf et al. (2011) obtained at 298.15 K a value of 20.7 mmol/L (γ_{cmc} = 33.4 mN/m), both using surface tension measurements. Due to the discrepancy of these values, obtained with the same experimental technique, the determination of this parameter at 298.15 K was repeated in this work and a value of 3.86 mmol/kg (γ_{cmc} = 41.0 mN/m) was obtained. Results are in agreement with values obtained by Tan et al. (2004a,b).

Regarding the capacity of aggregation of the synthesized ILs, **Figure 2** shows the determination of the cmc and results presented in **Table 3**. In comparison with the original surfactant, all the ILs have lower cmc values (ranging from 0.4 to 1.2 mmol/kg) and higher capacity to reduce the interfacial tension air/water (values ranging from 29.7 to 37.4 mN/m). The IL that led to the lowest cmc, and the greatest reduction of water surface tension was the imidazolium, and in the case of the pyridinium ILs, the lower the alkyl chain length the higher the cmc, with little variation in surface tension.

Dynamic Interfacial Tension

Applications of surface active compounds require that these chemicals drastically reduce the surface tension of water and its interfacial tension against oils. Thus, *n*-octane was selected as oil and the dynamic interfacial tension water-octane was measured at 298.15 K using aqueous solutions of the original surfactant and new synthesized ILs. A concentration of surfactant in the aqueous solution equal to twice the value of the cmc was selected for each surfactant. **Figure 3** shows the results. [C_1C_6Im][ONS] and [C_1Pyr][ONS] have the capacity of lowering the interfacial tension more than the original surfactant Na[ONS] using lower concentrations. The efficiency in IFT reduction decreases in the following order: [C_1C_6Im][ONS] > [C_1Pyr][ONS] > Na[ONS] ~ [C_4Py][ONS] > [C_2Py][ONS]. In this case, the longer alkyl chain of pyridinium ILs led to a better interaction with the oil, thus reducing the IFT.

With EOR applications in mind, the water-crude oil interfacial tension was also measured at 298.15 K. Similar results (see

Figure 4) to the case of *n*-octane were found. Equilibrium interfacial tensions achieved a range from 3.5 mN/m in the case of $[C_2Py][ONS]$ to 0.1 mN/m for $[C_1C_6im][ONS]$.

CONCLUSIONS

New alkylnaphthalenesulfonate surface active ILs were designed and successfully synthesized with high purity, namely: $[C_1Pyr][ONS]$, $[C_1C_6Im][ONS]$, $[C_2Py][ONS]$ and $[C_4Py][ONS]$. A synthetic procedure of three steps was required. First, sodium 4-(*n*-octyl)naphthalene-1-sulfonate, Na[ONS], was obtained by alkylation of 1-bromonaphthalene followed by sulfonation and later neutralization. Then the desired cations were introduced by the corresponding metathesis reaction with previously synthesized simple ILs. Unlike the starting product, Na[ONS], the new chemicals based on traditional IL cations (imidazolium, pyrrolidinium, and pyridinium) showed high solubility in water, which greatly favors their application in the form of aqueous formulations.

The incorporation of a large organic cation to the 4-(*n*-octyl)naphthalene-1-sulfonate anion led to a decrease in the glass transition/melting point of the synthesized compounds, and their IL nature was confirmed. Moreover, $[C_1Pyr][ONS]$ is liquid at room temperature and pressure which facilitates its manipulation at these conditions. Even when the inclusion of those cations decreased the decomposition temperatures in comparison to the starting product, the new chemicals can be used in a wide range of temperatures without suffering decomposition.

All the ILs self-aggregate in water, obtaining in all cases lower cmc and higher reduction of the surface tension of water than with Na[ONS]. This indicates that lesser amounts of the chemicals would be required if the ILs were selected for any application. Regarding the water/octane interfacial tension, $[C_1C_6Im][ONS]$ and $[C_1Pyr][ONS]$ are also able to reduce it to a greater extent than Na[ONS] with lower concentration of surfactant. Aiming at EOR applications, a very significant reduction of water-crude oil IFT was found with $[C_1C_6Im][ONS]$ ($\sim$0.1 mN/m). To achieve ultra-low values, as in the case of other naphthalene sulfonate surfactants (Chu et al., 2004; Gong et al., 2005), these chemicals must be formulated with electrolytes, co-surfactants, etc. to offer a promising formulation for this application.

DATA AVAILABILITY STATEMENT

The datasets generated for this study are available on request to the corresponding author.

AUTHOR CONTRIBUTIONS

All authors listed have made a substantial, direct and intellectual contribution to the work, and approved it for publication.

FUNDING

The authors acknowledge the Spanish Ministry of Science and Innovation, State Research Agency and European Regional Development Fund for financial support throughout project PGC2018-097342-B-I00, the Xunta de Galicia through the project EDA431D 2017/06, and the research support services of the Universidade de Vigo (CACTI) for the NMR and MS divisions.

SUPPLEMENTARY MATERIAL

The Supplementary Material for this article can be found online at: https://www.frontiersin.org/articles/10.3389/fchem.2020.00208/full#supplementary-material

REFERENCES

Abdel-Raouf, M. E., Maysour, N. E., Abdul-Raheim, A. M., El-Saeed, S. M., and Farag, R. K. (2011) Synthesis and study of the surface properties of alkylnaphthalene and alkylphenanthrene sulfonates. *J. Surfact. Deterg.* 14, 23–30. doi: 10.1007/s11743-010-1197-4

Berger, P. D., and Lee, C. H. (2002). New anionic alkylaryl surfactants based on olefin sulfonic acids. *J. Surfact. Deterg.* 5, 39–43. doi: 10.1007/s11743-002-0203-3

Calvar, N., Gómez, E., Macedo, E. A., and Domínguez, Á. (2013). Thermal analysis and heat capacities of pyridinium and imidazolium ionic liquids. *Thermochim. Acta* 565, 178–182. doi: 10.1016/j.tca.2013.05.007

Chu, Y. P., Gong, Y., Tan, X. L., Zhang, L., Zhao, S., An, J. Y., et al. (2004). Studies of synergism for lowering dynamic interfacial tension in sodium alpha-(n-alkyl) naphthalene sulfonate/alkali/acidic oil systems. *J. Colloid Interface Sci.* 276, 182–187. doi: 10.1016/j.jcis.2004.03.007

Gong, Y., Li, Z., and An, J. (2005). The properties of sodium naphthalene sulfonate in lowering interfacial tension and its possibility of application in EOR. *J. Dis. Sci. Techn.* 26, 503–507. doi: 10.1081/DIS-200054612

Green, D. W., and Willhite, G. P. (1998). *Enhanced Oil Recovery*. SPE Textbook Series Vol. 6, 2nd Edn. Richardson, TX: Society of Petroleum Engineers.

Hunter, M. E. (2017). "Alkylated naphthalenes," in *Lubricant Additives. Chemistry and Applications, 3rd Edn*, ed L. R. Rudnick (Wilmington, DE: CRC Press). doi: 10.1201/9781315120621-22

Lethesh, K. C., Evjen, S., Raj, J. J., Roux, D. C. D., Venkatraman, V., Jayasayee, K., et al. (2019). Hydroxyl functionalized pyridinium ionic liquids: experimental and theoretical study on physicochemical and electrochemical properties. *Front. Chem.* 7:625. doi: 10.3389/fchem.2019.00625

Lobo Ferreira, A. I., Rodrigues, A. S., Villas, M., Tojo, E., Rebelo, L. P. N., and Santos, L. M. (2019). Crystallization and glass-forming ability of ionic liquids: novel insights into their thermal behavior. *ACS Sustainable Chem. Eng.* 7, 2989–2997. doi: 10.1021/acssuschemeng.8b04343

Min, G. H., Yim, T., Yeong-Lee, H., Hu, D. H., Lee, E., Mun, J., et al. (2006). Synthesis and properties of ionic liquids: imidazolium tetrafluoroborates with unsaturated side chains. *Bull. Korean Chem. Soc.* 27, 847–852. doi: 10.1002/chin.200648138

Nietfeld, J. P., Schwiderski, R. L., Gonella, T. P., and Rasmussen, S. C. (2011). Structural effects on the electronic properties of extended fused-ring thieno[3,4-b]pyrazine analogues. *J. Org. Chem.* 76, 6383–6388. doi: 10.1021/jo200850w

Pal, A., and Saini, M. (2019). Aggregation behavior of task-specific acidic ionic liquid N-Methyl-2-Pyrrolidinium Dihydrogen Phosphate[NMP][H2PO4] in aqueous and aqueous salt solutions. *J. Surfact. Deterg.* 22, 491–499. doi: 10.1002/jsde.12232

Palmaerts, A., Lutsen, L., Cleij, T. J., Vanderzande, D., Pivrikas, A., Neugebauer, H., et al. (2009). Development of novel processable electron accepting conjugated polymers containing fluoranthene units in the main chain. *Polymer* 50, 5007–5015. doi: 10.1016/j.polymer.2009.08.031

Pirkwieser, P., Lopez-Lopez, J. A., Kandioller, W., Keppler, B. K., Moreno, C., and Jirsa, F. (2018). Novel 3-Hydroxy-2-Naphthoate-Based Task-Specific ionic liquids for an efficient extraction of heavy metals. *Front. Chem.* 6:172. doi: 10.3389/fchem.2018.00172

Potangale, M., Das, A., Kapoor, S., and Tiwari, S. (2017). Effect of anion and alkyl chain length on the structure and interactions of N-alkyl pyridinium ionic liquids. *J. Mol. Liquids* 240, 694–707. doi: 10.1016/j.molliq.2017.05.036

Tan, X., Zhang, L., Zhao, S., Yu, J., and An, J. (2004a). Synthesis and study of the surface properties of long-chain alkylnaphthalene sulfonates. *J. Surf. Deterg.* 7, 135–139. doi: 10.1007/s11743-004-0296-8

Tan, X. L., Zhang, L., Zhao, S., Li, W., Ye, J. P., Yu, J. Y., and An, J. Y. (2004b). Aggregation of sodium 1-(n-alkyl)naphthalene-4-sulfonates in aqueous solution: micellization and microenvironment characteristics. *Langmuir* 20, 7010–7014. doi: 10.1021/la049055v

Villanueva, M., Parajó J. J., Sánchez, P. B., García, J., and Salgado, J. (2015). Liquid range temperature of ionic liquids as potential working fluids for absorption heat pumps. *J. Chem. Thermodyn.* 91, 127–135. doi: 10.1016/j.jct.2015.07.034

Zhao, Z., Bi, C., Qiao, W., Li, Z., and Cheng, L. (2007). Dynamic interfacial tension behavior of the novel surfactant solutions and Daqing crude oil. *Colloid Surf. A* 294, 191–202. doi: 10.1016/j.colsurfa.2006.08.011

Zhao, Z., Liu, F., Qiao, W., Li, Z., and Cheng, L. (2006). Novel alkyl methylnaphthalene sulfonate surfactants,: A., good candidate for enhanced oil recovery. *Fuel* 85, 1815–1820. doi: 10.1016/j.fuel.2006.02.006

Conflict of Interest: The authors declare that the research was conducted in the absence of any commercial or financial relationships that could be construed as a potential conflict of interest.

frontiers in Chemistry

ORIGINAL RESEARCH
published: 08 May 2020
doi: 10.3389/fchem.2020.00295

Local Overheating of Biotissue Labeled With Upconversion Nanoparticles Under Yb^{3+} Resonance Excitation

*Ivan V. Krylov[1], Roman A. Akasov[1,2], Vasilina V. Rocheva[1], Natalya V. Sholina[1,2], Dmitry A. Khochenkov[1,3,4], Andrey V. Nechaev[1,5], Nataliya V. Melnikova[6], Alexey A. Dmitriev[6], Andrey V. Ivanov[2], Alla N. Generalova[1,7] and Evgeny V. Khaydukov[1,2]**

[1] Scientific Research Center "Crystallography and Photonics," Russian Academy of Sciences, Moscow, Russia, [2] Center of Biomedical Engineering, Institute of Molecular Medicine, Sechenov University, Moscow, Russia, [3] National Medical Research Center for Oncology, Ministry of Health of Russian Federation, Moscow, Russia, [4] Medicinal Chemistry Center, Togliatti State University, Togliatti, Russia, [5] Institute of Fine Chemical Technologies, Moscow Technological University, Moscow, Russia, [6] Engelhardt Institute of Molecular Biology, Russian Academy of Sciences, Moscow, Russia, [7] Laboratory of Polymers for Biology, Shemyakin-Ovchinnikov Institute of Bioorganic Chemistry, Russian Academy of Sciences, Moscow, Russia

OPEN ACCESS

Edited by:
Manoj K. Mahata, Gwangju Institute of Science and Technology, South Korea

Reviewed by:
Abdul K. Parchur, Medical College of Wisconsin, United States
Karina Nigoghossian, Tokyo University of Science, Japan

***Correspondence:**
Evgeny V. Khaydukov
khaydukov@mail.ru

Specialty section:
This article was submitted to Physical Chemistry and Chemical Physics, a section of the journal Frontiers in Chemistry

Received: *31 January 2020*
Accepted: *25 March 2020*
Published: *08 May 2020*

Citation:
Krylov IV, Akasov RA, Rocheva VV, Sholina NV, Khochenkov DA, Nechaev AV, Melnikova NV, Dmitriev AA, Ivanov AV, Generalova AN and Khaydukov EV (2020) Local Overheating of Biotissue Labeled With Upconversion Nanoparticles Under Yb^{3+} Resonance Excitation. Front. Chem. 8:295. doi: 10.3389/fchem.2020.00295

Local overheating of biotissue is a critical step for biomedical applications, such as photothermal therapy, enhancement of vascular permeability, remote control of drug release, and so on. Overheating of biological tissue when exposed to light is usually realized by utilizing the materials with a high-absorption cross section (gold, silica, carbon nanoparticles, etc.). Here, we demonstrate core/shell $NaYF_4$:Yb^{3+}, Tm^{3+}/$NaYF_4$ upconversion nanoparticles (UCNPs) commonly used for bioimaging as promising near-infrared (NIR) absorbers for local overheating of biotissue. We assume that achievable temperature of tissue labeled with nanoparticles is high enough because of Yb^{3+} resonance absorption of NIR radiation, whereas the use of auxiliary light-absorbing materials or shells is optional for photothermal therapy. For this purpose, a computational model of tissue heating based on the energy balance equations was developed and verified with the experimentally obtained thermal-graphic maps of a mouse in response to the 975-nm laser irradiation. Labeling of biotissue with UCNPs was found to increase the local temperature up to 2°C compared to that of the non-labeled area under the laser intensity lower than 1 W/cm^2. The cellular response to the UCNP-initiated hyperthermia at subcritical ablation temperatures (lower than 42°C) was demonstrated by measuring the heat shock protein overexpression. This indicates that the absorption cross section of Yb^{3+} in UCNPs is relatively large, and microscopic temperature of nanoparticles exceeds the integral tissue temperature. In summary, a new approach based on the use of UCNP without any additional NIR absorbers was used to demonstrate a simple approach in the development of photoluminescent probes for simultaneous bioimaging and local hyperthermia.

Keywords: upconversion nanoparticles, bioimaging, photothermal material, hyperthermia, local overheating, near-infrared irradiation, heat shock proteins, biotissue laser heating

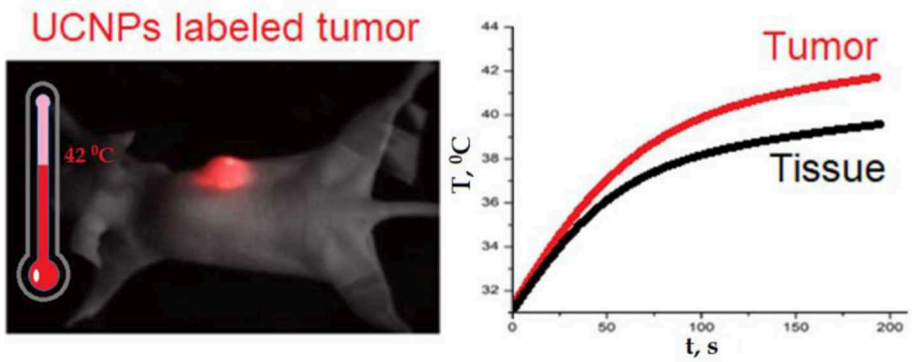

GRAPHICAL ABSTRACT | Overheating of UCNP-labeled tumor.

INTRODUCTION

Recently, upconversion nanoparticles (UCNPs) and UCNP-based nanoconstructions showed a great potential in biomedical applications for near-infrared (NIR)–to–NIR bioimaging (Chen et al., 2014; Wu et al., 2014; Li et al., 2015; Generalova et al., 2016), photodynamic (Khaydukov et al., 2016; Xu et al., 2017; Qiu et al., 2018; Liu et al., 2019), and photothermal therapy (PTT) (Zhu et al., 2016; Chan et al., 2018). Upconversion nanoparticles (NPs) consist of inorganic host matrix, typically $NaYF_4$, codoped with Yb^{3+}, Er^{3+} or Yb^{3+}, Tm^{3+} lanthanide ions. The UCNP luminescence and excitation lines are located in the so-called "biological transparency window," whereas the anti-Stokes luminescence signal shift allows the absence of autofluorescence. Unique UCNP properties provide NIR-to-visible and NIR-to-NIR luminescence suitable for bioimaging (Kobayashi et al., 2009), long-term visualization implemented even at the level of single NP (Liu et al., 2018), and the excellent excitation depth in biological tissue of up to 1 cm (Zhan et al., 2013). In addition, UCNPs are characterized by superior photostability, non-blinking (Wu et al., 2009), long lifetimes (Zhan et al., 2013; Pilch et al., 2017), low cytotoxicity (Guller et al., 2015, 2018; Vedunova et al., 2016), and high spatial resolution during bioimaging (Zhan et al., 2011; Chen et al., 2012; Xu et al., 2013; Khaydukov et al., 2014; González-Béjar et al., 2016; Generalova et al., 2017).

Nanoparticles have great potential for PTT. By providing heat at the nanoscale, they facilitate therapeutic efficacy and reduce side effects for normal tissue compared to conventional ultrasound and microwave methods. Heat generation from the NP consists of the absorption of incident photons, conversion of light energy into heat, and its transfer from the NP to the biotissue. Typically, the photothermal properties of UCNP nanoconstructions are achieved by shell formation or inclusion of NPs with a high-absorption cross section. For example, temperature feedback of UCNPs coated with carbon layer as a light absorber was used for the precise tumor PTT with minimal damage to normal tissue (Zhu et al., 2016). To enhance the absorption of plasmon resonance, a more complex double-coated UCNP structure with layers of iron and gold was proposed (Cheng et al., 2011). Graphene- and silica-based UCNP complexes for local overheating were also demonstrated (Liu et al., 2013; Gulzar et al., 2018). In addition, the specific optical properties of UCNPs are ideal for real-time luminescent temperature measurements in the physiological range (Sedlmeier et al., 2012; Li et al., 2017). However, the UCNP structure with additional layers or NPs as light-absorbing materials for PTT is often cumbersome and complicates the preparation of nanoprobes.

Magnetic NPs are often used as a model of NP-mediated hyperthermia. This approach was first proposed by Gilchrist et al. (1957), who introduced the concept of injecting magnetic NPs (20–100 nm) into lymphatic channels to heat residual cancer cells under an alternating magnetic field (AMF). Because delivering magnetic NPs via direct injection into the tumor could result in much more effective and selective heating when compared to other heating techniques, this approach was discussed as more safe and clinically promising (Jordan et al., 2009). Since then, significant efforts have been directed to the development of novel magnetic NPs, including targeted ones, and clinical AMF systems, resulting in clinical trials and industrial solutions (Cruz et al., 2017; Chang et al., 2018). Thus, within the past two decades, phases 1 and 2 of clinical studies of intratumorally delivered magnetic NPs treated by AMF were successfully conducted for patients with glioblastoma and prostate cancers (Johannsen et al., 2010; Maier-Hauff et al., 2011). We believe that UCNPs, which are comparatively new in medicine biotechnology, could be proposed as a promising alternative to magnetic NPs in terms of NP-mediated hyperthermia induction.

Herein, we synthesized core-shell UCNPs $NaYF_4$:Yb^{3+}:Tm^{3+}/$NaYF_4$ modified with a PEG shell aiming to demonstrate the possibility of PTT based on resonant excitation $^2F_{5/2} \rightarrow {}^2F_{7/2}$ of Yb^{3+} at low apparent absorption cross section. Our results indicate that Yb^{3+} absorption cross section in NPs is rather sufficient to increase the local temperature of the biological tissue to 2°C at a 975-nm radiation with intensity of <1 W/cm^2. Thus, theranostic NPs for simultaneous bioimaging and local hyperthermia can be easily designed because of their own absorption of UCNPs without impregnation with adjuvant light absorbers.

RESULTS AND DISCUSSION

In order to demonstrate simultaneous bioimaging and local hyperthermia, we synthesized UCNPs with a core/shell structure. The UCNP is an inorganic crystal matrix of the most popular composition $NaYF_4$ codoped with ytterbium (Yb^{3+}) and thulium (Tm^{3+}) ions with an undoped shell $NaYF_4$. The host matrix material should be optically transparent for light excitation and emission and have low phonon energy for efficient energy transfer inside the particle (Chen et al., 2014; Wu et al., 2014). In this study, we proposed that UCNPs consist of the hexagonal β-phase of $NaYF_4$ and two types of ions: a sensitizer (Yb^{3+}) and an activator (Tm^{3+}) (**Figure 1**). Yb^{3+} is capable of absorbing laser excitation at 975 nm and non-radiatively transfers this energy to Tm^{3+} ions. Tm^{3+} have multiple metastable excited states with long lifetimes (sub-ms) (Auzel, 2004). Energy transfer from Yb^{3+} to Tm^{3+} can occur several times. Eventually, Tm^{3+} has several emission lines from 800 to 345 nm (**Figure 1b**).

The as-synthesized hydrophobic UCNPs were hydrophilized using amphiphilic poly(maleic anhydrate-*alt-1*-octadecene) followed by surface modification using cross-linker poly(ethylene glycol) diglycidyl ether. This approach led to the formation of a "corona"-like negatively charged (ξ-potential was −41,1 mV) structure with PEG molecules on the UCNP surface. The PEG layer determines biocompatibility, non-cytotoxicity, and low blood protein adsorption of UCNPs (Generalova et al., 2016). The cross-linked shell on UCNP surface (PEG-UCNPs) maintained the colloidal stability for at least a month and was not affected by electrolytes (0.15 M NaCl and buffers). It should be noted that PEGylation of UCNPs is one of the most common methods to increase the biocompatibility of NPs, prolong circulation time, and, as a result, to increase passive accumulation in tumors due the enhanced permeability and retention effect (Generalova et al., 2016; Han et al., 2018).

Melanoma xenograft-bearing mice were used to demonstrate self-temperature effects of UCNPs for theranostic applications. For this purpose, 2×10^6 human melanoma A375 cells were subcutaneously inoculated into immunodeficient Balb/c nu/nu mice (see Methods section for details) and were grown for 15 days until the tumors reached 150 ± 20 mm^3 in volume, as shown in **Figure 2**. Then, 100-μL phosphate-buffered saline (PBS) solution containing 200 μg PEG-UCNPs was injected into the tumor-surrounding tissues and incubated for 2 h. In order to visualize the UCNPs in tumor, we performed an *in vivo* whole-animal imaging using custom-developed epiluminescence imaging system. The NIR-to-NIR system realizes raster scanning excitation at 975 nm with wide-field EMCCD detection at 800 nm. A strong luminescence signal was detected in the tumor, while normal tissues remained unlabeled (**Figure 2**).

After imaging the tumor, the *in vivo* heating procedure was started. Heating was provided by 975-nm laser beam scanning with an adjusted area due to a system of galvanic mirrors. A375 xenograft-bearing mouse was fixed to the plate with a duct tape. The mouse temperature was monitored by a Gobi-384-GigE-7098 Camera (Leuven, Belgium). The temperature of UCNP-labeled tumor was found to be higher than temperature of the surrounding tissue (**Figures 3A,B**). After 3 min of laser treatment, the detected temperature gap was ∼2°C. In order to prove that tumor overheating is associated with UCNPs impregnated in the tumor, a control group of unlabeled A375 melanoma xenografts was used. Surprisingly, the effect of overheating was not observed (**Figures 3C,D**). Note that the ablation temperature of biotissue is usually discussed as 42°C or higher (Zhu et al., 2016). In our experiments, this temperature was reached during 3 min of laser treatment, while the temperature of the treated normal tissue was in a safe range.

We have developed a computational model that predicts the heating of biotissue with variable parameters, namely, laser treatment time, NP concentration, and laser beam intensity.

For this purpose, we modified a temperature- and time-dependent model described earlier (Zhu et al., 2016). We proposed four temperature fields in the system "mouse-air" (**Figure 4**). In details, T_1 is the temperature of the tumor layer impregnated by UCNPs and irradiated by a 975-nm laser beam. T_2 corresponds to the temperature of the UCNP-free biotissue layer also irradiated with the laser beam. T_3 is the average temperature of the whole body, and T_4 is the environment temperature. The main model assumptions are as follows:

1. $Q_{i\to j} \sim (T_i - T_j)$, where $Q_{i->j}$ is the energy passing between i_{th} and j_{th} areas.
2. There is the same temperature T_i for a whole i_{th} area.
3. The absorber (NP) distribution is uniform.

A solid tumor is known to have the specific pressure distribution (Liu et al., 2016). Typically, the solid tumor divides into three regions: (1) the central region that contains the necrotic core; (2) the tumor periphery region with abundant blood vessels, which is the main source of tumor interstitial fluid; and (3) the intermediate region, where the increased core pressure equalizes with normal tissue fluid pressure (Liu et al., 2011). As a result, the injected NPs are redistributed into the tumor and form a specific surface layer impregnated with UCNPs. Based on our previous results (Generalova et al., 2016), we estimate the thickness of the layer with UCNPs as ∼2 mm. It should be noted that our estimation correlates with the data obtained in Liu et al. (2016). The energy balance equation in the first area can be written as follows:

$$\begin{aligned} Cm_1\frac{dT_1}{dt} &= Q_{in} - Q_{out} = Q_1 - (Q_{1\to 2} + Q_{1\to 3} + Q_{1\to 4}) \\ &= N\sigma I + P\left(1 - e^{-kd}\right) - h_{12}S_{12}(T_1(t) - T_2(t)) \\ &\quad -h_{13}S_{13}(T_1(t) - T_3(t)) - h_{14}S_{14}(T_1(t) - T_4), \end{aligned}$$

where C is the specific heat, m_1 is the mass of the surface layer, T_j is the temperature in the j-th area, t is time, N is the number of ytterbium ions absorbing laser radiation, σ is the absorption cross section of ytterbium, I is the intensity of the incident laser radiation, P is the power of the laser radiation, k is the absorption coefficient, S_{ij} is the heat exchange surface area between the i-th and j-th areas, and h_{ij} is the heat transfer coefficient.

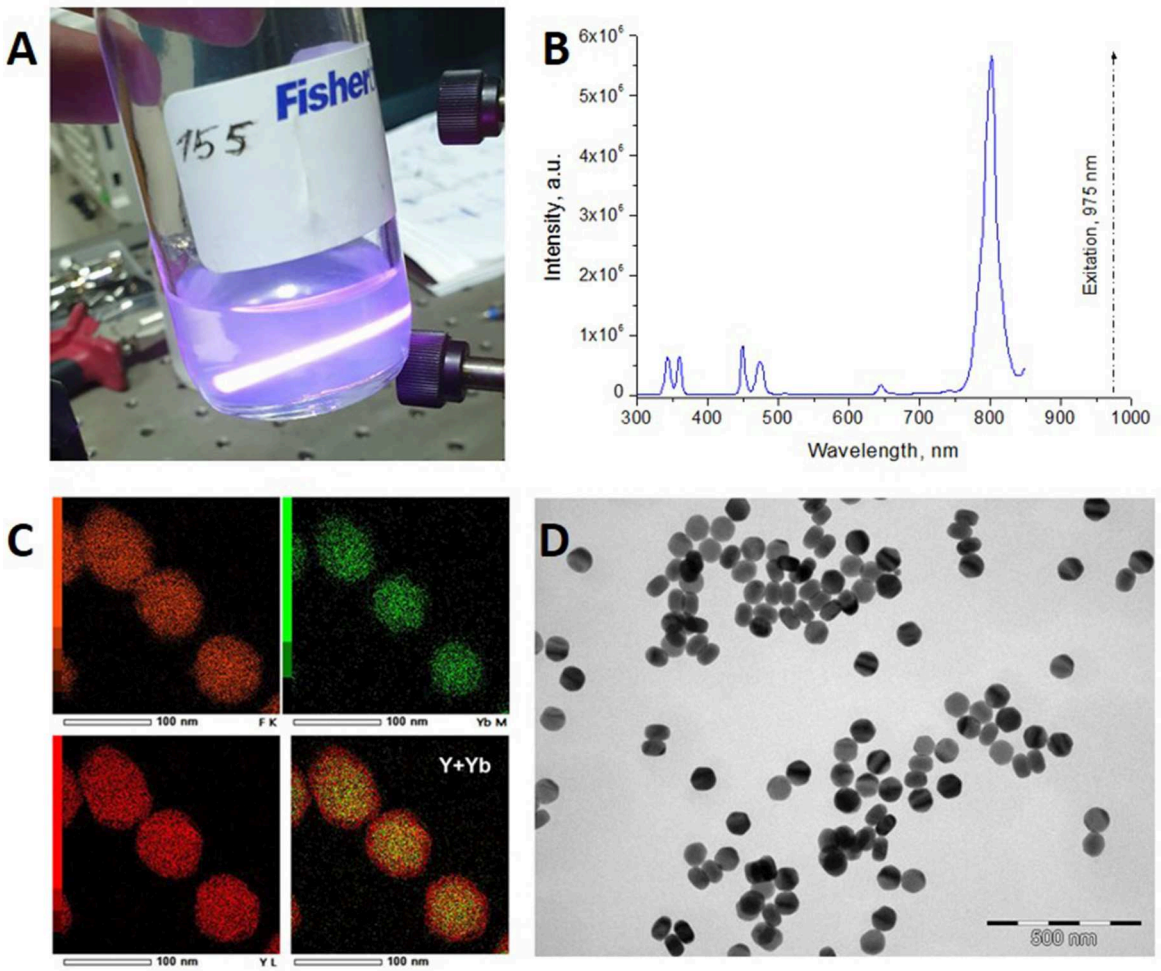

FIGURE 1 | (A) UCNPs colloid illuminated with a 975-nm laser beam. Blue traces of photoluminescence illustrate conversion of NIR radiation in NPs. The image was taken via the interference filter Semrock (842-nm blocking edge BrightLine® short-pass filter Semrock, New York, NY, USA) cutting off 15 W/cm^2 excitation at 975 nm. **(B)** Photoluminescence spectrum of UCNPs under excitation at 975 nm. **(C)** Elemental EDX mapping of NPs, overlay Y (red), and Yb (green) indicates core/shell structure of UCNPs. **(D)** Transmission electron microscopy (TEM) images of as-synthesized core/shell $NaYF_4$:Yb^{3+}, Tm^{3+}/$NaYF_4$ UCNPs with hexagonal prism shape (75-nm base and 50-nm height).

Simplifying, we obtain

$$\begin{aligned}\frac{dT_1}{dt} &= A_1 - B_{12}(T_1(t) - T_2(t)) - B_{13}(T_1(t) - T_3(t)) \\ &\quad -B_{14}(T_1(t) - T_4), \\ A_1 &= \frac{N\sigma I + P\left(1 - e^{-kd}\right)}{Cm_1}, B_{ij} = \frac{h_{ij}S_{ij}}{Cm_1}.\end{aligned}$$

Writing the similar energy balance equations in second and third areas, we obtain the following system:

$$\begin{aligned}\frac{dT_1}{dt} &= A_1 - B_{12}(T_1(t) - T_2(t)) - B_{13}(T_1(t) - T_3(t)) \\ &\quad - B_{14}(T_1(t) - T_4) \\ \frac{dT_2}{dt} &= A_2 + B_{21}(T_1(t) - T_2(t)) - B_{23}(T_2(t) - T_3(t)) \\ &\quad - B_{24}(T_2(t) - T_4) \\ \frac{dT_3}{dt} &= A_3 + B_{32}(T_2(t) - T_3(t)) + B_{31}(T_1(t) - T_3(t)) \\ &\quad - B_{34}(T_3(t) - T_4) \\ T_1(0) &= T_1^0 \\ T_2(0) &= T_2^0 \\ T_3(0) &= T_3^0\end{aligned}$$

This system was solved numerically, and the results are presented in **Figure 5**. The theoretical modeling allows predicting optimal physical parameters for overheating, taking into account the size and shape of the tumor. We have verified the theoretical model by comparing the experimental and calculated data (**Figure 5A**). **Figures 5B,C** show calculated laser intensities and NP concentrations with allowance for the need to maintain the

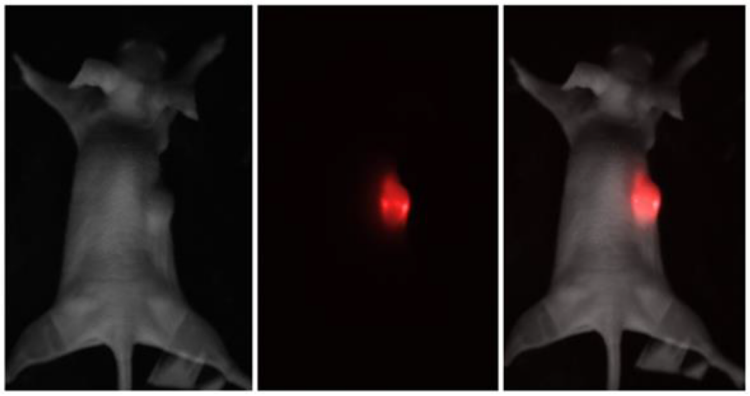

FIGURE 2 | Brightfield, epiluminescent, and overlay images of the immunodeficient mouse, bearing a grafted subcutaneous A375 tumor. The UCNP luminescence at 800 nm is represented in red color.

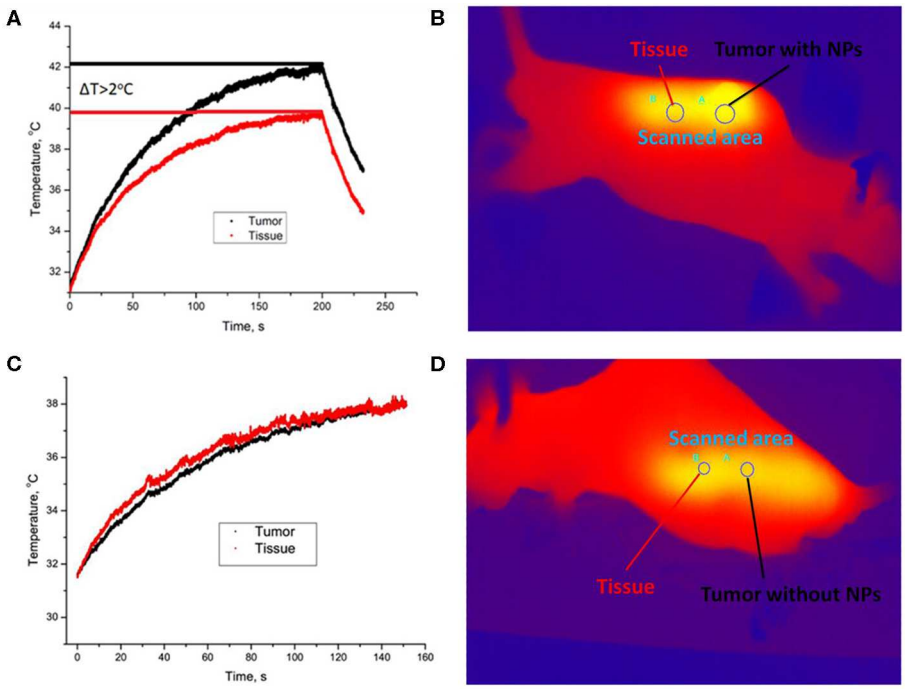

FIGURE 3 | Temperature image of immunodeficient mice bearing a grafted A375 tumor during 975-nm laser irradiation at the intensity of 1 W/cm^2. Melanoma xenograft labeled with UCNPs **(A)** and control (no UCNPs) **(B)**. Area A is for tumor, and area B is for normal tissue. A temperature increase during laser treatment in the UCNP-labeled **(C)** and control **(D)** mice. The tumor (area A) is shown with a black curve, and normal tissue (area B) is visualized with a red curve.

temperature in the range from 42°C to 45°C on the plateau because the exposure time in potential medical use is quite long.

We provide *in vitro* experiment on the heat shock protein (HSP) expression in response to overheating associated with UCNPs upon 975-nm irradiation. Overheating in biotissue causes several hazardous effects that lead to cell death through necrosis (proinflammatory response) or apoptosis, which is more attractive because apoptosis inhibits the inflammatory response (Melamed et al., 2015). Heat shock proteins are a family of proteins involved in the folding and maturation of proteins, and they have been identified as key determinants of cell survival under stressful conditions (Kennedy et al., 2014; Wu et al., 2017), and, in particular, in the apoptotic process (Lanneau et al., 2008). Here, we evaluated the expression of HSP70 family protein as a marker for the cellular response to overheating caused by UCNP photoactivation. For this purpose, cells were incubated with 0.1 mg/mL UCNPs, and rapid (within 30 min) accumulation of UCNPs in the cells was demonstrated, confirming high biocompatibility (**Figure 6A**). The cells were then irradiated until a critical temperature was reached for HSP expression.

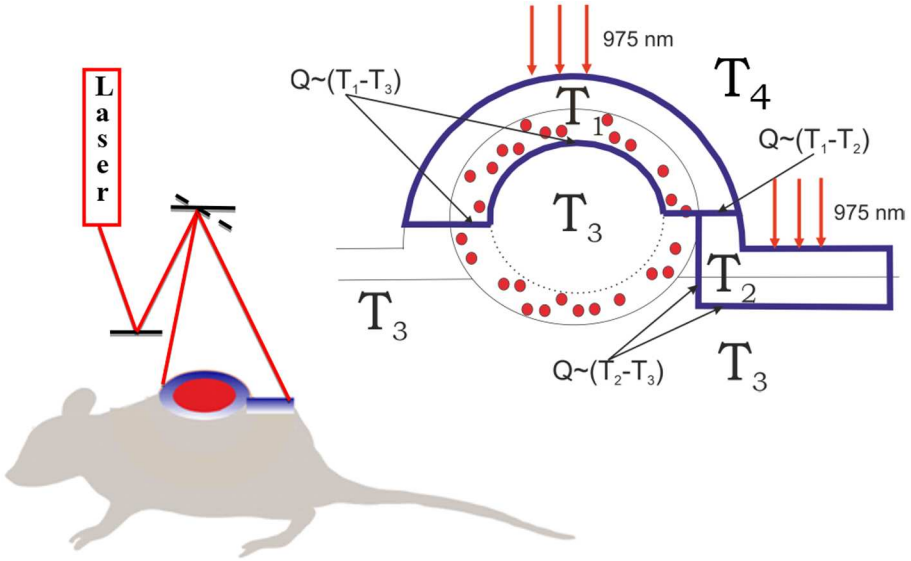

FIGURE 4 | Schematics of biotissue and tumor temperature modeling. The outer layer of the tumor tissue is labeled with UCNPs (red dots). The tumor and normal tissue were irradiated with 975-nm laser excitation. The laser dose was evenly released due to a galvanic mirror scanning system. The heated fields are marked with a blue line. T_3 is the temperature in the tumor core equal to the temperature of the non-irradiated tissue, T_2 is the temperature of the irradiated skin layer, T_1 is the temperature of the irradiated interstitial tumor tissue, and T_4 is the environment temperature. $T_1 \geq T_2 \geq T_3 \geq T_4$.

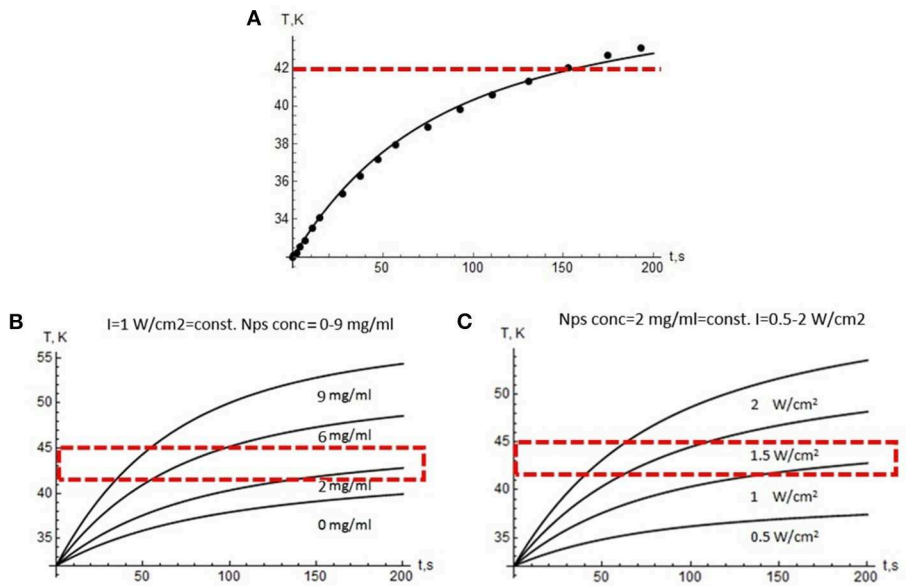

FIGURE 5 | Modeling results. **(A)** Temperature growth during laser treatment in the tumor (dots—experiment, curve—modeling data). Red dotted line indicates the lower edge of the overheating region. Temperature profiles vs. 975 nm treatment time: **(B)** at a constant laser power density of 1 W/cm^2 and the variable NP concentration, **(C)** at a constant NP concentration of 2 mg/mL and a variable power density from 0.5 to 2 W/cm^2. Red dotted line indicates the range suitable for PTT.

Although the temperature of the treated sample was 40.5°C ± 0.1°C that is lower than 41°C to 42°C usually required for HSP induction, the relative expression level of the *HSPA1A* gene (HSP70 family) was approximately 3.5 times higher compared to the untreated sample (**Figure 6B**). In contrast, there was no significant increase in *HSPA1A* gene expression for cells heated at the same laser settings and at a similar final temperature (39.5°C ± 0.3°C). Because this could be explained by the temperature gap between the UCNP-loaded sample and the UCNP-free sample, we performed an additional experiment with equal temperature for both samples (40.6°C ± 0.5°C). We found an increase in the relative level of *HSPA1A* expression for the UCNP-loaded

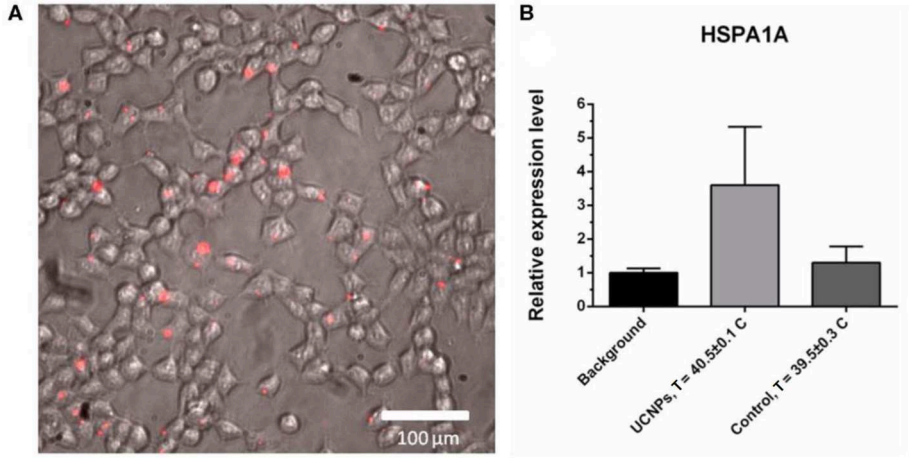

FIGURE 6 | Upconversion nanoparticle (in red) accumulation in A375 cells, 30-min incubation with 50 μg/mL UCNPs **(A)**. The *HSPA1A* expression in A375 human melanoma cells, quantitative PCR (qPCR) assay: background sample (no UCNPs, no NIR), treated sample (0.1 mg/mL UCNPs, NIR irradiation), control sample (no UCNPs, NIR irradiation). The *HSPA1A* expression in each sample was normalized to that in the background sample **(B)**.

sample that was about 4.5 times higher compared to the non-treated sample and no increase for the control heating without the UCNP. We suppose that this could be explained with the localized nature of UCNP-induced heating. In other words, the NP temperature can be significantly higher than the temperature of the medium. This effect was previously demonstrated for iron oxide NPs when particle-based hyperthermia has increased cytotoxicity compared to conventional hyperthermia in a water bath at the same measured heat dose (Ogden et al., 2009). Previously, it was also demonstrated that the exposure of A375 melanoma cells to temperatures below 43°C does not significantly affect viability levels (Mantso et al., 2018). Therefore, thermal damage caused by particles can be discussed as more effective than conventional integrated heating. It should be also noted that some metal-based NPs can themselves induce HSP expression through oxidative stress (Ahamed et al., 2010; Vecchio et al., 2012). However, in this study, the addition of UCNPs without NIR irradiation did not lead to significant HSP induction (**Supplementary Data 1**).

In order to explain the observed experimental facts and that theory converges with experimental data, we estimated the absorption cross section of $^2F_{5/2} \rightarrow {}^2F_{7/2}$ transition for Yb^{3+} ions in NPs, as 2×10^{-19} cm^2. At present, a relatively low value of 10^{-20} cm^2 as determined at 980 nm in the germanosilicate glass matrix (Paschotta et al., 1997) without allowance for the crystal matrix symmetry is widely accepted as the reference for the absorption cross section of Yb^{3+} in the literature. It is well-known that σ_{abs} can vary depending on the type of the crystalline matrix due to splitting Stark levels. For example, the effective energy absorption of Nd^{3+}, which is also used for optical imaging, can vary by three orders of magnitude (Kaminskii et al., 1980, 1982a,b). Fluoride materials with low symmetry, for example, $LiLnF_4$ and $BaLn_2F_8$ crystals, were shown to increase the absorption cross section by two orders of magnitude compared to oxide matrices with a cubic structure (Brown et al., 1969; Caspers and Rast, 1975; Esterowitz et al., 1979a,b; Da Gama et al., 1981).

Moreover, the question about the absorption cross section for doping ions in nanocrystals is probably even more complicated because the crystal symmetry at the nanoscale level can be violated because of geometric factors. We believe that the value of Yb^{3+} absorption cross section is an open question today and requires a detailed analysis. Further experiments are needed, although our data indicate the absorption cross section of Yb^{3+} in the β-$NaYF_4$ matrix is relatively large.

CONCLUSIONS

We demonstrated core/shell $NaYF_4$: Yb^{3+}, Tm^{3+}/$NaYF_4$ UCNPs as promising NIR absorbers for local biotissue overheating. The critical photothermal temperature (≥42°C) was achieved due to Yb^{3+} absorption of NIR radiation without the assistant light-absorbing materials. A computational model of tissue heating based on the energy balance equations was developed and verified with the experimentally obtained thermal-graphic maps of the mouse in response to the 975-nm laser exposure. Our modeling results indicate that the absorption cross section of Yb^{3+} in UCNPs is larger than the literature value, while microscopic temperature of NPs exceeds the integral tissue temperature. In summary, a novel approach based on UCNP application without additional NIR absorbers was developed and applied to demonstrate the possibility of these photoluminescent probes to be used for simultaneous bioimaging and local hyperthermia. We assume that demonstrated temperature modality of UCNPs will be perspective as a new strategy for combined cancer therapy.

METHODS

UCNP Synthesis

The synthesis of lanthanide-doped UCNPs based on $NaYF_4$ matrix was performed as described earlier (Grebenik et al., 2013; Generalova et al., 2016). Briefly, the synthesis is based on the coordinate stabilization of yttrium, ytterbium, and thulium metal salts in a solution of oleic acid and octadecene. It was carried

out under heating in an oxygen-free atmosphere. The product of synthesis is hydrophobic monodisperse NPs (75 ± 5 nm) (**Supplementary Data 2**) with a core@shell structure (β-$NaYF_4$: 18% Yb^{3+}, 0.6% Tm^{3+}@$NaYF_4$), which form stable colloids in non-polar organic solvents, such as hexane and chloroform.

Intercalation of UCNPs Using Amphiphilic Polymer Followed by Cross-Linking With PEG-Diglycidyl Ether

The coating of UCNPs with an amphiphilic polymer poly(maleic anhydrate-*alt-1*-octadecene) (PMAO) by solvent evaporation method was performed according to the previously described protocol (Guller et al., 2015). Resulted aqueous dispersion of UCNPs-PMAO containing 0.8 mg of UCNPs was centrifuged at 13,400 rpm for 10 min. The pellet was dispersed in 1 mL PBS buffer (pH 7.0), and 40 μL 1.5% PEG-diglycidyl ether aqueous solution was added. The mixture was vortexed, sonicated for 5 min, and stirred for 1 h at 95°C. Thereafter, the mixture was centrifuged again at 13,400 rpm for 10 min with a PBS buffer addition (this procedure was repeated three times to remove an unreacted cross-linker), and dispersed in 1 mL of PBS buffer (pH 7.0). For detail see Generalova et al. (2016).

Transmission Electron Microscopy ("TEM")

High-angle annular dark field (HAADF) scanning TEM and high-resolution TEM studies were performed using a JEOL ARM200F cold FEG double aberration corrected electron microscope operated at 200 kV and equipped with a large solid-angle CENTURIO EDX detector and Quantum EELS spectrometer (JEOL, Tokyo, Japan for all equipment). A TEM sample was prepared by sample dissolution in methanol and deposition on hollow carbon Cu grid.

Thermal Imaging Camera

The actual temperature of mice was measured by Xenics Gobi-384-GigE-7098 camera in real time. The working range of the camera is from 8 to 14 μm with an accuracy of 0.5°C and quantum yield 98% at the peak wavelengths 10 μm. Resolution of camera is 0.1 MPx, and the frame rate is 84 Hz. The data were transmitted by GigE-port to PC.

Visualization System

The custom-developed epiluminescent optical imaging system was used to visualize the accumulation of UCNPs in the tumor. The mice were scanned by a laser beam with a diameter of 1 cm. The laser intensity at 975 nm was limited to 1 W/cm^2. The detection of the photoluminescent signal was performed using a Falcon EMCCD camera (Raptor Photonics, Larne, Northern Ireland), equipped with the $F = 0.95$ objective. The interference filters (Semrock, New York, NY, USA) were placed in front of the lens, cutting the laser radiation. Exposure time of 2 seconds corresponded to two complete animal surface scans while taking the image by EMCCD camera.

Cell Culture

Human melanoma A375 and human embryonic kidney HEK 293 cells were used in this research. All cells were grown in Dulbecco modified eagle medium (DMEM) growth medium supplemented with 10% fetal bovine serum (FBS), 2 μM L-glutamine, 100 μg/mL streptomycin, and 100 U/mL penicillin at 37°C in a 5% CO_2 humidified atmosphere. The medium was replaced every 3 to 4 days.

Cell Treatment

Cells were seeded in 48-well plate (50,000 cells per each well) in DMEM supplemented with 10% FBS and incubated overnight in CO_2 incubator (37°C, 5% CO_2). Then, the UCNPs were added to the cells to the final concentration of 0.1 mg/mL for 30 min. Then, the cells were heated using NIR irradiation (parameters). Cells without UCNPs and NIR irradiation were used as controls.

RNA Isolation

RNA from A375 cells was isolated using Quick-RNA MiniPrep (Zymo Research, Irvine, CA, USA). RNA Lysis Buffer was added to the cells, and then RNA samples were purified with Zymo-Spin Columns according to the manufacturer's protocol. The RNA quality and concentration were evaluated on Agilent 2100 Bioanalyzer (Agilent Technologies, Santa Clara, CA, USA) and a Qubit 2.0 fluorometer (Thermo Fisher Scientific, Waltham, MA, USA).

Reverse Transcription

One microgram of RNA from each sample was treated with DNase I (Thermo Fisher Scientific). Random hexamer primers (Evrogen, Moscow, Russia) were added to DNase treated RNA or no template control, incubated at 70°C for 5 min, and chilled on ice. Sixteen microliters of reaction mix for first-strand cDNA synthesis (1× reaction buffer and 1 mM dNTP mix; Evrogen) was added to each sample and incubated for 5 min at 25°C. Then, each sample was separated for two parts: one was used for reverse transcription and the other one for no-reverse-transcriptase control (RT-minus control). To generate the first-strand cDNA, 200 U of RevertAid Reverse Transcriptase (Thermo Fisher Scientific) was added to samples for reverse transcription, and then all samples were incubated for 10 min at 25°C followed by 60 min at 42°C. Before quantitative PCR, each sample was 10-fold diluted.

Quantitative PCR

The qPCR was performed on 7500 Real-Time PCR System (Thermo Fisher Scientific) in 96-well plates. Reaction mix was prepared in 20 μL and contained: 1× PCR mix (GenLab, Moscow, Russia), 250 nM dNTP (Evrogen), 2 U of polymerase (GenLab), 300 nM primers and 200 nM short hydrolysis probes (Universal ProbeLibrary; Roche, Basel, Switzerland) or 1× TaqMan Gene Expression Assays (Thermo Fisher Scientific), and 1× LowROX (Evrogen). Quantitative PCR program was as follows: denaturation for 10 min at 95°C, 95°C for 15 s, and 60°C for 60 s for 50 cycles. All reactions were carried out in three technical replicates. TaqMan Gene Expression Assays representing primer–probe sets were used for reference genes: *RPN1*-Hs00161446_m1, *ACTB*-Hs01060665_g1. For the *HSPA1A* gene, we applied

custom primers (forward: AAGGACCGAGCTCTTCTCG, reverse: GGTTCCCTGCTCTCTGTCG) and probe #47 from Universal ProbeLibrary (Roche). The RT-minus controls were used for each sample and each pair of primers. The expression level of the target gene under each condition was calculated using the qGEPS (ATG) tool (Melnikova et al., 2016) as follows:

$$\text{Expression level} = 2^{\left(C_t^{\text{eff}}\right)^{\text{reference gene}} - \left(C_t^{\text{eff}}\right)^{\text{target gene}}}$$

$$C_t^{\text{eff}} = \text{C}_\text{t} \times \log_2(1+E)$$

where E is reaction efficiency for each pair of primers ($E = 1$ corresponds to 100% efficiency); Ct is replicate-averaged threshold cycle. All reaction efficiencies were more than 90%.

Mouse Model

Male Balb/c nu/nu mice aged 5 to 6 weeks were purchased at Shemyakin–Ovchinnikov Institute of Bioorganic Chemistry, Russian Academy of Sciences. All animal experiments were performed in accordance with European and Russian national guidelines for animal experimentation and were approved by the local animal and ethics review committee of the FSBSI "N.N. Blokhin NMRCO," reference number 2017-010. A375 cells were implanted subcutaneously into the right flank of the mice to ensure successful solid tumor initiation and tumor growth measurements. A tumor volume was estimated by the following formula: $V = (\text{length} \times [\text{width}]^2)/2$. Experiments started when the tumor size reached 150 ± 20 mm^3. Upconversion nanoparticles (100 μL, 2 mg/mL) were injected peritumorally. Tumor visualization and local overheating were demonstrated 2 h after administration. Near-infrared laser irradiation without UCNPs injection was used as a control.

DATA AVAILABILITY STATEMENT

The datasets generated for this study are available on request to the corresponding author.

ETHICS STATEMENT

The animal study was reviewed and approved by Ethics review committee of the FSBSI N.N. Blokhin NMRCO, reference number 2017-010.

AUTHOR CONTRIBUTIONS

IK: development of a theoretical model. RA: providing *in vitro* experiment. VR: imaging system construction. DK and NS: small animal experiments. AN: UCNPs synthesis. NM and AD: qPCR analysis. AI: Yb3+ absorption data analysis. AG: UCNPs surface modification. EK: manuscript preparation, author of idea.

FUNDING

This work was supported by the Ministry of Science and Higher Education within the State assignment of the Center of Crystallography and Photonics, RAS in part of UCNPs characterization. The study was also supported by the Russian Foundation for Basic research, project no. 17-03-01033 (in the part of UCNP modification) and project no. 18-29-01021 (in the part of PTT). Part of this work (qPCR analysis) was financially supported by the Russian Science Foundation, project no. 17-74-20064. Part of this work (UCNP synthesis) was financially supported by the Russian Science Foundation, project no. 18-79-10198. Part of this work (Yb3+ absorption data analysis) was supported by the Ministry of Science and Higher Education, project no. 075-15-2019-1927.

ACKNOWLEDGMENTS

The authors would like to acknowledge Prof. Vladislav Ya. Panchenko and Prof. Andrey V. Zvyagin for helpful discussion.

SUPPLEMENTARY MATERIAL

The Supplementary Material for this article can be found online at: https://www.frontiersin.org/articles/10.3389/fchem.2020.00295/full#supplementary-material

REFERENCES

Ahamed, M., Posgai, R., Gorey, T. J., Nielsen, M., Hussain, S. M., and Rowe, J. J. (2010). Silver nanoparticles induced heat shock protein 70, oxidative stress and apoptosis in *Drosophila melanogaster*. *Toxicol. Appl. Pharmacol.* 242, 263–269. doi: 10.1016/j.taap.2009.10.016

Auzel, F. (2004). Upconversion and anti-Stokes Processes with f and d Ions in Solids. *ChemInform* 35, 139–173. doi: 10.1002/chin.200416212

Brown, M. R., Roots, K. G., and Shand, W. A. (1969). Energy levels of Er3+in LiYF4. *J. Phys. C Solid State Phys.* 2, 593–602. doi: 10.1088/0022-3719/2/4/304

Caspers, H. H., and Rast, H. E. (1975). Electronic and vibronic spectra of Pr3+ in LiYF4. *J. Lumin.* 10, 347–369. doi: 10.1016/0022-2313(75)90001-0

Chan, M.-H., Chen, S.-P., Chen, C.-W., Chan, Y.-C., Lin, R. J., Tsai, D. P., et al. (2018). Single 808 nm laser treatment comprising photothermal and photodynamic therapies by using gold nanorods hybrid upconversion particles. *J. Phys. Chem. C* 122, 2402–2412. doi: 10.1021/acs.jpcc.7b10976

Chang, D., Lim, M., Goos, J. A. C. M., Qiao, R., Ng, Y. Y., Mansfeld, F. M., et al. (2018). Biologically targeted magnetic hyperthermia: Potential and limitations. *Front. Pharmacol.* 9:831. doi: 10.3389/fphar.2018.00831

Chen, G., Qiu, H., Prasad, P. N., and Chen, X. (2014). Upconversion nanoparticles: design, nanochemistry, and applications in theranostics. *Chem. Rev.* 114, 5161–5214. doi: 10.1021/cr400425h

Chen, G., Shen, J., Ohulchanskyy, T. Y., Patel, N. J., Kutikov, A., Li, Z., et al. (2012). (α-NaYbF4:Tm3+)/CaF2 Core/Shell nanoparticles with efficient near-infrared to near-infrared upconversion for high-contrast deep tissue bioimaging. *ACS Nano* 6, 8280–8287. doi: 10.1021/nn302972r

Cheng, L., Yang, K., Li, Y., Chen, J., Wang, C., Shao, M., et al. (2011). Facile preparation of multifunctional upconversion nanoprobes for multimodal imaging and dual-targeted photothermal therapy. *Angew. Chemie Int. Ed.* 50, 7385–7390. doi: 10.1002/anie.201101447

Cruz, M. M., Ferreira, L. P., Alves, A. F., Mendo, S. G., Ferreira, P., Godinho, M., et al. (2017). "Nanoparticles for magnetic hyperthermia," in *Nanostructures for*

Cancer Therapy, eds A. Ficai and A. M. Grumezescu (Amsterdam: Elsevier). doi: 10.1016/B978-0-323-46144-3.00019-2

Da Gama, A. A. S., De Sá, G. F., Porcher, P., and Caro, P. (1981). Energy levels of Nd 3+ in LiYF 4. *J. Chem. Phys.* 75, 2583–2587. doi: 10.1063/1.442410

Esterowitz, L., Bartoli, F. J., and Allen, R. E. (1979a). Spectroscopic determination of ground configuration energy levels in LiYF4 : Pr3+. *J. Lumin.* 21, 1–16. doi: 10.1016/0022-2313(79)90030-9

Esterowitz, L., Bartoli, F. J., Allen, R. E., Wortman, D. E., Morrison, C. A., and Leavitt, R. P. (1979b). Energy levels and line intensities of Pr3+ in LiYF4. *Phys. Rev. B.* 19:6442. doi: 10.1103/PhysRevB.19.6442

Generalova, A. N., Chichkov, B. N., and Khaydukov, E. V. (2017). Multicomponent nanocrystals with anti-Stokes luminescence as contrast agents for modern imaging techniques. *Adv. Colloid Interface Sci.* 245, 1–19. doi: 10.1016/j.cis.2017.05.006

Generalova, A. N., Rocheva, V. V., Nechaev, A. V., Khochenkov, D. A., Sholina, N. V., Semchishen, V. A., et al. (2016). PEG-modified upconversion nanoparticles for *in vivo* optical imaging of tumors. *RSC Adv.* 6, 30089–30097. doi: 10.1039/c5ra25304g

Gilchrist, R. L., Medal, R., Shorey, W. D., Hanselman, R. C., Parrott, J. C., and Taylor, C. B. (1957). Selective inductive heating of lymph nodes. *Ann. Surg.* 146:596. doi: 10.1097/00000658-195710000-00007

González-Béjar, M., Francés-Soriano, L., and Pérez-Prieto, J. (2016). Upconversion nanoparticles for bioimaging and regenerative medicine. *Front. Bioeng. Biotechnol.* 4:47. doi: 10.3389/fbioe.2016.00047

Grebenik, E. A., Nadort, A., Generalova, A. N., Nechaev, A. V., Sreenivasan, V. K. A., Khaydukov, E. V., et al. (2013). Feasibility study of the optical imaging of a breast cancer lesion labeled with upconversion nanoparticle biocomplexes. *J. Biomed. Opt.* 18:76004. doi: 10.1117/1.jbo.18.7.076004

Guller, A. E., Generalova, A. N., Petersen, E. V., Nechaev, A. V., Trusova, I. A., Landyshev, N. N., et al. (2015). Cytotoxicity and non-specific cellular uptake of bare and surface-modified upconversion nanoparticles in human skin cells. *Nano Res.* 8, 1546–1562. doi: 10.1007/s12274-014-0641-6

Guller, A. E., Nadort, A., Generalova, A. N., Khaydukov, E. V., Nechaev, A. V., Kornienko, I. A., et al. (2018). Rational surface design of upconversion nanoparticles with polyethylenimine coating for biomedical applications: better safe than brighter? *ACS Biomater. Sci. Eng.* 4, 3143–3153. doi: 10.1021/acsbiomaterials.8b00633

Gulzar, A., Xu, J., Yang, D., Xu, L., He, F., Gai, S., et al. (2018). Nano-graphene oxide-UCNP-Ce6 covalently constructed nanocomposites for NIR-mediated bioimaging and PTT/PDT combinatorial therapy. *Dalt. Trans.* 47, 3931–3939. doi: 10.1039/c7dt04141a

Han, Y., An, Y., Jia, G., Wang, X., He, C., Ding, Y., et al. (2018). Theranostic micelles based on upconversion nanoparticles for dual-modality imaging and photodynamic therapy in hepatocellular carcinoma. *Nanoscale* 10, 6511–6523. doi: 10.1039/c7nr09717d

Johannsen, M., Thiesen, B., Wust, P., and Jordan, A. (2010). Magnetic nanoparticle hyperthermia for prostate cancer. *Int. J. Hyperth.* 26, 790–795. doi: 10.3109/02656731003745740

Jordan, A., Wust, P., Fähling, H., John, W., Hinz, A., and Felix, R. (2009). Inductive heating of ferrimagnetic particles and magnetic fluids: physical evaluation of their potential for hyperthermia. *Int. J. Hyperth.* 9, 51–68. doi: 10.3109/02656730903287790

Kaminskii, A. A., Agamalyan, N. R., Deniseneo, G. A., Sarkisov, S. E., and Fedorov, P. P. (1982a). Spectroscopy and laser emission of disordered GdF3 CaF2: Nd3+ trigonal crystals. *Phys. status solidi.* 70, 397–406. doi: 10.1002/pssa.2210700206

Kaminskii, A. A., Ngoc, T., Sarkisov, S. E., Matrosov, V. N., and Timoshechkin, M. I. (1980). Growth, spectral and laser properties of La_2 Be_2 O_5:Nd^{3+} crystals in the $^4F_{3/2} \rightarrow {}^4I_{11/2}$ and $^4F_{3/2} \rightarrow {}^4I_{13/2}$ transitions. *Phys. status solidi.* 59, 121–132. doi: 10.1002/pssa.2210590117

Kaminskii, A. A., Sarkisov, S. E., Kürsten, H. D., and Schultze, D. (1982b). Crystal Growth and Spectroscopic Properties of Nd3+ Ions in Ferroelectric Pb5Ge3O11 Crystals. *Phys. status solidi.* 72, 207–213. doi: 10.1002/pssa.2210720121

Kennedy, D., Jäger, R., Mosser, D. D., and Samali, A. (2014). Regulation of apoptosis by heat shock proteins. *IUBMB Life* 66, 327–338. doi: 10.1002/iub.1274

Khaydukov, E. V., Mironova, K. E., Semchishen, V. A., Generalova, A. N., Nechaev, A. V., Khochenkov, D. A., et al. (2016). Riboflavin photoactivation by upconversion nanoparticles for cancer treatment. *Sci. Rep.* 6:35103. doi: 10.1038/srep35103

Khaydukov, E. V., Semchishen, V. A., Seminogov, V. N., Sokolov, V. I., Popov, A. P., Bykov, A. V., et al. (2014). Enhanced spatial resolution in optical imaging of biotissues labelled with upconversion nanoparticles using a fibre-optic probe scanning technique. *Laser Phys. Lett.* 11:95602. doi: 10.1088/1612-2011/11/9/095602

Kobayashi, H., Kosaka, N., Ogawa, M., Morgan, N. Y., Smith, P. D., Murray, C. B., et al. (2009). *In vivo* multiple color lymphatic imaging using upconverting nanocrystals. *J. Mater. Chem.* 19:6481. doi: 10.1039/b910512c

Lanneau, D., Brunet, M., Frisan, E., Solary, E., Fontenay, M., and Garrido, C. (2008). Heat shock proteins: essential proteins for apoptosis regulation: apoptosis review series. *J. Cell. Mol. Med.* 12, 743–761. doi: 10.1111/j.1582-4934.2008.00273.x

Li, Y., Li, Y., Wang, R., Xu, Y., and Zheng, W. (2017). Enhancing upconversion luminescence by annealing processes and the high-temperature sensing of ZnO:Yb/Tm nanoparticles. *New J. Chem.* 41, 7116–7122. doi: 10.1039/c7nj01358b

Li, Z., Zhang, Y., La, H., Zhu, R., El-Banna, G., Wei, Y., et al. (2015). Upconverting NIR Photons for Bioimaging. *Nanomaterials* 5, 2148–2168. doi: 10.3390/nano5042148

Liu, F., He, X., Liu, L., You, H., Zhang, H., and Wang, Z. (2013). Conjugation of NaGdF4 upconverting nanoparticles on silica nanospheres as contrast agents for multi-modality imaging. *Biomaterials* 34, 5218–5225. doi: 10.1016/j.biomaterials.2013.03.058

Liu, L. J., Brown, S. L., Ewing, J. R., Ala, B. D., Schneider, K. M., and Schlesinger, M. (2016). Estimation of Tumor Interstitial Fluid Pressure (TIFP) Noninvasively. *PLoS ONE* 11:e0140892. doi: 10.1371/journal.pone.0140892

Liu, L. J., Brown, S. L., Ewing, J. R., and Schlesinger, M. (2011). Phenomenological model of interstitial fluid pressure in a solid tumor. *Phys. Rev. E* 84:021919. doi: 10.1103/physreve.84.021919

Liu, Q., Zhang, Y., Peng, C. S., Yang, T., Joubert, L.-M., and Chu, S. (2018). Single upconversion nanoparticle imaging at sub-10 W cm−2 irradiance. *Nat. Photonics* 12, 548–553. doi: 10.1038/s41566-018-0217-1

Liu, Y., Meng, X., and Bu, W. (2019). Upconversion-based photodynamic cancer therapy. *Coord. Chem. Rev.* 379, 82–98. doi: 10.1016/j.ccr.2017.09.006

Maier-Hauff, K., Ulrich, F., Nestler, D., Niehoff, H., Wust, P., Thiesen, B., et al. (2011). Efficacy and safety of intratumoral thermotherapy using magnetic iron-oxide nanoparticles combined with external beam radiotherapy on patients with recurrent glioblastoma multiforme. *J. Neurooncol.* 103, 317–324. doi: 10.1007/s11060-010-0389-0

Mantso, T., Vasileiadis, S., Anestopoulos, I., Voulgaridou, G. P., Lampri, E., Botaitis, S., et al. (2018). Hyperthermia induces therapeutic effectiveness and potentiates adjuvant therapy with non-targeted and targeted drugs in an *in vitro* model of human malignant melanoma. *Sci. Rep.* 8:10724. doi: 10.1038/s41598-018-29018-0

Melamed, J. R., Edelstein, R. S., and Day, E. S. (2015). Elucidating the fundamental mechanisms of cell death triggered by photothermal therapy. *ACS Nano* 9, 6–11. doi: 10.1021/acsnano.5b00021

Melnikova, N. V., Dmitriev, A. A., Belenikin, M. S., Koroban, N. V., Speranskaya, A. S., Krinitsina, A. A., et al. (2016). Identification, expression analysis, and target prediction of flax genotroph microRNAs under normal and nutrient stress conditions. *Front. Plant Sci.* 7:399. doi: 10.3389/fpls.2016.00399

Ogden, J., Tate, J., Strawbridge, R., Ivkov, R., and Hoopes, P. (2009). Comparison of iron oxide nanoparticle and waterbath hyperthermia cytotoxicity. *Proc. SPIE–the Int. Soc. Opt. Eng.* 7181:71810K. doi: 10.1117/12.809818

Paschotta, R., Nilsson, J., Tropper, A. C., and Hanna, D. (1997). Ytterbium-doped fiber amplifier. *Quantum Electronics, IEEE J.* 33, 1049–1056. doi: 10.1109/3.594865

Pilch, A., Würth, C., Kaiser, M., Wawrzynczyk, D., Kurnatowska, M., Arabasz, S., et al. (2017). Bioimaging: shaping luminescent properties of Yb3+ and Ho3+ co-doped upconverting core-shell β-NaYF4 nanoparticles by dopant distribution and spacing (Small 47/2017). *Small* 13:1770246. doi: 10.1002/smll.201770246

Qiu, H., Tan, M., Ohulchanskyy, T., Lovell, J., and Chen, G. (2018). Recent progress in upconversion photodynamic therapy. *Nanomaterials* 8:344. doi: 10.3390/nano8050344

Sedlmeier, A., Achatz, D. E., Fischer, L. H., Gorris, H. H., and Wolfbeis, O. S. (2012). Photon upconverting nanoparticles for luminescent sensing of temperature. *Nanoscale* 4:7090. doi: 10.1039/c2nr32314a

Vecchio, G., Galeone, A., Brunetti, V., Maiorano, G., Sabella, S., Cingolani, R., et al. (2012). Concentration-dependent, size-independent toxicity of citrate capped AuNPs in *Drosophila melanogaster*. *PLoS ONE*. 7:e29980. doi: 10.1371/journal.pone.0029980

Vedunova, M. V., Mishchenko, T. A., Mitroshina, E. V., Ponomareva, N. V., Yudintsev, A. V., Generalova, A. N., et al. (2016). Cytotoxic effects of upconversion nanoparticles in primary hippocampal cultures. *RSC Adv.* 6, 33656–33665. doi: 10.1039/c6ra01272h

Wu, J., Liu, T., Rios, Z., Mei, Q., Lin, X., and Cao, S. (2017). Heat Shock Proteins and Cancer. *Trends Pharmacol. Sci.* 38, 226–256. doi: 10.1016/j.tips.2016.11.009

Wu, S., Han, G., Milliron, D. J., Aloni, S., Altoe, V., Talapin, D. V., et al. (2009). Non-blinking and photostable upconverted luminescence from single lanthanide-doped nanocrystals. *Proc. Natl. Acad. Sci. U.S.A.* 106, 10917–10921. doi: 10.1073/pnas.0904792106

Wu, X., Chen, G., Shen, J., Li, Z., Zhang, Y., and Han, G. (2014). Upconversion nanoparticles: a versatile solution to multiscale biological imaging. *Bioconjug. Chem.* 26, 166–175. doi: 10.1021/bc5003967

Xu, C. T., Zhan, Q., Liu, H., Somesfalean, G., Qian, J., He, S., et al. (2013). Upconverting nanoparticles for pre-clinical diffuse optical imaging, microscopy and sensing: current trends and future challenges. *Laser Photon. Rev.* 7, 663–697. doi: 10.1002/lpor.201200052

Xu, J., Xu, L., Wang, C., Yang, R., Zhuang, Q., Han, X., et al. (2017). Near-infrared-triggered photodynamic therapy with multitasking upconversion nanoparticles in combination with checkpoint blockade for immunotherapy of colorectal cancer. *ACS Nano* 11, 4463–4474. doi: 10.1021/acsnano.7b00715

Zhan, Q., He, S., Qian, J., Cheng, H., and Cai, F. (2013). Optimization of optical excitation of upconversion nanoparticles for rapid microscopy and deeper tissue imaging with higher quantum yield. *Theranostics* 3, 306–316. doi: 10.7150/thno.6007

Zhan, Q., Qian, J., Liang, H., Somesfalean, G., Wang, D., He, S., et al. (2011). Using 915 nm laser excited Tm3+/Er3+/Ho3+-Doped NaYbF4 upconversion nanoparticles for *in vitro* and deeper *in vivo* bioimaging without overheating irradiation. *ACS Nano* 5, 3744–3757. doi: 10.1021/nn200110j

Zhu, X., Feng, W., Chang, J., Tan, Y.-W., Li, J., Chen, M., et al. (2016). Temperature-feedback upconversion nanocomposite for accurate photothermal therapy at facile temperature. *Nat. Commun.* 7:10437. doi: 10.1038/ncomms10437

Conflict of Interest: The authors declare that the research was conducted in the absence of any commercial or financial relationships that could be construed as a potential conflict of interest.

frontiers in Chemistry

ORIGINAL RESEARCH
published: 26 May 2020
doi: 10.3389/fchem.2020.00399

Trap-Filling of ZnO Buffer Layer for Improved Efficiencies of Organic Solar Cells

Mingguang Li[1], Jing Li[1], Longsheng Yu[1], Ying Zhang[1], Yizhong Dai[1], Runfeng Chen[1] and Wei Huang[1,2]*

[1] *Key Laboratory for Organic Electronics and Information Displays & Jiangsu Key Laboratory for Biosensors, Institute of Advanced Materials (IAM), Jiangsu National Synergetic Innovation Center for Advanced Materials (SICAM), Nanjing University of Posts & Telecommunications, Nanjing, China,* [2] *Institute of Flexible Electronics, Northwestern Polytechnical University, Xi'an, China*

Trap-assisted recombination loss in the cathode buffer layers (CBLs) is detrimental to the electron extraction process and severely restricts the power conversion efficiencies (PCEs) of organic solar cells (OSCs). Herein, a novel organic–inorganic hybrid film composed of zinc oxide (ZnO) and 2,3,5,6-tetrafluoro-7,7,8,8-tetracyanoquinodimethane (F4TCNQ) is designed to fill the intrinsic charge traps of ZnO-based CBLs by doping F4TCNQ for high-performance inverted OSCs. Thus, constructed ZnO:F4TCNQ hybrid film exhibits enhanced surface hydrophobicity and adjustable energy levels, providing favorable interfacial condition for electron extraction process. Consequently, trap-assisted recombination loss in the CBLs was efficiently suppressed, leading to the significantly improved fill factor and PCEs of both fullerene- and non-fullerene-based OSCs using the ZnO:F4TCNQ hybrid CBLs. This work illustrates a convenient organic acceptor doping approach to suppress the internal charge traps of traditional inorganic CBLs, which will shed new light on the fabrication of high-performance CBLs with facile electron extraction processes in inverted OSC devices.

Keywords: ZnO, cathode buffer layers, organic solar cells, trap-filling, organic–inorganic hybrid film

OPEN ACCESS

Edited by:
Ye Zhou,
Shenzhen University, China

Reviewed by:
Tao Liu,
Hong Kong University of Science and Technology, Hong Kong
Zong-Xiang Xu,
Southern University of Science and Technology, China

****Correspondence:***
Runfeng Chen
iamrfchen@njupt.edu.cn

Specialty section:
This article was submitted to Physical Chemistry and Chemical Physics, a section of the journal Frontiers in Chemistry

Received: *09 January 2020*
Accepted: *15 April 2020*
Published: *26 May 2020*

Citation:
Li M, Li J, Yu L, Zhang Y, Dai Y, Chen R and Huang W (2020) Trap-Filling of ZnO Buffer Layer for Improved Efficiencies of Organic Solar Cells. Front. Chem. 8:399. doi: 10.3389/fchem.2020.00399

INTRODUCTION

Bulk heterojunction (BHJ) organic solar cells (OSCs) have attracted extensive attention due to their intrinsic merits of light weight, high mechanical flexibility, and easy processing (Li et al., 2012; Yan et al., 2018). In the construction of high-performance OSC devices, both the regulation of photoactive layers and interface engineering of the integrated functional layers plays important roles in achieving high power conversion efficiencies (PCEs) (Liu et al., 2016, 2018; Liu T. et al., 2017). As for a specified photoactive layer, interfacial modification by using an efficient cathode buffer layer (CBL) has been widely applied to further optimize the device structure and improve the device efficiency (Yin et al., 2016).

Among various interfacial materials, the zinc oxide (ZnO) film inserted between organic photoactive layer and inorganic electrode is one of the most widely used CBLs in the inverted OSCs, exhibiting many inherent advantages, including high electron mobility, high optical transparency, tuneable electronic properties, ease of preparation, and low toxicity (Hewlett and McLachlan, 2016). Moreover, a simple and extensively investigated sol-gel method can be applied to fabricate

ZnO-based CBLs at a relatively mild condition (Kamalasanan and Chandra, 1996). However, the low-temperature solution-processed ZnO films generally have high density of surface and bulk defects, which would introduce undesired intra-gap energy levels and thus suppress carrier transport processes in the CBLs. These intrinsic defects in ZnO lattice mainly comprise oxygen vacancies (V_O), oxygen interstitials (O_i), zinc vacancies (V_{Zn}), zinc interstitials (Zn_i), etc. (Spencer et al., 2012). Plenty of defects acting as charge recombination centers will reduce the charge collection efficiency, which is an obstacle to the application of ZnO material in the field of optoelectronic devices (Sun et al., 2011; Lee et al., 2019).

In view of the above adverse issues, there have been a general consensus to optimize charge transporting properties of ZnO-based CBLs by passivating the defect sites (Hu et al., 2015; Cai et al., 2017; Li et al., 2017; Wang et al., 2019). For example, a high-performance fullerene-free OSC with efficiency over 12% was reported by employing ethylene diamine tetraacetic acid (EDTA)/ZnO hybrid interlayer. The introduced EDTA efficiently passivizes defects in ZnO film due to its chelation function, leading to balanced hole and electron mobility (Li et al., 2017). Besides, amphiphilic fullerenes/ZnO hybrids were also used as novel CBLs to passivate the defects of ZnO and the corresponding efficiency of the OSC based on thieno[3,4-b]-thiophene/benzodithiophene (PTB7):$PC_{71}BM$ was up to 8.0% (Hu et al., 2015). Hybrid CBL consisting of ZnO and poly(2-ethyl-2-oxazoline) (PEOz) was also constructed and applied to the inverted non-fullerene OSCs. Due to the reduced oxygen deficiency of ZnO by the introduced PEOz, an improved PCE over 12% was achieved (Seo et al., 2018). Additionally, various other organic materials such as polyethylenimine (PEI) (Liu C. et al., 2017), fullerene derivatives (Liao et al., 2014; Hu et al., 2016), and non-fullerene acceptors (Xie and Wuerthner, 2017; Li et al., 2019) have also been utilized to construct high-performance organic–inorganic hybrid materials by passivating the inherent defects of metal oxide layers and remarkable efficiency improvements were all observed.

The reported organic defect-passivating agents can generally coordinate with ZnO due to the existence of various polar groups, such as hydroxyl groups, amino groups, carbonyl groups, and carboxylic groups. Here, we found that 2,3,5,6-tetrafluoro-7,7,8,8-tetracyanoquinodimethane (F4TCNQ) with four cyano (C=N) groups can also regulate the intrinsic property of ZnO CBLs with the assistance of coordination effects of C=N groups. In order to passivate the inherent defects originated from ZnO-based CBLs, we propose an organic–inorganic hybrid CBL composed of inorganic ZnO and organic dopant F4TCNQ and explore how the F4TCNQ doping in the CBLs affects device operation. The introduction of ZnO:F4TCNQ hybrid CBLs is able to improve the PCEs of both fullerene and non-fullerene OSCs by the remarkable increase of fill factor (FF) value. The use of F4TCNQ dopant can modify surface properties and regulate energy-level structure of ZnO-based CBLs simultaneously. Benefiting from the coordination effect of C=N groups, trap density in the ZnO film is reduced significantly, which suppresses non-geminate charge recombination in the ZnO:F4TCNQ-based OSCs. These results indicate that the construction of novel ZnO:F4TCNQ hybrid film is a promising approach in the interfacial modification of ZnO-based CBLs for the performance optimization of OSC devices.

RESULTS AND DISCUSSION

Photovoltaic Performance

To passivate the ZnO defects such as oxygen vacancies and zinc dangling bonds and modify interfacial contact between metal electrode and organic photoactive layer, a novel organic–inorganic hybrid material based on ZnO and F4TCNQ was used as CBLs in both fullerene- and non-fullerene-based OSCs. **Figure 1A** provides the molecular structure of photoactive materials: donor poly[4,8-bis(5-(2-ethylhexyl)thiophen-2-yl)benzo[1,2-b:4,5-b′]dithiophene-co-fluorothieno[3,4-b]thiophene-2-carboxylate] (PTB7-Th), fullerene-based acceptor $PC_{71}BM$, and non-fullerene-based acceptor 3,9-bis(2-methylene-(3-(1,1-dicyanomethylene)-indanone))-5,5,11,11-tetrakis(4-hexylphenyl)-dithieno[2,3-d:2′,3′-d′]-s-indaceno[1,2-b:5,6-b′]dithiophene) (ITIC). The molecular structure of organic dopant F4TCNQ is also supplied in **Figure 1A**. Meanwhile, **Figure 1B** shows the schematic device structure and the corresponding energy levels. Considering that sol-gel-derived ZnO generally has high density of defects, the organic dopant F4TCNQ was employed into the precursor solution to passivate the defects in both surface and bulk. Similar to the previous approach used to fabricate pure ZnO film, ZnO:F4TCNQ hybrid films with different doping concentrations were deposited by an identical sol-gel strategy (Sun et al., 2011; Li et al., 2019).

As shown in **Figure 2A**, *J–V* characteristics of the inversed OSCs based on the PTB7-Th:$PC_{71}BM$ system using ZnO:F4TCNQ hybrid CBLs are investigated under AM 1.5G irradiation. The corresponding photovoltaic parameters including open-circuit voltage (V_{OC}), short-circuit current density (J_{SC}), FF, PCE, series resistance (R_S), and shunt resistance (R_{sh}) are summarized in **Table 1**. The inverted OSC device with the structure of indium tin oxide (ITO)/CBL/PTB7-Th:$PC_{71}BM$/MoO_3/Al is shown in **Figure 2B**. For the devices fabricated with ZnO:F4TCNQ hybrid CBLs, the PCE value enhances from 7.17% for pristine device to 7.55% for ZnO:0.5 wt% F4TCNQ device, 8.14% for ZnO:1.0 wt% F4TCNQ device, and 7.56% for ZnO:5.0 wt% F4TCNQ device, respectively. When organic dopant F4TCNQ with the optimal concentration of 1.0 wt% is introduced into ZnO film, the J_{SC} value increases slightly from 14.24 to 15.00 mA/cm^2 while the FF improved from 62.2% to 67.1% significantly. The slightly enhanced external quantum efficiency (EQE) almost in the entire absorption range shown in **Figure 2B** is consistent with the minor variations of J_{SC} value as well as the slight reduction of R_S. Furthermore, the ZnO:F4TCNQ hybrid thin film used as a novel CBL was also applied to PTB7-Th:ITIC-based non-fullerene OSCs. Since the LUMO levels of $PC_{71}BM$ and ITIC are quite close, the V_{OC} values are the same for both fullerene- and non-fullerene-based OSCs. The non-fullerene-based device exhibits improved PCE values from 6.13 to 6.96%, which also mainly contributed to the enhancement of FF values (**Table 1** and

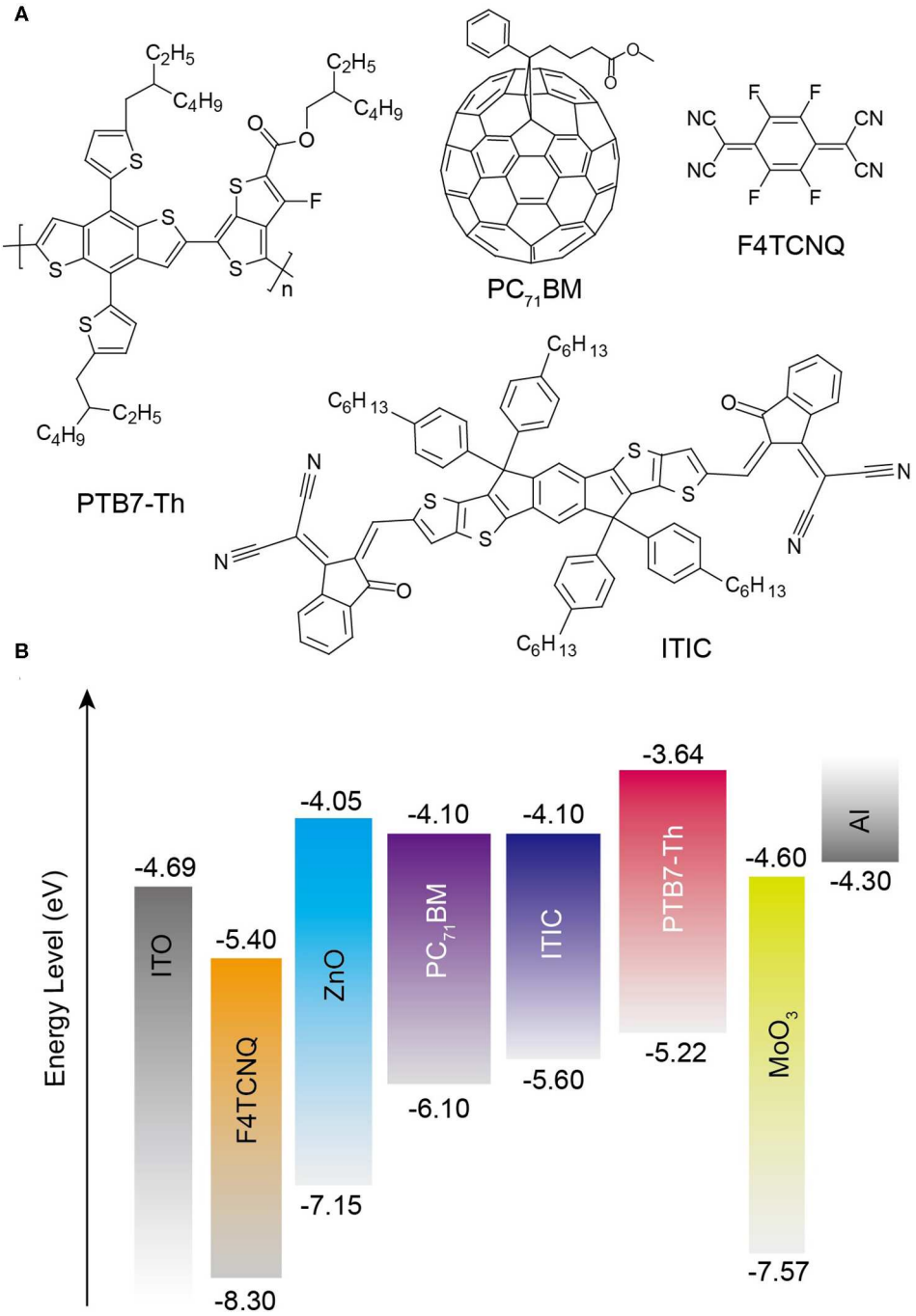

FIGURE 1 | (A) Molecular structures of PTB7-Th, ITIC, $PC_{71}BM$, and F4TCNQ. **(B)** A schematic device structure of the inverted OSCs and the corresponding molecular energy levels.

Supplementary Figure 1). Therefore, the construction of ZnO:F4TCNQ hybrid CBLs could efficiently improve the final device performance of both fullerene and non-fullerene OSCs by enhancing the FF values.

The *J*–*V* characteristics of inverted OSCs fabricated with ZnO:F4TCNQ hybrid CBLs in the dark condition were measured to investigate the inherent electrical properties, as shown in **Figure 2C**. Compared to the pristine ZnO-based device, the introduction of 1.0 wt% F4TCNQ leads to a significant reduction of leakage current, which demonstrates the efficient hole blocking capability of the ZnO:F4TCNQ hybrid film. On the contrary, the leakage current becomes strengthened with the

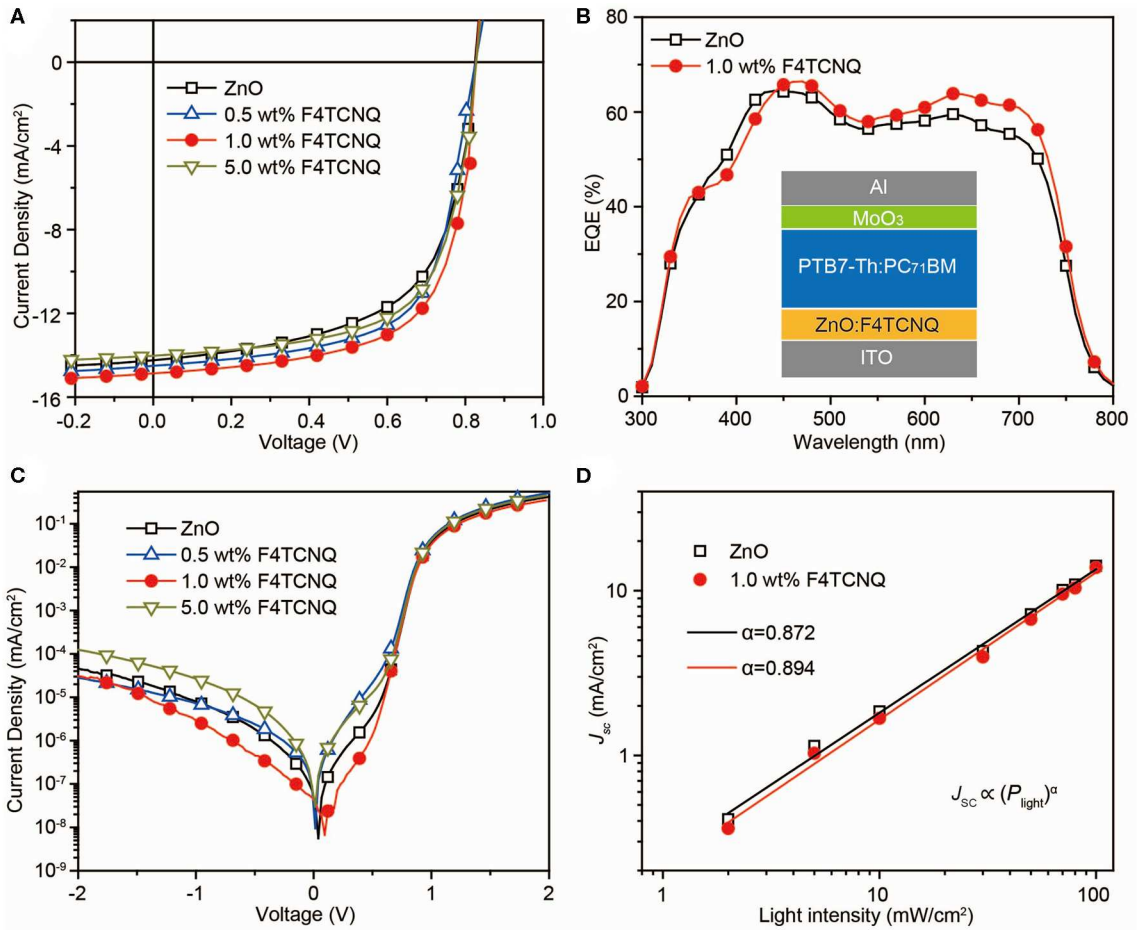

FIGURE 2 | (A) *J–V* characteristics and **(B)** EQE spectra of the inverted PTB7-Th:$PC_{71}BM$-based OSCs with various CBLs under illumination of AM 1.5G at 100 mW/cm^2. Inset: Device configuration of the OSCs. **(C)** Semi-logarithmic plots of *J–V* characteristics of the OSCs with various CBLs in dark. **(D)** Measured J_{SC} of different CBLs dependence on light intensity.

further increase of F4TCNQ content (5 wt%). To investigate the charge recombination dynamics in the PTB7-Th:$PC_{71}BM$ system, the dependence of J_{SC} on light intensity (P_{light}) was also conducted under the optimal F4TCNQ dopant content (**Figure 2D**). Generally, the dependence of J_{SC} on P_{light} can be expressed as $J_{SC} \propto (P_{light})^{\alpha}$ (Zhao et al., 2017). **Figure 2D** shows that the fitted slope ($\alpha = 0.897$) of the ZnO:F4TCNQ-based device is much closer to 1, thus demonstrating the beneficial effect of the introduced F4TCNQ dopant on the reduction of bimolecular recombination process. In addition, the significantly enhanced R_{sh} from 508.2 to 913.8 $\Omega \cdot cm^2$ for the ZnO:F4TCNQ-based device also indicates a weakened carrier recombination at the ZnO/photoactive layer interfaces (Yin et al., 2013). Therefore, the significantly enlarged R_{sh} and the restrained leakage current suggest that the introduced F4TCNQ component plays a significant role in optimizing the interfacial contact between different functional layers, thus facilitating the remarkable enhancement of FF value. When F4TCNQ was doped into ZnO film, a similar R_{sh} enhanced rule is observed for non-fullerene OSCs. Consequently, organic dopant F4TCNQ in both fullerene and non-fullerene systems is capable of suppressing charge recombination events, thus significantly enhancing the FF and PCE values of OSCs.

Properties of ZnO:F4TCNQ Hybrid Thin Films

X-ray photoelectron spectroscopy (XPS) measurements were conducted to explore the effect of F4TCNQ dopant on the formation of ZnO-based CBLs (**Supplementary Figure 2**). The high-resolution XPS spectra of Zn $2p_{1/2}$, Zn $2p_{3/2}$, O 1s, and N 1s are shown in **Figures 3A–C**. When 1.0 wt% F4TCNQ was doped, the peaks of Zn $2p_{1/2}$ (~1043.0 eV) and Zn $2p_{3/2}$ (~1019.9 eV) shift toward lower binding energy by ~0.2 and ~0.1 eV, respectively. Meanwhile, the main peak of O 1s (~528.8 eV) corresponding to O atoms in ZnO matrix also shifts toward lower binding energy by ~0.1 eV. The peak shifts shown in **Figures 3A,B** indicate that more Zn atoms are bound to O atoms and the oxygen-deficient defects originated from hydroxyl groups or carboxylate groups are passivated in the ZnO:F4TCNQ hybrid film (Sun et al., 2011; Li et al., 2017). In

TABLE 1 | Performance of inverted fullerene- and non-fullerene-based OSCs with different CBLs.

System	CBL	V_{oc} (V)	J_{sc} (mA/cm^2)	FF (%)	PCE (%)	R_s[a] ($\Omega \cdot$cm^2)	R_{sh}[b] ($\Omega \cdot$cm^2)
PTB7-Th:$PC_{71}BM$	ZnO	0.81	14.24	62.2	7.17	8.64	508.2
	0.5 wt% F4TCNQ	0.81	14.50	66.0	7.75	5.26	662.1
	1.0 wt% F4TCNQ	0.81	15.00	67.1	8.14	4.41	913.8
	5.0 wt% F4TCNQ	0.81	14.03	66.6	7.56	6.62	839.8
PTB7-Th:ITIC	ZnO	0.81	14.35	52.8	6.13	11.5	415.4
	0.5 wt% F4TCNQ	0.81	14.48	57.1	6.69	12.3	475.7
	1.0 wt% F4TCNQ	0.81	14.75	58.3	6.96	9.44	549.5
	5.0 wt% F4TCNQ	0.81	14.87	57.4	6.91	9.71	484.5

[a]*Series resistance (R_s) and* [b]*Shunt resistance (R_{sh}).*

addition, compared to the pure ZnO film, the appearance of N 1s peak for ZnO:F4TCNQ hybrid film further demonstrates that the organic dopant F4TCNQ has been incorporated into ZnO film.

Cyclic voltammetry (CV) measurements combined with UV-vis absorption spectra were performed to investigate the impact of introduced F4TCNQ on the energy levels of ZnO-based CBLs. As shown in **Figure 3D**, the employed F4TCNQ dopant exhibits a marginal impact on the optical properties of ZnO film and thus it can be approximately considered that the band gap of ZnO-based CBLs remains unchanged when a small amount of F4TCNQ molecules are added into ZnO precursor solution. Meanwhile, the highest occupied molecular orbital (HOMO) levels of ZnO and ZnO:F4TCNQ hybrid films were characterized by CV measurement (**Figure 3E**). The HOMO level of pure ZnO calculated from the onset potential of oxidation process is found to be −7.15 eV. While, the onset potential of ZnO:1.0 wt% F4TCNQ oxidation process shifts toward larger potential position and the corresponding HOMO level is calculated to be −7.29 eV. When the content of F4TCNQ is further raised to 5.0 wt%, the HOMO level of ZnO:F4TCNQ hybrid CBL reduces to −7.56 eV. According to the UV-vis absorption spectra and CV measurements of ZnO-based CBLs, the corresponding lowest unoccupied molecular orbital (LUMO) level can be obtained, as shown in the inset of **Figure 3E**. The optimized energy level structure by employing F4TCNQ dopant can lower the charge barrier of electron collection and thus be expected to facilitate the acquirement of high-performance OSCs.

In addition, we also performed atomic force microscopy (AFM) and contact angle (θ) measurement to reveal the influence of F4TCNQ dopant on the surface properties of ZnO-based CBLs, as shown in the inset of **Figure 3D**. Compared to the pure ZnO film with the roughness of 0.809 nm, the ZnO:1.0 wt% F4TCNQ hybrid film exhibits similar film roughness (0.961 nm). When the content of F4TCNQ reaches 5.0 wt%, the roughness is further increased to more than 1 nm and the remarkable aggregates can be observed at the film surface (**Supplementary Figure 3**). Therefore, the content of F4TCNQ dopant should be adjusted cautiously to fabricate the ZnO-based hybrid CBLs with excellent interfacial properties. Besides, the contact angle (θ) measurement provides the hydrophobic property of ZnO-based CBLs (the inset of **Figure 3D**). Due to the excellent hydrophobicity of F4TCNQ itself, the constructed ZnO:F4TCNQ hybrid CBL exhibits an enhanced hydrophobic property with the θ of 45.7°, which can perform a beneficial role in optimizing interfacial contact between CBL and organic photoactive layer (Hau et al., 2008; Liao et al., 2013). Furthermore, the conductivity measurements of the ZnO and ZnO:F4TCNQ films were also conducted (**Supplementary Table 1**). It was found that the ZnO:F4TCNQ film slightly decreases from 2.06×10^{-3} to 1.56×10^{-3} S/cm, indicating that the electron transfer from ZnO to the organic electron-acceptor molecule is not very efficient (Hewlett and McLachlan, 2016). This variation further demonstrates that the primary function of F4TCNQ is to optimize the interfacial contact rather than the inherent carrier transport properties of ZnO.

Trap-Filling Mechanism

Fourier transform infrared (FTIR) spectra are conducted to investigate the intermolecular interaction between F4TCNQ and ZnO (**Figure 4A**). In the pure F4TCNQ film, the stretching vibrations related to the four C=N groups appear at 2,224 and 2,178 cm^{-1}, respectively (Kato et al., 1991), while there is no characteristic peak that appeared at around 2,200 cm^{-1} for pure ZnO film. As soon as 1 wt% F4TCNQ was doped into ZnO, the two characteristic peaks of C=N stretching vibration shift to 2,204 and 2,158 cm^{-1}, respectively. Considering that the peak signal of C=N stretching vibration is relatively weak in the ZnO:1.0 wt% F4TCNQ film, the sample of ZnO:10.0 wt% F4TCNQ film was also detected and the same changes have been observed. The red shift of C=N stretching vibration peaks indicates that the C=N groups in F4TCNQ molecules coordinate with ZnO (Zhou et al., 2016). Benefiting from the coordination effects between F4TCNQ and ZnO, the passivation of various defects that existed in the ZnO matrix can be anticipated.

According to the previous reports, the photoluminescence (PL) properties of ZnO are very sensitive to the defects inside (Chen et al., 2012; Mishra et al., 2019). As shown in **Figure 4B**, the narrow emission peak at 363 nm is attributed to the band-to-band emission of ZnO, while the broad emission one at around 600 nm stems from the defect states in ZnO matrix (Mishra et al., 2019). The broad emissions correspond to various defects,

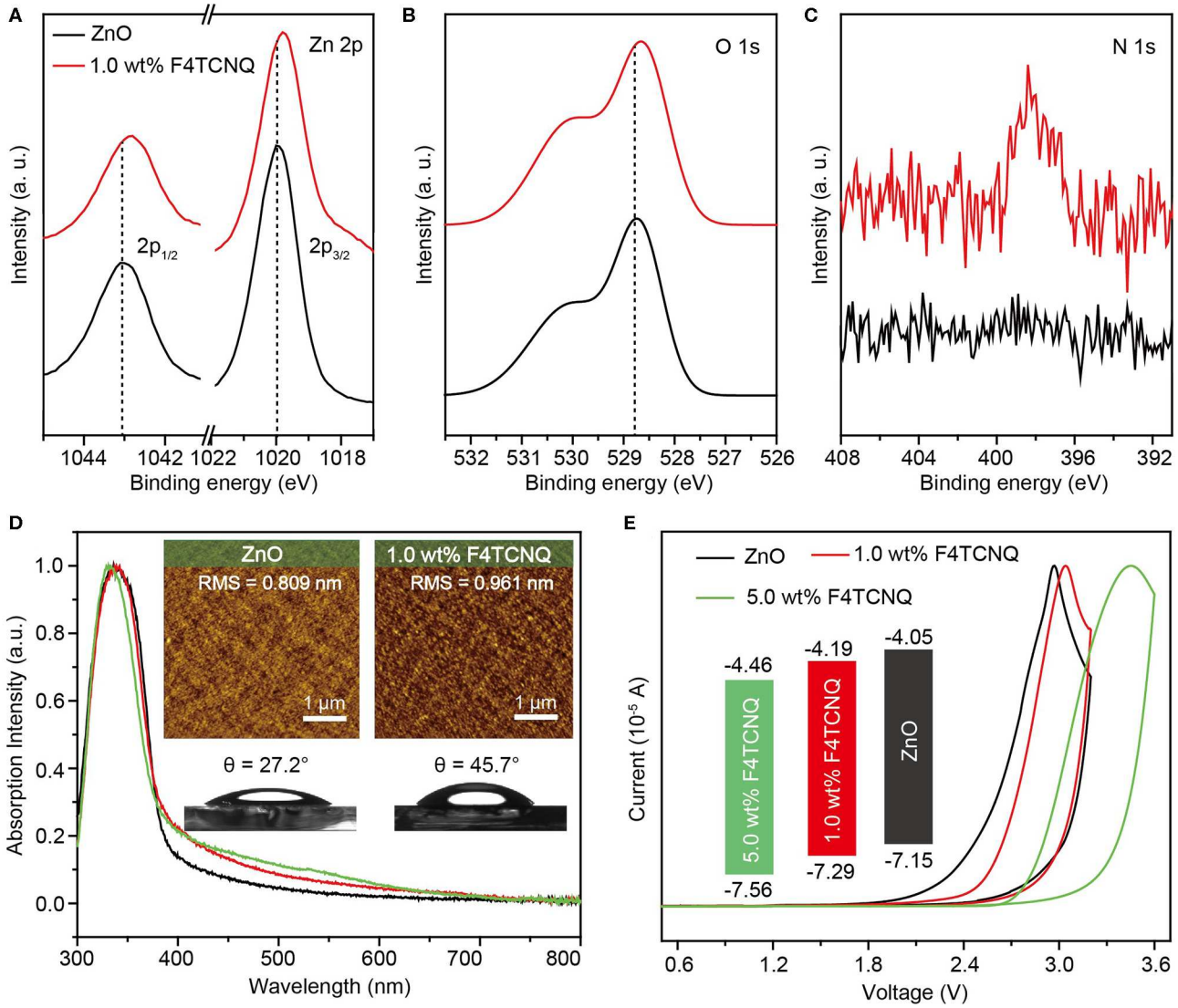

FIGURE 3 | (A) Zn 2p, **(B)** O 1s, and **(C)** N 1s high-resolution XPS spectra, **(D)** UV-vis absorption spectra, AFM height images (5 × 5 μm) and the contact angle images (inset), **(E)** CV measurements and energy level diagram (inset) of various ZnO-based CBLs.

e.g., Zn_i (violet), V_{Zn} (blue), V_O (green), and O_i (yellow, red), and the qualitative energy levels of these defect states in sol-gel ZnO are shown in **Figure 4C**. It should be noticed that the peak intensity of defect emission is remarkably stronger than that of ZnO emission for the pristine ZnO film, which demonstrates the existence of a large amount of defect states in the sol-gel-derived ZnO film. Upon introducing a few amount of F4TCNQ (0.5 wt% and 1.0 wt%), the broadband defect emission peak is effectively weakened, indicating a significant reduction of defect states. On the contrary, when the content of F4TCNQ is further increased to 5 wt%, the condition of defect states deteriorates and the emission peak corresponding to the defect states becomes even stronger. We speculate that excessive doping of F4TCNQ induces the formation of new defects in the ZnO-based CBLs. To exclude the impact of emission interference from F4TCNQ itself, the PL spectrum of the pure F4TCNQ film was also measured and the corresponding fluorescence signal in the range of visible region was found to be very weak (**Supplementary Figure 4**). The results indicate that an appropriate amount of F4TCNQ dopant can conduce to the construction of an excellent ZnO thin film with less defect states. In addition, the time-resolved PL spectra of pure $PC_{71}BM$ layers were also measured and the exciton lifetime of $PC_{71}BM$ on the ITO/ZnO:F4TCNQ substrate was found to be slightly longer than that on the ITO/ZnO substrate. This confirms that the photo-generated excitons prefer to transfer to the ZnO:F4TCNQ layer, leading to reduced charge recombination (**Supplementary Figure 5**).

Trap-assisted recombination that happened in the ZnO film can be regarded as a two-step process (**Supplementary Figure 6**); i.e., a hole is first trapped within the band gap; then, an oppositely

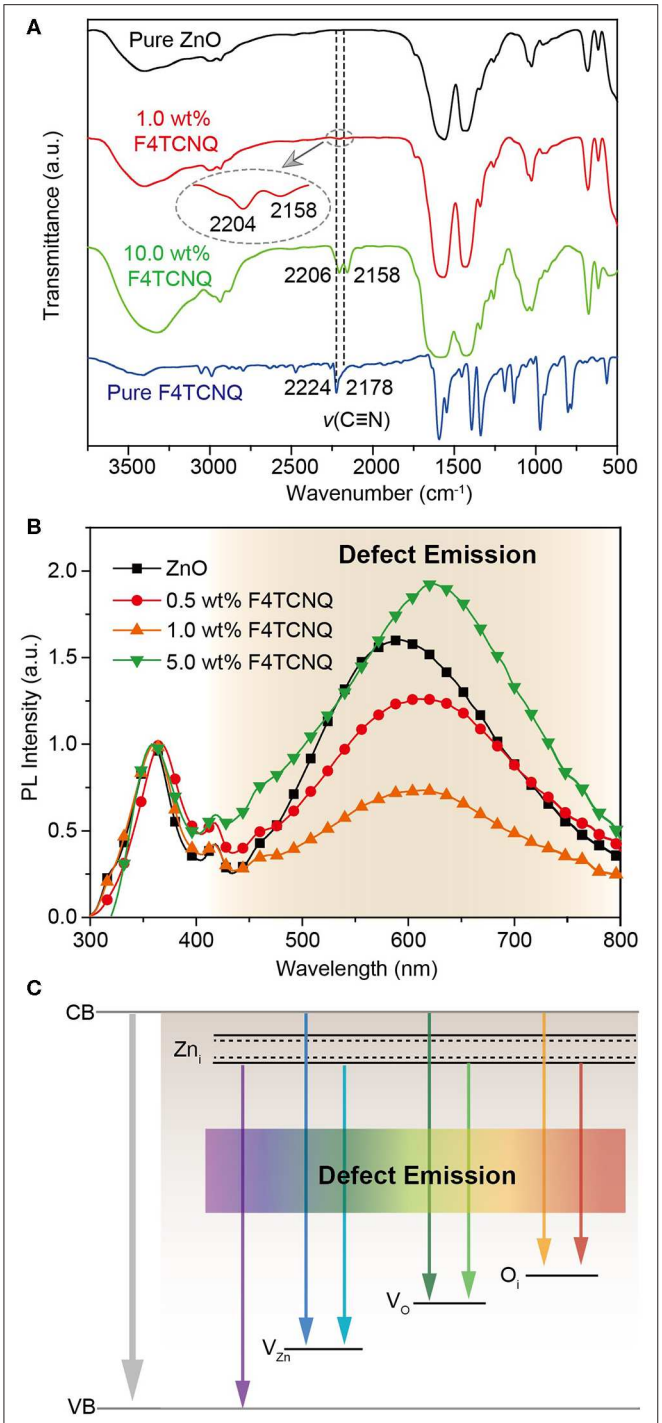

FIGURE 4 | (A) FTIR spectra of pure ZnO, pure F4TCNQ, and ZnO:x wt% F4TCNQ films (x = 1.0 and 10.0). **(B)** PL spectra of pristine ZnO and ZnO:x wt% F4TCNQ films (x = 0.5, 1.0, and 5.0) on top of the quartz substrates. **(C)** Energy level diagram of native defect states in sol-gel-derived ZnO.

charged electron finds the trapped hole and thus recombines with it (Proctor et al., 2013). Generally, the holes should be transported through the donor phase to the anode electrode when the photogenerated carriers have formed in the photoactive layer. However, a mass of defects generated in the ZnO film may induce hole transfer from the donor component to the ZnO CBL. When the electrons are collected through ZnO-based CBLs, they may enter the trap states with positively charged species and trap-assisted recombination process happens. According to the previous reports, the trap-assisted recombination rate is ultimately determined by the amount of trap sites and how quickly the free carrier can find the trapped carrier (Kirchartz et al., 2011; Proctor et al., 2013). As soon as F4TCNQ dopants were employed, the introduction of F4TCNQ dopants will fill the defects where traps reside, thus rendering them electronically inert (Yan et al., 2016). Based on the trap-filling strategy, the photogenerated holes will be blocked from entering trap states and thus the probability of trap-assisted recombination can be reduced efficiently during carrier transport process.

CONCLUSIONS

In conclusion, the ZnO:F4TCNQ hybrid films with good solution processability, tunable energy levels, and reduced defects have been developed as a new class of CBLs for both fullerene- and non-fullerene-based OSCs. While adding F4TCNQ into ZnO film, remarkable increases in FF were observed, leading to an obvious enhancement in overall device performance. The surface property and energy levels of ZnO-based CBLs can be regulated efficiently by the doping of organic acceptor. Owing to the coordination effects between cyano groups and ZnO, the introduced F4TCNQ contributes to suppressing the non-geminate recombination by filling the ZnO defects, thus allowing for efficient charge transport and extraction in ZnO-based CBLs. Consequently, the simple trap-filling strategy by organic dopants provides an efficient approach in adjusting electrical properties of interfacial layers, which is important for constructing high-performance CBLs of inverted OSCs.

EXPERIMENTAL

Materials

PTB7-Th, $PC_{71}BM$, and ITIC were purchased from Luminescence Technology Corp. O-dichlorobenzene (ODCB) and chlorobenzene (CB) were purchased from Aladdin Corp. Zinc acetate dihydrate [$Zn(CH_3COO)_2{\bullet}2H_2O$, 98%], ethanolamine ($NH_2CH_2CH_2OH$, 99.5%), and 2-methoxyethanol ($CH_3OCH_2CH_2OH$, 99.8%) were purchased from Acros. 2,3,5,6-Tetrafluoro-7,7,8,8-tetracyanoquinodimethane (F4TCNQ) was provided by Sigma-Aldrich. Molybdenum oxide (MoO_3) was provided by Shanghai Han Feng Chemical Corp. All chemicals were used as obtained.

Preparation of CBLs

Sol-gel-derived ZnO CBLs were prepared using zinc acetate in 2-methoxyethanol:ethanolamine as a precursor solution by spin-coating onto the ITO substrate followed by thermal annealing at 200°C for 30 min according to the reference (Sun et al., 2011). As for the ZnO:F4TCNQ hybrid CBLs, the ZnO:F4TCNQ precursor solutions were prepared by mixing with different contents of

F4TCNQ (0.5, 1.0, and 5.0 wt%) and dissolving in a mixture of 2-methoxyethanol as the solvent and ethanolamine as the stabilizer under sufficient stirring. After the spin-coating process has been completed, the hybrid film was also thermal-annealed at 200°C for 30 min.

Device Fabrication

The device structure was ITO/CBL/PTB7-Th:$PC_{71}BM$/MoO_3/Al. Firstly, the CBLs (∼30 nm) were spin-coated on top of the precleaned ITO substrate, which was treated with deionized water, acetone, and ethanol in an ultrasonic bath followed by ultraviolet (UV)-ozone treating for 15 min. A blend of PTB7-Th:$PC_{71}BM$ with the mass ratio of 4:7 in ODCB solvent was spin-coated on the surface of CBLs in the N_2 glovebox. The thickness of the active layer was controlled to be around 100 nm. Then, MoO_3 film (10 nm) as the anode interfacial layer was thermally evaporated on the active layer, followed by the thermal evaporation of Al (∼100 nm). The device of ITO/ZnO/PTB7-Th:ITIC/MoO_3/Al was prepared by adopting a similar approach. For the non-fullerene-based photoactive layer, a blend of PTB7-Th:ITIC with the mass ratio of 1:1.2 in CB solvent was spin-coated. The thickness of the active layer was also controlled to be around 100 nm. These OSCs, made on ITO glass substrate, have an active area of 0.09 cm^2.

Measurements and Characterization

Current density-voltage (*J–V*) characteristics of OSCs, which were detected under ambient situation, were recorded by Keithley-2400 digital source meter. SAN-EI electric solar simulator (XES-50S1) under simulated AM 1.5 illumination (100 mW/cm^2) was used for solar cell characterization. The EQE measurements of the PSCs were carried out with QE-R system (Enli Technology Co., Ltd.). The surface morphology of the CBLs was characterized by atomic force microscopy (AFM, FM-Nanoview 1000, FSM-Precision Co., Ltd.) in taping mode. Contact angle characterizations were carried out on pure ZnO layer, and ZnO:F4TCNQ layer using droplet shape analyzer (KRÜSS GmbH Germany). X-ray photoelectron spectroscopy (XPS) experiments were carried out with ESCALAB 250 system. The measurement chamber was equipped with a monochromatic Al Kγ X-ray source (hγ = 1486.6 eV). Ultraviolet-visible (UV-Vis) absorption spectra were measured on a lambda 35 PerkinElmer UV-Vis spectrophotometer. Photoluminescence (PL) spectra and time-resolved PL measurements were performed on an Edinburgh FLS980 fluorescence at room temperature. CV measurement was performed to estimate the HOMO from the onset potential of the electrochemical oxidation. The CV measurement was carried out on a CHI660E system in a three-electrode cell with a working electrode, a reference electrode, and a counter electrode in an acetonitrile solution of Bu_4NPF_6 (0.1 M). Fourier transform infrared (FTIR) spectroscopic analysis was performed using FT-IR spectrometer (PerkinElmer). The electrical conductivity was measured by Physical Property Measurement System (Quantum Design).

DATA AVAILABILITY STATEMENT

All relevant data is contained within the article. The raw data supporting the conclusions of this article will be made available by the authors, without undue reservation, to any qualified researcher.

AUTHOR CONTRIBUTIONS

ML and JL conceived the ideas and performed the device fabrication. LY and YZ conducted the XPS, UV-vis, and CV measurements. YD conducted the AFM and FTIR measurements. RC and WH supervised the research and contributed to manuscript preparation.

FUNDING

This study was supported in part by the National Natural Science Foundation of China (61704089, 61875090, and 21674049), China Postdoctoral Science Foundation (2019M661899), Jiangsu Planned Projects for Postdoctoral Research Funds (2019K140), and Scientific Starting Fund from Nanjing University of Posts and Telecommunications (NUPTSF) (NY217141).

SUPPLEMENTARY MATERIAL

The Supplementary Material for this article can be found online at: https://www.frontiersin.org/articles/10.3389/fchem.2020.00399/full#supplementary-material

REFERENCES

Cai, X., Yuan, T., Liu, X., and Tee, G. (2017). Self-assembly of 1-pyrenemethanol on ZnO surface toward combined cathode buffer layers for inverted polymer solar cells. *ACS Appl. Mater. Inter.* 9, 36082–36089. doi: 10.1021/acsami.7b10399

Chen, S., Small, C. E., Amb, C. M., Subbiah, J., Lai, T. H., Tsang, S. W., et al. (2012). Inverted polymer solar cells with reduced interface recombination. *Adv. Energy Mater.* 2, 1333–1337. doi: 10.1002/aenm.201200184

Hau, S. K., Yip, H. L., Ma, H., and Jen, A. K. Y. (2008). High performance ambient processed inverted polymer solar cells through interfacial modification with a fullerene self-assembled monolayer. *Appl. Phys. Lett.* 93:233304. doi: 10.1063/1.3028094

Hewlett, R. M., and McLachlan, M. A. (2016). Surface structure modification of ZnO and the impact on electronic properties. *Adv. Mater.* 28, 3893–3921. doi: 10.1002/adma.201503404

Hu, T., Chen, L., Yuan, K., and Chen, Y. W. (2015). Amphiphilic fullerene/ZnO hybrids as cathode buffer layers to improve charge selectivity of inverted polymer solar cells. *Nanoscale* 7, 9194–9203. doi: 10.1039/c5nr01456e

Hu, T., Jiang, P., Chen, L., Yuan, K., Yang, H., and Chen, Y. (2016). Amphiphilic fullerene derivative as effective interfacial layer for inverted polymer solar cells. *Org. Electron.* 37, 35–41. doi: 10.1016/j.orgel.2016.06.018

Kamalasanan, M. N., and Chandra, S. (1996). Sol-gel synthesis of ZnO thin films. *Thin Solid Films* 288, 112–115. doi: 10.1016/S0040-6090(96)08864-5

Kato, H., Nishikawa, O., Matsui, T., Honma, S., and Kokado, H. (1991). Fourier-transform infrared-spectroscopy study of dopants of polypyrrole. *J. Phys. Chem.* 95, 6011–6014. doi: 10.1021/j100168a054

Kirchartz, T., Pieters, B. E., Kirkpatrick, J., Rau, U., and Nelson, J. (2011). Recombination via tail states in polythiophene:fullerene solar cells. *Phys. Rev. B* 83:115209. doi: 10.1103/PhysRevB.83.115209

Lee, S., Hang, C. Y., Hong, A., Kim, J., Yang, H., Jung, B. J., et al. (2019). Inverted quantum dot light-emitting diodes with defect-passivated ZnO as an electron transport layer. *Semicond. Sci. Tech.* 34:085002. doi: 10.1088/1361-6641/ab2b52

Li, G., Zhu, R., and Yang, Y. (2012). Polymer solar cells. *Nat. Photonics* 6, 153–161. doi: 10.1038/NPHOTON.2012.11

Li, M., Li, J., Wang, J., Yu, L., Wang, T., Jin, J., et al. (2019). Enhancing photovoltaic performance by cathode interfacial modification with inorganic/organic gradient diffusion structures. *ACS Sustain. Chem. Eng.* 7, 12261–12269. doi: 10.1021/acssuschemeng.9b01601

Li, X., Liu, X., Zhang, W., Wang, H. Q., and Fang, J. (2017). Fullerene-free organic solar cells with efficiency over 12% based on EDTA-ZnO hybrid cathode interlayer. *Chem. Mater.* 29, 4176–4180. doi: 10.1021/acs.chemmater.7b01615

Liao, S. H., Jhuo, H. J., Cheng, Y. S., and Chen, S. A. (2013). Fullerene derivative-doped zinc oxide nanofilm as the cathode of inverted polymer solar cells with low-bandgap polymer (PTB7-Th) for high performance. *Adv. Mater.* 25, 4766–4771. doi: 10.1002/adma.201301476

Liao, S. H., Jhuo, H. J., Yeh, P. N., Cheng, Y. S., Li, Y. L., Lee, Y. H., et al. (2014). Single junction inverted polymer solar cell reaching power conversion efficiency 10.31% by employing dual-doped zinc oxide nano-film as cathode interlayer. *Sci. Rep.* 4:6813. doi: 10.1038/srep06813

Liu, C., Li, Z., Zhang, X., Guo, W., Zhang, L., and Ruan, S. (2017). Annealing-free ZnO:PEI composite cathode interfacial layer for efficient organic solar cells. *ACS Photonics* 4, 2952–2958. doi: 10.1021/acsphotonics.7b01096

Liu, T., Guo, Y., Yi, Y., Huo, L., Xue, X., Sun, X., et al. (2016). Ternary organic solar cells based on two compatible nonfullerene acceptors with power conversion efficiency >10%. *Adv. Mater.* 28, 10008–10015. doi: 10.1002/adma.20160257

Liu, T., Luo, Z., Fan, Q., Zhang, G., Zhang, L., Gao, W., et al. (2018). Use of two structurally similar small molecular acceptors enabling ternary organic solar cells with high efficiencies and fill factors. *Energ. Environ. Sci.* 11, 3275–3282. doi: 10.1039/C8EE01700J

Liu, T., Xue, X., Huo, L., Sun, X., An, Q., Zhang, F., et al. (2017). Highly efficient parallel-like ternary organic solar cells. *Chem. Mater.* 29, 2914–2920. doi: 10.1021/acs.chemmater.6b05194

Mishra, P. K., Ayaz, S., Srivastava, T., Tiwari, S., Meena, R., Kissinquinker, B., et al. (2019). Role of Ga-substitution in ZnO on defect states, carrier density, mobility and UV sensing. *J. Mater. Sci-Mater. Electron.* 30, 18686–18695. doi: 10.1007/s10854-019-02221-z

Proctor, C. M., Kuik, M., and Nguyen, T. (2013). Charge carrier recombination in organic solar cells. *Prog. Polym. Sci.* 38, 1941–1960. doi: 10.1016/j.progpolymsci.2013.08.008

Seo, J., Lee, C., Kim, H., and Kim, Y. (2018). Distinctive nanocrater structures in hybrid electron-collecting buffer layers for high efficiency polymer:nonfullerene solar cells. *Adv. Mater. Inter.* 5:1800912. doi: 10.1002/admi.201800912

Spencer, M. J. S., Wong, K. W. J., and Yarovsky, I. (2012). Surface defects on ZnO nanowires: implications for design of sensors. *J. Phys-Condens. Matter* 24:305001. doi: 10.1088/0953-8984/24/30/305001

Sun, Y., Seo, J. H., Takacs, C. J., Seifter, J., and Heeger, A. J. (2011). Inverted polymer solar cells integrated with a low-temperature-annealed sol-gel-derived ZnO film as an electron transport layer. *Adv. Mater.* 23, 1679–1683. doi: 10.1002/adma.201004301

Wang, C., Luo, D., Gao, Y., Wang, G., Wang, C., Ma, P., et al. (2019). Delicate energy-level adjustment and interfacial defect passivation of ZnO electron transport layers in organic solar cells by constructing ZnO/In nanojunctions. *J. Phys. Chem. C* 123, 16546–16555. doi: 10.1021/acs.jpcc.9b03776

Xie, Z., and Wuerthner, F. (2017). Hybrid photoconductive cathode interlayer materials composed of perylene bisimide photosensitizers and zinc oxide for high performance polymer solar cells. *Adv. Energy Mater.* 7:1602573. doi: 10.1002/aenm.201602573

Yan, C., Barlow, S., Wang, Z., Yan, H., Jen, A. K. Y., Marder, S. R., et al. (2018). Non-fullerene acceptors for organic solar cells. *Nat. Rev. Mater.* 3: 18003. doi: 10.1038/natrevmats.2018.3

Yan, H., Manion, J. G., Yuan, M., de Arquer, F. P. G., McKeown, G. R., Beaupre, S., et al. (2016). Increasing polymer solar cell fill factor by trap-filling with F4-TCNQ at parts per thousand concentration. *Adv. Mater.* 28, 6491–6496. doi: 10.1002/adma.201601553

Yin, Z., Wei, J., and Zheng, Q. (2016). Interfacial materials for organic solar cells: recent advances and perspectives. *Adv. Sci.* 3:1500362. doi: 10.1002/advs.201500362

Yin, Z., Zheng, Q., Chen, S. C., and Cai, D. (2013). Interface control of semiconducting metal oxide layers for efficient and stable inverted polymer solar cells with open-circuit voltages over 1.0 volt. *ACS Appl. Mater. Inter.* 5, 9015–9025. doi: 10.1021/am402175m

Zhao, F., Li, Y., Wang, Z., Yang, Y., Wang, Z., He, G., et al. (2017). Combining energy transfer and optimized morphology for highly efficient ternary polymer solar cells. *Adv. Energy Mater.* 7: 1602552. doi: 10.1002/aenm.201602552

Zhou, J., Fan, J. B., Nie, Q., and Wang, S. (2016). Three-dimensional superhydrophobic copper 7,7,8,8-tetracyanoquinodimethane biointerfaces with the capability of high adhesion of osteoblasts. *Nanoscale* 8, 3264–3267. doi: 10.1039/c5nr08305b

Conflict of Interest: The authors declare that the research was conducted in the absence of any commercial or financial relationships that could be construed as a potential conflict of interest.

frontiers in Chemistry

ORIGINAL RESEARCH
published: 12 June 2020
doi: 10.3389/fchem.2020.00497

Monodisperse Core-Shell $NaYF_4:Yb^{3+}/Er^{3+}@NaYF_4:Nd^{3+}$-PEG-GGGRGDSGGGY-$NH_2$ Nanoparticles Excitable at 808 and 980 nm: Design, Surface Engineering, and Application in Life Sciences

Uliana Kostiv[1], Hana Engstová[2], Bartosz Krajnik[3], Miroslav Šlouf[1], Vladimír Proks[1], Artur Podhorodecki[3], Petr Ježek[2] and Daniel Horák[1]**

[1] Institute of Macromolecular Chemistry of the Czech Academy of Sciences, Prague, Czechia, [2] Institute of Physiology of the Czech Academy of Sciences, Prague, Czechia, [3] Department of Experimental Physics, Wroclaw University of Science and Technology, Wroclaw, Poland

OPEN ACCESS

Edited by:
Manoj K. Mahata,
Gwangju Institute of Science and Technology, South Korea

Reviewed by:
Thuat Thanh Trinh,
Norwegian University of Science and Technology, Norway
Jinwoo Park,
University of Seoul, South Korea

***Correspondence:**
Uliana Kostiv
kostiv@imc.cas.cz
Daniel Horák
horak@imc.cas.cz

Specialty section:
This article was submitted to Physical Chemistry and Chemical Physics, a section of the journal Frontiers in Chemistry

Received: 28 January 2020
Accepted: 14 May 2020
Published: 12 June 2020

Citation:
Kostiv U, Engstová H, Krajnik B, Šlouf M, Proks V, Podhorodecki A, Ježek P and Horák D (2020) Monodisperse Core-Shell $NaYF_4:Yb^{3+}/Er^{3+}@NaYF_4:Nd^{3+}$-PEG-GGGRGDSGGGY-$NH_2$ Nanoparticles Excitable at 808 and 980 nm: Design, Surface Engineering, and Application in Life Sciences. Front. Chem. 8:497. doi: 10.3389/fchem.2020.00497

Lanthanide-doped upconversion nanoparticles (UCNPs) have a unique capability of upconverting near-infrared (NIR) excitation into ultraviolet, visible, and NIR emission. Conventional UCNPs composed of $NaYF_4:Yb^{3+}/Er^{3+}(Tm^{3+})$ are excited by NIR light at 980 nm, where undesirable absorption by water can cause overheating or damage of living tissues and reduce nanoparticle luminescence. Incorporation of Nd^{3+} ions into the UCNP lattice shifts the excitation wavelength to 808 nm, where absorption of water is minimal. Herein, core-shell $NaYF_4:Yb^{3+}/Er^{3+}@NaYF_4:Nd^{3+}$ nanoparticles, which are doubly doped by sensitizers (Yb^{3+} and Nd^{3+}) and an activator (Er^{3+}) in the host $NaYF_4$ matrix, were synthesized by high-temperature coprecipitation of lanthanide chlorides in the presence of oleic acid as a stabilizer. Uniform core (24 nm) and core-shell particles with tunable shell thickness (~0.5–4 nm) were thoroughly characterized by transmission electron microscopy (TEM), energy-dispersive analysis, selected area electron diffraction, and photoluminescence emission spectra at 808 and 980 nm excitation. To ensure dispersibility of the particles in biologically relevant media, they were coated by in-house synthesized poly(ethylene glycol) (PEG)-neridronate terminated with an alkyne (Alk). The stability of the $NaYF_4:Yb^{3+}/Er^{3+}@NaYF_4:Nd^{3+}$-PEG-Alk nanoparticles in water or 0.01 M PBS and the presence of PEG on the surface were determined by dynamic light scattering, ζ-potential measurements, thermogravimetric analysis, and FTIR spectroscopy. Finally, the adhesive azidopentanoyl-modified GGGRGDSGGGY-NH_2 (RGDS) peptide was immobilized on the $NaYF_4:Yb^{3+}/Er^{3+}@NaYF_4:Nd^{3+}$-PEG-Alk particles via Cu(I)-catalyzed azide-alkyne

cycloaddition. The toxicity of the unmodified core-shell $NaYF_4$:Yb^{3+}/Er^{3+}@$NaYF_4$:Nd^{3+}, $NaYF_4$:Yb^{3+}/Er^{3+}@$NaYF_4$:Nd^{3+}-PEG-Alk, and $NaYF_4$:Yb^{3+}/Er^{3+}@$NaYF_4$:Nd^{3+}-PEG-RGDS nanoparticles on both Hep-G2 and HeLa cells was determined, confirming no adverse effect on their survival and proliferation. The interaction of the nanoparticles with Hep-G2 cells was monitored by confocal microscopy at both 808 and 980 nm excitation. The $NaYF_4$:Yb^{3+}/Er^{3+}@$NaYF_4$:Nd^{3+}-PEG-RGDS nanoparticles were localized on the cell membranes due to specific binding of the RGDS peptide to integrins, in contrast to the $NaYF_4$:Yb^{3+}/Er^{3+}@$NaYF_4$:Nd^{3+}-PEG-Alk particles, which were not engulfed by the cells. The $NaYF_4$:Yb^{3+}/Er^{3+}@$NaYF_4$:Nd^{3+}-PEG-RGDS nanoparticles thus appear to be promising as a new non-invasive probe for specific bioimaging of cells and tissues. This development makes the nanoparticles useful for diagnostic and/or, after immobilization of a bioactive compound, even theranostic applications in the treatment of various fatal diseases.

Keywords: upconversion nanoparticles, core-shell, 808 nm excitation, luminescence, PEG-neridronate, RGDS peptide, Hep-G2 and HeLa cells

INTRODUCTION

Lanthanide-doped upconversion nanoparticles (UCNPs) have recently attracted a great deal of attention as promising materials for various biomedical applications including medical diagnostics, mainly for *in vitro* and *in vivo* imaging, but also in longer perspective for drug and gene delivery, and photothermal and photodynamic therapy of malignancies (Duan et al., 2018; Qin et al., 2019). The particles also find utilization in sensing applications, such as environmental hazard detection, food assays, and biological analysis (Chen et al., 2014; Poláchová et al., 2019; Zhang et al., 2019). Interest in the UCNPs comes from their superior optical properties, such as a narrow line emission, long luminescence lifetime, high photostability, and absence of background fluorescence interference (Wolfbeis, 2015). The main advantage of UCNPs is in their ability to convert low energy excitation photons (i.e., from NIR spectral range), which can penetrate deeper into biological tissues (up to 5 cm) (Li et al., 2017) than visible light, to high-energy photons, e.g., ultraviolet or visible, via anti-Stokes emission (Zhu et al., 2017). Moreover, UCNPs are characterized with low absorption and scattering rate. In contrast to the high energetic photons, NIR light is not harmful for the tissue and do not induce autofluoroscence, which provides significant contrast improvement.

Conventional UCNPs are mostly composed of an inorganic crystalline $NaYF_4$ matrix doped by two types of lanthanide ions, one acting as an activator and another acting as a sensitizer (Auzel, 2004). Due to a large absorption cross-section, Yb^{3+} is typically used as a sensitizer responsible for the accumulation of excitation light energy and its transfer to the activator ion via non-radiative energy transfer (Bagheri et al., 2019). Yb^{3+} matches several activator ions, such as Tm^{3+}, Er^{3+}, or Ho^{3+}, and in combination with them generates upconversion luminescence after absorption of NIR light at 980 nm (Zhou et al., 2015). Although excitation at 980 nm is very efficient, it is not beneficial for biomedical applications, especially for *in vivo* studies, because it overlaps with the absorption band of water, which can cause unwanted overheating and damage to cells and tissues (Zhan et al., 2011). Therefore, attention is recently focused on shifting the excitation of UCNPs to lower excitation wavelengths, where the absorption of water is minimal. It was found that when Nd^{3+} is codoped with Yb^{3+} and activator into a UCNP matrix, the nanoparticles can be excited at both 808 and 980 nm (Lai et al., 2014; Chen et al., 2015). Excitation of Nd^{3+}-sensitized UCNPs at 808 nm benefits from minimal photothermal effects and provides deeper living tissue penetration compared to that of conventional 980 nm excitation (Wang et al., 2014; Wiesholler et al., 2019).

A broad range of synthetic strategies have been utilized to produce UCNPs with well-controlled nanoparticle size, composition, crystalline fidelity, and luminescence efficiency. Among these approaches, thermal decomposition, conventional and high-temperature coprecipitation, hydro(solvo)thermal or sol-gel synthesis, and preparation in the presence of ionic liquids have been extensively used (Liu et al., 2009; Wang et al., 2011; Naccache et al., 2015). Despite the substantial effort devoted to the synthesis, modification and characterization of UCNPs, their translation to the clinic is still far from complete, and several important issues need to be resolved before their introduction in praxis. For example, knowledge about the chemical stability and interactions between the particles and their polymer coatings is insufficient, as well as the behavior and colloidal stability of the surface-coated UCNPs in organism (Wilhelm, 2017). UCNPs disintegrate in highly diluted water dispersions, decreasing the upconversion luminescence intensity (Plohl et al., 2017). This process can be accompanied by the release of fluoride and lanthanide ions from the particles into the plasma or tissue, inducing cell death (Lahtinen et al., 2017). An additional problem consists of a relatively low upconversion luminescence efficiency and water-related quenching of the luminescence (Arppe et al., 2015). To address these difficulties, a dense and thick coating,

preferably from an amphiphilic polymer, should be formed around the particles (Plohl et al., 2017). Modification of the UCNP surface with polymers affects not only the dispersibility in physiological media but also the chemical stability (preventing lanthanide ion leakage) and biocompatibility. Coating can be achieved by a ligand exchange, ligand oxidation, layer-by-layer technique, miniemulsion polymerization, self-assembly, or solvent evaporation technique (Muhr et al., 2014; Sedlmeier and Gorris, 2015). Nevertheless, the most frequently used inorganic coatings of UCNPs are still based on silica derivatives that can contain various reactive groups for the conjugation of drugs and other molecules. Strategies for silica coating typically include reverse microemulsion or the Stöber method (Stöber and Fink, 1968; Guerrero-Martinez et al., 2010). Different polymeric materials have also been suggested to change the hydrophobic UCNPs into hydrophilic UCNPs and to encapsulate biomolecules, including drugs. Such polymers include poly(acrylic acid), poly(ethylene glycol) (PEG) and its derivatives (e.g., PEG-neridronate), poly(vinylpyrrolidone), polyethyleneimine, poly(maleic anhydride-*alt*-1-octadecene), chitosan, dextran, etc. (Wilhelm et al., 2015; Gee and Xu, 2018; Mandl et al., 2019; Patsula et al., 2019).

The aim of this research was to develop biocompatible UCNP nanoparticles that absorb NIR light at both 808 and 980 nm excitation. Such particles might serve as a base for future development of UCNPs incorporating photoactivatable drugs, specifically those containing photosensitizers for photodynamic therapy of tumors. To achieve this goal, monodisperse spherical $NaYF_4:Yb^{3+}/Er^{3+}$ cores were synthesized, and homogeneous $NaYF_4:Nd^{3+}$ shells of different thicknesses were deposited on them to (*i*) enhance the upconversion luminescence at 980 nm excitation and (*ii*) simultaneously shift the excitation to 808 nm due to the presence of Nd^{3+} ions in the shell. The particles were modified by bisphosphonate- and alkyne-terminated PEG with a strong binding affinity to lanthanides on the particle surface and an ability to conjugate biomolecules, e.g., azido-modified RGDS peptide via Cu(I) catalyzed click reaction, respectively. The cytotoxicity of unmodified, PEGylated, and RGDS-conjugated core-shell $NaYF_4:Yb^{3+}/Er^{3+}@NaYF_4:Nd^{3+}$ nanoparticles was investigated using human cancer cell lines, hepatocellular carcinoma Hep-G2 cells, and cervical epithelioid carcinoma HeLa cells. The particle biodistribution in the cells was monitored by an inverted confocal fluorescence microscope with a laser at 980 nm excitation and a 140 fs pulse.

EXPERIMENTAL

Chemicals and Materials

Anhydrous neodymium(III), yttrium(III), ytterbium(III) and erbium(III) chlorides (99%), octadec-1-ene (90%), ammonium hydrogen difluoride, copper(II) sulfate, sodium L-ascorbate, Igepal CO-520 [polyoxyethylene(5) nonylphenyl ether], 2-amino-2-(hydroxymethyl)propane-1,3-diol (Tris), 2-[4-(2-hydroxyethyl)piperazin-1-yl]ethanesulfonic acid (HEPES), and phosphate-buffered saline (PBS) were obtained from Sigma-Aldrich (St. Louis, MO, USA). CellMask™ deep red was from Thermo Fisher Scientific (Waltham, MA, USA); α-NHS-ω-alkyne poly(ethylene glycol) (NHS-$PEG_{3,815}$-Alk; M_w = 3,815 Da and NHS-$PEG_{5,475}$-Alk; M_w = 5,475 Da) were purchased from Rapp Polymere (Tübingen, Germany). Oleic acid (OA), hexane, methanol, ethanol, and acetone were purchased from Lach-Ner (Neratovice, Czech Republic). Sodium neridronate and neridronate-PEG-alkyne (Ner-PEG-Alk) were prepared as described earlier (Kostiv et al., 2017c; Mickert et al., 2019). Azidopentanoyl-GGGRGDSGGGY-NH_2 (RGDS) peptide was synthesized by the standard Fmoc/tBu solid-phase technique on a TentaGel® Rink-Amide-R resin according to previously published procedures (Proks et al., 2012; Kostiv et al., 2016). Dulbecco's modified Eagle's medium (DMEM) and fetal calf serum were purchased from Life Technologies (Carlsbad, CA, USA). Other reagent grade chemicals were obtained from commercial sources and used as received. Cellulose dialysis membranes (MWCO 0.5, 3.5, 14, and 100 kDa) were purchased from Spectrum Europe (Breda, Netherlands). Ultrapure Q-water ultrafiltered on a Milli-Q Gradient A10 system (Millipore; Molsheim, France) was used in all experiments.

Synthesis of Core $NaYF_4:Yb^{3+}/Er^{3+}$ Nanoparticles

Core $NaYF_4:Yb^{3+}/Er^{3+}$ nanoparticles were synthesized according to previous publications with minor modifications (Kostiv et al., 2017a,b). In a 100-ml three-neck flask, a mixture of YCl_3 (0.78 mmol), $YbCl_3$ (0.2 mmol), $ErCl_3$ (0.02 mmol), OA (6 ml), and octadec-1-ene (15 ml) was heated at 160°C for 30 min with stirring under Ar flow. After cooling to room temperature (RT), a solution of NaOH (4 mmol) and $NH_4F{\cdot}HF$ (2.6 mmol) in methanol (5 ml) was added, and the mixture was slowly heated at 120°C under an Ar atmosphere until methanol evaporation; the reaction then continued at 300°C for 1.5 h. After cooling to RT, the resulting core $NaYF_4:Yb^{3+}/Er^{3+}$ nanoparticles were collected by centrifugation (6,000 rpm; 30 min), redispersed in hexane (16 ml), precipitated by ethanol (10 ml), and separated by centrifugation (6,000 rpm; 30 min). The sedimentation-redispersion cycle was repeated two times and the particles were finally dispersed in hexane (10 mg/ml).

Synthesis of Core-Shell $NaYF_4:Yb^{3+}/Er^{3+}@NaYF_4:Nd^{3+}$ Nanoparticles

Core-shell $NaYF_4:Yb^{3+}/Er^{3+}@NaYF_4:Nd^{3+}$ nanoparticles with 0.1, 0.3, 0.5, or 0.7 mmol of $NaYF_4:Nd^{3+}$ were synthesized according to an earlier procedure (Podhorodecki et al., 2018). Briefly, a mixture of YCl_3 (0.08, 0.24, 0.4, or 0.56 mmol), $NdCl_3$ (0.02, 0.06, 0.1, or 0.14 mmol), OA (6 ml), and octadec-1-ene (15 ml) was heated at 160°C for 30 min with stirring under an Ar atmosphere and cooled to RT. The core $NaYF_4:Yb^{3+}/Er^{3+}$ nanoparticles (125 mg) in hexane (12.5 ml), NaOH (0.4, 1.2, 2, or 2.8 mmol), and $NH_4F{\cdot}HF$ (0.26, 0.78, 1.3, or 1.82 mmol) in methanol were added, and the mixture was slowly heated to 70°C under an Ar atmosphere and then at 300°C for 1.5 h. The mixture was cooled to RT, and the resulting

core-shell $NaYF_4$:Yb^{3+}/Er^{3+}@$NaYF_4$:Nd^{3+} nanoparticles were washed with hexane and ethanol as described above and dispersed in hexane (10 mg/ml). In further experiments, $NaYF_4$:Yb^{3+}/Er^{3+}@$NaYF_4$:Nd^{3+} nanoparticles with 0.5 mmol of $NaYF_4$:Nd^{3+} were used due to their uniformity and high luminescence efficiency at both 808 and 980 nm excitation.

Synthesis of $NaYF_4$:Yb^{3+}/Er^{3+}-PEG-Alk, $NaYF_4$:Yb^{3+}/Er^{3+}@$NaYF_4$:Nd^{3+}-PEG-Alk, and $NaYF_4$:Yb^{3+}/Er^{3+}@$NaYF_4$:Nd^{3+}-PEG-RGDS Nanoparticles

The surface of the core $NaYF_4$:Yb^{3+}/Er^{3+} and core-shell $NaYF_4$:Yb^{3+}/Er^{3+}@$NaYF_4$:Nd^{3+} nanoparticles (containing 0.5 mmol of $NaYF_4$:Nd^{3+}) were modified by Ner-PEG-Alk of two different molecular weights, i.e., Ner-$PEG_{3,815}$-Alk and Ner-$PEG_{5,475}$-Alk. Prior to the modification, excess OA ligands were removed by washing the particles with hexane/ethanol (1/1 v/v), ethanol, ethanol/water (1/1 v/v), and water during five sedimentation-redispersion cycles; finally, the particles were dialyzed (MWCO = 14 kDa) against water. Ner-$PEG_{3,815}$-Alk (6 mg) or Ner-$PEG_{5,475}$-Alk (8 mg) was added to an aqueous particle dispersion (5 ml; 4 mg/ml), and the mixture was stirred at RT for 12 h. Excess PEG was removed by dialysis against water using a cellulose membrane (MWCO = 14 kDa) at RT for 48 h; the water (2.5 l) was exchanged two times. For biological experiments, the $NaYF_4$:Yb^{3+}/Er^{3+}@$NaYF_4$:Nd^{3+}-$PEG_{5,475}$-Alk nanoparticles were selected due to a high content of Ner-$PEG_{5,475}$-Alk bound to the particle surface, as confirmed by TGA analysis.

$NaYF_4$:Yb^{3+}/Er^{3+}@$NaYF_4$:Nd^{3+}-$PEG_{5,475}$-Alk nanoparticles were conjugated with azidopentanoyl-GGGRGDSGGGY-NH_2 peptide via a click reaction. Briefly, an aqueous $NaYF_4$:Yb^{3+}/Er^{3+}@$NaYF_4$:Nd^{3+}-$PEG_{5,475}$-Alk particle dispersion (1 ml; 20 mg/ml), azidopentanoyl-GGGRGDSGGGY-NH_2 peptide (20 µl; 1 mg/ml), and sodium ascorbate (20 µl; 20 µg/ml) were purged with Ar for 30 min, and aqueous 0.05 M $CuSO_4$ solution (10 µl) was added, and the mixture was purged with Ar for an additional 30 min. The resulting $NaYF_4$:Yb^{3+}/Er^{3+}@$NaYF_4$:Nd^{3+}-PEG-RGDS nanoparticle dispersion was sonicated for 10 min and washed by dialysis against water (MWCO = 100 kDa) at RT for 48 h; the water (2.5 l) was exchanged two times.

Characterization of Nanoparticles

The morphology, elemental composition, and crystal structure of the nanoparticles were analyzed using a Tecnai Spirit G2 transmission electron microscope (TEM; FEI; Brno, Czech Republic). Nanoparticles were deposited on a standard carbon-coated copper grid and characterized by three TEM modes at 120 kV. (*i*) The morphology of the nanoparticles was visualized by bright field imaging (BF), (*ii*) the elemental composition was obtained from energy-dispersive X-ray (EDX) analysis (EDAX detector; Mahwah, NJ, USA), and (*iii*) the crystal structure was verified by means of selected area electron diffraction (SAED). The nanoparticle size and distribution were determined by measuring at least 300 nanoparticles from TEM micrographs using ImageJ software. The number-average diameter (D_n), weight-average diameter (D_w) and uniformity (dispersity $Đ$) were calculated as follows:

$$D_n = \sum N_i D_i / \sum N_i, \quad (1)$$

$$D_w = \sum N_i D_i^4 / \sum N_i D_i^3, \quad (2)$$

$$Đ = D_w / D_n, \quad (3)$$

where N_i and D_i are the number and diameter of the nanoparticles, respectively. The elemental composition was calculated from TEM/EDX spectra by EDAX software and post-processed in the common MS Excel spreadsheet program. Elements (C and Cu) originating from the supporting carbon-coated copper TEM grid and possible impurities (small Si and O peaks originating from dust) were subtracted, and the remaining elements were normalized to 100%. The TEM/SAED patterns were processed with ProcessDiffraction software (Lábár, 2005) and compared to the theoretical X-ray diffraction patterns calculated with PowderCell software (Kraus and Nolze, 1996); the crystal structures for calculation of diffraction patterns were obtained from the freeware Crystallography Open Database (Glasser, 2016).

The hydrodynamic particle diameter (D_h), size distribution (polydispersity *PD*), and ζ-potential were determined by dynamic light scattering (DLS) on a ZEN 3600 Zetasizer Nano Instrument (Malvern Instruments; Malvern, UK). The particle dispersion was measured at 25°C, and D_h and *PD* were calculated from the intensity-weighted distribution function obtained by CONTIN analysis of the correlation function embedded in Malvern software.

ATR FTIR spectra were recorded on a Nexus Nicolet 870 FTIR spectrometer (Madison, WI, USA) equipped with a liquid nitrogen-cooled mercury cadmium telluride detector and a Golden Gate single reflection ATR cell (Specac; Orpington, UK). Thermogravimetric analysis (TGA) of the particles was performed in air in the temperature range 30–600°C at a heating rate of 10°C/min using a PerkinElmer Pyris 1 thermogravimetric analyzer (Shelton, CT, USA).

Upconversion luminescence spectra of nanoparticles in a hexane (2 ml; 1 mg/ml), hexane/water or hexane/D_2O (2 ml/10 µl) emulsion stabilized with Igepal CO-520 (100 µl) were measured using an FS5 spectrofluorometer (Edinburgh Instruments; Edinburgh, UK) coupled with a CW 980 nm laser diode as an excitation source (MDL-III-980-2W; output laser power 2 W and beam size 5 × 8 mm^2). The particle dispersion in hexane was stirred prior to the measurement, while the hexane/water or hexane/D_2O emulsions were sonicated with a USC 300 THD/HF ultrasonic bath (VWR; Lutterworth, UK) at RT for 10 min.

A custom-build experimental setup was used for measurements of the optical spectra of UCNPs excited by two CW fiber-coupled infrared diode lasers with nominal power 2 W (MDL-III-808/MDL-III-980; CNI Optoelectronics; Changchun, China) and emission wavelengths of 808 and

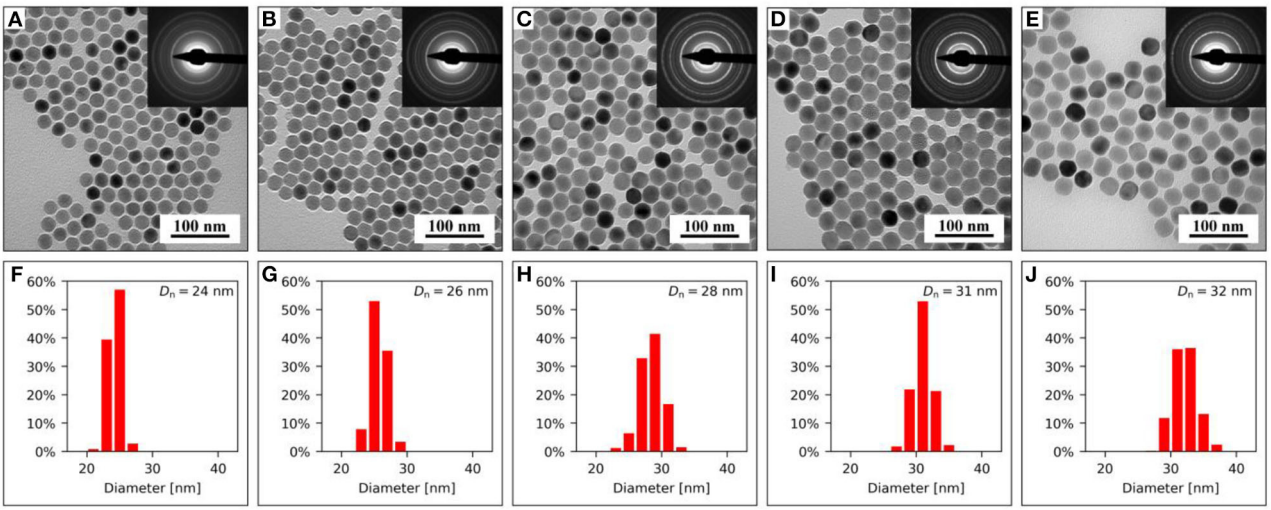

FIGURE 1 | (A–E) TEM/BF micrographs with TEM/SAED diffraction patterns (insets) and **(F–J)** corresponding particle size distributions of $NaYF_4:Yb^{3+}/Er^{3+}@NaYF_4:Nd^{3+}$ nanoparticles containing **(A,F)** 0, **(B,G)** 0.1, **(C,H)** 0.3, **(D,I)** 0.5, and **(E,J)** 0.7 mmol of $NaYF_4:Nd^{3+}$. Number-average particle diameters D_n are shown in the upper right corners of the histograms.

980 nm. A multimode fiber with core diameter 1 mm was used to homogenize both laser beams and ensure the same excitation beam profile focused on the sample. Laser light was collimated and focused at the center of the sample cuvette with an achromatic lens of focal length of 35 mm (Edmund Optics; Barrington, NJ, USA) to excite a large volume of the particle dispersion. The resulting beam waist was measured using a BP209-VIS scanning-slit optical beam profiler (Thorlabs; Newton, NH, USA). Due to the use of achromatic doublets, the beam waist at the focus was almost identical for both lasers. The values of the fitted waists equaled 1,260 ± 20 and 1,280 ± 20 μm for the 808 nm and 980 nm lasers, respectively, which corresponds to an average power density of ∼30 W/cm^2. The head of a FieldMax II thermal power sensor (Coherent; Palo Alto, CA, USA) was positioned 5 mm behind the cuvette rear wall to monitor the laser power during the experiment. Luminescence spectra were collected with a dry microscope objective (NA 0.12) equipped with a short-pass F38-749 filter (Semrock; Rochester, NY, USA) and focused on the multimode fiber attached to a Flame VIS spectrometer (Ocean Optics; Largo, FL, USA). Background-corrected spectra were collected with an acquisition time of 2.5 s.

Cell Cultivation and Monitoring

Human hepatocellular carcinoma Hep-G2 (ECACC 85011430) and human cervix epitheloid carcinoma HeLa cells (ECACC 93021013) were cultivated at 37°C in DMEM with 3 mM glutamine, 10% (v/v) fetal calf serum, 10 mM HEPES, 100 IU/ml penicillin, 100 μg/ml streptomycin, and 5 mM glucose in humidified air with 5 % CO_2. The cells were then cultured on poly(L-lysine)-coated glass coverslips in DMEM (2 ml) for 2 d, incubated with a nanoparticle dispersion (20, 40, and 150 μl; 5 mg/ml) for 24 h, transferred to a thermostable chamber at 37°C under 5% CO_2 atmosphere, mimicking normal cultivation conditions, and finally observed in a Leica TCS SP8 AOBS confocal inverted fluorescence microscope (Wetzlar, Germany) equipped with an objective HC PL APO 63×/1.20 NA W CORR CS2, WD = 0.3 mm. Particles were excited by a Chameleon Ultra I pulsed infrared tunable laser with wavelength range 690–1,040 nm, maximum output power 4 W, pulse frequency 80 MHz, pulse width ∼140 fs and laser intensity controlled by electrooptical EOM modulator (Coherent; Santa Clara, CA, USA) and attenuator at 980 nm excitation.

CellMask™ deep red-stained cell plasma membrane without the cell type-specific differences exhibited by lectins was visualized in a standard fluorescence confocal microscope with excitation and emission at 649 and 666 nm, respectively. A WLL2 supercontinuous pulsed laser for two-photon excitation (NKT Photonics; Birkerød, Denmark) was used for excitation at 470–670 nm with an average laser power ∼1.5 mW. The z-planes of the cells and nanoparticles were viewed by z-scan mode of the microscope with excitation at 808 and 980 nm. Overlaps of image planes showed the distribution of nanoparticles in the cell or their binding to the plasma membrane using λ-scan mode.

Cell Toxicity

Hep-G2 and HeLa cells (both 5×10^4) were cultured for 24 h as described above and incubated with $NaYF_4:Yb^{3+}/Er^{3+}@NaYF_4:Nd^{3+}$, $NaYF_4:Yb^{3+}/Er^{3+}@NaYF_4:Nd^{3+}$-PEG-Alk, and $NaYF_4:Yb^{3+}/Er^{3+}$@PEG-RGDS nanoparticles (0.001–1 mg per ml of DMEM) at 37°C for 72 h under a 5% CO_2 atmosphere. *In vitro* cell viability was determined by 0.4% trypan blue staining (Thermo Fisher Scientific), and the fraction of living cells

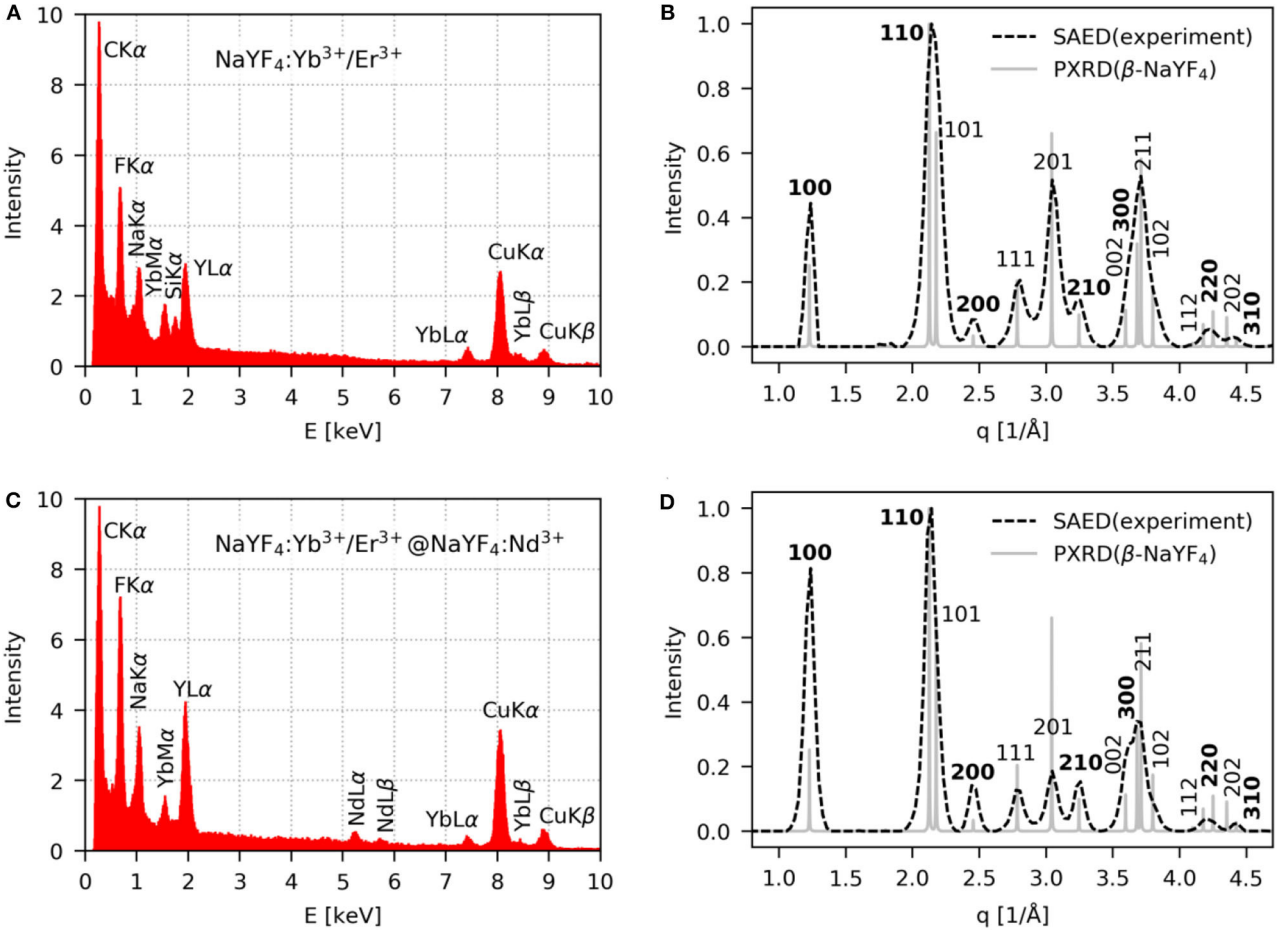

FIGURE 2 | (A,C) TEM/EDX and **(B,D)** TEM/SAED analysis of **(A,B)** $NaYF_4:Yb^{3+}/Er^{3+}$ and **(C,D)** $NaYF_4:Yb^{3+}/Er^{3+}@NaYF_4:Nd^{3+}$(0.5 mmol) nanoparticles. Experimental TEM/SAED diffractograms (dashed lines) were compared with theoretically calculated PXRD diffractograms for the hexagonal phase of β-$NaYF_4$ (full lines).

was counted on a Countess automated cell counter (Thermo Fisher Scientific).

RESULTS AND DISCUSSION

Synthesis and Structure of $NaYF_4:Yb^{3+}/Er^{3+}$ Core and $NaYF_4:Yb^{3+}/Er^{3+}@NaYF_4:Nd^{3+}$ Core-Shell Nanoparticles

Both the starting $NaYF_4:Yb^{3+}/Er^{3+}$ core and $NaYF_4:Yb^{3+}/Er^{3+}@NaYF_4:Nd^{3+}$ core-shell nanoparticles were synthesized in a high-boiling organic solvent (octadec-1-ene) in the presence of oleic acid (OA) as a stabilizer by high-temperature coprecipitation of lanthanide chlorides with different amounts of shell precursors.

The $NaYF_4:Yb^{3+}/Er^{3+}$ core was composed of an optically inert $NaYF_4$ host matrix and optically active sensitizer (Yb^{3+}) and activator (Er^{3+}), enabling excitation at 980 nm. The size distribution and average size of the nanoparticles were determined from the TEM/BF micrographs (**Figure 1**). The cores were spherical in shape with number-average diameter $D_n = 24.2 \pm 0.9$ nm and high uniformity ($Đ = 1$; **Figures 1A,F**). These cores served as seeds for the subsequent synthesis of differently thick $NaYF_4:Nd^{3+}$ shells to introduce a second sensitizer (Nd^{3+}) into the crystal matrix. The shell played two important roles: (*i*) it prevented surface quenching by passivation of optically active ions on the cores due to enhanced upconversion emission intensity and (*ii*) the presence of the Nd^{3+} sensitizer in the core-shell matrix enabled excitation of the particles at both 808 and 980 nm. The resulting $NaYF_4:Yb^{3+}/Er^{3+}@NaYF_4:Nd^{3+}$ core-shell nanoparticles were isometric and monodisperse ($Đ < 1.02$). The shell thickness was controlled by the amount of Y and Nd precursors, NaOH, and $NH_4F{\cdot}HF$ used in the synthesis. With increasing concentrations of the abovementioned precursors in the reaction feed and constant amounts of $NaYF_4:Yb^{3+}/Er^{3+}$ seeds, the $NaYF_4:Nd^{3+}$ shell became thicker, the average particle size became larger (D_n = 26–32 nm; **Figures 1B–E,G–J**; **Table S1**), and the Nd content in the particles increased, as determined by TEM/EDX analysis (**Figure S1**).

The crystalline structure corresponding to the hexagonal β-$NaYF_4$ phase was the same in all synthesized particles, as indicated by the very similar TEM/SAED patterns (**Figure 1**, insets in the TEM/BF micrographs). The diffraction positions were the same, and only their intensities slightly changed, which could be attributed to increasing preferred orientation, as will be discussed below. Representative TEM/EDX spectra and TEM/SAED analyses of starting $NaYF_4$:Yb^{3+}/Er^{3+} and $NaYF_4$:Yb^{3+}/Er^{3+}@$NaYF_4$:Nd^{3+} core-shell particles containing 0.5 mmol $NaYF_4$:Nd^{3+} confirmed the expected elemental composition of the nanoparticles (**Figure 2**). The TEM/EDX spectrum of $NaYF_4$:Yb^{3+}/Er^{3+} nanoparticles showed strong peaks of the main Na, Y, and F elements, a weaker Yb peak, and C and Cu peaks from the standard supporting carbon-coated copper TEM grid (**Figure 2A**). Two smaller peaks (Si and O at 1.74 and 0.52 eV, respectively) were attributed to a small amount of impurities, probably dust; the concentration of Si was <0.5%, and the content of Er was below the detection limit of the measurement. The spectrum of the $NaYF_4$:Yb^{3+}/Er^{3+}@$NaYF_4$:Nd^{3+} nanoparticles (0.5 mmol of $NaYF_4$:Nd^{3+}) contained additional Nd peaks and almost no signs of impurities (negligible amount of Si; **Figure 2C**). Note that the heights of the C and Cu peaks in the TEM/EDX spectra were somewhat arbitrary, depending on the relative amount of nanoparticles and the vicinity of the Cu mesh at a given location on the TEM grid. The experimental TEM/SAED diffraction patterns (**Figures 2B,D**; dashed lines) were compared to the theoretically calculated powder X-ray diffraction (PXRD) patterns of β-$NaYF_4$ (**Figures 2B,D**; full lines). Perfect agreement between the SAED and PXRD diffraction positions confirmed that all particles exhibited a hexagonal β-$NaYF_4$ phase structure. Differences among the diffraction intensities of the two particle types and the theoretically calculated PXRD diffractogram of β-$NaYF_4$ could be attributed to the preferred orientation. The smallest $NaYF_4$:Yb^{3+}/Er^{3+} nanocrystals were spherical, with random orientation, and, consequently, they exhibited almost the same SAED and PXRD diffraction intensities (**Figure 2B**). The larger $NaYF_4$:Yb^{3+}/Er^{3+}@$NaYF_4$:Nd^{3+} nanocrystals with 0.5 mmol of $NaYF_4$:Nd^{3+} were slightly faceted, with a tendency to lie on the facets; as a result, their orientation on the supporting carbon film was no longer random. The two strongest diffractions were (100) and (110), suggesting a preferred orientation with zone axis $[uvw] = [001]$ (**Figure 2D**); calculation of the zone axis from a pair of strong diffractions has been described elsewhere (Andrews et al., 1967; Beeston et al., 1972). The strongest peaks on the diffraction pattern should obey the Weiss zone law (WZL): $hu + kv + lw = 0$, where (h, k, l) are the diffraction indices of the planes, and $[u, v, w]$ are the indices of the zone axis (Andrews et al., 1967). If the zone axis $[uvw] = [001]$, the WZL takes a simple form $l = 0$, which means that the strongest diffractions should be of the (hk0) type. The diffractions of this type are marked in bold font in **Figures 2B,D**. For the core $NaYF_4$:Yb^{3+}/Er^{3+} nanocrystals, the intensity of (hk0) diffraction was comparable to that of other diffractions; the small intensity discrepancies could be attributed to the intrinsic differences between the SAED and PXRD methods and possible experimental errors (**Figure 2B**). For the $NaYF_4$:Yb^{3+}/Er^{3+}@$NaYF_4$:Nd^{3+} core-shell nanoparticles with 0.5 mmol of $NaYF_4$:Nd^{3+}, the (hk0) diffractions were stronger than both the theoretically calculated PXRD intensities (note that the SAED and PXRD diffractograms were normalized to the intensity of the strongest (110) diffraction) and experimentally determined SAED intensities of other diffractions of the general type (hkl). This consistent result confirmed the correctness of the TEM/SAED analysis. The enhanced relative intensity of the (hk0) diffractions corresponded to an increasing trend of forming faceted nanocrystals at higher Nd concentrations (**Figure 1**).

Surface Engineering of $NaYF_4$:Yb^{3+}/Er^{3+} and $NaYF_4$:Yb^{3+}/Er^{3+}@$NaYF_4$:Nd^{3+} Nanoparticles

The starting $NaYF_4$:Yb^{3+}/Er^{3+} core and $NaYF_4$:Yb^{3+}/Er^{3+}@$NaYF_4$:Nd^{3+} core-shell nanoparticles stabilized by OA are well-dispersible in a non-polar medium, e.g., hexane. However, before nanoparticle modification, to make them dispersible in aqueous media, as required for biological and/or medical applications, OA has to be removed from the surface by thorough washing with ethanol and water. After washing, the hydrodynamic diameters of the $NaYF_4$:Yb^{3+}/Er^{3+} core and $NaYF_4$:Yb^{3+}/Er^{3+}@$NaYF_4$:Nd^{3+} core-shell particles in water were 185 and 195 nm, respectively, with rather low polydispersity ($PD = 0.16$ and 0.18; **Figures S2a,b**). This observation was in agreement with the monodispersity of $NaYF_4$:Yb^{3+}/Er^{3+} and $NaYF_4$:Yb^{3+}/Er^{3+}@$NaYF_4$:Nd^{3+} particles in water measured by TEM/BF (**Figures S3a,c,e,g**). Note that the nanoparticle size and shape were not affected by washing. It is not surprising that $D_h > D_n$, as the former was measured in water and represented an intensity-based mean diameter that is sensitive to the presence of large particles, while the latter was sensitive to small particles and was analyzed in a dry state; moreover, a partial particle aggregation in water could also increase the size. The surface charge of both core and core-shell particles was positive ($\zeta = 37$ and 41 mV, respectively) due to the presence of lanthanide atoms on the surface. Such a high ζ-potential supports particle repulsion, ensuring good colloidal stability in water; let us note that particles with ζ-potential <30 mV typically have a tendency to aggregate (Lowry et al., 2016). Though the purified $NaYF_4$:Yb^{3+}/Er^{3+} and $NaYF_4$:Yb^{3+}/Er^{3+}@$NaYF_4$:Nd^{3+} particles were well-dispersible in water, they irreversibly aggregated in PBS used in biomedical applications. Therefore, we modified the $NaYF_4$:Yb^{3+}/Er^{3+} and $NaYF_4$:Yb^{3+}/Er^{3+}@$NaYF_4$:Nd^{3+} nanoparticle surfaces with both Ner-$PEG_{3,815}$-Alk and Ner-$PEG_{5,475}$-Alk. The size and shape of the modified nanoparticles remained the same as those measured by TEM/BF (**Figures S3b,d,f,h**). After modification with Ner-$PEG_{3,815}$-Alk, the hydrodynamic particle diameter of $NaYF_4$:Yb^{3+}/Er^{3+} and $NaYF_4$:Yb^{3+}/Er^{3+}@$NaYF_4$:Nd^{3+} in water decreased from 185 and 195 nm to 86 and 110 nm, respectively, with $PD = 0.14$ and 0.13 (**Figures S2c,e**); if the particles were modified with Ner-$PEG_{5,475}$-Alk, their D_h reached 92 and 116 nm, respectively, with $PD = 0.12$ (**Figures S2d,f**). The ζ-potential

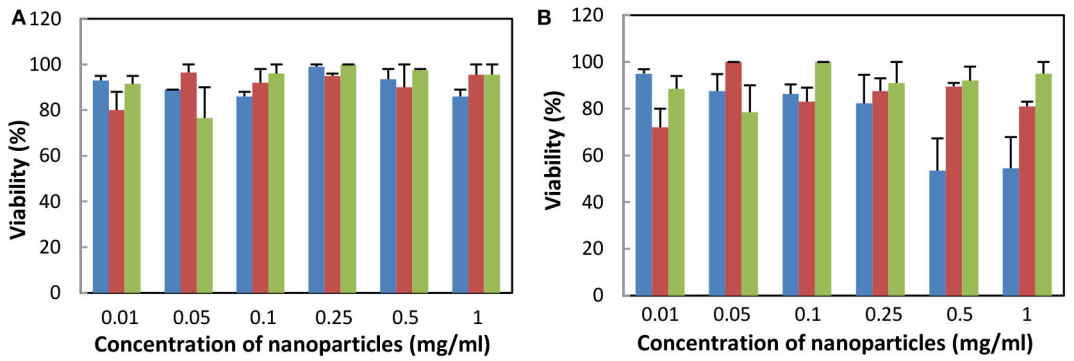

FIGURE 3 | Dependence of viability of **(A)** Hep-G2 and **(B)** HeLa cells on the concentration of $NaYF_4:Yb^{3+}/Er^{3+}@NaYF_4:Nd^{3+}$ (blue), $NaYF_4:Yb^{3+}/Er^{3+}@NaYF_4:Nd^{3+}$-$PEG_{5,475}$-Alk (red), and $NaYF_4:Yb^{3+}/Er^{3+}@NaYF_4:Nd^{3+}$-$PEG_{5,475}$-RGDS nanoparticles (green) using the trypan blue exclusion test. All differences between data were statistically non-significant, except for blue vs. other two bars at concentration 0.5 and 1 mg/ml for Hela cells, where $P < 0.01$.

of the $NaYF_4:Yb^{3+}/Er^{3+}$-$PEG_{3,815}$-Alk and $NaYF_4:Yb^{3+}/Er^{3+}$-$PEG_{5,475}$-Alk particles decreased to 9 and 5 mV, respectively, while that of $NaYF_4:Yb^{3+}/Er^{3+}@NaYF_4:Nd^{3+}$-$PEG_{3,815}$-Alk and $NaYF_4:Yb^{3+}/Er^{3+}@NaYF_4:Nd^{3+}$-$PEG_{5,475}$-Alk particles was only 2 and 4 mV, respectively. The nearly neutral surface charge of the PEGylated UCNPs, compared to the highly positive unmodified nanoparticles, indicated successful surface modification of the particles by PEG.

The colloidal stability of the particles was further investigated in 0.01 M PBS buffer used in experiments with cells and animals. Here, aggregation of the starting $NaYF_4:Yb^{3+}/Er^{3+}$ core and $NaYF_4:Yb^{3+}/Er^{3+}@NaYF_4:Nd^{3+}$ core-shell nanoparticles was due to the chelation of phosphates to lanthanides exposed on the particle surface and the relatively high ionic strength of PBS compared to water. In contrast, the colloidal stability of PEGylated nanoparticles in PBS remained similar to that in water, reaching D_h = 90 and 126 nm with PD = 0.13 and 0.15 for $NaYF_4:Yb^{3+}/Er^{3+}$-$PEG_{3,815}$-Alk and $NaYF_4:Yb^{3+}/Er^{3+}@NaYF_4:Nd^{3+}$-$PEG_{3,815}$-Alk, respectively (**Figures S2c,e**). According to the DLS measurements, the $NaYF_4:Yb^{3+}/Er^{3+}$-$PEG_{5,475}$-Alk and $NaYF_4:Yb^{3+}/Er^{3+}@NaYF_4:Nd^{3+}$-$PEG_{5,475}$-Alk particles had D_h = 93 and 129 nm, respectively, with PD = 0.13 (**Figures S2d,f**). This result shows that modification by Ner-PEG-Alk endowed the UCNPs with colloidal stability even in PBS due to the strong binding of neridronate to their surface and highly efficient steric stabilization by PEG.

The presence of functional alkyne groups on the UCNP surface is necessary to facilitate efficient conjugation of targeting moieties, such as peptides, vitamins, or antibodies. In this report, arginine-glycine-aspartic acid (RGD) peptide was used as a model biomolecule that was conjugated to the nanoparticle surface via copper (I)-catalyzed azide-alkyne 1,3-cycloaddition (click reaction). Compared to conventional bioconjugation reactions, the click reaction is beneficial due to its high selectivity, high reaction yield, and use of ambient reaction conditions, i.e., RT and aqueous media. After conjugation, the resulting $NaYF_4:Yb^{3+}/Er^{3+}@NaYF_4:Nd^{3+}$-$PEG_{5,475}$-RGDS nanoparticles were colloidally stable in water and 0.01 M PBS, reaching D_h = 116 and 130 nm, respectively, with PD = 0.14 and 0.13 (**Figure S2g**).

To further confirm the particle surface modification, ATR FTIR spectra of the unmodified and PEGylated $NaYF_4:Yb^{3+}/Er^{3+}$ core and $NaYF_4:Yb^{3+}/Er^{3+}@NaYF_4:Nd^{3+}$ core-shell particles were acquired (**Figures S4a,b**). The spectrum of the unmodified nanoparticles displayed characteristic bands of oleyl groups at 2,927 and 2,854 cm^{-1} attributed to asymmetric and symmetric CH_2 stretching vibrations (Shukla et al., 2003). The intensity of the characteristic OA bands was low, especially in the spectrum of the $NaYF_4:Yb^{3+}/Er^{3+}@NaYF_4:Nd^{3+}$ core-shell nanoparticles (**Figure S4b**, black line), due to the removal of OA adsorbed during the synthesis, thus confirming the efficacy of the washing procedure. After particle surface modification by Ner-$PEG_{3,815}$-Alk and Ner-$PEG_{5,475}$-Alk, the FTIR spectra revealed strong peaks at 2,886, 1,467, 1,342, 1,284, 1,112, 960, and 844 cm^{-1} (**Figures S4a,b**), which confirmed the presence of PEG on both the $NaYF_4:Yb^{3+}/Er^{3+}$ core and $NaYF_4:Yb^{3+}/Er^{3+}@NaYF_4:Nd^{3+}$ core-shell nanoparticles, in agreement with analogous modification of silver nanoparticles by PEG (Shameli et al., 2012). Although all the particles were lyophilized after washing and dialysis, residual water was still adsorbed on the particles, as the ATR FTIR spectra contained broad peaks of water O-H stretching vibrations in the 3,700–3,100 cm^{-1} region. The intensities of the water bands were low compared to the intensities of the other bands.

TGA of both unmodified and $PEG_{3,815}$- or $PEG_{5,475}$-coated $NaYF_4:Yb^{3+}/Er^{3+}$ core and $NaYF_4:Yb^{3+}/Er^{3+}@NaYF_4:Nd^{3+}$ core-shell nanoparticles was used to determine weight changes due to polymer decomposition at temperatures ranging from 25 to 600°C (**Figures S4c,d**). Residual water that was evaporated up to 150°C amounted to 0.5–5 wt.%, while OA on the $NaYF_4:Yb^{3+}/Er^{3+}$ core and $NaYF_4:Yb^{3+}/Er^{3+}@NaYF_4:Nd^{3+}$ core-shell nanoparticles decomposed at 300–400°C, reaching 3.5 and 2 wt.%, respectively. Thermal decomposition of PEG on the PEGylated particles started at 200°C and was completed at 500°C. The weight loss corresponded to 15 and 20 wt.% $PEG_{3,815}$

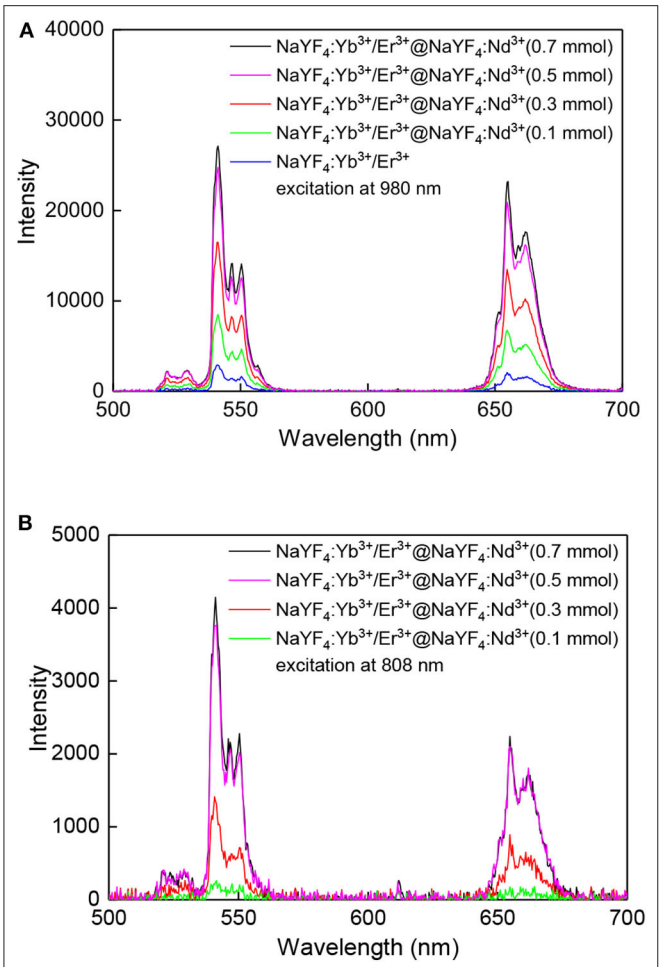

FIGURE 4 | Upconversion photoluminescence spectra of nanoparticles (1 mg/ml) in hexane/water emulsion stabilized with Igepal CO-520 at **(A)** 980 and **(B)** 808 nm excitation; average power density of both lasers ~30 W/cm^2.

or 21 and 25 wt.% $PEG_{5,475}$ in the $NaYF_4$:Yb^{3+}/Er^{3+}-$PEG_{3,815}$-Alk core and $NaYF_4$:Yb^{3+}/Er^{3+}@$NaYF_4$:Nd^{3+}-$PEG_{3,815}$-Alk core-shell or $NaYF_4$:Yb^{3+}/Er^{3+}-$PEG_{5,475}$-Alk core and $NaYF_4$:Yb^{3+}/Er^{3+}@$NaYF_4$:Nd^{3+}-$PEG_{5,475}$-Alk core-shell nanoparticles, respectively. This result means that more PEG molecules were bound on the $NaYF_4$:Yb^{3+}/Er^{3+}@$NaYF_4$:Nd^{3+}-PEG-Alk core-shell nanoparticles than on the $NaYF_4$:Yb^{3+}/Er^{3+}-PEG-Alk core particles (by ~5 wt.%), which can be explained by size effects. Moreover, $PEG_{5,475}$ was superior to $PEG_{3,815}$ in terms of efficient particle surface modification, and therefore the $NaYF_4$:Yb^{3+}/Er^{3+}@$NaYF_4$:Nd^{3+}-$PEG_{5,475}$-Alk core-shell nanoparticles were preferred in the subsequent biological experiments.

Cytotoxicity of Particles

As the developed UCNPs are prospectively intended for photodynamic therapy of tumors, Hep-G2 and HeLa cancer cell lines were selected for cytotoxicity investigation using a trypan blue exclusion test (**Figure 3**). Trypan blue, a hydrophilic tetrasulfonated anionic dye containing two azo chromophores, is commonly used to selectively detect dead cells. Incubation and/or penetration of $NaYF_4$:Yb^{3+}/Er^{3+}@$NaYF_4$:Nd^{3+}, $NaYF_4$:Yb^{3+}/Er^{3+}@$NaYF_4$:Nd^{3+}-$PEG_{5,475}$-Alk, and $NaYF_4$:Yb^{3+}/Er^{3+}@$NaYF_4$:Nd^{3+}-$PEG_{5,475}$-RGDS nanoparticles (0–1 mg/ml) in the cells for 72 h virtually did not decrease their viability. The possible viability variations were within statistical error. Decrease of HeLa cell viability was observed only at a high concentration of the $NaYF_4$:Yb^{3+}/Er^{3+}@$NaYF_4$:Nd^{3+} particles (>0.5 mg/ml). Amounts of the nanoparticles >1 mg/ml could affect dilution of the culture medium, possibly skewing the results of the cytotoxicity assay. The results were comparable with those from previous studies (Kostiv et al., 2015), demonstrating the biocompatibility of the particles in the above concentration range. For further cell monitoring, particle concentrations that did not affect Hep-G2 viability were used.

Upconversion Photoluminescence of $NaYF_4$:Yb^{3+}/Er^{3+} Core and $NaYF_4$:Yb^{3+}/Er^{3+}@$NaYF_4$:Nd^{3+} Core-Shell Nanoparticles at 808 and 980 nm Excitation

To investigate the optical properties of the $NaYF_4$:Yb^{3+}/Er^{3+} core and $NaYF_4$:Yb^{3+}/Er^{3+}@$NaYF_4$:Nd^{3+} core-shell nanoparticles, their upconversion photoluminescence spectra were measured at both 808 and 980 nm excitation wavelengths. Due to colloidal instability and sedimentation of the particles in hexane, a hexane/water emulsion stabilized with Igepal CO-520 was prepared for optical analysis. The particles dispersed in hexane quickly settled down, which decreased the intensity of the detected light. For example, the luminescence intensity of $NaYF_4$:Yb^{3+}/Er^{3+}@$NaYF_4$:Nd^{3+} (0.5 mmol) core-shell nanoparticles in hexane (1 mg/ml) decreased by 10-fold after 30 min, while nanoparticles dispersed in hexane/water emulsion stabilized with Igepal CO-520 exhibited similar luminescence intensities during the experiments (**Figure S5**). Therefore, all the photoluminescence spectra were measured in hexane/water emulsion with a concentration of 1 mg of particles/ml and a power density of ~30 W/cm^2 at both 808 and 980 nm excitation wavelengths. Lasers were warmed-up for 30 min prior measurements and the laser power was monitored continuously during the experiment. To ensure that the luminescence intensity was not affected by variations in the particle concentration, spectra of all samples were measured in triplicate.

The emission spectra acquired at 980 nm excitation wavelength showed typical emission lines of Er^{3+} at 520 nm ($^2H_{11/2} \rightarrow {}^2I_{15/2}$), 541 nm ($^4S_{3/2} \rightarrow {}^2I_{15/2}$), and 655 nm ($^4F_{9/2} \rightarrow {}^2I_{15/2}$) (**Figure 4**). After growth of the $NaYF_4$:Nd^{3+} shell around the $NaYF_4$:Yb^{3+}/Er^{3+} core, the emission intensity of green and red light of $NaYF_4$:Yb^{3+}/Er^{3+}@$NaYF_4$:Nd^{3+}(0.1 mmol), $NaYF_4$:Yb^{3+}/Er^{3+}@$NaYF_4$:Nd^{3+}(0.3 mmol), $NaYF_4$:Yb^{3+}/Er^{3+}@$NaYF_4$:Nd^{3+}(0.5 mmol) and $NaYF_4$:Yb^{3+}/Er^{3+}@$NaYF_4$:Nd^{3+}(0.7 mmol) increased by 2.9×, 5.7×, 8.6×, and 9.4× and by 3.3×, 6.6×, 10.5×, and 11.9×, respectively, compared to that of the starting $NaYF_4$:Yb^{3+}/Er^{3+}

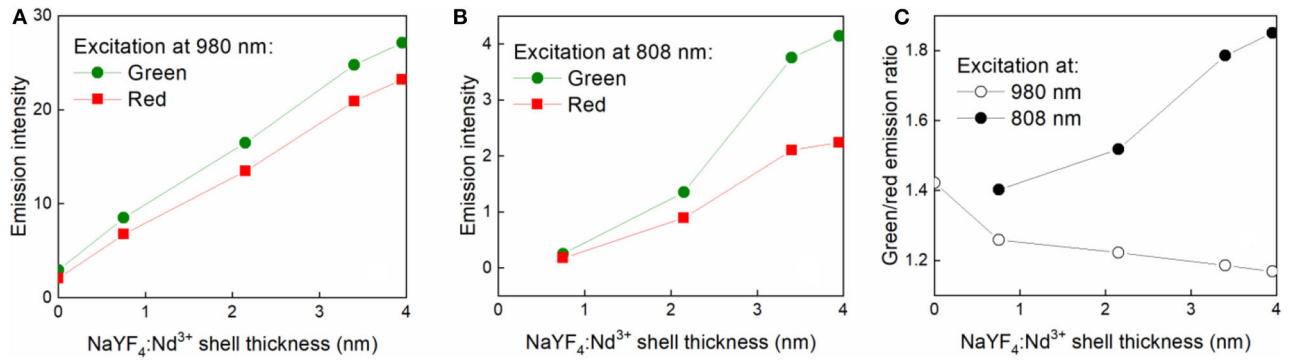

FIGURE 5 | Dependence of green (541 nm) and red (655 nm) emission intensity of nanoparticles (1 mg/ml) in hexane/water emulsion stabilized with Igepal CO-520 on $NaYF_4:Nd^{3+}$ shell thickness at **(A)** 980 and **(B)** 808 nm excitation. **(C)** Gresen-to-red emission intensity ratio for different excitation wavelengths measured for different shell thickness; average power density of both lasers ~30 W/cm^2.

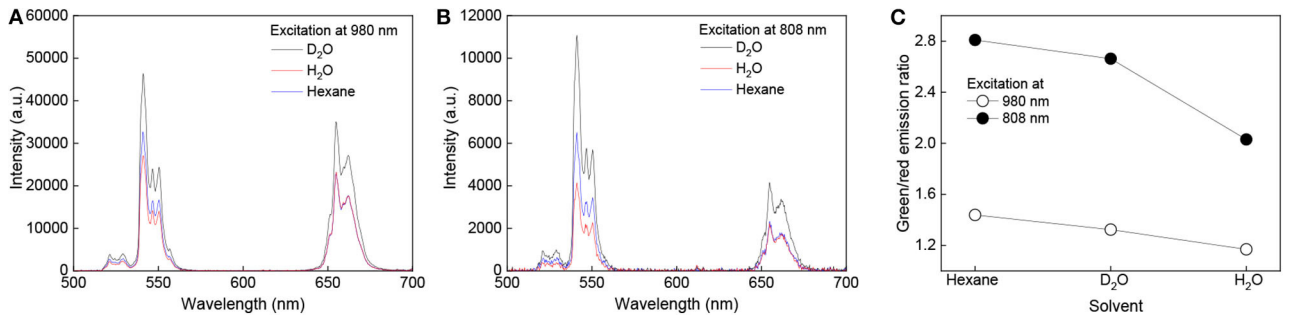

FIGURE 6 | Photoluminescence upconversion spectra of $NaYF_4:Yb^{3+}/Er^{3+}@NaYF_4:Nd^{3+}$(0.7 mmol) core-shell nanoparticles (1 mg/ml) in D_2O (black), water (red), and hexane (blue) at **(A)** 808 and **(B)** 980 nm excitation. **(C)** Green-to-red emission intensity ratio for different solvents; average power density of both lasers ~30 W/cm^2.

cores (**Figure 4A**). This increase was linear for both green and red light (**Figure 5A**). It is worth of mentioning that this dependence can differ for various Yb/Er ratios and UCNP sizes, as shown in our previous paper (Podhorodecki et al., 2018). Under 808 nm excitation, characteristic peaks of green and red light originating from Er^{3+} ions were observed in the spectrum of the $NaYF_4:Yb^{3+}/Er^{3+}@NaYF_4:Nd^{3+}$(0.1 mmol) nanoparticles. With increasing shell thickness in the $NaYF_4:Yb^{3+}/Er^{3+}@NaYF_4:Nd^{3+}$(0.3 mmol), $NaYF_4:Yb^{3+}/Er^{3+}@NaYF_4:Nd^{3+}$(0.5 mmol), and $NaYF_4:Yb^{3+}/Er^{3+}@NaYF_4:Nd^{3+}$(0.7 mmol) particles, the intensity of green and red emission increased by 5.5×, 15.3×, and 16.9× and by 5.1×, 12.1×, and 12.9×, respectively, compared to that of the $NaYF_4:Yb^{3+}/Er^{3+}@NaYF_4:Nd^{3+}$(0.1 mmol) particles (**Figure 4B**). The largest intensity increase in green and red emission was observed in the $NaYF_4:Yb^{3+}/Er^{3+}@NaYF_4:Nd^{3+}$(0.5 mmol) particles, while it was smallest in the $NaYF_4:Yb^{3+}/Er^{3+}@NaYF_4:Nd^{3+}$(0.7 mmol) particles (**Figure 5B**). This result can be explained by small diffusion efficiency of Nd^{3+} ions at the core-shell interface and small number of Nd^{3+} ions at low concentration in the shell. This reduces efficient energy transfer from Nd^{3+} to Er^{3+} ions located in UCNP core. Increasing Nd^{3+} concentration increases the probability of non-radiative energy transfer as the intermixing becomes more efficient and number Nd^{3+} ions increases as well. Green/red emission intensity ratio was significantly different at different excitation wavelengths (**Figures 5C**, **6C**). The 808 nm excitation wavelength favored green luminescence. As expected, effect was stronger with increasing shell thickness, due to higher Nd^{3+} content in UCNPs. Let us note that intensity of the photoluminescence emission at 808 nm excitation was lower compared to 980 nm excitation (**Figure 4**). This difference can be attributed to different amount of Nd^{3+} and Yb^{3+} ions in the core-shell structure of the $NaYF_4:Yb^{3+}/Er^{3+}@NaYF_4:Nd^{3+}$ nanoparticles. The Yb^{3+} ions that absorb light at 980 nm were present in the core, while the Nd^{3+} ions, absorbing photons at 808 nm and transferring the absorbed energy to Yb^{3+}, were localized in the shell. The $NaYF_4:Nd^{3+}$ shell, which protects the particle surface from quenchers, facilitates enhancement of upconversion photoluminescence at 980 nm; at the same time, the presence of Nd^{3+} ions in the shell allows excitation at 808 nm, though these ions remain vulnerable to the surface quenchers. This, and additional energy losses during energy transfer between Nd^{3+} and Yb^{3+} ions, can explain the observed lower photoluminescence emission intensity at 808 nm compared to 980 nm excitation.

The upconversion photoluminescence spectra of the $NaYF_4:Yb^{3+}/Er^{3+}@NaYF_4:Nd^{3+}$(0.7 mmol) particles (1 mg/ml) were measured in hexane, hexane/water, and hexane/D_2O

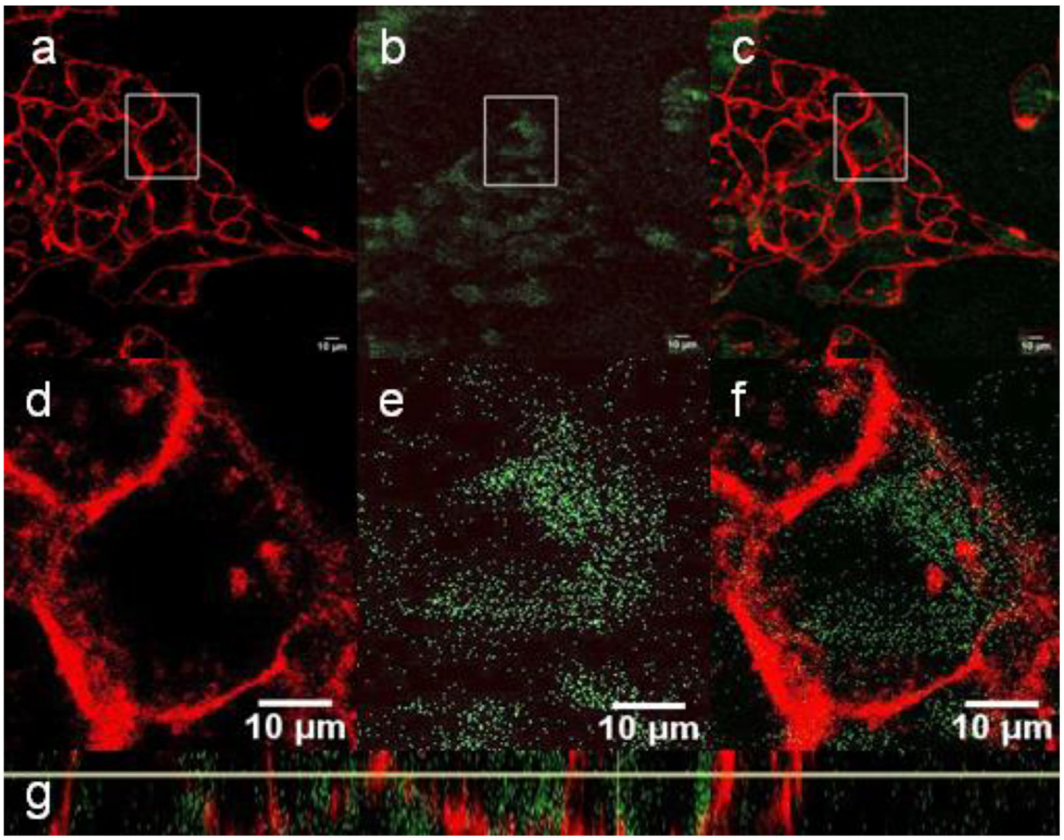

FIGURE 7 | (a–f) Confocal micrographs showing the distribution of $NaYF_4:Yb^{3+}/Er^{3+}@NaYF_4:Nd^{3+}$ nanoparticles (200 μl) in Hep-G2 cells at 980 nm excitation with a laser power of 30–50 mW. **(d–f)** Detailed micrographs of **(a–c)**. **(a,d)** CellMask™ deep red cell-stained cell membrane, **(b,e)** nanoparticles (green), and **(c,f)** overlay of **(a,b,d,e)**. **(g)** The xz-plane of $NaYF_4:Yb^{3+}/Er^{3+}@NaYF_4:Nd^{3+}$ nanoparticle-labeled Hep-G2 cells.

emulsions at 808 and 980 nm excitation and power density ~30 W/cm^2. Significant enhancement of the luminescence intensity was observed in hexane and hexane/D_2O compared to that in hexane/water emulsion. The green luminescence intensity of $NaYF_4:Yb^{3+}/Er^{3+}@NaYF_4:Nd^{3+}$ (0.7 mmol) in hexane/D_2O emulsion and hexane at 808 nm excitation was ~2.7- and 1.6-fold higher, respectively, than that of particles dispersed in hexane/water emulsion (**Figure 6A**). This enhancement can be explained by substitution of the O-H luminescence quencher with O-D. The energy of the O-D stretching vibration (2,500 cm^{-1}) is lower than that of O-H (3,450 cm^{-1}), which leads to a decrease in multiphoton relaxation rate in the case of D_2O and enhancement of luminescence (Luwang et al., 2010). The same mechanism could also explain the high luminescence intensity of the $NaYF_4:Yb^{3+}/Er^{3+}@NaYF_4:Nd^{3+}$ (0.7 mmol) particles in hexane. Additionally, in this case, the energy of the C-H stretching vibration (2,900 cm^{-1}) is lower than that of O-H and thus more phonons are needed in hexane to dissipate the excitation energy and depopulate excited carriers from green to red energy level (**Figure 6C**). This makes green emission more intense. The effect is stronger under excitation at 808 nm due to the proximity of the luminescence sensitizer (Nd^{3+}) and solvent molecules. In the case of 980 nm excitation, the green luminescence intensity was 7 × and 1.2 × higher in the hexane/D_2O emulsion and hexane, respectively, due to the small effect of hexane on the Yb^{3+} ions (**Figure 6B**).

UCNP Upconversion Spectra With a Pulsed Excitation

Upconversion luminescence of the $NaYF_4:Yb^{3+}/Er^{3+}@NaYF_4:Nd^{3+}$, $NaYF_4:Yb^{3+}/Er^{3+}@NaYF_4:Nd^{3+}$-$PEG_{5,475}$, and $NaYF_4:Yb^{3+}/Er^{3+}@NaYF_4:Nd^{3+}$-$PEG_{5,475}$-RGDS nanoparticles was confirmed by the emission spectra at 980 nm obtained with excitation by 140 fs pulses (**Figure S6**). The particles exhibited two typical upconversion peaks at 535 and 635 nm (Kostiv et al., 2015).

Cell Monitoring

In this set of experiments, Hep-G2 cells were incubated with all types of nanoparticles to monitor their cell distribution by confocal microscopy. Various volumes of the particle dispersions (20, 40, 60, 100, and 200 μl) were added to the DMEM-based medium containing the cells. A volume amounting to 200 μl was found to be optimal, avoiding damage to cells and at the same

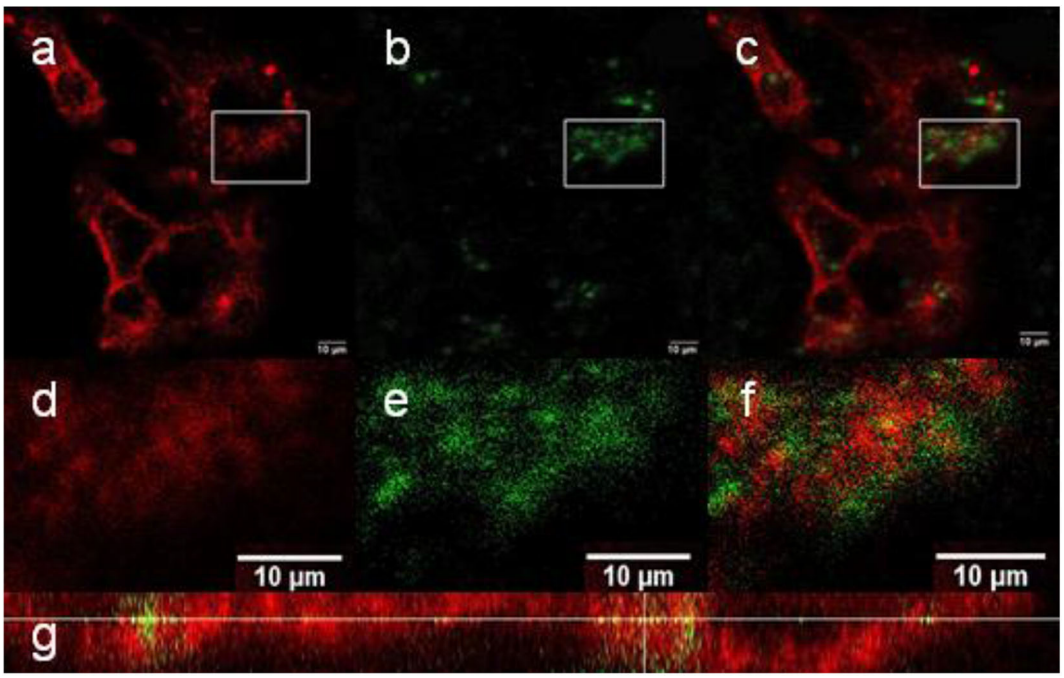

FIGURE 8 | (a–f) Confocal micrographs showing the distribution of $NaYF_4:Yb^{3+}/Er^{3+}@NaYF_4:Nd^{3+}$-$PEG_{5,475}$-RGDS nanoparticles in Hep-G2 cells at 980 nm excitation with a laser power of 30–50 mW. **(d–f)** Detailed micrographs of **(a–c)**. **(a,d)** CellMask™ deep red cell-stained cell membrane, **(b,e)** nanoparticles, and **(c,f)** overlay of **(a,b,d,e)**. **(g)** The xz-plane of $NaYF_4:Yb^{3+}/Er^{3+}@NaYF_4:Nd^{3+}$-$PEG_{5,475}$-RGDS nanoparticle-labeled Hep-G2 cells.

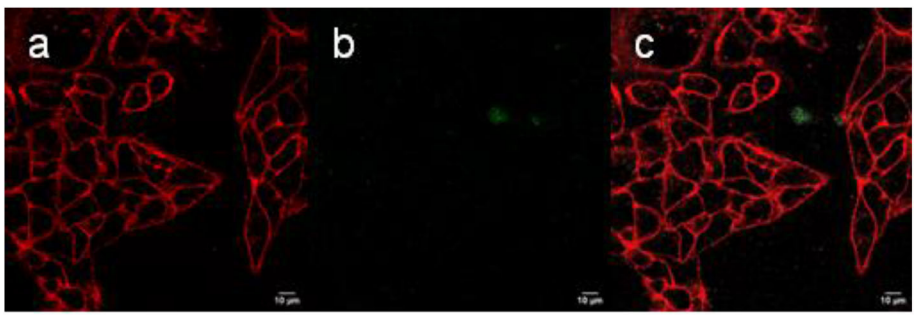

FIGURE 9 | (a–c) Confocal micrographs showing the distribution of $NaYF_4:Yb^{3+}/Er^{3+}@NaYF_4:Nd^{3+}$-$PEG_{5,475}$-Alk nanoparticles in Hep-G2 cells at 980 nm excitation with a laser power of 30–50 mW. **(a)** CellMask™ deep red cell-stained cell membrane, **(b)** nanoparticles, and **(c)** overlay of **(a,b)**.

time providing good particle visibility; this volume was therefore used in further biological experiments.

Upconversion luminescence was determined after incubation of the $NaYF_4:Yb^{3+}/Er^{3+}@NaYF_4:Nd^{3+}$, $NaYF_4:Yb^{3+}/Er^{3+}@NaYF_4:Nd^{3+}$-$PEG_{5,475}$, and $NaYF_4:Yb^{3+}/Er^{3+}@NaYF_4:Nd^{3+}$-$PEG_{5,475}$-RGD particles with Hep-G2 cells, the membranes of which were stained with CellMask™ deep red. Localization of the particles in the cells was demonstrated within the confocal plane by confocal microscopy in the range of 500-670 nm using z-scan via the xy and xz plane, as exemplified on the $NaYF_4:Yb^{3+}/Er^{3+}@NaYF_4:Nd^{3+}$ particles (**Figure 7**). This approach allowed us to determine the biodistribution of the particles, particularly on the cell membrane and in the cell cytosol. Since the emission spectra of nanoparticles in the cells at 535 and 640 nm under 980 nm pulsed excitation with 140 fs pulses corresponded to those of neat particles, the presence of $NaYF_4:Yb^{3+}/Er^{3+}@NaYF_4:Nd^{3+}$ particles in the Hep-G2 cells was proven (**Figure S6**). Moreover, penetration of the $NaYF_4:Yb^{3+}/Er^{3+}@NaYF_4:Nd^{3+}$ nanoparticles into the cells was confirmed by particle localization inside the cells, which were contoured in their plasma membranes by CellMask™ deep red. Artificial nanoparticle adherence to the top of cell

surface is excluded by colocalization of the two confocal images of cell section (nanoparticle emission vs. CellMask™ deep red emission) within the xz plane (**Figure 7g**).

In contrast to the $NaYF_4:Yb^{3+}/Er^{3+}@NaYF_4:Nd^{3+}$ nanoparticles, the $NaYF_4:Yb^{3+}/Er^{3+}@PEG_{5,475}$-RGDS nanoparticles adhered to the cell membrane (**Figure 8**), while the $NaYF_4:Yb^{3+}/Er^{3+}@NaYF_4:Nd^{3+}$-$PEG_{5,475}$-Alk particles were located outside of the cells (**Figure 9**). Colocalization of the $NaYF_4:Yb^{3+}/Er^{3+}@PEG_{5,475}$-RGDS particles with CellMask™ deep red-marked cell membranes was apparent only within the xz plane (**Figure 8g**). Hence, unlike to the $NaYF_4:Yb^{3+}/Er^{3+}@NaYF_4:Nd^{3+}$ nanoparticles, the $NaYF_4:Yb^{3+}/Er^{3+}@PEG_{5,475}$-RGDS particles were absent inside the cells in the xy images, but colocalizations occurred at the edge of the cells within the xz plane. Finally, colocalizations of $NaYF_4:Yb^{3+}/Er^{3+}@NaYF_4:Nd^{3+}$-$PEG_{5,475}$-Alk nanoparticles were not observed, either intracellularly or within the plasma membrane (**Figure 9**). Both z- and λ-scans (emission spectrum) confirmed that the emission originated from particle upconversion, distinguishing the emission from background cell autofluorescence, as exemplified by the $NaYF_4:Yb^{3+}/Er^{3+}@NaYF_4:Nd^{3+}$ particles (**Figure S6**).

As a result, UCNP surface engineering with PEG and/or RGDS peptide enabled us to target the particles in various cell compartments that are important for prospective biomedical applications, in particular photodynamic therapy of tumors.

CONCLUSIONS

In conclusion, the hexagonal β-$NaYF_4$ phase of $NaYF_4:Yb^{3+}/Er^{3+}@NaYF_4:Nd^{3+}$ core-shell nanoparticles was successfully synthesized by thermal coprecipitation of lanthanide precursors. The number-average size of the core particles was ∼24 nm and the shell thickness could be adjusted in the range of 1–4 nm, depending on the amount of precursors used in the synthesis. The particles were monodisperse, which is important in terms of controlling their properties, reproducible photoluminescence, and improved performance in drug release systems. To make both the starting $NaYF_4:Yb^{3+}/Er^{3+}$ core and $NaYF_4:Yb^{3+}/Er^{3+}@NaYF_4:Nd^{3+}$ core-shell nanoparticles long-term dispersible in PBS, they were coated with in-house synthesized Ner-PEG-Alk. While bisphosphonate terminal groups of neridronate strongly conjugated to the surface of UCNPs, alkyne groups were available for the copper-catalyzed click reaction with azido-RGDS peptide. The presence of PEG on the UCNPs was confirmed by FTIR analysis and TGA, which proved that the $NaYF_4:Yb^{3+}/Er^{3+}@NaYF_4:Nd^{3+}$-$PEG_{5,475}$-Alk nanoparticles contained up to 25 wt.% PEG. Spectroscopic studies showed significant difference in the activator luminescence (Er^{3+}) upon the excitation of the first (Yb^{3+}) and the second (Nd^{3+}) sensitizer. Interestingly, in the latter, the luminescence spectra strongly depended on the shell thickness. Precise control of this parameter could be potentially used for tuning the optical properties of $NaYF_4:Yb^{3+}/Er^{3+}@NaYF_4:Nd^{3+}$ nanoparticles. We have also observed a noticeable $NaYF_4:Yb^{3+}/Er^{3+}@NaYF_4:Nd^{3+}$ luminescence quenching in water, predominantly for the green luminescence bands.

The particles were non-cytotoxic as confirmed by the trypan blue exclusion test. It was interesting to note that the $NaYF_4:Yb^{3+}/Er^{3+}@NaYF_4:Nd^{3+}$ particles were well-internalized by the Hep-G2 cells, while the $NaYF_4:Yb^{3+}/Er^{3+}@NaYF_4:Nd^{3+}$-$PEG_{5,475}$-RGDS nanoparticles accumulated on the cell membranes, which is in contrast to the $NaYF_4:Yb^{3+}/Er^{3+}@NaYF_4:Nd^{3+}$-$PEG_{5,475}$-Alk particles that were neither engulfed by the cells nor tightly adsorbed on the cell membrane surface. This finding confirmed that the RGDS peptide was effective for adhesion of UCNPs to the cell membranes. Specific binding of the $NaYF_4:Yb^{3+}/Er^{3+}@NaYF_4:Nd^{3+}$-$PEG_{5,475}$-RGDS nanoparticles to membranes of various cell types can also be achieved using antibodies, which might be important for addressing specific cell types. In contrast, the $NaYF_4:Yb^{3+}/Er^{3+}@NaYF_4:Nd^{3+}$ particles (without RGDS) could be useful for example for photodynamic therapy (PDT) of tumors, if a proper photosensitizer is attached to the particle coating. PDT with excitation at 808 nm is a newly developing field, as 808 nm light can penetrate tissue up to a depth of 5 cm. Such an application would greatly increase the number of conditions that can be treated using infrared PDT. Moreover, $NaYF_4:Yb^{3+}/Er^{3+}@NaYF_4:Nd^{3+}$-based systems can be prospectively modified to serve as drug delivery vehicles for any general therapy, releasing the attached or adsorbed drug in the affected cells and/or tissues.

DATA AVAILABILITY STATEMENT

All datasets generated for this study are included in the article/**Supplementary Material**.

AUTHOR CONTRIBUTIONS

UK synthesized and characterized the particles. HE cultivated and monitored the cells. BK measured the optical spectra. MŠ investigated morphology and crystal structure of the particles. VP synthesized RGDS peptide. AP measured upconversion photoluminescence spectra. PJ measured upconversion spectra with a pulsed excitation. DH supervised the work and together with UK wrote the publication.

ACKNOWLEDGMENTS

Main financial support of the Czech Science Foundation (19-00676S) was gratefully acknowledged. Electron microscopy was supported by the Technology Agency of the CR (TE01020118) and the Ministry of Education, Youth and Sports (POLYMAT LO1507 program NPU I). Peptide synthesis and click bioconjugation was supported by the Czech Science Foundation (18-05510S). Czech-Polish exchange visits were supported by the Ministry of Education, Youth and Sports (8JPL19006), the Polish National Agency for Academic Exchange, and the RECOOP HST Association and Cedars-Sinai

Medical Center. Polish authors would like to acknowledge financial support from the Polish National Science Center (Sonata Bis 3 project UMO-2013/10/E/ST5/00651). BK would like to thank the Polish National Science Center FUGA program (UMO 2016/20/S/ST3/00277).

SUPPLEMENTARY MATERIAL

The Supplementary Material for this article can be found online at: https://www.frontiersin.org/articles/10.3389/fchem.2020.00497/full#supplementary-material

REFERENCES

Andrews, K. W., Dyson, D. J., and Keown, S. R. (1967). *Interpretation of Electron Diffraction Patterns*. *New York*, NY*: Plenum Press.*

Arppe, R., Hyppänen, I., Perälä, N., Peltomaa, R., Kaiser, M., Würth, C., et al. (2015). Quenching of the upconversion luminescence of $NaYF_4$:Yb^{3+},Er^{3+} and $NaYF_4$:Yb^{3+},Tm^{3+} nanophosphors by water: the role of the sensitizer Yb^{3+} in non-radiative relaxation. *Nanoscale* 7, 11746–11757. doi: 10.1039/C5NR02100F

Auzel, F. (2004). Upconversion and anti-stokes processes with f and d ions in solids. *Chem. Rev*. 104, 139–173. doi: 10.1021/cr020357g

Bagheri, N., Liu, Q., Bergstrand, J., Pu, R., Zhan, Q., Ara, M. H. M., et al. (2019). Change in the emission saturation and kinetics of upconversion nanoparticles under different light irradiations. *Opt. Mater*. 97:109389. doi: 10.1016/j.optmat.2019.109389

Beeston, B. E. P., Horne, R., and Markham, R. (1972). *Electron Diffraction and Optical Diffraction Techniques*. Amsterdam: North-Holland Publishing Company.

Chen, G., Damasco, J., Qiu, H., Shao, W., Ohulchanskyy, T. Y., Valiev, R. R., et al. (2015). Energy-cascaded upconversion in an organic dye-sensitized core/shell fluoride nanocrystal. *Nano Lett*. 15, 7400–7407. doi: 10.1021/acs.nanolett.5b02830

Chen, G., Qiu, H., Prasad, P. N., and Chen, X. (2014). Upconversion nanoparticles: design, nanochemistry, and applications in theranostics. *Chem. Rev*. 114, 5161–5214. doi: 10.1021/cr400425h

Duan, C., Liang, L., Li, L., Zhang, R., and Xu, Z. P. (2018). Recent progress in upconversion luminescence nanomaterials for biomedical applications. *J. Mater. Chem. B* 6, 192–209. doi: 10.1039/C7TB02527K

Gee, A., and Xu, X. (2018). Surface functionalisation of upconversion nanoparticles with different moieties for biomedical applications. *Surfaces* 1, 96–121. doi: 10.3390/surfaces1010009

Glasser, L. (2016). Crystallographic information resources. *J. Chem. Educ*. 93, 542–549. doi: 10.1021/acs.jchemed.5b00253

Guerrero-Martinez, A., Perez-Juste, J., and Liz-Marzan, L. M. (2010). Recent progress on silica coating of nanoparticles and related nanomaterials. *Adv. Mater*. 22, 1182–1195. doi: 10.1002/adma.200901263

Kostiv, U., Janoušková, O., Šlouf, M., Kotov, N., Engstová, H., Smolková, K., et al. (2015). Silica-modified monodisperse hexagonal lanthanide nanocrystals: Synthesis and biological properties. *Nanoscale* 7, 18096–18104. doi: 10.1039/C5NR05572E

Kostiv, U., Kotelnikov, I., Proks, V., Šlouf, M., Kučka, J., Engstová, H., et al. (2016). RGDS- and TAT-conjugated upconversion $NaYF_4$:Yb^{3+}/Er^{3+}@SiO_2 nanoparticles: *In vitro* human epithelioid cervix carcinoma cellular uptake, imaging and targeting. *ACS Appl. Mater. Interfaces* 8, 20422–20431. doi: 10.1021/acsami.6b07291

Kostiv, U., Lobaz, V., Kučka, J., Švec, P., Sedláček, O., Hrubý, M., et al. (2017c). A simple neridronate-based surface coating strategy for upconversion nanoparticles: Highly colloidally stable ^{125}I-radiolabeled $NaYF_4$:Yb^{3+}/Er^{3+}@PEG nanoparticles for multimodal *in vivo* tissue imaging. *Nanoscale* 9, 16680–16688. doi: 10.1039/C7NR05456D

Kostiv, U., Patsula, V., Noculak, A., Podhorodecki, A., Větvička, D., Poučková, P., et al. (2017a). Phthalocyanine-conjugated upconversion $NaYF_4$:Yb^{3+}/Er^{3+}@SiO_2 nanospheres for NIR-triggered photodynamic therapy in a tumor mouse model. *ChemMedChem* 12, 2066–2073. doi: 10.1002/cmdc.201700508

Kostiv, U., Rajsiglová, L., Luptáková, D., Pluháček, T., Vannucci, L., Havlíček, V., et al. (2017b). Biodistribution of upconversion/magnetic silica-coated $NaGdF_4$:Yb^{3+}/Er^{3+} nanoparticles in mouse models. *RSC Adv*. 7, 45997–46006. doi: 10.1039/C7RA08712H

Kraus, W., and Nolze, G. (1996). POWDER CELL - a program for the representation and manipulation of crystal structures and calculation of the resulting X-ray powder patterns. *J. Appl. Cryst*. 29, 301–303. doi: 10.1107/S0021889895014920

Lábár, J. L. (2005). Consistent indexing of a (set of) SAED pattern(s) with the ProcessDiffraction program. *Ultramicroscopy* 103, 237–249. doi: 10.1016/j.ultramic.2004.12.004

Lahtinen, S., Lyytikäinen, A., Päkkilä, H., Hömppi, E., Perälä, N., Lastusaari, M., et al. (2017). Disintegration of hexagonal $NaYF_4$:Yb^{3+},Er^{3+} upconverting nanoparticles in aqueous media: the role of fluoride in solubility equilibrium. *J. Phys. Chem. C* 121, 656–665. doi: 10.1021/acs.jpcc.6b09301

Lai, J., Zhang, Y., Pasquale, N., and Lee, K. B. (2014). An upconversion nanoparticle with orthogonal emissions using dual NIR excitations for controlled two-way photoswitching. *Angew. Chem*. 126, 14647–14651. doi: 10.1002/ange.201408219

Li, T., Xue, C., Wang, P., Li, Y., and Wu, L. (2017). Photon penetration depth in human brain for light stimulation and treatment: a realistic Monte Carlo simulation study. *J. Innov. Opt. Health Sci*. 10:17430027. doi: 10.1142/S1793545817430027

Liu, X., Zhao, J., Sun, Y., Song, K., Yu, Y., Du, C., et al. (2009). Ionothermal synthesis of hexagonal-phase $NaYF_4$:Yb^{3+},Er^{3+}/Tm^{3+} upconversion nanophosphors. *Chem. Commun*. 43, 6628–6630. doi: 10.1039/b915517a

Lowry, G. V., Hill, R. J., Harper, S., Rawle, A. F., Hendren, C. O., Klaessig, F., et al. (2016). Guidance to improve the scientific value of zeta-potential measurements in nanoEHS. *Environ. Sci. Nano* 3, 953–965. doi: 10.1039/C6EN00136J

Luwang, M. N., Ningthoujam, R. S., Jagannath, Srivastava, S. K., and Vatsa, R.K. (2010). Effects of Ce^{3+} codoping and annealing on phase transformation and luminescence of Eu^{3+}-doped YPO_4 nanorods: D_2O solvent effect. *J. Am. Chem. Soc*. 132, 2759–2768. doi: 10.1021/ja909578s

Mandl, G. A., Cooper, D. R., Hirsch, T., Seuntjens, J., and Capobianco, J. A. (2019). Perspective: lanthanide-doped upconverting nanoparticles. *Methods Appl. Fluoresc*. 7:012004. doi: 10.1088/2050-6120/aafa3d

Mickert, M. J., Farka, Z., Kostiv, U., Hlaváček, A., Horák, D., Skládal, P., et al. (2019). Measurement of sub-femtomolar concentrations of prostate-specific antigen through single-molecule counting with an upconversion-linked immunosorbent assay. *Anal. Chem*. 91, 9435–9441. doi: 10.1021/acs.analchem.9b02872

Muhr, V., Wilhelm, S., Hirsch, T., and Wolfbeis, O. S. (2014). Upconversion nanoparticles: from hydrophobic to hydrophilic surfaces. *Acc. Chem. Res*. 47, 3481–3493. doi: 10.1021/ar500253g

Naccache, R., Yu, Q., and Capobianco, J. A. (2015). The fluoride host: Nucleation, growth, and upconversion of lanthanide-doped nanoparticles. *Adv. Optical. Mater*. 3, 482–509. doi: 10.1002/adom.201400628

Patsula, V., Horák, D., Kučka, J., Macková, H., Lobaz, V., Francová, P., et al. (2019). Synthesis and modification of uniform PEG-neridronate-modified magnetic nanoparticles determines prolonged blood circulation and biodistribution in a mouse preclinical model. *Sci. Rep*. 9:10765. doi: 10.1038/s41598-019-47262-w

Plohl, O., Kralj, S., Majaron, B., Fröhlich, E., Ponikvar-Svet, M., Makovec, D., et al. (2017). Amphiphilic coatings for the protection of upconverting nanoparticles against dissolution in aqueous media. *Dalton Trans*. 46, 6975–6984. doi: 10.1039/C7DT00529F

Podhorodecki, A., Krajnik, B., Golacki, L. W., Kostiv, U., Pawlik, G., Kaczmarek, M., et al. (2018). Percolation limited emission intensity from upconverting $NaYF_4$:Yb^{3+},Er^{3+} nanocrystals – a single nanocrystal optical study. *Nanoscale* 10, 21186–21196. doi: 10.1039/C8NR05961F

Poláchová, V., Pastucha, M., Mikušová, Z., Mickert, M. J., Hlaváček, A., Gorris, H. H., et al. (2019). Click-conjugated photon-upconversion nanoparticles in

an immunoassay for honeybee pathogen *Melissococcus plutonius*. *Nanoscale* 11, 8343–8351. doi: 10.1039/C9NR01246J

Proks, V., Jaros, J., Pop-Georgievski, O., Kucka, J., Popelka, S., Dvorak, P., et al. (2012). "Click & seed" approach to the biomimetic modification of material surfaces. *Macromol. Biosci.* 12, 1232–1242. doi: 10.1002/mabi.201200095

Qin, X., Xu, J., Wu, Y., and Liu, X. (2019). Energy-transfer editing in lanthanide-activated upconversion nanocrystals: a toolbox for emerging applications. *ACS Cent. Sci.* 5, 29–42. doi: 10.1021/acscentsci.8b00827

Sedlmeier, A., and Gorris, H. H. (2015). Surface modification and characterization of photon-upconverting nanoparticles for bioanalytical applications. *Chem. Soc. Rev*. 44, 1526–1560. doi: 10.1039/C4CS00186A

Shameli, K., Ahmad, M. B., Jazayeri, S. D., Sedaghat, S., Shabanzadeh, P., Jahangirian, H., et al. (2012). Synthesis and characterization of polyethylene glycol mediated silver nanoparticles by the green method. *Int. J. Mol. Sci*. 13, 6639–6650. doi: 10.3390/ijms13066639

Shukla, N., Liu, C., Jones, P. M., and Weller, D. (2003). FTIR study of surfactant bonding to FePt nanoparticles. *J. Magn. Magn. Mater*. 266, 178–184. doi: 10.1016/S0304-88530300469-4

Stöber, W., and Fink, A. (1968). Controlled growth of monodisperse silica spheres in the micron size range. *J. Colloid Interface Sci.* 26, 62–69. doi: 10.1016/0021-97976890272-5

Wang, M., Abbineni, G., Clevenger, A., Mao, C., and Xu, S. (2011). Upconversion nanoparticles: synthesis, surface modification and biological applications. *Nanomedicine* 7, 710–729. doi: 10.1016/j.nano.2011.02.013

Wang, R., Li, X., Zhou, L.,., and Zhang, F. (2014). Epitaxial seeded growth of rare-earth nanocrystals with efficient 800 nm near-infrared to 1525 nm short-wavelength infrared downconversion photoluminescence for *in vivo* bioimaging. *Angew. Chem*. 126, 12282–12286. doi: 10.1002/ange.201407420

Wiesholler, L. M., Frenzel, F., Grauel, B., Würth, C., Resch-Genger, U., and Hirsch, T. (2019). Yb,Nd,Er-doped upconversion nanoparticles: 980 nm versus 808 nm excitation. *Nanoscale* 11, 13440–13449. doi: 10.1039/C9NR03127H

Wilhelm, S. (2017). Perspectives for upconverting nanoparticles. *ACS Nano* 11, 10644–10653. doi: 10.1021/acsnano.7b07120

Wilhelm, S., Kaiser, M., Würth, C., Heiland, J., Carrillo-Carrion, C., Muhr, V., et al. (2015). Water dispersible upconverting nanoparticles: effects of surface modification on their luminescence and colloidal stability. *Nanoscale* 7, 1403–1410. doi: 10.1039/C4NR05954A

Wolfbeis, O. S. (2015). An overview of nanoparticles commonly used in fluorescent bioimaging. *Chem. Soc. Rev*. 44, 4743–4768. doi: 10.1039/C4CS00392F

Zhan, Q., Qian, J., Liang, H., Somesfalean, G., Wang, D., He, S., et al. (2011). Using 915 nm laser excited $Tm^{3+}/Er^{3+}/Ho^{3+}$-doped $NaYbF_4$ upconversion nanoparticles for *in vitro* and deeper *in vivo* bioimaging without overheating irradiation. *ACS Nano* 5, 3744–3757. doi: 10.1021/nn200110j

Zhang, Z., Shikha, S., Liu, J., Zhang, J., Mei, Q., and Zhang, Y. (2019). Upconversion nanoprobes: recent advances in sensing applications. *Anal. Chem*. 91, 548–568. doi: 10.1021/acs.analchem.8b04049

Zhou, B., Shi, B., Jin, D., and Liu, X. (2015). Controlling upconversion nanocrystals for emerging applications. *Nat. Nanotechnol*. 10, 924–936. doi: 10.1038/nnano.2015.251

Zhu, X., Su, Q., Feng, W., and Li, F. (2017). Anti-Stokes shift luminescent materials for bio-applications. *Chem. Soc. Rev*. 46, 1025–1039. doi: 10.1039/C6CS00415F

Conflict of Interest: The authors declare that the research was conducted in the absence of any commercial or financial relationships that could be construed as a potential conflict of interest.

frontiers in Chemistry

ORIGINAL RESEARCH
published: 10 July 2020
doi: 10.3389/fchem.2020.00583

Experimental Analyses Emphasize the Stability of the Meisenheimer Complex in a S_NAr Reaction Toward Trends in Reaction Pathways

Paola R. Campodónico[1]*, *Belén Olivares*[1] and *Ricardo A. Tapia*[2]

[1] Centro de Química Médica, Facultad de Medicina, Clínica Alemana Universidad del Desarrollo, Santiago, Chile, [2] Facultad de Química y Farmacia, Pontificia Universidad Católica de Chile, Santiago, Chile

The mechanism of S_NAr reactions between 2-chloro-5-nitropyrimidine with primary and secondary alicyclic amines, respectively, have been studied by kinetic measurements. The kinetic data obtained in aqueous media opens a controversial discussion based on Brönsted-type plots analysis. The first approach based on the kinetic data reveals a non-catalyzed pathway. Then, the subtlety of the mathematical treatment of the kinetic data is discussed over a concerted or stepwise mechanism, respectively.

Keywords: S_NAr reaction, reaction mechanism, Brönsted-type plots, border mechanisms, Meisenheimer complex

OPEN ACCESS

Edited by:
Ramesh L. Gardas, Indian Institute of Technology Madras, India

Reviewed by:
Sugata Chowdhury, National Institute of Standards and Technology (NIST), United States
Vito Di Noto, University of Padova, Italy
Taoufik Boubaker, University of Monastir, Tunisia

****Correspondence:***
Paola R. Campodónico
pcampodonico@udd.cl

Specialty section:
This article was submitted to Physical Chemistry and Chemical Physics, a section of the journal Frontiers in Chemistry

Received: *29 July 2019*
Accepted: *05 June 2020*
Published: *10 July 2020*

Citation:
Campodónico PR, Olivares B and Tapia RA (2020) Experimental Analyses Emphasize the Stability of the Meisenheimer Complex in a S_NAr Reaction Toward Trends in Reaction Pathways. Front. Chem. 8:583. doi: 10.3389/fchem.2020.00583

INTRODUCTION

The nucleophilic aromatic substitution (S_NAr) reactions have been the object of several studies, especially in solvation analysis and solvent effects studies in water, conventional organic solvents (COS), ionic liquids (ILs), and mixtures of them (Nudelman et al., 1987; Newington et al., 2007; D'Anna et al., 2010; Park and Lee, 2010; Alarcón-Espósito et al., 2015, 2016, 2017; Marullo et al., 2016; Sánchez et al., 2018a,b). However, only in the last time these reactions have been investigated systematically in order to acquire knowledge about the rate determining step (RDS) on the reaction mechanism based on Brönsted type-plots (Um et al., 2007; Ormazábal-Toledo et al., 2013a,b; Gallardo-Fuentes et al., 2014; Gazitúa et al., 2014). This free energy relationship correlates the logarithm of the nucleophilic rate coefficients (k_N) and the pK_a values of the nucleophiles from Brönsted Equation:

$$logk_N = \beta_{nuc}\, pK_a + log\ log\ G \tag{1}$$

where G is a constant that depends of the solvent and temperature and β_{nuc} corresponds to the development of charge between the reaction sites of the nucleophile/electrophile pair, respectively, along to the potential energy surface (PES) (Brönsted and Pedersen, 1924). Therefore, β_{nuc} gives information about the transition state (TS) structure related to the RDS on the reaction mechanism (Buncel et al., 1993).

The established mechanism for S_NAr reactions occurs in activated aromatic substrates with strong electron withdrawing groups (EWG) containing a good leaving group (LG) through an addition-elimination process (Crampton et al., 2004; Um et al., 2007; Ormazábal-Toledo et al., 2013a,b; Terrier, 2013; Gallardo-Fuentes et al., 2014; Gazitúa et al., 2014; Alarcón-Espósito et al., 2015, 2016, 2017; Mortier, 2015; Sánchez et al., 2018a,b). The first step of this stepwise mechanism is the nucleophilic attack to the substrate (k_1 channel in **Scheme 1**) leading to the formation of an anionic σ-adduct named Meisenheimer complex (MC). Subsequent to the MC development,

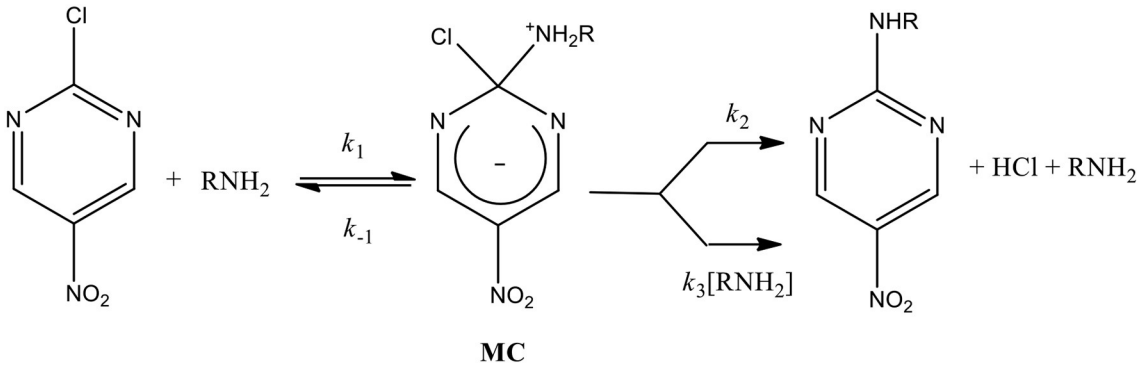

SCHEME 1 | General reaction mechanism for a S_NAr reaction between 2-chloro-5-nitropyrimidine as substrate with primary amines as nucleophiles (general chemical structure).

two processes for its decomposition have been postulated: (i) expulsion of the LG followed by fast proton loss to give the reaction product (k_2 channel in **Scheme 1**) and (ii) the base-catalyzed deprotonation of the zwitterionic complex that loss the LG to give the reaction product (k_3 channel in **Scheme 1**) (Crampton et al., 2004; Um et al., 2007; Ormazábal-Toledo et al., 2013a,b; Terrier, 2013; Gallardo-Fuentes et al., 2014; Gazitúa et al., 2014; Alarcón-Espósito et al., 2015, 2016, 2017; Mortier, 2015; Sánchez et al., 2018a,b) **Scheme 1** shows the general reaction mechanism for a S_NAr considering the reaction of this study and the decomposition channel cited above (k_2 and k_3, respectively) (Bunnett and Zahler, 1951; Bunnett and Cartano, 1981; Bunnett et al., 1981) See details in **Scheme 1** and Results and Discussions.

Nowadays, researchers have opened the discussion over concerted vs. stepwise mechanisms on S_NAr reactions. For instance, Um et al. postulated a concerted route based on the evidence of a cyclic TS structure for the reaction between 1-(Y-substituted-phenoxy)-2,4-dinitrobenzenes with cyclic secondary amines in acetonitrile (Um et al., 2014). Recently, Jacobsen et al. provides experimental and computational evidences that S_NAr reactions proceed through concerted mechanism (Kwan et al., 2018) Ritter et al. has proposed concerted S_NAr mechanism based on theoretical analysis validated by experimental studies on the deoxyfluorination reaction of phenols (Neumann et al., 2016; Neumann and Ritter, 2017).

In S_NAr reactions proceeding through a stepwise mechanism that discard the general-base catalyzed mechanism (k_3 *in Scheme* 1), Crampton et al. obtained β_{nuc} values close to 0.5 which were attributed to the MC formation (nucleophilic attack) as RDS on the reaction mechanism (see **Scheme 1**) (Crampton et al., 2004, 2006; Um et al., 2007; Stenlid and Brinck, 2017). Up to date there are no reports that can establish a range for β_{nuc} values that could separate the nucleophilic attack and the LG departure steps on the reaction mechanism for S_NAr processes indicating a non-catalyzed pathway. For instance, β_{nuc} values were reported for the S_NAr reaction between 2,4-dinitrophenylsulfonylchloride with secondary alicyclic amines in aqueous media (Gazitúa et al., 2014), where the LG departure is the RDS for a non-catalyzed pathway (k_2 channel in **Scheme 1**). This result was obtained using the β_{nuc} values proposed by Jencks in nucleophilic substitution reactions of carbonates with amine series, attributing β_{nuc} values of 1.0 for the LG departure and 0.3 for the nucleophilic attack, respectively, obtained from linear Brönsted-type plots (Jencks and Gilchrist, 1968) These analysis were performed considering that the reactions proceeded through: (i) a MC intermediate (stepwise mechanism) and (ii) non-catalyzed pathway, both in agreement to **Scheme 2**. However, the stability of the MC opens the possibility toward a concerted pathway (without MC) instead of a stepwise mechanism (Gallardo-Fuentes and Ormazábal-Toledo, 2019).

On the other hand, linear Brönsted-type plots for nucleophilic substitution have been associated with concerted mechanisms, in which the nucleophilic attack at the electrophilic center occurs concertedly with the LG departure within a single step pathway (Perrin, 2000). A range of slope values have been reported by Castro et al. from 0.40 to 0.60 for aminolysis of carboxylic esters derivatives (Castro, 1999). Note that, this range of β_{nuc} values assigned to concerted mechanisms for nucleophilic substitution is similar to β_{nuc} values associated to the nucleophilic attack in S_NAr reactions.

Plotting log k_N and pK_a values in the traditional way affording curved Brönsted type-plots have been reported. The later, can be associated to a stepwise mechanism with a change in the TS structure associated to the RDS. Statistically downward curvatures for corrected Brönsted-type plots defined β_{nuc} values associated to the LG departure in the range between 0.8–1.1 and 0.1–0.3 for the nucleophilic attack, respectively (Jencks and Gilchrist, 1968; Williams, 1989). Subsequently, the above range was also obtained by Castro et al. in the reaction of carbonate and thiocarbonate derivatives with *N*-nucleophiles series (Jencks and Gilchrist, 1968; Perrin, 2000). However, other analysis associated to curved Brönsted-type plots postulate a concerted pathway. In this case, the reported mechanism is attributable to strong EWG in the electrophile (substrate) that could destabilize the hypothetical intermediate (in a hypothetical stepwise mechanism, see **Scheme 2**) (Castro et al., 2001, 2002a; Knipe, 2019). Note that, the difference between nucleophilic substitution and S_NAr reactions is the type of intermediate given by the nature of the reacting pair. For nucleophilic substitution is postulated a zwitterionic tetrahedral intermediate

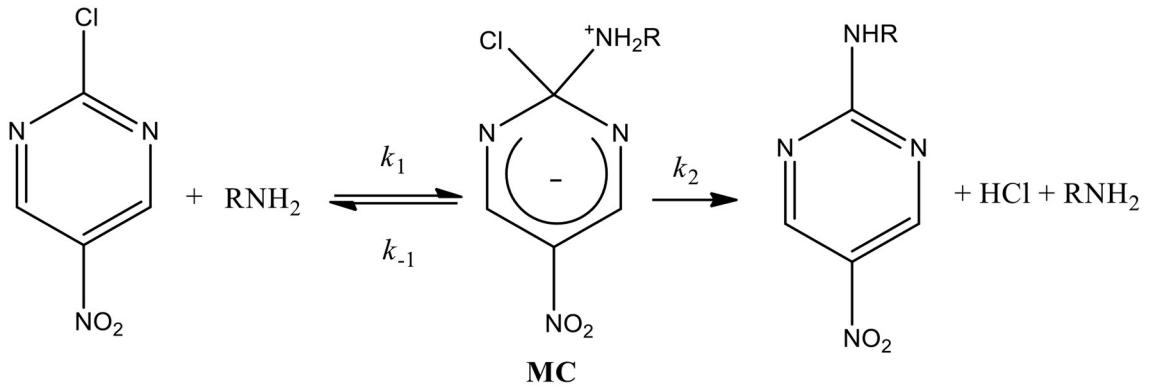

SCHEME 2 | General reaction mechanism for a S_NAr reaction between 2-chloro-5-nitropyrimidine as substrate with primary amines as nucleophiles. It excludes the general-base catalyzed mechanism (k_3 *in Scheme* 1).

($T^{\pm}$) (Satterthwait and Jencks, 1974; Castro et al., 2002a), while in a S_NAr reaction is suggested an anionic σ-adduct (MC in **Schemes 1**, **2**, respectively).

Jacobsen et al. summarize the mechanistic trends in S_NAr reactions centered on the chemical structures of the substrates, specifically groups or atoms attached to the permanent group (PG) and the nature of the LG as shown below (Kwan et al., 2018).

PG	LG	Suggested Mechanism
Strong EWG	Poor	Stepwise
Heterocycles that contain nitrogen atoms	Good	Concerted
Strong EWG	Good	Borderline

Note that, this description excludes the nucleophile nature. Nevertheless, it is known that the nature of the reacting pair (solute) plays a key role on the reactivity added to the hydrogen bond (HB) effect involved in solute-solvent interactions over the stabilization of species along the PES for S_NAr reactions (Bernasconi and De Rossi, 1976; Newington et al., 2007; Ormazábal-Toledo et al., 2013a,b; Gallardo-Fuentes et al., 2014; Sánchez et al., 2018a,b). Furthermore, it is known that secondary alicyclic amines (SAA) are better nucleophiles than primary amines (PA) (Ormazábal-Toledo et al., 2013a,b). On the other hand, the substrate or electrophile is highly reactive, because it contains nitrogen atoms in its chemical structure added to an EWG group and chlorine is considered a good LG. Then, applying the table that summarize the mechanistic trends based on the nature of the reacting pair, the possibility for a reaction between SAA and 2-chloro-5-nitropyrimidine suggests a concerted pathway. However, depending of the nature of the LG, two routes could be possible: (i) poor LG, the LG departure step will be the RDS (stepwise mechanism) and (ii) good LG, the nucleophilic attack could be occurring at the same time to the leaving group departure or the nucleophilic attack will be the rate determining step. Therefore, the meaning of a borderline mechanism will be the uncertainty of which reaction channel will follow a solute.

As a result, the number of factors controlling reactivity in S_NAr reactions is large, and could produce effects over the reaction mechanism given by the stabilization of the MC toward stepwise ($stwS_NAr$) or concerted mechanisms (cS_NAr).

In this context, we have recently studied the reactivity of 2-chloro-5-nitropyrimidine with benzohydrazides, establishing that the HB between the reacting pair activate the pyrimidine moiety and increases the nucleophilicity of the nitrogen atom of the benzohydrazide fragment (Campodónico et al., 2010; Gallardo-Fuentes et al., 2014). Note that, in this case the nucleophile series are not very reactive, promoting a *stw*S_NAr mechanism, where the nucleophilic attack is the RDS of the reaction mechanism (see **Scheme 1**). Other studies for nitrogen heterocyclic compounds have shown a borderline mechanism, such as the reaction between atrazine and bio-thiols (Calfumán et al., 2017). On the other hand, the reaction between 4-chloroquinazoline with aniline suggested a *stw*S_NAr route being the first step (nucleophilic attack) the RDS of the reaction mechanism (Sánchez et al., 2018b). These previous kinetic studies and others based on heterocyclic substrates that contain nitrogen atoms in its chemical structures opened an interesting discussion over mechanistic features of S_NAr reactions (Taylor and Thompson, 1961; Cherkasov et al., 1982; Cullum et al., 1995, 1996), especially with ambident substrates, which would be showing more than one site toward the nucleophilic attack and another alternative mechanism (Guo and Mayr, 2014; Gabsi et al., 2018).

In this work, we report a complete kinetic study to better understand the reaction mechanism which is operative between the substrate 2-chloro-5-nitropyrimidine with two series of N-nucleophiles: PA and SAA in aqueous media (see **Scheme 3**). Both series of nucleophiles proceed through of a S_NAr route for which reaction mechanisms were assigned. These results were discussed in terms of the comparison of Brönsted slope parameters (β_{nuc}) given by the Brönsted type-plots analysis, as well as examination of chemical structures of the reacting pairs.

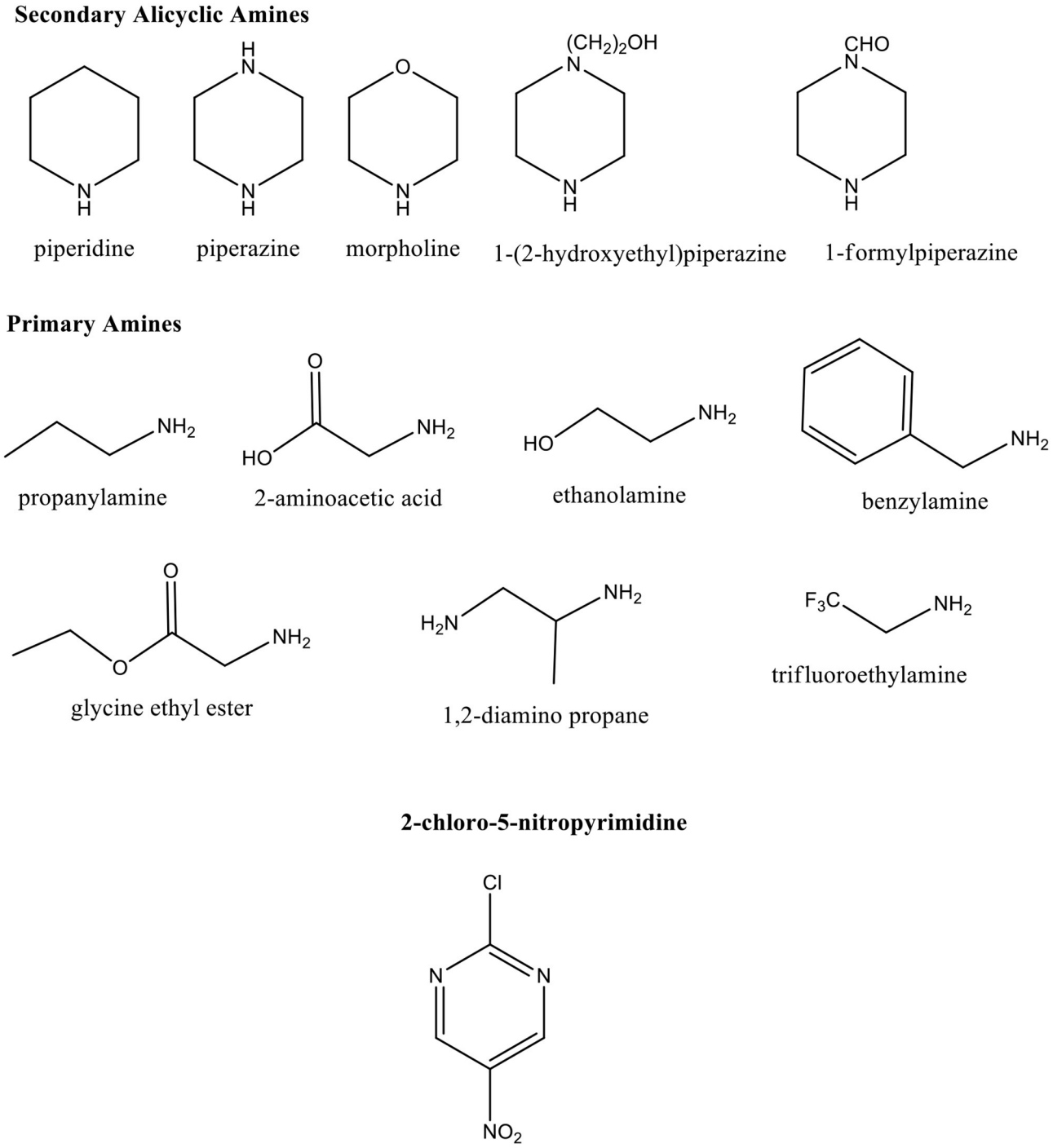

SCHEME 3 | Chemical structures of secondary alicyclic and primary amines, respectively and the substrate 2-chloro-5-nitropyrimidine.

MATERIALS AND METHODS

Reactants and Solvents

All the reagents used were the commercially available by Sigma-Aldrich and Merck. The certificate of analysis guarantees purity $\geq$ 99%.

Kinetic Measurements

The kinetics of the studied reactions were carried out spectrophotometrically by means of a diode array spectrophotometer for slow reactions and a stopped-flow spectrophotometer for fast reactions equipped with a constant temperature circulating bath. In aqueous solution, the

experimental conditions were 25.0 ± 0.1°C, ionic strength 0.2 M (KCl), at three different pH values maintained by partial protonation of the amines. All the reactions were studied under excess of the amine over the substrate and were started by injection of a substrate stock solution in acetonitrile (10 μL) into the amine solution (2.5 mL in the spectrophotometric cell). The initial substrate concentration was about 0.1 M. The pseudo first order constant (k_{obs}) values were found for all reactions; which were determined by means of the spectrophotometer kinetic software for first order reactions at the wavelength corresponding at the kinetic products. Note that, in aqueous media each pH values correspond to: pH = pK_a and 0.3 units up and down in order to analyze the possibility of acid and/or basic catalysis by the reaction media. On the other hand, a Brönsted type-plot requires a broad range of pK_a values for the nucleophiles. For this reason, in this study is used a family of nucleophiles with similar chemical features, 7 SAA and 7 PA, respectively. Then, the relationships between k_{obs} vs. [Nucleophile] should be straight lines or straight lines with smooth deviations, which will discard a catalysis processes by the media. All the reactions were carried out under pseudo first-order conditions in which the amine concentrations were at least 10 times greater than the substrate concentration (Um et al., 2007, 2012).

TABLE 1 | Summary of nucleophiles and their statistically corrected pK_a values in water and the second-order rate constant (k_N) for the nucleophile series with 2-chloro-5-nitropyrimidine.

Name	pK_a	k_N (sM)$^{-1}$
PRIMARY AMINES		
Propylamine	11.14	6.93 ± 0.47
Glycine	10.24	3.16 ± 0.09
Ethanolamine	9.98	1.95 ± 0.04
Benzylamine	9.82	2.78 ± 0.06
Glycine ethyl ester	8.23	0.43 ± 0.01
1,2-Diamino propane	7.31	0.220 ± 0.007
Trifluoroethylamine	6.18	0.0260 ± 0.00005
SECONDARY ALICYCLIC AMINES		
Piperidine	11.54	100 ± 2.78
Piperidine*	11.54	52.39 ± 2.10
Piperazine	9.94	65.2 ± 2.50
1–(2–Hidroxyethyl) piperazine	9.38	50 ± 1.50
Morpholine	8.78	41.6 ± 0.95
1–Formylpiperazine	7.93	20 ± 0.52
Piperazinium anion	6.28	1.83 ± 0.052

Kinetic data for piperidine obtained using stop flow equipment.

Product Analysis

In the studied reactions, the increase of a band centered in the range of 330–550 nm was observed; and it was attributed to the corresponding 5-nitro-(2-amine-1-yl) pyrimidine like reaction products for all amines studied.

Synthesis of Products

5-Nitro-*N*-Propylpyrimidin-2-Amine

To a mixture of 2-chloro-5-nitropyrimidine (40 mg, 0.25 mmol) in tetrahydrofuran (THF, 5 mL), containing triethylamine (25.3 mg, 0.25 mmol), was added dropwise a solution of piperidine (14.8 mg, 0.25 mmol) in THF (2.0 mL). The reaction mixture was stirred for 20 h at room temperature, the solvent was removed under vacuum and the residue was dissolved in ethyl acetate (15 mL). The organic layer was washed with 0.5 N HCl, water, brine and dried over Na_2SO_4. After evaporation of the solvent the crude product was purified by flash chromatography on silica gel (CH_2Cl_2–hexane 1:1) to give a yellow solid (35 mg, 77%), mp 117–118°C (Lit. Barlin and Young, 1972116°C). IR (KBr) ν_{max} cm^{-1} 3246, 1602, 1580, 1560, 1334, 1300. ^{1}H-NMR (200 MHz, $CDCl_3$) ð*: 1.01 (t, J = 7.2 Hz, 3H), 1.68 (sext, J = 7.2 Hz, 2H), 3.51 (q, J = 7.2 Hz, 2H), 6.09 (br s, 1H), 9.03 (s, 1H), 9.10 (s, 1H); ^{13}C-NMR (50.4 MHz, $CDCl_3$/DMSO-d_6) ð*: 11.5, 22.3, 43.6, 133.6, 154.9, 155.2, 163.3.

5-Nitro-2-(Piperidin-1-yl)Pyrimidine

Using the above procedure, from 2-chloro-5-nitropyrimidine (40 mg, 0.25 mmol) and piperidine (22 mg, 0.258 mmol), was obtained a yellow solid (27 mg, 52%), mp 154–156°C (Lit. Boarland and McOmie, 1951147–148°C). IR (KBr) ν_{max} cm^{-1} 1602, 1580, 1332, 1303. ^{1}H-NMR (200 MHz, $CDCl_3$) ð*: 1.60–1.80 (m, 6 H), 3.95 (t, J = 5.0 Hz, 4 H), 8.90 (s, 2H); ^{13}C-NMR (50.4 MHz, $CDCl_3$) ð*: 23.6, 25.1 (2C), 44.8 (2C), 99.4, 154.1 (2C), 167.2. HRMS (ESI) calcd for $C_9H_{12}N_4O_2$[M +] 208.0960, found 208.0955.

RESULTS AND DISCUSSION

Under the experimental conditions used, the formation of only one product was spectrophotometrically observed for all the reactions studied. Therefore, the possibility of nucleophilic attack at the unsubstituted ring positions, substitution of hydrogen (Gabsi et al., 2018), was discarded (Um et al., 2007). This fact was confirmed by synthesis and study of the reaction products (see Experimental Section and **Supplementary Material**), discarding the possibility of nucleophilic attack at the unsubstituted positions on the aromatic ring (4 and 6, positions).

The kinetic study for the reaction of 2-chloro-5-nitropyrimidine with the whole set of amines considered in this study (see **Scheme 3** and **Table 1**) was performed in aqueous solution at 25°C and ionic strength 0.2 M in KCl. The formation of colored amino-substituted nitropyrimidine compounds were monitored by UV–vis spectroscopy. In all runs, an excess of amines over the substrate were used in order to achieve pseudo-first-order kinetic conditions and the pseudo-first-order rate constant (k_{obs}) was found for all the reactions. See more details in **Figures S1–S14** and **Tables S1–S42**, respectively in **Supplementary Material**.

The kinetic analysis (Terrier, 2013; Mortier, 2015) shows that the k_{obs} for the studied reactions can be expressed as Equation (2), in which [*Nu*] represents the concentration of nucleophile and k_1, k_2 and k_3 are the micro-constants associated to the reaction

mechanism of a S_NAr reaction (see **Scheme 1**).

$$k_{obs} = \frac{k_1 k_2 [Nu] + k_1 k_3 [Nu]^2}{k_{-1} + k_2 + k_3 [Nu]} \quad (2)$$

The values of k_{obs} for all the reactions are in accordance with Equation (3) where k_0 and k_N are the rate coefficients for hydrolysis and aminolysis, respectively. Then, the k_{obs} values were obtained at different concentrations of the nucleophile in aqueous media. These results were plotted through of k_{obs} vs. $[Nu]$ in order to obtain the k_N values from Equationn 3:

$$k_{obs} = k_0 + k_N [Nu] \quad (3)$$

These linear plots passed through the origin or close to it, suggesting that the contribution of hydroxide and/or water to k_{obs} values is negligible and the reactions do not follow a catalyzed route in agreement with **Scheme 2** ($k_{-1} + k_2 \gg k_3 [Nu]$ *in Scheme* 1) (see more details in SM). Then, k_{obs} is expressed by Equation 4:

$$k_{obs} = k_N [Nu], \text{ where } k_N = \frac{k_1 k_2}{(k_{-1} + k_2)} \quad (4)$$

Table 1 summarizes the pK_a values in water and the rate coefficients values obtained for the amination of the pyrimidine derivative in aqueous media at 25°C and ionic strength 0.2 M in KCl. The pK_a and k_N values were statistically corrected using p (numbers of protons which can be deprotonated from the conjugate acid of the amine) and q (numbers of nucleophilic sites of the amine). The value accompanying k_N coefficients corresponds to the error associated to the slope to obtain these values (Bell, 1973).

Figure 1 shows the Brönsted-type plots for the studied reactions in agreement to Equation 1, where the k_N and pK_a values were statistically corrected by p and q parameters, respectively. The analysis of the statistically corrected Brönsted-type plots is based on the discussion of two trends (linear and curve) for each amine series (see **Scheme 3**) in order to elucidate the RDS on the reaction mechanisms if its channel follows a stepwise route or to get highlights about the meaning of curved Brönsted-type plots.

First part in **Figure 1** (empty circles in bottom) corresponds to PA serie. Note for these amines, that the rate coefficients increase together with its pK_a values showing a weak curvature. However, it will perfectly be a linear trend (see dotted and continued lines in **Figure 1**). From this linear behavior, a β_{nuc} value of 0.46 ± 0.03 is obtained, which is comparable to those reported for the S_NAr reaction of 2,4-dinitrochlorobenzene with SAA and PA in water, suggesting that the RDS is the nucleophilic attack (Um et al., 2007, 2012) For this serie, with $N = 7$, the parameters for a straight line are: $R^2 = 0.976$, SD = 0.141 and $p < 0.0001$, respectively. On the other hand, and maintaining N, the values for the curved plot (polynomial fit of 2nd order) are $R^2 = 0.994$, SD = 0.077 and $p < 0.0001$, respectively.

Second part in **Figure 1** (full squares in top) corresponds to SAA. Note that for these nucleophiles, the curvature is more stressed in comparison with PA, specifically toward the most basic amine (piperidine). See the comparison between continued and dotted lines. Therefore, for the complete series of these amines the strength trend is discarded (see **Figure 1**, dotted line). However, a rude first approximation for these SAA, will be eliminating the k_N value obtained for piperidine, obtaining a β_{nuc} value of 0. 44 ± 0.04. Note that, this value will be comparable with the β_{nuc} value obtained for PA suggesting the same reaction route. For this serie, with $N = 8$, the parameters for a straight line are: $R^2 = 0.791$, SD = 0.271 and $p = 0.003$, respectively.

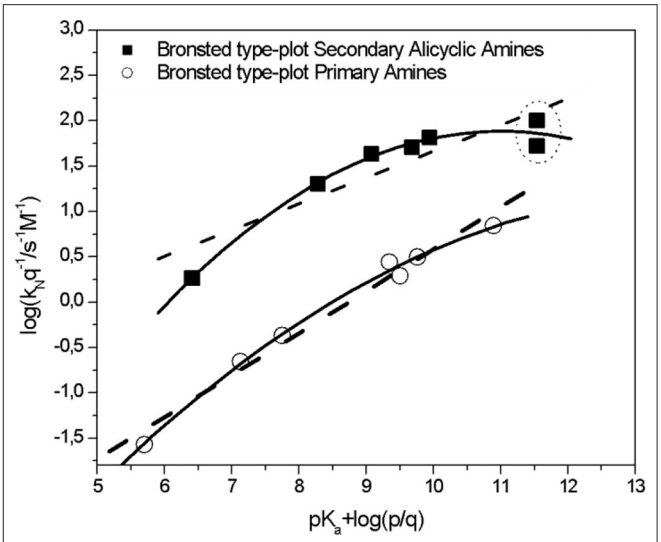

FIGURE 1 | Brönsted-type plots (statistically corrected) obtained for the reactions of 2-choro-5-nitropyrimidine with Secondary Alicyclic Amines series (full squares, see **Scheme 3** and **Table 1**) and Primary Amines series (empty circles, see **Scheme 3** and **Table 1**), respectively in aqueous solution, at 25.0°C and ionic strength of 0.2 M in KCl. Data enclosed in dots correspond to piperidine. Continued and dotted lines correspond to the free energy relationships that correlates the logarithm of the nucleophilic rate coefficients (k_N) and the pK_a values of the nucleophiles from Brönsted Equation. See below in the text the analysis of those trends.

Continuing with the same section of the **Figure 1**, a new analysis considering all the kinetic data for the SAA shown a Brönsted-break plot (see continued line in **Figure 1**). Note that, all the kinetic data in this study were carried out spectrophotometrically by a diode array spectrophotometer. However, piperidine shows kinetic measurements extremely fast and high k_{obs} values (see **Figure S8** and **Tables S22–S24**, respectively in SM). This fact was corrected using a stop flow equipment connected to the diode array spectrophotometer maintaining the same experimental conditions. The k_{obs} values are reported in **Figure S14** and **Tables S40–S42**, respectively in SM and k_N value is shown in **Table 1**. Note that, this k_N value emphases the curvature on the Brönsted-type plot (see dotted circle in **Figure 1** and data in **Table 1**). Maintaining $N = 8$, the parameter values for the curved plot (polynomial fit of 2nd order) are $R^2 = 0.977$, SD = 0.093 and $p < 0.0001$, respectively.

Castro et al. reported a similar behavior in aminolysis of carbonate derivatives, suggesting a concerted mechanism (Castro

et al., 2002a). The observed curvature on the Brönsted-type plots given by the reaction between piperidine and 2-choro-5-nitropyrimidine, will be attributed to the electron-withdrawing effect of the nitro group added to the high nucleophilic strength of piperidine. The synergy of both effects over the reaction would destabilize the MC intermediate in a hypothetical stepwise process promoting the concerted route. This fact added to the Jacobsen et al. analysis: heterocycles that contain nitrogen atoms plus good LG follow a cS_NAr route (Kwan et al., 2018).

Then, if a Brönsted-type plot is considered as a definitive proof to validate a concerted mechanism, it implies the prediction of the pK_a position at the break of the biphasic Brönsted type-plot (pK_a^0) for the hypothetical stepwise mechanism. This condition establish that this value should fall within the pK_a range of the amines employed (Chrystiuk and Williams, 1987; Williams, 1989; Castro et al., 2006). It is also important to obtain a large number of data, which cover a substantial pK_a range above and below the pK_a^0 value (Williams, 2007). Equation 5 is a semiempirical equation of 4 parameters based on the existence of an intermediate on the reaction mechanism (Castro et al., 2002b).

$$\begin{aligned} log\frac{k_N}{k_N^0} &= \beta_2\ (pK_a - pK_a^0) - log\ log\left[\frac{(1+a)}{2}\right]; \\ log\ log\ a &= (\beta_2 - \beta_1)\,(pK_a - pK_a^0) \end{aligned} \tag{5}$$

The Brönsted slopes are β_1 and β_2 at high and low pK_a, respectively and k_N^0 and pK_a^0 are the corresponding values at the center of curvature. The Brönsted curve for SAA shown a pK_a^0 value of 9.0 and 9.15 for PA, respectively. Note that, the pK_a values for the complete series of nucleophiles of this study, cover a range of pK_a values in aqueous media between 5.81 to 11.24 (SAA) and 5.70 to 10.66 (PA), respectively. The higher pK_a^0 values obtained could be explained by the nature of the PG. The presence of a strong electron withdrawing group (-NO_2) and its high electronic delocalization would promote the high reactivity of the reacting pair allowing the LG departure and the nucleophilic attack at the same time promoting a cS_NAr route for these reactions.

Finally, the nature of the reacting pair is determinant on the reaction channel and it may be used to predict the degree of polar character at the TS structure. The latter, is achieved on the basis of the electronic information given by the nature of the LG and PG, solvent effects, strength of the nucleophile, electrofugality and nucleofugality of the fragment associated to the reaction. The studied reactions have: basic amines, a good LG (chlorine atom) and heterocyclic ring. The high nucleophilicity of these amines added to the high nucleofugality of the chlorine atom promoted by a heterocyclic ring highly stabilized by nitrogen atoms that improve the electrophilicity of the ipso carbon in the PG suggests that the intermediate specie is not stable and the reactions proceed without a MC intermediate only with one TS structure suggesting a concerted route for the studied reactions.

In summary, the subtlety of the mathematical treatment of the kinetic data and the analysis of the reacting pair suggest a concerted mechanism for the studied reactions of both amine series. A pertinent alternative is to complete the experimental study with reliable theoretical and computational studies in order to validate the proposed reaction route, specifically oriented in these amines that produce the curvature on the Brönsted type-plots. However, a complete and detailed experimental work is enough to validate a mechanistic study.

CONCLUSIONS

The mechanism of the S_NAr reaction between PA and SAA with 2-chloro-5-nitro pyrimidine, respectively have been elucidated by kinetic measurements. The first approach of the kinetic data reveals a non-catalyzed pathway. Then, the Brönsted type-plots analysis opened a complete discussion based on the subtlety of the mathematical treatment of the kinetic data suggesting a concerted mechanism for both amines discarding a nucleophilic attack as RDS on the reaction mechanism. The information given by curved Brönsted type-plots was complemented with the analysis of the chemical structures of the reacting pair and its relationships with the reaction pathway, validating the proposed concerted pathway. This article emphasizes the importance of Brönsted type-plots analysis highlighting the significance of the β value as a measure to determine the bond formation and the reaction mechanisms.

DATA AVAILABILITY STATEMENT

All datasets generated for this study are included in the article/**Supplementary Material**.

AUTHOR CONTRIBUTIONS

BO performed kinetic experiments, RT synthesized the reaction products and PC designed the experiments, analyzed the results, wrote and revised the manuscript. All the authors have approved the final revised manuscript. PC on behalf of The Collaborative Working Group.

FUNDING

This work was supported by FONDECYT grant N°1150759.

SUPPLEMENTARY MATERIAL

The Supplementary Material for this article can be found online at: https://www.frontiersin.org/articles/10.3389/fchem.2020.00583/full#supplementary-material

REFERENCES

Alarcón-Espósito, J., Contreras, R., and Campodónico, P. R. (2017). Iso-solvation effects in mixtures of ionic liquids on the kinetics of a model SNAr reaction. *N. J. Chem.* 41, 13435–13441. doi: 10.1039/C7NJ03246C

Alarcón-Espósito, J., Contreras, R., Tapia, R. A., and Campodónico, P. R. (2016). Gutmann's donor numbers correctly assess the effect of the solvent on the kinetics of SNAr reactions in ionic liquids. *Chem. - A Eur. J.* 22, 13347–13351. doi: 10.1002/chem.201602237

Alarcón-Espósito, J., Tapia, R. A., Contreras, R., and Campodónico, P. R. (2015). Changes in the SNAr reaction mechanism brought about by preferential solvation. *RSC Adv.* 5, 99322–99328. doi: 10.1039/C5RA20779G

Barlin, G. B., and Young, A. C. (1972). Useful preparations involving the reactions of nucleophiles with some trimethylammonio-derivatives of nitrogen heterocycles. *J. Chem. Soc.* 1, 1269–1272. doi: 10.1039/p19720001269

Bell, R. P. (1973). *The Proton in Chemistry.* London: Methuen.

Bernasconi, C. F., and De Rossi, R. H. (1976). Influence of the o-nitro group on base catalysis in nucleophilic aromatic substitution. Reactions in Benzene solution. *J. Org. Chem.* 41, 44–49. doi: 10.1021/jo00863a010

Boarland, M. P. V., and McOmie, J. F. W. (1951). Monosubstituted pyrimidines, and the action of thiourea on chloropyrimidines. *J. Chem. Soc.* 1218–1221. doi: 10.1039/jr9510001218

Brönsted, J. N., and Pedersen, K. (1924). Die katalytische Zersetzung des Nitramids und ihre physikalisch-chemische Bedeutung. *Zeitschrift für Physikalische Chemie* 108, 185–235. doi: 10.1515/zpch-1924-10814

Buncel, E., Tarkka, R., and Hoz, S. (1993). The phenomenology of differently constructed Brønsted-type plots. *J. Chem. Soc. Chem. Commun.* 109–110. doi: 10.1039/C39930000109

Bunnett, J. F., and Cartano, A. V. (1981). Differing behavior of pyrrolidine and piperidine as nucleophiles toward 2,4-dinitrophenyl and 2,4-dinitro-6-methylphenyl phenyl ethers. *J. Am. Chem. Soc.* 103, 4861–4865. doi: 10.1021/ja00406a031

Bunnett, J. F., Sekiguchi, S., and Smith, L. A. (1981). Kinetics of reactions of cyclic secondary amines with 2,4-dinitro-1-naphthyl ethyl ether in dimethyl sulfoxide solution. Spectacular difference between the behavior of pyrrolidine and piperidine. *J. Am. Chem. Soc.* 103, 4865–4871. doi: 10.1021/ja00406a032

Bunnett, J. F., and Zahler, R. E. (1951). Aromatic nucleophilic substitution reactions. *Chem. Rev.* 49, 273–412. doi: 10.1021/cr60153a002

Calfumán, K., Gallardo-Fuentes, S., Contreras, R., Tapia, R. A., and Campodónico, P. R. (2017). Mechanism for the SNAr reaction of atrazine with endogenous thiols: experimental and theoretical study. *N. J. Chem.* 41, 12671–12677. doi: 10.1039/C7NJ02708G

Campodónico, P. R., Aliaga, M. E., Santos, J. G., Castro, E. A., and Contreras, R. (2010). Reactivity of benzohydrazide derivatives towards acetylation reaction. Experimental and theoretical studies. *Chem. Phys. Lett.* 488, 86–89. doi: 10.1016/j.cplett.2010.01.052

Castro, E. A. (1999). Kinetics and mechanisms of reactions of thiol, thiono, and dithio analogues of carboxylic esters with nucleophiles. *Chem. Rev.* 99, 3505–3524. doi: 10.1021/cr990001d

Castro, E. A., Aliaga, M., Campodónico, P., and Santos, J. G. (2002a). Kinetics and mechanism of the aminolysis of methyl 4-nitrophenyl, methyl 2,4-dinitrophenyl, and phenyl 2,4-dinitrophenyl carbonates. *J. Org. Chem.* 67, 8911–8916. doi: 10.1021/jo026390k

Castro, E. A., Andujar, M., Campodonico, P., and Santos, J. G. (2002b). Kinetics and mechanism of the aminolysis of 4-nitrophenyl and 2,4-dinitrophenyl 4-methylphenyl carbonates in aqueous ethanol. *Int. J. Chem. Kinet.* 34, 309–315. doi: 10.1002/kin.10046

Castro, E. A., Campodónico, P. R., Contreras, R., Fuentealba, P., Santos, J. G., Ramón Leis, J., et al. (2006). Experimental and theoretical study on the substitution reactions of aryl 2,4-dinitrophenyl carbonates with quinuclidines. *Tetrahedron* 62, 2555–2562. doi: 10.1016/j.tet.2005.12.044

Castro, E. A., Pavez, P., and Santos, J. G. (2001). Concerted mechanisms of the reactions of methyl aryl carbonates with substituted phenoxide ions. *J. Org. Chem.* 66, 3129–3132 doi: 10.1021/jo010022j

Cherkasov, V. M., Ya. Remennikov, G., and Kisilenko, A. A. (1982). Sigma complexes in the pyrimidine series. 5. Reaction of 5-nitromethoxypyrimidines with the anion of malonic acid dinitrile. *Chem. Heterocycl. Compds.* 18, 526–530. doi: 10.1007/BF00526093

Chrystiuk, E., and Williams, A. (1987). A single transition-state in the transfer of the methoxycarbonyl group between isoquinoline and substituted pyridines in aqueous solution. *J. Am. Chem. Soc.* 109, 3040–3046. doi: 10.1021/ja00244a028

Crampton, M. R., Emokpae, T. A., Howard, J. A. K., Isanbor, C., and Mondal, R. (2004). Leaving group effects on the mechanism of aromatic nucleophilic substitution (SNAr) reactions of some phenyl 2,4,6-trinitrophenyl ethers with aniline in acetonitrile. *J. Phys. Org. Chem.* 17, 65–70. doi: 10.1002/poc.690

Crampton, M. R., Emokpae, T. A., Isanbor, C., Batsanov, A. S., Howard, J. A. K., and Mondal, R. (2006). Effects ofortho- andpara-Ring activation on the kinetics of SNAr reactions of 1-Chloro-2-nitro- and 1-Phenoxy-2-nitrobenzenes with aliphatic amines in acetonitrile. *Eur. J. Org. Chem.* 2006, 1222–1230. doi: 10.1002/ejoc.200500774

Cullum, N. R., Renfrew, A. H. M., Rettura, D., Taylor, J. A., Whitmore, J. M. J., and Williams, A. (1995). Effective charge on the nucleophile and leaving group during the stepwise transfer of the triazinyl group between pyridines in aqueous solution. *J. Am. Chem. Soc.* 117, 9200–9205. doi: 10.1021/ja00141a012

Cullum, N. R., Rettura, D., Whitmore, J. M. J., and Williams, A. (1996). The aminolysis and hydrolysis of N-(4,6-diphenoxy-1,3,5-triazin-2-yl) substituted pyridinium salts: concerted displacement mechanism. *J. Chem. Soc.* 2, 1559–1563. doi: 10.1039/p29960001559

D'Anna, F., Marullo, S., and Noto, R. (2010). Aryl azides formation under mild conditions: a kinetic study in some ionic liquid solutions. *J. Org. Chem.* 75, 767–771. doi: 10.1021/jo9022952

Gabsi, W., Essalah, K., Goumont, R., Tangour, B., and Boubaker, T. (2018). The ambident electrophilic behavior of 5-nitro-3-X-thiophenes in σ-complexation processes. *Int. J. Chem. Kinet.* 50, 659–669. doi: 10.1002/kin.21190

Gallardo-Fuentes, S., and Ormazábal-Toledo, R. (2019). σ-Holes promote the concertedness in nucleophilic aromatic substitution reactions of nitroarenes. *N. J. Chem.* 43, 7763–7769. doi: 10.1039/C9NJ01493D

Gallardo-Fuentes, S., Tapia, R. A., Contreras, R., and Campodónico, P. R. (2014). Site activation effects promoted by intramolecular hydrogen bond interactions in SNAr reactions. *RSC Adv.* 4, 30638–30643. doi: 10.1039/C4RA04725G

Gazitúa, M., Tapia, R. A., Contreras, R., and Campodónico, P. R. (2014). Mechanistic pathways of aromatic nucleophilic substitution in conventional solvents and ionic liquids. *N. J. Chem.* 38, 2611–2618. doi: 10.1039/C4NJ00130C

Guo, X., and Mayr, H. (2014). Quantification of the ambident electrophilicities of halogen-substituted quinones. *J. Am. Chem. Soc.* 136, 11499–11512. doi: 10.1021/ja505613b

Jencks, W. P., and Gilchrist, M. (1968). Nonlinear structure-reactivity correlations. The reactivity of nucleophilic reagents toward esters. *J. Am. Chem. Soc.* 90, 2622–2637. doi: 10.1021/ja01012a030

Knipe, A. C. (2019). Organic Reaction Mechanism 2015. Chapter 2. West Sussex: John Wiley and Sons.

Kwan, E. E., Zeng, Y., Besser, H. A., and Jacobsen, E. N. (2018). Concerted nucleophilic aromatic substitutions. *Nat. Chem.* 10, 917–923. doi: 10.1038/s41557-018-0079-7

Marullo, S., D'Anna, F., Campodonico, P. R., and Noto, R. (2016). Ionic liquid binary mixtures: how different factors contribute to determine their effect on the reactivity. *RSC Adv.* 6, 90165–90171. doi: 10.1039/C6RA12836J

Mortier, J. (2015). *Arene Chemistry: Reaction Mechanisms and Methods for Aromatic Compounds*. New Jersey: John Wiley and Sons.

Neumann, C. N., Hooker, J. M., and Ritter, T. (2016). Concerted nucleophilic aromatic substitution with (19)F(-) and (18)F(-). *Nature* 534, 369–373. doi: 10.1038/nature17667

Neumann, C. N., and Ritter, T. (2017). Facile C–F bond formation through a concerted nucleophilic aromatic substitution mediated by the phenofluor reagent. *Acc. Chem. Res.* 50, 2822–2833. doi: 10.1021/acs.accounts.7b00413

Newington, I., Perez-Arlandis, J. M., and Welton, T. (2007). Ionic liquids as designer solvents for nucleophilic aromatic substitutions. *Org. Lett.* 9, 5247–5250. doi: 10.1021/ol702435f

Nudelman, N. S., Mancini, P. M. E., Martinez, R. D., and Vottero, L. R. (1987). Solvents effects on aromatic nucleophilic substitutions. Part 5. Kinetics of the reactions of 1-fluoro-2,4-dinitrobenzene with piperidine in aprotic solvents. *J. Chem. Soc. Perkin Trans. 2*, 951–954. doi: 10.1039/p29870000951

Ormazábal-Toledo, R., Contreras, R., Tapia, R. A., and Campodónico, P. R. (2013a). Specific nucleophile–electrophile interactions in nucleophilic aromatic substitutions. *Org. Biomol. Chem.* 11, 2302–2309. doi: 10.1039/c3ob27450k

Ormazábal-Toledo, R., Santos, J. G., Ríos, P., Castro, E. A., Campodónico, P. R., and Contreras, R. (2013b). Hydrogen bond contribution to preferential solvation in SNAr reactions. *J. Phys. Chem. B* 117, 5908–5915. doi: 10.1021/jp4005295

Park, S., and Lee, S. (2010). Effects of ion and protic solvent on nucleophilic aromatic substitution (SNAr) reactions. *Bull. Korean Chem. Soc.* 31, 2571–2573. doi: 10.5012/bkcs.2010.31.9.2571

Perrin, C. L. (2000). Concerted Organic and Bio-organic Mechanisms By Andrew Williams (University Chemical Laboratory, Canterbury, UK). CRC Press LLC: Boca Raton, FL. 2000. *J. Am. Chem. Soc.* 122, 9569–9569. doi: 10.1021/ja0047020

Sánchez, B., Calderón, C., Garrido, C., Contreras, R., and Campodónico, P. R. (2018a). Solvent effect on a model SNAr reaction in ionic liquid/water mixtures at different compositions. *N. J. Chem.* 42, 9645–9650. doi: 10.1039/C7NJ04820C

Sánchez, B., Calderón, C., Tapia, R. A., Contreras, R., and Campodónico, P. R. (2018b). Activation of Electrophile/Nucleophile pair by a nucleophilic and electrophilic solvation in a SNAr reaction. *Front. Chem.*6, 509–517. doi: 10.3389/fchem.2018.00509

Satterthwait, A. C., and Jencks, W. P. (1974). Mechanism of the aminolysis of acetate esters. *J. Am. Chem. Soc.* 96, 7018–7031. doi: 10.1021/ja00829a034

Stenlid, J. H., and Brinck, T. (2017). Nucleophilic aromatic substitution reactions described by the local electron attachment energy. *J. Org. Chem.* 82, 3072–3083. doi: 10.1021/acs.joc.7b00059

Taylor, E. C., and Thompson, M. J. (1961). On the Reaction of 2,4-Dichloro-5-nitropyrimidine with amines 1. *J. Org. Chem.* 26, 5224–5226. doi: 10.1021/jo01070a524

Terrier, F. (2013). *Modern Nucleophilic Aromatic Substitution.* New-York, NY: John Wiley and Sons.

Um, I.-H., Im, L.-R., Kang, J. S., Bursey, S. S., and Dust, J. M. (2012). Mechanistic assessment of SNAr displacement of halides from 1-Halo-2,4-dinitrobenzenes by selected primary and secondary amines: brønsted and mayr analyses. *J. Org. Chem.* 77, 9738–9746. doi: 10.1021/jo301862b

Um, I.-H., Kim, M.-Y., Kang, T.-A., and Dust, J. M. (2014). Kinetic study on SNAr reaction of 1-(Y-Substituted-phenoxy)-2,4-dinitrobenzenes with cyclic secondary amines in acetonitrile: evidence for cyclic transition-state structure. *J. Org. Chem.* 79, 7025–7031. doi: 10.1021/jo5011872

Um, I.-H., Min, S.-W., and Dust, J. M. (2007). Choice of Solvent (MeCN vs H2O) decides rate-limiting step in SNAr aminolysis of 1-Fluoro-2,4-dinitrobenzene with Secondary Amines: Importance of Brønsted-Type Analysis in Acetonitrile. *J. Org. Chem.* 72, 8797–8803. doi: 10.1021/jo701549h

Williams, A. (1989). Concerted mechanisms of acyl group transfer reactions in solution. *Acc. Chem. Res.* 22, 387–392. doi: 10.1021/ar00167a003

Williams, A. (2007). *Free Energy Relationships in Organic and Bio-Organic Chemistry*. Canterbury: Royal Society of Chemistry.

Conflict of Interest: The authors declare that the research was conducted in the absence of any commercial or financial relationships that could be construed as a potential conflict of interest.

frontiers in Chemistry

ORIGINAL RESEARCH
published: 17 July 2020
doi: 10.3389/fchem.2020.00567

Enhancing Singlet Oxygen Generation in Conjugates of Silicon Nanocrystals and Organic Photosensitizers

Deski Beri[1], *Marius Jakoby*[1], *Dmitry Busko*[1], *Bryce S. Richards*[1,2]* *and Andrey Turshatov*[1]*

[1] *Institute of Microstructure Technology, Karlsruhe Institute of Technology, Eggenstein-Leopoldshafen, Germany,* [2] *Light Technology Institute, Karlsruhe Institute of Technology, Karlsruhe, Germany*

Silicon nanocrystals (SiNCs) are regarded as a green and environmentally friendly material when compared with other semiconductor nanocrystals. Ultra-small SiNCs (with the size 4.6–5.2 nm) demonstrate strong UV absorption and photoluminescence in the near infrared (NIR) range with the high photoluminescence quantum yield (PLQY) up to 60%. In contrast to nanoporous silicon, ultra-small SiNCs do not possess an intrinsic ability to generate singlet oxygen ($^1O_2$). However, we demonstrate that SiNC-dye conjugates synthesized *via* microwave assistant hydrosilylation reaction produce $^1O_2$ with moderate quantum yield (Φ_Δ) up to 27% in cyclohexane. These interesting results were obtained *via* measurements of singlet oxygen phosphorescence at 1,270 nm. SiNCs play an important role in the production of singlet oxygen as SiNCs harvest UV and blue radiation and transfer absorbed energy to a triplet state of the attached dyes. It increases the population of the triplet states and leads to the enhancement of the singlet oxygen generation. Simultaneously, the SiNC-dye conjugates demonstrate NIR luminescence with the PLQY up to 22%. Thus, the luminescence behavior and photosensitizing properties of the SiNC-dye conjugates can attract interest as a new multifunctional platform in the field of bio-applications.

Keywords: singlet oxygen, silicon nanocrystals, photosensitizers, NIR luminescence, microwave synthesis

OPEN ACCESS

Edited by:
Manoj K. Mahata, Gwangju Institute of Science and Technology, South Korea

Reviewed by:
Mengistie Debasu, University of New Mexico, United States
Dayane Batista Tada, Federal University of São Paulo, Brazil

***Correspondence:**
Bryce S. Richards
bryce.richards@kit.edu
Andrey Turshatov
andrey.turshatov@kit.edu

Specialty section:
This article was submitted to Physical Chemistry and Chemical Physics, a section of the journal Frontiers in Chemistry

Received: *27 February 2020*
Accepted: *02 June 2020*
Published: *17 July 2020*

Citation:
Beri D, Jakoby M, Busko D, Richards BS and Turshatov A (2020) Enhancing Singlet Oxygen Generation in Conjugates of Silicon Nanocrystals and Organic Photosensitizers. Front. Chem. 8:567. doi: 10.3389/fchem.2020.00567

INTRODUCTION

Singlet oxygen ($^1O_2$) is an extremely reactive species and powerful oxidant for many types of organic materials (Ogilby, 2010). The study of $^1O_2$ has attracted increasing attention due to its potential applications in many fields such as chemical synthesis (Manfrin et al., 2019), photocatalysis (Nosaka and Nosaka, 2017), water purification (García-Fresnadillo, 2018), and photodynamic therapy of cancer (Wang et al., 2004; Vlaskin et al., 2009; Ghogare and Greer, 2016). In chemistry, $^1O_2$ has been used to produced oxygenated hydrocarbons such as endoperoxide (Ahuja et al., 2018), deoxetanes (Camussi et al., 2019), as well as hydroperoxide and phosphine oxide for biomimetic organic synthesis of natural products and drugs (You and Nam, 2014). In the field of water treatment, $^1O_2$ has demonstrated its efficiency in the degradation of water born pollutants (Lyubimenko et al., 2019). In photodynamic therapy, $^1O_2$ has displayed a huge potential to destroy cancer cells (Campillo et al., 2019; Sun et al., in press). When a source of $^1O_2$ is selectively delivered to a tumor affected tissue, $^1O_2$ can react with many biological molecules—amino acid

residues in proteins and the nucleobases in DNA and RNA resulting in photo induced degradation of cancer cells (Castano et al., 2004; Yang et al., 2019).

The most important conventional method to produce $^1O_2$ is irradiation of photosensitizers (PSs) with ultraviolet or visible (UV/Vis) light. In the past, many potential organic and inorganic PSs have been proposed, for example, organic chromophores (Yogo et al., 2005), metal complexes (Monro et al., 2019), metal organic frameworks (Hu et al., 2018; Zheng et al., 2018), semiconductor quantum dots (QDs) (Bakalova et al., 2004; Rakovich et al., 2010), graphene QDs (Ge et al., 2014), perovskite nanocrystals (Gu et al., 2020) as well as metal nanoparticles (Chadwick et al., 2016) and metal nanowires (Smith et al., 2015). Among these, organic chromophores have been most intensively studied for $^1O_2$ generation as they exhibit strong UV/Vis absorption, fast and efficient intersystem crossing (ISC), and a long triplet lifetime (Callaghan and Senge, 2018). When exposed to UV/Vis light, organic PSs produce a large number of long-lived triplet states, which transfer energy to the ground (triplet) molecular oxygen state *via* triplet energy transfer (Wang et al., 2004; Maisch et al., 2007). Despite the forbidden nature of ISC in quantum mechanics under the El-Sayed rule, this process can be partially allowed in organic systems if the ISC involves a change of the orbital type (Marian, 2012) or in systems with strong spin-vibronic coupling (Penfold et al., 2018). Heavy elements anchored to a chromophore can also significantly enhance the rate of population of the triplet state *via* spin–orbit effect (Marian, 2012). Recently, the population of triplet state *via* a SOCT (spin–orbit charge transfer)-ISC have been proved to be efficient for generation of $^1O_2$ in different organic and water media (Filatov, 2020).

Interestingly, it has also been observed that the abundant and non-toxic chemical element of silicon (Si) can also produce $^1O_2$. A pioneering work by Kovalev et al. (2002) described generation of $^1O_2$ using silicon nanocrystals (SiNCs) distributed in a solid state porous Si layer. Several follow-up communications reported generation of $^1O_2$ in organic and aqueous media by relatively large (with size 50–150 nm) porous SiNCs (Osminkina et al., 2011; Xiao et al., 2011). Photosensitization of $^1O_2$ using ultra-small blue-emitting silicon nanocrystals (SiNCs) with size of 3 $\pm$ 1 nm and short photoluminescence (PL) decay lifetime of 1 ns was described by Llansola Portolés et al. (2010). Unlike SiNCs with blue PL resulting from surface defects, $^1O_2$ generation with SiNCs demonstrating quantum confinement effect and optical properties similar to semiconductor QDs has not yet been reported. These SiNCs typically demonstrate strong UV absorption and bright long-lived PL ($\sim$100 μs PL decay time) in the red and near-infrared (NIR) spectral range. The long-lived NIR PL and low toxicity (Durnev et al., 2010; Cao et al., 2017; Mazzaro et al., 2017; Pramanik et al., 2018; Zhi et al., 2018) of SiNCs attract high attention of researchers in many application fields (Mazzaro et al., 2017).

The conjugation of organic dyes and SiNCs is a little explored topic relevant for many potential applications. It is known that an interaction between dyes and QDs can modified photophysical properties of the both (Lu et al., 2020). In particularly, the triplet exciton transfer between a dye and QD rises strong interest in the luminescent energy harvesting by singlet fission (Gray et al., 2020) and triplet fusion (Xia et al., 2020). Beside of that, QDs can enhance ISC in organic dyes anchored to their surface (Ahmed et al., 2015; Jin et al., 2019), that can be used for efficient generation of and $^1O_2$ for PDT and photocatalytic applications.

Recently, we investigated conjugates of SiNCs and organic chromophores (Beri et al., 2020) in order to enhance visible absorption of SiNCs. To our surprise, we observed significant quenching SiNCs PL induced by organic chromophores covalently attached to the surface of SiNCs. We postulated that the quenching of the PL signal can originate from energy transfer from the SiNCs to the triplet state of the anchored dye molecule. These interesting findings motivated us to investigate in detail the role of SiNCs in photosensitization of the dye triplet state and a possible use of this process for generation of $^1O_2$.

In the current paper, we anchored two different perylene derivatives to the surface of SiNCs using a thermal hydrosilylation reaction. The perylene unit in the close proximity to the surface of SiNCs plays the role of an energy acceptor mediating the energy transfer from SiNCs to the triplet state of molecular oxygen. Utilizing this mechanism of the $^1O_2$ generation, we intended to enhance the potential value of SiNCs as a non-toxic and environmentally friendly material to sensitize reactive $^1O_2$ for applications in chemical synthesis and photodynamic therapy.

MATERIALS AND METHODS

Silicon monoxide (99.9%, 325 mesh) and phenalenone (*phe*) (also known as perinaphtenone, 97%) were purchased from Sigma-Aldrich. Hydrofluoric acid (48%) was purchased from Fisher Scientific. Ethanol (98%), methanol (HPLC grade), toluene (99%+) were purchased from Merck. 1-hexene (C6) (99%) was purchased from Acros. Cyclohexane (spectroscopic grade) was purchased from Alfa Aesar. 3-ethynylperylene (*dye-1*) was purchased from Lumiprobe GmbH, Germany and 3-ethenylperylene (*dye-2*) was purchased from Fluorochem. Ltd, U.K. All chemicals were used without further purification and the chemical structure the most important substances are presented in **Figure 1A**.

Synthetic Methods

Silicon nanocrystals were produced by a top-down method using the disproportionation reaction of silicon monoxide (SiO_x), x < 1. The reaction initialized by annealing of 3.0 g SiO_x powder in a quartz boat at 900°C for 60 min under continuous H_2/Ar (5:95%) flow. During this annealing process, the nucleation of SiNCs seeds inside a silicon dioxide matrix occurs (Hessel et al., 2012). Details regarding the annealing procedure can be found in the literature (Beri et al., 2018). After annealing, the sample was transferred to an agate mortar and ground.

Synthesis of Hydrogen Terminated SiNCs (H-SiNCs)

1.0 g the ground powder was transferred to a PTFE flask, followed by the addition of 10 ml absolute ethanol and stirring for 5 min. Subsequently, 10 ml of HF 48% was added to the flask and the solution was stirred for the next 2.5 h. In 50 ml PTFE separatory

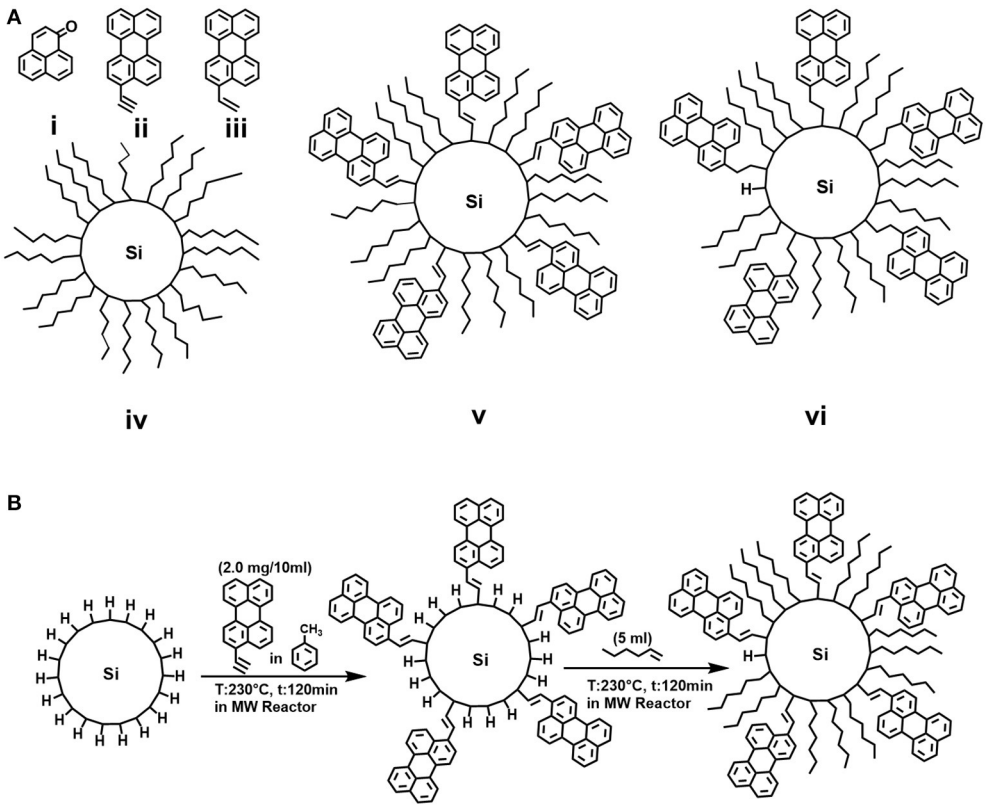

FIGURE 1 | (A) Molecular structures of (i) phenalenone (*phe*), (ii) 3-ethynylperylene (*dye-1*), (iii) 3-ethenylperylene (*dye-2*), (iv) hexyl-functionalized SiNCs (*C6-SiNCs*), (v) 3-ethynylperylene/hexyl-functionalized SiNCs (*C6-1-SiNCs*) and (vi) 3-ethenylperylene/hexyl-functionalized SiNCs (*C6-2-SiNCs*); **(B)** Schematic representation of the hydrosilylation reaction of hydrogen-terminated SiNCs with dye and 1-hexene.

funnel, 15 mL of toluene was added followed by the addition of the ethanol/HF mixture. The separation of *H-SiNCs* was performed by extracting the non-polar (toluene) part from the polar (ethanol/HF) media. The toluene solution transferred to the centrifuge tube to remove the large particles. The centrifugation was performed at 2,000 rpm for 2 min. The big particles were discarded and the toluene solution was transferred to the G30 microwave (MW) tube (Anton Paar) and Ar was purged through the dispersion in order to remove dissolved O_2. These *H-SiNCs* was ready for further reaction inside the MW reactor.

Synthesis of Hexyl Terminated SiNCs (C6-SiNCs)

Five milliliter of 1-hexene (C6) injected into G30 MW tube with the solution of *H-SiNCs* in toluene and purged for another 20 min. The tube with the solution was heated at 230°C for 120 min inside the MW reactor (Anton Paar GmbH). Unreacted C6 and toluene were removed with rotary evaporator and *C6-SiNCs* were re-dispersed in cyclohexane.

Synthesis of dye Terminated SiNCs (C6-1-SiNCs and C6-2-SiNCs)

A solution of *dye-1* in toluene (2 mg in 10 ml of toluene) was added to the solution of *H-SiNCs* in the G30 MW tube and the resulted solution was purged with Ar for 20 min. The tube with the solution was heated at 230°C for 120 min inside the MW reactor (Anton Paar GmbH). Five milliliter of *C6* was injected into the tube and again purged with Ar for another 20 min. The reaction in the MW reactor was repeated at 230°C for another 120 min. The schematic representative of the synthetic method is shown in **Figure 1B**. The product of the reaction with a dark orange color was transferred to the rotary evaporator flask and unreacted *C6* as well as toluene were removed. The obtained solid powder was rinsed with MeOH/EtOH (1:1) to remove unreacted dye. The precipitate was further redispersed in *cyclohexane* and stored in a glovebox and will be referred to as *C6-1-SiNCs*. The same procedure was applied for synthesis of *C6-2-SiNCs*.

Sample Characterization

Size and Size Distribution

Transmission electron microscope (TEM) investigations were carried out on a TITAN 60–300 microscope at accelerating voltage 300 kV (**Figure S1**). Dynamic Light Scattering (DLS) using Anton Paar Litesizer 500 was used for characterization of the particle size distribution.

Absorption and Photoluminescence Excitation (PLE) Spectra

Absorption spectra were taken by UV-Vis-NIR spectrophotometer (Perkin Elmer Lambda 950). with a 2 nm resolution. Photoluminescence excitation (PLE) spectra were measured with a spectrofluorometer (Varian Cary Eclipse). The PLE scan was conducted monitoring the 800 nm emission (close to maximum peak of SiNCs emission) and exploring the excitation range from 300 to 550 nm.

Photoluminescence (PL) and Photoluminescence Quantum Yield (PLQY) Measurements

PLQY, PL-lifetimes and PL-emission were determined by the methods, which have been earlier described (Beri et al., 2020).

Singlet Oxygen Quantum Yields (Φ_Δ)

Samples (2.5 ml) dispersed in cyclohexane were placed in a quartz cuvette (Starna) with path length 1 cm were irradiated with 405 nm diode lasers (75 mW, DL-7146-1012S, Roithner Laser Technique GmbH) or with a narrow-linewidth Ti:Sa laser (45 mW, SolsTiS, EMM-532, M-Squared Lasers) for the 317.5 nm excitations. The PL of $^1O_2$ was measured with irradiance calibrated NIR spectrometer (NIRQuest 512-1.7, Ocean Optics) operating in 900–1,700 nm range. Integration time of 100 s was used for collection of the $^1O_2$ phosphorescence spectra. The quantum yield of singlet $^1O_2$ generation (Φ_Δ) was calculated in agreement with Equation 1 using the *phe* as quantum yield as standard:

$$\Phi_\Delta^{\mathbf{x}} = \Phi_\Delta^{\mathbf{R}} \frac{\left[\mathbf{S}_{\mathbf{em}}^{\mathbf{x}}\right]}{\left[\mathbf{S}_{\mathbf{em}}^{\mathbf{R}}\right]} \frac{\left[\mathbf{I}_{\mathbf{abs}}^{\mathbf{R}}\right]}{\left[\mathbf{I}_{\mathbf{abs}}^{\mathbf{x}}\right]} \quad (1)$$

where $\Phi_\Delta^{\mathbf{x}}$ and $\Phi_\Delta^{\mathbf{R}}$ are singlet oxygen quantum yields of the sample and the reference, respectively. $\left[\mathbf{S}_{\mathbf{em}}^{\mathbf{x}}\right]$ and $\left[\mathbf{S}_{\mathbf{em}}^{\mathbf{R}}\right]$ are integrated area of $^1O_2$ PL generated by the sample and the reference, while $\left[\mathbf{I}_{\mathbf{abs}}^{\mathbf{x}}\right]$ and $\left[\mathbf{I}_{\mathbf{abs}}^{\mathbf{R}}\right]$ are the number of absorbed photons by the sample and the reference. In case of the excitation with monochromatic light, absorption (% of absorbed light $\left[\mathbf{A}_{\%}^{\mathbf{x}}\right]$ and $\left[\mathbf{A}_{\%}^{\mathbf{R}}\right]$ at the excitation wavelength) of the sample and the reference can be used instead of $\left[\mathbf{I}_{\mathbf{abs}}^{\mathbf{x}}\right]$ and $\left[\mathbf{I}_{\mathbf{abs}}^{\mathbf{R}}\right]$.

The reported value of Φ_Δ^R for *phe* in cyclohexane is 92 ± 10% (Schmidt et al., 1994). The concentrations of two sets of *phe*, *dye-1*, *dye-2*, *C6-1-SiNCs,* and *C6-2-SiNCs* solutions were adjusted to have roughly similar absorbance (*a*) at 405 and 317.5 nm.

Temperature-Dependent Photoluminescence Measurements

Dye molecules are dispersed in cyclohexane and placed in quartz cuvette with a path length of 2 mm and purged with argon gas for 30 min. Subsequently, the cuvette was clamped to the cryostat sample holder (Cryospares A7-103) and placed inside the sample chamber of the closed cycle cryostat (Oxford Instruments, Optistat Dry TLEX). After evacuating the sample chamber to $\sim 10^{-5}$hPa, the chamber was flooded with helium (purity >99.999mol%) to improve thermal coupling between the sample and the heat exchanger of the cryostat. PL emission spectra were measured at 20K for both *dye-1* and *dye-2* samples. For the excitation, a mode-locked ytterbium laser (Light Conversion, Pharos) with a pulse width of 190 fs and a repetition rate of 20 kHz was used. The 1028 nm output of the laser was converted to 440 nm using an optical parametric amplifier (Light Conversion, Orpheus) and second harmonic generator (Light Conversion, Lyra). The steady state photoluminescence spectra were recorded by a fiber-coupled UV/VIS spectrometer (Avantes, AvaSpec-2048L).

RESULT AND DISCUSSION

The molecular structures of the reference PS—*phe*, perylene derivatives *dye-1* and *dye-2*, as well as hexyl functionalized SiNCs (*C6-SiNCs*), hexyl-dye functionalized SiNCs (*C6-1-SiNCs* and *C6-2-SiNCs*) are shown in **Figure 1A**.

The unsaturated bonds of *dye*-1 and *dye-2* can react with the surface of *H-SiNCs* resulting in dye-functionalized SiNCs. The obtained dye-functionalized SiNCs exhibit enhanced absorption in the visible range and broad NIR emission with maximum of 860 nm and PLQYs of 15 ± 1% (for *C6-1-SiNCs*) and 22 ± 1% (for *C6-2-SiNCs*) as shown in **Table 1**. To improve the stability of SiNCs during and after the passivation reaction (**Figure 1B**), 1-hexene was employed as an additional surface ligand. A detailed investigation of the photophysical properties of *C6-SiNCs*, *C6- 1-SiNCs* and *C6-2-SiNCs* have been reported previously (Beri et al., 2020). In this previous publication, we found that the anchored dyes reduce both the PLQY of the NIR emission of SiNCs as well as the luminescence lifetime (at the NIR PL peak). As the NIR PL peak of SiNCs does not overlap with the absorption peak of the dyes (observed between 350 and 500 nm), we assumed that the NIR PL of SiNCs is quenched by the triplet state of the dyes *via* Dexter energy transfer. The resulting enhancement of the dye triplet population in the *C6-1-SiNCs* and *C6-2-SiNCs* can be probed *via* measurements of the yield of $^1O_2$ generated by the triplet states of the dye. Thus, the main goal of the present study is to compare Φ_Δ under the direct excitation of the attached dyes (with 405 nm laser) and SiNCs (with 317.5 nm laser), with the two chosen wavelengths enabling this selectivity.

There are two well-established methods to determine the Φ_Δ. The first method uses a particular trap compound such as 9,10-dimethylanthracene (DMA), 1,3-diphenylisobenzofuran (DPBF), singlet oxygen sensor green, etc. (You, 2018). For instance, the DMA trap reacts specifically with $^1O_2$ to form peroxide. This chemical reaction results in changes of the absorption spectrum of DMA decaying with irradiation time. By measuring the absorption decay, the Φ_Δ could be determined quantitatively *via* the comparison with the absorption decay induced by a reference PS with a known Φ_Δ^R. The second method is based on measurements of $^1O_2$ phosphorescence and Equation 1. The radiative relaxation process from excited $^1O_2$ to the ground triplet state ($^1\Delta_g \rightarrow {}^3\Sigma_g$) yields an emission at 1,270 nm with relatively long lifetime (ms-to-s, depending on solvent) (Khan and Kasha, 1979; DeRosa and Crutchley, 2002). Similar to the first method, it also requires a reference material with known Φ_Δ^R for the comparison of intensities of $^1O_2$ phosphorescence.

TABLE 1 | Absorbance (α), normalized intensity of $^1O_2$ phosphorescence (I_{em}), photoluminescence quantum yield (*PLQY*), and singlet oxygen quantum yields (Φ_Δ) measured with 317.5 nm and 405 nm lasers.

PS	a(317.5nm)	$I_{em}^{\dagger}$	a(405nm)	$I_{em}^{\ddagger}$	PLQY,%	Φ_Δ,%†	Φ_Δ,%‡
phe	0.576	1	0.760	1	–	92 ± 10*	92 ± 10*
dye-1	0.138	0.111	0.763	0.381	68 ± 1‡,§	45 ± 14	35 ± 5
dye-2	0.081	0.090	0.760	0.382	52 ± 1‡,§	56 ± 25	34 ± 5
C6-SiNc	0.780	–	0.773	–	33 ± 1$^{\dagger,\blacklozenge}$	–	–
C6-1-SiNCs	0.576	0.213	0.693	0.264	15 ± 1$^{\dagger,\blacklozenge}$	20 ± 5	27 ± 5
C6-2-SiNCs	0.331	0.052	n/a	n/a	22 ± 1$^{\dagger,\blacklozenge}$	9 ± 6	n/a

*†Corresponds to the 317.5 nm excitation; ‡corresponds to the 405 nm excitation; *reference $\Phi_\Delta = 0.92 \pm 10$ (Schmidt et al., 1994) §PLQY of dyes visible emission integrated in the range 350–500 nm; ♦PLQY of SiNCs NIR emission integrated in the range 650–1,000 nm; I_{em} was normalized using the emission of $^1O_2$ excited via phe ($I_{em} = 1$ for phe); The uncertainty of Φ_Δ was calculated in agreement with Equation S1 (**Supporting Information**). The uncertainty of PLQY measurements were earlier reported in Saleta Reig et al. (2020). The Φ_Δ for dye-2 under 405 excitation is not reported because luminescence of $^1O_2$ was too weak.*

It should be noted that the first method has a significant disadvantage for the estimation of Φ_Δ. Several factors must be taken into account to determine the correct value of Φ_Δ, including: overlap of absorption spectra of the sample and trap; self-degradation of the trap; as well as trap decomposition induced by other reactive oxygen species. For instance, we were not able to measure Φ_Δ *via* either DMA or DPBF due to the spectral overlap with the broad absorption spectra of *C6-1-SiNCs* and *C6-2-SiNCs*. A subsequent attempt to use rubrene (absorbing in range 450–550 nm) as the $^1O_2$ trap also failed, as rubrene displayed a fast rate of the self-degradation upon irradiation with 405 nm and 317.5 nm lasers (**Figure S2**). Thus, the second method of the estimation of Φ_Δ based on the detection of $^1O_2$ phosphorescence was chosen as the most reliable.

Singlet Oxygen Generation With *Dye-1* and *Dye-2*

Before conducting the experiments related to $^1O_2$ generation, the photostability of the reference PS—*phe* was evaluated (**Figure S3**). The degradation of 20% *phe* was found after long-time (1 h) irradiation of a solution of the reference PS in cyclohexane using 15 mW UV LED. Taking into account that acquisition of $^1O_2$ luminescence (using 317.5 nm laser with intensity of 45 mW) takes ∼100 s, we considered the reference PS as photostable. When we were satisfied that the *phe* was photostable, we investigated $^1O_2$ generation by *dye-1* and *dye-2*. Perylene by itself exhibits a very high PLQY of 94% in cyclohexane (Taniguchi et al., 2018) and is thus a very poor PS. However, perylene derivatives have demonstrated ability to generate $^1O_2$ with high quantum yield (Wu et al., 2010; Filatov et al., 2018; Blacha-Grzechnik et al., 2020). **Figures 2B,D** demonstrates phosphorescence of $^1O_2$ generated *via* photoexcitation of *dye-1* and *dye-2* solutions in cyclohexane via both 405 and 317.5 nm laser excitation. The concentration of solutions with *dye-1*, *dye-2,* and *phe* was adjusted to have similar absorption at the excitation wavelengths (**Figures 2A,C**). The absorption of the samples $A^x_\%$ was estimated from absorbance a_x using Equation 2:

$$\mathbf{A^x_\% = 100\% - 10^{(2-a_x)}}, \quad (2)$$

where $A^x_\%$ is % of absorbed light and a_x is absorbance measured experimentally.

A calculation using Equation 1 gives the value of $\Phi_\Delta = 35 \pm 5\%$ for *dye-1* and $\Phi_\Delta = 34 \pm 5\%$ for *dye-2* when excited with the 405 nm laser. Measurements with the other excitation wavelength (317.5 nm) result to very weak $^1O_2$ phosphorescence with very high uncertainty in $\Phi_\Delta = 45 \pm 14\%$ (for *dye*-1) and $\Phi_\Delta = 56 \pm 25\%$ (for *dye-2*) because of the weak dye absorption at 317.5 nm.

Interestingly, the dyes demonstrate unusually large values of Φ_Δ together with large values of absolute PLQY of 68 ± 1% and 52 ± 1% measured for *dye-1* and *dye-2*, respectively. Note, that absolute PLQYs were estimated in the integrating sphere and have a higher precision than Φ_Δ. To gain inside $^1O_2$ photosensitization we measured PLQY for dye solutions prepared inside a glovebox under oxygen-free conditions. We found PLQY of 98% for *dye-1* and 80% for *dye-2*. The obtained result indicates that photosensitization of $^1O_2$ occurs solely *via* the excite singlet state in case of *dye-1* and predominantly in case of *dye-2*. It appears that, around two-thirds of the excited singlet states relax *via* the radiative transition for *dye-1*, whereas around one-third of the excited singlets transfer the energy to oxygen molecules. For *dye-2*, ∼50% of the excitation energy decaying *via* radiative relaxation, whereas the remainder (∼30%) transfers the energy to oxygen. Earlier, the highest Φ_Δ of 67% for perylene-like molecules was reported for rather complex di-(perylenebisimide) derivatives (Wu et al., 2010). However, our measurements indicate that moderate Φ_Δ of 35 ± 5% can be achieved with the simple molecules, which can be produced without expensive and time-consuming multistep synthesis.

To obtain additional information about triplet states of *dye-1* and *dye-2*, we measured the emission spectra of their glassy solutions (in cyclohexane) at low temperature (20 K). Assuming small, but non-zero probability of ISC, we expected to detect phosphorescence of *dye-1* and *dye-2* at low temperature. **Figure 3** demonstrates a comparison of PL spectra collected at room temperature and 20 K. Indeed, new emission bands appear in the low temperature spectra with maxima at 674 and 735 nm for *dye-1* and 670 and 735 nm for *dye-2*. We attributed the appearance of these bands to the radiative T_1–S_0 transition. The position of these peaks is slightly blue-shifted

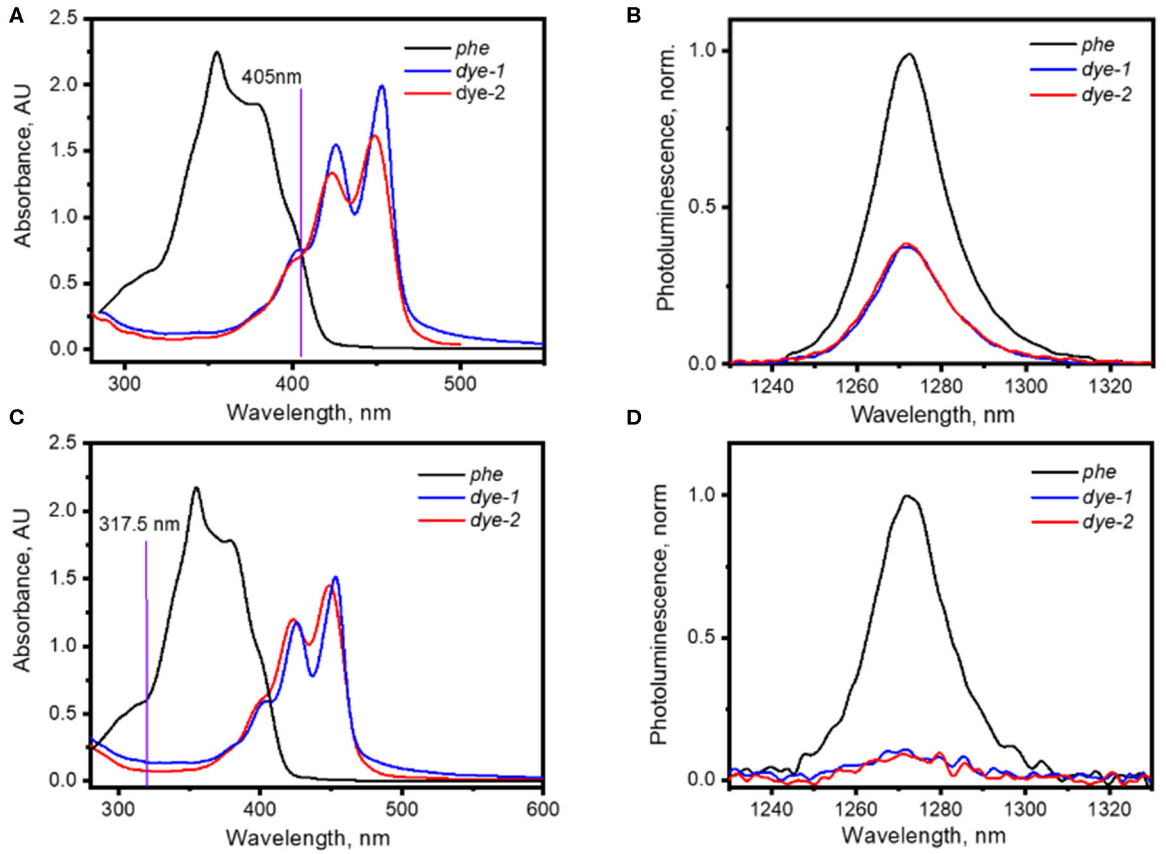

FIGURE 2 | (A) UV-Vis absorption spectra of solutions of *phe*, *dye-1,* and *dye-2* in cyclohexane used for the generation of $^1O_2$ with 405 nm laser; **(B)** $^1O_2$ phosphorescence excited *via* irradiation of solutions of *phe* and *dye-1* with 405 nm laser (75 mW); **(C)** UV-Vis absorption spectra of solutions of *phe*, *dye-1,* and *dye-2* in cyclohexane used for the generation of $^1O_2$ with 317.5 nm laser; **(D)** $^1O_2$ phosphorescence excited via irradiation of solutions of *phe*, *dye-1,* and *dye-2* with 317.5 nm laser (excitation intensity of 15 mW).

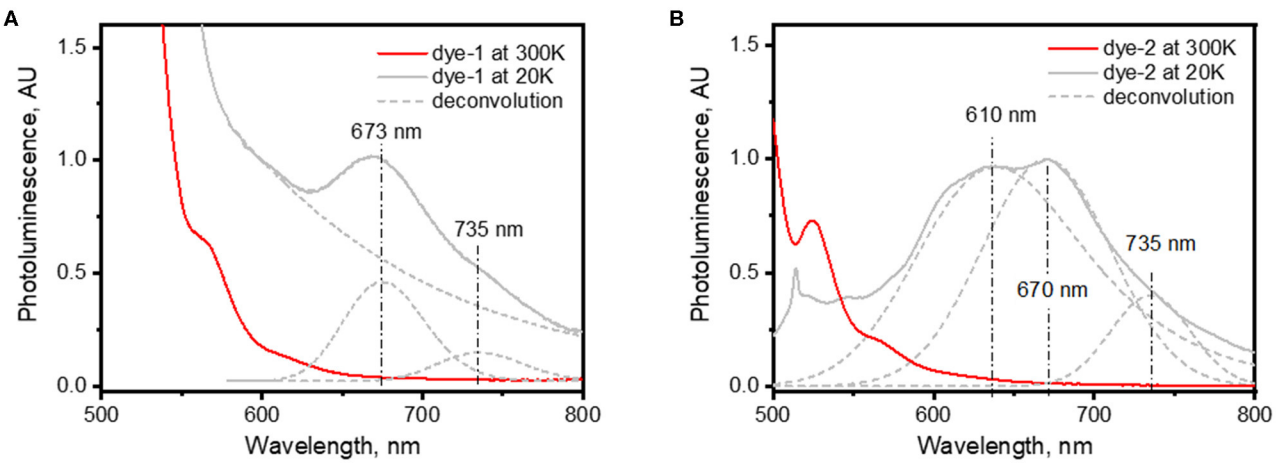

FIGURE 3 | Photoluminescence of **(A)** *dye-1* and **(B)** *dye-2* at temperature of 300 and 20 K. Dashed lines represent results of deconvolution of low-temperature photoluminescence using Gaussian peaks centered at 673 and 735 nm for *dye 1* and 610, 670, and 735 nm for *dye 2*.

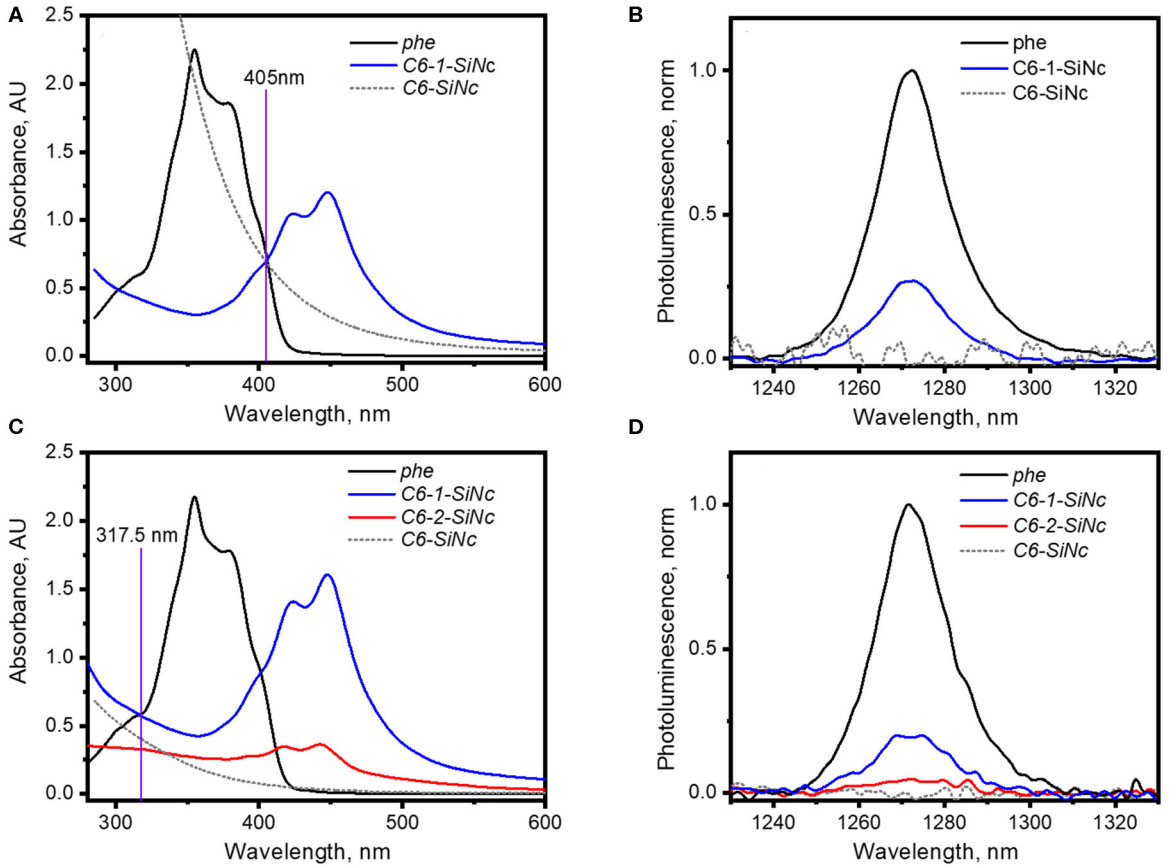

FIGURE 4 | (A) UV-Vis absorption spectra of solutions of *phe, C6-SiNCs* and *C6-1-SiNCs* in cyclohexane used for the generation of $^1O_2$ with 405 nm laser; **(B)** $^1O_2$ phosphorescence excited *via* irradiation of solutions of *phe*, *C6-SiNCs* and *C6-1-SiNCs* with 405 nm laser (excitation intensity of 75 mW); **(C)** UV-Vis absorption spectra of solutions of *phe*, *C6-SiNCs*, *C6-1-SiNCs* and *C6-2-SiNCs* in cyclohexane used for the generation of $^1O_2$ with 317.5 nm laser; **(D)** $^1O_2$ phosphorescence excited via irradiation of solutions of *phe*, *C6-SiNCs*, *C6-1-SiNCs* and *C6-2-SiNCs* with 317.5 nm laser (excitation intensity of 45 mW).

when compared with the position of T_1 state of 800–850 nm in the unsubstituted perylene molecule (Turshatov et al., 2012). However, it is highly likely that the dye triplet with the T_1 energy of ∼1.7 eV (740 nm) can be excited *via* the energy transfer process utilizing the energy of SiNCs with PL in range 1.2–1.9 eV (650–1,000 nm).

Singlet Oxygen Generation With *C6-1-SiNCs* and *C6-2-SiNCs*

The chemical reaction of the dyes with *H-SiNCs* yields a product of conjugation that demonstrates absorption of both components. The PLE spectra of *C6-1-SiNCs* (**Figure S4**) and *C6-2-SiNCs* (**Figure S5**) confirm the dye attachment. The excitation of SiNCs becomes possible *via* dye excitation in the range of 400–450 nm, which indicates the very short distance between dyes and SiNCs. In contrast, the physical mixture of *C6-SiNCs* and the dyes does not demonstrate NIR luminescence when the sample is excited with blue light (400–450 nm).

It should be pointed out that the irradiation of *C6-1-SiNCs* and *C6-2-SiNCs* with 317.5 and 405 nm lasers excites different species. The 405 nm laser mainly excites the dye molecule anchored to the surface of SiNCs, whereas the 317.5 nm laser directly excites SiNCs as the dyes exhibit an absorption minimum at this wavelength. The results of the calculation with Equation 1 (using the data presented in **Figures 4A,B** and **Table 1**) indicate that *C6-1-SiNCs* excited with 405 nm laser generate $^1O_2$ with $\Phi_\Delta = 27 \pm 5\%$. This quantum yield is lower than Φ_Δ of pure *dye-1*. However, the experiment emphasizes that the *C6-1-SiNCs* conjugate exhibits synergistic behavior. Under blue light excitation at room temperature, the nanoparticles demonstrate NIR emission (originating from the SiNCs core) with PLQY of 15 ± 1% and $^1O_2$ generation (originated from the anchored dye). Thus, this new conjugate can attract potential interest in photomedicine as a new chemical agent combining properties of PS and a NIR phosphor.

The irradiation of *C6-1-SiNCs* with the 317.5 nm laser should lead to selective excitation of SiNCs. To the best of our knowledge, the SiNCs synthesized from SiO_x are not able to generate $^1O_2$. Indeed, the excitation of *C6-SiNCs* with 317.5 and 405 nm lasers do not produce $^1O_2$ phosphorescence (**Figures 4B,D**). However, the excitation of the *C6-1-SiNCs*

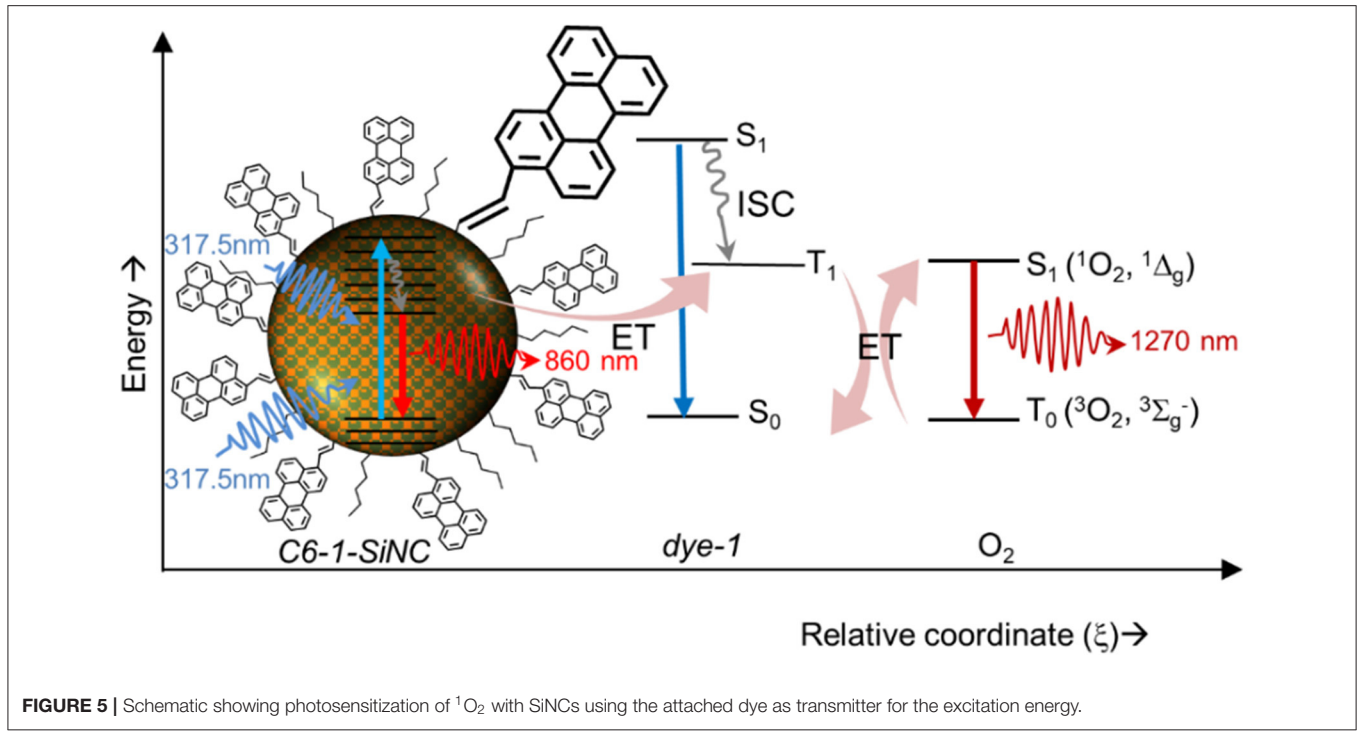

FIGURE 5 | Schematic showing photosensitization of $^1O_2$ with SiNCs using the attached dye as transmitter for the excitation energy.

conjugate with the 317.5 nm laser results in $^1O_2$ phosphorescence with $\Phi_\Delta = 20 \pm 5\%$. The enhancement factor (F) of $^1O_2$ oxygen generation with UV light (317.5 nm) for *C6-1-SiNCs* vs. *dye-1* can be determined using Equation 3:

$$\mathbf{F}=\frac{[\Phi_\Delta^{(\mathbf{C6})-\mathbf{1}-\mathbf{SiNCs}}]}{[\Phi_\Delta^{\mathbf{dye}}]}\frac{\left[\mathbf{a}_{(\mathbf{C6})-\mathbf{1}-\mathbf{SiNCs}}\right]}{\left[\mathbf{a}_{\mathbf{dye}}\right]} \quad (3)$$

where we assume that two solutions (*C6-1-SiNCs* and *dye-1)* exhibit similar absorbance at the 450 nm peak (indication of similar perylene concentration); $\Phi_\Delta^{(C6)-1-SiNCs}$ and Φ_Δ^{dye} are quantum yields of $^1O_2$ generation measured at the 317.5 nm excitation for the *C6-1-SiNCs* conjugate and *dye-1,* respectively; $a_{(C6)-1-SiNCs}$ and a_{dye} are absorbance of the two solutions at 317.5 nm.

The enhancement factor $F = 2.3$ indicates that the solution with *C6-1-SiNCs* is able produce 2.3 times more $^1O_2$ then the solution with *dye-1* with similar concentration of perylene chromophore. We performed here the calculation of F only for one single wavelength (317.5 nm). However, this conclusion can be also valid for the broad UV range (∼300–350 nm) with strong absorption of SiNCs. Thus, the *C6-1-SiNCs* conjugate demonstrate the ability of efficient $^1O_2$ generation over very broad spectral range utilizing the absorption of SiNCs (∼300–350 nm) and the absorption of dye-1 (∼350–460 nm).

It has been mentioned in our previous publication (Beri et al., 2020) that energy transfer from SiNCs to the triplet state of *dye-2* is less efficient. This observation was also confirmed in the experiment with $^1O_2$ generation. The *C6-2-SiNCs* conjugate exhibits significant lower $\Phi_\Delta = 9 \pm 6\%$ under excitation with UV light (317.5 nm) (**Figures 4C,D** and **Table 1**).

Energy Transfer From SiNCs to Perylene Chromophore

The schematic at **Figure 5** displays a $^1O_2$ generation pathway under UV excitation of *C6-1-SiNCs*. Under excitation with 317.5 nm laser, the crystals emit NIR photons with the wavelength of 860 nm. At the same time, the excitation energy can be transferred to the triplet state of the dye. The triplet state interacts with molecular oxygen. The interaction produces $^1O_2$ that emits NIR photons with the wavelength of 1,270 nm with the overall quantum efficiency of $^1O_2$ production around 20%

Finally, we were able to evaluate the efficiency of energy transfer (η_{ET}) from the SiNC core to the perylene chromophore from the calculations of Φ_Δ. At 317.5 nm excitation, the efficiency of the energy transfer can be calculated using Equation 4 and the values contained in **Table 1**:

$$\eta_{\mathbf{ET}}=\frac{\left[\Phi_\Delta^{\mathbf{317.5nm}}\right]-\left[\mathbf{P}_{\mathbf{dye}}^{\mathbf{317.5nm}}\right]\left[\Phi_\Delta^{\mathbf{405nm}}\right]}{\left[\mathbf{P}_{\mathbf{SiNCs}}^{\mathbf{317.5nm}}\right]\left[\Phi_\Delta^{\mathbf{405nm}}\right]}, \quad (4)$$

where η_{ET} is energy transfer efficiency from SiNCs to attached dyes, $\left[\Phi_\Delta^{317.5nm}\right] = 20\%$ is the quantum yield of $^1O_2$ generation by *C6-1-SiNCs* under 317.5 nm excitation; $\left[\Phi_\Delta^{405nm}\right] = 27\%$ is the quantum yield of $^1O_2$ generation by *C6-1-SiNCs* under 405 nm excitation; $\left[P_{dye}^{317.5nm}\right] = 24\%$ is a part of the excitation light (with wavelength of 317.5 nm) absorbed by the dye; $\left[P_{SiNCs}^{317.5nm}\right] = 76\%$ is a part of the excitation light (with wavelength of 317.5 nm) absorbed by the SiNC core.

The calculation of η_{ET} with Equation 4 gives a value of 66%. This value is in very good agreement with the value of η_{ET} of 55% calculated using PL lifetimes of the NIR emission of *C6-SiNCs* and *C6-1-SiNCs* nanocrystals (Beri et al., 2020).

CONCLUSIONS

The SiNCs were modified with organic dyes *via* the hydrosilylation reaction in the microwave reactor. The SiNC-dye conjugates were investigated for the first time within the context of singlet oxygen generation. The singlet oxygen yield was determined *via* measurements of singlet oxygen phosphorescence (at 1,270 nm) in cyclohexane solutions using the comparison with the singlet oxygen phosphorescence produced by the reference PS—*phe*. The Φ_Δ values were estimated for two excitation wavelengths: 317.5 nm at 405 nm. The calculation of Φ_Δ for the *C6- 1- SiNC* conjugate results $\Phi_\Delta = 27 \pm 5\%$ and $\Phi_\Delta = 20 \pm 5\%$ for 405 nm and 317.5 nm excitations, respectively. We attributed high yield of singlet oxygen generation under 317.5 nm with efficient energy transfer from photoexcited SiNCs to the triplet states of attached molecules of *dye-1*. In contrast to *dye-1*, *dye-2* is a less efficient acceptor for SiNCs. As results, the Φ_Δ value of the *C6-2-SiNCs* conjugates is smaller—$\Phi_\Delta = 9 \pm 6\%$. We assumed that *C6-1-SiNCs* demonstrate high Φ_Δ over entire absorption spectrum of *C6-1-SiNCs* (∼300–460 nm). Thus, this finding indicates a large potential of the dye modified SiNCs for the production of singlet oxygen.

DATA AVAILABILITY STATEMENT

All datasets generated for this study are included in the article/ **Supplementary Material**.

AUTHOR CONTRIBUTIONS

DBe: synthesis of the dye functionalized SiNCs, characterization of SiNCs, measurement of singlet oxygen, evaluation and interpretation of the data, and writing. MJ: temperature dependent photoluminescence measurement. DBu: measurement of singlet oxygen. BR: supervision, data interpretation, and writing. AT: development of a paper concept, supervision data interpretation, and writing. All authors contributed to the manuscript revision, read, and approved the submitted version.

FUNDING

The authors would like to acknowledge the financial support provided by the Helmholtz Association: (i) a Recruitment Initiative Fellowship for BR; (ii) the funding of chemical synthesis equipment from the Helmholtz Materials Energy Foundry (HEMF); and (iii) the Science and Technology of Nanosystems research programme. DBe acknowledges the Directorate General of Higher Education (DGHE) of the Republic of Indonesia for the Ph.D. fellowship 101.2/E4.4/K/2015 and DAAD-STIBET doctoral graduation scholarships.

ACKNOWLEDGMENTS

A. Mazilkin (INT, KIT) is acknowledged for TEM measurements.

SUPPLEMENTARY MATERIAL

The Supplementary Material for this article can be found online at: https://www.frontiersin.org/articles/10.3389/fchem.2020.00567/full#supplementary-material

REFERENCES

Ahmed, G. H., Aly, S. M., Usman, A., Eita, M. S., Melnikov, V. A., and Mohammed, O. F. (2015). Quantum confinement-tunable intersystem crossing and the triplet state lifetime of cationic porphyrin–CdTe quantum dot nano-assemblies. *Chem. Commun.* 51, 8010–8013. doi: 10.1039/C5CC01542A

Ahuja, S., Raghunathan, R., Kumarasamy, E., Jockusch, S., and Sivaguru, J. (2018). Realizing the photoene reaction with alkenes under visible light irradiation and bypassing the favored [2+2]-photocycloaddition. *J. Am. Chem. Soc.* 140, 13185–13189. doi: 10.1021/jacs.8b08100

Bakalova, R., Ohba, H., Zhelev, Z., Ishikawa, M., and Baba, Y. (2004). Quantum dots as photosensitizers? *Nat. Biotechnol.* 22, 1360–1361. doi: 10.1038/nbt1104-1360

Beri, D., Busko, D., Mazilkin, A., Howard, I. A., Richards, B. S., and Turshatov, A. (2018). Highly photoluminescent and stable silicon nanocrystals functionalized via microwave-assisted hydrosilylation. *RSC Adv.* 8, 9979–9984. doi: 10.1039/C7RA13577G

Beri, D., Jakoby, M., Howard, I. A., Busko, D., Richards, B. S., and Turshatov, A. (2020). Improved photon absorption in dye-functionalized silicon nanocrystals synthesized via microwave-assisted hydrosilylation. *Dalton Trans.* 49, 2290–2299. doi: 10.1039/C9DT04497C

Blacha-Grzechnik, A., Drewniak, A., Walczak, K. Z., Szindler, M., and Ledwon, P. (2020). Efficient generation of singlet oxygen by perylene diimide photosensitizers covalently bound to conjugate polymers. *J. Photochem. Photobiol. A* 388:112161. doi: 10.1016/j.jphotochem.2019.112161

Callaghan, S., and Senge, M. O. (2018). The good, the bad, and the ugly – controlling singlet oxygen through design of photosensitizers and delivery systems for photodynamic therapy. *Photochem. Photobiol. Sci.* 17, 1490–1514. doi: 10.1039/C8PP00008E

Campillo, N., Falcones, B., Otero, J., Colina, R., Gozal, D., Navajas, D., et al. (2019). Differential oxygenation in tumor microenvironment modulates macrophage and cancer cell crosstalk: novel experimental setting and proof of concept. *Front. Oncol.* 9:43. doi: 10.3389/fonc.2019.00043

Camussi, I., Mannucci, B., Speltini, A., Profumo, A., Milanese, C., Malavasi, L., et al. (2019). g-C3N4 - singlet oxygen made easy for organic synthesis: scope and limitations. *Acs Sustain. Chem. Eng.* 7, 8176–8182. doi: 10.1021/acssuschemeng.8b06164

Cao, Z., Peng, F., Hu, Z., Chu, B., Zhong, Y., Su, Y., et al. (2017). *In vitro* cellular behaviors and toxicity assays of small-sized fluorescent silicon nanoparticles. *Nanoscale* 9, 7602–7611. doi: 10.1039/C7NR00530J

Castano, A. P., Demidova, T. N., and Hamblin, M. R. (2004). Mechanisms in photodynamic therapy: part one—photosensitizers, photochemistry and cellular localization. *Photodiagn. Photodyn. Ther.* 1, 279–293. doi: 10.1016/S1572-1000(05)00007-4

Chadwick, S. J., Salah, D., Livesey, P. M., Brust, M., and Volk, M. (2016). Singlet oxygen generation by laser irradiation of gold nanoparticles. *J. Phys. Chem. C* 120, 10647–10657. doi: 10.1021/acs.jpcc.6b02005

DeRosa, M. C., and Crutchley, R. J. (2002). Photosensitized singlet oxygen and its applications. *Coord. Chem. Rev.* 233–234, 351–371. doi: 10.1016/S0010-8545(02)00034-6

Durnev, A. D., Solomina, A. S., Daugel-Dauge, N. O., Zhanataev, A. K., Shreder, E. D., Nemova, E. P., et al. (2010). Evaluation of genotoxicity and reproductive toxicity of silicon nanocrystals. *Bull. Exp. Biol. Med.* 149, 445–449. doi: 10.1007/s10517-010-0967-3

Filatov, M. A. (2020). Heavy-atom-free BODIPY photosensitizers with intersystem crossing mediated by intramolecular photoinduced electron transfer. *Org. Biomol. Chem.* 18, 10–27. doi: 10.1039/C9OB02170A

Filatov, M. A., Karuthedath, S., Polestshuk, P. M., Callaghan, S., Flanagan, K. J., Wiesner, T., et al. (2018). BODIPY-pyrene and perylene dyads as heavy-atom-free singlet oxygen sensitizers. *Chemphotochem* 2, 606–615. doi: 10.1002/cptc.201800020

García-Fresnadillo, D. (2018). Singlet oxygen photosensitizing materials for point-of-use water disinfection with solar reactors. *Chemphotochem* 2, 512–534. doi: 10.1002/cptc.201800062

Ge, J., Lan, M., Zhou, B., Liu, W., Guo, L., Wang, H., et al. (2014). A graphene quantum dot photodynamic therapy agent with high singlet oxygen generation. *Nat. Commun.* 5:4596. doi: 10.1038/ncomms5596

Ghogare, A. A., and Greer, A. (2016). Using singlet oxygen to synthesize natural products and drugs. *Chem. Rev.* 116, 9994–10034. doi: 10.1021/acs.chemrev.5b00726

Gray, V., Allardice, J. R., Zhang, Z., Dowland, S., Xiao, J., Petty, A. J., et al. (2020). Direct vs delayed triplet energy transfer from organic semiconductors to quantum dots and implications for luminescent harvesting of triplet excitons. *ACS Nano* 14, 4224–4234. doi: 10.1021/acsnano.9b09339

Gu, K., Wang, Y., Shen, J., Zhu, J., Zhu, Y., and Li, C. (2020). Effective singlet oxygen generation in silica-coated CsPbBr3 quantum dots through energy transfer for photocatalysis. *Chemsuschem* 13, 682–687. doi: 10.1002/cssc.201903157

Hessel, C. M., Reid, D., Panthani, M. G., Rasch, M. R., Goodfellow, B. W., Wei, J. W., et al. (2012). Synthesis of ligand-stabilized silicon nanocrystals with size-dependent photoluminescence spanning visible to near-infrared wavelengths. *Chem. Mater.* 24, 393–401. doi: 10.1021/cm2032866

Hu, F., Mao, D., Kenry, W.ang, Y., Wu, W., Zhao, D., Kong, D., et al. (2018). Metal–organic framework as a simple and general inert nanocarrier for photosensitizers to implement activatable photodynamic therapy. *Adv. Funct. Mater.* 28:1707519. doi: 10.1002/adfm.201707519

Jin, T., Uhlikova, N., Xu, Z., Zhu, Y., Huang, Y., Egap, E., et al. (2019). Enhanced triplet state generation through radical pair intermediates in BODIPY-quantum dot complexes. *J. Chem. Phys.* 151:241101. doi: 10.1063/1.5136045

Khan, A. U., and Kasha, M. (1979). Direct spectroscopic observation of singlet oxygen emission at 1268 nm excited by sensitizing dyes of biological interest in liquid solution. *Proc. Natl. Acad. Sci. U.S.A.* 76, 6047–6049. doi: 10.1073/pnas.76.12.6047

Kovalev, D., Gross, E., Kunzner, N., Koch, F., Timoshenko, V. Y., and Fujii, M. (2002). Resonant electronic energy transfer from excitons confined in silicon nanocrystals to oxygen molecules. *Phys. Rev. Lett.* 89, 137401. doi: 10.1103/PhysRevLett.89.137401

Llansola Portolés, M. J., David Gara, P. M., Kotler, M. L., Bertolotti, S., San Román, E., Rodríguez, H. B., et al. (2010). Silicon nanoparticle photophysics and singlet oxygen generation. *Langmuir* 26, 10953–10960. doi: 10.1021/la100980x

Lu, H., Huang, Z., Martinez, M. S., Johnson, J. C., Luther, J. M., and Beard, M. C. (2020). Transforming energy using quantum dots. *Energy Environ. Sci.* 13, 1347–1376. doi: 10.1039/C9EE03930A

Lyubimenko, R., Busko, D., Richards, B. S., Schäfer, A. I., and Turshatov, A. (2019). Efficient photocatalytic removal of methylene blue using a metalloporphyrin–poly(vinylidene fluoride) hybrid membrane in a flow-through reactor. *ACS Appl. Mater. Interfaces* 11, 31763–31776. doi: 10.1021/acsami.9b04601

Maisch, T., Baier, J., Franz, B., Szeimies, R., Landthaler, M., and Baumler, W. (2007). The role of singlet oxygen and oxygen concentration in photodynamic inactivation of bacteria. *Proc. Natl. Acad. Sci. U.S.A.* 104, 7223–7228. doi: 10.1073/pnas.0611328104

Manfrin, A., Borduas-Dedekind, N., Lau, K., and Mcneill, K. (2019). Singlet oxygen photooxidation of peptidic oxazoles and thiazoles. *J. Org. Chem.* 84, 2439–2447. doi: 10.1021/acs.joc.8b02684

Marian, C. M. (2012). Spin–orbit coupling and intersystem crossing in molecules. *WIREs Comput. Mol. Sci.* 2, 187–203. doi: 10.1002/wcms.83

Mazzaro, R., Romano, F., and Ceroni, P. (2017). Long-lived luminescence of silicon nanocrystals: from principles to applications. *Phys. Chem. Chem. Phys.* 19, 26507–26526. doi: 10.1039/C7CP05208A

Monro, S., Colón, K. L., Yin, H., Roque, J., Konda, P., Gujar, S., et al. (2019). Transition metal complexes and photodynamic therapy from a tumor-centered approach: challenges, opportunities, and highlights from the development of TLD1433. *Chem. Rev.* 119, 797–828. doi: 10.1021/acs.chemrev.8b00211

Nosaka, Y., and Nosaka, A. Y. (2017). Generation and detection of reactive oxygen species in photocatalysis. *Chem. Rev.* 117, 11302–11336. doi: 10.1021/acs.chemrev.7b00161

Ogilby, P. R. (2010). Singlet oxygen: there is indeed something new under the sun. *Chem. Soc. Rev.* 39, 3181–3209. doi: 10.1039/b926014p

Osminkina, L. A., Gongalsky, M. B., Motuzuk, A. V., Timoshenko, V. Y., and Kudryavtsev, A. A. (2011). Silicon nanocrystals as photo- and sono-sensitizers for biomedical applications. *Appl. Phys. B* 105, 665–668. doi: 10.1007/s00340-011-4562-8

Penfold, T. J., Gindensperger, E., Daniel, C., and Marian, C. M. (2018). Spin-vibronic mechanism for intersystem crossing. *Chem. Rev.* 118, 6975–7025. doi: 10.1021/acs.chemrev.7b00617

Pramanik, S., Hill, S. K. E., Zhi, B., Hudson-Smith, N. V., Wu, J. J., White, J. N., et al. (2018). Comparative toxicity assessment of novel Si quantum dots and their traditional Cd-based counterparts using bacteria models *Shewanella oneidensis* and *Bacillus subtilis*. *Environ. Sci. Nano* 5, 1890–1901. doi: 10.1039/C8EN00332G

Rakovich, A., Savateeva, D., Rakovich, T., Donegan, J. F., Rakovich, Y. P., Kelly, V., et al. (2010). CdTe quantum dot/dye hybrid system as photosensitizer for photodynamic therapy. *Nanoscale Res. Lett.* 5, 753–760. doi: 10.1007/s11671-010-9553-x

Saleta Reig, D., Grauel, B., Konyushkin, V. A., Nakladov, A. N., Fedorov, P. P., Busko, D., et al. (2020). Upconversion properties of SrF2:Yb3+,Er3+ single crystals. *J. Mater. Chem. C.* 8, 4093–4101. doi: 10.1039/C9TC06591A

Schmidt, R., Tanielian, C., Dunsbach, R., and Wolff, C. (1994). Phenalenone, a universal reference compound for the determination of quantum yields of singlet oxygen O2(1-Delta-G) sensitization. *J. Photochem. Photobiol. A* 79, 11–17. doi: 10.1016/1010-6030(93)03746-4

Smith, J. G., Faucheaux, J. A., and Jain, P. K. (2015). Plasmon resonances for solar energy harvesting: a mechanistic outlook. *Nano Today* 10, 67–80. doi: 10.1016/j.nantod.2014.12.004

Sun, Y., Zhao, D., Wang, G., Wang, Y., Cao, L., Sun, J., et al. (in press). Recent progress of hypoxia-modulated multifunctional nanomedicines to enhance photodynamic therapy: opportunities, challenges, and future development. *Acta Pharm. Sin. B*. doi: 10.1016/j.apsb.2020.01.004

Taniguchi, M., Du, H., and Lindsey, J. S. (2018). PhotochemCAD 3: diverse modules for photophysical calculations with multiple spectral databases. *Photochem. Photobiol.* 94, 277–289. doi: 10.1111/php.12862

Turshatov, A., Busko, D., Avlasevich, Y., Miteva, T., Landfester, K., and Baluschev, S. (2012). Synergetic effect in triplet–triplet annihilation upconversion: highly efficient multi-chromophore emitter. *Chemphyschem* 13, 3112–3115. doi: 10.1002/cphc.201200306

Vlaskin, V. A., Beaulac, R., and Gamelin, D. R. (2009). Dopant-carrier magnetic exchange coupling in colloidal inverted core/shell semiconductor nanocrystals. *Nano Lett.* 9, 4376–4382. doi: 10.1021/nl9026499

Wang, S. Z., Gao, R. M., Zhou, F. M., and Selke, M. (2004). Nanomaterials and singlet oxygen photosensitizers: potential applications in photodynamic therapy. *J. Mater. Chem.* 14, 487–493. doi: 10.1039/b311429e

Wu, Y., Zhen, Y., Ma, Y., Zheng, R., Wang, Z., and Fu, H. (2010). Exceptional intersystem crossing in di(perylene bisimide)s: a structural platform toward photosensitizers for singlet oxygen generation. *J. Phys. Chem. Lett.* 1, 2499–2502. doi: 10.1021/jz1008328

Xia, P., Raulerson, E. K., Coleman, D., Gerke, C. S., Mangolini, L., Tang, M. L., et al. (2020). Achieving spin-triplet exciton transfer between silicon and molecular acceptors for photon upconversion. *Nat. Chem.* 12, 137–144. doi: 10.1038/s41557-019-0385-8

Xiao, L., Gu, L., Howell, S. B., and Sailor, M. J. (2011). Porous silicon nanoparticle photosensitizers for singlet oxygen and their phototoxicity against cancer cells. *ACS Nano* 5, 3651–3659. doi: 10.1021/nn1035262

Yang, B., Chen, Y., and Shi, J. (2019). Reactive oxygen species (ROS)-based nanomedicine. *Chem. Rev.* 119, 4881–4985. doi: 10.1021/acs.chemrev.8b00626

Yogo, T., Urano, Y., Ishitsuka, Y., Maniwa, F., and Nagano, T. (2005). Highly efficient and photostable photosensitizer based on BODIPY chromophore. *J. Am. Chem. Soc.* 127, 12162–12163. doi: 10.1021/ja05 28533

You, Y. (2018). Chemical tools for the generation and detection of singlet oxygen. *Org. Biomol. Chem.* 16, 4044–4060. doi: 10.1039/C8OB 00504D

You, Y., and Nam, W. (2014). Designing photoluminescent molecular probes for singlet oxygen, hydroxyl radical, and iron-oxygen species. *Chem. Sci.* 5, 4123–4135. doi: 10.1039/C4SC01637H

Zheng, X., Wang, L., Liu, M., Lei, P., Liu, F., and Xie, Z. (2018). Nanoscale mixed-component metal–organic frameworks with photosensitizer spatial-arrangement-dependent photochemistry for multimodal-imaging-guided photothermal therapy. *Chem. Mater.* 30, 6867–6876. doi: 10.1021/acs.chemmater.8b 03043

Zhi, B., Mishra, S., Hudson-Smith, N. V., Kortshagen, U. R., and Haynes, C. L. (2018). Toxicity evaluation of boron- and phosphorus-doped silicon nanocrystals toward *Shewanella oneidensis* MR-1. *ACS Appl. Nano Mater.* 1, 4884–4893. doi: 10.1021/acsanm.8b01053

Conflict of Interest: The authors declare that the research was conducted in the absence of any commercial or financial relationships that could be construed as a potential conflict of interest.

frontiers in Physics

ORIGINAL RESEARCH
published: 27 August 2020
doi: 10.3389/fphy.2020.00331

Unorthodox Dimensional Interpolations for He, Li, Be Atoms and Hydrogen Molecule

Kumar J. B. Ghosh[1], *Sabre Kais*[1] *and Dudley R. Herschbach*[2]*

[1] Department of Chemistry and Physics, Purdue University, West Lafayette, IN, United States, [2] Department of Chemistry and Chemical Biology, Harvard University Cambridge, Cambridge, MA, United States

We present a simple interpolation formula using dimensional limits $D = 1$ and $D = \infty$ to obtain the $D = 3$ ground-state energies of atoms and molecules. For atoms, these limits are linked by first-order perturbation terms of electron-electron interactions. This unorthodox approach is illustrated by ground-states for two, three, and four electron atoms, with modest effort to obtain fairly accurate results. Also, we treat the ground-state of H_2 over a wide range of the internuclear distance R, and compares well with the standard exact results from the Full Configuration Interaction method. Similar dimensional interpolations may be useful for complex many-body systems.

Keywords: dimensional interpolation, dimensional scaling, large-d limit, one-dimension, hydrogen molecule, ground state energy and ground state binding energy

OPEN ACCESS

Edited by:
Bretislav Friedrich,
Fritz-Haber-Institut, Germany

Reviewed by:
John Stuart Briggs,
University of Freiburg, Germany
David A. Mazziotti,
University of Chicago, United States

***Correspondence:**
Dudley R. Herschbach
dherschbach@gmail.com

Specialty section:
This article was submitted to Physical Chemistry and Chemical Physics, a section of the journal Frontiers in Physics

Received: *08 June 2020*
Accepted: *16 July 2020*
Published: *27 August 2020*

Citation:
Ghosh KJB, Kais S and Herschbach DR (2020) Unorthodox Dimensional Interpolations for He, Li, Be Atoms and Hydrogen Molecule. Front. Phys. 8:331. doi: 10.3389/fphy.2020.00331

1. INTRODUCTION

Dimensional scaling, as applied to chemical physics, offers promising computational strategies and heuristic perspectives to study electronic structures and obtain energies of atoms, molecules, and extended systems [1–4]. Taking a spatial dimension other than $D = 3$ can make a problem much simpler and then use perturbation theory or other techniques to obtain an approximate result for $D = 3$. Years ago, a D-scaling technique used with quantum chromodynamics [5] was prompted for helium [2–4]. The approach began with the $D \to \infty$ limit and added terms in powers of $\delta = 1/D$. It was arduous and asymptotic but by summation techniques attained very high accuracy for $D = 3$ [6]. Other dimensional scaling approaches were extended to N-electron atoms [7], renormalization with $1/Z$ expansions [8], random walks [9], interpolation of hard sphere virial coefficients [10], resonance states [11], and dynamics of many-body systems in external fields [12, 13].

Recently, a simple analytical interpolation formula emerged using both the $D = 1$ and $D \to \infty$ limits for helium [14]. It makes use of only the dimensional dependence of a hydrogen atom, together with the exactly known first-order perturbation terms with $\lambda = 1/Z$ for the dimensional limits of the electron-electron $\langle 1/r_{12} \rangle$ interaction. In the $D = 1$ limit, the Coulombic potentials are replaced by delta functions in appropriately scaled coordinates [15]. In the $D \to \infty$ limit, the electrons assume positions fixed relative to another and to the nucleus, with wave functions replaced by delta functions [16]. Then at $D = 3$, the ground state energy of helium ϵ_3 can be obtained by linking ϵ_1 and ϵ_∞ together with the first-order perturbation coefficients $\epsilon_1^{(1)}$ and $\epsilon_\infty^{(1)}$ of the $1/Z$ expansion. The first-order terms actually provide much of the dimension dependence. This article exhibits the applicability of an unorthodox formula, a blend of dimensions with first-order perturbations, to more complex many-body systems.

We outline the following sections: in section 2 the interpolation formula; in section 3 treat helium; in section 4 lithium; in section 5 beryllium; in section 6 hydrogen molecule. Each atom section 3–5 has four subsections: A for $D = 1$; B for $D \to \infty$; C for $\epsilon_D^{(1)}$, the first-order perturbation terms; D for ϵ_3, the ground-state energy at $D = 3$ is obtained from the interpolation formula. For the hydrogen molecule section 6, the subsections deal how the internuclear distance R varies in the $D = 1$ and $D \to \infty$ dimensions and mesh into $D = 3$. Finally, in section 7 we comment on prospects for blending dimensional limits to serve other many-body problems.

2. DIMENSIONAL INTERPOLATION

For dimensional scaling of atoms and molecules the energy erupts to infinity as $D \to 1$ and vanishes as $D \to \infty$. Hence, we adopt scaled units (with hartree atomic units) whereby $E_D = (Z/\beta)^2\epsilon_D$ and $\beta = \frac{1}{2}(D-1)$, so the reduced energy ϵ_D remains finite in both limits. When expressed in a $1/Z$ perturbation expansion, the reduced energy is given by

$$\epsilon_D = -1 + \epsilon_D^{(1)}\lambda + \epsilon_D^{(2)}\lambda^2 + \ ... \tag{1}$$

with $\lambda = 1/Z$, where Z is the total nuclear charge of the corresponding atom. The first-order perturbation coefficient is (1, 6):

$$\epsilon_D^{(1)} = f(D) = \frac{\Gamma(\frac{D}{2}+\frac{1}{2})\Gamma(D+\frac{1}{2})}{\Gamma(\frac{D}{2})\Gamma(D+1)}. \tag{2}$$

It represents the expectation value, $\langle\frac{1}{r_{12}}\rangle$, of the electron-electron repulsion evaluated with the zeroth-order hydrogenic wave function, $\exp(-r_1 - r_2)$. Accordingly, $\epsilon_D^{(1)}$ is universal. For $D = 1, 3, \infty$ the corresponding term $\epsilon_D^{(1)} = 1/2, 5/8, 2^{-1/2}$, respectively.

Our interpolation for atoms, developed in [14], weights the dimensional limits by $\delta = 1/D$, providing $\delta\epsilon_1$ and $(1-\delta)\epsilon_\infty$ in a simple analytic formula

$$\epsilon_D = \delta\epsilon_1 + (1-\delta)\epsilon_\infty + [\epsilon_D^{(1)} - \delta\epsilon_1^{(1)} - (1-\delta)\epsilon_\infty^{(1)}]\lambda, \tag{3}$$

We aim to illustrate the interpolation formula more fully, presenting results with modest calculations having respectable accuracy for two, three, and four electrons.

For the hydrogen molecule, a different scaling scheme will be used and illustrated. The rescaling of the internuclear distance $R \to R'$ is given by:

$$R \to \delta R' \text{ for } D \to 1;\ R \to (1-\delta)R' \text{ for } D \to \infty. \tag{4}$$

An approximation for $D = 3$ (where $R = R'$) emerges:

$$\epsilon_3(R') = \frac{1}{3}\epsilon_1(\frac{1}{3}R') + \frac{2}{3}\epsilon_\infty(\frac{2}{3}R'), \tag{5}$$

on interpolating linearly between the dimensional limits, developed by Loeser in [17–19]; especially see the paragraphs around Equations (23) and (24) of [17] for more details.

3. TWO-ELECTRONS: HELIUM

The formula worked very well for $D = 3$, helium with $\lambda = 1/2$:

$$\epsilon_3 = \frac{1}{3}\epsilon_1 + \frac{2}{3}\epsilon_\infty + \left[\epsilon_3^{(1)} - \frac{1}{3}\epsilon_1^{(1)} - \frac{2}{3}\epsilon_\infty^{(1)}\right]\lambda \tag{6}$$

The input ingredients are exact limit energies: $\epsilon_1 = -0.788843$ from Ref. [15]; $\epsilon_\infty = -0.684442$ from [4]; and the three first-order perturbation terms $\epsilon_D^{(1)}$ displayed in Equation (2). The interpolation delivered $\epsilon_3 = -0.725780$, a result very close to the exact ground-state energy -0.725931 [4]. The interpolation accuracy of 2 millihartrees is better than current density functional theory.

3.1. One-Dimension: D = 1

We will calculate the ground-state energy of the Hamiltonian operator using the variational principle. It is less accurate than [15], but much easier to deal with two and more electrons [20]. The Hamiltonian with electrons in delta functions is:

$$\mathcal{H} = -\frac{1}{2}\frac{\partial^2}{\partial r_1^2} - \frac{1}{2}\frac{\partial^2}{\partial r_2^2} - \delta(r_1) - \delta(r_2) + \lambda\delta(r_1 - r_2), \tag{7}$$

with $\lambda = 1/Z$. The electronic wave function is as follows:

$$\phi(r_1, r_2) = \chi_1(r_1)\chi_2(r_2), \tag{8}$$

where the normalized wave functions χ_1 and χ_2 are defined as:

$$\chi_1(r_1) = (\xi)^{1/2}e^{-\xi|r_1|} \tag{9}$$

and

$$\chi_2(r_2) = (\xi)^{1/2}e^{-\xi|r_2|}. \tag{10}$$

We optimize the parameter ξ, defined in (9, 10), and calculate the minimum value of the operator $E_\phi(\xi)$ defined as:

$$E_\phi(\xi) = \langle\phi \mid \mathcal{H} \mid \phi\rangle = \langle\phi \mid -\frac{1}{2}\frac{\partial^2}{\partial r_1^2} - \frac{1}{2}\frac{\partial^2}{\partial r_2^2} - \delta(r_1) - \delta(r_2) + \lambda\delta(r_1 - r_2) \mid \phi\rangle. \tag{11}$$

We divide the above Hamiltonian into three parts, where

$$\langle\phi \mid \mathcal{H}_{KE} \mid \phi\rangle = \langle\phi \mid -\frac{1}{2}\frac{\partial^2}{\partial r_1^2} - \frac{1}{2}\frac{\partial^2}{\partial r_2^2} \mid \phi\rangle = \xi^2 \tag{12}$$

is the kinetic energy of the two electrons,

$$\langle\phi \mid \mathcal{H}_{PE} \mid \phi\rangle = \langle\phi \mid -\delta(r_1) - \delta(r_2) \mid \phi\rangle = -2\xi \tag{13}$$

is the potential energy of the two electrons due to nuclear attraction, and

$$\langle\phi \mid \mathcal{H}_{ee} \mid \phi\rangle = \lambda\langle\phi \mid \delta(r_1 - r_2) \mid \phi\rangle = \lambda\frac{\xi}{2} \tag{14}$$

is the interaction energy for electron-electron repulsion in the system.

We minimize the Hamiltonian operator $E_\phi(\xi)$ with respect to ξ, with

$$E_\phi(\xi) = \xi^2 - 2\xi + \lambda\frac{\xi}{2}, \tag{15}$$

such that

$$\frac{dE_\phi}{d\xi} = 2\xi - 2 + \frac{\lambda}{2} = 0, \tag{16}$$

and obtain $\xi_0 = 0.875$, which put into Equation (15) gives the ground-state energy, $\epsilon_1 = -0.765625$. This result is found in [20–22], but it is approximated by 2.9% since noted the exact value is $\epsilon_1 = -0.788843$.

3.2. Infinite-Dimension: $D \to \infty$

At large-D limit, the effective ground state Hamiltonian for a two electron atom, with inter-electronic correlation can be written as:

$$\mathcal{H} = \frac{1}{2\sin^2\theta}\left(\frac{1}{r_1^2} + \frac{1}{r_2^2}\right) - \frac{Z}{r_1} - \frac{Z}{r_2} + J(r_1, r_2, \theta), \tag{17}$$

with

$$J(r_1, r_2, \theta) = \frac{1}{\sqrt{r_1^2 + r_2^2 - 2r_1 r_2\cos\theta}}, \tag{18}$$

where θ is the angle between r_1 and r_2; see [7] for more details.

We minimize the above effective-Hamiltonian with respect to the parameters r_1, r_2, and θ respectively, and obtain the corresponding ground state energy to be: $\epsilon_\infty = -0.684442$ (see Table 1 in [14], and [22]).

3.3. First-Order Perturbations: $\epsilon_D^{(1)}$

In a two-electron atom, with nuclear charge Z, the exact Hamiltonian in D-dimension using atomic units can be written as:

$$\mathcal{H} = -\frac{1}{2}\nabla_1^2 - \frac{1}{2}\nabla_2^2 - \frac{1}{r_1} - \frac{1}{r_2} + \lambda\frac{1}{r_{12}}, \tag{19}$$

where the Laplacian operator ∇_r^2 in D-dimension is defined as:

$$\nabla_r^2 = \frac{\partial^2}{\partial r^2} + \left(\frac{D-1}{r}\right)\frac{\partial}{\partial r} + \left(\text{angular part involving } \partial_\theta, \partial_\phi \text{etc}\right). \tag{20}$$

For helium-like atoms we consider the two electrons are in a 1s-like state with spatial part being symmetric (both electrons are in the same state) and the spin part in the antisymmetric spin singlet. The spatial part of the electronic wave function can be written as:

$$\phi(r_1, r_2) = \chi_1(r_1)\chi_2(r_2), \tag{21}$$

where the normalized wave functions $\chi_1(r_1)$ and $\chi_2(r_2)$ are defined as:

$$\chi_1(r_1) = \mathcal{N}e^{-r_1} \tag{22}$$

and

$$\chi_2(r_2) = \mathcal{N}e^{-r_2}. \tag{23}$$

The normalization constant $\mathcal{N}$ is calculated as:

$$\mathcal{N} = \frac{2^{D/2}}{\sqrt{(D-1)!\Omega(D)}}, \tag{24}$$

with

$$\Omega(D) = \frac{2\pi^{D/2}}{\Gamma(D/2)} \tag{25}$$

is the surface area of an unit sphere in D-dimension.

In D-dimension, with the above wave functions, we obtain the following first-order coefficient [14]:

$$\epsilon_D^{(1)} = f(D) = \langle\phi \mid \frac{1}{r_{12}} \mid \phi\rangle = \frac{\Gamma(\frac{D}{2}+\frac{1}{2})\Gamma(D+\frac{1}{2})}{\Gamma(\frac{D}{2})\Gamma(D+1)}. \tag{26}$$

As shown in Equation (2) and for $D = 1, 3, \infty$, respectively $\epsilon_D^{(1)} = \frac{1}{2}, \frac{5}{8}, \frac{1}{\sqrt{2}}$.

3.4. Interpolation for D = 3

We use the formula shown in Equation (6), already noting that the exact limit energies and first-order perturbation terms, gave $\epsilon_3 = -0.725780$; accurate to 0.02%. If we replace the variational result $\epsilon_1 = -0.765625$ (from section 3.1), the formula would give $\epsilon_3 = -0.71839$, accurate to 2.9%. However, if we evaluate ϵ_1 by using Equation (3), a subformula is

$$\epsilon_D = \epsilon_\infty + \left[\epsilon_D^{(1)} - \epsilon_\infty^{(1)}\right]\lambda, \tag{27}$$

with $D = 1$. This yielded a good approximation of 0.11% for $\epsilon_1 = -0.787996$, near the exact $\epsilon_1 = -0.788843$. With this better ϵ_1 we obtain $\epsilon_3 = -0.725496$, with accuracy of 0.06%.

In conventional quantum chemistry textbooks treating $D = 3$ helium, the electron-electron interaction, $\langle 1/r_{12}\rangle$, is evaluated by first-order perturbation theory. The result is $\epsilon_3 = -0.687529$ with accuracy of 5.29%.

4. THREE-ELECTRONS: LITHIUM

The ground-state of the lithium atom had been calculated a long ago by using the variational method with complicated wave functions [23–25]. Here we present the interpolation formula, using the $D = 1$ and $D = \infty$ limits and the first-order perturbation terms. For the ground-state of the lithium atom our formula gave $\epsilon_3 = -0.839648$, with approximation 1.04% compared the exact result $\epsilon_3 = -0.830896$ [26].

4.1. One-Dimension: D=1

In a three-electron atom, with nuclear charge Z, the exact Hamiltonian in one-dimension using atomic units can be written as:

$$\mathcal{H} = \sum_{i=1}^{3}\left(-\frac{1}{2}\frac{\partial^2}{\partial r_i^2} - \delta(r_i)\right) + \lambda\sum_{i,j=1}^{3}\delta(r_i - r_j), \tag{28}$$

with $\lambda = 1/Z$.

In the lithium atom we consider that two electrons are in the 1*s* state and the third electron is in a 2*s* state, with the spatial part being symmetric (both electrons are in the same state) and the spin part in the antisymmetric state. We write spatial part of the electronic wave function as:

$$\phi(r_1, r_2, r_3) = \chi_1(r_1)\chi_2(r_2)\chi_3(r_3). \tag{29}$$

The two normalized wave functions $\chi_1(r_1)$, $\chi_2(r_2)$ are described in Equations (9) and (10). We assume that the 1*s* wave functions are orthogonal to the 2*s* wave function:

$$\chi_3(r_3) = \left(\frac{9\xi}{20}\right)^{1/2}\left(\frac{2}{3} - \xi \mid r_3 \mid\right) e^{-\xi|r_3|/2}. \tag{30}$$

We calculate the ground state energy of a three-electron atom using variational principle. We optimize the parameter ξ, defined in the wave functions $\chi_1(r_1), \chi_2(r_2), \chi_3(r_3)$, and obtain the minimum value of the Hamiltonian operator $E_\phi(\xi)$, which is defined as

$$E_\phi(\xi) = \langle\phi \mid \mathcal{H} \mid \phi\rangle = \langle\phi \mid \sum_{i=1}^{3}\left(-\frac{1}{2}\frac{\partial^2}{\partial r_i^2} - \delta(r_i)\right) + \lambda\sum_{i,j=1}^{3}\delta(r_i - r_j) \mid \phi\rangle. \tag{31}$$

We divide the above Hamiltonian (31) into five parts, where

$$\langle\phi \mid \mathcal{H}_{KE} \mid \phi\rangle = \langle\phi \mid \sum_{i=1}^{3} -\frac{1}{2}\frac{\partial^2}{\partial r_i^2} \mid \phi\rangle = \frac{1}{2}\left(2\xi^2 + \frac{17}{20}\xi^2\right) \tag{32}$$

is the kinetic energy of the three electrons,

$$\langle\phi \mid \mathcal{H}_{PE} \mid \phi\rangle = \langle\phi \mid -\sum_{i=1}^{3}\delta(r_i) \mid \phi\rangle = -\left(2\xi + \frac{\xi}{5}\right) \tag{33}$$

is the potential energy of the three electrons due to nuclear attraction, and

$$\langle\phi \mid \mathcal{H}_{12} \mid \phi\rangle = \langle\phi \mid \lambda\delta(r_1 - r_2) \mid \phi\rangle = \lambda\frac{\xi}{2}, \tag{34}$$

$$\langle\phi \mid \mathcal{H}_{13} \mid \phi\rangle = \lambda\langle\phi \mid \delta(r_1 - r_3) \mid \phi\rangle = \lambda\frac{\xi}{15}, \tag{35}$$

$$\langle\phi \mid \mathcal{H}_{23} \mid \phi\rangle = \lambda\langle\phi \mid \delta(r_2 - r_3) \mid \phi\rangle = \lambda\frac{\xi}{15}, \tag{36}$$

are the interaction energies for inter-electronic repulsions in the system.

We minimize the Hamiltonian operator $E_\phi(\xi)$ with respect to ξ, with

$$E_\phi(\xi) = \frac{1}{2}\left(2\xi^2 + \frac{17}{20}\xi^2\right) - \left(2\xi + \frac{\xi}{5}\right) + \lambda\frac{2\xi}{15} + \lambda\frac{\xi}{2}, \tag{37}$$

such that

$$\frac{dE_\phi}{d\xi} = \frac{57}{20}\xi - \frac{11}{5} + \frac{19}{30}\lambda = 0, \tag{38}$$

and obtain $\xi_0 = 0.697856$, which put into Equation (37) gives the ground-state energy, $\epsilon_1 = -0.693979$.

4.2. Infinite-Dimension: $D \to \infty$

At large-D-limit the effective ground state Hamiltonian for three-electron atoms, with correlation can be written as:

$$\mathcal{H} = \frac{1}{2}\left(\frac{1}{r_1^2}\frac{\Gamma^{(1)}}{\Gamma} + \frac{1}{r_2^2}\frac{\Gamma^{(2)}}{\Gamma} + \frac{4}{r_3^2}\frac{\Gamma^{(3)}}{\Gamma}\right) - \frac{1}{r_1} - \frac{1}{r_2} - \frac{1}{r_3} + \lambda J(r_1, r_2, r_3), \tag{39}$$

where

$$J(r_1, r_2, r_3) = \frac{1}{\sqrt{r_1^2 + r_2^2 - 2r_1r_2\gamma_{12}}} + \frac{1}{\sqrt{r_1^2 + r_3^2 - 2r_1r_3\gamma_{13}}} + \frac{1}{\sqrt{r_2^2 + r_3^2 - 2r_2r_3\gamma_{23}}}, \tag{40}$$

with $\gamma_{ij} = \gamma_{ij} = \cos\theta_{ij}$, and θ_{ij} is the angle between r_i and r_j. The quantities $\Gamma^{(i)}$ and Γ are called the Gramian determinants. In Equation (39) the quantity $\frac{\Gamma^{(i)}}{\Gamma}$ is effectively defined as:

$$\frac{\Gamma^{(i)}}{\Gamma} = 1 + \sum_{\substack{i,j \\ (j\neq i)}}\gamma_{ij}^2 - \sum_{\substack{i,j,k \\ (j\neq i\neq k)}} 2\gamma_{ij}\gamma_{jk}\gamma_{ki} \quad \text{for} i, j, k = 1, 2, 3. \tag{41}$$

See page 111, Equation (35) in [7] for more details.

We minimize the above effective-Hamiltonian with respect to the parameters r_1, r_2, r_3, and $\theta_{12}, \theta_{13}, \theta_{23}$, respectively and obtain the corresponding ground state energy $\epsilon_\infty = -0.795453$.

4.3. First-Order Perturbations: $\epsilon_D^{(1)}$

As the electrons reside in two orbits, $1s^2 2s$, there are three electron-electron pairs: one $\langle\frac{1}{r_{12}}\rangle$ from $1s^2$, the two others $\langle\frac{1}{r_{13}}\rangle$ and $\langle\frac{1}{r_{23}}\rangle$ from $1s2s$. Thus, each $\epsilon_D^{(1)}$ coefficient is comprised from the three electron pairs:

$$\epsilon_1^{(1)} = 1/2 + 2(1/15) = 0.633333 \tag{42}$$

$$\epsilon_\infty^{(1)} = 2^{-1/2} + 2(0.447212) = 1.601531 \tag{43}$$

$$\epsilon_3^{(1)} = 5/8 + 2(17/81) = 1.044753. \tag{44}$$

The $D = 1$ item is obtained via section 4.1. The $D = 3$ item is attained from [27]. Here we will develop both $D = 3$ and $D \to \infty$ bringing the third electron akin with the two-electron treatment in section 3.3. As the Hamiltonian is evident in Equations (19) and (20), we start with the electronic wave function:

$$\phi(r_1, r_2, r_3) = \chi_1(r_1)\chi_2(r_2)\chi_3(r_3). \tag{45}$$

The two normalized functions $\chi_1(r_1)$, $\chi_2(r_2)$ are taken care of in Equations (22), (23), (24), and (25). We assume that the 1*s* wave functions are orthogonal to the 2*s* wave function:

$$\chi_3(r_3) = \mathcal{N}_1(1-\alpha r_3)e^{-r_3/2}. \tag{46}$$

The normalization is:

$$\mathcal{N}_1 = \frac{1}{\sqrt{(1+\alpha^2 D(D+1)-2\alpha D)(D-1)!\Omega(D)}}, \tag{47}$$

with $\alpha = \frac{3}{2D}$.

To obtain the first-order terms for $D = 3$ and $D \to \infty$ we need to assemble some integrals associated with the key $f(D)$ function shown in Equations (2) and (26). The output is:

$$\langle\frac{1}{r_{13}}\rangle = \langle\frac{1}{r_{23}}\rangle = f(D)F\left(\frac{1}{2}, \frac{3-D}{2}; \frac{D}{2}; y\right)\left(\frac{ab}{a+b}\right), \tag{48}$$

with

$$y = \left(\frac{a-b}{a+b}\right)^2, \tag{49}$$

and the hypergeometric function $F\left(\frac{1}{2}, \frac{3-D}{2}; \frac{D}{2}; y\right)$ enters in (26).

The parent integral is,

$$\begin{aligned} G_D(a,b) &= \int d^D r_1 \int d^D r_2 \frac{e^{-ar_1}}{r_1}\frac{e^{-br_2}}{r_2}\frac{1}{r_{12}} \\ &= N_D F\left(\frac{1}{2}, \frac{3-D}{2}; \frac{D}{2}; y\right)\frac{1}{(ab)^{D-2}(a+b)}, \end{aligned} \tag{50}$$

and

$$N_D = \frac{(4\pi)^{D-1}\Gamma(D-1)\Gamma(D-\frac{3}{2})\Gamma(\frac{D-1}{2})^3}{\Gamma(D-1)^2\Gamma(D/2)}. \tag{51}$$

From $G_D(a,b)$ we compute the following integral:

$$\begin{aligned} K_D(i,j) &= \int d^D r_1 \int d^D r_2 e^{-ar_1}e^{-br_2}r_1^{i-1}r_2^{j-1}\frac{1}{r_{12}} \\ &= \left(-\frac{\partial}{\partial a}\right)^i\left(-\frac{\partial}{\partial b}\right)^j G_D(a,b). \end{aligned} \tag{52}$$

In the integrals, we used the normalized wave functions $\chi_1(r_1)$, $\chi_2(r_2)$, and $\chi_3(r_3)$ already specified, such a typical term:

$$\begin{aligned} \langle\frac{1}{r_{13}}\rangle &\sim \int d^D r_1 \int d^D r_3 \chi_1^*(r_1)^*\chi_3^*(r_3)\frac{1}{r_{13}}\chi_1(r_1)\chi_3(r_3) \\ &\sim \int d^D r_1 \int d^D r_3 (1-\alpha r_3)^2 e^{-2r_1}e^{-r_3}\frac{1}{r_{13}}. \end{aligned} \tag{53}$$

From Equation (53), we see that we have to put $a = 2$ and $b = 1$, so $y = 1/9$. In Equations (48) and (55) the hypergeometric function is available in tabulations [28]. We computed up to $D = 10^6$ to see that the function converges to

$$F\left(\frac{1}{2}, -\frac{D}{2}; \frac{D}{2}; \frac{1}{9}\right) \to 0.948683 \text{for } D \to \infty. \tag{54}$$

At the $D \to \infty$ limit

$$\langle\frac{1}{r_{13}}\rangle = \langle\frac{1}{r_{23}}\rangle = (2/3)2^{-1/2}(0.948683) = 0.447212. \tag{55}$$

For $D = 3$, the function gives

$$F\left(\frac{1}{2}, 0; \frac{3}{2}; \frac{1}{9}\right) = 0.503703 \tag{56}$$

and,

$$\langle\frac{1}{r_{13}}\rangle = \langle\frac{1}{r_{23}}\rangle = (2/3)(5/8)(0.503703) = 17/81. \tag{57}$$

4.4. Interpolation for D = 3

Again we use the interpolation formula shown in Equation (6),

$$\epsilon_3 = \frac{1}{3}\epsilon_1 + \frac{2}{3}\epsilon_\infty + \left[\epsilon_3^{(1)} - \frac{1}{3}\epsilon_1^{(1)} - \frac{2}{3}\epsilon_\infty^{(1)}\right]\lambda, \tag{58}$$

now with $\lambda = 1/Z = 1/3$. The input from our A, B, C subsections was:

$$\epsilon_1 = -0.693979, \epsilon_\infty = -0.795453,$$

and

$$\epsilon_3^{(1)} = 1.044753, \epsilon_1^{(1)} = 0.633333, \epsilon_\infty^{(1)} = 1.601531.$$

Our interpolation gave the Li atom ground-state energy with error 1%: $\epsilon_3 = -0.839648$, compared with the exact result $\epsilon_3 = -0.830896$ [26].

5. FOUR-ELECTRON: BERYLLIUM

The electronic structure of the beryllium atom is highly interesting because it's implication in different areas of modern science, for e.g. stellar astrophysics and plasmas, high-temperature physics, etc. The ground-state energy for the Be-atom has been calculated by applying various methods for e.g., the Configuration Interaction (CI) method with Slater-type orbitals (STOs) [29], the Hylleraas method (Hy) [30], the Hylleraas-Configuration Interaction method (Hy-CI) [31], and the Exponential Correlated Gaussian (ECG) method [32, 33]. In this section, we present the dimensional interpolation formula, by using the results from $D = 1$ and $D = \infty$ limit, to obtain the ground state energy of the four-electron atoms. With dimensional interpolation we obtain the ground state energy of beryllium atom to be $\epsilon_3 = -0.910325$, compared to the exact energy $\epsilon_3 = -0.916709$, with a percentage error of 0.6%.

5.1. One-Dimension: D=1

In Four-electron atoms, with nuclear charge $Z = 1/\lambda$, the exact Hamiltonian in one-dimension using atomic units can be written as:

$$\mathcal{H} = \sum_{i=1}^{4}\left(-\frac{1}{2}\frac{\partial^2}{\partial r_i^2} - \delta(r_i)\right) + \lambda\sum_{i,j=1}^{4}\delta(r_i - r_j). \tag{59}$$

In beryllium atom we consider that two electrons are in the 1*s* state, and the other two electrons are in the 2*s* state with the spatial part being symmetric (both electrons are in the same state) and the spin part in the antisymmetric state. We write spatial part of the electronic wave function as follows:

$$\phi(r_1, r_2, r_3, r_4) = \chi_1(r_1)\chi_2(r_2)\chi_3(r_3)\chi_4(r_4), \tag{60}$$

The three normalized wave functions $\chi_1(r_1)$, $\chi_2(r_2)$, $\chi_3(r_3)$ are described in Equations (9), (10), and (30). We assume that the 1*s* wave functions are orthogonal to the two 2*s* wave functions $\chi_3(r_3)$ and

$$\chi_4(r_4) = \left(\frac{9\xi}{20}\right)^{1/2}\left(\frac{2}{3} - \xi \mid r_4 \mid\right) e^{-\xi|r_4|/2}. \tag{61}$$

We calculate the ground state energy of a four-electron atom with variational principle. We optimize the parameter ξ, defined in the wave functions $\chi_1(r_1)$, $\chi_2(r_2)$, $\chi_3(r_3)$, $\chi_4(r_4)$, and obtain the minimum value of the Hamiltonian operator $E_\phi(\xi)$, which is defined as:

$$E_\phi(\xi) = \langle\phi \mid \mathcal{H} \mid \phi\rangle = \langle\phi \mid \sum_{i=1}^{4}\left(-\frac{1}{2}\frac{\partial^2}{\partial r_i^2} - \delta(r_i)\right) + \lambda\sum_{i,j=1}^{4}\delta(r_i - r_j) \mid \phi\rangle. \tag{62}$$

We divide the above Hamiltonian into five parts, where

$$\langle\phi \mid \mathcal{H}_{KE} \mid \phi\rangle = \langle\phi \mid \sum_{i=1}^{4} -\frac{1}{2}\frac{\partial^2}{\partial r_i^2} \mid \phi\rangle = \left(\xi^2 + \frac{17}{20}\xi^2\right) \tag{63}$$

is the kinetic energy of the four electrons,

$$\langle\phi \mid \mathcal{H}_{PE} \mid \phi\rangle = \langle\phi \mid -\sum_{i=1}^{4}\delta(r_i) \mid \phi\rangle = -2\left(\xi + \frac{1}{5}\xi\right) \tag{64}$$

is the potential energy of the four electrons due to nuclear attraction, and

$$\langle\phi \mid \mathcal{H}_{12} \mid \phi\rangle = \langle\phi \mid \lambda\delta(r_1 - r_2) \mid \phi\rangle = \lambda\frac{\xi}{2}, \tag{65}$$

$$\langle\phi \mid \mathcal{H}_{i3} \mid \phi\rangle = \langle\phi \mid \lambda\delta(r_i - r_3) \mid \phi\rangle = \lambda\frac{\xi}{15} = \langle\phi \mid \mathcal{H}_{i4} \mid \phi\rangle, \text{ for i=1,2,} \tag{66}$$

$$\langle\phi \mid \mathcal{H}_{34} \mid \phi\rangle = \langle\phi \mid \lambda\delta(r_3 - r_4) \mid \phi\rangle = \lambda\frac{71}{800}\xi \tag{67}$$

are the interaction energies for inter-electronic repulsions in the system.

We minimize the Hamiltonian operator $E_\phi(\xi)$ with respect to ξ, with

$$E_\phi(\xi) = \left(\xi^2 + \frac{17}{20}\xi^2\right) - 2\left(\xi + \frac{\xi}{5}\right) + \lambda\frac{4\xi}{15} + \lambda\frac{\xi}{2} + \lambda\frac{71}{800}\xi, \tag{68}$$

such that

$$\frac{dE_\phi}{d\xi} = \frac{37}{10}\xi - \frac{12}{5} + \frac{2053}{2400}\lambda = 0, \tag{69}$$

and obtain $\xi_0 = 0.590850$, which put into Equation (68) gives the ground-state energy, $\epsilon_1 = -0.645842$.

5.2. Infinite-Dimension: $D \to \infty$

In large-D-limit the effective ground state Hamiltonian for four-electron atoms, with inter-electronic correlation can be written as:

$$\mathcal{H} = \frac{1}{2}\left(\frac{1}{r_1^2}\frac{\Gamma^{(1)}}{\Gamma} + \frac{1}{r_2^2}\frac{\Gamma^{(2)}}{\Gamma} + \frac{4}{r_3^2}\frac{\Gamma^{(3)}}{\Gamma} + \frac{4}{r_4^2}\frac{\Gamma^{(4)}}{\Gamma}\right) - \frac{1}{r_1} - \frac{1}{r_2} - \frac{1}{r_3} - \frac{1}{r_4} + \lambda J(r_1, r_2, r_3, r_4), \tag{70}$$

where

$$J(r_1, r_2, r_3, r_4) = \sum_{i,j=1}^{4}\frac{1}{\sqrt{r_i^2 + r_j^2 - 2r_i r_j\gamma_{ij}}}, \tag{71}$$

with $\gamma_{ij} = \gamma_{ij} = \cos\theta_{ij}$, and θ_{ij} are the angle between r_i and r_j. The quantities $\Gamma^{(i)}$ and Γ are the Gramian determinants. In Equation (70) the quantity $\frac{\Gamma^{(i)}}{\Gamma}$ is effectively defined as follows:

$$\frac{\Gamma^{(i)}}{\Gamma} = 1 + \sum_{\substack{i,j \\ (j\neq i)}}\gamma_{ij}^2 - \sum_{\substack{i,j,k \\ (j\neq i\neq k)}} 2\gamma_{ij}\gamma_{jk}\gamma_{ki} + \sum_{\substack{i,j,k,l \\ (j\neq i\neq k\neq l)}}\left(2\gamma_{ij}\gamma_{jk}\gamma_{kl}\gamma_{li} - \gamma_{ij}^2\gamma_{kl}^2\right) \text{for} i, j, k, l = 1, 2, 3, 4. \tag{72}$$

See page 111, Equation (35) in [7] for more details.

We minimize the above effective-Hamiltonian with respect to the parameters r_1, r_2, r_3, r_4, and $\theta_{12}, \theta_{13}, \theta_{14}, \theta_{23}, \theta_{24}, \theta_{34}$ respectively and obtain the corresponding ground state energy $\epsilon_\infty = -0.875837$.

5.3. First-Order Perturbations: $\epsilon_D^{(1)}$

As the electrons reside in two orbits, $1s^2 2s^2$, there are six electron-electron pairs: one $\langle\frac{1}{r_{12}}\rangle$ from $1s^2$, four others $\langle\frac{1}{r_{13}}\rangle$, $\langle\frac{1}{r_{14}}\rangle$, $\langle\frac{1}{r_{23}}\rangle$, $\langle\frac{1}{r_{24}}\rangle$ from $1s2s$; and another lonely $\langle\frac{1}{r_{34}}\rangle$ from $2s^2$. Each $\epsilon_D^{(1)}$ coefficient is comprised from the six electron pairs:

$$\epsilon_1^{(1)} = 1/2 + 4(1/15) + (71/800) = 0.855417, \tag{73}$$

$$\epsilon_\infty^{(1)} = 2^{-1/2} + 4(0.447212) + 0.353553 = 2.849508, \tag{74}$$

$$\epsilon_3^{(1)} = 5/8 + 4(17/81) + 0.275696 = 1.740202, \tag{75}$$

The $D = 1$ item is obtained via section 5.1. Here we will develop both $D = 3$ and $D \to \infty$ bringing the fourth electron akin with the three-electron treatment in section 4.3. As the Hamiltonian

is evident in Equations (19) and (20), we start with the electronic wave function:

$$\phi(r_1, r_2, r_3, r_4) = \chi_1(r_1)\chi_2(r_2)\chi_3(r_3)\chi_4(r_4), \tag{76}$$

The two normalized 1*s* wave functions $\chi_1(r_1)$, $\chi_2(r_2)$ are taken care of in Equations (22), (23), (24), and (25). We assume that the 1*s* wave functions are orthogonal to the 2*s* wave functions $\chi_2(r_2)$, defined in (46), and:

$$\chi_4(r_4) = \mathcal{N}_1 (1 - \alpha r_4)\, e^{-r_4/2}, \tag{77}$$

with normalization constant $\mathcal{N}_1$ defined in (47).

We take the same approach as section 4.3 to calculate the first-order term (the $2s^2$ electron-electron repulsion term) at $D \to \infty$ limit with the help of Equations (50, 52):

$$\langle \frac{1}{r_{34}} \rangle = f(D) F\left(\frac{1}{2}, \frac{3-D}{2}; \frac{D}{2}; y\right)\left(\frac{ab}{a+b}\right) \tag{78}$$

with $y = \left(\frac{a-b}{a+b}\right)^2$ and $f(D)$ function shown in Equations (2) and (26). This is the same functional expression as in lithium atom (53), but the arguments are different.

To calculate the first-order perturbation coefficient $\langle \frac{1}{r_{34}} \rangle$ for beryllium we use the normalized wave functions $\chi_1(r_1), \chi_2(r_2), \chi_3(r_3)$, and $\chi_4(r_4)$ already specified, which gives rise to a typical term like

$$\begin{aligned}\langle \frac{1}{r_{34}} \rangle &\sim \int d^D r_3 \int d^D r_4 \chi_3^*(r_3)\chi_4^*(r_4)\frac{1}{r_{34}}\chi_3(r_3)\chi(r_4) \\ &\sim \int d^D r_3 \int d^D r_4 (1-\alpha r_3)^2(1-\alpha r_4)^2 e^{-r_3} e^{-r_4}\frac{1}{r_{34}}.\end{aligned} \tag{79}$$

From the above Equation (79), we see that we have to put $a = 1$ and $b = 1$, so $y = 0$. In Equation (78) the hypergeometric function

$$\lim_{D\to\infty} F\left(\frac{1}{2}, \frac{3-D}{2}; \frac{D}{2}; y\right) = \lim_{D\to\infty} F\left(\frac{1}{2}, -\frac{D}{2}; \frac{D}{2}; 0\right) = 1, \tag{80}$$

and $f(D) \to 2^{-1/2}$ at $D \to \infty$ limit.

At $D \to \infty$ limit (78) gives

$$\langle \frac{1}{r_{34}} \rangle = 0.353553. \tag{81}$$

For $D = 3$ we use the following formula from [1] and [28]:

$$\begin{aligned}G_3^k(a,b) &= \int d^3 r_1 \int d^3 r_2 \frac{e^{-ar_1}}{r_1}\frac{e^{-br_2}}{r_2} r_{12}^{k-1} \\ &= (4\pi)^2 \Gamma(k+1)\left(a^2 - b^2\right)^{-1}\left(b^{-k-1} - a^{-k-1}\right),\end{aligned} \tag{82}$$

From the above relation (82) we can compute the following integral:

$$\begin{aligned}K_3(i,j,k) &= \int d^3 r_1 \int d^3 r_2 e^{-ar_1} e^{-br_2} r_1^{i-1} r_2^{j-1} r_{12}^{k-1} \\ &= \left(-\frac{\partial}{\partial a}\right)^i \left(-\frac{\partial}{\partial b}\right)^j G_3^k(a,b).\end{aligned} \tag{83}$$

At $D = 3$ the 2*s* wave function

$$\psi_{2s}(r) = \sqrt{\frac{\alpha^3}{32\pi}}(2 - \alpha r) e^{-\alpha r/2}, \tag{84}$$

with $\alpha = 1$ such that

$$\langle \frac{1}{r_{34}} \rangle = \int d^3 r_3 \int d^3 r_4 |\psi_{2s}(r_3)|^2 \left(\frac{1}{r_{34}}\right) |\psi_{2s}(r_4)|^2. \tag{85}$$

To calculate the inter-electronic repulsion energy $\langle \frac{1}{r_{34}} \rangle$ from (85) we use the above type of integrals $G_3^k(a,b)$ in Equation (82) and $K_3(i,j,k)$ in Equation (83), with $a = 1, b = 1$, and $k = 0$.

With the help of (82, 83) we calculate the first-order coefficient (2*s*-2*s* part) for the beryllium atom in three dimension:

$$\langle \frac{1}{r_{34}} \rangle = 0.275696. \tag{86}$$

5.4. Interpolation for D=3

We again use the interpolation formula shown in Equation (6),

$$\epsilon_3 = \frac{1}{3}\epsilon_1 + \frac{2}{3}\epsilon_\infty + \left[\epsilon_3^{(1)} - \frac{1}{3}\epsilon_1^{(1)} - \frac{2}{3}\epsilon_\infty^{(1)}\right]\lambda, \tag{87}$$

now with $\lambda = 1/Z = 1/4$. The input from our A, B, C subsections was:

$$\epsilon_1 = -0.645842, \epsilon_\infty = 0.875837,$$

and

$$\epsilon_3^{(1)} = 1.740202, \epsilon_1^{(1)} = 0.855417, \epsilon_\infty^{(1)} = 2.849508.$$

Our interpolation gives the Be atom ground-state energy with error 0.6%: $\epsilon_3 = -0.910325$, compared with the exact result $\epsilon_3 = -0.916709$.

6. HYDROGEN MOLECULE

The ground state potential energy function, $V(R)$, of the hydrogen molecule has been calculated by many methods [34–37]. Recently, Olivares-Pilón and Turbiner [38] presented a general theory for obtaining the $V(R)$ function for diatomic molecules. They dealt with the Born-Oppenheimer approximation, based on matching R in short and long distances via a two-point Padé approximation. Here, we present a simpler approach obtaining $V(R)$ for H_2 at $D = 3$ by using interpolation between $D = 1$ and $D \to \infty$ dimensional limits. Key aspects of dimensional scaling had been developed years ago by Tan and Loeser [18], Lòpez-Cabrera et al. [19] and Frantz and Herschbach [17]. They did an excellent treatment on H_2^+ and partial on H_2. Now we will complete $V(R)$ for H_2 by interpolation.

6.1. One-Dimension: D=1

In H_2, with nuclear charge of each atom Z, the electronic part of the Hamiltonian in one-dimension using atomic units can be written as [20, 39]:

$$\mathcal{H} = -\frac{1}{2}\frac{\partial^2}{\partial r_1^2} - \frac{1}{2}\frac{\partial^2}{\partial r_2^2} - \delta(r_1 - a) - \delta(r_1 + a) - \delta(r_2 - a) - \delta(r_2 + a) + \lambda\delta(r_1 - r_2), \quad (88)$$

with $a = R/2$, where R is the distance between the two nuclei located at $r = \pm a$; also $\lambda = 1/Z = 1$. The Hamiltonian energy eigenvalues provide symmetric and antisymmetric states under exchange of the electrons. The symmetric state pertains to the ground-state potential energy [20]:

$$\epsilon_1(R) = -\frac{1 + \left(4 + 2R + R^2\right) e^{-2R}}{1 + (1 + R)^2 e^{-2R}}, \quad (89)$$

The total binding energy is obtained by adding the nucleus-nucleus-interaction term $(1/R)$ with the electronic energy.

6.2. Infinite-Dimension: $D \to \infty$

Many important features of the H_2 molecule are calculated in cylindrical coordinates because this problem has a natural cylindrical symmetry about the z-axis. The D-dimensional space in cylindrical coordinates is described by a linear coordinate z and a $(D-1)$-dimensional subspace specified by spherical coordinates, which are orthogonal to each other. The coordinate ρ is the radius of a $(D-1)$-dimensional sphere; see section 2 of [17] for more details.

For H_2, convention locates the two nuclei A and B on the z-axis at $-R/2$ and $R/2$, respectively, with equal charges $Z_A = Z_B = Z$. The electrons are located at (ρ_1, z_1) and (ρ_2, z_2), with a dihedral angle ϕ specifying their relative azimuthal orientation about the molecular axis. The effective Hamiltonian for large-D limit in cylindrical coordinates is [17, 40]:

$$\mathcal{H} = \frac{1}{2}\left(\frac{1}{\rho_1^2} + \frac{1}{\rho_2^2}\right)\frac{1}{\sin^2\phi} - \sum_{i=1}^{2}\left[\frac{Z}{\sqrt{\rho_i^2 + (z_i + a)^2}} + \frac{Z}{\sqrt{\rho_i^2 + (z_i - a)^2}}\right] + J(\rho_1, \rho_2, z_1, z_2, \phi), \quad (90)$$

with $a = R/2$ and

$$J(\rho_1, \rho_2, z_1, z_2, \phi) = \frac{1}{\sqrt{(z_1 - z_2)^2 + \rho_1^2 + \rho_2^2 - 2\rho_1\rho_2\cos\phi}}.$$

In the $D \to \infty$ limit, the Hamiltonian has two locations for electrons, namely: symmetric, with $\rho_1 = \rho_2$ and $z_1 = z_2$, and antisymmetric, with $\rho_1 = \rho_2$ and $z_1 = -z_2$. When R has the nuclei well apart, in the symmetric case, both electrons cluster near one of the nuclei ($H_2 \to H^- + H^+$); in the antisymmetric case, each electron resides near just one of the nuclei ($H_2 \to H + H$). Thus, the antisymmetric case is much more favorable for the ground-state energy.

We minimize the Hamiltonian (90) with respect to ρ's and z's to obtain the ground state energy, $\epsilon_\infty(R)$; we numerically evaluate the corresponding optimized parameters $\rho_1^*, \rho_2^*, z_1^*, z_2^*$, and ϕ^* for different values of R.

The total binding energy is obtained by adding to $\epsilon_\infty(R)$ the internuclear-interaction term $(1/R)$.

6.3. Interpolation for D=3

Unlike the atoms, our interpolation will be different for a molecule. An atom has only one nucleus, with the electrons orbiting about the positive charge; our interpolation with the first-order perturbation works well for atoms but not for a molecule. For a diatomic molecule, $V(R)$ is fundamental, with the internuclear distance R. As mentioned in Equations (4) and (5), our interpolation for H_2 uses a modified rescaling scheme developed by [17–19] with the $D = 1$ and $D \to \infty$ dimensional limits:

$$\epsilon_3(R) = \frac{1}{3}\epsilon_1(R) + \frac{2}{3}\epsilon_\infty(R), \quad (91)$$

The rescaled distances are:

$$\text{In } D = 1 : r_i \to r_i'/3 \text{ and } R \to R'/3, \text{ for } i = 1, 2\,; \quad (92a)$$

$$\text{In } D \to \infty : \rho_i \to 2\rho_i'/3, z_i \to 2z_i'/3, \text{ and } R \to 2R'/3, \text{ for } i = 1, 2\,. \quad (92b)$$

The rescaled Hamiltonians have distinct factors in the kinetic and potential energy parts: In $D = 1$: Hamiltonian (88) becomes:

$$\mathcal{H}_{D=1} = -\frac{9}{2}\frac{\partial^2}{\partial r_1^2} - \frac{9}{2}\frac{\partial^2}{\partial r_2^2} - 3\delta(r_1 - a) - 3\delta(r_1 + a) - 3\delta(r_2 - a) - 3\delta(r_2 + a) + 3\lambda\delta(r_1 - r_2)\,. \quad (93a)$$

In $D \to \infty$: Hamiltonian (90) becomes:

$$\mathcal{H}_{D=\infty} = \frac{9}{4}\left(\frac{1}{\rho^2\sin^2\phi}\right) - 3\left[\frac{Z}{\sqrt{\rho^2 + (z + a)^2}} + \frac{Z}{\sqrt{\rho^2 + (z - a)^2}}\right] + \frac{3}{2}J(\rho, z, \phi)\,, \quad (93b)$$

with $a = R/2$ and

$$J(\rho, z, \phi) = \frac{1}{\sqrt{(2z)^2 + 2\rho^2 - 2\rho^2\cos\phi}}\,.$$

We minimized these rescaled Hamiltonians (93) with respect to the rescaled distances (92).

In **Figure 1**, we have plotted the binding energies of H_2 as functions of R, in the three dimensions (91), adding the nuclear

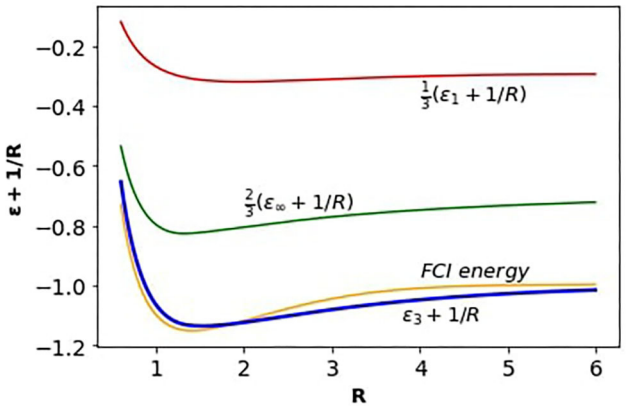

FIGURE 1 | The binding $V(R)$ curves for H_2, shown from different dimensions. The red and green curves pertain to $D = 1$ and $D \to \infty$, respectively, parts from Equations (92) and (93) of the interpolaiton. The blue curve, $\epsilon_3(R) + 1/R$, represents $D = 3$, the interpolation result at Equation (91). The orange curve is a highly accurate result obtained from computation [43].

repulsion term, $1/R$. The curves are colored: red for $D = 1$, green for $D \to \infty$, and blue for $D = 3$, the interpolation. It compares fairly well with the nominally exact $V(R)$ curve, colored orange, for H_2 obtained from the full configuration interaction (FCI) method [41, 42]. We have obtained the FCI by using the OpenFermion quantum computational chemistry software [43].

7. CONCLUSION AND PROSPECTS

The formula used for atoms we consider unorthodox, as it recently emerged [14] whereas other D-interpolations are elderly [44, 45]. The fresh aspect links the energies ϵ_1 and ϵ_∞ together with the first-order perturbation coefficients $\epsilon_1^{(1)}$ and $\epsilon_\infty^{(1)}$ plus $\epsilon_3^{(1)}$ from their $1/Z$ expansions. Those perturbations arise from of electron-electron pair interactions, $\langle 1/r_{ij} \rangle$; they actually provide much of the dimension dependence. For H_2 we used a different scaling than with the atoms, since H_2 links the distance R between the two nuclei. Then the rescaling is: $R \to 1/3R'$ for $D \to 1$; $R \to 2/3R'$ for $D \to \infty$. Interpolating between the dimensional limits gave a fair approximation of the binding energy for $D = 3$, when compared with the full configuration interaction (FCI).

In tally, our sections 3, 4, and 5 treat He, Li, Be; in section 6 dealt with H_2. In subsections we describe the $D = 1$ limit, the $D = \infty$ limit, the first-order perturbations, and the interpolation output.

The ingredients of the interpolation are well suited for computing. In our calculation we treat the electrons exclusively in *s* states with spherical or, in the molecular case, cylindrical symmetry. However, we expect the possibility to extend our method to encompass atoms with electrons of finite angular momentum, although this could be more challenging. We also expect the method to hold true for larger atomic, molecular and extended systems. More than ground-state energies are accessible. However, there are prospects for combining dimensional limits to serve other many-body problems. One is examining dimensional dependence of quantum entanglement [46, 47]. Another is the isomorphism between the Ising model [48] and two-level quantum mechanics [49]. Long ago the Ising model was solved in one, two and infinite dimensions [50–52], as well much activity near four dimensions [53]. The unknown solution at $D = 3$ remains a challenge even by quantum computing [54, 55]. More light on the solution might come by blending of dimensions akin to our unorthodox interpolated formula.

DATA AVAILABILITY STATEMENT

The original contributions presented in the study are included in the article/supplementary material, further inquiries can be directed to the corresponding author/s.

AUTHOR CONTRIBUTIONS

All authors listed have made a substantial, direct and intellectual contribution to the work, and approved it for publication.

ACKNOWLEDGMENTS

The authors (SK and KG) acknowledge the partial financial support by the U.S. Department of Energy (Office of Basic Energy Sciences) under Award No. DE-SC0019215 and the Integrated Data Science Initiative Grant (IDSI F.90000303), Purdue University. This manuscript has been released as a pre-print at arXiv:2004.11489 [quant-ph] [56].

REFERENCES

1. Herrick DR, Stillinger FH. Variable dimensionality in atoms and its effect on the ground state of the helium isoelectronic sequence. *Phys Rev A*. (1975) **11**:42–53. doi: 10.1103/PhysRevA.11.42
2. Mlodinow LD, Papanicolaou N. SO(2,1) algebra and the large N expansion in quantum mechanics. *Ann Phys*. (1980) **128**:314–334.
3. Yaffe LG. Large N limits as classical mechanics. *Rev Mod Phys*. (1982) **54**:407.
4. Herschbach DR. Dimensional interpolation for two-electron atoms. *J Chem Phys*. (1986) **84**:838–51. doi: 10.1063/1.450584
5. Witten E. Quarks, atoms, and the 1/N expansion. *Phys Today*. (1980) **33**:38–43.
6. Goodson DZ, López-Cabrera M, Herschbach DR, Morgan JD III. Large-order dimensional perturbation theory for two-electron atoms. *J Chem Phys*. (1992) **97**:8481–96.
7. Zhen Z, Loeser J. In: Herschbach DR, Avery J, Goscinski O. (eds.). *Large-D Limit for N-Electron Atoms*. Dordrecht: Springer Netherlands (1993). p. 83–114.
8. Kais S, Herschbach DR. The 1/Z expansion and renormalization of the large-dimension limit for many-electron atoms. *J Chem Phys*. (1994) **100**:4367–76.
9. Rudnick J, Gaspari G. The shapes of random walks. *Science*. (1987) **237**:384–9.
10. Loeser JG, Zhen Z, Kais S, Herschbach DR. Dimensional interpolation of hard sphere virial coefficients. *J Chem Phys*. (1991) **95**:4525–44.
11. Kais S, Herschbach DR. Dimensional scaling for quasistationary states. *J Chem Phys*. (1993) **98**:3990–8.

12. Wei Q, Kais S, Herschbach DR. Dimensional scaling treatment of stability of simple diatomic molecules induced by superintense, high-frequency laser fields. *J Chem Phys*. (2008) **129**:214110. doi: 10.1063/1.3027451
13. Wei Q, Kais S, Herschbach DR. Dimensional scaling treatment of stability of atomic anions induced by superintense, high-frequency laser fields. *J Chem Phys*. (2007) **127**:094301. doi: 10.1063/1.2768037
14. Herschbach DR, Loeser JG, Virgo WL. Exploring unorthodox dimensions for two-electron atoms. *J Phys Chem A*. (2017) **121**:6336–40. doi: 10.1021/acs.jpca.7b06148
15. Rosenthal CM. Solution of the delta function model for heliumlike ions. *J Chem Phys*. (1971) **55**:2474–83. doi: 10.1063/1.1676436
16. Loeser JG, Herschbach DR. Dimension dependence of correlation energies in two-electron atoms. *J Chem Phys*. (1987) **86**:3512–21. doi: 10.1063/1.451954
17. Frantz DD, Herschbach DR. Lewis electronic structures as the large-dimension limit for H_2^+ and H_2 molecules. *Chem Phys*. (1988) **126**:59–71.
18. Tan AL, Loeser JG. In: Herschbach DR, Avery J, Goscinski O, editors. Simple molecules and variant scalings. *Dimensional Scaling in Chemical Physics*. Dordrecht: Springer Netherlands (1993). p. 230–55. doi: 10.1007/978-94-011-1836-1_3
19. López-Cabrera M, Tan AL, Loeser JG. Scaling and interpolation for dimensionally generalized electronic structure. *J Phys Chem*. (1993) **97**:2467–78.
20. Lapidus IR. One-dimensional models for two-electron systems. *Am J Phys*. (1975) **43**:790–2. doi: 10.1119/1.9708
21. White RJ, Stillinger FH. Analytic approach to electron correlation in atoms. *J Chem Phys*. (1970) **52**:5800–14. doi: 10.1063/1.1672862
22. Loeser JG, Herschbach DR. Hylleraas-Pekeris treatment of D-dimensional two-electron atoms. *J Chem Phys*. (1986) **84**:3882–92. doi: 10.1063/1.450099
23. James HM, Coolidge AS. On the ground state of Lithium. *Phys Rev*. (1936) **49**:688.
24. Weiss AW. Configuration interaction in simple atomic systems. *Phys Rev*. (1961) **122**:1826.
25. Larsson S, Burke EA. Variational calculation of the ground state of the lithium atom. *Phys Rev*. (1969) **184**:248.
26. Scherr CW, Silverman JN, Matsen FA. Perturbation energy coefficients and ionization potentials of the ground state of three-to ten-electron isoelectronic atomic series. *Phys Rev*. (1962) **127**:830.
27. Wilson EB Jr. Wave functions for the ground state of lithium and three-electron ions. *J Chem Phys*. (1933) **1**:210–8.
28. Abramowitz M, Stegun IA. *Handbook of Mathematical Functions With Formulas, Graphs, and Mathematical Tables, Vol. 55*. US Government Printing Office (1948).
29. Bunge CF. Configuration interaction benchmark for Be ground state. *Theor Chem Acc*. (2010) **126**:139–50. doi: 10.1007/s00214-009-0601-5
30. Büsse G, Kleindienst H, Lüchow A. Nonrelativistic energies for the Be atom: double-linked Hylleraas-CI calculation. *Int J Quantum Chem*. (1998) **66**:241–7.
31. Sims JS, Hagstrom SA. Hylleraas-configuration-interaction study of the 1s ground state of neutral beryllium. *Phys Rev A*. (2011) **83**:032518. doi: 10.1103/PHYSREVA.83.032518
32. Puchalski M, Komasa J, Pachucki K. Testing quantum electrodynamics in the lowest singlet states of the beryllium atom. *Phys Rev A*. (2013) **87**:030502. doi: 10.1103/PhysRevA.87.030502
33. Stanke M, Komasa J, Bubin S, Adamowicz L. Five lowest S 1 states of the Be atom calculated with a finite-nuclear-mass approach and with relativistic and QED corrections. *Phys Rev A*. (2009) **80**:022514. doi: 10.1103/PhysRevA.80.022514
34. James HM, Coolidge AS. The ground state of the hydrogen molecule. *J Chem Phys*. (1933) **1**:825–35. doi: 10.1063/1.1749252
35. Kolos W, Roothaan CCJ. Accurate electronic wave functions for the H_2 molecule. *Rev Mod Phys*. (1960) **32**:219. doi: 10.1103/RevModPhys.32.219
36. Svidzinsky AA, Scully MO, Herschbach DR. Simple and surprisingly accurate approach to the chemical bond obtained from dimensional scaling. *Phys Rev Lett*. (2005) **95**:080401. doi: 10.1103/PhysRevLett.95.080401
37. Chen G, Chin SA, Dou Y, Kapale KT, Kim M, Svidzinsky AA, et al. The two electron molecular bond revisited: from Bohr orbits to two-center orbitals. *Adv At Mol Opt Phys*. (2005) **51**:93–238. doi: 10.1016/S1049-250X(05)51015-2
38. Olivares-Pilón H, Turbiner AV. Towards the theory of Potential Energy Curves for diatomic molecular ions: He_2^+ case. *arXiv [preprint]*. arXiv:1904.06614. (2019). Available online at: https://arxiv.org/abs/1904.06614
39. Lapidus IR. One-dimensional hydrogen molecule revisited. *Am J Phys*. (1982) **50**:453–6. doi: 10.1119/1.12833
40. Herrick DR. Degeneracies in energy levels of quantum systems of variable dimensionality. *J Math Phys*. (1975) **16**:281–3. doi: 10.1063/1.522538
41. Bauschlicher CW, Langhoff SR, Taylor PR. Accurate quantum chemical calculations. *Adv Chem Phys*. (1990) **77**:103–61.
42. Sherrill CD, Schaefer HF III. The configuration interaction method: advances in highly correlated approaches. In: Löwdin P-O, Sabin JR, Zerner MC, Brändas E, editors. *Advances in Quantum Chemistry*. Vol. 34. San Diego, CA: Elsevier (1999). p. 143–269.
43. McClean JR, Rubin NC, Sung KJ, Kivlichan ID, Monroig XB, Cao Y, et al. OpenFermion: the electronic structure package for quantum computers. *Quant Sci Technol*. (2020) **5**:034014. doi: 10.1088/2058-9565/ab8ebc
44. Kais S, Sung SM, Herschbach DR. Large-Z and-N dependence of atomic energies from renormalization of the large-dimension limit. *Int J Quantum Chem*. (1994) **49**:657–74. doi: 10.1002/qua.560490511
45. Cardy J. *Scaling and Renormalization in Statistical Physics*. Vol. 5. Cambridge, UK: Cambridge University Press (1996).
46. Kais S. Entanglement, electron correlation, and density matrices. *Adv Chem Phys*. (2007) **134**:493. doi: 10.1002/9780470106600.ch18
47. Huang Z, Wang H, Kais S. Entanglement and electron correlation in quantum chemistry calculations. *J Mod Opt*. (2006) **53**:2543–58. doi: 10.1080/09500340600955674
48. Chandler D. *Introduction to Modern Statistical Mechanics*. Oxford: Oxford University Press (1987).
49. Loeser JG, Herschbach DR. In: Tsipis CA, Popov VS, Herschbach DR, Avery JS, editors. Dimensional Scaling. *New Methods in Quantum Theory*. 1st Edn. Dordrecht: Kluwer Academic Pub (1996) 1–32.
50. Ising E. Beitrag zur theorie des ferromagnetismus. *Z Phys*. (1925) **31**:253–8. doi: 10.1007/BF02980577
51. Stanley HE. Spherical model as the limit of infinite spin dimensionality. *Phys Rev*. (1968) **176**:718–22. doi: 10.1103/PhysRev.176.718
52. Berlin TH, Kac M. The spherical model of a ferromagnet. *Phys Rev*. (1952) **86**:821–35. doi: 10.1103/PhysRev.86.821
53. Herschbach DR. Dimensional scaling and renormalization. *Int J Quantum Chem*. (1996) **57**:295–308. doi: 10.1002/(SICI)1097-461X(1996)57:3<295::AID-QUA3>3.0.CO;2-T
54. Xia R, Bian T, Kais S. Electronic structure calculations and the Ising Hamiltonian. *J Phys Chem B*. (2017) **122**:3384–95. doi: 10.1021/acs.jpcb.7b10371
55. Nielsen MA, Chuang IL. *Quantum Computation and Quantum Information: 10th Anniversary Edition*. Cambridge, UK: Cambridge University Press (2010).
56. Ghosh KJB, Kais S, Herschbach DR. Unorthodox dimensional interpolations for He, Li, Be atoms and hydrogen molecule. *arXiv [preprint]*. arXiv:2004.11489. (2020). Available online at: https://arxiv.org/abs/2004.11489

Conflict of Interest: The authors declare that the research was conducted in the absence of any commercial or financial relationships that could be construed as a potential conflict of interest.

frontiers in Chemistry

ORIGINAL RESEARCH
published: 28 August 2020
doi: 10.3389/fchem.2020.00734

Fluid Behavior in Nanoporous Silica

Salim Ok[1], Bohyun Hwang[1], Tingting Liu[1], Susan Welch[1], Julia M. Sheets[1], David R. Cole[1,2], Kao-Hsiang Liu[3] and Chung-Yuan Mou[4]*

[1] School of Earth Sciences, The Ohio State University, Columbus, OH, United States, [2] Department of Chemistry, The Ohio State University, Columbus, OH, United States, [3] Shull Wollan Center-A Joint Institute for Neutron Sciences, Oak Ridge National Laboratory, Oak Ridge, TN, United States, [4] Department of Chemistry, National Taiwan University, Taipei, Taiwan

We investigate dynamics of water (H_2O) and methanol (CH_3OH and CH_3OD) inside mesoporous silica materials with pore diameters of 4.0, 2.5, and 1.5 nm using low-field (LF) nuclear magnetic resonance (NMR) relaxometry. Experiments were conducted to test the effects of pore size, pore volume, type of fluid, fluid/solid ratio, and temperature on fluid dynamics. Longitudinal relaxation times (T_1) and transverse relaxation times (T_2) were obtained for the above systems. We observe an increasing deviation in confined fluid behavior compared to that of bulk fluid with decreasing fluid-to-solid ratio. Our results show that the surface area-to-volume ratio is a critical parameter compared to pore diameter in the relaxation dynamics of confined water. An increase in temperature for the range between 25 and 50°C studied did not influence T_2 times of confined water significantly. However, when the temperature was increased, T_1 times of water confined in both silica-2.5 nm and silica-1.5 nm increased, while those of water in silica-4.0 nm did not change. Reductions in both T_1 and T_2 values as a function of fluid-to-solid ratio were independent of confined fluid species studied here. The parameter T_1/T_2 indicates that H_2O interacts more strongly with the pore walls of silica-4.0 nm than CH_3OH and CH_3OD.

Keywords: low viscous fluids, confined state, relaxation, low-field NMR, subsurface

OPEN ACCESS

Edited by:
Doo Soo Chung,
Seoul National University, South Korea

Reviewed by:
Bin Ding,
Donghua University, China
Ahmet Akin Uenal,
Max Born Institute for Nonlinear Optics and Short-Term Spectroscopy (LG), Germany

****Correspondence:***
Salim Ok
sok@uos.de

Specialty section:
This article was submitted to Physical Chemistry and Chemical Physics, a section of the journal Frontiers in Chemistry

Received: *08 October 2019*
Accepted: *16 July 2020*
Published: *28 August 2020*

Citation:
Ok S, Hwang B, Liu T, Welch S, Sheets JM, Cole DR, Liu K-H and Mou C-Y (2020) Fluid Behavior in Nanoporous Silica. Front. Chem. 8:734. doi: 10.3389/fchem.2020.00734

INTRODUCTION

There has been enormous interest in understanding the behavior of nanoconfined fluids due to its relevance in various areas such as biology and geochemistry (Vogel, 2010; Millischuk and Ladanyi, 2014). The behavior of molecules in confined geometries differs significantly from bulk behavior (Vogel, 2010; D'Agostino et al., 2012). This deviation arises from several factors including the relation between fluid and nanoporous matrix, and the effects of the size, shape, and geometry of the solid matrix on fluid behavior (Vogel, 2010; D'Agostino et al., 2012; Millischuk and Ladanyi, 2014). The issues on physical and chemical properties of confined fluids are heavily discussed (D'Agostino et al., 2012; Mallamace et al., 2014) along with the characterization of mesoporous solids with precise pore structure (Webber and Dore, 2004). Fundamental understanding of porous systems and their interaction with confined liquids is essential because mesoporous solids are used as model systems relevant to geological materials in the subsurface and have applications in separations, nanofluids, and catalysis (Millischuk and Ladanyi, 2014).

Mesoporous silica systems are a group of nanoporous materials with distinct cylindrical mesochannels, easily adjustable pore sizes, large surface areas, and even tunable particle sizes and shapes (Asefa and Tao, 2012). These mesoporous materials have generated interest because of their possible uses as supports for practical innovative materials (Al-Othman, 2012). Due to their large surface areas, these engineered proxies are ideal nanoporous systems for exploring confined fluid

behavior at pore surfaces. For porous silica glasses, various degree of pore filling as compared to total pore volume of the nanoporous material with distilled water have been investigated with both relaxation and diffusion NMR approaches (Bhattachrja et al., 1989; D'Orazio et al., 1990a,b). Both longitudinal (T_1) and transverse (T_2) relaxation measurements showed a linear relationship with respect to fluid filling equivalent to monolayer coverage. This arises from the homogeneity of nanopores where the water molecules are evenly distributed. In the current study, we provide detailed characterization on the properties of mesoporous materials and discuss how the properties of these mesoporous materials influence the dynamics of confined fluids.

There are contradictory conclusions on the confined fluid behavior of nanoporous systems. For instance, D'Agostino et al. (2012) observed that diols, such as ethylene glycol and 1,2-propanediol, showed increased diffusivity within the pore space of titania (22 nm average pore size) and silica (13 nm average pore size) compared to alkanes including n-hexane and n-octane. T_1 measurements also demonstrated that tumbling rate of polyols was not influenced by the porous medium while there was a significant drop of T_1 for the alkanes. Among confined fluids, water has central significance for gaining insight into a wide range of systems including various geological and technological materials. In general, despite large number of literature work on confined water, the behaviors such as diffusion property of water in confined geometry is not fully understood (Ricci and Rovere, 2000; Swenson et al., 2001). The contradictory results are attributed to different factors such as competition between confinement and surface effects, dependence on temperature, and the characteristics of the surface interactions-hydrophilic vs. hydrophobic (Swenson et al., 2001). Experimental studies on water showed decreasing motion with increasing confinement for various surface substrates (Bellisent-Funel et al., 1995; Denisov and Halle, 1996; Zanotti et al., 1999). Contradictory results, such as an extensive hydrogen bonded network of water close to the surface (Steytler and Dore, 1985) vs. a reduction in number of hydrogen bonds per water molecule near cavity walls (Bruni et al., 1998) have been observed. Besides that, the influence of confinement is less pronounced in two-dimensional substrate type confinements than in three-dimensional confinements such as pores (Barut et al., 1998; Bergman and Swenson, 2000). Because of the controversial interpretations of the behaviors of confined fluids and water in particular, there is still a need to probe the molecular-level behavior of fluids as a function of a number of key parameters including, but not limited to, pore size, pore volume, fluid type, fluid-to-solid ratio, and temperature. In addition, conducting research on simple fluids such as water in confined state and developing models on confined behavior of low viscous fluids could be extended and utilized for better experimental design and understanding of complex fluids under confinement. For instance, mesoporous silica type materials are of special interest in crude oil industry, and these materials are ideal engineering proxies to investigate larger organic molecules such as decalin and tetradecane, and their mixtures to mimic a micro-environment resembling a petroleum aromatic fraction (Kapur et al., 2000) under confinement.

The novelty of the current work is studying dynamical behavior of fluids in confined states systematically by varying fluid volume, temperature, and pore diameter of the confining solid to better understand complex heterogeneous subsurface systems. These include fluids such as water and hydrocarbons in rock that have various wetting behaviors in the subsurface. The remarkable aspect of the mesoporous silica materials used in the present study is the utilization of them as catalyst materials in petroleum industry. Therefore, the projection of this work will be to extend the current efforts in terms of investigating more complex mixtures of fluids under confinement. In order to focus on that, first emphasis is showing distinguishability of confined vs. bulk-like fluids.

Our approach to distinguish the signals of fluids between confined and bulk-like states in different pore networks may have applications in rock core analysis using low-field NMR. To this end, in addition to using nanoporous silica powder, nanoporous silica rods (monolith samples) also were used, allowing for the study of confinement of water without excess water. Excess water has been observed in the case of mixtures of white powder nanoporous silica with water upon centrifugation, and it is bulk-like water. However, in the case of silica rods, there is no excess water outside the rod itself. First, the dynamical behaviors of bulk fluids in an NMR were determined by NMR relaxation measurements. Then the same NMR measurements were conducted on nanoporous silica powders having *confined* fluid (fluid in mesoporous silica and fluid interacting with the pore walls), as well as fluid in the interparticle regions of nanoporous silica powder and outside the pores, and *excess* fluid (fluid observed upon centrifugation of mixtures of nanoporous silica and fluids and showing bulk-like dynamical behavior). Hence, we aim to achieve the following goals: (i) to characterize the nanoporous silica systems in detail, (ii) to determine the degree of deviation of confined fluid behavior with respect to bulk fluid, (iii) to clarify the influence of pore parameters to the deviation of confined fluid behavior from bulk, and (iv) to show how to differentiate signals of confined fluid in nanopores from excess fluid.

MATERIALS AND METHODS

Samples

Mesoporous silica with mean nanopore diameter and particle size of 4 and 200 nm, respectively, was purchased from Sigma-Aldrich. The silica porous monolith samples with nominal pore diameter of 5.0 nm, total pore volume of 0.7 cm^3, specific density of 1.1 cm^3, and BET surface area of 580 m^2/g were purchased from Particle Solutions, LLC (Alachua, FL). Silica-1.5 nm was prepared by calcination of micellar template silica matrices made up of micrometer size grains. Pre-formed β-zeolite kernels (composed of tetraethylammonium hydroxide), NaOH, and fumed silica reacted with decylmethylammonium bromide solution in order to synthesize the silica matrix (Liu et al., 2013). The β-zeolite seeds were utilized to make the silica nanopore walls semi-crystalline and resilient to hydrolysis deterioration (Liu et al., 2000). The mixture was first relocated into an autoclave at 120°C for 2 days, then decreased to room temperature while

adjusting the pH to 10. Upon sealing in an autoclave at 100°C for 2 days, the probe was accumulated by filtration in solid state, washed by water and ethanol, and dried at 60°C in air overnight. The ultimate mesoporous silica was obtained by calcination at 540°C for 8 h (Liu et al., 2013). Silica-2.5 nm was produced by an analogous procedure. The minor difference was the utilization of different carbon chain length surfactants or hydrothermal curing (Liu et al., 2013). Both silica-2.5 nm and silica-1.5 nm are cured with the second hydrothermal treatment; hence have even stronger structure and better hydrolysis resilience. Liu et al. (2006) provides further description on the synthesis of these two samples of silica-2.5 nm and silica-1.5 nm. It should be emphasized that the determined pore diameters of the samples in the present study are average values.

Characterization

Pore size, pore volume, and surface area measurements were made with a Micromeritics ASAP 2020 gas sorption analyzer. The mesoporous silica samples were degassed at 423 K for 20 h under a vacuum pressure of 10 μm Hg to eliminate the impurities and gases within the pores. Nitrogen was the adsorbate used to acquire the adsorption and desorption isotherms at 77 K (see **Table S1** and **Figure S1** in Supporting Information). Transmission X-ray diffraction (TXRD) experiments were conducted with a PANalytical X'Pert Pro diffractometer. Transmission geometry permits accurate and precise measurement at the low 2θ angle range required for obtaining the long-range ordered pore structure. A thin layer of specimen was mounted between two films of Kapton foil to reduce beam absorption. TXRD measurements on nanoporous silica-4.0 nm and silica-1.5 nm were acquired using Cu Kα radiation and an X'Celerator detector. Data were acquired from 1 to 43° 2θ, with a step size of 0.02° 2θ and a speed of 20 s/step. Applied voltage and tube current for the measurements were 45 kV and 40 mA. TRXD measurement on silica-2.5 nm was acquired using a scintillation detector. Data were collected from 1 to 15° 25, with a step size of 0.02° 2. and a speed of 12 s/step. Applied voltage and tube current for the measurements were 45 kV and 40 mA (see **Figures S2a–c)** for TXRD scans of nanoporous silica samples).

Samples for thermogravimetric analysis (TGA) measurements were prepared by blending 150 mg of each silica sample with 1.0 ml distilled water in a 4 ml clear vial. The mixtures were kept at 20°C for a week for complete saturation of the pores with water. After centrifugation of the samples for 20 min at 5,000 rpm on an Eppendorf Centrifuge 5340 V 4.4, supernatant was taken. The samples were left again overnight after stirring with small glass rods. This procedure of centrifugation, removal of supernatant, and overnight keeping were repeated at least 10 days to make it sure that no excess water was left between the grains. Then water saturated porous silica samples were dried under continuous flow of neat air for durations ranging from 5 to 85 min. Successively, 10–20 mg samples were placed into a Pt crucible. Finally, the TGA measurements were run on a Perkin Elmer TGA7 Thermogravimetric Analyzer from 25 to 900°C under the flow of nitrogen gas with a flow rate of 15 ml/min and a heat rate of 20°C/min (see **Figures S3a,b** showing the TGA results). TG curves of silica samples prepared by different drying times exhibit weight loss behavior. The weight losses correspond to the elimination of water, and hence pore volume comparison of the mesoporous silica materials.

Sample Preparation for Low-Field NMR Measurements

Hundred and fifty milligrams of each mesoporous silica sample were filled with three different amounts of distilled water 0.8, 0.6, and 0.4 ml. The samples were left overnight at least prior to conducting measurements for complete filling of the pores (see **Figures S4a–e**) in supporting information showing the photos of excess water after centrifugation and homogenization by sonication). For confining CH_3OH and CH_3OD, silica-4.0 nm was mixed with 0.9, 0.6, and 0.4 ml of each of these fluids. As with water, the samples were left overnight at minimum prior to conducting measurements to ensure complete filling of the pores. The samples were capped to prevent evaporation. Each sample was homogenized by sonication for 15 min immediately prior to the low-field NMR measurements. Controlled measurements were done to distinguish excess fluid signal from confined fluid signal (see **Figures S4a–e**). As seen in **Figure S4**, this was achieved by centrifugation of samples for 20 min at 5,000 rpm so that excess water migrated on top of the silica and water mixture (see **Table 1** for the summary of the experimental conditions of the samples).

A second set of samples was prepared as follows: 218.0 mg silica-4.0 nm, 100.0 mg silica-2.5 nm, and 173.0 mg silica-1.5 nm were mixed with 0.4 ml deionized H_2O. This adjustment was made to keep the pore volume of each nanoporous silica powder consistent around 120 cm^3, for a given amount of surface area (see **Table 2** for detailed values). The samples were left for soaking overnight at minimum prior to the measurements to ensure complete pore fillings. The samples were sonicated for 15 min to homogenize throughout the sample right before the measurements. The measurements were conducted at 313 K.

The third set of samples was prepared using porous silica monolith samples that were thermally treated overnight at 400°C to remove moisture and any organics left from the synthesis of the monolith samples. Upon cooling to 25°C, the samples were soaked in water for 10 min, measured and then soaked until 90 min. Visual inspection showed that the sample soaked for 10 min had non-transparent region in the middle of the sample, while such a region was not seen in the sample soaked for 90 min. This non-transparent region is attributed to volume not filled with water.

^{1}H Low-Field NMR Relaxometry Measurements

Low-field NMR T_1 and T_2 relaxation measurements were performed on a Bruker Minispec mq20 NF Series instrument with a magnetic field strength of 0.47 T equivalent to a proton resonance frequency of 20 MHz (see **Table 1** showing the details of experimental conditions), and the data were acquired utilizing Minispec software. The instrument contains a 10 mm temperature-variable probe. Temperature control is

TABLE 1 | Experimental conditions of the low-field NMR measurements.

Measurements	Variable	Fluid type	Nanoporous matrix	Number of fluid/solid ratio
T_1	Pore diameter, temperature, fluid/solid ratio	H_2O	Silica-4.0 nm; silica-2.5 nm; silica-1.5 nm	3
T_2	Pore diameter, temperature, fluid/solid ratio	H_2O	Silica-4.0 nm; silica-2.5 nm; silica-1.5 nm	3
T_1	Pore diameter, temperature, fluid/solid ratio, fluid chemistry	CH_3OH; H_2O	Silica-4.0 nm	2
T_2	Pore diameter, temperature, fluid/solid ratio, fluid chemistry	CH_3OH; CH_3OD	Silica-4.0 nm	3
T_1, T_2	Soaking time into water, temperature	H_2O	Nanoporous silica rod-6.0 nm	2
Measurements	**Fluid/solid ratio**	**Temperature (K) (H_2O)**	**Temperature (K) (CH_3OH/CD_3OD)**	**Figures**
T_1	0.80 ml; 0.60 ml; 0.40 ml/0.150 g	298; 313; 323	-	2 (A–C)
T_2	0.80 ml; 0.60 ml; 0.40 ml/0.150 g	298; 313; 323	-	3 (A–C)
T_1, T_2	0.60 ml; 0.40 ml/0.150 g	298; 313; 323	298; 313; 323	4 (A,B)
T_1, T_2	0.90 ml; 0.60 ml; 0.40 ml/0.150 g	-	298; 313; 323	5 (A,B)
T_1, T_2	10 and 90 min water soaking time	298; 313; 323	-	6 (A,B)

TABLE 2 | T_1 and T_2 values of confined water obtained by keeping pore volumes approximately constant.

	Silica-4.0 nm	Silica-2.5 nm	Silica-1.5 nm
Amount (mg)	218.0	100.0	173.0
Total surface of given amount (m^2)	130.1	116.7	143.9
Pore volume (cm^3/g), single point at $P/P_0 = 0.99$	1.04	0.97	1.20
Pore volume for given amount of surface area (cm^3)	125.1	120.3	119.9
T_1 (1) (ms)	500 ± 80	2,850 ± 60	2,670 ± 10
T_1 (2) (ms)	270 ± 50	-	-
T_2 (1) (ms)	19.6 ± 0.2	23.2 ± 0.4	18.5 ± 0.1
T_2 (2) (ms)	-	70.0 ± 2.0	

The measurements were conducted at 313 K.

achieved using N_2 flow and BVT temperature control unit. T_1 measurements were completed using the inversion recovery pulse sequence found in the pulse sequence library of Bruker. T_2 relaxation measurements were performed utilizing the standard Carr-Pucell-Meiboom-Gill (CPMG) pulse sequence, with τ of 1.0 ms between the 90 and 180° pulses. A continuous distribution of T_2 exponential decays and T_1 exponential growths correlated to confined and excess fluids were fitted for all T_2 and T_1 data using the CONTIN algorithm (Provencher, 1982). This analysis results in T_2 and T_1 distribution data. Bi-exponential decay and growth fittings of T_2 and T1 curves, respectively, were completed using Origin 9.1 employing the following equations:

$$y = A_{21}e^{-x/T_{21}} + A_{22}e^{-x/T_{22}} \quad (1)$$

$$y = A_{21}e^{x/T_{11}} + A_{22}e^{x/T_{12}} \quad (2)$$

where T_{21}, T_{22}, T_{11}, and T_{12} are the relaxation constituents, and A_{21} and A_{22} are the corresponding scales. The amplitudes A_{21} and A_{22} are directly proportional to the amount of fluid either in confined state or as excess. The fraction of T_{21} or T_{11} component is calculated as $A_{21}/(A_{21}+A_{22})$ while portion of T_{22} or T_{12} component is determined as $A_{22}/(A_{21}+A_{22})$.

RESULTS AND DISCUSSION

Characterization of the Nanoporous Silica Materials

Figure S1 integrates the N_2 adsorption and desorption isotherms for the three samples. Based on the shapes of the isotherms, the 2.5 and 4.0 nm samples can be classified as *Type IV* (Sing et al., 1985), which possesses mesoporous structure and poses the hysteresis loop caused by capillary condensation in mesopores (Thommes et al., 2015). The silica-2.5 nm material does not show strong hysteresis character because it is near the boundary of mesopore and micropore size ranges. The silica-1.5 nm isotherm is complicated by a *Type I* isotherm (micropore) below 0.8 P/P_0, and a mesoporous hysteresis loop above 0.8 P/P_0. The hysteresis is like the *H1* type (Tangestaninejad et al., 2009), which is composed of regular pores that have narrow pore distribution. The insets in **Figure S1** show the pore size distributions for the three materials, where we can see that the silica-4.0 nm

and silica-2.5 nm have uniform pore sizes, as determined by the Barrett-Joyner-Halenda (BJH) desorption and adsorption models, respectively. On the other hand, the silica-1.5 nm shows a bimodal pore distribution, as determined by density functional theory (DFT) model, where the dominant pore sizes are ∼1.5 and ∼2.5 nm (see **Figure S1**-inset).

Table S1 lists surface areas, volumes, and sizes of nanopores for the silica materials characterized for use in experiments. It needs to be mentioned that *meso,* which means "in between" in Greek, describes pore sizes ranging from 2.0 to 50.0 nm (Al-Othman, 2012; Thommes et al., 2015). In the present study, one of the silica samples, silica-1.5 nm, is out of the necessary range to be defined as *mesoporous*. This 1.5 nm material has higher surface area than the 4.0 nm material, contributed by the existence of micropores. In addition, the 2.5 nm material has relatively low pore volume, but the highest surface area measured, due to its nearly-microporous nature, and the highest surface-to-volume (S/V) ratio of the three porous silica systems. We will use the S/V ratio as a parameter for comparison in the discussion below.

Figure S2 shows TXRD scans for the three samples, with the contribution from kapton foil removed. The three peaks of silica-4.0 nm, shown in **Figure S2a**, can be indexed as (100), (110), and (200) reflections, respectively (Sarawade et al., 2013). A hexagonal mesostructure with an interplanar distance of 4.5 nm [$d_{(100)}$] can be determined, and based on the hexagonal geometry, the sum of the pore wall and pore diameter is about 5.2 nm. This long range ordered structure is consistent with the single peak (∼4.2 nm) in the pore size distribution plot (**Figure S1**) determined from gas sorption analysis. In addition, the TEM imaging of this nanoporous silica shows an ordered arrangement of about 4.0 nm pores in parallel (Ok et al., 2017).

Figure S2b shows the five diffraction maxima observed in the TXRD scan of silica-2.5 nm, with *d*-spacings 3.1, 2.1, 1.9, 1.5, and 1.3 nm, respectively. According to their ratios, they can be indexed as (110), (200), (211), (310), and (222) reflections, and this ordered structure belongs to the cubic *Im3m* space group. Therefore, the sum of the pore wall and the pore diameter is ∼4.2 nm, indicating that the pore wall is relatively thick, considering the pore diameter of 2.8 nm as determined by the BJH adsorption model. **Figure S2c** shows the silica-1.5 nm TXRD scan with diffraction maxima corresponding to *d*-spacings 2.2 and 1.5 nm. Although the specific pore structure arrangement is not identified in this case, these measurements, along with the pore distribution plot for silica-1.5 nm (**Figure S1**), suggest that it may have two dominant pore dimensions.

Pore volume is directly related to the amount of confined fluid. As demonstrated in **Figure S3a**, all of the porous silica samples where water was confined showed one-step mass loss. However, the samples with shorter drying times had fractions of water that persist till higher temperatures such as 200°C, as shown in **Figure S3a,** demonstrating representative weight loss in the case of silica-4.0 nm. As the sample-drying time was increased, complete weight-loss temperature shifted toward 95°C. In other words, all the water weight loss only required heating 95°C when the sample was dried for longer period of time. Similar results were observed when water was confined into silica samples with 2.5 and 1.5 nm pore diameters. At temperatures higher than 200°C no weight-loss occurred, and this shows that mesopores may intensely restrict water molecules and offer media for both thermodynamic and kinetic barrier to the elimination of water molecules (Wu and Navrotsky, 2013). These effects may resemble the consequences of confinement in geological environments with widely-ranging pore sizes. As shown in **Figure S3b**, the weight loss of water was less in silica-2.5 nm than for both silica-4.0 nm and silica-1.5 nm at the end of 12 min of drying time. This clearly showed that silica-2.5 nm has lower pore volume than the other two-engineered proxies of interest. Comparing the mass loss at the end of 20 min drying, we suggest that silica-1.5 nm has higher volume than that of silica-4.0 nm.

Excess Fluid vs. Confined Fluid

For discriminating excess water signal from signal of water confined into nanoporous silica samples, first T_1 (inversion recovery) and T_2 (CPMG) measurements at 40°C on the low-field NMR instrument were conducted. **Figure S4a** shows excess water showing bulk-like behavior on top of the mixture of silica-4.0 nm and confined water. As seen in **Figure 1** and **Table 3A**, it is possible to differentiate excess water signal from that of confined water. T_1 time values of bulk like water on top of the mixture without sonication are closer to that of water in bulk, while T_1 values of confined water signal is lower than that of T_1 values of confined water in the case of homogenized sample by sonication. This also exhibits that T_1 values measured by homogenizing (sonication) are average values of water with two different environments: in between the grains and in the mesopores. Buntkowsky et al. (2007) mentioned that the sticking together is mainly the consequence of H_2O molecules high polarity and their capability to establish hydrogen bond networks among the water molecules. However, dynamics of water become more complicated in confined geometries due to opposition between the surface-liquid and liquid-liquid relations. This opposition forms new structures of water as in the case of partial ordering water molecules in the neighborhood of the restraining surface.

The other approach of the T_2 data analysis belonging to the samples without sonication and with excess water on top (see **Figures S4a,d**) is determination of the percentages of bulk like water and confined water based on the Equation (1) as suggested in the literature (Aursand et al., 2008). This is a simple and robust technique to evaluate the T_2 relaxation data. At first we compare the results of bi-exponential fitting of the data belonging to water mixtures with either silica-4.0 nm or silica-1.5 nm having bulk-like water on top as shown in **Figures S4a,d**. As seen in **Table 3A**, longer T_2 values are assigned to bulk-like water. The percentage of bulk-like water on top of the mixture is not ∼ <60% (**Table 3B**). Then in this case, nearly 40% of H_2O is in between grains and confined establishing a dynamic system. Referring to **Table S1**, it is possible to calculate the pore volume given that the mass of the nanoporous silica is known. Thus, we can differentiate the volume of confined water from the volume of water in between the grains.

In the case of homogenized samples by sonication, because the nanoporous silica materials of interest in the current study have the same structure of MCM-41, we refer to the proposed filling mechanism of MCM-41 having 4.6 nm of pore-to-pore

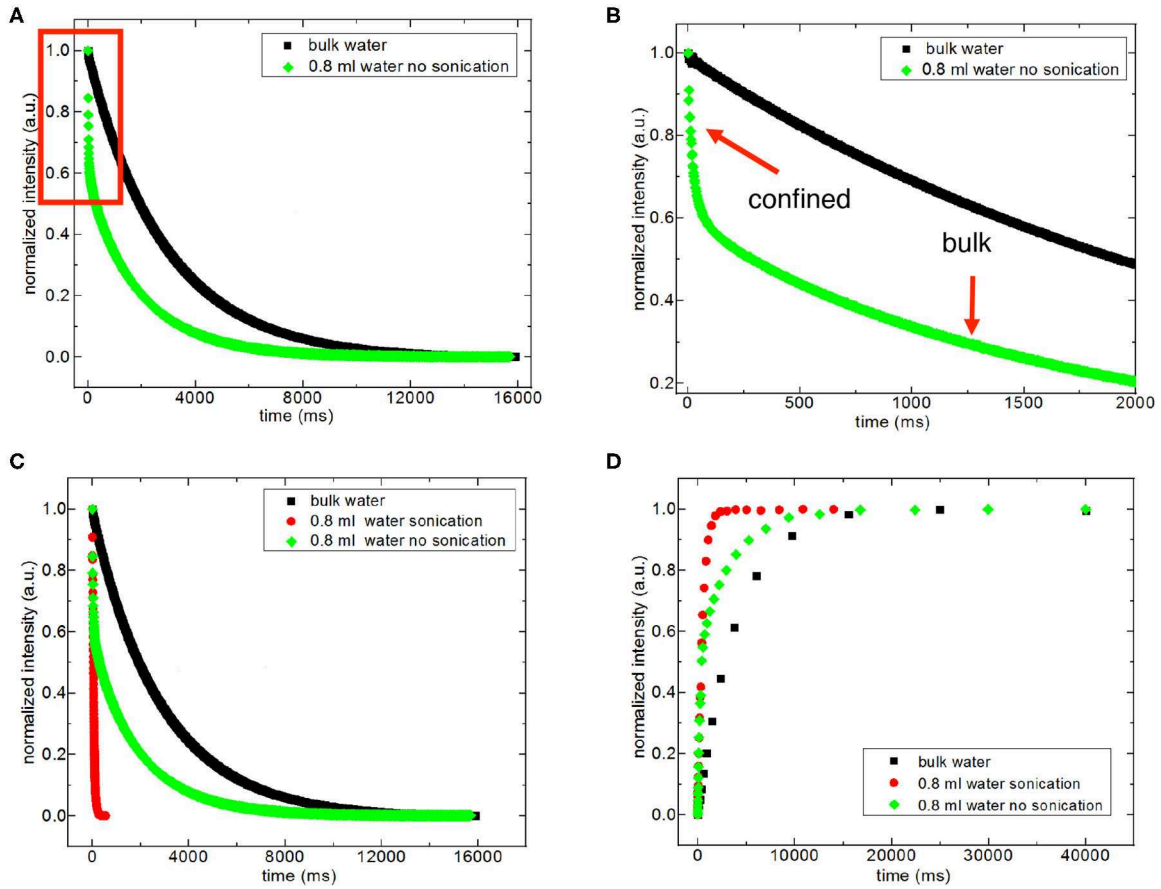

FIGURE 1 | Representative comparison of T_2 data of 0.8 ml water in the mixture with 150 mg silica-4.0 nm (S/V = 574) with and without sonication acquired at 40°C **(A–C)**. **(B)** is the zoom in for the red box in **(A)**. Representative comparison of T_1 data of 0.8 ml water in 150 mg silica-4.0 nm with and without sonication acquired at 40°C **(D)**.

distance by water (Grünberg et al., 2004). Water was studied as a guest molecule in mesoporous silica, MCM-41 and SBA-15, with two-dimensional hexagonally arranged of cylindrical pores in identical size ranging from 2 to 10 nm. Due to the high density of pores and relatively small pore diameters, these silica materials have bigger inner surfaces with respect to the volume of the single particle. There is a favored axis present in the direction of the pores cylinder axis arising from highly anisotropic geometry of the pores. In MCM-41, following the first wetting of the pore surfaces, a co-presence of filled pores or partially filled pores occurs. Additional filling of the pores happens as an enlargement of the filled pores till whole filling is obtained once more. Therefore, for MCM-41 the water layer grows axially in the direction of the pore axis. In the case of 0.4 ml H_2O wetted silica-4.0 nm or silica-1.5 nm there were initially wetted pore surfaces, filled pores and not wetted pore (dry) segments coexisted. In mixtures of nanoporous silica samples mixed with either 0.6 or 0.8 ml H_2O, after homogenization by 15 min sonication, the confined water molecules were in rapid "conversation" with the excess water molecules occupying the space in between the grains. The water molecules inside the nanoporous silica did the fast exchange with the excess water molecules by moving axially in the direction of the pores. On the NMR time scale, average T_1 or T_2 values were obtained. These average relaxation times are shorter than not only these of bulk water but also bulk-like water on top of the silica and water mixtures. There was no apparent bulk-like water in the case of mixtures with 0.4 ml water. For this reason, we did not apply bi-exponential fitting analysis for these samples having the lowest fluid-to-solid ratio.

Dynamics of Confined Fluids

Then we focus on dynamical behaviors of confined fluids by varying temperature, fluid-to-solid ratio, and pore diameter. **Table 4A** lists T_1 values of bulk and confined water. As seen in **Figures 2A–C**, deviation and change of confined fluid behavior from that of bulk fluid is independent of pore size of the nanoporous matrix systems. At the fluid-to-solid ratios of 0.8, 0.6, and 0.4 ml to 150 mg silica-2.5 nm, T_1 times increased as the temperature was increased. However, in the case of fluid-to-solid ratios of 0.8, 0.6, and 0.4 ml to 150 mg silica-4.0 nm, T_1 times did not show significant change when temperature

TABLE 3A | T_1 and T_2 values of confined water measured on the 20 MHz instrument at 40°C with either excess water on top or after homogenization with sonication.

Sample	T_2 (ms)	T_1 (ms)	Experimental treatment
Bulk water	2,883.3 ± 0.5	3,960 ± 20	-
150 mg silica-4.0 nm + 0.8 ml H_2O	(1): 50.48 ± 0.08	(1): 478 ± 6	After sonication
150 mg silica-4.0 nm + 0.8 ml H_2O	(1): 34.5 ± 0.2	***(1): 200 ± 8***	Without sonication/with excess fluid
	(2): 1,956 ± 1	***(2): 3,300 ± 100***	
150 mg silica-4.0 nm + 0.6 ml H_2O	(1): 36.48 ± 0.06	(1): 350 ± 10	After sonication
		(2): 470 ± 20	
150 mg silica-4.0 nm + 0.6 ml H_2O	(1): 29.4 ± 0.1	***(1): 201 ± 87***	Without sonication/with excess fluid
	(2): 2,315 ± 1	***(2): 3,500 ± 100***	
150 mg silica-2.5 nm + 0.8 ml H_2O	(1): 24.2 ± 0.3	(1): 2,830 ± 20	After sonication
	(2): 91.0 ± 3.0		
150 mg silica-2.5 nm + 0.8 ml H_2O	(1): 15 ± 2.0	(1): 2,760 ± 20	Without sonication/with excess fluid
	(2): 38.6 ± 0.7		
150 mg silica-2.5 nm + 0.6 ml H_2O	(1): 17.0 ± 5.0	(1): 2,660 ± 20	After sonication
150 mg silica-2.5 nm + 0.6 ml H_2O	(1): 17.57 ± 0.10	(1): 70 ± 20	Without sonication/with excess fluid
		(2): 2,600 ± 10	
150 mg silica-1.5 nm + 0.8 ml H_2O	(1): 9.6 ± 0.2	(1): 2,200 ± 200	After sonication
	(2): 55.1 ± 0.6	(2): 1,100 ± 200	
150 mg silica-1.5 nm + 0.8 ml H_2O	(1): 5.74 ± 0.03	**(1): 110 ± 2**	Without sonication/with excess fluid
	(2): 1,406.9 ± 0.4	**(2): 2,800 ± 100**	
150 mg silica-1.5 nm + 0.6 ml H_2O	(1): 5.1 ± 0.5	(1): 1,000 ± 50	After sonication
	(2): 41.7 ± 0.1	(2): 2,100 ± 100	
150 mg silica-1.5 nm + 0.6 ml H_2O	(1): 16.7 ± 0.10	**(1): 680 ± 20**	Without sonication/with excess fluid
	(2): 927.1 ± 0.6	**(2): 3,500 ± 10**	

Bold and italic values are with excess fluid on top. In particular, T_1(2) are the values closer to that of bulk fluid.

TABLE 3B | Quantification of confined vs. excess water.

Sample	Treatment	A_{21} (longer T_2)	A_{22} (shorter T_2)	Amount of H_2O on top (ml)	The rest of H_2O (ml)[a]	Amount of H_2O between grains (ml)[b]	Confined H_2O (ml)[c]	Pore volume (ml)[d]
150 mg silica-4.0 nm + 0.8 ml H_2O	Centrifuge/with excess fluid	0.61	0.39	0.49	0.31	0.16	0.16	0.16
150 mg silica-4.0 nm + 0.6 ml H_2O	Centrifuge/with excess fluid	0.63	0.38	0.38	0.23	0.07	0.16	0.16
150 mg silica-1.5 nm + 0.8 ml H_2O	Centrifuge/with excess fluid	0.53	0.47	0.42	0.38	0.20	0.18	0.18
150 mg silica-1.5 nm + 0.6 ml H_2O	Centrifuge/with excess fluid	0.60	0.40	0.36	0.24	0.06	0.18	0.18

[a] *Volume of water confined and between grains.*
[b] *Difference between 1 and 3.*
[c] *Volume of confined water which is equal to pore volume.*
[d] *Pore volume determined by using density data in* ***Table S1****.*

was varied. When 0.8 ml water was confined to 150 mg silica-1.5 nm, as the temperature was increased, T_1 times also increased. However, with the fluid-to-solid ratios of 0.6 and 0.4 ml water to 150 mg silica-1.5 nm, first there was an increase in T_1 time as the temperature was increased, but when the temperature was increased further, T_1 time decreased. Sattig et al. (2014) studied temperature-dependent rotational motion of super-cooled H_2O in MCM-41 type silica pores of diameters 2.93, 2.76, and 2.14 nm using ^2H NMR. There was a first sharp twist observed in the temperature reliance escorted by a solidification of a portion of the confined H_2O. This implied an alteration from bulk-like to interface-dominated water dynamics instead of a liquid-liquid phase changeover. In the temperature range above 225 K, there was the confinement effect observed. Above 225 K, the temperature reliance of H_2O re-location was weaker in the smaller pores, and in the bigger pores bulk-like water behavior was seen. Near 225 K, longitudinal magnetization relaxation (T_1) times for the ice in silica-2.1 nm confinement became very long for a dependable determination within a sensible duration, while T_1 times for confined water in liquid state passes a minimum, showing that confined H_2O has correlation times $\tau \approx 1/\omega_0 \approx 1$ ns. It was suggested that ^2H NMR line-shape analysis evidenced pronounced dynamical heterogeneities for confined H_2O. However, in our study we did not conduct line-shape

TABLE 4A | Longitudinal magnetization relaxation times (T_1) of confined water obtained after sonication of the mixtures for 15 min.

	Temperature (°C)		
Samples	**25°C**	**40°C**	**50°C**
Bulk H_2O	2,960 ± 20 ms	3,960 ± 20 ms	4,440 ± 50 ms
150 mg silica-4.0 nm + 0.8 ml H_2O	(1): 413 ± 30 ms	(1): 478 ± 6 ms	(1): 550 ± 10 ms
150 mg silica-4.0 nm + 0.6 ml H_2O	(1): 270 ± 8 ms	(1): 350 ± 10 ms	(1): 405 ± 3 ms
	(2): 360 ± 10 ms	(2): 470 ± 20 ms	
150 mg silica-4.0 nm + 0.4 ml H_2O	(1): 210 ± 20 ms	(1): 254 ± 9 ms	(1): 30 ± 6 ms
	(2): 310 ± 30 ms	(2): 400 ± 10 ms	(2): 329 ± 5 ms
150 mg silica-2.5 nm + 0.8 ml H_2O	(1): 2,230 ± 20 ms	(1): 2,830 ± 20 ms	(1): 3,510 ± 80 ms
150 mg silica-2.5 nm + 0.6 ml H_2O	(1): 2,120 ± 20 ms	(1): 2,660 ± 20 ms	(1): 3,120 ± 20 ms
150 mg silica-2.5 nm + 0.4 ml H_2O	(1): 1,970 ± 60 ms	(1): 2,370 ± 10 ms	(1): 2,720 ± 30 ms
150 mg silica-1.5 nm + 0.8 ml H_2O	(1): 1,000 ± 200 ms	(1): 1,100 ± 200 ms	(1): 1,390 ± 70 ms
	(2): 1,800 ± 300 ms	(2): 2,200 ± 200 ms	(2): 3,100 ± 300 ms
150 mg silica-1.5 nm + 0.6 ml H_2O	(1): 900 ± 100 ms	(1): 1,000 ± 50 ms	(1): 700 ± 200 ms
	(2): 1,700 ± 400 ms	(2): 2,100 ± 100 ms	(2): 2,200 ± 400 ms
150 mg silica-1.5 nm + 0.4 ml H_2O	(1): 670 ± 100 ms	(1): 500 ± 100 ms	(1): 130 ± 40 ms
	(2): 800 ± 100 ms	(2): 1,440 ± 40 ms	(2): 1,060 ± 10 ms

analysis; rather focus on T_1 measurements at high temperatures. Temperature range of the study was out of interest of the current contribution. However, Sattig et al. (2014) mentioned that the temperature reliance of water re-location is largely independent of the confinement dimensions. We observe a similar result that deviation of confined water behavior from that of bulk water is independent of pore diameter, while degree of confinement effect on dynamics of confined water is more pronounced in the case of silica-4.0 nm. This is reflected in the T_1 values as follows: the longest T_1 values were observed when water was confined to silica-2.5 nm, while the shortest T_1 values were seen when water was confined to silica-4.0 nm. We explain this situation with surface-to-volume (S/V) ratios of the nanoporous silica materials rather than pore diameter. Timur (1969) claimed that in a three-component NMR model, the pore volumes of a porous medium were classified as three sub-groups, based on their S/V ratio distribution. He explained that the longer T_1 times would correspond to the smaller S/V ratios, and the larger pores. In our case, the T_1 times do not show systematic change as a function of pore diameter. Rather, T_1 times become longer when water molecules are confined into silica-2.5 nm with the highest S/V ratio, while the shortest T_1 times are observed upon confining H_2O molecules into silica-4.0 nm with the lowest S/V ratio. For this reason, the trend in T_1 times of water confined into silica materials is attributed to the S/V ratios rather than pore diameter.

Besides analyzing T_1 times, T_2 times of the confined fluids were also analyzed. **Table 4B** lists the T_2 results. As seen in **Figures 3A–C**, when the fluid-to-solid ratio is decreased, T_2 values also decrease. This is independent of the pore diameter of the nanoporous silica materials. T_2 values in the case of the fluid-to-solid ratio of 0.4 ml to 150 mg silica (partial filling of the pores) are longer for silica-4.0 nm than silica-1.5 nm and silica-2.5 nm. In the case of 0.6 ml fluid to 150 mg silica ratio, T_2 values of water confined into silica-4.0 nm and silica-1.5 nm are closer to each other, and longer than confined into silica-2.5 nm. With the highest fluid-to-solid ratio, the longest T_2 values are observed when water is confined into silica-2.5 nm. Having smaller fluid-to-solid ratio means filling the pores with lower volume easily. Because silica-2.5 nm has lower pore volume as shown by TGA measurements (see **Figures S3a,b**), in the case of the lowest fluid-to-solid ratio "majority" of the fluid molecules completely fill the pores. This in turn is indicated with shorter T_2 values. There is an important trend in T_2 values. As the fluid-to-solid ratio is decreased, T_2 values also decrease. However, the decrease is more effective in the case of silica-2.5 nm, which has the lowest pore volume.

The other set of measurements was conducted by keeping the pore volume of each nanoporous silica constant around 120 cm^3 (see **Table 2**). Among the three silica samples, silica-2.5 nm has the highest S/V ratio. When the pore volume is kept constant at ∼120 cm^3, water has the longest T_1 value in the mixture with silica-2.5 nm. Similarly, the highest T_2 was obtained for the same water and silica-2.5 nm mixture. The T_1 value of water in the mixture with silica-1.5 nm is slightly lower than that of water in the mixture with silica-2.5 nm. The results on relaxation of water obtained by keeping pore volumes of porous matrixes constant for the given amounts of the porous materials indicate clearly that pore diameter does not affect the dynamics of confined water significantly. Rather, S/V ratio along with pore diameter reflects information on filling mechanism of nanoporous silica materials with water. In particular, when the pore diameter is big and S/V ratio is small, at first water molecules wet the surface of the pore walls. Additional filling happens easily from the pore wall to the midpoint of the pore. Then complete filling of the pores is achieved (Grünberg et al., 2004). In the case of nanoporous silica with small pore diameter and large S/V ratio, the filling mechanism occurs in a different way: first the center is filled; hence there is a co-presence of filled pore fragments with wetted pores. Further filling of the pores develops axially in the direction

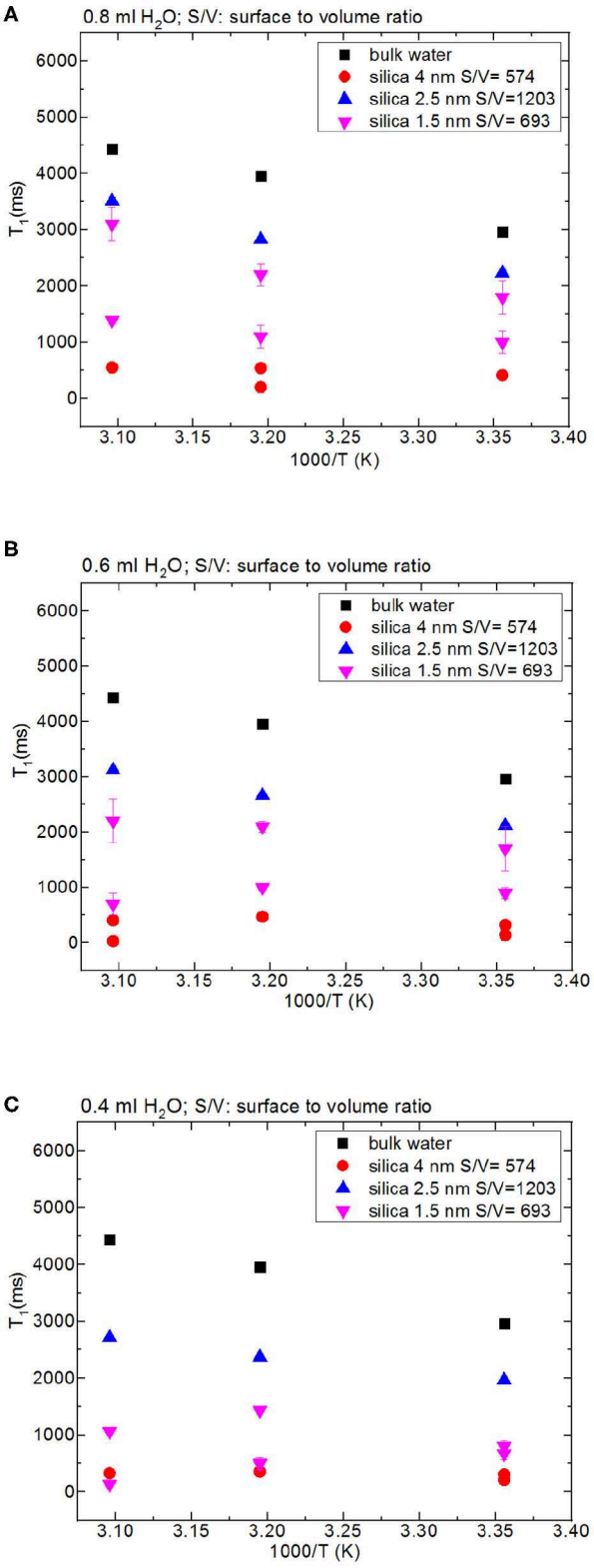

FIGURE 2 | Comparison of T_1 values of bulk water and water mixed with nanoporous silica where the variables are pore diameter of nanoporous silica with the amount of 150 mg (silica-4.0 nm, silica-2.5 nm, silica-1.5 nm), temperature (298, 313, 323 K) and volume of water [0.8 ml water **(A)**, 0.6 ml water **(B)**, 0.4 ml water **(C)**].

of the pore axis. The pore volume is also related to pore length when we assume cyclindrical pores. The nanoporous silica with small pore diameter and long pore axis leads to larger pore volumes. The long pore length (large pore volume) gives enough degree of freedom for confined water molecules. Relatively free confined water molecules prefer motion in axial direction, and this results in weaker interactions with pore walls. This is a possible explanation of larger T_1 values for pores with smaller pore diameter and larger pore volume.

In addition to the effect of pore volume and S/V ratios of the porous systems on dynamical behaviors of confined H_2O, fluid chemistry is also studied by confining CH_3OH and CH_3OD into nanoporous silica-4.0 nm. **Tables 5A,B** list T_1 and T_2 values of bulk and confined CH_3OH and CH_3OD. First, T_1 and T_2 relaxation times of confined methanol deviated from those of bulk methanol. The second remarkable point is the higher T_1 and T_2 values of CH_3OD with respect of those of CH_3OH in confined state. Internal rotation of the $-CH_3$ group is faster than the –OD group rotation in turn leading to longer T_1 times of CH_3OD compared to that of CH_3OH. As seen in **Figures 4A,B**, confined methanol (CH_3OH) has slightly higher T_1 relaxation values than these of confined H_2O. This result is independent of fluid-to-solid ratio. This is also related to the faster internal rotation of $-CH_3$ group. As expected, when the fluid-to-solid ratio is decreased, T_1 values of confined methanol also decreased. Methanol has two T_1 values in confined state. In the case of higher fluid-to-solid ratio, longer T_1 increases as temperature increases, while shorter T_1 does not show significant change upon elevating temperature. In the case of lower fluid-to-solid ratio for both longer and shorter T_1 values, T_1 minimum is observed as a function of temperature.

Methanol has also two T_2 values in confined state (**Figures 5A,B**). The longer T_2 value is greater than of that H_2O. The longer T_2 value increases as temperature increases, while the shorter T_2 does not indicate significant change when temperature is varied. When the fluid-to-solid ratio was decreased, T_2 values also decreased. The short T_2 value of CH_3OH in the confined state became even shorter as the temperature was elevated. This is independent of the fluid-to-solid ratios. This observation is explained by layering of CH_3OH on the pore walls via interacting with –OH groups of the pores, which are proven to exist by solid-state magic angle spinning (MAS) cross-polarization (CP) NMR (Sindorf and Maciel, 1983). In addition, water molecules near the interface had preferred directions due to the interaction with surface –OH groups (Millischuk and Ladanyi, 2011). There are two layers, and as temperature was elevated the molecules of the second layer having weaker interactions with the molecules forming the first layer with –OH of the pore walls gained mobility, and moved to the region of the molecules clustered in the middle of the pores. The number of methanol molecules in the second layer was reduced when the temperature was increased, while methanol molecules of the first layer still interact with the pore walls. Thus, the shorter T_2 value attributed to the average motions of the first and second layers of CH_3OH interacting with the pore walls became shorter at high temperatures. However, there is weaker hydrogen bonding interaction between CH_3OH and –OH of the pore walls that is indicated in relatively longer T_1

TABLE 4B | Transverse magnetization relaxation times (T_2) of confined water obtained after sonication of the mixtures for 15 min.

	Temperature (°C)		
Samples	**25°C**	**40°C**	**50°C**
Bulk H_2O	2,440 ± 0.2	2,883.3 ± 0.5	3,122.2 ± 0.2
150 mg silica-4.0 nm + 0.8 ml H_2O	(1): 47.0 ± 2.0 ms	(1): 50.5 ± 0.1 ms	(1): 75.3 ± 0.1 ms
	(2): 53.0 ± 2.0 ms		
150 mg silica-4.0 nm + 0.6 ml H_2O	(1): 37.6 ± 0.1 ms	(1): 36.5 ± 0.1 ms	(1): 58.8 ± 0.1 ms
150 mg silica-4.0 nm + 0.4 ml H_2O	(1): 29.4 ± 0.2 ms	(1): 27.8 ± 0.1 ms	(1): 44.3 ± 0.6 ms
	(2): 6.1 ± 0.9 ms		(2): 14.0 ± 2.0 ms
150 mg silica-2.5 nm + 0.8 ml H_2O	(1): 27.2 ± 0.4 ms	(1): 24.2 ± 0.3 ms	(1): 27.5 ± 0.2 ms
	(2): 99.0 ± 4.0 ms	(2): 91.0 ± 3.0 ms	(2): 119 ± 4.0 ms
150 mg silica-2.5 nm + 0.6 ml H_2O	(1): 19.7 ± 0.1 ms	(1): 17.0 ± 5.0 ms	(1): 19.3 ± 0.1 ms
150 mg silica-2.5 nm + 0.4 ml H_2O	(1): 12.5 ± 0.1 ms	(1): 11.0 ± 0.1 ms	(1): 12.8 ± 0.1 ms
		(2): 24.3 ± 0.4 ms	
150 mg silica-1.5 nm + 0.8 ml H_2O	(1): 10.1 ± 0.5 ms	(1): 9.6 ± 0.2 ms	(1): 10.7 ± 0.2 ms
	(2): 42.8 ± 0.3 ms	(2): 55.1 ± 0.6 ms	(2): 62.2 ± 0.3 ms
150 mg silica-1.5 nm + 0.6 ml H_2O	(1): 13.3 ± 1.0 ms	(1): 5.1 ± 0.5 ms	(1): 4.9 ± 0.5 ms
	(2): 44.4 ± 0.5 ms	(2): 41.7 ± 0.1 ms	(2): 43.3 ± 0.1 ms
150 mg silica-1.5 nm + 0.4 ml H_2O	(1): 8.3 ± 0.5 ms	(1): 7.4 ± 0.5 ms	(1): 15.9 ± 0.1 ms
	(2): 21.3 ± 0.3 ms	(2): 19.1 ± 0.3 ms	

values of CH_3OH with respect to these of H_2O. As discussed above, the contribution of faster internal $-CH_3$ rotation to the overall dynamics of CH_3OH molecules should not be neglected as well.

Dynamics of Water Confined in Nanoporous Silica Monoliths Without Excess Fluid

First, it needs to be mentioned that there was no excess fluid in the medium when both of the T_1 and T_2 measurements were conducted upon soaking the nanoporous silica monoliths into water. The surface area of the nanoporous silica monolith is closer to that of silica-4.0 nm. **Table 6** lists T_1 and T_2 values of water confined in the nanoporous silica monolith by varying soaking duration and temperature (see **Figure 6**). In this case, 10 min and 90 min of soaking time correspond to partial filling and more complete saturation of water in pores, respectively. Both T_1 and T_2 times of confined water in the nanoporous silica monoliths show strong deviation from bulk values (see **Tables 4A,B**) for bulk T_1 and T_2 relaxation values of water, respectively). The deviation from bulk is independent of the water soaking time. Comparison of the T_1 values water molecules inside the nanoporous silica monoliths shows the negligible effect of soaking duration. However, T_2 times get shorter approximately twice as the soaking time was increased to 90 min. As expected, when the temperature was increased, both T_1 and T_2 times of confined water within the nanoporous silica monoliths get longer, and again independent of the soaking time. The shortest T_2 value observed is explained by the strong interaction between the confined water molecules and the pore walls of the nanoporous silica monolith surface. We suggest that there is first a monolayer established on top of the pore walls of the monolith. This layer gains mobility when the temperature was increased in the case of short soaking time. However, such a mobility and hence increase in the shorter T_2 time component is not observed in the case of 90 min soaking time sample. In other words, partial filling of the pores due to shorter soaking time gives free volume within the nanoporous silica monolith for confined water molecules. The elevation in temperature helps with overcoming energy barrier that water molecules forming the monolayer gain freedom. This gain in mobility is reflected as longer relaxation times. In comparing the relaxation times of confined water in nanoporous silica monoliths with respect to the relaxation values of H_2O confined into nanoporous powdered silica samples (silica-4.0 nm, silica-2.5 nm, and silica-1.5 nm), we prefer to consider the samples where only 0.4 ml water was confined into the powdered silica samples. T_1 values of water within the nanoporous silica monoliths are significantly shorter than those of water confined into silica-2.5 nm and silica-1.5 nm, while closer but still shorter than that of water confined into silica-4.0 nm. T_2 times of water confined into nanoporous silica monolith for 10 min of soaking time are longer than those of T_2 times of water confined into powdered nanoporous silica samples, but T_2 times of water confined into nanoporous silica monolith for 90 min of soaking time are within the same range with T_2 values of water confined into powdered nanoporous silica matrixes. The comparison shows that confinement effect for water is independent of water soaking time. The water molecules remaining between powdered nanoporous silica grains upon sonication, where only 0.4 ml water was confined into the powdered silica samples, contribute to the averaged relaxation times so that relatively longer T_1 and T_2 times than those of water within the nanoporous silica monoliths were observed. There is an overall decreasing trend in relaxation times of water as going from smaller pore diameters of 1.5 and 2.5 nm to larger diameters of 4.0 and 6.0 nm. As a result, we suggest that taking the pore diameters of both the powdered and monolith samples into

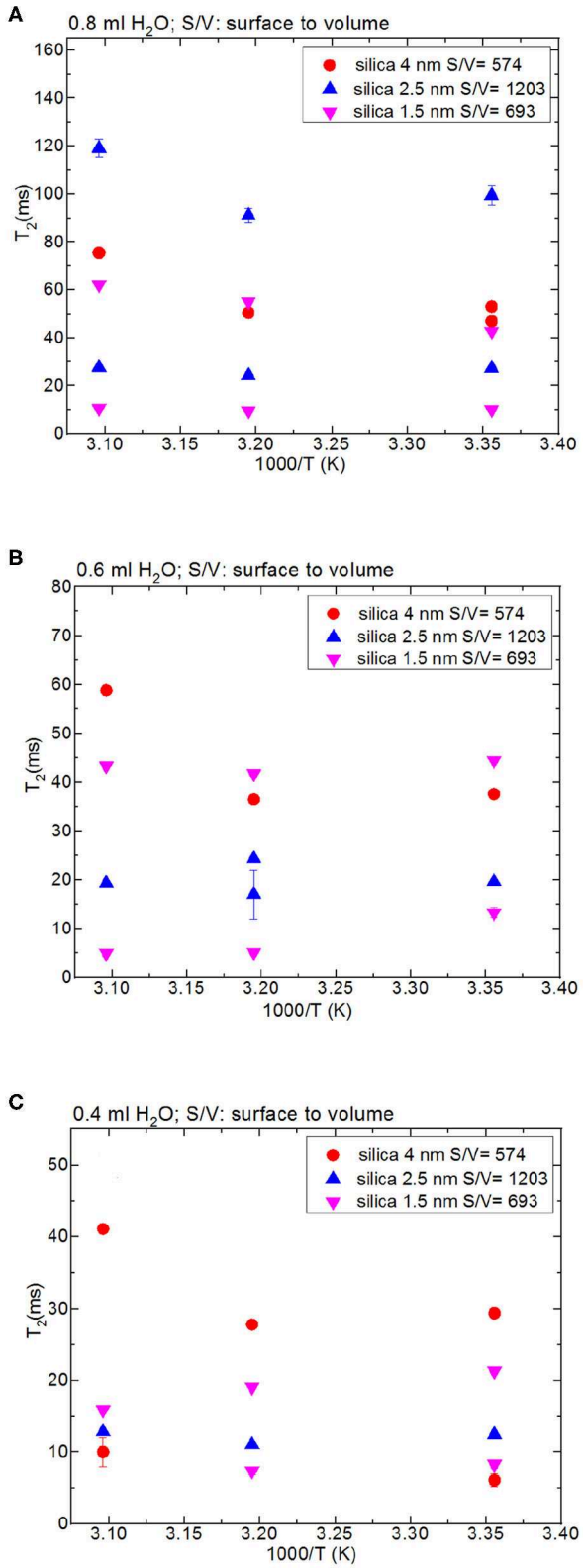

FIGURE 3 | Comparison of T_2 values of bulk water and water mixed with nanoporous silica where the variables are pore diameter nanoporous silica materials with the amount 150 mg (silica-4.0 nm, silica-2.5 nm, silica-1.5 nm) and temperature (298, 313, and 323 K); 0.8 ml water **(A)**, 0.6 ml water **(B)**, 0.4 ml water **(C)**.

account, pore volume is a significant factor reducing the mobility of water.

T_1/T_2 Ratio of Confined Fluid Interaction With the Pore Walls

Regarding NMR relaxation in porous media, T_1/T_2 ratio indicates how strongly or weakly molecules interact with the uppermost layer of the porous system (Mitchell et al., 2009; Weber et al., 2009). Therefore, T_1/T_2 ratio is an important parameter showing the degree of wettability of the fluid toward pore walls in confined geometry. The NMR T_1 time in liquids arises from time-dependent local magnetic fields persuading changeovers that permit nuclear spins to restore the equilibrium. The major driving force for variations in local magnetic fields at a nucleus is the rotational motion of molecules, regularly defined as molecular tumbling. The correlation time of molecular tumbling is defined as τ_c. The approximate definition of τ_c is the duration for a molecule to finish a rotation of 1 rad. The BPP (Bloemberg-Purcell-Pound) relaxation theory describes that for $\tau_c \rightarrow 0$, $T_1 \rightarrow \infty$. As a result, small, and rapid tumbling molecules will show a gradual relaxation rate and thus longer T_1 values (Bloembergen et al., 1948; D'Agostino et al., 2012). There is the resulting correlation between T_1 and τ_c:

$$\frac{1}{T_1} \propto \frac{\tau_c}{1 + (2\omega_0\tau_c)^2} \tag{3}$$

where ω_0 is the precession frequency of the target nucleus. This equation tells that for very fast molecular motion (when $1/\tau_c >> 2\omega_0$), T_1 is inversely proportional to τ_c. That is, as correlation time decreases (fast molecular motion), relaxation time increases (the rate of relaxation decreases). Conversely, for slow molecular motion (when $1/\tau_c << 2\omega_0$), T_1 is directly proportional to τ_c. Therefore, they both increase together. The minimum in T_1, and hence the most efficient spin-lattice relaxation, occurs when $\tau_c \propto (\omega_0)^{-1}$ (Slichter, 1990; Macomber, 1998; Nicotera et al., 2012). Viscous molecules or molecules under confinement of geometrical constraints will have shorter T_1 values and thus a faster relaxation rate (D'Agostino et al., 2012). In analyzing and explaining the longitudinal relaxation data obtained, we refer to Equation (4) described below. We first think of a cylindrical pore with a radius of R and a length of l, completely filled with water molecules. Due to water-substrate interactions, the water molecules at the surface will experience a restricted motion when compared to the bulk like water in the middle of pore. We assume that the water molecules within a distance *a* from the surface are affected by the surface and the rest acts as bulk like fluid as mentioned above while discussing layering of methanol on the pore walls via interactions with –OH groups decorating the pore walls. Under these assumptions the observed proton relaxation time constant $T_{1,observed}$ will have a weighted average from water molecules near the surface and bulk like water molecules, where the weights are proportional to the volume (Gallegos et al., 1988; Weber et al., 2009). The number of protons/water molecules at the uppermost layer and in bulk-like state is proportional to the $V_{Surface}$ and V_{Bulk}, respectively. Thus, the observed $T_{1,observed}$

TABLE 5A | Longitudinal magnetization relaxation times (T_1) of confined CH_3OH and CH_3OD obtained after sonication of the mixtures for 15 min.

	Temperature (°C)		
Samples	**25°C**	**40°C**	**50°C**
Bulk CH_3OH	**2,800 ± 20 ms**	**3,300 ± 100 ms**	**3,320 ± 20**
150 mg silica-4.0 nm + 0.9 ml CH_3OH	(1): 50 ± 30 ms	(1): 200 ± 40 ms	(1): 520 ± 70 ms
	(2): 540 ± 10 ms	(2): 670 ± 20 ms	(2): 900 ± 100 ms
150 mg silica-4.0 nm + 0.6 ml CH_3OH	(1): 100 ± 10 ms	(1): 100 ± 30 ms	(1): 150 ± 20 ms
	(2): 465 ± 6 ms	(2): 530 ± 10 ms	(2): 630 ± 30 ms
150 mg silica-4.0 nm + 0.4 ml CH_3OH	(1): 120 ± 20 ms	(1): 40 ± 20 ms	(1): 140 ± 30 ms
	(2): 400 ± 21 ms	(2): 390 ± 10 ms	(2): 470 ± 20 ms
Bulk CH_3OD	**2,790 ± 30 ms**	**3,170 ± 50 ms**	**3,280 ± 40 ms**
150 mg silica-4.0 nm + 0.9 ml CH_3OD	(1): 1,290 ± 10 ms	(1): 1,560 ± 30 ms	(1): 1,300 ± 200 ms
			(2): 2,000 ± 200 ms
150 mg silica-4.0 nm + 0.6 ml CH_3OD	(1): 100 ± 20 ms	(1): 780 ± 20 ms	(1): 680 ± 80 ms
	(2): 670 ± 6 ms		(2): 1,000 ± 100 ms
150 mg silica-4.0 nm + 0.4 ml CH_3OD	(1): 390 ± 40 ms	(1): 580 ± 20 ms	(1): 650 ± 20 ms
	(2): 630 ± 60 ms		

TABLE 5B | Transverse magnetization relaxation times (T_2) of confined CH_3OH obtained after sonication of the mixtures for 15 min.

	Temperature (°C)		
Samples	**25°C**	**40°C**	**50°C**
Bulk CH_3OH	2,589.5 ± 0.1 ms	2,780.9 ± 0.2 ms	2,985.6 ± 0.2 ms
150 mg silica-4.0 nm + 0.9 ml CH_3OH	(1): 59.1 ± 0.8 ms	(1): 61.9 ± 0.6 ms	(1): 53.0 ± 0.3 ms
	(2): 338.5 ± 0.4 ms	(2): 396.1 ± 0.3 ms	(2): 434.5 ± 0.3 ms
150 mg silica-4.0 nm + 0.6 ml CH_3OH	(1): 49.9 ± 0.5 ms	(1): 44.2 ± 0.5 ms	(1): 39.1 ± 0.3 ms
	(2): 307.3 ± 0.4 ms	(2): 327.1 ± 0.4 ms	(2): 386.2 ± 0.3 ms
150 mg silica-4.0 nm + 0.4 ml CH_3OH	(1): 32.1 ± 0.4 ms	(1): 28.2 ± 0.3 ms	(1): 23.2 ± 0.2 ms
	(2): 171.3 ± 0.4 ms	(2): 196.1 ± 0.3 ms	(2): 209.8 ± 0.3 ms
Bulk CH_3OD	2,588.6 ± 0.2 ms	2,790.3 ± 0.4 ms	2,937.3 ± 0.2 ms
150 mg silica-4.0 nm + 0.9 ml CH_3OD	(1): 58 ± 2 ms	(1): 64 ± 2 ms	(1): 38 ± 1 ms
	(2): 636.1 ± 0.3 ms	(2): 732.8 ± 0.3 ms	(2): 807.2 ± 0.2 ms
150 mg silica-4.0 nm + 0.6 ml CH_3OD	(1): 48 ± 1 ms	(1): 145 ± 3 ms	(1): 32.7 ± 1.0 ms
	(2): 422.0 ± 0.3 ms	(2): 521.5 ± 0.8 ms	(2): 527.5 ± 0.2 ms
150 mg silica-4.0 nm + 0.4 ml CH_3OD	(1): 58 ± 2 ms	(1): 59 ± 3 ms	(1): 50 ± 2 ms
	(2): 231.9 ± 0.6 ms	(2): 259.2 ± 0.8 ms	(2): 273.4 ± 0.5 ms

relaxation can be written as:

$$\frac{1}{T_{1,observed}} = \frac{2a}{R}\left[\frac{1}{T_{1,surface}} - \frac{1}{T_{1,bulk}}\right] + \left[\frac{1}{T_{1,bulk}}\right] \quad (4)$$

This equation assumes an ideal case where the pores are filled in whole with the liquid of interest. In the current study, there is gradual increase in the amount of fluid mixed with the porous systems. This leads to an increase in the amount of confined fluid. **Tables 7A,B** lists the $T_{1,surface}$ values, where $T_{1,surface}$ was calculated by the following restrictions: (i) only 0.4 ml fluid added samples are taken into consideration, (ii) for *a*, 0.25 nm as the silica layer thickness is assumed. As shown in **Table 7A**, $T_{1,surface}$ values decreased as the temperature was increased only in the case of silica-4.0 nm and silica-1.5 nm. On the contrary, in the case of silica-2.5 nm, $T_{1,surface}$ values increased as the temperature was increased. This shows that water molecules form layers on the pore walls of silica-4.0 nm and silica-1.5 nm, and these layers have strong interaction with the pore walls. The contrary dynamical attitude of water in silica-2.5 nm is a reflection of the effect of surface-to-volume ratio. **Table 7B** shows that $T_{1,surface}$ values of CH_3OH in the nanopores of silica-4.0 nm do not change significantly as a function of temperature. However, there is a systematic increase in $T_{1,surface}$ values of CH_3OD in the nanopores of silica-4.0 nm when the temperature was elevated. This is attributed to the fluid chemistry.

Sattig et al. (2014) suggested that ^2H NMR line-shape analysis evidenced pronounced dynamical heterogeneities for confined H_2O. In another study on characteristic properties of H_2O dynamical attitudes in confined forms explored by quasi-elastic

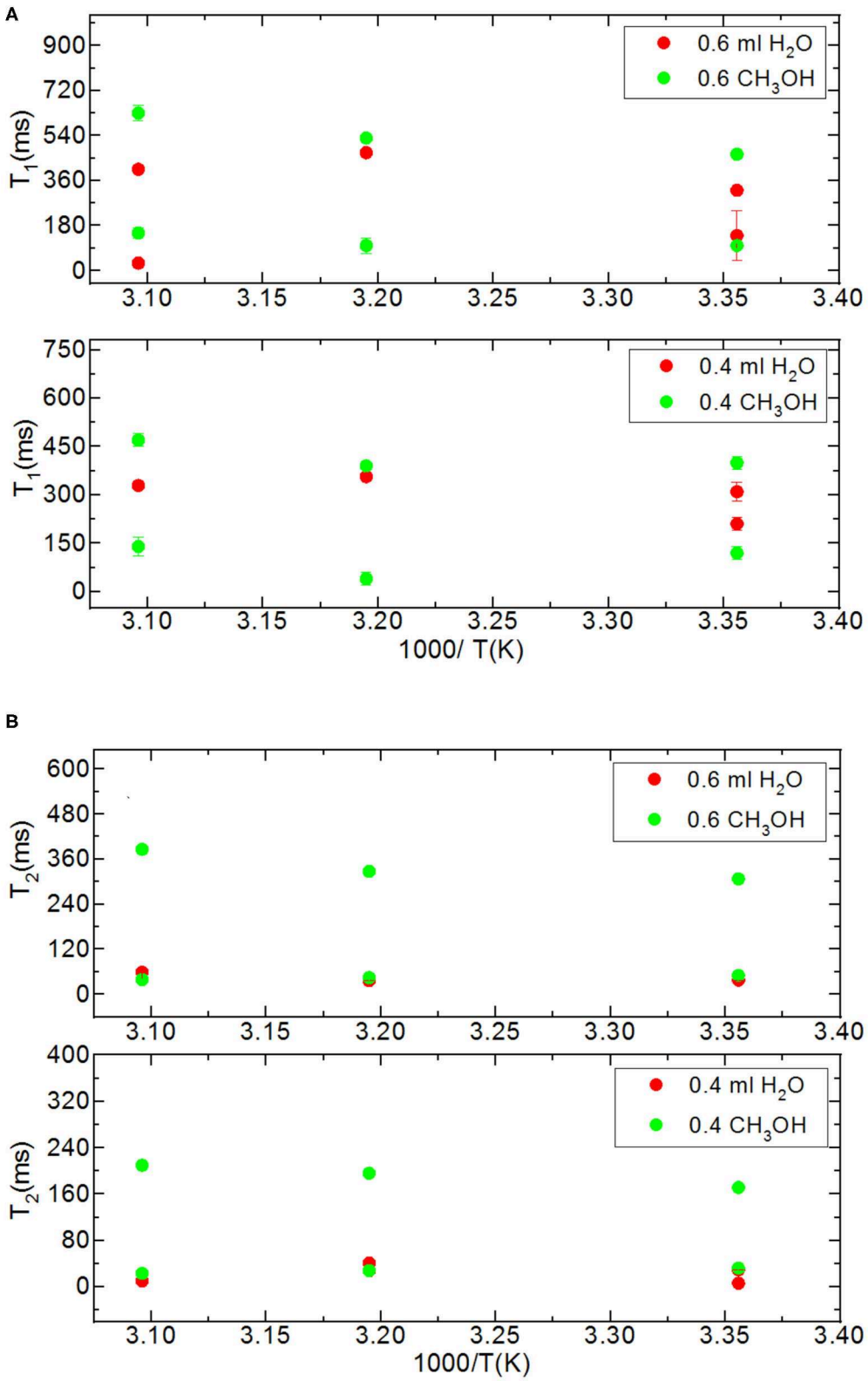

FIGURE 4 | Comparison of relaxation values of H_2O and CH_3OH confined into silica-4.0 nm with the amount of 150 mg and S/V = 574 where the variables are temperature values (298, 313, and 323 K), and fluid-to-solid ratios (0.60 ml/150 mg, 0.40 ml/150 mg); T_1 **(A)** and T_2 **(B)**.

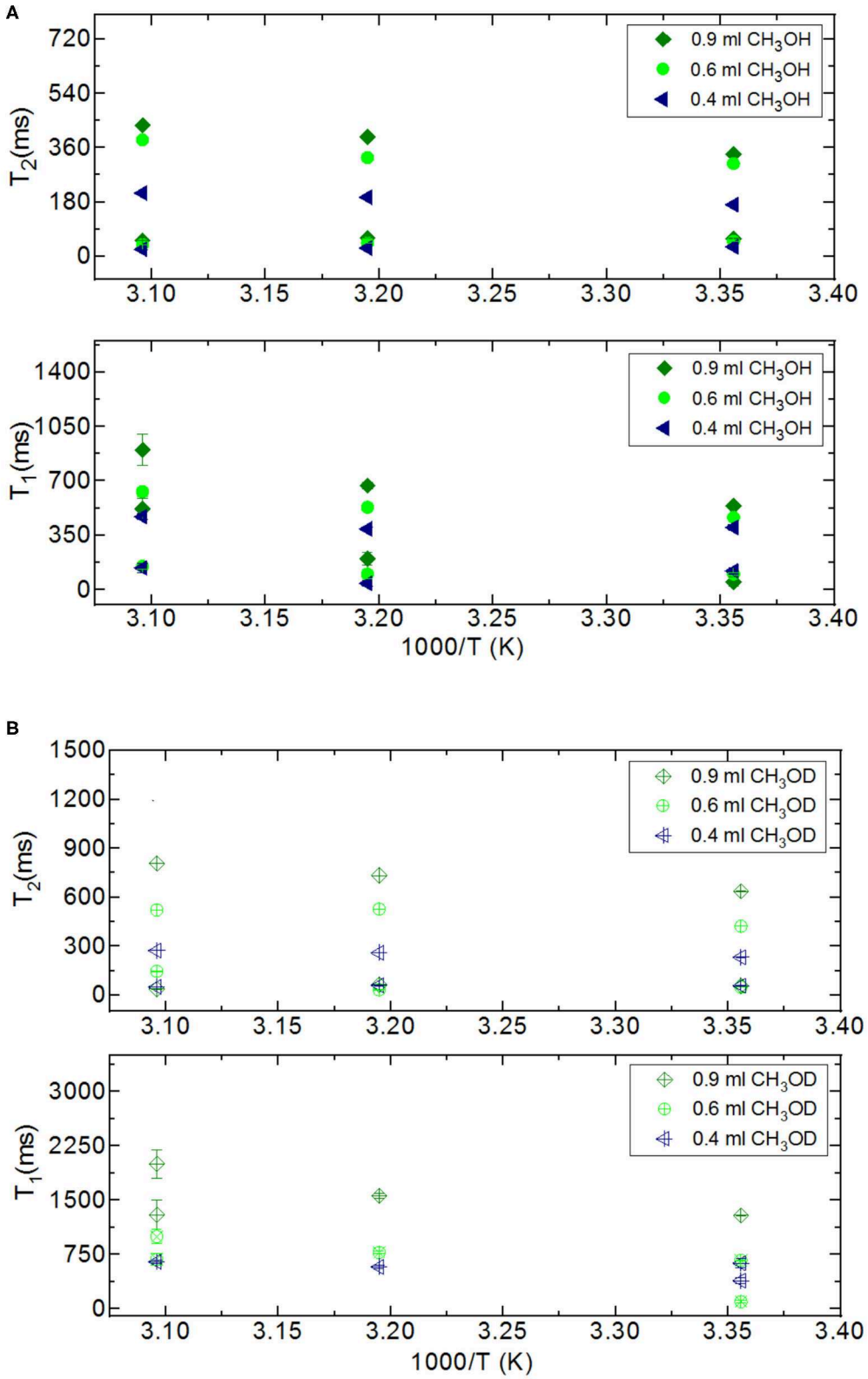

FIGURE 5 | Comparison of relaxation values of CH_3OH and CH_3OD confined into silica-4.0 nm with the amount of 150 mg and S/V = 574 where the variables are temperature values (298, 313, and 323 K), and fluid-to-solid ratios (0.90 ml/150 mg, 0.60 ml/150 mg, 0.40 ml/150 mg); CH_3OH **(A)**, CH_3OD **(B)**.

TABLE 6 | T_1 and T_2 values of water confined into nanoporous silica rod.

Silica_rod_6 nm			Silica_rod_6 nm		
Water soaking time 10 min			Water soaking time 90 min		
Temperature (°C)	**T_1 (ms)**	**T_2 (ms)**	**Temperature (°C)**	**T_1 (ms)**	**T_2 (ms)**
25	160 ± 2.4	31.5 ± 0.2	25	164.3 ± 3.4	15.8 ± 0.1
		2.3 ± 0.6			1.5 ± 1.0
40	191.1 ± 2.5	31.3 ± 0.2	40	190.4 ± 2.9	14.2 ± 0.2
		2.9 ± 0.7			1.5 ± 0.0
50	204.4 ± 4.9	47.8 ± 0.8	50	203.4 ± 5.0	25.89 ± 0.1
		20.3 ± 3.3			

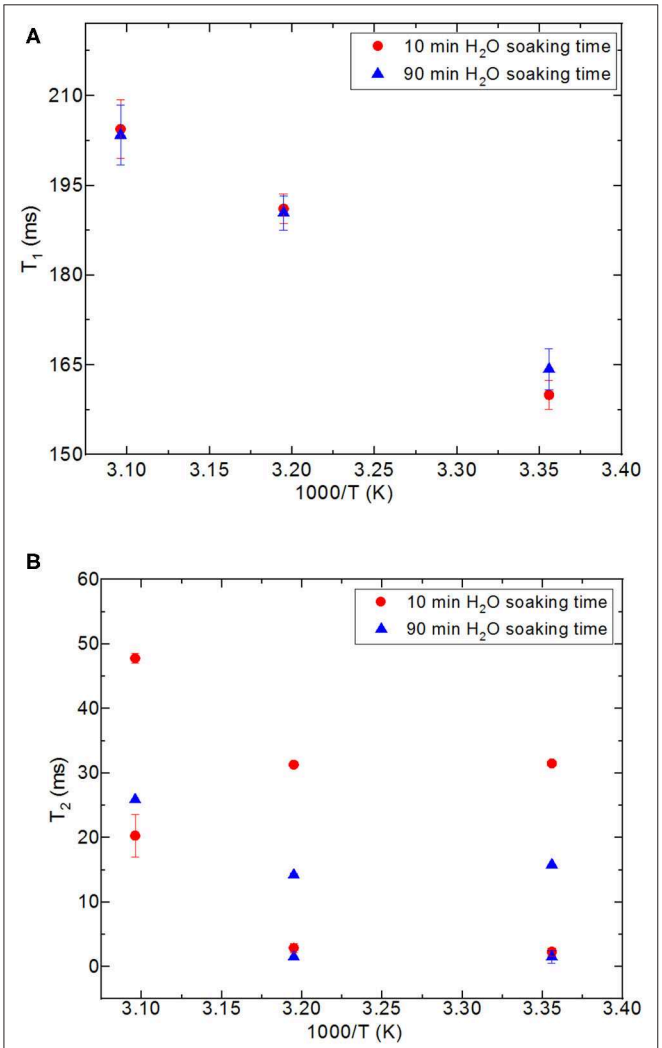

FIGURE 6 | Comparison of relaxation values of H_2O confined into 6 nm silica rod at 298, 313, and 323 K, and with 10 and 90 min of water soaking times; T_1 **(A)**, T_2 **(B)**.

TABLE 7A | $T_{1,surface}$ values of water in confined state.

	$T_{1,surface}$ (ms) with 0.4 ml water		
	25°C	**40°C**	**50°C**
Silica-4.0 nm	28.0	47.4	3.8
Silica-2.5 nm	842.7	909.4	1066.9
Silica-1.5 nm	263.0	182.0	44.2

TABLE 7B | $T_{1,surface}$ values of CH_3OH and CH_3OD in confined state.

	$T_{1,surface}$ (ms): silica-4.0 nm + 0.4 ml fluid		
	25°C	**40°C**	**50°C**
CH_3OH	15.6	5.1	18.2
CH_3OD	55.5	86.3	98.3

neutron scattering, Osti et al. (2016) mentioned primary single parameter θ, which is the ratio of the mean number of water molecules that are mostly affected by pore walls to the total number of H_2O molecules under confinement. If we consider θ as equal to a constant value such as (X) for a complete saturation with and without excess water by taking filling mechanism of MCM-41 with H_2O mentioned by Grünberg et al. (2004) into account, we suggest that there are both $\theta \approx X$ and $\theta \leq X$ where there is dynamic exchange between confined water molecules (the ones not interacting with the pore walls) and the bulk excess water. For the samples with excess fluid as in the case of silica-4 nm, θ for different fluid-solid-ratios is equal to each other. When the fluid-to-solid ratio is decreased for the partially filled samples, θ also decreases down. Because θ is utilized for the slit-type, cylindrical, and spherical geometries, θ is applicable in the current study as well. Osti et al. (2016) used exact analytical techniques to explain H_2O adsorption in three model geometries of slit-type, cylinder, and sphere to have deeper explanation of the change of θ with the restricted geometry. In the present study, characterization of the engineered nanoporous proxies and the analysis of confined fluids are done in detail. For example, although nanoporous silica materials are known amorphous, degree of regular patterns of each sample was studied by XRD thoroughly to clarify the alignment and geometry of the pores.

A rough consideration of T_1/T_2 ratios for both confined water and methanol clearly indicate a straightforward deducing

arrangement of comparative intensity of interaction with the pore uppermost layer of silica-4.0 nm: water has greater interaction with the pore surface than methanol (Weber et al., 2010; D'Agostino et al., 2012). For this reason, we think that methanol molecules establish clusters with extensive hydrogen bond formation in the pores rather than interacting with the pore surface (Tsotsalas et al., 2013). It was argued that the existence of porous medium disrupts the widespread intermolecular hydrogen-bonding system of some polyols such as glycerol and ethylene glycol, and this disruption in hydrogen bonding system resulted in boosted translation and tumbling movement degree, therefore longer T_1 values. In our case, such a disruption might exist with respect to bulk liquids. However, this disruption is less effective for confined CH_3OH molecules than confined water molecules given that the same nanoporous matrix system is utilized for confining the molecules. In addition, we observe shorter T_1 times for both of the confined fluids with respect to their bulk state. It is already known that NMR relaxation time values of confined fluids in porous media are relatively shorter than their corresponding fluids in bulk (Barrie, 2000). This situation is attributed to the uppermost layer and dipolar interactions and a decreased degree of reorientation of molecules at the pore uppermost layer (D'Agostino et al., 2012). We suggest these interactions dominate in terms of reducing the T_1 times of both of the confined fluids.

In addition to comparing relaxation behaviors of confined H_2O and CH_3OH, we also compare relaxation behaviors of CH_3OH and CH_3OD under confinement. When we switch from CH_3OH to CH_3OD, we only measure confined behavior of $-CH_3$ group. Both T_1 and T_2 of CH_3OD are longer than those of CH_3OH. T_1/T_2 ratio of confined CH_3OD is also smaller as in the case of confined CH_3OH. This shows that there is weaker interaction between $-CH_3$ and mesoporous silica-4.0 nm. Although confined CH_3OD behavior deviated from that of bulk CH_3OD upon confining into silica-4.0 nm, deviation is lesser than these of confined H_2O and CH_3OH. This also shows that hydrogen bonding capability of the molecules such as H_2O and CH_3OH with –OH groups decorating the pore walls influences both dynamics of the confined fluids and the layers formation on the pore walls.

T_2 Distributions of Fluids Under Nanoporous Confinement

Figure 7 shows T_2 distribution curves, obtained using Contin software, of H_2O, CH_3OH, and CH_3OD confined in silica-4.0 nm. The distributed exponential approach utilizes a governing approach to the inverse Laplace transform yielding a continuous distribution of T_2 relaxation times (Provencher, 1982). Mathematically speaking, the distributed exponential fitting is an ill-defined process because it is sensitive to the restrictions applied (Martens and Thybo, 2000; Hansen et al., 2010). Furthermore, there is a shorter T_2 relaxation component observed in the range 10–15 ms. Such a component is mostly explained as a treating artifact due to the Contin processing stage (Aursand et al., 2008). For this reason, this component in the T_2 distributions is not taken into account in evaluating T_2 distribution curves of the fluids confined into silica-4.0 nm.

In the case of the confined water inside silica-4.0 nm, when the fluid-to-solid ratio is lowered, T_2 curves shifted toward shorter times. In addition, T_2 curves became broader and had lower intensity (**Figure 7A**). On the other hand, confined CH_3OH has longer T_2 components as seen in **Figure 7B**. The T_2 curves with the highest intensities between 150 and 450 ms range exhibited the same tendency as in the case of confined water. In other words, lower fluid-to-solid ratio was reflected as lower intensity T_2 distribution curves at shorter T_2 times. For the range between 20 and 80 ms the same result was observed. However, line broadening in T_2 distribution curves of confined CH_3OH was less pronounced. When the fluid-to-solid ratio was at the lowest value (0.4 ml CH_3OH confined to 150 mg silica 4.0 nm), there was a third T_2 curve around 55 ms with broader distribution. When the fluid chemistry was switched to CH_3OD, T_2 distribution curves with the higher intensities were in the range between 100 and 900 ms. Consistently with the two other confined fluids, as the fluid-to-solid ratio was decreased, T_2 curves shifted to shorter times with lower intensities. However, there were three T_2 curves for each fluid-to-solid ratio. As the T_2 curve shifts toward lower values, the T_2 curve loses intensity. For this reason, the observation of three T_2 curves for confined CH_3OD inside silica-4.0 nm might correspond to different proportions of the confined CH_3OD molecules (Bertram et al., 2002): (1) the ones forming layers on the pore walls by weak interactions with the –OH of the pore wall, (2) the ones closer to the middle of the pores and having lesser interactions with ones forming layers on the pore walls, (3) the ones clustering in the center of the pores. As reflected in longer T_2 values, and continuous T_2 distribution curves, among the three fluids of interest, CH_3OD has the weakest interaction with the pore walls.

CONCLUSION

Specific pore volumes (cm^3/g) of the nanoporous silica samples studied exhibit the following order: silica-1.5 nm > silica-4.0 nm > silica-2.5 nm. Nanopore diameter does not influence the dynamics of confined water significantly as revealed by the results on relaxation of water obtained by keeping pore volumes of porous matrixes constant for the given amounts of the porous materials. Rather than pore diameter, S/V ratio along with pore diameter reflects information on filling mechanism the nanopores with water. In the case of relatively larger pore diameter and small S/V ratio, wetting the surface of the nanopore walls is followed by additional filling from the pore wall to the midpoint of the pore until achieving complete filling of the pores (Grünberg et al., 2004). In the case of nanoporous silica with small pore diameter and large S/V ratio, the filling mechanism follows a different path: first, fluid fills the center of the pores leading to a co-presence of filled pore fragments with wetted pores. Further filling of the pores develops axially in the direction of the pore axis.

The possibility of distinguishing among relaxation times of excess and confined fluids, and to quantify excess fluid, fluid

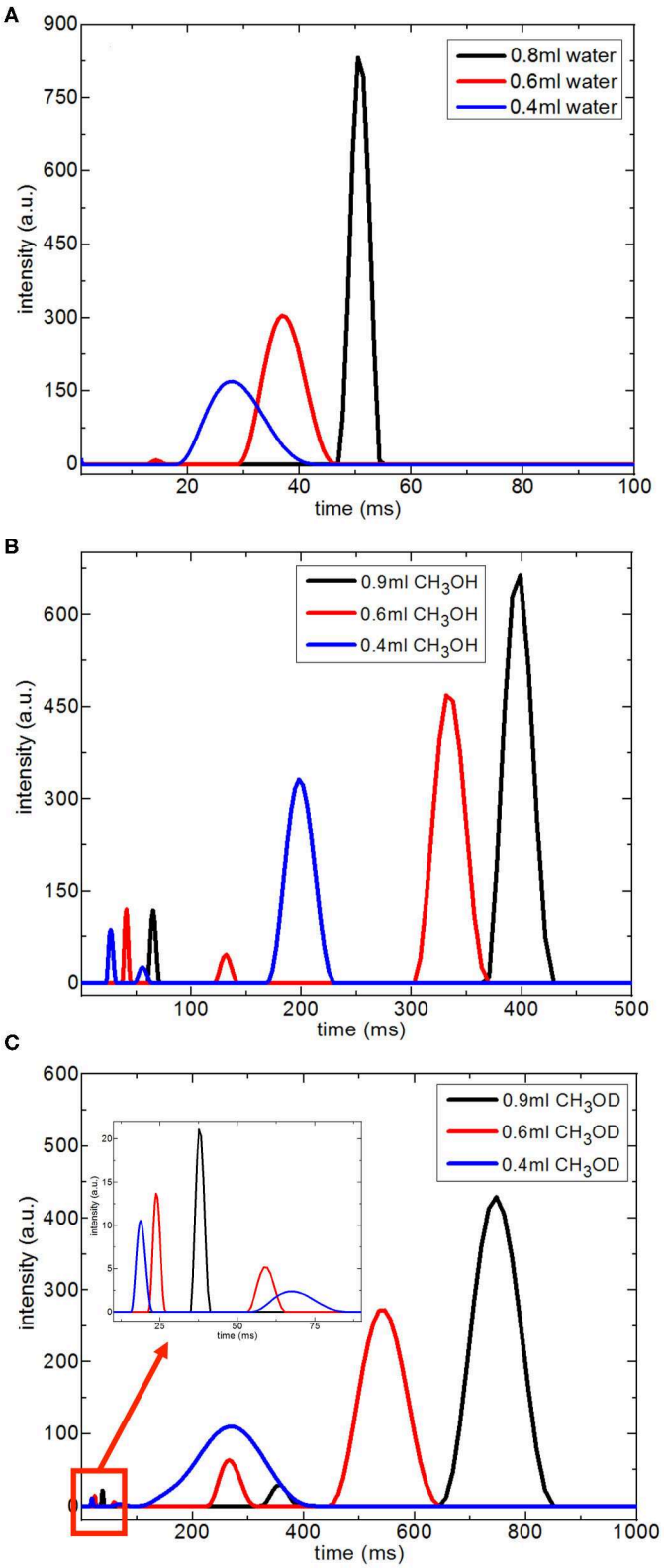

FIGURE 7 | Continuous T_2 relaxation time data for H_2O **(A)**, CH_3OH **(B)**, and CH_3OD **(C)** confined into silica-4.0 nm with the amount of 150 mg and S/V = 574 as a function of fluid-to-solid ratio.

found in the interparticle regions of nanoporous silica powder and outside the pores, and fluid confined in the nanopores of silica matrices might have applications in the petroleum industry, where characterization of rock with various pore sizes has significance for better definition of reservoirs. However, the highest S/V ratio leads to the longest T_1 times of confined water, while the lowest S/V ratio resulted in the shortest T_1 times of confined water. The decrease in T_2 values as decreasing the fluid-to-solid ratio is more pronounced in the case of silica-2.5 nm having the lowest pore volume. These results clearly show the importance and influence of S/V ratio on dynamical behaviors of fluids confined into nanoporous proxies.

Comparison of T_1/T_2 ratios, showing the affinity of the confined fluid to the pore walls, of both confined H_2O and CH_3OH clearly show that H_2O has stronger interaction with the pore surface of silica-4.0 nm than CH_3OH. The degree of deviation of confined CH_3OD behavior in silica-4.0 nm from that of bulk is less than those of confined H_2O and CH_3OH. It was claimed that a porous medium disrupts the extensive intermolecular hydrogen-bonding network of some polyols, and this disruption led to longer T_1 values (D'Agostino et al., 2012). Such a disruption in hydrogen-bonding network is less effective for confined CH_3OH molecules than confined H_2O molecules for the same nanoporous matrix system. In addition to S/V ratio, chemistry of confined fluids also affects the dynamical measurements. This is an important observation, for example, in interpreting dynamical behaviors of confined and saturated mixtures of water and hydrocarbons at natural confined systems, where wettability alteration occurring inside the porous structures of the rocks influences the crude oil production.

The continuous T_2 distribution curves suggest that weaker interaction between CH_3OD and nanoporous silica-4.0 nm with three different environments: (i) layered structure by weak interactions with the pore walls, (ii) the ones closer to the center of pores and interacting weakly with the first layer on the pore wall, (iii) the ones forming cluster in the middle of the nanopores.

Finally, the characteristics and properties of the nanoporous matrix systems are defined in a better way. Furthermore, low-field ^{1}H NMR is a powerful technique when exploring confined fluid dynamics as a function of the aforementioned parameters. These nanoporous silica samples are ideal examples that mimic the natural geological systems such as heterogeneous subsurface materials containing crude oil and brine solutions to mimic nano-environments present in natural systems such as rocks. Based on the findings on the properties of mesoporous silica proxies and dynamical behavior of confined crude oil and brine confined into mesoporous silica materials, we also analyzed sandstone rock cores flooded with crude oil and brine with hydrophobic/oleophilic nanoparticles in addition to characterizing natural carbonate rock cores saturated with water and crude oil. The results of these measurements are to be discussed in forthcoming publications.

DATA AVAILABILITY STATEMENT

All datasets generated for this study are included in the article/**Supplementary Material**.

AUTHOR CONTRIBUTIONS

SO planned and conducted the low-field NMR measurements in addition to TGA measurements. BH contributed to the low-field NMR measurements. TL completed the BET and TXRD measurements. JS and SW contributed to each and every step of the study, and in particular on both TXRD and BET parts. K-HL and C-YM synthesized silica-2.5 nm and silica-1.5 nm. DC was the research leader. All authors contributed to the article and approved the submitted version.

FUNDING

Support for SO was provided by the A.P. Sloan Foundation sponsored Deep Carbon Observatory. DC, JS, and SW were supported by the Department of Energy, Basic Energy Sciences Geosciences Program under grant DE-SC0006878.

SUPPLEMENTARY MATERIAL

The Supplementary Material for this article can be found online at: https://www.frontiersin.org/articles/10.3389/fchem.2020.00734/full#supplementary-material

REFERENCES

Al-Othman, Z. A. (2012). A review: fundamental aspects of silicate mesoporous materials. *Materials* 5, 2874–2902. doi: 10.3390/ma5122874

Asefa, T., and Tao, Z. (2012). Mesoporous silica and organosilica materials-review of their synthesis and organic functionalization. *Can. J. Chem.* 90, 1015–1031. doi: 10.1139/v2012-094

Aursand, I. G., Gallart-Jornet, L., Erikson, U., Axelson, D. E., and Rustad, T. (2008). Water distribution in brine salted cod (*Gadus morhua*) and aalmon (*Salmo salar*): a low-field ^{1}H NMR study. *J. Agric. Food Chem.* 56, 6252–6260. doi: 10.1021/jf800369n

Barrie, P. J. (2000). Characterization of porous media using NMR methods. *Annu. Rep. NMR Spectrosc.* 41, 265–316. doi: 10.1016/S0066-4103(00)41011-2

Barut, G., Pissis, P., Pelster, R., and Nimtz, G. (1998). Glass transition in liquids: two versus three-dimensional confinement. *Phys. Rev. Lett.* 79, 3543–3546. doi: 10.1103/PhysRevLett.80.3543

Bellisent-Funel, M.-C., Chen, S. H., and Zanotti, J. M. (1995). Single-particle dynamics of water molecules in confined space. *Phys. Rev. E* 51, 4558–4569. doi: 10.1103/PhysRevE.51.4558

Bergman, R., and Swenson, J. (2000). Dynamics of supercooled water in confined geometry. *Nature* 403, 283–285. doi: 10.1038/35002027

Bertram, H. C., Purslow, P. P., and Andersen, H. J. (2002). Relationship between meat structure, water mobility, and distribution: a low-field nuclear magnetic resonance study. *J. Agric. Food Chem.* 50, 824–829. doi: 10.1021/jf010738f

Bhattachrja, S., D'Orazio, F., Tarczon, J. C., Halperin, W. P., and Gerhardt, R. (1989). Internal structure of porous silica: a model system for characterization

by nuclear magnetic resonance. *J. Am. Ceram. Soc.* 72, 2126–2130. doi: 10.1111/j.1151-2916.1989.tb06043.x

Bloembergen, N., Purcell, E. M., and Pound, R. V. (1948). Relaxation effects in nuclear magnetic resonance absorption. *Phys. Rev.* 73, 679–746. doi: 10.1103/PhysRev.73.679

Bruni, F., Ricci, M. A., and Soper, A. K. (1998). Water confined in vycor glass. I. A neutron diffraction study. *J. Chem. Phys.* 109, 1478–1485. doi: 10.1063/1.476698

Buntkowsky, G., Breitzke, H., Adamczyk, A., Roelofs, F., Emmler, T., Gedat, E., et al. (2007). Structural and dynamical properties of guest molecules confined in mesoporous silica materials revealed by NMR. *Phys. Chem. Chem. Phys.* 9, 4843–4853. doi: 10.1039/b707322d

D'Agostino, C., Mitchell, J., Gladden, L. F., and Mantle, M. D. (2012). Hydrogen bonding network disruption in mesoporous catalyst supports probed by PFG-NMR diffusometry and NMR relaxometry. *J. Phys. Chem. C* 116, 8975–8982. doi: 10.1021/jp2123295

Denisov, V., and Halle, B. (1996). Protein hydration dynamics in aqueous solution. *Faraday Discuss.* 103, 227–244. doi: 10.1039/fd9960300227

D'Orazio, F., Bhattaharja, S., Halperin, W. P., Eguchi, K., and Mizusaki, T. (1990b). Molecular diffusion and nuclear-magnetic-resonance relaxation of water in unsaturated porous silica glass. *Phys. Rev. B* 42, 9810–9818. doi: 10.1103/PhysRevB.42.9810

D'Orazio, F., Bhattaharja, S., Halperin, W. P., and Gerhardt, R. (1990a). Fluid transport in partially filled porous sol-gel silica glass. *Phys. Rev. B* 42, 6503–6508. doi: 10.1103/PhysRevB.42.6503

Gallegos, D. P., Smith, D. M., and Brinker, C. J. (1988). An NMR technique for the analysis of pore structure: application to mesopores and micropores. *J. Coll. Inter. Sci.* 124, 186–198. doi: 10.1016/0021-9797(88)90339-6

Grünberg, B., Emmler, T., Gedat, E., Shenderovich, I., Findenegg, G. H., Limbach, H.-H., et al. (2004). Hydrogen bonding of water confined in mesoporous silica MCM-41 and SBA-15 studied by ^{1}H solid-state NMR. *Chem. Eur. J.* 10, 5689–5696. doi: 10.1002/chem.200400351

Hansen, C. L., Thybo, A. K., Bertram, H. C., Viereck, N., van den Berg, F., and Engelsen, S. B. (2010). Determination of dry matter content in potato tubers by low-field nuclear magnetic resonance (LF-NMR). *J. Agric. Food Chem.* 58, 10300–10304. doi: 10.1021/jf101319q

Kapur, G. S., Findeisen, M., and Berger, S. (2000). Analysis of hydrocarbon mixtures by diffusion-ordered NMR spectroscopy. *Fuel* 79, 1347–1351. doi: 10.1016/S0016-2361(99)00271-9

Liu, K.-H., Zhang, Y., Lee, J.-J., Chen, C.-C., Yeh, Y.-Q., Chen, S.-H., et al. (2013). Density and anomalous thermal expansion of deeply cooled water confined in mesoporous silica investigated by synchrotron x-ray diffraction. *J. Chem. Phys.* 139:064502. doi: 10.1063/1.4817186

Liu, L., Chen, S. H., Faraone, A., Yen, C. W., Mou, C. Y., Kolesnikov, A. I., et al. (2006). Quasielastic and inelastic neutron scattering investigation of fragile-to-strong crossover in deeply supercooled water confined in nanoporous silica matrices. *J. Phys. Condens. Matter* 18, S2261–S2284. doi: 10.1088/0953-8984/18/36/S03

Liu, Y., Zhang, W. Z., and Pinnavaia, T. J. (2000). Steam-stable aluminosilicate mesostructures assembled from zeolite type Y seeds. *J. Am. Chem. Soc.* 122, 8791–8792. doi: 10.1021/ja001615z

Macomber, R. S. (1998). *A Complete Introduction to Modern NMR Spectroscopy*. New York, NY: John Wiley and Sons, Inc.

Mallamace, F., Corsaro, C., Mallacame, D., Vasi, S., Vasi, C., and Stanley, H. E. (2014). Thermodynamic properties of bulk and confined water. *J. Chem. Phys.* 141:18C504. doi: 10.1063/1.4895548

Martens, H. J., and Thybo, A. K. (2000). An integrated microstructural, sensory and instrumental approach to describe potato texture. *LWT Food Sci. Technol.* 33, 471–482. doi: 10.1006/fstl.2000.0688

Millischuk, A. A., and Ladanyi, B. M. (2011). Structure and dynamics of water confined *in silica* nanopores. *J. Chem. Phys.* 135:174709. doi: 10.1063/1.3657408

Millischuk, A. A., and Ladanyi, B. M. (2014). Polarizability anisotropy relaxation in nanoconfinement: molecular simulation study of water in cylindrical silica pores. *J. Chem. Phys.* 141, 18C513-1–18C513-9. doi: 10.1063/1.4896218

Mitchell, J., Hurlimann, M. D., and Fordham, E. J. (2009). A rapid measurement of T1/T2: the DECPMG sequence. *J. Magn. Reson.* 200, 198–206. doi: 10.1016/j.jmr.2009.07.002

Nicotera, I., Angjeli, K., Coppola, L., Arico, A. S., and Baglio, V. (2012). NMR and electrochemical investigation of the transport properties of methanol and water in nafion and clay-nanocomposites membranes for DMFCs. *Membranes* 2, 325–345. doi: 10.3390/membranes2020325

Ok, S., Hoyt, D. W., Andersen, A., Sheets, J., Welch, S. A., Cole, D. R., et al. (2017). Surface interactions and confinement of methane: a high pressure magic angle spinning NMR and computational chemistry study. *Langmuir* 33, 1359–1367. doi: 10.1021/acs.langmuir.6b03590

Osti, N. C., Cote, A., Mamontov, E., Ramirez-Cuesta, A., Wesolowski, D. J., and Diallo, S. O. (2016). Characteristic features of water dynamics in restricted geometries investigated with quasi-elastic neutron scattering. *Chem. Phys.* 465–466, 1–8. doi: 10.1016/j.chemphys.2015.11.008

Provencher, S. W. (1982). A constrained regularization method for inverting data represented by linear algebraic of integral equations. *Comput. Phys. Commun.* 27, 213–227. doi: 10.1016/0010-4655(82)90173-4

Ricci, M. A., and Rovere, M. (2000). Studies of water in confinement by experiments and simulations. *J. Phys.* 10, 187–193. doi: 10.1051/jp4:2000737

Sarawade, P. B., Shao, G. N., Quang, D. V., and Kim, H. T. (2013). Effect of various structure directing agents on the physicochemical properties of the silica aerogels prepared at an ambient pressure. *Appl. Surf. Sci.* 287, 84–90. doi: 10.1016/j.apsusc.2013.09.072

Sattig, M., Reutter, S., Fujara, F., Werner, M., Buntkowsky, G., and Vogel, M. (2014). NMR studies on the temperature-dependent dynamics of confined water. *Phys. Chem. Chem. Phys.* 16, 19229–19240. doi: 10.1039/C4CP02057J

Sindorf, D. W., and Maciel, G. E. (1983). Silicon-29 NMR study of dehydrated/rehydrated silica gel using cross polarization and magic-angle spinning. *J. Am. Chem. Soc.* 105, 1487–1493. doi: 10.1021/ja00344a012

Sing, K. S. W., Everett, D. H., Haul, R. A. W., Moscou, L., Pierotti, R. A., Rouquerol, J., et al. (1985). Reporting physisorption data for gas–solid systems. *Pure Appl. Chem.* 57, 603–619. doi: 10.1351/pac198557040603

Slichter, C. P. (1990). *Principles of Magnetic Resonance, 3rd Edn.* New York, NY: Springer Series in Solid State Science. doi: 10.1007/978-3-662-09441-9

Steytler, D. C., and Dore, J. C. (1985). Neutron diffraction studies of water in porous silica. *Mol. Phys.* 56, 1001–1015. doi: 10.1080/00268978500102851

Swenson, J., Bergman, R., and Longeville, S. (2001). A neutron spin-echo study of confined water. *J. Chem. Phys.* 115, 11299–11305. doi: 10.1063/1.1420728

Tangestaninejad, S., Moghadam, M., Mirkhani, V., Baltork, I. M., and Ghani, K. (2009). Alkene epoxidation catalyzed by molybdenum supported on functionalized MCM-41 containing N–S chelating schiff base ligand. *Catal. Commun.* 10, 853–858. doi: 10.1016/j.catcom.2008.12.010

Thommes, M., Kaneko, K., Neimark, A. V., Olivier, F. R.-R., Rouquerol, J., and Sing, K. S. W. (2015). Physisorption of gases, with special reference to the evaluation of surface area and pore size distribution, IUPAC Technical Report. *Pure Appl. Chem.* 87, 1051–1069. doi: 10.1515/pac-2014-1117

Timur, A. (1969). Pulsed nuclear magnetic resonance studies of porosity, movable fluid, and permeability of sandstones. *J. Petrol. Technol.* 21, 775–786. doi: 10.2118/2045-PA

Tsotsalas, M., Hejcik, P., Sumida, K., Kalay, Z., Furukawa, S., and Kitagawa, S. (2013). Impact of molecular clustering inside nanopores on desorption processes. *J. Am. Chem. Soc.* 135, 4608–4611. doi: 10.1021/ja312115x

Vogel, M. (2010). NMR studies on simple liquids in confinement. *Eur. Phys. J.* 189, 47–64. doi: 10.1140/epjst/e2010-01309-9

Webber, B., and Dore, J. (2004). Structural and dynamic studies of water in mesoporous silicas using neutron scattering and nuclear magnetic resonance. *J. Phys. Condens. Matter* 16, S5449–S5470. doi: 10.1088/0953-8984/16/45/009

Weber, D., Mitchell, J., McGregor, J., and Gladden, L. F. (2009). Comparing strengths of surface interactions for reactants and solvents in porous catalysts

using two-dimensional NMR relaxation correlations. *J. Phys. Chem. C* 113, 6610–6615. doi: 10.1021/jp811246j

Weber, D., Sederman, A. J., Mantle, M. D., Mitchell, J., and Gladden, L. F. (2010). Surface diffusion in porous catalysts. *Phys. Chem. Chem. Phys.* 12, 2619–2624. doi: 10.1039/b921210h

Wu, D., and Navrotsky, A. (2013). Small molecule-silica interactions in porous silica structures. *Geochim. Cosmochim. Acta* 109, 38–50. doi: 10.1016/j.gca.2013.01.038

Zanotti, J. M., Bellisent-Funel, M.-C., and Chen, S. H. (1999). Relaxational dynamics of supercooled water in porous glass. *Phys. Rev. E* 59, 3084–3093. doi: 10.1103/PhysRevE.59.3084

Conflict of Interest: The authors declare that the research was conducted in the absence of any commercial or financial relationships that could be construed as a potential conflict of interest.

frontiers in Chemistry

REVIEW
published: 23 December 2020
doi: 10.3389/fchem.2020.598662

Use of Ionic Liquids in Protein and DNA Chemistry

Shashi Kant Shukla[1]* *and Jyri-Pekka Mikkola*[1,2]*

[1] Technical Chemistry, Department of Chemistry, Chemical-Biological Centre, Umeå University, Umeå, Sweden, [2] Industrial Chemistry and Reaction Engineering, Department of Chemical Engineering, Johan Gadolin Process Chemistry Centre, Åbo Akademi University, Åbo-Turku, Finland

Ionic liquids (ILs) have been receiving much attention as solvents in various areas of biochemistry because of their various beneficial properties over the volatile solvents and ILs availability in myriad variants (perhaps as many as 10^8) owing to the possibility of paring one cation with several anions and *vice-versa* as well as formulations as zwitterions. Their potential as solvents lies in their tendency to offer both directional and non-directional forces toward a solute molecule. Because of these forces, ionic liquids easily undergo intermolecular interactions with a range of polar/non-polar solutes, including biomolecules such as proteins and DNA. The interaction of genomic species in aqueous/non-aqueous states assists in unraveling their structure and functioning, which have implications in various biomedical applications. The charge density of ionic liquids renders them hydrophilic and hydrophobic, which retain intact over long-range of temperatures. Their ability in stabilizing or destabilizing the 3D-structure of a protein or the double-helical structure of DNA has been assessed superior to the water and volatile organic solvents. The aptitude of an ion in influencing the structure and stability of a native protein depends on their ranking in the Hofmeister series. However, at several instances, a reverse Hofmeister ordering of ions and specific ion-solute interaction has been observed. The capability of an ionic liquid in terms of the tendency to promote the coiling/uncoiling of DNA structure is noted to rely on the basicity, electrostatic interaction, and hydrophobicity of the ionic liquid in question. Any change in the DNA's double-helical structure reflects a change in its melting temperature (T_m), compared to a standard buffer solution. These changes in DNA structure have implications in biosensor design and targeted drug-delivery in biomedical applications. In the current review, we have attempted to highlight various aspects of ionic liquids that influence the structure and properties of proteins and DNA. In short, the review will address the issues related to the origin and strength of intermolecular interactions, the effect of structural components, their nature, and the influence of temperature, pH, and additives on them.

Keywords: ionic liquid (IL), DNA, protein, Hofmeister series, intermolecular interaction, circular dichroism, double-helical structure, salting phenomenon

OPEN ACCESS

Edited by:
Janno Torop,
University of Tartu, Estonia

Reviewed by:
Itthipon Jeerapan,
Prince of Songkla University, Thailand
Jens Smiatek,
University of Stuttgart, Germany
Ramesh L. Gardas,
Indian Institute of Technology Madras, India

***Correspondence:**
Shashi Kant Shukla
shashi.kant.shukla@umu.se;
shasi271283@gmail.com
Jyri-Pekka Mikkola
jyri-pekka.mikkola@umu.se

Specialty section:
This article was submitted to Physical Chemistry and Chemical Physics, a section of the journal Frontiers in Chemistry

Received: *25 August 2020*
Accepted: *01 December 2020*
Published: *23 December 2020*

Citation:
Shukla SK and Mikkola J-P (2020) Use of Ionic Liquids in Protein and DNA Chemistry. Front. Chem. 8:598662. doi: 10.3389/fchem.2020.598662

INTRODUCTION

The energetics of a biological reaction/process change upon perturbing the solvent systems around it (Yancey et al., 1982). Molecular solvents, depending upon its nature, might offer various interactions ranging from dipole-dipole, electrostatic, van der Waals, hydrogen bonding, hydrophobic interactions, and so on. However, it is impossible to accommodate all the said interactions in a single molecular solvent. Water, despite its recognition as a universal solvent, offers only dipole-dipole, hydrogen bonding, and hydrophobic interactions for a solute. Almost all basic biological entities necessarily require a medium for their stabilization and functioning. Out of various basic biological candidates, we are, in particular, addressing the proteins and DNA in detail. As both proteins and DNA possess basic moieties, electrostatic, and hydrophobic centers, they require a medium that has all these interactions for their stabilization, functioning, long-term storage, and separation.

In quest of the "green" solvents, the past few decades have witnessed the upsurge of ionic liquids (ILs) as a suitable replacement of volatile organic solvents (VOCs) in various applications. Ionic liquids (IL) are typically liquid at room temperature and mainly consists of asymmetric organic cation and organic/ inorganic anion (Wilkes and Zaworotko, 1992). Ionic liquids are classified as protic ionic liquids (PILs) and aprotic ionic liquids (AILs), depending on the quaternization of base by proton (H^+) or alkyl group (-R), respectively. These two ionic liquids differ a lot in terms of the activity and strength of the directional and non-directional forces between ions. Protic ionic liquids possess higher strength of Coulomb- and hydrogen bonding-interactions as compared to their aprotic counterparts and resembles closely to water, owing to their extensive network of hydrogen bonding (Fumino et al., 2009) Similar to PILs are Brønsted acidic ionic liquids, in which protons occupy either the cation or the anion (not necessarily on the cation as in protic ionic liquids), and therefore, they are categorized with the protic/aprotic ionic liquids. The reputation of ionic liquids in several fields is because of their attractive properties such as significantly low vapor pressures, high thermal stability, wide liquidus range, non-flammability, and recyclability (Welton, 1999; Weingärtner, 2008; Castner and Wishart, 2010; Hayes et al., 2015; Egorova et al., 2017). Their relevance in various chemical and biological processes is owing to their ability to interact through the variety of forces toward a solute. The physicochemical properties of ionic liquids depend on the coordination of asymmetric cation with a symmetric or asymmetric organic/inorganic anion (Rogers and Seddon, 2003). Depending on the charge density of anion, ionic liquids behaves as hydrophilic or hydrophobic in water and therefore can react with both polar and non-polar solutes. Besides, a long alkyl chain either on cation or on anion also imparts hydrophobic character to the ionic liquid. Ionic liquids in neat and in aqueous state affects the structure and stability of proteins and hence are being tried as a potential media in storage and crystallization. Despite the huge interests in ionic liquids, the molecular mechanism involved in protein-ionic liquid are not yet fully comprehended. The availability of different kinds of ionic liquids and various features of proteins make the generalization about the intermolecular interactions very difficult. Addition of water though alleviates the solubility problem and maintains the structure over a longer time period; however, it complicates the understanding of the intermolecular interactions between the ionic liquid and biomolecules as water also undergoes strong hydrogen bonding with both species. The physical parameters for the aqueous ionic liquids, however, cannot be accounted for by the screened forces of the ionic liquid toward the biomolecule. In this regard, different solvation models have been employed to derive the interaction parameters that explain the stabilizing/destabilizing behavior of aqueous ionic liquid systems toward biomolecules. The structure and stability of the DNA's double-helical structure also get affected in the dilute solution of an ionic liquid. **Figure 1** and **Table 1** shows the interactions between ionic liquids and protein and DNA molecules.

There are some excellent review articles available on the use of ionic liquids in the stabilization and functioning of protein and DNA. The review article by Schindl et al. thoroughly discusses the use of different classes of ionic liquids in the dissolution and processing of different types of proteins (Schindl et al., 2019). The review by Gough et al. presents a critical discussion on the use of ionic liquids as potential media for protein and polysaccharide biopolymers fibrillation by different fiber fabrication methods (Gough et al., 2020). The topical review by Smiatek presents detailed discussion about the role of ionic liquids as solvents in deciding the fate of protein to the native and denatured state by using a preferential binding model, where the strength of ions in influencing the protein dynamics is given in terms of the value of preferential binding coefficient (Smiatek, 2017). The role of water on the self-aggregation of ionic liquids is also discussed with recent experimental and theoretical findings in light of the binding coefficient values. Wakayama et al. presented a review based on various model parameters to construct the enzyme-derived catalyst in the production of important chemicals (Wakayama et al., 2019). The review by Saha and Mukherjee enlists the simulation results on the effect of water in altering the structural and dynamical properties of ionic liquids and biomolecules present in it (Saha and Mukherjee, 2018). Reslan and Kayser compiled all the experimental and theoretical results available on the ionic liquid-protein interactions and discussed the effect of toxicity and viscosity on it (Reslan and Kayser, 2018). Oprzeska-Zingrebe and Smiatek discussed the relative importance of the aqueous ionic liquids and standard co-solutes in stabilizing or destabilizing the protein and DNA structure (Oprzeska-Zingrebe and Smiatek, 2018). The extent of stabilization/destabilization by the ionic liquids are discussed in terms of the enthalpic and entropic contributions obtained from the Gibbs free energy change. The review by Schröder gives a detailed account of the various properties of ionic liquids that could affect the protein stability and crystallization in view of the various classical theories (Schröder, 2017). Contrary to the multiple reviews available on the behavior and functioning of protein in ionic liquid systems, information on DNA stabilization in ionic liquid systems is scarce. The review by Zhao though gives a good account of the use of ionic liquids on the DNA

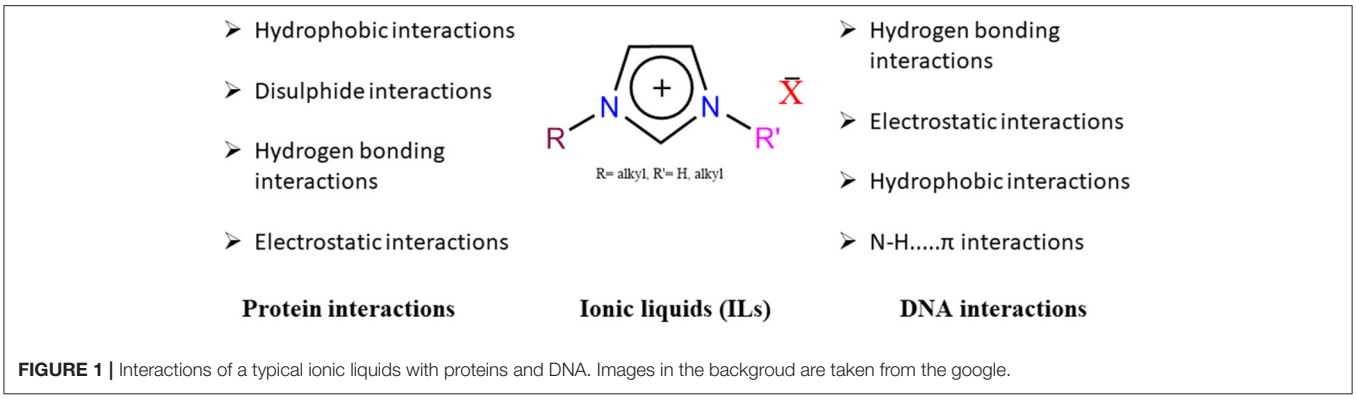

FIGURE 1 | Interactions of a typical ionic liquids with proteins and DNA. Images in the backgroud are taken from the google.

TABLE 1 | Summary of interactions between ionic liquids and biomolecules and responsible functionality/moiety.

Type of interactions	Responsible group/moiety on ionic liquids
Hydrophobic interactions	Hydrophobic surfaces of protein/DNA and alkyl chain on cation
Disulphide (S-S) interactions	Anion and protein linkage
Hydrogen bonding interactions	Anion and electron donor moiety on protein and DNA bases
Electrostatic interactions	Cation with P=O bonds on DNA strands and anion with negatively charged surface on protein
NH—π interactions	Aromatic cation and DNA bases

stabilization in terms of various specific and non-specific-interactions between them (Zhao, 2015).

In the current review, we aim to discuss the role of intermolecular interactions of ionic liquids on the structure and functioning of various proteins and DNA. These interactions are discussed in terms of the change of cation, anion, length of alkyl chain, and presence of functional group on them. A brief introduction of various theories/concepts in the protein stabilization by electrolytes solutions and their utility in case of ionic liquids is presented. Besides the variation of structural components, the influence of the reaction conditions such as pH, temperature, and effect of water on the intermolecular interactions are also described. The importance of ionic liquid-biomolecules interactions on, stability, solubility and separations are also covered. The negative impact of toxicity of ionic liquids on the storage and functioning of biomolecules and recyclability is also taken into the consideration.

ION-PROTEIN INTERACTIONS

We begin this section with a brief discussion about the solvent property such as polarity and hydrophobicity that have implications on the protein and DNA chemistry. Subsequently, various theories/concepts related to the ion-protein interactions like the Hofmeister series, Collins law of matching water affinity, Jones-Dole coefficient, and the influence of ionic strength will be discussed. The validity and deviation of Hofmeister series is also extended to the ionic liquids. At the end, specific role of water on the protein-ionic liquid interactions is discussed.

Nearly all proteins contain a lower or higher amount of sulfur (3–6%) in their structures that impart rigidity to the 3-D structure owing to the formation of disulfide (-S-S-) bonds (Simpson and Crawshaw, 2002). Besides, various inter- and intra-molecular hydrogen bonds in protein also contribute to the rigidity and hence posing a challenge in their processing. Therefore, a solvent/mixture whose components outshine the –S-S- and inter- and intra-molecular interactions are desired for protein processing. The use of molecular solvents in protein processing has lingered with various issues. They poses a risk of volatility, corrosiveness, environmental impact, recycling, and renewability (Idris et al., 2013). In addition to this, their inapplicability in multi-step processes and the degradation of proteins are the prime issues related to solvent mixtures. Due to these shortcomings, there has been a growing demand to develop a new solvent that can fulfill the entire solvent properties for protein processing. The solvation behavior among different classes of ionic liquids is not similar and can be assessed from the polarity parameters and hydrophobicity. We would discuss in detail the characteristics of ionic liquids such as polarity, hydrophobicity and potential of ion, that come-in-aid to stabilize the protein structure.

Polarity

The solvation capability of a solvent is best to describe in terms of a single polarity parameter that accounts for the entire specific- and non-specific-interactions (Reichardt, 2005). There are various scales of solvent polarity such as static dielectric constant (ε_r), Reichardt polarity scale ($E_T(30)$), refractive index (η), and permanent dipole moment (μ) (Reichardt, 1994). Out of these, the static dielectric constant and Reichardt polarity scales are largely utilized to account for the "solvation effects/polarity." The non-specific electrostatic interactions are measured by dielectric spectroscopy (Huang and Weingärtner, 2008). The protic ionic liquids possesses a higher dielectric constant whereas the polarity of aprotic ionic liquids is in the range of lower alcohols. In the case of ionic liquids, which possess charged ions, static conductivity σ (0) dominates in the dielectric constant. However, it is noted that the dielectric constant of ionic liquids is lower than that measured by the diffusion coefficient due to

the interaction of ions itself rather than the neutral ion-pair. The mobility of ions poses a problem in the measurements of dielectric constant (Krüger et al., 2010).

The "Reichardt polarity scale" is devoid of any complications and determines all the specific, non-specific, π-π and dipole-dipole interactions of ionic liquids and molecular solvents (Reichardt, 2008). In this method, any change in the electronic transition due to the transfer of the Reichardt's dye from non-polar to polar medium is measured by UV-visible spectrophotometer and is represented as the electronic transition energy ($E_T(30)$) measured in kcal.mol^{-1}. Kamlet, Abboud, and Taft proposed the idea of a complementary polarity scale using a set of dyes that are known as polarity index (π^*), hydrogen bond donor acidity (α), and hydrogen bond acceptor basicity (β) (Kamlet and Taft, 1976; Taft and Kamlet, 1976; Kamlet et al., 1977). α denotes the hydrogen bond donor capacity and is a characteristic of cation whereas the β accounts for the hydrogen bond acceptor basicity and depends on the anion. The strength of electrostatic interaction between ions of ionic liquid is determined in terms of the polarity index, π^*. Protic ionic liquids possess higher α and lower β than their aprotic counterparts. The interaction of cations and anions of ionic liquids to the protein and DNA depends on the charge and acidity/basicity of the interacting sites on biomolecules.

Hydrophobicity

Hydrophobicity is a phenomenon in which a non-polar solute molecule tends to stay away from water (Zhao, 2006). It has a crucial role in protein solubilization and enzyme functioning. The low charge density on protein and enzymes makes them hydrophobic in water. A saturated 1-octanol-water mixture is used to measure the hydrophobicity of a solute in terms of the partition coefficient shown as log P, which denotes the partitioning of solute in 1-octanol as compared to water. Solvents with high log P are more hydrophobic compared to those with lower log P-values. Ionic liquids possess lower log P-values than short-chain alcohols. For example, 1-butyl-3-methylimidazolium with acetate, nitrate, and hexafluorophosphate anions have log P−2.8,−2.9, and−2.4, respectively than ethanol−0.24. Thus, ionic liquids are less hydrophobic or more hydrophilic than ethanol. The tethering of longer alkyl chain on cation or anion increases the log P (Yamamoto et al., 2011). Though hydrophobicity was found significant in enzyme catalysis, it inversely affects the solubility of the protein (Laane et al., 1987). In the case of proteins, hydrophobicity overshadows the basicity of anion or coulombic interactions (Kaar et al., 2003).

Effect of Ion on Protein Solubility: Hofmeister Series

Ion-induced effects are universal in chemistry and biology and emerged through the alteration in the hydrogen bonding network of water (Hofmeister, 1888). These effects were important in protein and enzyme stabilization and crystallization but the fundamental mechanism behind these effects were not well-understood (Collins, 2004; Kunz et al., 2004; Broering and Bommarius, 2005; Nostro et al., 2005). In 1888, Franz Hofmeister arranged several cations and anions into their capability of precipitating the egg white protein (Hofmeister, 1888). For a given cation, anions' coagulating power was in the order,

$$SO_4^{2-} > HPO_4^{2-} > F^- > CH_3COO^- > Cl^- > Br^- > NO_3^- > I^- > ClO_4^- > SCN^-$$

A reverse of the above ordering was noted operative in predicting the precipitating power of anions though not universally obeyed. Afterwards several experimental and theoretical reports claimed that protein stabilization in an electrolytic medium depends on the specific solute-ion interactions (Omta et al., 2003a,b; Zhang et al., 2005). Later, Gurney, Washbaugh and Collins, and Green explained the confusion over the validity of the Hofmeister series (Gurney, 1953; Collins, 2004, 2006).

Gurney classified salts as structure–maker (kosmotropic) and structure-breaker (chaotropic) depending on their ability to strongly- or weakly-interact with hydration layer of solute, respectively (Gurney, 1953). Collins and Washbaugh proposed the "law of matching water affinity" which states that a kosmotropic cation forms an ion-pair only with a kosmotropic anion and a chaotropic cation forms ion-pair only with a chaotropic anion (Collins, 2004). The ion-pairs of the mixed types do not exist. A perfect match between the hydration enthalpies of oppositely charged ions inhibits them to interact with water. A mismatch in the hydration enthalpy allows the ions to dissolve in water and make ion-induced effects visible. A kosmotrope (water structure-maker) offers strong interaction to water molecules beyond its hydration layer than a chaotrope (water structure-breaker; Collins, 2006). However, these concepts were soon disproved by spectroscopic and thermodynamic considerations (Omta et al., 2003a; Batchelor et al., 2004; Funkner et al., 2012). According to these evidences, a salt ion only affects its first hydration layer and has no effect on the bulk water as expected.

For a classical ion, the kosmotropic and chaotropic character correlates with the relative viscosity by the Equation (1),

$$\frac{\eta}{\eta_0} = 1 + A\sqrt{c} + B.c \quad (1)$$

where, η_0 is the viscosity of solvent, η is the viscosity of salt solution at concentration c, A is the Falkenhagen coefficient that depends on the electrostatics of the system and are small and B is the Jones-Dole coefficient and represent the characteristic of ions (Collins, 1997). A kosmotropic ion interacts intensely with water layers, consequently increase the viscosity η and thus increase B, whereas the chaotropic ion due to their water-immiscible character possesses lower B. Except for some minor issues with anions, the Jones-Dole coefficient value is quite questionable for ionic liquid cations. The ionic liquid containing a longer alkyl chain on cation exhibits positive B values and hence considered as kosmotropic (more than eight carbon) (Zhao, 2006). The increase in the solution viscosity might be due to the hydrophobic hydration or because of the high viscosity of ionic liquids in water. Nevertheless, kosmotropic/chaotropic assignment of an ionic liquid cation is based on the B values, and their order in the Hofmeister series is different (Zhao, 2005, 2015; Yang, 2009). To

avoid any complications, the Hofmeister series for anions used only for accounting the ion-induced effects.

Green noted that the protein solubility does not depend on the concentration of salt but also its ionic strength (I) in the solution (Green, 1932). For a solvent with protein solubility S_0, which changes to S after addition of salt, depends on the ionic strength I by the Equation (2),

$$log\frac{s}{s_0} = \frac{1}{2}\frac{z_1.z_2\sqrt{I}}{1+A\sqrt{I}} - K_s.I \quad (2)$$

where, z_1 and z_2 are the valences of the salt ions and K_s is salt coefficient and depends on the characteristic of salts. As K_s depends on the volume of ion, chaotropic ions noted to decrease the protein solubility (Salis and Ninham, 2014). Based on these factors, it is evident that the Hofmeister series do not depend on the ion but also its concentration and ionic strength in the solution.

Ionic Liquid-Protein Interactions and Hofmeister Series

Similar to aqueous electrolytes, ionic liquids are constituted by oppositely charged ions held together by hydrogen-bonding and van der Waals interactions rather than strong electrostatic attractions as in case of electrolytes. The reduced charge density of ionic liquid ions weakens their interaction with the oppositely charged surfaces of proteins compared to the aqueous electrolytes. However, hydrophobic- and hydrogen bonding-interactions are noted to play anchoring role in the stabilizing protein structure. Hippel and Wong were the first to observe the Hofmeister ordering of tetraalkylammonium and guanidinium salts on the thermal stability of Ribonuclease A (RNase A), gelatin-collagen, DNA and precipitation of benzoic acid from aqueous state (Von Hippel and Wong, 1964). However, they did not overrule the possibility of the specific solute-ion interactions. Zhao et al. observed the Hofmeister ordering of ionic liquid ions during the hydrolysis of enantiomeric phenylalanine methyl ester catalyzed by *Bacillus licheniformis* protease in different aqueous ionic liquid solutions (Zhao et al., 2006). The kosmotropic anion and chaotropic cation were noted effective in enhancing the enzyme enantioselectivity. The decreasing order of anions: PO_4^{3-} > citrate^{3-}, CH_3COO^-, $EtSO_4^-$, CF_3COO^- > Br^- > OTs^-, BF_4^- and for cations: $[emim]^+$ > $[bmim]^+$ > $[hmim]^+$.

An ionic liquid solution with high kosmotropicity (which is given in terms of the difference of Jones-Dole B-coefficient of anion and cation) resulted in high enzyme enantioselectivity (Zhao et al., 2006). Mazzini et al. investigated the role of water, methanol, propylene carbonate (PC), dimethyl sulfoxide (DMSO) and formamide on the Hofmeister ordering of CH_3COO^-, F^-, Cl^-, Br^-, I^-, ClO_4^-, and SCN^- in the Size Exclusion Chromatography (SEC) of electrolyte solutions on *Sephadex*® G-10 and the investigation of the conformation of a polymer brush in the presence of the different electrolytes by Quartz Crystal Microbalance with Dissipation (QCM-D) (Mazzini et al., 2018). The fundamental Hofmeister ordering of ions maintained in the methanol and water (CH_3COO^- > F^- > Cl^- > Br^- > I^- > ClO_4^- > SCN^-) whereas it reversed in case of DMSO and PC. There was no discrete ordering of ions in case of formamide (Mazzini et al., 2018). Constantinescu et al. measured the melting temperature (T_m) of RNase A in presence of major cations such as 1-alkyl-3-methyl imidazolium ($[Rmim]^+$), 1-alkyl-1-methylpyrrolidinium ($[Rmpyrr]^+$), tetraalkylammonium ($[R_4N]^+$) and guanidinium ($[Guan]^+$) and anions thiocyanate ($[SCN]^-$), methylsulfate $[MeOSO_3]^-$), ethylsulfate ($[EtOSO_3]^-$), trifluoromethanesulfonate ($[TfO]^-$), bis(tri-fluoromethanesulfonyl)imide ($[Tf_2N]^-$), and dicyanimide ($[N(CN)_2]^-$) (Constantinescu et al., 2007). The cation series in terms of decreasing T_m with Br^- and Cl^- as common anion is as,

$$K^+ > Na^+ > [C_{1,1,1,1}N]^+ > Li^+ > [C_{2,2,2,2}N]^+ \approx [emim]^+ > [bmpyrr]^+ > [bmim]^+ \approx [C_{3,3,3,3}N]^+ > [C_6mim]^+ \approx [C_{4,4,4,4}N]^+$$

The thermal stabilization of RNase A by these cations was in the order of their hydrophobicity (**Figure 2**). The thermal stability data of lysozyme in presence of three imidazolium chloride-based ionic liquids fortifies this observation (Lange et al., 2005). The different ordering of structurally similar $[emim]^+$ and $[bmpyrr]^+$ ions was attributed to the charge delocalization in $[emim]^+$. For a common cation $[emim]^+$, the order of anions in terms of decreasing T_m values is as,

$$[SO_4]^{2-} > [HPO_4]^{2-} > Cl^- > [EtOSO_3]^- > [BF_4]^- \approx Br^- > [MeOSO_3]^- > [TfO]^- > [SCN]^- \approx [N(CN)_2]^- > [Tf_2N]^-$$

The series suggests that weak hydration and high hydrophobicity tends to decrease the T_m more (**Figure 3**). However, this should not be taken as a rule of thumb in arranging the anions on the basis of their effectiveness in stabilizing/destabilizing the RNase A since all these anions belong to different homologous series. Even for the chemically-related anions, the order of hydrophobicity is not valid as observed from their effect on T_m (Zhao, 2006). The reverse ordering at various places in the cation and anion series suggests that the simple hydration theory cannot be applied for the complex ions and thus, this assumption is not valid in case of ionic liquids. Zhao also noted that enzyme activity in aqueous ionic liquids seems to follow the Hofmeister series as ions remain separated but predicting their activity in absence of water is not a straightforward affair (Zhao, 2005). Lau et al. had similar observation upon testing the influence of pure ionic liquids on the activity of *Candida antarctica* Lipase B (CaL B) (Lau et al., 2004). They noticed that the concept of kosmotropicity/chaotropicity and Jones-Dole B-coefficient cannot be applied to account for the influence of ionic liquids over the activity of CaL B. Even for the similar $[NTf_2]^-$ anion counter cation such as Li^+ destabilizing behavior was noted for Cal B while a stabilizing behavior was evident with $[emim]^+$ (de Diego et al., 2005; Constantinescu et al., 2007). These observations suggest that binding of ionic liquids to protein surface depends on the charge and hydrophobicity and thus indicates specific ion-protein interactions.

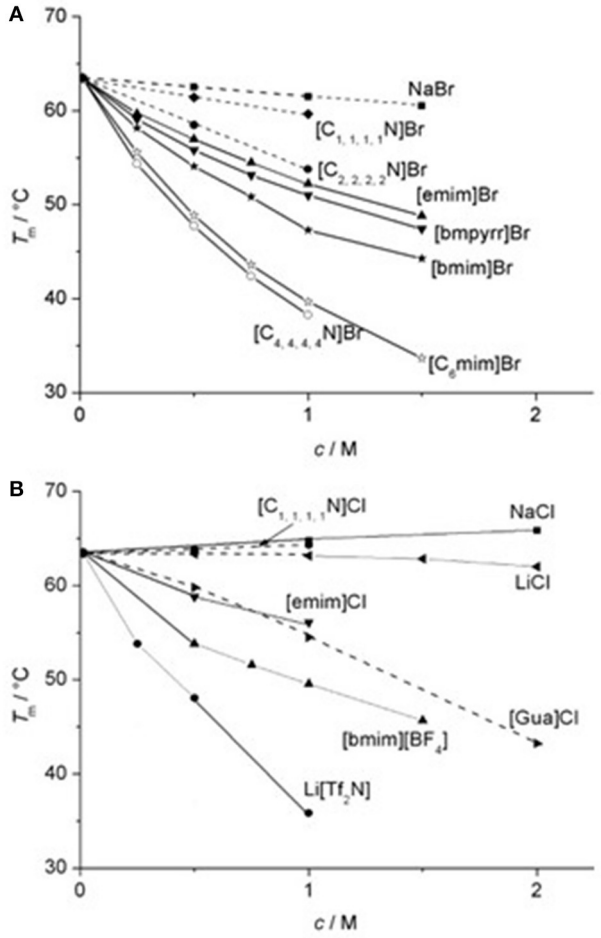

FIGURE 2 | Transition temperatures T_m for the thermal denaturation of RNase A as a function of the concentration c of added ILs with **(A)** Br^- and **(B)** Cl^- as a common anion. Reprinted with permission from Constantinescu et al. (2007).

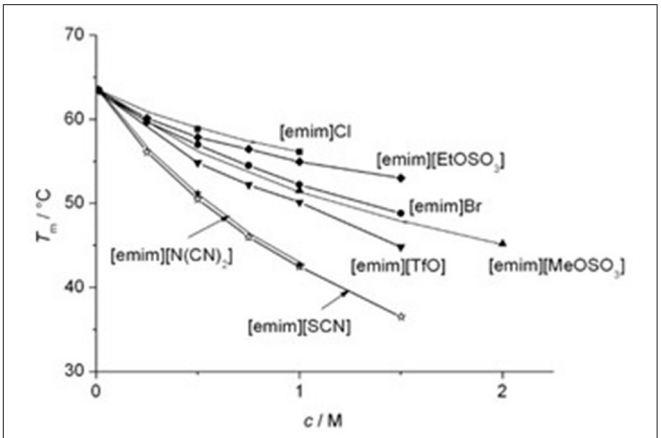

FIGURE 3 | Transition temperature T_m for the thermal denaturation of RNase A as a function of the concentration c of added ILs with $[emim]^+$ as a common cation. Reprinted with permission from Constantinescu et al. (2007).

Beyond Hofmeister: Specific Ion-Solute Interactions

The reports by Omta, Jungwirth, and Funkner on the protein interaction in aqueous electrolytes strongly suggested that the ions interaction toward the protein backbone is driven by specific ion-protein interactions and not necessarily due to the perturbation of the bound water to the protein (Omta et al., 2003a; Batchelor et al., 2004; Heyda et al., 2010; Algaer and van der Vegt, 2011; Funkner et al., 2012; Jungwirth and Cremer, 2014). These observations were confirmed as valid in several studies utilizing ionic liquids. Kumar et al. compared the stabilizing power of SCN^-, SO_4^{2-}, HSO_4^- Cl^-, Br^-, I^-, and CH_3COO^- for ionic liquids with 1-butyl-3-methylimidaolium ($[bmim]^+$) cation and for inorganic salt with sodium ion on α-chymotrypsin (CT) (Kumar et al., 2014). The comparison showed that the SCN^-, SO_4^{2-}, HSO_4^- Cl^-, Br^-, I^-, and CH_3COO^- of sodium salt have a destabilizing effect whereas the Cl^-, Br^-, and CH_3COO^- with $[bmim]^+$ have a stabilizing effect on the CT. The arrangement of these anions in the stabilizing/destabilizing order of CT does not necessarily follow the Hofmeister ordering and depends a lot on the counter cation and nature of the protein in question. Similarly, the influence of ionic liquids on the stability of collagen and activity of laccase do not follow the Hofmeister ordering of anions and indicate specific anion-protein binding (Sun et al., 2017; Tarannum et al., 2019). Reid et al. investigated various theories predicting the behavior of ionic liquid in water by statistical thermodynamic. The structure of water-IL mixture was water dependent (Reid et al., 2015). At a lower concentration, water binds strongly with ion whereas at higher concentrations, water molecules aggregate themselves and interact less with ionic liquid. Kobayashi et al. noted similar behavior of water at the water-ionic liquid interface in their study of ionic liquid-water interaction study by molecular dynamics and sum frequency generation (SFG) spectroscopy, at different concentrations of water (Kobayashi et al., 2017, 2019). Bui-Le et al. used a set of analytical techniques such as circular dichroism (CD), fluorescence, UV-visible, NMR and small-angle X-ray scattering to probe the protein [green fluorescent protein (GFP)] interaction with imidazolium and pyrrolidinium as cation and chloride, acetate and triflate as complementary anions (Bui-Le et al., 2020). The site-specific protein-ionic liquid interactions through various analytical methods exhibited triflate as the stabilizing anion while to chloride and acetate as the destabilizing anions. Singh et al. studied the thermal unfolding of lysozyme in 1-ethyl-3-methylimidazolium ethylsulphate ($[emim][EtSO_4]$) and 1-ethyl-3-methylimidazolium diethylphosphate ($[emim][Et_2PO_4]$) both experimentally and theoretically (Singh et al., 2020). The destabilizing power of $[emim][EtSO_4]$ and $[emim][Et_2PO_4]$ was higher than that of a strong denaturant as observed from lowering in the T_m. Among ionic liquids, $[emim][Et_2PO_4]$ was more destabilizing for lysozyme and required lower energy, as is evident from ΔH, than $[emim][EtSO_4]$. The fluorescence study showed that both ionic liquids interact with the tryptophan

residue of lysozyme. MD simulation revealed that cation interacts in a "local-manner" while anion in a "global-manner" due to the negative charge of the lysozyme. The $[Et_2PO_4]^-$ was found to have closer first coordination shell and stronger coulombic interaction with lysozyme than $[EtSO_4]^-$.

Besides the experimental work, several theoretical studies on the ionic liquid-protein interactions indicated a trend pointing toward the specific ion-solute interactions. Lesch et al. studied the influence of aqueous [emim][CH_3COO] on the stability of β-hairpin peptide using atomistic MD simulation and Kirkwood-Buff theory. The simulation work suggested that the cation ($[emim]^+$) binds with both folded and unfolded peptide but anion ($[CH_3COO]^-$) binds only with the unfolded peptide (Lesch et al., 2015). In an another work Diddens et al. compared the behavior of different anions ($[BF_4]^-$, $[CH_3COO]^-$, and Cl^-) with the same cation on the ionic l iquid-protein using the atomistic MD simulation and Kirkwood-Buff theory (Diddens et al., 2017). The simulation outcome suggests that the larger anion interacts with protein surface more strongly, followed by dehydration, than the smaller anion and the interaction was enthalpic in nature. Jaegar and Pfaendtner studied the stability of human serum albumin (HSA) in 1-butyl-3-methylimidazolium tetrafluoroborate ([bmim][BF_4]) and choline dihydrogenphosphate ([chol][dhp]) by MD simulations and enhanced sampling techniques (Jaeger and Pfaendtner, 2016). The RMSD and RMSF calculations indicated that at higher ionic liquid concentrations, the protein adopts structure similar to their crystallographic structure. The structure of HSA in 20% [chol][dhp] is similar to that in water and thus it is unlikely that [chol][dhp] destabilize the HSA in its pure state. Burney et al. investigated the modification of the enzyme surface charge for *Candida rugosa* lipase and *Bos taurus* α-chymotrypsin in aqueous 1-butyl-3-methylimidazolium chloride ([bmim]Cl) and 1-ethyl-3-methylimidazolium ethylsulphate ([emim][$EtSO_4$]) using MD simulations (Burney et al., 2015). The calculated solvent charge density indicated that for both enzymes in ionic liquids changed their positively charge surface to the negatively charged one upon an increase in the solvent concentration near the enzyme surface. The radial distribution of ionic liquid components with respect to enzyme reveals the decreased interaction of anion with the modified surface and more to the cation. Ghanta et al. showed in their MD simulation on α-lactalbumin in aqueous [bmim][BF_4] the conformational changes in the protein as well as the distribution of water and ionic liquid around it (Ghanta et al., 2020). The calculations revealed an enhanced rigidity of protein due to the rearrangement of protein-water hydrogen bond and the formation of protein-ionic liquid hydrogen bond. The formation of greater number of salt bridges in presence of ionic liquid also account for the enhanced rigidity. Jaegar et al., compared the aqueous ionic liquid ([bmim][CH_3COO]) tolerance on cellulases from *Trichoderma viride, Thermogata maritima*, and *Pyrococcus horikoshii* at different temperatures and different concentrations of ionic liquid in water (Jaeger et al., 2014). The simulation results indicated dissimilar effects of the ionic liquid on enzyme deactivation. The most negatively charged enzyme was least destabilized and had similar behavior in water and binary mixtures of ionic liquids. A summary of interactions between ionic liquid moieties and protein and DNA surfaces are given in **Table 2**. Majority of research about the protein-ionic liquid interactions do not account the solvation properties of ionic liquids. A correlation between the solvation parameters of ionic liquids and their influence on the fate of protein can be of paramount value in designing the potential optimum ionic liquids. Tomlinson et al. studied the solubility of corn protein zein in aprotic ionic liquids, namely, 1-butyl-3-methylimidazolium acetate ([bmim][CH_3COO]), 1-ethyl-3-methylimidazolium acetate ([emim][CH_3COO]), and 1-butyl-3-methylimidazolium dicyanamide ([bmim][$N(CN)_2$]) and protic ionic liquids containing 1-methylimidazolium ($[Hmim]^+$) cation with $[HSO_4]^-$, $[CH_3COO]^-$, and $[HCOO]^-$ as anions (Tomlinson et al., 2014). Zein dissolved in all ionic liquids except [Hmim][HSO_4]. While comparing the zein solubility among ionic liquids, [bmim][$N(CN)_2$] exhibited the highest solubility owing to the denaturing action of dicyanamide anion. The other aprotic ionic liquids [emim][CH_3COO] and [bmim][CH_3COO] showed similar solubilization properties despite their different solvation properties. The importance of solvation properties [$E_T(30)$, α, β, and π^*] is however more evident in protic ionic liquids. At 60°C, zein had a maximum solubility in [Hmim][CH_3COO] (26.2 wt%) followed by [Hmim][HCOO] (12.3 wt%) whereas the lowest solubility was found in [Hmim][HSO_4] ($<$ 1 wt%). The decreasing order of zein solubility was in line with the increasing order of polarity [$E_T(30)$], indicating that least polar protic ionic liquid are required for higher solubility. Single and multivariate regression using polarity parameters and molar volume on zein's solubility in ionic liquids suggested that a small molecular size and low $E_T(30)$, α, β, and π^* are required to attain maximum solubility of zein in an ionic liquid. The higher solubility of zein in [bmim][CH_3COO] than in [emim][CH_3COO] is due to the lower π^* for former than latter. The lower correlation coefficient for α suggests that acidity has lower impact on the zein's solubility. π^* is noted as the important parameter and at higher temperature its highly responsible for the non-polar character to achieve higher solubility. Despite the effective correlation between zein's solubility and polarity parameters, more studies are needed before reaching any definite conclusions.

Influence of Water on Ionic Liquid-Protein Interactions

An aqueous solution of ionic liquids is used in the storage of biomolecules to alleviate the solubility problem and to maintain their structural features intact. Aqueous ionic liquids have different properties than neat ionic liquids but resemble closely to dilute electrolytes solution. The amphiphilic character of ionic liquids makes them heterogeneous, at the molecular level, that further increases with the size of alkyl chain on cation (Hayes et al., 2015; Bruce et al., 2017). Addition of water alters the heterogeneity of ionic liquids (Jiang et al., 2007). Blesic et al. showed that imidazolium chloride-based ionic liquids with alkyl chain greater than octyl undergoes self-aggregation whereas an ionic liquid with shorter chains (butyl to hexyl) do not show such behavior (Blesic et al., 2007). Liu et al., observed rod-like micelle

TABLE 2 | Summary of interactions between ionic liquids and sites of proteins and DNA.

Functional group on ionic liquids	Interaction with protein/DNA	References
Alkyl chain on cation	Hydrophobic sites on the proteins [human serum albumin (HSA), bovine serum albumin (BSA), and lipase A] and major grooves of DNA	Chandran et al., 2012; Singh et al., 2012; Nordwald et al., 2014
Electron-donor substituents on cation	Disulphide linkages on protein	Liu et al., 2015
Nucleophilicity of anion	Disulphide linkages, positively charged surface on protein [*Candida antarctica* lipase B (CAL-B)], cytochrome c (Cyt. C), DNA bases (adenine, guanine, and cytosine), and G-quadruplexes	Fujita et al., 2005; Cardoso and Micaelo, 2011; Klähn et al., 2011a; Fujita and Ohno, 2012; Liu et al., 2015
Electrophilicity of cation	Phosphate groups on DNA strands and negatively charged surfaces on protein	Klähn et al., 2011a; Sarkar et al., 2020;
Hydroxyl group (-OH) on choline cation	Hydrogen bonding with carbonyl (C=O), imine (-N-H) and hydroxyl (OH) group on protein (e.g., collagen protein)	Tarannum et al., 2018
Anionic aggregates (e.g., octylsulphate, [OS])	Acidic sites on protein [e.g., lysozyme (tryptophan, arginine, *etc.*)] and hydrophobic sites on BSA	Mandal et al., 2015
Cationic aggregates (e.g., 1-methyl-3-octylimidazolium cation, $[Omim]^+$)	Hydrophobic and electrostatic interactions with carboxyl and amine functionality on BSA	Singh et al., 2012
Hydrophobic cation (e.g., cyclic alkylmethylguanidinium cation $[RR'GUA]^+$)	Hydrophobic core of protein [e.g., CAL-B, Ribonuclease A (RNase A), and α-helical protein (Im7)]	Constantinescu et al., 2007; Klähn et al., 2011b; Figueiredo et al., 2013
Highly polar ionic liquid (e.g., [bmim][NO_3] and [OHemim][BF_4])	Polar surfaces of protein CAL-B	Klähn et al., 2011b
Hydrophobic anion (e.g., $[N(CN)_2]^-$, $[NTf_2]^-$)	Hydrophobic core of RNase A	Constantinescu et al., 2007
Acidic proton on cation	Negatively charged residues on protein and base-pair of DNA	Sarkar et al., 2020
π-electrons on cation	NH—π interactions with DNA bases	Cardoso and Micaelo, 2011

in imidazolium-based ionic liquids whereas Vincent-Luna et al. noticed that critical micelle concentration required for micelle formation was lowered with an increase in the anisotropy in the imidazolium-based ionic liquids (Liu et al., 2015; Vicent-Luna et al., 2017). Cammarata et al. showed that water binds with ionic liquid anion in 1:2 ratio and the water content of ionic liquids increases with the basicity of anion (Cammarata et al., 2001). Simulation studies also indicate that water cluster size in ionic liquids are independent of the size of alkyl chain length on cation although the hydrophobicity of anion is crucial in deciding the miscibility with water (Méndez-Morales et al., 2011). The orientation of water molecules at the surface of hydrophilic and hydrophobic ionic liquids are different (Anthony et al., 2001; Rivera-Rubero and Baldelli, 2004). In hydrophilic ionic liquids, water molecules experience stable dipole-dipole and hydrogen bonding interactions and remain in solvated state whereas water molecules undergo surface orientation at gas-liquid interface in case of the hydrophobic ionic liquids (Anthony et al., 2001; Rivera-Rubero and Baldelli, 2004). Addition of water in ionic liquids also affects the dynamics of ions as observed in many studies (Araque et al., 2015; Sharma and Ghorai, 2016).

The consequence of water addition to the protein-ionic liquid interactions cannot be generalized based on its influence over the ionic liquids. In reality, both stabilizing and destabilizing effects of water on the protein-ionic liquid interactions were observed. Micaêlo and Soares study on a model protein in presence of [bmim][PF_6] suggested that a higher fraction of water molecules resides in the solvation shell of protein and hence higher stability was observed compared to that in case of [bmim][NO_3] (Micaêlo and Soares, 2008). Similarly, a decrease in the hydrodynamic radius of lysozyme was observed upon addition of 1-propyl-3-methylimidazolium bromide ([pmim]Br) in aqueous lysozyme (Ghosh et al., 2015). Conversely, higher activity of α-chymotrypsin was observed in [bmim][NTf_2] compared to the organic solvents at low water concentration (Eckstein et al., 2002). These contradictory observations about the role of water on protein stability in presence of ionic liquids indicate that the fate of the protein depends on its direct interaction with ionic liquids and do not depend on the interaction of water on the ionic liquids as assumed in the simple hydration theory. However, addition of water alters the stabilizing/destabilizing role of ionic liquids toward proteins and enzymes. As noted by Constatinescu et al., a strong interaction between cation and anion in ionic liquids might reduce the destabilizing effect of cation or anion of ionic liquids (Constantinescu et al., 2010). The role of water in protein stabilization in presence of ionic liquid is also controversial. In some cases, higher concentrations of ionic liquids were needed for the long-term stability. However, a change in the tertiary structure of protein was also reported at higher concentrations of ionic liquids (Byrne et al., 2007; Bihari et al., 2010). Singh et al. showed that long-chain imidazolium-based ionic liquids stabilize the horse heart cytochrome c (h-cyt-c) for a long term and at very low concentrations (1mM) (Singh et al., 2018). However, the presence of water in ionic liquid-protein mixtures is shown to have a distinct effect on the structural features. Proteins with the radius of gyration below 20 Å interact with water and remain in solvated state whereas proteins having radius of gyration above 20 Å do not react with

water and undergo protein-protein interactions and result in larger aggregates (Takekiyo et al., 2014). The review articles by Smiatek (2017) and Saha and Mukherjee (2018) present more evidence about the inconclusive role of water on the ionic liquid-protein interactions.

IMPLICATIONS OF IONIC LIQUID-PROTEIN INTERACTIONS

This section accounts for various applications of ionic liquid-protein interactions in protein chemistry. Firstly, the effect of various features of ionic liquid systems on the protein solubility is discussed. Secondly, use of ionic liquids in protein separation is discussed by making use of the ionic liquids-based aqueous biphasic systems (ABSs) and electrophoretic processes. Lastly, protein stability in ionic liquids-based systems is also discussed by using enthalpy-entropy compensation, role of the Hofmeister series on stabilizing protein and thermodynamics of the Hofmeister effects.

Protein Solubility

Though protein is fairly soluble in ionic liquids, however, an aqueous mixture of ionic liquids is used for low cost and high solubility of biomolecules. A mixture of ionic liquid and water better interacts with the polar, non-polar, or amphiphilic surfaces of proteins because of the hydrophilic, hydrophobic, and amphiphilic characters than the neat ionic liquids. These interactions cause either the precipitation or stabilization of proteins. In ionic liquids, the anion remains in the hydrated state more than the cation and hence the concentration of cation at the surface of the protein remains higher as obtained by various simulation results (Haberler and Steinhauser, 2011; Haberler et al., 2011, 2012; Klähn et al., 2011a,b; Lesch et al., 2015). The cation tethered with a long alkyl chain exhibits amphiphilic character; the cation being polar and alkyl moiety acts as a non-polar region (Zhang and Cremer, 2006). Because of the non-polar character, the alkyl chain orients toward the non-polar surface of proteins and the cation remains at the polar surface (Lim et al., 2014). According to the "iceberg model," water molecules surround the alkyl chain and consequently lower the entropy of water molecules, and result in the hydrophobic hydration (Zangi, 2010). The ionic liquid cation competes with the anion toward the polar surface of proteins. The negatively charged amino acid moiety such as glutamic- and aspartic-acid exclusively attract the cation but as water molecules also remain in the equilibrium toward the site, due to hydrogen bond formation, the extent of attraction remains lower (Haberler and Steinhauser, 2011; Klähn et al., 2011a). As compared to cation, high charge density anion strongly interacts with amino acid moiety *per se* histidine, arginine, and lysine by the coulombic interactions that decide the fate of protein in aqueous ionic liquid solutions (Seduraman et al., 2012). Overall, the ionic components interact stronger at the protein surface than water hence replacing the bound water from the protein surface and hence resulting in coagulation or crystallization of a protein (Zaks and Klibanov, 1988). On the contrary, hydrophobic molecules stabilize the protein surface owing to their tendency of not interacting with water (Laszlo and Compton, 2002; Dang et al., 2013).

Additionally, the ionic liquid concentration also affects the protein solubility as the ion interacts strongly with the surrounding water hydrogen-bonding network of protein. At moderate ion concentrations up to 1 $mol.l^{-1}$, the ion breaks the hydrogen bonding network of protein and increases its solubility by the phenomenon called "salting-in" (Thomas and Elcock, 2007). The strong chaotropic anion promotes the salting-in while a reverse effect noticed with the kosmotropic ions referred to as "salting-out." The energetics of salting-in might be entropic/enthalpic, but in the case of salting-out, it is purely enthalpic (Zangi et al., 2007). Later, several MD simulation results indicated that the salting-in and salting-out not rely on the ion concentration but also depends on the specific ion-protein interactions because of the non-homogenous charge distribution, hydrophobicity/hydrophilicity, and difference in the functional structures of the protein (Zangi, 2010; Schwierz et al., 2013). The Hofmeister ordering was intact in case of the negatively charged ions but completely reversed for cations (Schwierz et al., 2016).

The control of protein precipitation and subsequent crystallization by tuning the salt concentration in protein solution is necessary for the structure determination of protein by X-ray diffraction (Judge et al., 2009). Ionic liquids, because of large availability and recyclability considered as a better co-solvent, and initial results established them as an excellent crystallizing agent for protein. The other benefits using ionic liquids in protein crystallization were less polymorphism and improved tolerance to concomitant impurities in crystals. The method was used to obtain the highly pure crystals of protein at the required salt concentrations. In 1999, Garlitz et al. reported lysozyme crystallization using ethylammonium nitrate (Garlitz et al., 1999). Later, Judge et al. noticed that proteins such as lysozyme, catalase, myoglobin, trypsin, glucose, and isomerase grow bigger crystals with ionic liquids as co-solvents and provide better resolution in x-ray crystallography (Judge et al., 2009). Kowacz et al. observed a reduction in nucleation density and improved crystal quality at higher ionic liquid concentration (Muldoon et al., 2012). In a comparison, choline chloride was noted less efficient than imidazolium-based ionic liquids in protein crystallization. The efficacy of imidazolium-based ionic liquids in crystallization was noted to increase with the length of the alkyl chain upon cation. Green observed the importance of electrostatic interaction at low ion concentrations (Ajaj, 2010). The electrostatic force is first screened by the like-charged biomolecular region that helps in protein crystallization (Muldoon et al., 2012).

Protein Separations

The efficiency and viability of any biotechnological process are in its efficiency to downstream processing to maintain the purity and quality, as it costs 60–90% of the overall process (Kula et al., 1982). The metabolites and bioproducts separation depends on the delicate change in pH, temperature, osmotic pressure, ionic strength, and surface charges; therefore, the techniques/methods utilized for the separation must be reliable and compatible with the bioproducts (Banik et al., 2003; Neves et al., 2009).

Conventional methods used for the bioproducts separation from biotechnological processes are cost-ineffective and result in poor yields (Silva and Franco, 2000). In pure ionic liquids, most proteins get dissolved but not homogeneously dispersed. Besides, they can also denature the protein. In place of pure ionic liquids, an aqueous-biphasic solution (ABS) of the ionic liquid has emerged as an effective tool in biomolecular separation. An aqueous solution of ionic liquid with a salt solution can be used to create phase separation between aqueous ionic liquid and aqueous salt solution and therefore allows easier separation of bioproducts than conventional methods. Although hydrophobic ionic liquids form a biphasic solution with water but their high cost and protein denaturation ability render them unsuitable for biomolecule separations.

Aqueous-Biphasic Solution (ABS)

An ABS is formed when two mutually immiscible but water-soluble polymer/polymer, polymer/salt, and salt/salt systems are employed together. For the first time, Gutowaski et al. exhibited that 1-butyl-3-methylimidazolium chloride ([bmim]Cl), a hydrophilic ionic liquid, undergoes aqueous biphasic separation (ABS formation) upon mixing with the concentrated solution of K_3PO_4, a water-structuring salt (Gutowski et al., 2003). The upper layer remains rich in ionic liquid and lower layer rich in K_3PO_4. These new ABSs were first supposed to be used in the recycling of hydrophilic ionic liquids and metathesis in the formation of new ionic liquids but were later used in the extraction and separation of biomolecules and transition metal elements. The first use of ionic liquid-based ABS was noted by He et al. where they coupled [bmim]Cl + K_2HPO_4 + water-based ABS with reversed-phase high-performance liquid chromatography (RP-HPLC) for concentration and analysis of testosterone and epitestosterone (He et al., 2005). Later, Coutinho et al. extensively studied the utilization of ionic liquid-based ternary ABSs in the separation of the amino acid L-tryptophan with the major emphasis on the role of structural features of ionic liquids. They observed that separation of L-tryptophan increases with the length of alkyl chain on the cation because of elevated hydrophobicity. Further, the cation hydrophilicity increases the biphasic separation whereas the tethering of polar group such as hydroxyl, benzylic, and allylic increases the interaction with water and hence decreases the phase separation (Gutowski et al., 2003; Neves et al., 2009). The role of the anion in biphasic separation and extraction of L-tryptophan was studied by Ventura et al. by employing 1-ethyl-3-methylimidazolium-([emim]) and 1-butyl-3-methylimidazolium ([bmim])-based ionic liquids with chloride, bromide, acetate, hydrogensulfate, methanesulfonate, methylsulfate, ethylsulfate, trifluomethanesulfonate, trifluoroacetate, and dicyanamide as the anion (Ventura et al., 2009). The results indicated that the extraction ability of prepared ABSs depends inversely on the hydrogen bond donor basicity of anion with water. Dreyer et al. pointed out that extraction of protein in ionic liquid (Ammoeng^{TM} 110)-based two-phase ABS depends on the electrostatic interactions between the positively charged cation and charged surface of the protein (Dreyer et al., 2009). Rather than polymer-based ABS, where hydrophobicity is a deciding parameter, ionic liquid-based ABSs remain unaffected of the hydrophobicity or surface area. It was concluded that the protein separation using ionic liquid -based ABSs does not simply depend on the biphasic separation but, in reality, is a complex phenomenon. Pei et al. used aqueous K_2HPO_4 + [$C_n$mim]Br] (where $n = 4$, 6, and 8)-based ABSs for the extraction of bovine serum albumin (BSA), cytochrome c, trypsin, and γ-globulin at different temperatures and pH conditions to achieve 75–100% extraction efficiency (Pei et al., 2009). The extraction efficiency was noted to change with the temperature and alkyl chain length on the cation. A small change in the extraction efficiency was observed with the pH change for cytochrome c due to the change of isoelectric point and hence electrostatic interaction between cytochrome c and ionic liquid cation. The thermodynamic study confirmed that increased extraction efficiency with temperature is owing to the endothermic nature of the process in ABSs keeping in mind that the temperature change should be below the denaturation temperature of protein. The standard Gibbs free energy for the extraction process at a given temperature can be correlated by the van't Hoff Equation (3)

$$\Delta G_o^T = -RTlnK \tag{3}$$

where, K is the partition coefficient of protein between two phases at temperature T (K) at gas constant R.

The standard enthalpy (ΔH^o)- and standard entropy (ΔS^o)-change associated with protein partitioning can be obtained by Equation (4)

$$lnK = -\frac{\Delta H^o}{RT} + \frac{\Delta S^o}{R} \tag{4}$$

The ΔH^o and ΔS^o can be obtained from slope and intercept by plotting lnK *vs* $\frac{1}{T}$.

The values of both enthalpy (ΔH^o) and entropy (ΔS^o) are positive but ΔG_o^T is negative. The $T\Delta S^o > \Delta H^o$ indicated that the separation process is entropically favored in studied ABSs. The UV-vis- and IR-spectra showed that the protein structure remains intact even after the extraction with ABSs.

Capillary Electrophoresis (CE) and Micro-Capillary Electrophoresis (μCE)

Apart from the use of biphasic solution in protein separation, a capillary electrophoretic method is also used in protein separation and detection. In this method, the ionic liquid is used as a running electrolyte solution that causes a reversal of surface charge on the column wall (Jiang et al., 2003). By employing 1-ethyl-3-methylimidazolium tetrafluoroborate ([emim][BF_4]) as a dynamic coating, the absorption of the protein was reduced at the wall of column and paved way for the separation and detection of proteins such as lysozyme, cytochrome c, trypsinogen, and α-chymotrypsinogen A. The separation was observed to facilitate upon increasing the length of alkyl chain on cation. Li et al. used 3% (v/v) ionic liquid solution in capillary electrophoresis for the detection of model protein avidin (Li et al., 2007). Protein detection was bettered by increasing ionic liquid concentration. Corradini et al. in their study showed that flushing a solution

of 1-alkyl-3-methylimidazolium-based ionic liquid into a bare-fused silica capillary produces a non-covalent layer on the inner surface of coating that affects the untoward interaction of the protein with the capillary wall even if ionic liquid not present with the electrolyte (BGE) used for separation (Corradini et al., 2009). This effect was attributed to the adsorption of ionic liquid on the silica wall, which subsequently reduces the electrophoretic behavior of basic proteins up to different extent depending on ionic liquid. Xu and Wang published a detailed account on the use of ionic liquids in the improvement of capillary and microchip electrophoresis for the separation and detection of analytes such as phenols and aromatic acids, metal ions, medicines, enantiomers, biological materials, etc. (Xu and Wang, 2009).

Protein Stability

Protein is a heterogeneous class of biomolecule whose stability depends on the preservation of its functional secondary structure, which is α-helical, β-sheet and coil region. The functional structure of protein is a complex phenomenon and depends on the hydrogen bonding, disulfide (S-S) bond, hydrophobic, and intramolecular interactions. To maintain its functionality, a protein requires a specific solvent, pH, co-solvent and temperature. Any change in these conditions alters the functionality of the secondary structure of the protein. Apart from these conditions, viscosity of solvent also affects the dynamics of solvent and protein (van Rantwijk and Sheldon, 2007). At higher viscosity, the diffusion of protein is slow with the insignificant change in the catalytic ability. The hydrolysis of some $[PF_6]$- and $[BF_4]$-based ionic liquids form HF and alters the protein functionality (van Rantwijk and Sheldon, 2007). The enthalpy-entropy compensation and the relevance of the Hofmeister series of ions on protein stabilization is discussed below.

Enthalpy-Entropy Compensation

The marginal/low stability of protein is represented in terms of Gibb's free energy of unfolding (ΔG_u) using enthalpic (ΔH_u) and entropic (ΔS_u) contributions (Equation 5).

$$\Delta G_u = \Delta H_u - T\Delta S_u \tag{5}$$

The ΔG_u accounts for the thermodynamic stability of a protein from native to the unfolded state and should be positive for a stable conformation (Lumry and Rajender, 1970). However, a low ΔG_u indicates that protein stabilization largely depends on the higher enthalpic and entropic contributions that are also called "enthalpy-entropy" compensation, whose value can be manipulated by the addition of co-solute in the system (Senske et al., 2014). In general, the co-solute which can be excluded from the protein structure favors folded state while those binds to the protein surface shift the equilibrium toward the unfolded state of the protein. Macromolecular crowders, like polyethylene glycol and dextran, are noted to be excluded co-solute. They protect protein either due to the entropic excluded volume effect or enthalpic effects (Zhou et al., 2008; Sapir and Harries, 2015). Urea and guanidinium salts are chemical denaturant and destabilize the proteins by direct interactions that reduce ΔH_u (Benton et al., 2012; Senske et al., 2014).

Similar to the inorganic/organic materials, ionic liquids may also cause a subtle change between the ΔH_u and ΔS_u when used as a co-solute and hence shift the equilibrium between the folded to unfolded states. For example, choline dihydrogen phosphate stabilizes cytochrome *c* and lysozymes for months (Fujita et al., 2006, 2007; Vrikkis et al., 2009). The stabilization mechanism involves the protection of the hydrophobic part of protein by the cation of ionic liquids (Summers and Flowers, 2000; Kumar and Venkatesu, 2013, 2014).

Apart from stabilization, ionic liquids have also been employed in accelerating the protein activity. The mechanism may involve either the chemical modification or stabilization or immobilization of the protein surface for chemical reactions (Zhao, 2006; van Rantwijk and Sheldon, 2007). However, the activity of lipase-catalyzed transesterification of methyl methacrylate and the polytransesterification of divinyl adipate and 1,4-butanediol in hydrophilic ionic liquids exhibited no reaction despite the high activity of the enzyme in 1-butyl-3-methylimidazolium hexafluorophosphate ($[bmim][PF_6]$) (Kaar et al., 2003). The ineffectiveness of lipase is tested by adsorption, PEG-modification, and covalent immobilization in polyurethane foams in the hydrophilic ionic liquids.

Protein Stability and Hofmeister Series

Based on the change in the melting temperature (T_m) of ribonuclease A (RNase A) in various ionic liquids and inorganic salts, Weingärtner observed the trend of ions similar to the Hofmeister series (Weingärtner et al., 2012). The series shows that both the stabilizing and destabilizing effects to the native structure of protein depends on the choice of ions and hence to the extent of intermolecular interactions between them (Constantinescu et al., 2007, 2010).

$$\begin{aligned} &K^+ > Na^+ > \left[Me_4N^+\right] \parallel Li^+ > [chol^+] > [Et_4N^+] \\ &\simeq [C_2mim^+] > gua^+ > [C_4C_1p_y^+] > [C_4mim^+] \simeq [Pr_4N^+] \\ &> [C_6mim^+] \simeq [Bu_4N^+] \end{aligned}$$

where, $chol^+$ and gua^+ are acronyms for choline and guanidinium, respectively.

$$\begin{aligned} &SO_4^{2-} > H_2PO_4^- > CH_3COO^- > F^- > Cl^- \parallel E_tSO_4^- > BF_4^- \\ &\approx Br^- > OTf^- > I^- > SCN^- \simeq N(CN)_2^- \gg N(Tf)_2^- \end{aligned}$$

The above ordering of ions remains valid at the dilute concentration of inorganic salts and ionic liquids; whereas, a higher concentration is required during actual processing that may lead an interchange of the ion position due to the secondary interactions at elevated concentrations. For example, [Chol]Cl has a denaturing effect both for lysozyme and α-lactalbumin only at a lower concentration as exhibited by the dip in their T_m. The nature of [Chol]Cl toward lysozyme and α-lactalbumin start reversing at a higher concentration as suggested by their increasing T_m (Ajaj, 2010).

Klähn et al. studied the solvation stability of enzyme *Candida Antarctica* lipase B (CAL-B) in eight different ionic liquids and compared the results with that in water (Klähn et al., 2011a). The calculated solvation enthalpy indicated stronger interaction and hence lower solubility of the enzyme in ionic liquids than water. The lower solvation of CAL-B in ionic liquids is owing to the higher cavitation energy that further increases with IL-CAL-B interactions and subsequently denature the enzyme. The stronger interactions between the cation and anion lead to lower surface charge reduction from the surface of CAL-B as indicated by larger electrostatic potential values. Furthermore, charge density was more toward the polar surface of enzyme whereas the non-polar alkyl remains oriented toward the non-polar segment. During the investigation of CAL-B unfolding at a higher temperature in similar ionic liquids, Klähn et al. noted that hydrophobic ionic liquid causes higher stabilization of CAL-B than the hydrophilic ionic liquids (Klähn et al., 2011a). The interaction of CAL-B with ionic liquids was mainly at the polar surface and the non-polar core. The high polarizability of anion increases the extent of hydrogen bonding with the protein surface and destabilizes the CAL-B whereas the hydrophobic alkyl chain interacts with the CAL-B core. In the case of most hydrophobic cation acyclicbutylpentamethylguanidinium ($[BAGUA]^+$), the protein core destabilizes due to the conformation change in the CAL-B. This exposes the protein core to the ionic liquids and stabilizes the unfolded protein. However, these observations could not be observed in the case of other hydrophobic ionic liquids due to the low solubility and weaker dispersion of protein. Fujita et al. reported the stabilizing role of biocompatible ionic liquids in solubilizing and stabilizing the cytochrome c (Fujita et al., 2005). As suggested by the study, the stabilizing role of biocompatible ionic liquids was bound to the dihydrogen phosphate (dhP). The addition of excess water has a negative destabilizing effect as revealed by the DSC spectra. An interesting, unfolding/refolding equilibria for lysozyme was noticed in a sugar solution of ethylammonium nitrate, EAN ($[CH_3CH_2NH_3^+][NO_3^-]$) with 97% refolding success by Byrne et al. (2007).

The experimental and theoretical studies indicated the dominance of anion in controlling the unfolding/folding equilibria (Haberler and Steinhauser, 2011; Haberler et al., 2011). The pronouncing role of the anion is attributed to the high polarizability that enables them to undergo coulombic and hydrogen bonding interactions at the protein surface also confirmed by the longer residence time (Haberler, M., and Steinhauser). Despite being the more influential in protein unfolding, anion approach to the positively charged surface of the protein in the form of ion-pair. The repulsive interaction between the surface and cation is compensated by the strong Coulomb interaction between the ions (Klähn et al., 2011b). The unfolding of the hen egg-white lysozyme (HEWL) in a dilute solution of EAN represents one such case where despite a strong coulomb interaction nearly 75% activity of HEWL was restored. The EAN was effective in high doses (1.6 mg/ml) compared to other renaturing agents (e.g., urea and guanidinium chloride) and the refolding efficiency increase up to 90% upon dilution (Summers and Flowers, 2000). The strong efficiency of EAN as a renaturating agent is because of its ability to extend hydrogen bonding network to the active sites similar to water.

Thermodynamics of the Hofmeister Series

Protein stability largely depends on the concentration of the ionic liquid. At lower ionic liquid concentration, say $c_{IL} < 0.5$ M, all ionic liquids behave as a denaturing agent for proteins. At $c_{IL} > 1$ M, ion-specific effects become dominant and follow Hofmeister ordering in protein stabilization (Senske et al., 2016). This shift in the behavior of ionic liquids is different than the inorganic salts mainly because of the diffused charges on ions. The folding/refolding behavior is reported as the change in melting temperature (ΔT_m) upon transferring the protein from an ionic liquid solution to an ionic liquid-free buffer solution. At lower concentration, $c_{IL} < 0.5$ M, denaturation starts and results in negative (ΔT_m). As the concentration increases beyond 1 M, renaturation starts in protein that brings a positive change in the ΔT_m values. However, a positive ΔT_m for [Chol][dhp] was observed even at 0.25 and 0.5 M. T_m is defined as the midpoint of the unfolding transition, where $\Delta G_u = 0$. The cosolute-induced changes relative to the cosolute-free, buffered solution can be expressed as the excess functions (Equation 6),

$$\Delta\Delta G_u = \Delta G_{u,\,IL} - \Delta G_{u,\,buffer} = \Delta\Delta H_u - T\Delta\Delta S_u \quad (6)$$

where, $\Delta\Delta G_u$ is the excess Gibbs free energy and $\Delta\Delta H_u$ and $T\Delta\Delta S_u$ are the enthalpic and entropic contributions, respectively, that provide intriguing thermodynamic fingerprinting of the molecular mechanism involving a solute. Both $\Delta\Delta H_u$ and $T\Delta\Delta S_u$ are cosolute-dependent and favor either the direct or reverse Hofmeister ordering for ions. For the favorable unfolding at $c_{IL} > 1$ M, the $G_u > 0$. This trend in $\Delta\Delta G_u$ is parallel to that of ΔT_m during unfolding of RNase A. An *enthalpy-entropy* compensation between $\Delta\Delta H_u$ and $T\Delta\Delta S_u$ is observed in case of analyzing the role of cosolute on protein unfolding. Based on the sign of excess function $\Delta\Delta G_u$, $\Delta\Delta H_u$ and $T\Delta\Delta S_u$ eight possibilities are there as shown in **Figure 4**. According to **Figure 4**, hydrophobic ionic liquids (alkyl chain length from 4 to 6 and more carbons) have more positive $T\Delta\Delta S_u$ than $\Delta\Delta H_u$ leading to enthalpic stabilization and entropic destabilization. For hydrophilic salts, both $T\Delta\Delta S_u$ and $\Delta\Delta H_u$ were negative and the classification of ionic liquids into the stabilizing and destabilizing salts was depending on the magnitude of the relative values of these values. As the magnitude of thermodynamic parameters of cosolute-protein interactions depends on the pH, isoelectric point, charge on the protein and hydrophobicity, the arrangements of ionic liquid ions into the direct or reverse Hofmeister ordering is inconclusive. The increasing hydrophobicity of the cosolute promotes both the stabilizing enthalpic contribution and the destabilizing entropic contribution.

IONIC LIQUID-DEOXYRIBONUCLEIC ACID (DNA) INTERACTION

Deoxyribonucleic acid (DNA) is a negatively charged, naturally occurring double-helical structure made up of phosphate

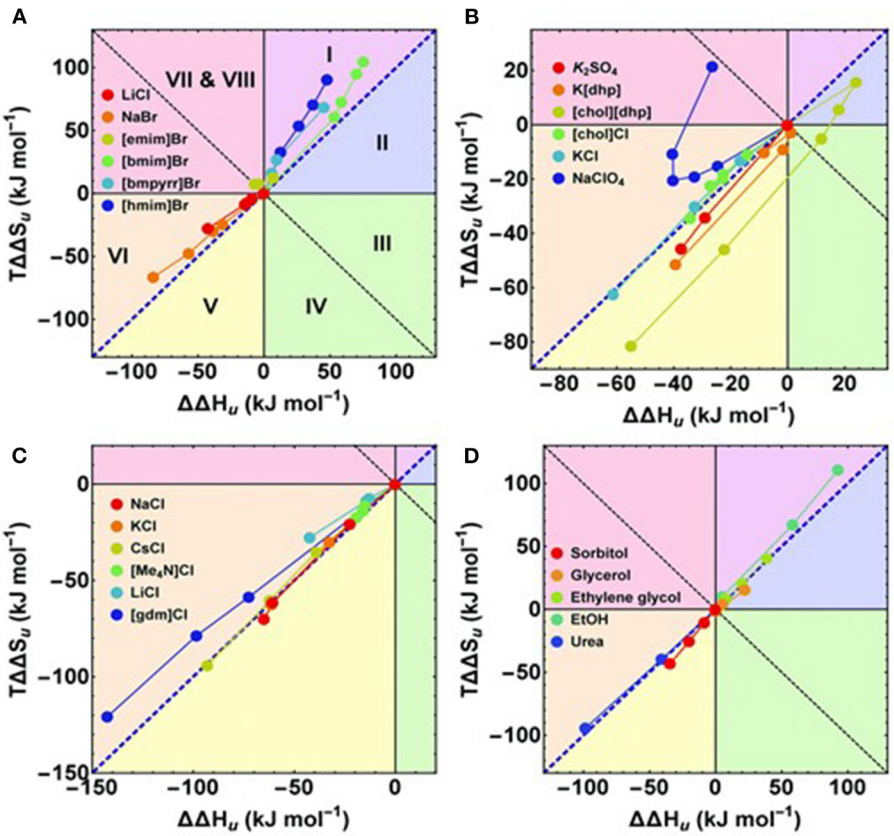

FIGURE 4 | (A–D) Enthalpy–entropy compensation plots. The different segments correspond to different contributions of $\Delta\Delta G_u$, $\Delta\Delta H_u$, and $T\Delta\Delta S_u$. The blue diagonal corresponds to a complete enthalpy–entropy compensation. Data points correspond to different concentrations of the respective cosolute. **(A,C,D)** The first or the first two data points (≤0.5 M) of some compounds are omitted for clarity. Adopted from Senske et al. (2016).

groups, sugars, and nitrogenous bases. The DNA forms duplex *via* base-pairing in the cells and carries genetic information (Saenger, 1984). In the double-helical structure, nitrogenous bases project into the helix and are responsible for stabilizing the structure through a hydrogen bond, stacking- and charge-charge-interactions. The nucleotide base pairs in DNA are adenine-thymine (A-T) and cytosine-guanine (C-G). The A-T base pair stabilizes the double-helical structure of DNA less efficiently than the G-C base pair owing to the two hydrogen bonds in former than three in later (Yakovchuk et al., 2006). The two strands of DNA connects through phosphodiester bonds (Sinden, 1994). Owing to the phosphodiester bonds, sugars remain oriented in the same plane in the nucleotides and add more stability to the double-helical structure because of more van der Waals interactions. The nitrogenous bases exert a hydrophobic effect on the DNA structure and remain toward the cavity of helix while the phosphate and sugar groups are hydrophilic and orient toward the exterior side and interacts with water. The negatively charged phosphate groups are stabilized by the positively charged moieties for maximum stability. The phosphodiester bonds further add up to the strength of the electrostatic interactions by bringing the bases in close vicinity (Hunter, 1993). Apart from the number of A-T base pairs in the DNA, a base-pair mismatch during replication also affects the stability of DNA double helix. It has been observed that a T-C mismatch destabilizes the duplex by up to 5.8 kcal/mol. If a hydrogen bond stabilizes the double helix by 1.5 kcal/mol, the destabilization due to base-pair mismatch is way more than the stabilization and might cause structural distortion to the helix (Kool et al., 2000).

Depending on the choice of the solvent, nucleic acids [DNA and ribonucleic acid (RNA)] exist in three forms viz. A-, B-, and Z-form. RNA exists exclusively in the A-form while DNA in the B-form. However, under dehydrating conditions DNA exist in the A-form (Tateishi-Karimata and Sugimoto, 2014). The Z-form of DNA is highly unfavorable and noted only upon unfavorable base sequencing, under the high salt concentration, or the influence of a cation (Pan et al., 2014). Although the B-form of DNA is stable in water but owing to its large dependency on the electrostatic interactions; it undergoes denaturation upon changing the pH, temperature and ionic strength (Lerman, 1964; McFail-Isom and Sines, 1999; Bonner and Klibanov, 2000). Besides, co-solutes and osmolytes can also affect the stability of the DNA structure. The concentration of sodium and chloride ions attached to the DNA directly affects its stability as shown by the molecular dynamic simulation (Feig and Pettitt, 1999). The interaction of co-solutes with the unfolded DNA strands is used

as a quantitative probe to reveal important information about the changes in structural conformation (Sasaki et al., 2007). In drug delivery application, drug molecules are used to perturb the DNA structure (Neidle et al., 1987). The stability of DNA is reflected in its melting temperature, T_m. In the coming sections, we will discuss the effect of various ionic liquid systems on the stability, and extraction and purification of DNA.

DNA Melting

The stability of DNA helix reflects in its melting temperature, T_m. Because of the dependency of T_m on the polymerase chain reaction (PCR), any change in the double-helical structure during DNA hybridization can be accounted in terms of the T_m (Wittwer, 2009). The stability of the DNA double-helical structure upon rising the temperature changes depending on the mismatch in the DNA strands during hybridization and the strength of the buffer solution (Rouzina and Bloomfield, 2001; Gudnason et al., 2007). The T_m method can be used to account for the effect of solution conditions such as buffers, pH, hydrophobicity, solutes, analytes, or even surfactants. High salt concentration and high molecular weight polyethylene glycol were observed to stabilize the double-helical structure of DNA and, consequently, result in higher T_m (Khimji et al., 2013a). Cationic surfactants have been noticed to stabilize the DNA strands and therefore reduces the T_m (Bhattacharya and Mandal, 1997).

The excluded volume of a solvent is another factor that affects the DNA T_m. The excluded volume is the free space of a solvent that can be occupied by another molecule. The salts containing polyanion possess large excluded volume than alkali halide salts viz. NaCl, NaBr, etc. Upon denaturation, DNA strands require a larger volume to expand than the duplex. In the presence of polyanions, which possess large excluded volume, the expansion of DNA duplex into the single stranded DNA gets thermodynamically less favored due to overcrowding and consequently, an increase in T_m is noticed (Khimji et al., 2013a).

DNA Stability in Ionic Liquid Systems

The effect of ionic liquids on the structure of DNA and its subsequent stability has been a subject of major interest among researchers. Circular dichroism (CD) is normally used to assess any change in the DNA structure. An ionic liquid stabilizes DNA mainly through electrostatic bonding between the negatively charged phosphate group and the cation of the ionic liquid. At a higher concentration of ionic liquid, cation binds to several sites including phosphate and results in the destabilization of the structure. However, an adequate blend of specific and electrostatic interactions in ionic liquids has been noted to stabilize the structure more efficiently.

DNA Stability in Neat Ionic Liquids

The CD spectrum of DNA duplexes from salmon testes in choline dihydrogenphosphate ([ChCl][dhp]) exhibited only B-form of DNA. Besides, both quadruplexes (G-quadruplex and i-motifs) of DNA where noted stable in [ChCl][dhp], similar to water (Fujita and Ohno, 2010; Vijayaraghavan et al., 2010; Tateishi-Karimata et al., 2015). Thermodynamic parameters determination indicated abnormally higher stability of A-T base pairs than G-C base pairs (Watson-Crick base pairs) in 4 M [ChCl][dhp] solution compared to that in buffered NaCl solution due to the differences in the enthalpy contributions (Tateishi-Karimata and Sugimoto, 2012). Molecular dynamics (MD) and NMR results revealed choline binding to the minor groove of A-T base pairs in B-form of DNA and stabilize it via hydrogen bonding (Nakano et al., 2014a; Marusic et al., 2015). In the case of G-C base pairs, choline undergoes for specific binding with the guanine in the single strand of DNA that further inhibits the duplex formation via base pairing (Tateishi-Karimata and Sugimoto, 2012). This unusual behavior of ionic liquid solution toward A-T base pairs was more investigated further by experimental *in vitro* and MD *in silico* studies. In this succession, Chandran et al. observed that apart from the electrostatic interactions, groove binding of ionic liquid cation through hydrophobic and polar interactions significantly add up to the stability of DNA duplex (Chandran et al., 2012). The intrusion of DNA's minor groove by ionic liquid cation was further confirmed by the fluorescent intercalation dye replacement experiment. Portella et al. showed using MD simulations that G-C base pairs possess preferably higher solvation energy than the A-T base pairs in an ionic liquid solution and solvation differences greatly affect the DNA stability (Portella et al., 2014). It is concluded that the specific behavior of ionic liquid solution toward the DNA arises from the groove binding. The interaction of DNA with ionic liquid components are shown in **Figure 1** and summarized in **Tables 1**, **2**.

Zhang et al. showed that poly[3-butyl-1-vinylimidazolium L-proline salt] could condense plasmid DNA to form stable complexes against enzymatic degradation by deoxyribonuclease I (Zhang et al., 2009). Chen et al. studied the solubility and chain conformation of DNA in 1-allyl-3-methylimidazolium chloride ([Amim]Cl) and 1-butyl-3-methylimidazolium formate ([bmim][HCOO]) using laser light scattering (Chen et al., 2011). The DNA chain was observed in random conformation in [Amim]Cl and denatured and condensed in [bmim][HCOO]. Cardoso and Micaelo investigated the molecular solvation of single-stranded DNA (ssDNA) and double-stranded DNA (dsDNA) in detail in a variety of ionic liquids comprised of imidazolium, oxazolium, pyrrolidinium, pyrimidinium, quaternary ammonium, and choline as cation and tetrafluoroborate ($[BF_4]$) and hexafluorophosphate ($[PF_6]$) as counterpart anion (Cardoso and Micaelo, 2011). The modeling and MD simulation studies exhibited that dsDNA retains its B-form in all ionic liquids as shown by crystallographic data. The most stabilizing ionic liquids toward the dsDNA were based on choline and pyridine as cation and $[PF_6]$ as a binding anion. The $[BF_4]$ anion was observed to undergo stronger hydrogen bond formation than the $[PF_6]$. The ssDNA was more accessible toward the hydrogen bonding *via* fluorinated anions. The cation of ionic liquid was located close to the DNA main chain owing to the electrostatic interactions with a phosphate group and hydrogen bonding and edge-to-face NH—π interaction with the bases, while anion forms hydrogen bonding with the cytosine, adenine and guanine bases. Mukesh et al. reported high solubility (3.5%) and long-term stability (up to 6 months) of

B-form of DNA, obtained from salmon testes, in bio-based ionic liquid choline indole-3-acetate (Mukesh et al., 2013). Singh et al. reported long term storage capability (1 year) and high solubility (25 w/w%) of salmon tests DNA in 2-hydroxyethylammonium formate (2-HEAF) at ambient temperature (Singh et al., 2017). ITC results indicated the hydrogen bonding between DNA and 2-HEAF responsible for the high concentration solubility and extended stability. The DNA docking analysis exhibited a higher preference for minor-groove binding over DNA surface with 2-HEAF than the major-groove binding and thus confirming the importance of hydrogen bonding in stabilizing DNA. Sarkar and group investigated the role of hydrogen bonding in the DNA stabilization by employing ionic liquids, namely, 1,1,3,3-tetramethylguanidinium acetate (TMG) and 2,2-diethyl-1,1,3,3-tetramethylguanidinium acetate (DETMG), in which former has a hydrogen bonding N-H moiety whereas the latter has a different mode of bonding (Sarkar et al., 2020). MD simulation and spectroscopic results indicated that only the groove binding of ionic liquid to the DNA is not sufficient for stabilization of the structure. The TMG cation stabilized the Watson-Crick pair more efficiently than larger DETMG cation owing to the hydrogen bonding interaction differences with DNA grooves.

DNA Stability in Aqueous Ionic Liquids

As hydration itself has a major impact on DNA stability, ionic liquid as co-solvent in water has been explored as suitable media in DNA stabilization and storage. Wang et al. observed that [bmim][PF_6] effectively extracts the salmon tests DNA from aqueous solution; in which [bmim]$^+$ cation displace the Na^+ from the phosphate group (Wang et al., 2007). In a further study, they noted that [bmim][PF_6] replaces the ethidium bromide from the dsDNA as fortified by the lowering in the signals of the resonance light scattering (RLS) (Cheng et al., 2007). Khimji et al. contrarily observed the inefficiency of the hydrophobic ionic liquids [bmim][PF_6] and 1-hexyl-3-methylimidazolium hexafluorophosphate ([hmim][PF_6]) in extracting DNA from aqueous solutions despite their efficacy in extracting DNA staining dyes (Khimji et al., 2013b). Guo et al. examined the molecular mechanism and binding characteristics of DNA and [bmim]Cl in the aqueous medium (Ding et al., 2010). They reported a lowering in the critical aggregation concentration of [bmim]Cl in presence of DNA and a reduction in the fluorescence quenching of ethidium bromide upon addition of [bmim]Cl in DNA suggesting a competitive interaction between the dye, [bmim]Cl and DNA. Based on the experimental and quantum chemical results they proposed a DNA-ionic liquid interaction mechanism. At a concentration of [bmim]Cl below 0.06 M, the cationic head group locates at several Å of DNA phosphate with the alkyl chain lying parallel to the DNA surface, whereas, at higher concentrations (>0.06 M), the cationic head group situates nearer to the phosphate while butyl chain attached perpendicularly to the DNA surface. He et al. extensively studied the interaction between the 1-dodecyl-3-methylimidazolium bromide ([ddmim]Br) and DNA in dilute brine using isothermal titration calorimetry (ITC), micropolarity, dynamic light scattering, UV–Vis transmittance, atomic force microscopy (AFM), circular dichroism (CD) and molecular dynamics simulation (He et al., 2013). They observed strong electrostatic interaction between DNA and ionic liquid cation and hydrophobic interaction between the [ddmim]Br alkyl chains. Very high thermal stability (up to 100°C) and long-term storage stability (up to 6 months) observed for salmon tests DNA in [choline][lactate], [choline][H_2PO_4] (containing 20–50 wt% water) and [choline] [nitrate] (containing 20% water), as defined by CD and fluorescence spectra as well as gel electrophoresis.

Tateishi-Karimata et al. noted that DNA triplexes that are difficult to achieve in aqueous solution at neutral pH, can be stabilized in [ChCl][dhp] solution at neutral pH (Tateishi-Karimata et al., 2014). Surprisingly, the Hoogsteen base pairs and Watson-Crick base pairs exhibited similar stability in hydrated ionic liquid. MD simulation results of DNA triplex in [ChCl][dhp] by Nakano et al. indicated the groove binding of choline to the third strand of DNA (Nakano et al., 2014b). Stable G-quadruplexes were shown to occur in [ChCl][dhp] with choline location at the center of the quadruplex (Fujita and Ohno, 2012). Thermodynamic calculations coupled with MD simulation results showed higher stability of i-motifs than G-quadruplex in [ChCl][dhp] owing to the binding of the choline to the loops and grooves of i-motifs (Tateishi-Karimata et al., 2015). A detailed account of various studies involving ionic liquids and their influences on the DNA structure stability is given by Zhao (2015) and Tateishi-Karimata and Sugimoto (2018) groups.

Extraction and Purification of DNA

The extraction, purification and storage of DNA are required for the biological experiments. The quantification of transcript and protein level of target genes Hyde and Read, 1993 is essential for understanding gene regulatory mechanisms and drug design that controls gene expression. The current liquid-liquid extraction methodology for the separation, purification and storage of nucleic acids involves highly toxic reagents such as phenol and chloroform; therefore, a simpler method involving an environmentally-benign solvent is highly sought (Tan and Yiap, 2009).

DNA is not stable in an aqueous medium at room temperature for a long period owing to the degradation by contaminating nucleases and inherent stability (Sasaki et al., 2007; Armand et al., 2009). Additionally, the lower vapor pressure of the water makes them unsuitable in the small scale operational methods as it quickly vaporizes; therefore, solvents that alleviate the problem of aqueous buffers are desirable for the development of functional devices (Armand et al., 2009). Because of the vaporless characteristic even at zero pressure, the extensive network of hydrogen bonding akin to water and coulombic nature, ionic liquids emerged as the most suitable alternative compared to the toxic organic solvents (Earle and Seddon, 2000). The solvation capability for both polar and apolar moieties and ease of tailoring makes ionic liquid a smarter solvent from the DNA-ionic liquid interaction perspective.

Shi et al. proposed a bicyclic imidazolium-based ionic liquid [b-4C-im][Br] for promoting the PCR signal of G-C rich DNA by minimizing non-specific amplifications (Shi et al., 2012). The ionic liquid also facilitated the PCR of normal-GC DNA under

mild conditions because of the destabilization of DNA duplexes under mild conditions. Anderson group reported the efficiency of hydrophobic magnetic ionic liquids (MILs) in the extraction of long and short plasmid DNA from bacterial cell lysate and salmon tests (Clark et al., 2015a). Benzyltrioctylammoniumbromotrichloroferrate(III) ($[(C_8)_3B_nN^+]$-$[FeCl_3Br^-]$) MIL was efficient in selective extraction of smaller single-stranded and double-stranded DNA whereas the dicationic 1,12-di(3-hexadecylbenzimidazolium)dodecane bis[(trifluoromethyl)-sulfonyl]imide bromotrichloroferrate(III) ($[(C_{16}B_nIM)_2C_{12}^{2+}][NTf_2^-$, $FeCl_3Br^-]$) MIL were excellent in extraction for the higher DNA molecules. In another report, MIL with metal-containing cations (Ni^{2+}, Mn^{2+}, or Co^{2+}) and chloride anion were applied for *in situ* dispersive liquid–liquid microextractions (DLLME) for the extraction of long and short double-stranded DNA (Bowers et al., 2019). These hydrophilic MILs were further converted to hydrophobic MILs during the extraction by exchanging the chloride anion with that of bis[(trifluoromethyl)sulfonyl]imide anion to ease the separation. To make the whole process faster and sensitive, extraction methodology was coupled with anion-exchange high-performance liquid chromatography with diode array detection (HPLC-DAD) and fluorescence spectroscopy. The developed *in situ* MIL-DLLME method noted effective than the conventional DLLME method as it required only 3 min for DNA extraction and yielded 1.1–1.5 times higher extraction efficiency (EFs). In another attempt, the Anderson group developed a method to remove the DNA further from MIL by designing the PCR buffer and coupling it with the process (Clark et al., 2015b). Clark et al. further developed a particle-free approach to sequence-specific DNA extraction using a magnetic liquid support and ion-tagged oligonucleotide (ITO) probes that can distinguish nucleotide mismatch and was more sensitive than a commercial magnetic bead-based method for the capture of target DNA from a pool of interfering genomic DNA (Clark et al., 2017).

Another aspect of DNA extraction comes from the bacterial gene transformation that implies the gene cloning technology (Lorenz and Wackernagel, 1994). In this technology, bacteria receives a new genetic trait through foreign DNA. Such gene transformation occurs spontaneously in few prokaryotes naturally; however, most of the bacterial cells require artificial transformation, stemming from the slow diffusion of hydrophilic DNA's entry across the hydrophobic lipid bilayer membrane and the slight electrostatic repulsion due to anionic DNA as well as the anionic head-groups of the bilayer membrane (van Die et al., 1983). Also, DNA molecules undergo hydrolysis and enzymatic degradation during transformation (Caruso et al., 2012). During transformation, DNA molecules are loaded onto the delivery vectors that efficiently transfer the genetic material across the lipid bilayer without any possibility of enzymatic degradation. The DNA delivery vectors mainly involve the encapsulation of DNA within the delivery vectors such as cationic surfactants, triblock copolymer vesicles, viral capsids, protein superstructures, lipid assemblies, polymer nanocapsules, and mesoporous structure and are crafted within the self-assembled superstructures, followed by transformation studies (Kikuchi et al., 1999; Vijayanathan et al., 2002; Guo, 2005; Li et al., 2011; Mingozzi and High, 2011). In addition to this DNA delivery vehicle-mediated transformation, some physical techniques such as a biolistic method, microinjection, electroporation, and heat shock, and poly(ethylene glycol) also required during the transformation to increase the efficiency (Klebe et al., 1983; Smith et al., 1992; Amoozgar and Yeo, 2012). The well-established calcium chloride method proposes that Ca^{2+} binds with anionic DNA and gets transferred via the transient pores formed during the heat shock. The necessity of heat shock and the inability to induce self-assembly in DNA during transformation renders calcium chloride method less lucrative. Instead, involving a hydrophobic ionic liquid that contains organic cation and also provides electrostatic interaction owing to the oppositely-charged ions and induces DNA self-assembly during the transformation. Soni et al. reported the formation of novel functional nanostructures during the electrostatic interaction between the phosphate group of DNA and the cationic part of hydrophobic ionic liquid [bmim][PF_6] (Soni et al., 2015). The self-assembling nanostructures acted as promising synthetic non-viral vectors for the efficient bacterial pGFP gene transformation in cells. TGA analysis of the DNA-IL functional nanostructures revealed that nanostructures consist of about 16 wt% ionic liquid, which may stabilize the pDNA and eventually enhance transformation efficiency. Samarkina et al. studied the behavior of supramolecular systems based on homologous series of amphiphiles bearing imidazolium fragment ($C_nH_{2n+1}Im^+Br^-$, where $n = 14, 16, 18$) toward the aggregation behavior, solubilization activity toward the hydrophobic guest, interaction with DNA decamer as well as integration with the lipid bilayer (Samarkina et al., 2017). The elongation of hydrophobic moiety by two methylene groups was noted to decrease critical micelle concentration by 4-folds without any change in the solubility. The ability of amphiphiles to integrate with lipid bilayer strongly depends on the length of the hydrophobic fragments. The lower homolog $C_{14}H_{29}Im^+Br^-$ increases the permeability of lipid bilayer whereas the higher homologs $C_{16}H_{33}Im^+Br^-$ and $C_{18}H_{37}Im^+Br^-$ stabilize it. Serker et al. noted positive zeta potential when employed [bmim][PF_6] for plasmid DNA transformation (Sarker et al., 2019). [bmim][PF_6] protected the plasmid DNA against ultrasonic shear stress and also enhanced *in vitro* gene transfection efficiency.

TOXICITY AND RECYCLABILITY OF IONIC LIQUIDS

The enormous interests in ionic liquids as biostabilizers necessitates the documentation of their toxicity on the environmental systems and various organisms. The toxicity of different ionic liquids is summarized by Thuy Pham et al. (2010). The inhibitory action of various ionic liquids on the activity of enzyme acetylcholinesterase is reported by many workers (Stock et al., 2004; Jastorff et al., 2005; Matzke et al., 2007; Ranke et al., 2007; Arning et al., 2008). The enzyme acetylcholinesterase has a major role in nerve response and function. The repressive action of ionic liquids on the activity of acetylcholinesterase has been observed to arise from the cation

(Arning et al., 2008). However, later, several studies suggested that the toxicity depends on both cation and anion (Thuy Pham et al., 2010). The measurements showed that pyridine-based ionic liquids were less toxic than the imidazolium- and phosphonium-based ionic liquids. Contrary to the cations, anions are non-inhibitory to the enzyme activity except those containing fluoride and complex anions of fluorine ($[BF_4]^-$, $[PF_6]^-$, $[OTf]^-$, $[NTf_2]^-$, $[SbF_6]^-$) (Stolte et al., 2006). The hydrolysis of complex anions of fluorine produces hydrofluoric acid which is a potential inhibitor of Na^+-K^+-ATPase, at the cell surface, and may interfere with essential cellular processes. The non-inhibitory action of anions might arise because of the binding to active site of enzyme (Matzke et al., 2007). However, the presence of alkyl chain on cation or anion increases the toxic effect of ionic liquids. The hydrophobicity of ionic liquids is also indicative of its toxicity (Kumar et al., 2009). The hydrophobicity of ionic liquids mainly arises due to the low charge density of anions. It is linked with the presence of fluorine atom in anion and increase with the number of fluorine atoms. However, a comparison between the alkyl chain length and anion in affecting the toxicity showed that the alkyl chain lengths on the cation gave rise to a larger impact on toxicity than a fluorinated anion. The effect of fluorinated anion ($[NTf_2]^-$) vanishes as the alkyl chain length reaches beyond octyl. Similarly, the unsaturation in cationic core and alkyl group on cation promotes toxicity (Kumar et al., 2009). Despite the distinct effect of different features of ionic liquids on toxicity, ionic liquids are noted as less toxic than their precursors (Kumar et al., 2009). Pyrrolidinium- and piperidinium-based ionic liquids containing propyl and butyl alkyl chain and bromide as the counter anion are less toxic than pyrrolidine and piperidine, respectively (Kumar et al., 2009). The task-effective ionic liquids containing nitrile, dimethyldisulphide, hydroxy, and polar ether group on cation reduces the toxicity compared to the non-functionalized ionic liquids (Stolte et al., 2006; Kumar et al., 2009). Thus, aprotic ionic liquids without modification cannot be considered as biocompatible ionic liquids due to their toxicity.

The protic ionic liquids have been shown to possess low cytotoxicity due to the lack of hydrophobic cation and perfluorinated anion (Gouveia et al., 2014). Choline-based protic ionic liquids are excellent example of biocompatible ionic liquids due to the low toxicity of choline and hence, have been involved as stabilizers for biopharmaceuticals (Gouveia et al., 2014). Weaver et al. studied the toxicity of choline-based protic ionic liquids combined with phosphate-based anions. The [Chol][DHP] exhibited the lowest cytotoxicity. Thus, choline family is one of the most suitable candidates of biocompatible protic ionic liquids and can be utilized as medium for protein and DNA stabilization. The development of biocompatible ionic liquids makes the toxicity issue irrelevant for their use as medium in many therapeutic applications and as stabilizers for biomolecules.

The wide applicability of ionic liquid systems in biomolecules stabilization, purification and storage makes them the frontrunner in the quest of the sustainable solvents. However, the efficient recyclability and reuse of ionic liquids are required to reach the economic and environmental goals. The recovery of ionic liquids is also essential as these solvents are toxic and non-biodegradable and releasing them to the aquatic environment might cause sever contamination (Frade and Afonso, 2010). These are the prime issues while using ionic liquids at a large scale. Several methods have been proposed to recover ionic liquids from solution, namely, distillation, adsorption, membrane separation, ion-exchange, and liquid-liquid extraction processes. The choice of the method in recovery depends on the medium characteristics, nature, and concentration of ionic liquids.

The negligible vapor pressure of ionic liquids makes their recovery easy from the ionic liquid-solvent mixtures by evaporation. However, a large difference in their boiling point is needed for adopting this method. Hydrophobic ionic liquids are easier to separate from aqueous mixture than hydrophilic one because of their water-immiscible nature. Membrane separation is a well-known, cost-effective, and commercially applicable method of separation for biomolecules (Haerens et al., 2010). In membrane separations, a membrane capable of separation retains specific compounds while allowing the passage to others. In pressure-driven membrane separation processes *viz.* microfiltration, ultrafiltration, nanofiltration, etc., when a pressure is applied across the membrane, the feed stream is split into permeate and retentate. Ionic liquids can be separated from permeate. Ultrafiltration method is used widely to separate ionic liquids from the proteins. Ultrafiltration membranes have a pore size 2–100 nm that allows the ionic liquid solution to pass through it while retaining the protein (Van Der Bruggen et al., 2003). The recovery of ionic liquids by ultrafiltration can be further improved by tuning the flow rate, concentration ratio, and temperature as suggested by Liu and Wu (1998).

Ionic liquid recovery from the DNA does not require special techniques. Precipitation of both DNA and ionic liquid upon addition of suitable solvents followed by the filtration and evaporation is normally used. In general, an ice-cold isopropyl alcohol (IPA)/ethanol is added to the ionic liquid-DNA mixture to precipitate the DNA (Mukesh et al., 2013; Singh et al., 2017). Upon adding ethyl acetate, the ionic liquid separates at the bottom and remaining DNA forms a hazy layer at the top that becomes transparent in 3–4 h. The traces of DNA can be completely removed from the ionic liquid by applying the same treatment again.

CONCLUSIONS AND OUTLOOK

Despite the large volume of research on ionic liquids in various physical and chemical transformations, their employment in the area of biochemistry has only seen growth in the last two decades. The remarkable properties such as insignificantly low vapor pressure and structure-tunability render ionic liquids more superior over the hazardous volatile organic solvents (VOSs) and, therefore, can be employed as a potent medium in controlling the functionality and stability of biomolecules like protein and DNA. Protein solubility, structural stability, crystallization, and separation in ionic liquids are often scaled either in the direct or indirect order of the Hofmeister ordering of ions. However,

the overall influence of a particular ionic liquid on a protein cannot be predicted and necessitates further investigation both from the experimental and computational researches. Compared to the dubious conclusions drawn from the ionic liquid-protein interactions owing to the structural variations, ionic liquid-DNA interactions are facile as the expected outcome of a particular ionic liquid on the structure and stability can be foreseen based on the available research. In the case of DNA, ionic liquids emerged as a natural long-term stabilizer and nuclease inhibitor that causes slow degradation to the stored DNA. Ionic liquids provide the five major interacting forces like hydrogen bonding, base stacking, conformational entropy, hydration, and cation binding that determine the structure and stability of ionic liquids. Despite the growing interests of ionic liquids in biochemistry, their moderate toxicity and involvement of volatile organic compounds during synthesis and recyclability are foremost concerns lingered with these coulombic media and ought to be addressed shortly. However, the introduction of biocompatible ionic liquids eliminates the problem of toxicity up to a certain length.

AUTHOR CONTRIBUTIONS

All authors have made significant contributions to the reading, writing sections of the manuscripts, and approved the final version submitted to the journal.

ACKNOWLEDGMENTS

We are thankful to the Wallenberg Wood Science Center (WWSC), Kempe Foundations, the Swedish Research Council, the Swedish Energy Agency, and the Bio4Energy (B4E) programme. This work is also part of the activities of the Johan Gadolin Process Chemistry Center at Åbo Akademi University.

REFERENCES

Ajaj, Y. (2010). *Dynamics and thermodynamics of protein folding and interactions in water-cosolvent systems*. (*Ph.D. thesis)*. Ruhr-University Bochum, Bochum, Germany.

Algaer, E. A., and van der Vegt, N. F. A. (2011). Hofmeister ion interactions with model amide compounds. *J. Phys. Chem. B* 115, 13781–13787. doi: 10.1021/jp208583w

Amoozgar, Z., and Yeo, Y. (2012). Recent advances in stealth coating of nanoparticle drug delivery systems. *Wiley Interdiscip. Rev. Nanomed. Nanobiotechnol.* 4, 219–233. doi: 10.1002/wnan.1157

Anthony, J. L., Maginn, E. J., and Brennecke, J. F. (2001). Solution thermodynamics of imidazolium-based ionic liquids and water. *J. Phys. Chem. B* 105, 10942–10949. doi: 10.1021/jp0112368

Araque, J. C., Yadav, S. K., Shadeck, M., Maroncelli, M., and Margulis, C. J. (2015). How is diffusion of neutral and charged tracers related to the structure and dynamics of a room-temperature ionic liquid? *Large deviations from Stokes–Einstein behavior explained. J. Phys. Chem. B* 119, 7015–7029. doi: 10.1021/acs.jpcb.5b01093

Armand, M., Endres, F., MacFarlane, D. R., Ohno, H., and Scrosati, B. (2009). Ionic liquid materials for the electrochemical challenges of the future. *Nat. Mater.* 8, 621–629. doi: 10.1038/nmat2448

Arning, J., Stolte, S., Böschen, A., Stock, F., Pitner, W.-R., Welz-Biermann, U., et al. (2008). Qualitative and quantitative structure activity relationships for the inhibitory effects of cationic head groups, functionalized side chains and anions of ionic liquids on acetylcholinesterase. *Green Chem.* 10, 47–58. doi: 10.1039/B712109A

Banik, R. M., Santhiagu, A., Kanari, B., Sabarinath, C., and Upahyay, S. N. (2003). Technological aspects of extractive fermentation using aqueous two-phase systems. *World J. Microbiol. Biotechnol.* 19, 337–348. doi: 10.1023/A:1023940809095

Batchelor, J. D., Olteanu, A., Tripathy, A., and Pielak, G. J. (2004). Impact of protein denaturants and stabilizers on water structure. *J. Am. Chem. Soc.* 126, 1958–1961. doi: 10.1021/ja039335h

Benton, L. A., Smith, A. E., Young, G. B., and Pielak, G. J. (2012). Unexpected effects of macromolecular crowding on protein stability. *Biochemistry* 51, 9773–9775. doi: 10.1021/bi300909q

Bhattacharya, S., and Mandal, S. (1997). Interaction of surfactants with DNA. *Role of hydrophobicity and surface charge on intercalation and DNA melting. Biochim. Biophys. Acta Biomembr.* 1323, 29–44. doi: 10.1016/S0005-2736(96)00171-X

Bihari, M., Russell, T. P., and Hoagland, D. A. (2010). Dissolution and dissolved state of cytochrome c in a neat, hydrophilic ionic liquid. *Biomacromolecules* 11, 2944–2948. doi: 10.1021/bm100735z

Blesic, M., Marques, M. H., Plechkova, N. V., Seddon, K. R., Rebelo, L. P. N., and Lopes, A. (2007). Self-aggregation of ionic liquids: micelle formation in aqueous solution. *Green Chem.* 9, 481–490. doi: 10.1039/b615406a

Bonner, G., and Klibanov, A. M. (2000). Structural stability of DNA in nonaqueous solvents. *Biotechnol. Bioeng.* 68, 339–344. doi: 10.1002/(sici)1097-0290(20000505)68:3<339::aid-bit12>3.0.co;2-o

Bowers, A. N., Trujillo-Rodríguez, M. J., Farooq, M. Q., and Anderson, J. L. (2019). Extraction of DNA with magnetic ionic liquids using *in situ* dispersive liquid–liquid microextraction. *Anal. Bioanal. Chem.* 411, 7375–7385. doi: 10.1007/s00216-019-02163-9

Broering, J. M., and Bommarius, A. S. (2005). Evaluation of Hofmeister effects on the kinetic stability of proteins. *J. Phys. Chem. B* 109, 20612–20619. doi: 10.1021/jp053618+

Bruce, D. W., Cabry, C. P., Lopes, J. N. C., Costen, M. L., D'Andrea, L., Grillo, I., et al. (2017). Nanosegregation and structuring in the bulk and at the surface of ionic-liquid mixtures. *J. Phys. Chem. B* 121, 6002–6020. doi: 10.1021/acs.jpcb.7b01654

Bui-Le, L., Clarke, C. J., Bröhl, A., Brogan, A. P. S., Arpino, J. A. J., Polizzi, K. M., et al. (2020). Revealing the complexity of ionic liquid–protein interactions through a multi-technique investigation. *Commun. Chem.* 3:55. doi: 10.1038/s42004-020-0302-5

Burney, P. R., Nordwald, E. M., Hickman, K., Kaar, J. L., and Pfaendtner, J. (2015). Molecular dynamics investigation of the ionic liquid/enzyme interface: application to engineering enzyme surface charge. *Proteins* 83, 670–680. doi: 10.1002/prot.24757

Byrne, N., Wang, L.-M., Belieres, J.-P., and Angell, C. A. (2007). Reversible folding–unfolding, aggregation protection, and multi-year stabilization, in high concentration protein solutions, using ionic liquids. *Chem. Commun.* 2007, 2714–2716. doi: 10.1039/B618943A

Cammarata, L., Kazarian, S. G., Salter, P. A., and Welton, T. (2001). Molecular states of water in room temperature ionic liquids. *Phys. Chem. Chem. Phys.* 3, 5192–5200. doi: 10.1039/b106900d

Cardoso, L., and Micaelo, N. M. (2011). DNA molecular solvation in neat ionic liquids. *ChemPhysChem* 12, 275–277. doi: 10.1002/cphc.201000645

Caruso, F., Hyeon, T., and Rotello, V. M. (2012). Nanomedicine. *Chem. Soc. Rev.* 41, 2537–2538. doi: 10.1039/C2CS90005J

Castner, J. E. W., and Wishart,. J. F. (2010). Spotlight on ionic liquids. *J. Chem. Phys.* 132, 120901–120909. doi: 10.1063/1.3373178

Chandran, A., Ghoshdastidar, D., and Senapati, S. (2012). Groove binding mechanism of ionic liquids: a key factor in long-term stability of DNA in hydrated ionic liquids? *J. Am. Chem. Soc.* 134, 20330–20339. doi: 10.1021/ja304519d

Chen, Y., Zhang, Y., Ke, F., Zhou, J., Wang, H., and Liang, D. (2011). Solubility of neutral and charged polymers in ionic liquids studied by

laser light scattering. *Polymer* 52, 481–488. doi: 10.1016/j.polymer.2010.11.034

Cheng, D.-H., Chen, X.-W., Wang, J.-H., and Fang, Z.-L. (2007). An abnormal resonance light scattering arising from ionic-liquid/DNA/ethidium interactions. *Chem. Eur. J.* 13, 4833–4839. doi: 10.1002/chem.200601544

Clark, K. D., Nacham, O., Yu, H., Li, T., Yamsek, M. M., Ronning, D. R., et al. (2015a). Extraction of DNA by magnetic ionic liquids: tunable solvents for rapid and selective DNA analysis. *Anal. Chem.* 87, 1552–1559. doi: 10.1021/ac504260t

Clark, K. D., Varona, M., and Anderson, J. L. (2017). Ion-tagged oligonucleotides coupled with a magnetic liquid support for the sequence-specific capture of DNA. *Angew. Chem. Int. Ed.* 56, 7630–7633. doi: 10.1002/anie.201703299

Clark, K. D., Yamsek, M. M., Nacham, O., and Anderson, J. L. (2015b). Magnetic ionic liquids as PCR-compatible solvents for DNA extraction from biological samples. *Chem. Commun.* 51, 16771–16773. doi: 10.1039/C5CC07253K

Collins, K. D. (1997). Charge density-dependent strength of hydration and biological structure. *Biophys. J.* 72, 65–76. doi: 10.1016/S0006-3495(97)78647-8

Collins, K. D. (2004). Ions from the Hofmeister series and osmolytes: effects on proteins in solution and in the crystallization process. *Methods* 34, 300–311. doi: 10.1016/j.ymeth.2004.03.021

Collins, K. D. (2006). Ion hydration: implications for cellular function, polyelectrolytes, and protein crystallization. *Biophys. Chem.* 119, 271–281. doi: 10.1016/j.bpc.2005.08.010

Constantinescu, D., Herrmann, C., and Weingärtner, H. (2007). Protein denaturation by ionic liquids and the Hofmeister series: a case study of aqueous solutions of Ribonuclease A. *Angew. Chem. Int. Ed.* 46, 8887–8889. doi: 10.1002/anie.200702295

Constantinescu, D., Herrmann, C., and Weingärtner, H. (2010). Patterns of protein unfolding and protein aggregation in ionic liquids. *Phys. Chem. Chem. Phys.* 12, 1756–1763. doi: 10.1039/B921037G

Corradini, D., Nicoletti, I., and Bonn, G. K. (2009). Co-electroosmotic capillary electrophoresis of basic proteins with 1-alkyl-3- methylimidazolium tetrafluoroborate ionic liquids as non-covalent coating agents of the fused-silica capillary and additives of the electrolyte solution. *Electrophoresis* 30, 1869–1876. doi: 10.1002/elps.200800447

Dang, L. P., Fang, W. Z., Li, Y., Wang, Q., Xiao, H. Z., and Wang, Z. Z. (2013). Ionic liquid-induced structural and activity changes in hen egg white lysozyme. *Appl. Biochem. Biotechnol.* 169, 290–300. doi: 10.1007/s12010-012-9986-z

de Diego, T., Lozano, P., Gmouh, M., Voltier, M., and Iborra, I. M. (2005). Understanding structure-stability relationships of *Candida antartica* lipase B in ionic liquids. *Biomacromolecules* 6, 1457–1464. doi: 10.1021/bm049259q

Diddens, D., Lesch, V., Heuer, A., and Smiatek, J. (2017). Aqueous ionic liquids and their influence on peptide conformations: denaturation and dehydration mechanisms. *Phys. Chem. Chem. Phys.* 19, 20430–20440. doi: 10.1039/C7CP02897K

Ding, Y., Zhang, L., Xie, J., and Guo, R. (2010). Binding characteristics and molecular mechanism of interaction between ionic liquid and DNA. *J. Phys. Chem. B* 114, 2033–2043. doi: 10.1021/jp9104757

Dreyer, S., Salim, P., and Kragl, U. (2009). Driving forces of protein partitioning in an ionic liquid-based aqueous two-phase system. *Biochem. Eng. J.* 46, 176–185. doi: 10.1016/j.bej.2009.05.005

Earle, M. J., and Seddon, K. R. (2000). Ionic liquids. *Green solvents for the future. Pure Appl. Chem.* 72, 1391–1398. doi: 10.1351/pac200072071391

Eckstein, M., Sesing, M., Kragl, U., and Adlercreutz, P. (2002). At low water activity α-chymotrypsin is more active in an ionic liquid than in non-ionic organic solvents. *Biotechnol. Lett.* 24, 867–872. doi: 10.1023/A:1015564608261

Egorova, K. S., Gordeev, E. G., and Ananikov, V. P. (2017). Biological activity of ionic liquids and their application in pharmaceutics and medicine. *Chem. Rev.* 117, 7132–7189. doi: 10.1021/acs.chemrev.6b00562

Feig, M., and Pettitt, B. M. (1999). Sodium and chlorine ions as part of the DNA solvation shell. *Biophys. J.* 77, 1769–1781. doi: 10.1016/S0006-3495(99)77023-2

Figueiredo, A. M., Sardinha, J., Mooreb, G. R., and Cabrita, E. J. (2013). Protein destabilisation in ionic liquids: the role of preferential interactions in denaturation. *Phys. Chem. Chem. Phys.* 15, 19632–19643. doi: 10.1039/c3cp53395f

Frade, R. F., and Afonso, C. A. (2010). Impact of ionic liquids in environment and humans: an overview. *Hum. Exp. Toxicol.* 29, 1038–1054. doi: 10.1177/0960327110371259

Fujita, K., Forsyth, M., MacFarlane, D. R., Reid, R. W., and Elliott, G. D. (2006). Unexpected improvement in stability and utility of cytochrome C by solution in biocompatible ionic liquids. *Biotechnol. Bioeng.* 94, 1209–1213. doi: 10.1002/bit.20928

Fujita, K., MacFarlane, D. R., and Forsyth, M. (2005). Protein solubilizing and stabilizing ionic liquids. *Chem. Commun.* 2005, 4804–4806. doi: 10.1039/b508238b

Fujita, K., MacFarlane, D. R., Foryth, M., Yoshizawa-Fujita, M., Murata, K., Nakamura, N., et al. (2007). Solubility and stability of cytochrome C in hydrated ionic liquids: effect of oxo acid residues and kosmotropicity. *Biomacromolecules* 8, 2080–2086. doi: 10.1021/bm070041o

Fujita, K., and Ohno, H. (2010). Enzymatic activity and thermal stability of metalloproteins in hydrated ionic liquids. *Biopolymers* 93, 1093–1099. doi: 10.1002/bip.21526

Fujita, K., and Ohno, H. (2012). Stable G-quadruplex structure in a hydrated ion pair: cholinium cation and dihydrogen phosphate anion. *Chem. Commun.* 48, 5751–5753. doi: 10.1039/c2cc30554b

Fumino, K., Wulf, A., and Ludwig, R. (2009). Hydrogen bonding in protic ionic liquids: reminiscent of water. *Angew. Chem. Int. Ed.* 48, 3184–3186. doi: 10.1002/anie.200806224

Funkner, S., Niehues, G., Schmidt, D. A., Heyden, M., Schwaab, G., Callahan, K. M., et al. (2012). Watching the low-frequency motions in aqueous salt solutions: the terahertz vibrational signatures of hydrated ions. *J. Am. Chem. Soc.* 134, 1030–1035. doi: 10.1021/ja207929u

Garlitz, J. A., Summers, C. A., Flowers, R. A. I. I., and Borgstahl, G. E. (1999). Ethylammonium nitrate: a protein crystallization reagent. *Acta Crystallogr. D* 55, 2037–2038. doi: 10.1107/S0907444999011774

Ghanta, K. P., Pal, T., Mondal, S., and Bandyopadhyay, S. (2020). Microscopic understanding of the effect of ionic liquid on protein from molecular simulation studies. *J. Phys. Chem. B* 124, 3909–3921. doi: 10.1021/acs.jpcb.0c02001

Ghosh, S., Parui, S., Jana, B., and Bhattacharyya, K. (2015). Ionic liquid induced dehydration and domain closure in lysozyme: FCS and MD simulation. *J. Chem. Phys.* 143:125103. doi: 10.1063/1.4931974

Gough, C. R., Rivera-Galletti, A., Cowan, D. A., Cruz, D. S., and Hu, X. (2020). Protein and polysaccharide-based fiber materials generated from ionic liquids: a review. *Molecules* 25:3362. doi: 10.3390/molecules25153362

Gouveia, W., Jorge, T. F., Martins, S., Meireles, M., Carolino, M., Cruz, C., et al. (2014). Toxicity of ionic liquids prepared from biomaterials. *Chemosphere* 104, 51–56. doi: 10.1016/j.chemosphere.2013.10.055

Green, A. A. (1932). Studies in the physical chemistry of the proteins: x. *The solubility of hemoglobin in solutions of chlorides and sulfates of varying concentration. J. Biol. Chem.* 95, 47–66.

Gudnason, H., Dufva, M., Bang, D. D., and Wolff, A. (2007). Comparison of multiple DNA dyes for real-time PCR: effects of dye concentration and sequence composition on DNA amplification and melting temperature. *Nucleic Acids Res.* 35:e127. doi: 10.1093/nar/gkm671

Guo, P. (2005). RNA nanotechnology: engineering, assembly and applications in detection, gene delivery and therapy. *J. Nanosci. Nanotechnol.* 5, 1964–1982. doi: 10.1166/jnn.2005.446

Gurney, R. W. (1953). *Ionic Processes in Solution;* New York, NY: McGraw-Hill.

Gutowski, K. E., Broker, G. A., Willauer, H. D., Huddleston, J. G., Swatloski, R. P., Holbrey, J. D., et al. (2003). Controlling the aqueous miscibility of ionic liquids: aqueous biphasic systems of water-miscible ionic liquids and water-structuring salts for recycle, metathesis, and separations. *J. Am. Chem. Soc.* 125, 6632–6633. doi: 10.1021/ja0351802

Haberler, M., Schröder, C., and Steinhauser, O. (2011). Solvation studies of a zinc finger protein in hydrated ionic liquids. *Phys. Chem. Chem. Phys.* 13, 6955–6969. doi: 10.1039/c0cp02487b

Haberler, M., Schröder, C., and Steinhauser, O. (2012). Hydrated ionic liquids with and without solute: the influence of water content and protein solutes. *J. Chem. Theory Comput.* 8, 3911–3928. doi: 10.1021/ct300191s

Haberler, M., and Steinhauser, O. (2011). On the influence of hydrated ionic liquids on the dynamical structure of model proteins: a computational study. *Phys. Chem. Chem. Phys.* 13, 17994–18004. doi: 10.1039/c1cp22266j

Haerens, K., Van Deuren, S., Matthijs, E., and Van der Bruggen, B. (2010). Challenges for recycling ionic liquids by using pressure driven membrane processes. *Green Chem.* 12, 2182–2188. doi: 10.1039/c0gc00406e

Hayes, R., Warr, G. W., and Atkin, R. (2015). Structure and nanostructure in ionic liquids. *Chem. Rev.* 115, 6357–6426. doi: 10.1021/cr500411q

He, C., Li, S., Liu, H., Li, K., and Liu, F. (2005). Extraction of testosterone and epitestosterone in human urine using aqueous two-phase systems of ionic liquid and salt. *Chromatogr. A* 1082, 143–149. doi: 10.1016/j.chroma.2005.05.065

He, Y., Shang, Y., Liu, Z., Shao, S., Liu, H., and Hu, Y. (2013). Interactions between ionic liquid surfactant [C_{12}mim]Br and DNA in dilute brine. *Colloid Surface B* 101, 398–404. doi: 10.1016/j.colsurfb.2012.07.027

Heyda, J., Vincent, J. C., Tobias, D. J., Dzubiella, J., and Jungwirth, P. (2010). Ion specificity at the peptide bond: molecular dynamics simulations of N-methylacetamide in aqueous salt solutions. *J. Phys. Chem. B* 114, 1213–1220. doi: 10.1021/jp910953w

Hofmeister, F. (1888). On the theory of the effects of salts. *Arch. Exp. Pathol. Pharmakol.* 1888, 247–260. doi: 10.1007/BF01918191

Huang, M.-M., and Weingärtner, H. (2008). Protic ionic liquids with unusually high dielectric permittivities. *ChemPhysChem* 9, 2172–2173. doi: 10.1002/cphc.200800523

Hunter, C. A. (1993). Sequence-depenent DNA structure: the role of base stacking interactions. *J. Mol. Biol.* 230, 1025–1054. doi: 10.1006/jmbi.1993.1217

Hyde, J. E., and Read, M. (1993). The extraction and purification of DNA and RNA from *in vitro* cultures of the malaria parasite plasmodium falciparum. *Methods Mol. Biol.* 21, 133–143. doi: 10.1385/0-89603-239-6:133

Idris, A., Vijayaraghavan, R., Rana, U. A., Fredericks, D., Pattia, A. F., and MacFarlane, D. R. (2013). Dissolution of feather keratin in ionic liquids. *Green Chem.* 15, 525–534. doi: 10.1039/c2gc36556a

Jaeger, V. W., Burney, P., and Pfaendtner, J. (2014). Comparison of three ionic liquid-tolerant cellulases by molecular dynamics. *Biophys J.* 108, 880–892. doi: 10.1016/j.bpj.2014.12.043

Jaeger, V. W., and Pfaendtner, J. (2016). Destabilization of human serum albumin by ionic liquids studied using enhanced molecular dynamics simulations. *J. Phys. Chem. B* 120, 12079–12087. doi: 10.1021/acs.jpcb.6b09410

Jastorff, B., Mölter, K., Behrend, P., Bottin-Weber, U., Filser, J., Heimers, A., et al. (2005). Progress in evaluation of risk potential of ionic liquids-basis for an eco-design of sustainable products. *Green Chem.* 7, 362–372. doi: 10.1039/b418518h

Jiang, T.-F.-, Gu, Y.-L., Liang, B., Li, J.-B., Shi, Y.-P., and Ou, Q.-Y. (2003). Dynamically coating the capillary with 1-alkyl-3-methylimidazolium-based ionic liquids for separation of basic proteins by capillary electrophoresis. *Anal. Chim. Acta* 479, 249–254. doi: 10.1016/S0003-2670(02)01537-4

Jiang, W., Wang, Y., and Voth, G. A. (2007). Molecular dynamics simulation of nanostructural organization in ionic liquid/water mixtures. *J. Phys. Chem. B* 111, 4812–4818. doi: 10.1021/jp067142l

Judge, R. A., Takahashi, S., Longenecker, K. L., Fry, E. H., Abad-Zapatero, C., and Chiu, M. L. (2009). The effect of ionic liquids on protein crystallization and X-ray diffraction resolution. *CrystGrowthDes* 9, 3463–3469. doi: 10.1021/cg900140b

Jungwirth, P., and Cremer, P. S. (2014). Beyond hofmeister. *Nat. Chem.* 6, 261–263. doi: 10.1038/nchem.1899

Kaar, J. L., Jesionowski, A. M., Berberich, J. A., Moulton, R., and Russell, A. J. (2003). Impact of ionic liquid physical properties on lipase activity and stability. *J. Am. Chem. Soc.* 125, 4125–4131. doi: 10.1021/ja028557x

Kamlet, M. J., Abboud, J. L., and Taft, R. W. (1977). The solvatochromic comparison method 6. The π^* scale of solvent polarities. *J. Am. Chem. Soc.* 99, 6027–6038. doi: 10.1021/ja00460a031

Kamlet, M. J., and Taft, R. W. (1976). The solvatochromic comparison method. I. The *beta-scale of solvent hydrogen-bond acceptor (HBA) basicities. J. Am. Chem. Soc.* 98, 377–383. doi: 10.1021/ja00418a009

Khimji, I., Doan, K., Bruggeman, K., Huang, P.-J. J., Vajha, P., and Liu, J. (2013b). Extraction of DNA staining dyes from DNA using hydrophobic ionic liquids. *Chem. Commun.* 49, 4537–4539. doi: 10.1039/c3cc41364k

Khimji, I., Shin, J., and Liu, J. (2013a). DNA duplex stabilization in crowded polyanion solutions. *Chem. Comm.* 49, 1306–1308. doi: 10.1039/c2cc38627e

Kikuchi, H., Suzuki, N., Ebihara, K., Morita, H., Ishii, Y., Kikuchi, A., et al. (1999). Gene delivery using liposome technology. *J. Control Rel.* 1999, 269–277. doi: 10.1016/S0168-3659(99)00047-4

Klähn, M., Lim, G. S., Seduraman, A., and Wu, P. (2011a). On the different roles of anions and cations in the solvation of enzymes in ionic liquids. *Phys. Chem. Chem. Phys.* 13, 1649–1662. doi: 10.1039/C0CP01509A

Klähn, M., Lim, G. S., and Wu, P. (2011b). How ion properties determine the stability of a lipase enzyme in ionic liquids: A molecular dynamics study. *Phys. Chem. Chem. Phys.* 13, 18647–18660. doi: 10.1039/c1cp22056j

Klebe, R. J., Harriss, J. V., Sharp, Z. D., and Douglas, M. G. (1983). A general method for polyethylene-glycol-induced genetic transformation of bacteria and yeast. *Gene* 25, 333–341. doi: 10.1016/0378-1119(83)90238-X

Kobayashi, T., Kemna, A., Fyta, M., Braunschweig, B., and Smiatek, J. (2019). Aqueous mixtures of room-temperature ionic liquids: entropy-driven accumulation of water molecules at interfaces. *J. Phys. Chem. C* 123, 13795–13803. doi: 10.1021/acs.jpcc.9b04098

Kobayashi, T., Reid, J. E. S. J., Shimiju, S., Fyta, M., and Smiatek, J. (2017). The properties of residual water molecules in ionic liquids: a comparison between direct and inverse Kirkwood–Buff approaches. *Phys. Chem. Chem. Phys.* 19, 18924–18937. doi: 10.1039/C7CP03717A

Kool, E., Morales, J., and Guckian, K. (2000). Mimicking the structure and function of DNA: insights into DNA stability and replication. *Angew. Chem. Int. Ed.* 39, 990–1009. doi: 10.1002/(SICI)1521-3773(20000317)39:6<990::AID-ANIE990>3.0.CO;2-0

Krüger, M., Bründermann, E., Funkner, S., Weingärtner, H., and Havenith, M. (2010). Communications: polarity fluctuations of the protic ionic liquid ethylammonium nitrate in the terahertz regime. *J. Chem. Phys.* 132, 101101–101104. doi: 10.1063/1.3352585

Kula, M.-R., Kroner, K. H., and Hustedt, H. (1982). Purification of enzymes by liquid–liquid extraction. *Adv. Biochem. Eng.* 24, 73–118. doi: 10.1007/3-540-11699-0_11

Kumar, A., Rani, A., and Venkatesu, P. (2014). A comparative study of the effects of the Hofmeister series anions of the ionic salts and ionic liquids on the stability of a-chymotrypsin. *New J. Chem.* 39, 938–952. doi: 10.1039/C4NJ01596G

Kumar, A., and Venkatesu, P. (2013). Prevention of insulin self-aggregation by a protic ionic *liquid. RSV Adv.* 3, 362–367. doi: 10.1039/C2RA22277A

Kumar, A., and Venkatesu, P. (2014). The stability of insulin in the presence of short alkyl chain imidazolium-based ionic liquids. *RSC Adv.* 4, 4487–4499. doi: 10.1039/C3RA44477E

Kumar, R. A., Papaiconomou, N., Lee, J.-M., Salminen, J., Clark, D. S., and Prausnitz, J. M. (2009). In vitro cytotoxicities of ionic liquids: effect of cation rings, functional groups, and anions. *Environ. Toxicol.* 24, 388–395. doi: 10.1002/tox.20443

Kunz, W., Nostro, P. L., and Ninham, B. W. (2004). The present state of affairs with Hofmeister effects. *Curr. Opin. Colloid Interface Sci.* 9, 1–18. doi: 10.1016/j.cocis.2004.05.004

Laane, C., Boeren, S., Vos, K., and Veeger, C. (1987). Rules for optimization of biocatalysis in organic *solvents. Biotechnol. Bioeng.* 30, 81–87. doi: 10.1002/bit.260300112

Lange, C., Patil, G., and Rudolph, R. (2005). Ionic liquids as refolding additives: N′-alkyl and N′-(ω-hydroxyalkyl) N-methylimidazolium chlorides. *Protein Sci.* 14, 2693–2701. doi: 10.1110/ps.051596605

Laszlo, J. A., and Compton, D. L. (2002). Comparison of peroxidase activities of hemin, cytochrome c and microperoxidase-11 in molecular solvents and imidazolium-based ionic liquids. *J. Mol. Catal. B Enzym.* 18, 109–120. doi: 10.1016/S1381-1177(02)00074-7

Lau, R. M., Sorgetrager, M. J., Carrea, G., van Rantwijk, F., Secundo, F., and Sheldon, R. A. (2004). Dissolution of candida antarctica lipase B in ionic liquids: effects on structure and activity. *Green Chem.* 6, 483–487. doi: 10.1039/b405693k

Lerman, L. S. (1964). Acridine mutagens and DNA structure. *J. Cell. Physiol.* 64, 1–18. doi: 10.1002/jcp.1030640403

Lesch, V., Heuer, A., Tatsis, V. A., Holm, C., and Smiatek, J. (2015). Peptides in the presence of aqueous ionic liquids: tunable co-solutes as denaturants or protectants? *Phys. Chem. Chem. Phys.* 17, 26049–26053. doi: 10.1039/C5CP03838C

Li, T., Li, B., Dong, S., and Wang, E. (2007). Ionic liquids as selectors for the enhanced detection of proteins. *Chem. Eur. J.* 13, 8516–8521. doi: 10.1002/chem.200700275

Li, X., Xie, Q. R., Zhang, J., Xia, W., and Gu, H. (2011). The packaging of siRNA within the mesoporous structure of silica nanoparticles. *Biomaterials* 32, 9546–9556. doi: 10.1016/j.biomaterials.2011.08.068

Lim, G. S., Zidar, J., Cheong, D. W., Jaenicke, S., and Klähn, M. (2014). Impact of lonic liquids in aqueous solution on bacterial plasma membranes studied with molecular dynamics simulations. *J. Phys. Chem. B* 118, 10444–10459. doi: 10.1021/jp5060952

Liu, C., and Wu, X. (1998). Optimization of operation parameters in ultrafiltration process. *J. Biotechnol.* 66, 195–202. doi: 10.1016/S0168-1656(98)00161-8

Liu, X., Zhou, G., He, H., Zhang, X., Wang, J., and Zhang, S. (2015). Rodlike micelle structure and formation of ionic liquid in aqueous solution by molecular simulation. *Ind. Eng. Chem. Res.* 54, 1681–1688. doi: 10.1021/ie503109z

Lorenz, M. G., and Wackernagel, W. (1994). Bacterial gene transfer by natural genetic transformation in the environment. *Microbiol. Rev.* 58, 563–602. doi: 10.1128/MMBR.58.3.563-602.1994

Lumry, R., and Rajender, S. (1970). Enthalpy-entropy compensation phenomena in water solutions of proteins and small molecules: a ubiquitous property of water. *Biopolymers* 9, 1125–1227. doi: 10.1002/bip.1970.360091002

Mandal, B., Mondal, S., Pan, A., Moulik, S. P., and Ghosh, S. (2015). Physicochemical study of the interaction of lysozyme with surface active ionic liquid 1-butyl-3-methylimidazolium octylsulfate [BMIM] [OS] in aqueous and buffer media. *Colloids Surf. A Physicochem. Eng. Asp.* 484, 345–353. doi: 10.1016/j.colsurfa.2015.07.052

Marusic, M., Tateishi-Karimata, H., Sugimoto, N., and Plavec, J. (2015). Structural foundation for DNA behavior in hydrated ionic liquid: an NMR study. *Biochimie* 108, 169–177. doi: 10.1016/j.biochi.2014.11.015

Matzke, M., Stolte, S., Thiele, K., Juffernholz, T., Arning, J., Ranke, J., et al. (2007). The influence of anion species on the toxicity of 1-alkyl-3-methylimidazolium ionic liquids observed in an (eco)toxicological test battery. *Green Chem.* 9, 1198–1207. doi: 10.1039/b705795d

Mazzini, V., Liu, G., and Craig, V. S. J. (2018). Probing the Hofmeister series beyond water: specific-ion effects in non-aqueous solvents. *J. Chem. Phys.* 148, 222805–222812. doi: 10.1063/1.5017278

McFail-Isom, L., Sines, C. C., and Williams, L. D. (1999). DNA structure: cations in charge? *Curr. Opin. Struc. Boil.* 9, 298–304. doi: 10.1016/s0959-440x(99)80040-2

Méndez-Morales, T., Carrete, J., Cabeza, Ó., Gallego, L. J., and Varela, L. M. (2011). Molecular dynamics simulation of the structure and dynamics of water-1-Alkyl-3-methylimidazolium ionic liquid mixtures. *J. Phys. Chem. B* 115, 6995–7008. doi: 10.1021/jp202692g

Micaêlo, N. M., and Soares, C. M. (2008). Protein structure and dynamics in ionic liquids. *Insights from molecular dynamics simulation studies. J. Phys. Chem. B* 112, 2566–2572. doi: 10.1021/jp0766050

Mingozzi, F., and High, K. A. (2011). Therapeutic *in vivo* gene transfer for genetic disease using AAV: progress and challenges. *Nat. Rev. Genet.* 12, 341–355. doi: 10.1038/nrg2988

Mukesh, C., Mondal, D., Sharma, M., and Prasad, K. (2013). Rapid dissolution of DNA in a novel bio-based ionic liquid with long-term structural and chemical stability: successful recycling of the ionic liquid for reuse in the process. *Chem. Commun.* 49, 6849–6851. doi: 10.1039/c3cc42829j

Muldoon, M., Lagunas-Castedo, C., and Nockemann, P. (2012). Hofmeister effects of ionic liquids in protein crystallization: direct and water-mediated interactions. *Cryst. Eng. Comm.* 14, 4912–4921. doi: 10.1039/c2ce25129a

Nakano, M., Tateishi-Karimata, H., Tanaka, S., and Sugimoto, N. (2014a). Choline ion interactions with DNA atoms explain unique stabilization of A-T base pairs in DNA duplexes: a microscopic view. *J. Phys. Chem. B* 118, 379–389. doi: 10.1021/jp406647b

Nakano, M., Tateishi-Karimata, H., Tanaka, S., and Sugimoto, N. (2014b). Affinity of molecular ions for DNA structures is determined by solvent accessible surface area. *J. Phys. Chem. B* 118, 9583–9594. doi: 10.1021/jp505107g

Neidle, S., Pearl, L., and Skelly, J. (1987). DNA structure and perturbation by drug *binding*. *Biochem. J.* 243, 1–13. doi: 10.1042/bj2430001

Neves, C. M. S. S., Ventura, S. P. M., Freire, M. G., Marrucho, I. M., and Coutinho, J. A. P. (2009). Evaluation of cation influence on the formation and extraction capability of ionic-liquid-based aqueous biphasic systems. *J. Phys. Chem. B* 113, 5194–5199. doi: 10.1021/jp900293v

Nordwald, E. M., Armstrong, G. S., and Kaar, J. L. (2014). NMR-guided rational engineering of an ionic-liquid-tolerant lipase. *ACS Catal.* 4, 4057–4064. doi: 10.1021/cs500978x

Nostro, P. L., Ninham, B. W., Nostro, A. L., Pesavento, G., Fratoni, L., and Baglioni, P. (2005). Specific ion effects on the growth rates of *Staphylococcus aureus* and *Pseudomonas aeruginosa*. *Phys. Biol.* 2, 1–7. doi: 10.1088/1478-3967/2/1/001

Omta, A. W., Kropman, M. F., Woutersen, S., and Bakker, H. J. (2003a). Negligible effect of ions on the hydrogen-bond structure in liquid water. *Science* 301, 347–349. doi: 10.1126/science.1084801

Omta, A. W., Kropman, M. F., Woutersen, S., and Bakker, H. J. (2003b). Influence of ions on the hydrogen-bond structure in liquid water. *J. Chem. Phys.* 119, 12457–12461. doi: 10.1063/1.1623746

Oprzeska-Zingrebe, E. A., and Smiatek, J. (2018). Aqueous ionic liquids in comparison with standard co-solutes. *Biophys. Rev.* 10, 809–824. doi: 10.1007/s12551-018-0414-7

Pan, F., Roland, C., and Sagui, C. (2014). Ion distributions around left- and right-handed DNA and RNA duplexes: a comparative study. *Nucleic Acids Res.* 42, 13981–13996. doi: 10.1093/nar/gku1107

Pei, Y., Wang, J., Wu, K., Xuan, X., and Lu, X. (2009). Ionic liquid-based aqueous two-phase extraction of selected proteins. *Sep. Purif. Techol.* 64, 288–295. doi: 10.1016/j.seppur.2008.10.010

Portella, G., Germann, M. W., Hud, N. V., and Orozco, M. (2014). MD and NMR analyses of choline and TMA binding to duplex DNA: on the origins of aberrant sequence-dependent stability by alkyl cations in aqueous and water-free solvents. *J. Am. Chem. Soc.* 136, 3075–3086. doi: 10.1021/ja410698u

Ranke, J., Stolte, S., Störmann, R., Arning, J., and Jastorff, B. (2007). Design of sustainable chemical products – the example of ionic liquids. *Chem. Rev.* 107, 2183–2206. doi: 10.1021/cr050942s

Reichardt, C. (1994). Solvatochromic dyes as solvent polarity indicators. *Chem. Rev.* 94, 2319–2358. doi: 10.1021/cr00032a005

Reichardt, C. (2005). Polarity of ionic liquids determined empirically by means of solvatochromic pyridinium N-phenolate betaine dyes. *Green Chem.* 7, 339–351. doi: 10.1039/b500106b

Reichardt,. C. (2008). Pyridinium-N-phenolate betaine dyes as empirical indicators of solvent polarity: some new findings. *Pure Appl. Chem.* 80, 1415–1432. doi: 10.1351/pac200880071415

Reid, J. E. S. J., Walker, A. J., and Shimizu, S. (2015). Residual water in ionic liquids: clustered or dissociated? *Phys. Chem. Chem. Phys.* 17, 14710–14718. doi: 10.1039/C5CP01854D

Reslan, M., and Kayser, V. (2018). Ionic liquids as biocompatible stabilizers of proteins. *Biophys. Rev.* 10, 781–793. doi: 10.1007/s12551-018-0407-6

Rivera-Rubero, S., and Baldelli, S. (2004). Influence of water on the surface of hydrophilic and hydrophobic room-temperature ionic liquids. *J. Am. Chem. Soc.* 126, 11788–11789. doi: 10.1021/ja0464894

Rogers, R. D., and Seddon, K. R. (2003). Ionic liquids—solvents of the future? *Science* 302, 792–793. doi: 10.1126/science.1090313

Rouzina, I., and Bloomfield, V. (2001). Force-induced melting of the DNA double helix. 2. Effect of solution conditions. *Biophys. J.* 80, 894–900. doi: 10.1016/S0006-3495(01)76068-7

Saenger, W. (1984). *Principles of Nucleic Acid Structure. New York, NY: Springer-Verlag.* doi: 10.1007/978-1-4612-5190-3

Saha, D., and Mukherjee, A. (2018). Effect of water and ionic liquids on biomolecules. *Biophys. Rev.* 10, 795–808. doi: 10.1007/s12551-018-0399-2

Salis, A., and Ninham, B. W. (2014). Models and mechanisms of Hofmeister effects in electrolyte solutions, and colloid and protein systems revisited. *Chem. Soc. Rev.* 43, 7358–7377. doi: 10.1039/C4CS00144C

Samarkina,. D. A., Gabdrakhmanov, D. R., Lukashenko, S. S., Khamatgalimov, A. R., Kovalenko, V. I., and Zakharova, L. Y. (2017). Cationic amphiphiles bearing imidazole fragment: from aggregation properties to potential in biotechnologies. *Colloids Surf. A Physicochem. Eng. Asp. A* 529, 990–997. doi: 10.1016/j.colsurfa.2017.07.018

Sapir, L., and Harries, D. (2015). Macromolecular stabilization by excluded cosolutes: mean field theory of crowded solutions. *J. Chem. Theory Comput.* 11, 3478–3490. doi: 10.1021/acs.jctc.5b00258

Sarkar, S., Rajdev, P., and Singh, P. C. (2020). Hydrogen bonding of ionic liquids in the groove region of DNA controls the extent of its stabilization: synthesis, spectroscopic and simulation studies. *Phys. Chem. Chem. Phys.* 22, 15582–15591. doi: 10.1039/D0CP01548B

Sarker, S. R., Ball, A. S., Bhargava, S. K., and Soni, S. K. (2019). Evaluation of plasmid DNA stability against ultrasonic shear stress and its *in vitro* delivery efficiency using ionic liquid [Bmim][PF_6]. *RSC Adv.* 9, 29225–29231. doi: 10.1039/C9RA03414E

Sasaki, Y., Miyoshi, D., and Sugimoto, N. (2007). Regulation of DNA nucleases by molecular crowding. *Nucl. Acids Res.* 35, 4086–4093. doi: 10.1093/nar/gkm445

Schindl, A., Hagen, M. L., Muzammal, S., Gunasekera, H. A., and Croft, A. K. (2019). Proteins in ionic liquids: reactions, applications and futures. *Front. Chem.* 7:347. doi: 10.3389/fchem.2019.00347

Schröder, C. (2017). Proteins in ionic liquids: current status of experiments and simulations. *Top Curr Chem* 375:25. doi: 10.1007/s41061-017-0110-2

Schwierz, N., Horinek, D., and Netz, R. R. (2013). Anionic and cationic Hofmeister effects on hydrophobic and hydrophilic surfaces. *Langmuir* 29, 2602–2614. doi: 10.1021/la303924e

Schwierz, N., Horinek, D., Sivan, U., and Netz, R. R. (2016). Reversed hofmeister series—the rule rather than the exception. *Curr. Opin. Coll. Interf. Sci.* 23, 10–18. doi: 10.1016/j.cocis.2016.04.003

Seduraman, A., Wu, P., and Klähn, M. (2012). Extraction of tryptophan with ionic liquids studied with molecular dynamics simulations. *J. Phys. Chem. B* 116, 296–304. doi: 10.1021/jp206748z

Senske, M., Constantinescu-Aruxandei, D., Havenith, M., Herrmann, C., Weingärtner, H., and Ebbinghaus, S. (2016). The temperature dependence of the Hofmeister series: thermodynamic fingerprints of cosolute–protein interactions. *Phys. Chem. Chem. Phys.* 18, 29698–29708. doi: 10.1039/C6CP05080H

Senske, M., Törk, L., Born, B., Havenith, M., Herrmann, C., and Ebbinghaus, S. (2014). Protein stabilization by macromolecular crowding through enthalpy rather than entropy. *J. Am. Chem. Soc.* 136, 9036–9041. doi: 10.1021/ja503205y

Sharma, A., and Ghorai, P. K. (2016). Effect of water on structure and dynamics of [BMIM][PF6] ionic liquid: an all-atom molecular dynamics simulation investigation. *J. Chem. Phys.* 144:114505. doi: 10.1063/1.4944083

Shi, Y., Liu, Y.-L., Lai, P.-Y., Tseng, M.-C., Tseng, M.-J., Li, Y., et al. (2012). Ionic liquids promote PCR amplification of DNA. *Chem. Commun.* 48, 5325–5327. doi: 10.1039/c2cc31740k

Silva, M. E., and Franco, T. T. (2000). Liquid-liquid extraction of biomolecules in downstream processing—a review paper. *Braz. J. Chem. Eng.* 17, 1–17. doi: 10.1590/S0104-66322000000100001

Simpson, W. S., and Crawshaw, G. H. (2002). *Wool: Science and Technology*. Cambridge; Boca Raton, FL: *WOODHEAD* Publishing; CRC Press.

Sinden, R. R. (1994). DNA Structure and Function; Elsevier Science, Academic press, New York, 398

Singh, N., Sharma, M., Mondal, D., Pereira, M. M., and Prasad, K. (2017). Very high concentration solubility and long-term stability of DNA in an ammonium-based ionic liquid: a suitable medium for nucleic acid packaging and preservation. *ACS Sustain. Chem. Eng.* 5, 1998–2005. doi: 10.1021/acssuschemeng.6b02842

Singh, O., Lee, P.-Y., Matysiak, S., and Bermudez, H. (2020). Dual mechanism of ionic liquid-induced protein unfolding. *Phys. Chem. Chem. Phys.* 22, 19779–19786. doi: 10.1039/D0CP03138K

Singh, T., Bharmoria, P., Morikawa, M.-a., Kimizuka, N., and Kumar, A. (2012). Ionic liquids induced structural changes of bovine serum albumin in aqueous media: a detailed physicochemical and spectroscopic study. *J. Phys. Chem. B* 116, 11924–11935. doi: 10.1021/jp303609h

Singh, U. K., Kumari, M., Khan, S. H., Bohidar, H. B., and Patel, R. (2018). Mechanism and dynamics of long-term stability of cytochrome c conferred by long-chain imidazolium ionic liquids at low concentration. *ACS Sustain. Chem. Eng.* 6, 803–815. doi: 10.1021/acssuschemeng.7b03168

Smiatek, J. (2017). Aqueous ionic liquids and their effects on protein structures: an overview on recent theoretical and experimental results. *J. Phys. Condens. Matter.* 29:233001. doi: 10.1088/1361-648X/aa6c9d

Smith, F. D., Harpending, P. R., and Sanford, J. C. (1992). Biolistic transformation of prokaryotes: factors that affect biolistic transformation of very small cells. *J. Gen. Microbiol.* 138, 239–248. doi: 10.1099/00221287-138-1-239

Soni, S. K., Sarkar, S., Mirzadeh, N., Selvakannan, P. R., and Bhargava, S. K. (2015). Self-assembled functional nanostructure of plasmid DNA with ionic liquid [Bmim][PF_6]: enhanced efficiency in bacterial gene transformation. *Langmuir* 31, 4722–4732. doi: 10.1021/acs.langmuir.5b00402

Stock, F., Hoffmann, J., Ranke, J., Störmann, R., Ondruschka, B., and Jastorff, B. (2004). Effects of ionic liquids on the acetycholinesterase–a structure-activity relationship consideration. *Green Chem.* 6, 286–290. doi: 10.1039/B402348J

Stolte, S., Arning, J., Bottin-Weber, U., Matzke, M., Stock, F., Thiele, K., et al. (2006). Anion effects on the cytotoxicity of ionic liquids. *Green Chem.* 8, 621–629. doi: 10.1039/b602161a

Summers, C. A., and Flowers, R. A. II. (2000). Protein renaturation by the liquid organic salt ethylammonium nitrate. *Protein Sci.* 9, 2001–2008. doi: 10.1110/ps.9.10.2001

Sun, J., Liu, H., Yang, W., Chen, S., and Fu, S. (2017). Molecular mechanisms underlying inhibitory binding of alkylimidazolium ionic liquids to laccase. *Molecules* 22, 1353–1366. doi: 10.3390/molecules22081353

Taft, R. W., and Kamlet,. M. J. (1976). The solvatochromic comparison method. 2. The α-scale of solvent hydrogen-bond donor (HBD) acidities. *J. Am. Chem. Soc.* 98, 2886–2894. doi: 10.1021/ja00426a036

Takekiyo, T., Fukudome, K., Yamazaki, K., Abe, H., and Yoshimura, Y. (2014). Protein aggregation and partial globular state in aqueous 1-alkyl-3-methylimidazolium nitrate solutions. *Chem. Phys. Lett.* 602, 22–27. doi: 10.1016/j.cplett.2014.03.089

Tan, S. C., and Yiap, B. C. (2009). DNA, RNA, and protein extraction: the past and the present. *J. Biomed. Biotechnol.* 2009, 574398. doi: 10.1155/2009/574398

Tarannum, A., Jonnalagadda, R. R., and Nishter, N. F. (2019). Stability of collagen in ionic liquids: ion specific hofmeister series effect. *Spectrochim. Acta A* 212, 343–348. doi: 10.1016/j.saa.2019.01.029

Tarannum, A., Rao, J. R., and Fathima, N. N. (2018). Choline-based amino acid ils-collagen interaction: enunciating its role in stabilization/destabilization phenomena. *J. Phys. Chem. B* 122, 1145–1151. doi: 10.1021/acs.jpcb.7b10645

Tateishi-Karimata, H., Nakano, M., Pramanik, S., Tanaka, S., and Sugimoto, N. (2015). i-Motifs are more stable than G-quadruplexes in a hydrated ionic liquid. *Chem. Commun.* 51, 6909–6912. doi: 10.1039/C5CC00666J

Tateishi-Karimata, H., Nakano, M., and Sugimoto, N. (2014). Comparable stability of Hoogsteen andWatson-Crick base pairs in ionic liquid choline dihydrogen phosphate. *Sci. Rep.* 4:3593. doi: 10.1038/srep03593

Tateishi-Karimata, H., and Sugimoto, N. (2012). A-T base pairs are more stable than G-C base pairs in a hydrated ionic liquid. *Angew. Chem. Int. Ed.* 51, 1416–1419. doi: 10.1002/anie.201106423

Tateishi-Karimata, H., and Sugimoto, N. (2014). Structure, stability and behaviour of nucleic acids in ionic liquids. *Nucleic Acids Res.* 42, 8831–8844. doi: 10.1093/nar/gku499

Tateishi-Karimata, H., and Sugimoto, N. (2018). Biological and nanotechnological applications using interactions between ionic liquids and nucleic acids. *Biophys. Rev.* 10, 931–940. doi: 10.1007/s12551-018-0422-7

Thomas, A. S., and Elcock, A. H. (2007). Molecular dynamics simulations of hydrophobic associations in aqueous salt solutions indicate a connection between water hydrogen bonding and the Hofmeister effect. *J. Am. Chem. Soc.* 129, 14887–14898. doi: 10.1021/ja073097z

Thuy Pham, T. P., Cho, C.-W., and Yun, Y.-S. (2010). Environmental fate and toxicity of ionic liquids: a review. *Water Res.* 44, 352–372. doi: 10.1016/j.watres.2009.09.030

Tomlinson, S. R., Kehr, C. W., Lopez, M. S., Schlup, J. R., and Anthony, J. L. (2014). Solubility of the corn protein zein in imidazolium-based ionic liquids. *Ind. Eng. Chem. Res.* 53, 2293–2298. doi: 10.1021/ie403659x

Van Der Bruggen, B., Vandecasteele, C., Van Gestel, T., Doyen, W., and Leysen, R. (2003). A review of pressure-driven membrane processes in wastewater treatment and drinking water production. *Environ. Prog.* 22, 46–56. doi: 10.1002/ep.670220116

van Die, I. M., Bergmans, H. E. N., and Hoekstra, W. P. M. (1983). Transformation in *Escherichia coli*: Studies on the role of the heat shock in induction of competence. *J. Gen. Microbiol.* 129, 663–670. doi: 10.1099/00221287-129-3-663

van Rantwijk, F., and Sheldon, R. A. (2007). Biocatalysis in ionic liquids. *Chem. Rev.* 107, 2757–2785. doi: 10.1021/cr050946x

Ventura, S. P. M., Neves, C. M. S. S., Freire, M. G., Marrucho, I. M., Oliveira, J., and Coutinho, J. A. P. (2009). Evaluation of anion influence on the formation and extraction capacity of ionic liquid-based aqueous biphasic systems. *J. Phys. Chem. B* 113, 9304–9310. doi: 10.1021/jp903286d

Vicent-Luna, J. M., Romero-Enrique, J. M., Calero, S., and Anta, J. A. (2017). Micelle formation in aqueous solutions of room temperature ionic

liquids: a molecular dynamics study. *J. Phys. Chem. B* 121, 8348–8358. doi: 10.1021/acs.jpcb.7b05552

Vijayanathan, V., Thomas, T., and Thomas, T. J. (2002). DNA nanoparticles and development of DNA delivery vehicles for gene therapy. *Biochemistry* 41, 14085–14094. doi: 10.1021/bi0203987

Vijayaraghavan, R., Izgorodin, A., Ganesh, V., Surianarayanan, M., and MacFarlane, D. R. (2010). Long-term structural and chemical stability of DNA in hydrated ionic liquids. *Angew. Chem. Int. Ed.* 49, 1631–1633. doi: 10.1002/anie.200906610

Von Hippel, P. H., and Wong, K.-Y. (1964). Neutral salts: the generality of their effects on the stability of macromolecular conformations. *Science* 145, 577–580. doi: 10.1126/science.145.3632.577

Vrikkis, R. M., Fraser, K. J., Fujita, K., MacFarlane, D. R., and Elliott, G. D. (2009). Biocompatible ionic liquids: a new approach for stabilizing proteins in liquid formulation. *J. Biomech. Eng.* 131, 74514–74517. doi: 10.1115/1.3156810

Wakayama, R., Uchiyama, S., and Hall, D. (2019). Ionic liquids and protein folding—old tricks for new solvents. *Biophys. Rev.* 11, 209–225. doi: 10.1007/s12551-019-00509-2

Wang, J.-H., Cheng, D.-H., Chen, X.-W., Du, Z., and Fang, Z.-L. (2007). Direct extraction of double-stranded DNA Into ionic liquid 1-butyl-3-methylimidazolium hexafluorophosphate and its quantification. *Anal. Chem.* 79, 620–625. doi: 10.1021/ac061145c

Weingärtner, H. (2008). Understanding ionic liquids at the molecular level: facts, problems, and controversies. *Angew. Chem. Int. Ed.* 47, 654–670. doi: 10.1002/anie.200604951

Weingärtner, H., Cabrele, C., and Herrmann, C. (2012). How ionic liquids can help to stabilize native proteins. *Phys. Chem. Chem. Phys.* 14, 415–426. doi: 10.1039/C1CP21947B

Welton, T. (1999). Room-temperature ionic liquids. *Solvents for synthesis and catalysis. Chem. Rev.* 99, 2071–2083. doi: 10.1021/cr980032t

Wilkes, J. S., and Zaworotko, M. J. (1992). Air and water stable 1-ethyl-3-methylimidazolium based ionic liquids. *J. Chem. Soc. Chem. Commun.* 965–967. doi: 10.1039/c39920000965

Wittwer, C. T. (2009). High-resolution DNA melting analysis: advancements and limitations. *Hum. Mutat.* 30, 857–859. doi: 10.1002/humu.20951

Xu, Y., and Wang,. E. (2009). Ionic liquids used in and analyzed by capillary and microchip electrophoresis. *J. Chromatogr. A* 1216, 4817–4823. doi: 10.1016/j.chroma.2009.04.024

Yakovchuk, P., Protozanova, E., and Frank-Kamenetskii, M. D. (2006). Base-stacking and base-pairing contributions into thermal stability of the DNA double helix. *Nucl. Acids Res.* 34, 564–574. doi: 10.1093/nar/gkj454

Yamamoto, E., Yamaguchi, S., and Nagamune, T. (2011). Protein refolding by N-alkylpyridinium and N-alkyl-N-methylpyrrolidinium ionic liquids. *Appl. Biochem. Biotechnol.* 164, 957–967. doi: 10.1007/s12010-011-9187-1

Yancey, P. H., Clark, M. E., Hand, S. C., Bowlus, R. D., and Somero, G. N. (1982). Living with water stress: evolution of osmolyte systems. *Science* 217, 1214–1222. doi: 10.1126/science.7112124

Yang, Z. (2009). Hofmeister effects: an explanation for the impact of ionic liquids on Biocatalysis. *J. Biotechnol.* 144, 12–22. doi: 10.1016/j.jbiotec.2009.04.011

Zaks, A., and Klibanov, A. M. (1988). The effect of water on enzyme action in organic media. *J. Biol. Chem.* 263, 8017–8021.

Zangi, R. (2010). Can salting-in/salting-out ions be classified as chaotropes/kosmotropes? *J. Phys. Chem. B* 114, 643–650. doi: 10.1021/jp909034c

Zangi, R., Hagen, M., and Berne, B. J. (2007). Effect of ions on the hydrophobic interaction between two plates. *J. Am. Chem. Soc.* 129, 4678–4686. doi: 10.1021/ja068305m

Zhang, Y., Chen, X., Lan, J., You, J., and Chen, L. (2009). Synthesis and biological applications of imidazolium-based polymerized ionic liquid as a gene delivery vector. *Chem. Biol. Drug. Des.* 74, 282–288. doi: 10.1111/j.1747-0285.2009.00858.x

Zhang, Y., and Cremer, P. S. (2006). Interactions between macromolecules and ions: the Hofmeister series. *Curr. Opin. Chem. Biol.* 10, 658–663. doi: 10.1016/j.cbpa.2006.09.020

Zhang, Y. J., Furyk, S., Bergbreiter, D. E., and Cremer P. S. (2005). Specific ion effects on the water solubility of macromolecules: PNIPAM and the Hofmeister series. *J. Am. Chem. Soc.* 127, 14505–14510. doi: 10.1021/ja0546424

Zhao, H. (2005). Effect of ions and other compatible solutes on enzyme activity, and its implication for biocatalysis using ionic liquids. *J. Mol. Catal. B Enzym.* 37, 16–25. doi: 10.1016/j.molcatb.2005.08.007

Zhao, H. (2006). Are ionic liquids kosmotropic or chaotropic? *An evaluation of available thermodynamic parameters for quantifying the ion kosmotropicity of ionic liquids. J. Chem. Technol. Biotechnol.* 81, 877–891. doi: 10.1002/jctb.1449

Zhao, H. (2015). DNA stability in ionic liquids and deep eutectic solvents. *J. Chem. Technol. Biotechnol.* 90, 19–25. doi: 10.1002/jctb.4511

Zhao, H., Campbell, S. M., Jackson, L., Song, Z., and Olubajo, O. (2006). Hofmeister series of ionic liquids: kosmotropic effect of ionic liquids on the enzymatic hydrolysis of enantiomericphenylalanine methyl ester. *Tetrahedron* 17, 377–383. doi: 10.1016/j.tetasy.2006.01.015

Zhou, H. X., Rivas, G., and Minton, A. P. (2008). Macromolecular crowding and confinement: biochemical, biophysical, and potential physiological consequences. *Annu. Rev. Biophys.* 37, 375–397. doi: 10.1146/annurev.biophys.37.032807.125817

Conflict of Interest: The authors declare that the research was conducted in the absence of any commercial or financial relationships that could be construed as a potential conflict of interest.

Advantages of publishing in Frontiers

OPEN ACCESS
Articles are free to read for greatest visibility and readership

FAST PUBLICATION
Around 90 days from submission to decision

HIGH QUALITY PEER-REVIEW
Rigorous, collaborative, and constructive peer-review

TRANSPARENT PEER-REVIEW
Editors and reviewers acknowledged by name on published articles

Frontiers
Avenue du Tribunal-Fédéral 34
1005 Lausanne | Switzerland

Visit us: www.frontiersin.org
Contact us: frontiersin.org/about/contact

REPRODUCIBILITY OF RESEARCH
Support open data and methods to enhance research reproducibility

DIGITAL PUBLISHING
Articles designed for optimal readership across devices

FOLLOW US
@frontiersin

IMPACT METRICS
Advanced article metrics track visibility across digital media

EXTENSIVE PROMOTION
Marketing and promotion of impactful research

LOOP RESEARCH NETWORK
Our network increases your article's readership